X62-10107

[redacted]

CCN

Space Programs Summary No. 37-13, Volume II

for the period November 1, 1961 to January 1, 1962

CLASSIFICATION CHANGE

TO - UNCLASSIFIED [redacted]

By authority of T.D. No. 24-126

Changed by D. L. Merritt Date 1/10/64

jpl

JET PROPULSION LABORATORY
CALIFORNIA INSTITUTE OF TECHNOLOGY
PASADENA, CALIFORNIA

February 1, 1962

(NASA-CR-136577) SPACE PROGRAMS SUMMARY NO. 37-13, VOLUME 2, 1 NOVEMBER 1961 - 1 JANUARY 1962 (Jet Propulsion Lab.) 252 p

N74-72180

Unclas
00/99 27113

[redacted] an unauthorized person is prohibited by law.

[redacted]

[redacted]

CONFIDENTIAL

NATIONAL AERONAUTICS AND SPACE ADMINISTRATION
CONTRACT NO. NAS 7-100

Space Programs Summary No. 37-13, Volume II

for the period November 1, 1961 to January 1, 1962

JET PROPULSION LABORATORY
CALIFORNIA INSTITUTE OF TECHNOLOGY
PASADENA, CALIFORNIA

JA 64

February 1, 1962

CONFIDENTIAL

[redacted]

Preface

The *Space Programs Summary* is a two-volume bimonthly publication of the Jet Propulsion Laboratory. Research and development activities conducted by JPL having specific application to space programs under the sponsorship of the National Aeronautics and Space Administration are reported in this publication. Unclassified and classified activities will be documented in Volumes I and II, respectively.

The projects reported herein were undertaken in partial fulfillment of National Aeronautics and Space Administration Contract NAS 7-100.

W. H. Pickering, *Director*
Jet Propulsion Laboratory

This document contains information affecting the national defense of the United States, within the meaning of the Espionage Laws, Title 18, U.S.C., Sections 793 and 794, the transmission or revelation of which in any manner to an unauthorized person is prohibited by law.

Space Programs Summary No. 37-13
Volume II

Copyright© 1962
Jet Propulsion Laboratory
California Institute of Technology

Contents

PART ONE: RÉSUMÉ 1
I. Lunar Program 1
II. Planetary–Interplanetary Program 1
III. Deep Space Instrumentation Facility 1

PART TWO: LUNAR PROGRAM 3
I. *Ranger* 3
A. Systems 4
B. Engineering Mechanics 9
C. Propulsion 10
D. Lunar Capsule 10
E. High Resolution TV Experiment 23

References 58

II. *Surveyor* 60
A. System Design Summary 60
B. Scientific Instrument Payload 63
C. System Analysis 64
D. Flight Control 71
E. Electronics 92
F. Electrical Power Supply 129
G. Thermal Control 134
H. Engineering Mechanics 141
I. Propulsion 150
J. Spacecraft Vehicle and Mechanisms 157
K. Reliability and System Test 172
L. Mission Operations 181
M. Scientific Experiments 188

Reference 194

PART THREE: PLANETARY–INTERPLANETARY PROGRAM . . . 195
I. Program Status 195
A. Objectives 195
B. Missions 195
C. Program Activities 196

II. *Mariner* R 197
A. Systems 197
B. Engineering Mechanics 202
C. Propulsion 202

Contents (cont'd)

III. *Mariner* B 207
A. Spacecraft Design 207

IV. *Voyager* 217
A. Synopsis 217

PART FOUR: ADVANCED DEVELOPMENT 219

I. Lunar 219
A. Ultra-High-Speed Optical System 219
B. Sun Simulator 220

II. Planetary–Interplanetary 221
A. Synopsis 221
B. Space Sciences 222
C. Spacecraft Secondary Power 228
D. Engineering Mechanics 231
E. Propulsion 232

References 244

III. *Syncom* 245

Editor's Note:

Additional documentation of the Lunar and Planetary–Interplanetary Programs and material on the DSIF can be found in Volume I of this summary.

In order to expedite this publication, Figures, Tables, and References are sequentially numbered within each section.

I. Lunar Program

At 03:12 EST on November 18, 1961, *Ranger II* was launched from Cape Canaveral into a low Earth orbit. The spacecraft re-entered the atmosphere that same night. As in the case of *Ranger I*, scientific results of the flight were slight, but spacecraft engineering data again showed that the spacecraft survived the launch environment and performed all of its programmed functions in orbit.

The *Ranger* RA-3 spacecraft and launch vehicle are at Air Force Missile Test Center (AFMTC) being prepared for the first *Ranger* lunar mission attempt.

II. Planetary–Interplanetary Program

Procurement and fabrication of *Mariner* R assemblies have been largely completed. Assembly of the first spacecraft is scheduled to begin in early January 1962. Preliminary design of *Mariner* B is proceeding as planned.

III. Deep Space Instrumentation Facility

Telemetry data from the nonstandard *Ranger II* trajectory was obtained by the Mobile Tracking Station on 2 passes.

To aid in the design of the Advanced Antenna System (AAS) various tests and studies have been conducted. These include foundation studies, wind measurements, wind tunnel tests, and structural, servo and RF feed tests. The Echo Site 85-ft Az-El antenna will soon be moved to a new location at Goldstone where it will be used for research and development. A new 30-ft antenna will be installed near it, and a new 85-ft HA-Dec antenna will be installed at the Echo Site for operational use.

Performance of the Cassegrain feed system has been improved by a modification in its optical design.

Page intentionally left blank

PART TWO
LUNAR PROGRAM

I. *Ranger*

Ranger II was launched on November 18 at 03:12 EST, after a countdown that was unusually smooth; the only delays were for correction of minor difficulties in the *Agena* umbilicals and in the *Atlas* LOX tanking measurement.

The *Atlas* performance was completely satisfactory, despite a minor error in staging time, and the *Agena* 1st burn (to acquire parking-orbit speed) took place on schedule. The 2nd burn did not occur. As in the case of *Ranger I*, the spacecraft was left in a low Earth orbit, instead of the desired near-escape trajectory. *Agena* telemetry records show that the cause of the *Ranger II* failure was entirely different from that of *Ranger I*. On *Ranger II* the *Agena* roll gyro was inoperative throughout the flight. With no roll control, the *Agena* depleted its attitude-control gas supply shortly after the 1st burn, and was tumbling at the time of 2nd burn. The 2nd burn start sequence began on schedule, and the engine ignited but immediately shut down, probably because of gas ingestion due to the tumbling motion.

Data was received from *Ranger II* at all DSIF stations during its brief flight, which probably terminated after 6 orbits. As in the case of *Ranger I*, all spacecraft subsystems were determined to be operating, but the scientific results of the flight were slight. The ground portion of the system operated better than in *Ranger I*, in that real time data operations were achieved both before and after injection. All functions other than *Agena* 2nd burn (e.g., spacecraft separation, solar panel extensions, etc.) took place as planned.

The risk of the *Ranger* RA-3 mission is, of course, increased by the *Ranger I* and *II* failures, because the stabilized cruise mode of the spacecraft attitude-control system still remains to be demonstrated; until it is, little confidence can be placed in the mid-course and terminal maneuver sequences required for the lunar mission. Nevertheless, the preparations for launching RA-3 remain on schedule. The RA-3 spacecraft, *Agena* 6003, and *Atlas* 117D successfully completed a joint flight acceptance and compatibility (J-FACT) test on January 5, 1962, at AMR. The Aeronutronic lunar capsule was shipped to AMR on the same day. The spare capsule, however, developed a destructive internal short circuit, and efforts to prepare a 2nd spare were immediately started.

A. Systems

1. Ranger I *Trajectory*

The *Ranger I* spacecraft was placed in a low Earth orbit on August 23, 1961. The standard trajectory was essentially achieved up to ejection from the parking orbit; a component failure in the propulsion system of the *Agena* B prevented *Ranger I* from achieving the required velocity increment for standard flight.

a. Ascent. Liftoff was normal, with all systems operating properly. The *Atlas* performance during ascent was satisfactory (Ref 1). The guidance system initiated the cutoffs of the engines at near-nominal times, and the coast ellipse prior to *Atlas–Agena* B separation was within specifications. The *Atlas–Agena* B separation sequence was performed satisfactorily followed by expected stabilization and pitch-down controls. The *Agena* B timers were started by *Atlas* guidance commands and the 2nd stage sequence of events was normal. *Agena* 1st burn data indicated that the proper parking orbit was achieved.

A malfunction in the *Agena* B engine 2nd burn ignition sequence allowed the gas generator to start but kept the main fuel valve closed. A small velocity gain of 84 m/sec was obtained during the programmed 2nd burn due to the expulsion of oxidizer. The net loss of approximately 3100 m/sec of velocity to be gained during 2nd burn resulted in an Earth orbit having an apogee altitude of only 313 mi.

Since 2nd burn was not attained, the velocity meter did not initiate the engine shutdown function; this event was performed by the timer backup signal. Separation of the spacecraft from the *Agena* at 1530 sec followed. Telemetry indicated a separation velocity of approximately 0.6 m/sec with approximately 0.15-sec separation time. Following separation of the spacecraft, the *Agena* performed the required yaw–pitch maneuver in preparation for firing of its retrorocket. The retrorocket fired and the subsequent altering of the *Agena* trajectory (to prevent the *Agena* from following the spacecraft trajectory) was successful.

b. Postinjection. The characteristics of the postinjection trajectory are presented in Table 1. These are the best obtainable parameters using an orbit determination program (ODP) available at JPL. The ODP is designed for use with deep space probes similar to the *Ranger I* standard trajectory and, therefore, lacks certain features which are mandatory for the determination of low orbits. The most important of these features is the exclusion of any type of drag effect experienced by the spacecraft during the decay of its orbit. As a result, it was necessary to

Table 1. Orbital parameters of *Ranger I*

August 1961	Time of injection						Epoch of pericenter passage			Period, min Apogee, mi Perigee, mi
	X R	Y ϕ	Z θ	$\dot{X}$ v	$\dot{Y}$ γ	$\dot{Z}$ σ	a e	i Ω	ω ν	
23	8-23-61, 10:26:36						8-23-61, 10:27:23.106			91.1483
	−0.24370486E4[a] 0.65421648E4	0.60054081E4 −0.78371254E1	−0.89207321E3 0.34396299E3	−0.59845351E1 0.75058997E1	−0.30579307E1 −0.83381240E1	−0.41566759E1 0.12400118E3	6709.03 0.024911	32.9283 279.8169	197.788 −3.2601	313.337 105.597
24	8-24-61, 5:20:00						8-24-61, 4:38:42.202			90.8346
	0.15937675E4 0.68277538E4	−0.66002189E4 0.60346574E1	0.71780167E3 0.23132487E3	0.61159252E1 0.71507338E1	0.18709918E1 0.34833794E0	0.40379101E1 0.55444856E2	6693.63 0.020846	32.9237 274.1791	206.828 164.324	286.614 113.172
25	8-25-61, 1:50:00						8-25-61, 1:47:48.742			90.4836
	−0.36687562E4 0.65356489E4	0.48113055E4 −0.22215657E2	−0.24710883E4 0.12673406E3	−0.49436399E1 0.74935728E1	−0.53200141E1 0.19903683E0	−0.30874395E1 0.11633590E3	6676.37 −0.021334	32.9008 268.1813	215.029 9.084	277.692 100.645
26	8-26-61, 0:20:00						8-26-61, 0:23:29.176			90.1401
	−0.20031848E4 0.65393933E4	0.59413022E4 −0.16505720E2	−0.18579142E4 0.12961566E3	−0.61797660E1 0.74802883E1	−0.32606133E1 −0.27501244E0	−0.36375649E1 0.12057164E3	6659.47 0.018598	32.9074 261.3796	225.978 −14.448	255.625 101.686
27	8-27-61, 0:15:00						8-27-61, 0:22:46.763			89.7370
	−0.32633687E3 0.65485475E4	0.64037421E4 −0.11718777E2	−0.13300636E4 0.11416857E3	−0.66805933E1 0.74581758E1	−0.12279096E1 −0.51101682E0	−0.39452968E1 0.12282820E3	6639.59 0.016117	32.9141 254.2260	234.132 −32.182	232.818 99.806
28	8-28-61, 0:10:00						8-28-61, 0:16:1.986			89.1915
	−0.13595608E4 0.65346669E4	0.59559554E4 −0.20790533E2	−0.23194963E4 0.12437762E3	−0.65960181E1 0.74585742E1	−0.28048166E1 −0.32683821E0	−0.32160637E1 0.11760648E3	6612.66 0.012979	32.9076 246.9342	245.768 −24.974	202.914 96.231

$X, Y, Z, \dot{X}, \dot{Y}, \dot{Z}$ = a right-handed, Earth centered, equatorial, space fixed rectangular cartesian coordinate system. Z is assumed to lie along the Earth spin axis, positive north, X is normal to Z and positive in the direction of the vernal equinox, km, km/sec.

$R, \phi, \theta, v, \gamma, \sigma$ = a right-handed, Earth centered, equatorial, Earth fixed spherical coordinate system. R is from Earth center in km, ϕ is geocentric latitude measured from equatorial plane positive north in deg, θ is longitude measured eastward from the Greenwich meridian positive eastward in deg, v is Earth fixed velocity in km/sec, γ is path angle of spacecraft with respect to local horizontal in deg, σ is azimuth angle of v measured east of true north in deg.

a = semi-major axis, km.
e = eccentricity.
i = inclination of orbit plane to equatorial plane, deg.
Ω = longitude of ascending node, deg.
ω = argument of perigee, deg.
ν = true anomaly, deg.
All times are in GMT.

[a] −0.24370486E4 = −2437.0486.

Table 2. Sequence of flight events

Event	Predicted time, sec	Actual time, sec
Liftoff (GMT)	0	10:04:10.32
Atlas booster cutoff	137.7	136.23
Atlas booster engine separation	—	138.90
Start *Agena* restart timer	247.3	246.27 ±0.11
Atlas sustainer cutoff	276.4	273.50
Start *Agena* primary D-timer	285.8	288.06 ±0.11
Atlas vernier cutoff	295.3	289.91
Nose shroud pin puller squibs *Fire*	296.8	291.80
Mid-body pin pullers and retrorockets *Fire*	299.8	294.97
Jettison horizon scanner fairing	307.56[a]	307.60
Initiate −180 deg/min pitch rate	314.06[a]	314.01 ±0.11
Transfer to −3.54 deg/min pitch rate	317.06[a]	317.07 ±0.11
Ullage rockets *Fire* (1st burn)	337.06[a]	337.12
Telemeter signal acquire (Antigua, station 9.1)	—	346.68
Gas Generator 1 *Fire* (1st burn)	349.06[a]	349.05 ±0.11
Thrust attainment, 90% P_c (1st burn)	350.31[a]	350.58
Telemeter signal loss (Cape Canaveral, Station 1)	—	458
Engine cutoff, 70% P_c (1st burn)	499.41[a]	499.48
Burning duration (1st burn)	149.10	148.90
Horizon scanner position squib *Fire*	516.06[a]	516.10
Helium valve *Off* Squib 2 *Fire*	516.06[a]	516.10
Stop *Agena* primary D-timer	520.06[a]	520.10
Telemeter signal loss (Antigua, Station 9.1)	—	766.00
Telemeter signal acquire (Ascension, Station 12)	—	1152.39
Restart *Agena* primary D-timer	1266.27[b]	1267.25 ±0.11
Ullage rockets *Fire* (2nd burn)	1271.25[c]	1271.37 ±0.11
Transfer to −4.74 deg/min pitch rate	1271.25[c]	1271.37 ±0.11
Gas Generator 2 *Fire* (2nd burn)	1283.25[c]	1283.35 ±0.03
Thrust attainment, 90% P_c (2nd burn)	1284.50[c]	—
Engine cutoff, 70% P_c (2nd burn)	1373.50[c]	1380.32 ±0.03[d]
Burning duration (2nd burn)	89.00	96.97[e]
Start telemetry Calibrate	1380.25[c]	1381.35
Payload interface connector *Fire*	1525.25[c]	1525.35
Payload pin pullers *Fire*	1530.25[c]	1530.35
Agena–Ranger separation complete	—	1530.51
Initiate 180-deg/min yaw rate	1533.25[c]	1533.31 ±0.11
Telemetry signal loss (Ascension, Station 12)	—	1583.08
Remote yaw program	1593.25[c]	—[f]
Transfer to 5.55-deg/min pitch rate	1593.25[c]	—[f]
Retrorocket *Fire*	1920.25[c]	—[g]

[a]Adjusted for primary D-timer start of 288.06 sec.
[b]Adjusted for restart D-timer start of 246.27 sec.
[c]Adjusted for primary D-timer restart of 1267.25 sec.
[d]Shutdown of relay signal.
[e]Duration of gas generator operation.
[f]Not available.
[g]Verification of event only.

redetermine the orbit for each excursion about the Earth. The final orbit of *Ranger I* will be determined by Goddard Space Flight Center using techniques developed for low altitude satellites.

There are 6 orbits available in Table 1, 1 for each day. The epoch on each day was chosen to be just prior to the start of the set of new periods at Woomera. The orbit defined is representative of the actual orbit up to the last new period at Johannesburg, a duration of approximately 14 hr.

c. Standard and actual trajectories. A comparison of standard and actual trajectory parameters is presented in Tables 2 through 6. Table 2 compares the sequence of flight events; Table 3 compares the *Atlas* coast apogee conditions; Table 4 compares the parking orbit parameters; Table 5 compares the injection conditions, and Table 6 compares the orbit parameters at injection. In general, satisfactory agreement exists with the exception

Table 3. *Atlas* coast apogee conditions

Parameter	Predicted	G.E.–Burroughs Vector 1	Real time Vector 2	FPS-16 radar simulation
Inertial velocity, m/sec	5646.72	5654.65	5645.52	5650.08
Altitude, km	184.3369	181.9107	184.6296	184.4558
Orbital inclination angle, deg	32.62	32.63	32.62	32.61

Table 4. Parking orbit parameters

Item	(N + N)[a]	(A + N)[b]	(A + N + S)[c]	JPL data
Perigee, km	6553.477	6548.028	6554.054	6545.784
ΔPerigee		5.449	− 0.577	7.693
Apogee, km	6567.648	6583.615	6596.530	6614.216
ΔApogee		−15.967	−28.882	−46.568
Period, min	88.139	88.245	88.436	88.531
ΔPeriod		− 0.106	− 0.297	− 0.392
Eccentricity	0.00108	0.00271	0.00323	0.0052
ΔEccentricity		− 0.00163	− 0.00215	− 0.00412
Apogee–perigee, km	14.171	35.587	42.476	68.422
Inclination angle, deg	32.699	32.770	32.778	32.85
Node Ω, deg	—	—	—	279.80
Argument of perigee ω, deg	—	—	—	194.60
Position of epoch, ω + v_0, deg	—	—	—	136.50
Epoch	—	—	—	Aug. 23, 1961 15:12:28

[a]N + N = nominal *Atlas* + nominal *Agena*.
[b]A + N = actual *Atlas* + nominal *Agena*.
[c]A + N + S = A + N + actual ignition and burnout.

of Tables 5 and 6 which show large differences since nominal injection was not obtained (Fig 1).

2. Ranger II *Trajectory*

Ranger II was placed in a low Earth orbit on November 18, 1961. The standard trajectory was essentially achieved up to ejection from the parking orbit; a component failure in the attitude control system of the *Agena* B prevented *Ranger II* from achieving the required velocity increment for standard flight.

a. Ascent. Liftoff was normal. *Atlas* performance during ascent was satisfactory (Ref 2). The guidance system initiated the cutoffs of the engines at near-nominal times, and the coast ellipse prior to *Atlas–Agena* B separation was within specifications. The *Atlas–Agena* B separation sequence was performed satisfactorily. After separation, the *Agena* B spacecraft vehicle exhibited instability in roll due to lack of proper signals from the *Agena* B roll gyro. Analysis of the *Agena* B flight data shows that the *Agena* B roll gyro stopped spinning between the gyro checks made at T −260 min

Table 5. Injection conditions

Parameter	Predicted	Actual (first orbit)
Time from launch, sec	1373.4233	1346.32
Radius vector, km	6569.4743	6542.1648
Earth-fixed velocity, m/sec	10,588.0223	7505.8997
Earth-fixed flight path angle, deg	1.6251180	−0.0833812
Geocentric latitude, deg	−9.1929791	−7.8371254
Longitude, deg	346.178965	343.962990
Earth-fixed azimuth, deg	122.970366	124.001180

Table 6. Orbit parameters

Conic parameters at injection	Predicted	Actual
Twice total energy/unit mass C_3, km²/sec²	−0.662,272	−59.4131
Angular Momentum C_1, km²/sec	72,155.9	51,696.9
Semi-major axis a, km	640,561	6709.03
Semi-minor axis b, km	91,470	6688.18
Eccentricity e	0.989752	0.024911
Period of revolution, min	85,035.2	91.1483
Inclination of the plane of the orbit to the equatorial plane i, deg	32.8032	32.9283
Longitude of the ascending node Ω, deg	279.761	279.8169
Argument of perigee ω, deg	194.003	197.788
Closest approach distance, km	6564.54	6564.19
Apogee distance, km	1,274,557	6876.11
Time from perigee passage, sec	32.83	−47.11
True anomaly v, deg	3.14822	−3.2601

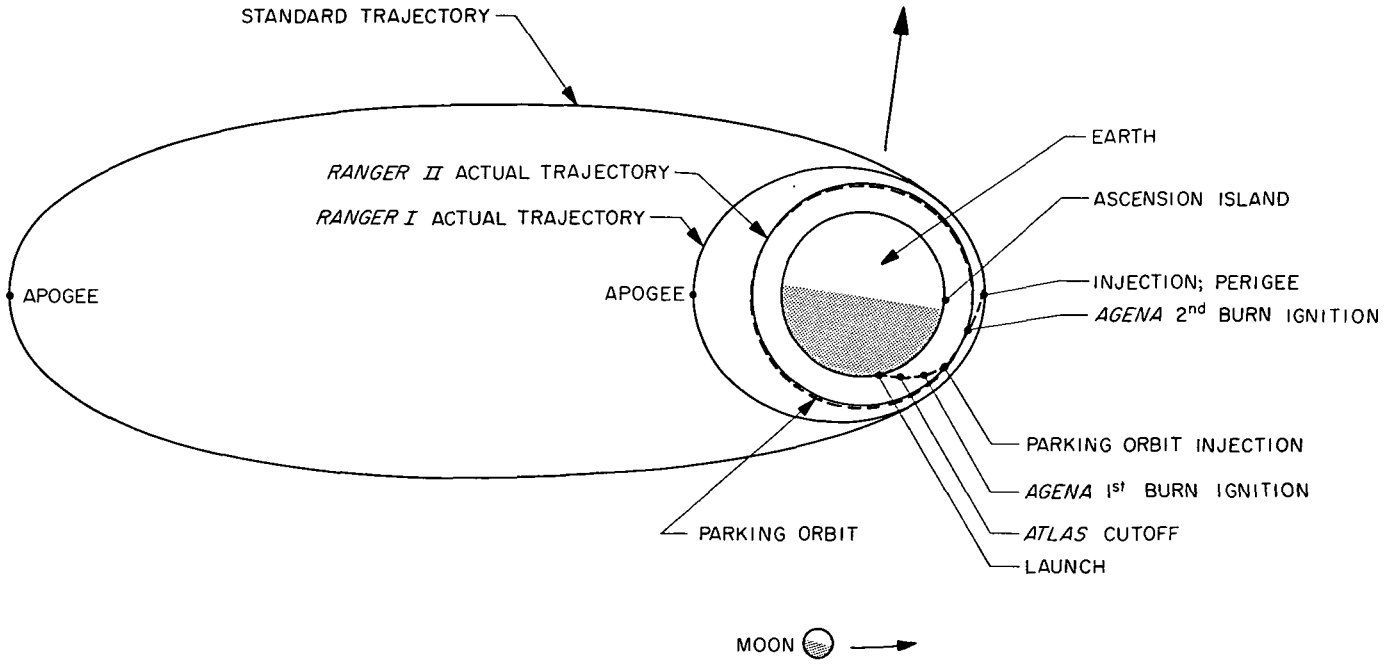

Figure 1. *Ranger I* and *II* orbits

during the countdown and the *Atlas* roll program executed shortly after liftoff.

The *Agena* B pitch-down program, occurring soon after *Atlas–Agena* B separation, was satisfactory so that the *Agena* B 1st burn carried the vehicle safely under the jettisoned shroud and into a nominal parking orbit. However, a high roll rate occurred during the 1st burn period due to the roll gyro failure. As a result, *Agena* B guidance gas depletion occurred shortly after the burn period. The

Table 7. Orbital parameters of *Ranger II*, November 18, 1961

Time of injection						Epoch of pericenter passage			Period, min Apogee, mi Perigee, mi
X R	Y ϕ	Z θ	$\dot{X}$ v	$\dot{Y}$ γ	$\dot{Z}$ σ	a e	i Ω	ω ν	
8:33:44.302 sec						8:01:32.460 sec			88.5274
−0.63459188E4[a]	0.16854436E4	−0.65343558E3	−0.12939232E1	−0.64001960E1	−0.41955106E1	6579.81	33.3153	59.085	146.029
0.65983621E4	−0.56833149E1	0.33954339E3	0.73638873E1	0.19510606E0	0.12490519E3	0.004292	336.4170	131.3020	111.231

$X, Y, Z, \dot{X}, \dot{Y}, \dot{Z}$ = a right-handed, Earth centered, equatorial, space fixed rectangular cartesian coordinate system. Z is assumed to lie along the Earth spin axis, positive north, X is normal to Z and positive in the direction of the vernal equinox, km, km/sec.

$R, \phi, \theta, v, \gamma, \sigma$ = a right-handed, Earth centered, equatorial, Earth fixed spherical coordinate system. R is from Earth center in km, ϕ is geocentric latitude measured from equatorial plane positive north in deg, θ is longitude measured eastward from the Greenwich meridian positive eastward in deg, v is Earth fixed velocity in km/sec, γ is path angle of spacecraft with respect to local horizontal in deg, σ is azimuth angle of v measured east of true north in deg.

a = semi-major axis, km.
e = eccentricity.
i = inclination of orbit plane to equatorial plane, deg.
Ω = longitude of ascending node, deg.
ω = argument of perigee, deg.
ν = true anomaly, deg.
All times are in GMT.

[a] −0.63459188E4 = −6345.9188

Table 8. Sequence of flight events

Event	Predicted time, sec	Actual time, sec
Liftoff (GMT)	0	08:12:21.502
Atlas booster cutoff	138.3	136.4
Atlas booster engine separation	—	—[b]
Start *Agena* restart timer	249.0	253.9
Atlas sustainer cutoff	278.1	280.2
Start *Agena* primary D-timer	286.5	292.0
Atlas vernier cutoff	295.2	295.7
Nose shroud pin puller squibs *Fire*	297.5	297.7
Mid-body pin pullers and retrorockets *Fire*	300.5	300.7
Jettison horizon scanner fairing	313.0[a]	313.2
Initiate −173 deg/min pitch rate	318.0[a]	318.2
Transfer to −3.36 deg/min pitch rate	321.0[a]	321.3
Ullage rockets Fire (1st burn)	341.0[a]	341.2
Telemeter signal acquire (Antigua, Station 9.1)	—	352.0
Gas Generator 1 *Fire* (1st burn)	353.0[a]	353.0
Thrust attainment, 90% P_c (1st burn)	354.5[a]	354.4
Telemeter signal loss (Cape Canaveral, Station 1)	—	473.0
Engine cutoff, 70% P_c (1st burn)	506.6[a]	508.4
Burning duration (1st burn)	151.7	154.0
Horizon scanner position squib *Fire*	523.0[a]	—[b]
Helium valve Off Squib 2 Fire	523.0[a]	—[b]
Stop *Agena* primary D-timer	527.0[a]	527.1
Telemeter signal loss (Antigua, Station 9.1)	—	783.0
Telemeter signal acquire (Ascension, Station 12)	—	1125.0
Restart primary D-timer	1265.9[c]	1265.9
Ullage rockets *Fire* (2nd burn)	1269.9[d]	1269.9 (No. 3) 1282.7 (No. 1)
Transfer to −4.68 deg/min pitch rate	1269.9[d]	—[b]
Gas Generator 2 *Fire* (2nd burn)	1281.9[d]	1281.9
Thrust attainment, 90% P_c (2nd burn)	1283.9[d]	1282.8
Engine cutoff, 70% P_c (2nd burn)	1374.2[d]	1282.8
Burning duration (2nd burn)	90.3	0
Start telemetry calibrate	1381.9[d]	1382.4
Payload interface connector *Fire*	1526.9[d]	—[e]
Payload pin pullers *Fire*	1531.9[d]	1531.8
Agena–Ranger separation complete	—	—[e]
Initiate 180 deg/min yaw rate	1534.9[d]	1534.7
Remove yaw program	1534.9[d]	1595.0
Transfer to 5.55 deg/min pitch rate	1534.9[d]	1595.0
Telemetry signal loss (Ascension, Station 12)	—	1640.0
Retrorocket *Fire*	1921.9[d]	—[e]

[a] Adjusted for primary D-timer start of 292.0 sec.
[b] Not available.
[c] Adjusted for restart D-timer start of 253.9 sec.
[d] Adjusted for primary D-timer restart of 1265.9 sec.
[e] Verification of event only.

exhaustion of guidance gas caused vehicle tumbling in all 3 axes.

Vehicle tumbling apparently prevented proper propellant ullage control. Engine shutdown occurred immediately after 2nd burn ignition, probably due to ingestion of pressurization gas. Second burn ignition imparted approximately 6.2 m/sec impulse to the vehicles. The net loss of approximately 3176 m/sec of velocity to be gained during 2nd burn resulted in an Earth orbit having an apogee altitude of only 146 mi.

Spacecraft separation and *Agena* B retrorocket firing occurred at the proper times. No 180-deg yaw maneuver was performed by the *Agena* B due to guidance gas depletion.

b. Postinjection. The characteristics of the postinjection trajectory (Ref 3) are presented in Table 7. These are the best obtainable parameters using the ODP. The final orbit of *Ranger II* will be determined by Goddard Space Flight Center using techniques developed especially for low altitude satellites.

Table 7 presents only 1 representative orbit since the lifetime of *Ranger II* was approximately 1 day. The decay due to drag was significant after the 1st several orbits.

c. Standard and actual trajectories. A comparison of standard and actual trajectory parameters is presented in Tables 8 through 12. Table 8 compares the sequence of flight events, Table 9 compares the *Atlas* coast apogee conditions, Table 10 compares the parking orbit parameters, Table 11 compares the injection conditions, and Table 12 compares the orbit parameters at injection. In general, satisfactory agreement exists with the exception of Tables 11 and 12 which show large differences since nominal injection was not obtained (Fig 1).

Table 9. *Atlas* coast apogee conditions

Parameter	Predicted	G.E.–Burroughs	
		Veco[a] + 0.5 sec	Veco[a] + 0.1 sec
Inertial velocity, m/sec	5646.4	5650.7	5652.5
Altitude, km	185.5	185.9	184.3
Orbital inclination, deg	32.614	32.605	32.603

[a]Vernier engine cutoff.

Table 10. Parking orbit parameters

Parameter	Nominal	JPL data
Perigee, km	6561.4	6502.331
Δ Perigee		59.1
Apogee, km	6575.1	6640.055
Δ Apogee		−65.0
Period, min	88.3	88.354
Δ Period		−0.1
Eccentricity	0.00105	0.0105
Δ Eccentricity		−0.00945
Apogee–perigee, km	13.7	137.724
Inclination angle, deg	32.584	33.173
Node Ω, deg	—	336.62
Argument of perigee, ω deg	—	54.04
Position of epoch, $\omega + \gamma_0$, deg	—	137.76
Epoch	—	November 18, 1961 8:20:49

Table 11. Injection conditions

Parameter	Predicted	Actual (first orbit)
Time from launch, sec	1373.4055	1282.8
Radius vector, km	6568.9782	6598.3621
Earth-fixed velocity, m/sec	10,587.8210	7363.8873
Earth-fixed flight path, angle, deg	1.7238	0.1951
Geocentric latitude, deg	−9.0679	−5.6833
Longitude, deg	346.1921	339.543
Earth-fixed azimuth, deg	122.8447	124.9052

Table 12. Orbit parameters

Conic parameters at injection	Predicted	Actual
Twice total energy/unit mass C_3, km²/sec²	−0.621,909	−60.5798
Angular momentum C_1, km²/sec	72,150.0	51,212.1
Semi-major axis a, km	640,934.0	6579.81
Semi-minor axis b, km	91,488.0	6579.75
Eccentricity e	0.989760	0.004292
Period of revoluation, min	85,104.0	88.5274
Inclination of the plane of the orbit to the equatorial plane i, deg	32.6557	33.3153
Longitude of the ascending node Ω, deg	325.832	336.4170
Argument of perigee ω, deg	193.644	59.0854
Closest approach distance, km	6563.43	6551.57
Apogee distance, km	1,275,304.5	6608.04
Time from perigee passage, sec	34.82	1931.8
True anomaly v, deg	3.33910	131.3020

B. Engineering Mechanics

1. Equipment Packaging

The major portion of the *Ranger* RA-6, -7, -8, and -9 equipment packaging remains unchanged from the RA-3, -4, and -5 configuration. However, there are some additions and changes which were necessitated due to repackaging of the L-Band communications assembly, the replacement of the scientific instruments and telescope electronics assembly of Electronics Assembly III with the S-band ranging experiment, and the addition of scientific instruments for radiation measurements.

a. Electronics Assembly II, L-band communications. This assembly has been completely repackaged to incorporate the electronics and other RF equipment into standard module form. The drawings of this new assembly have been released and many of the subchassis and assembly chassis have been ordered or delivered. A band separator will be housed in the communications chassis when the S-band ranging experiment is flown. This additional subassembly will be used on RA-8 and -9.

b. Electronics Assembly III, S-band ranging experiment. This assembly will be flown only on RA-8 and -9, and will require dummy modules for RA-5, -6, and -7. In addition to the modules required for operation of the S-band ranging experiment, 4 modules of the data contioning system will be housed in the assembly case for RA-5 through -9. Drawings of the S-band subassemblies are in process and procurement of the associated packaging hardware will follow.

c. Scientific instruments. These instruments consist of 3 radiation experiments: a tissue equivalent ionization chamber, a particle flux detector, and a Neher-type ionization chamber. The particle flux detector and the Neher ionization chamber are similar to *Mariner* R configurations. The tissue equivalent ionization chamber is a completely new unit.

Due to procurement scheduling problems of electronic equipment, the Neher ionization chamber will be aboard the RA-5 through -9; the particle flux detector and the tissue equivalent ionization chamber will be on RA-8 and -9. The addition of the latter experiments will require shifting the associated electronics within Cases III and VI.

2. Spacecraft Design

a. Mechanical and structural system. Analysis of telemetry data from the *Ranger I* and *II* flights indicates that the spacecraft mechanical and structural system functioned properly; no modifications to these areas are necessary for future flights. Despite the nonstandard orbits attained in these flights, it was possible to analyze the spacecraft temperature data. It is concluded that the temperature control system of the spacecraft functioned satisfactorily on these flights, and also would have done so had the spacecraft attained the proper orbits.

For *Rangers* RA-6, -7, -8, and -9, the electronic and structural requirements for the high gain L- and S-band antennas require no changes to the existing *Agena–Ranger* interface, thus ensuring complete interchangeability.

Similarly, the mechanical and thermal interfaces between TV capsule and bus require only minor differences in fittings and paint patterns. The basic requirement of bus interchangeability between *Ranger* RA-3 and -6 type missions remains unimpaired.

3. Modal Vibration Tests

Mode shapes and natural frequencies have been investigated for the *Ranger* RA-3 vehicle. The test vehicle was the *Ranger* proof test model, which is structurally the same as RA-3. The test specimen was mounted to a rigid support ring, which in turn was bolted to a concrete floor. Several modal vibration shakers were used to excite the

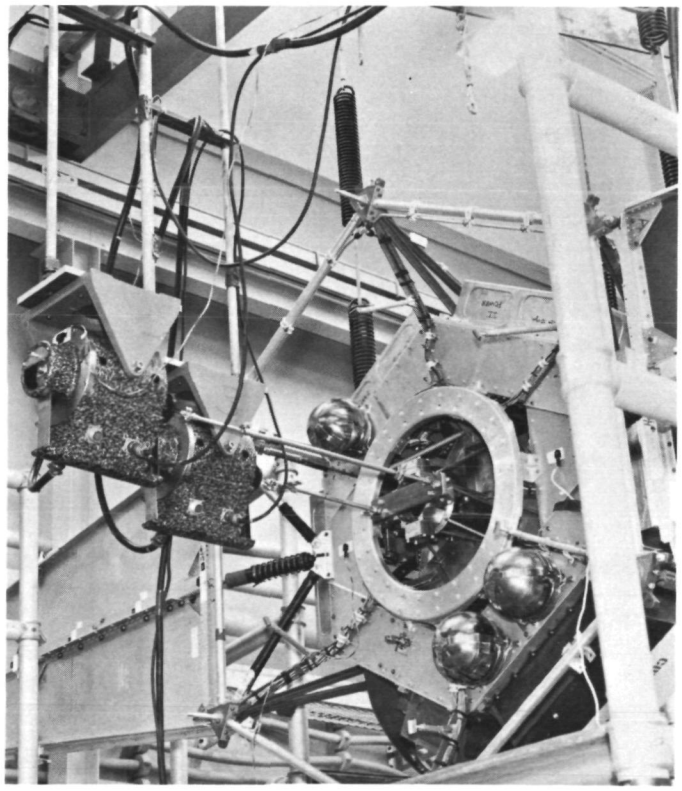

Figure 2. Setup for angle vs torque tests

various normal modes. Significant results were natural vehicle cantilever frequencies of 16.1 16.3, 34.5, and 35.1 cps and a natural vehicle torsional frequency of 37.8 cps. Structural damping coefficients were found to be 0.04 in the 1st mode and 0.08 in the 2nd mode.

A shake test was conducted on the freely suspended *Ranger* RA-3 dynamic equivalent mockup (Figs 2, 3). The purpose of the test was to allow investigation of the vehicle angle versus applied torque for a limited frequency range. The test verified the theoretical calculation for this frequency range.

Figure 3. Freely suspended *Ranger* RA-3 dynamic equivalent mockup

C. Propulsion

The *Ranger* spacecraft will perform a single mid-course propulsion maneuver to remove or reduce the injection dispersion errors.

This maneuver will be accomplished using a small, monopropellant hydrazine-fueled propulsion system of 50-lb vacuum thrust. This propulsion system will be capable of delivering a variable total impulse in conjunction with an integrating accelerometer system.

All valving functions on the propulsion system are accomplished using explosively actuated valves. On *Rangers* RA-5 through RA-9, recently developed dual-bridgewire hermetically sealed squibs will be used in the explosive valves in lieu of single-bridgewire squibs to attain a high degree of reliability. A detailed description of the propulsion system, the operational design philosophy, and a system schematic are contained in *SPS 37-3*. Developmental progress is reported in *SPS 37-3* through *37-12*.

During this reporting period, project activities have consisted primarily of fabrication and procurement of parts for the RA-5 through RA-9 propulsion systems, flight acceptance testing of the parts, and the generation of specifications and operating procedures required for pre-launch and launch activities.

D. Lunar Capsule

1. Introduction and Summary

Under subcontract for the development of a complete lunar capsule subsystem, Aeronutronic Division of Ford Motor Company is supplying a lunar seismographic capsule and ancillary equipments for *Rangers* RA-3, -4, and -5. As the *Ranger* spacecraft approaches the Moon, the capsule will be separated from the spacecraft and braked to allow a survivable landing which will emplace a sensitive seismometer on the lunar surface. Data from the seismometer will then be relayed to Earth receiving stations.

As a result of the simulated lunar landing (SLL) tests and subsequent mechanical modifications, a series of separate, major developmental tests were instituted on the capsule electronics, the ordnance assemblies, the insulation and thermal control system, and basic structure of the survival sphere and the impact limiter.

Two subassemblies of the survival sphere, the main batteries and the voltage-controlled subcarrier oscillator (VCO), both fabricated under subcontract, developed problems. Both had been previously qualified and were regarded to be nearly finished items. Because of changes or errors in fabrication procedures, the units delivered

failed in late development tests. Efforts were required in design and quality control to make required revisions and produce new units on a schedule consistent with design proof testing to meet the flight schedule. A parallel VCO effort was also instituted. All the vendors are now delivering units constructed to rigid process standards on the required schedule.

Two final design proof tests of complete landing spheres were planned, 1 an airplane drop, the other a testing machine impact. Tests were delayed several weeks by unfavorable development test results and subassembly deliveries. Furthermore, it was deemed necessary to introduce 2 more design proof test impacts of partially completed landing spheres to provide necessary assurance that the revised parts were qualified in a manner consistent with the entire sphere.

The altimeter has been completed, and Wiley Electronics has delivered them on schedule.

The retrorocket program, after an extensive staffing revision, has proceeded well. Previously encountered failures were successfully diagnosed, and corrections were confirmed by test firings. The support structures, squibs, clamps and associated equipment, and the power and sequencing assembly are completed and available for flight.

Table 13. Design proof test program summary

Test No.	Component	Completed date	Results
B1	Separation clamp	11-27-61	Change in clamp configuration to add guard for radiation shield retraction and minor change in electrical contacts required repeat of separation test to obtain tip off impulse and separation time, and repeat of shake test. Clamp separation met specification.
B2	Spin motor	12-20-61	Test fixture problems held up test. Five rounds fired successfully. Design adequate for flight.
B4	Explosive bolt cutter	11-17-61	Design qualified.
B5	Altimeter	9-15-61	Design qualified.
B6	Payload (separation)	9-9-61	Design qualified. Separation meets specification.
B7	Major capsule structure	8-11-61	Design qualified. Structure good for all flight loads.
B8	Landing sphere	11-24-61	Thirteen test vehicles built and tested with varying degrees of success to separately investigate functional subsystems. Final test on S/N DPT-5 successful. Meets flight requirements.
B9	Acceleration switch	11-8-61	Design qualified.
B10	Retromotor igniter squib	9-6-61	Lot qualified.
B11	Capsule battery	—	Failed in Nov. Battery redesigned for 2nd time. Battery structure suitable for impact. Failure was due to internal leakage not caused by environmental tests. Additional battery now being tested.
B13	Retromotor structure	3-61	Design qualified.
B14	Caging pin motor	10-10-61	Lot qualified.
B15	Squib switch	10-28-61	One lot previously rejected. Present lot accepted without sterilization.
B16	Altimeter support and erection system (structure and function)	10-2-61 and 12-6-61	Addition of structural members will require repeat of shake part of test scheduled Nov. 20 and 21.
B17	Thermal radiation shield	10-21-61 (thermal test) 12-18-61	Design qualified thermally. Final design of support and retraction system fabricated for design proof structural and vacuum cold retraction test.
B18	Thermal control valve	9-7-61	Lot qualified.
B19	Capsule position switch	11-8-61	Design qualified.
B20	Bulkhead terminal seal	10-6-61	Lot qualified.
B21	Power and sequencing assembly	12-22-61	Initial test failed because of battery. Battery redesigned. Also power and sequencing assembly redesigned to include arming timer. Development tests gave good results. Formal design proof test gave good results.
B23	Penetrator (venting) squib	10-24-61	Lot qualified.
B24	External wiring	9-1-61	Successful. Tested with B7 and B16. Also tested in joint systems tests at JPL. To be retested.
B26	Altimeter battery	12-22-61	One ESB battery (alternate design) failed in Nov. test. Yardney battery pack partially failed in Dec. After design modification both batteries are acceptable.

2. Test Program

a. Design proof test. The lunar capsule design proof test program has been completed on schedule during this reporting period with 2 minor exceptions. The survival sphere battery is still under electrical test and several rounds of the spin motor qualification test remain to be fired. The spin motor qualification will be completed in early January. The battery is being tested for long term discharge to simulate the flight batteries. Status of each of the major design proof tests is shown in Table 13.

b. Acceptance testing. Implementation of formal acceptance tests for assemblies and parts fabricated for flight use has continued during this period. With the exception of the batteries to be used in the power and sequencing assembly and in the altimeter, all parts to support the *Ranger* RA-3 have been tested. Testing will continue during the coming period on parts and assemblies to be used in support of *Rangers* RA-4 and -5. Test plans, previously prepared, have been modified in some instances to improve the tests or to reduce the time required to perform each test.

c. Landing sphere development and qualification testing. During this reporting period, the developmental and qualification program has been successfully concluded in a final demonstration design proof test of a complete landing sphere. The first tests of major significance, beyond the initial subsystem empirical developmental tests, were conducted in May in the initial simulated lunar landing tests. All major objectives of these first tests were met; it was demonstrated that the laboratory impact tests were adequate for further testing of landing spheres and survival sphere systems.

As a consequence of these tests, however, the mechanical design of nearly every portion of the survival sphere was revised or modified to produce a more reliable overall system. All of the development involving these changes was conducted on a series of separate but major tests on the several, separable subsystems of the survival sphere. Detailed revisions of the final design were not completed until the fabrication of DPT-5, the final test vehicle. Table 14 shows this developmental process. Table 15 indicates in more detail failures observed and information gained during this testing process.

DPT-4. The batteries in this unit failed during the buildup phase of the unit. Since there was insufficient power for operation of the timer and other equipment, functions depending on electrical power could not be tested.

The capsule was balanced and subsequently fired on the Hyge testing machine at 166 ft/sec and impacted at 90 deg. Following this the penetrators were fired with an external power source. There was no visible damage of the payload due to impact or to the penetrator blast.

Table 14. Landing sphere test history

Test vehicles	Functional equipments								
	Thermal control and insulation	Uncage and cage	Erection	Venting	Seismometer and amplifier	Control electronics	Transmitter	Antenna and feed	Battery
DPT-1	—[d]	—[c]	—[a]	—[d]	—[a]	—[a]	—[c]	—[b]	—[a]
DPT-2	—[d]	—[c]	—[c]	—[c]	—[d]	—[a]	—[d]	—[c]	—[c]
ITV-1	—[c]	—[d]	—[d]	—[d]	—[d]	—[d]	—[d]	—[d]	—[d]
ITV-2	—[c]	—[d]	—[d]	—[d]	—[d]	—[d]	—[d]	—[d]	—[d]
ITV-3	—[b]	—[d]	—[d]	—[d]	—[d]	—[d]	—[d]	—[d]	—[d]
ITV-4	—[c]	—[d]	—[d]	—[d]	—[d]	—[d]	—[d]	—[d]	—[d]
BOV-1	—[c]	—[d]	—[d]	—[d]	—[a]	—[d]	—[d]	—[d]	—[d]
ETV-1	—[d]	—[d]	—[d]	—[d]	—[b]	—[a]	—[b]	—[b]	—[b]
OTV-1	—[c]	—[a]	—[b]	—[c]	—[d]	—[c]	—[d]	—[d]	—[c]
OTV-2	—[c]	—[a]	—[a]	—[d]	—[d]	—[c]	—[d]	—[b]	—[c]
BTV-2	—[d]	—[d]	—[d]	—[d]	—[d]	—[d]	—[c]	—[d]	—[b]
DPT-3	—[c]	—[a]	—[a]	—[c]	—[a]	—[a]	—[c]	—[a]	—[c]
DPT-4	—[c]	—[d]	—[d]	—[a]	—[c]	—[b]	—[d]	—[a]	—[b]
DPT-5	—[a]	—[a]	—[a]	—[a]	—[a]	—[a]	—[a]	—[a]	—[b]

[a] Good results.
[b] Failure.
[c] Tested but with some deviation or only a partial system.
[d] No test.

The DPT-4 vehicle limiter and upper insulation shell half were removed after sled impact. The necessary instrumentation for conducting a thermal boiloff test was installed. The upper half of the insulation shell was installed and sealed inside the impact limiter. This assembly was subjected to vacuum in the high-altitude test facility. The test could not be completed due to a small leak in the brazed aluminum payload structure, which prevented evacuation of the chamber and insulation.

The insulation and shells were removed and placed on a dummy structure equipped with carbon resistor heaters and a thermistor for temperature measurement. The antenna coax and caging device wires were also installed resulting in a representative thermal mockup which was placed in a double wall, liquid nitrogen-cooled vacuum chamber. An equilibrium heat rate of 3.05 w was established with the payload temperature being maintained at 32°F and the chamber at −320°F.

DPT-5. Initial electronic system checks were made on November 20. The transmitter frequency measured 960.14095 mc, the VCO 558.3 cps; the sphere was balanced the same day. On November 24 the capsule was subjected to a Hyge impact. The preimpact velocity was 151 ft/sec. Frequency measurements made before and after impact are:

Relative time	Transmitter frequency, mc
Before	960.14240
After	960.13940
After ½ hr	960.13891
After 1 day	960.13944

Both penetrators fired 15 min after impact. The sphere was observed to roll over a few degrees as a result of the firing. The sphere was resting on the smooth concrete of the Hyge pit floor. Subsequent measurement of the angle between the axis of the payload and vertical was about 26 deg. This is attributed to displacement due to the penetrators. The postimpact caging mechanism functioned as it should.

The DPT-5 insulation was constructed identical to the *Ranger* RA-3 units using 31 layers of 0.0085-in. thick Dacron felt interlined with 30 layers of 0.00045-in. thick aluminum foil and 0.0048-in. thick Dexiglas paper. Insulation muffs were sewn around all holes and equator. A preimpact thermal test was performed on the insulation with resulting equilibrium heat rates of 2.09 w at 33°F and 2.42 w at 67°F while enclosed in the −320°F vacuum chamber.

A postimpact thermal test was performed by removing the insulation muffs and shells and installing them on the dummy payload structure. The caging wires and antenna coax were installed during both tests. Three equilibrium heat rates were established during this test. The first was 3.15 w with the dummy payload at 199°F and the chamber at 76°F. This approximates the lunar day environment with the heat loss in the opposite sense. The other 2 were run with a chamber temperature of −320°F with resulting heat loss rates of 3.80 w at 68°F and 3.37 w at 33°F. The increase in postimpact heat loss over preimpact can be attributed almost wholly to the radiation foil surface inside the shell, which was damaged by the penetrator blast. There was no apparent physical damage nor appreciable shifting of adjacent layers due to the Hyge impact.

3. Equipment Status

a. Weights and performance.

Weight control. Latest revisions to the capsule weight status are presented in Table 16. Also shown is the previous evaluation. The changes shown reflect redistribution in the classification of potting materials and wiring in order that the categories be more meaningful in weight control. Accompanying this table is Table 17 which gives weights and center-of-gravity stations. Final weight trimming by adjustment of the impact limiter weight has been employed to achieve the particular retrovelocity increment. This weight trimming was not accomplished until completion of the retromotor qualification tests, which provided accurate motor performance data.

Performance. Final evaluation of the expected inflight performance for the whole lunar capsule system is now in process. Table 18 gives current estimates of the variances of capsule axial velocity, transverse velocity, and altitude at retromotor burnout. The transverse velocity data for the spin motor and retromotor are estimates based on limited data and are believed to be conservative to a factor of 2. Considerably more experimental and analytical effort would be required to refine these estimates, although further analysis continues.

Mean values and 95 percentile points are estimated as follows:

Parameter	Mean value	95 percentile
Burnout altitude, ft	930	–
Vertical velocity, ft/sec	105	140
Transverse velocity, ft/sec	110	214
Impact velocity, ft/sec	156	235

Table 15. Lunar landing sphere test performance chart

Test vehicles	Functional equipment										
	Uncage and cage	Erection	Venting	Seismometer and amplifier	Control electronics	Transmitter and VCO	Antenna and feed	Battery	Thermal control and insulation	Impact limiter	Structure elements
DPT-1	Test wiring did not permit caging system to operate. OK in subsystem test	5 deg	No test. Penetrators fired in lab prior to test	OK (preliminary design)	OK	Preliminary design partial success	Coax broken	OK	Preliminary design no thermal data	Airplane drop 20-deg angle, 200 ft/sec. Good limiter	Good test of preliminary design
DPT-2	Preliminary design used	11 deg	System worked. Design changed to give bigger holes	—	OK	—	Antenna structure OK	One-half OK, other half poor before assembly	Preliminary design no thermal data	Airplane drop 45-deg angle, 200 ft/sec. Good limiter	Good test of preliminary design
ITV-1	—	—	—	—	—	—	—	—	Development models of insulation, fair thermally, poor structurally	No limiter, sled test, 154 ft/sec	—
ITV-2	—	—	—	—	—	—	—	—	Development models of insulation, fair thermally, poor structurally	No limiter, sled test, 138 ft/sec	—
ITV-3	—	—	—	—	—	—	—	—	Failed, insulation shifted in shell	No limiter, sled test, 136 ft/sec	Insulation shell cracked
ITV-4	—	—	—	—	—	—	—	—	Heat loss of 2.3 w	No limiter, sled test, 120 ft/sec	Insulation shell cracked
BOV-1	—	—	—	Seismometer operated with thermal valve. OK	—	—	—	—	Water boiloff system good	No test	—
ETV-1	—	—	—	Two diodes failed probably due to procedural failures	OK	VCO failed. Two capacitors failed mechanically	Coax broken but antenna OK	Electrolyte leak	—	No limiter, sled test, 179 ft/sec	Severe test in sled. Insulation shell cracked
OTV-1	OK	Failed due to antenna structure failure allowed fluid in top	Venting occurred but one blast shield malfunctioned	—	Battery lead unsoldered. Broken resistor	—	Shells failed	Only ½ battery tested. OK	Minor structural problems	Normal impact 168 ft/sec. Good limiter	Impacted on top, both shells broke, cover bent, structural sound valve seal leaked

CONFIDENTIAL

CONFIDENTIAL

Table 15. Lunar landing sphere test performance chart (cont'd)

Test vehicles	Functional equipment										
	Uncage and cage	Erection	Venting	Seismometer and amplifier	Control electronics	Transmitter and VCO	Antenna and feed	Battery	Thermal control and insulation	Impact limiter	Structure elements
OTV-2	OK	7 deg after drying from leak due to antenna structure failure	—	—	Resistor immersed in fluid	—	Coax failed, antenna redesigned to include rubber cover	Only ½ battery tested. OK	Minor structural problems	45-deg impact, 187 ft/sec. Good limiter	Insulation shell broke at ground plane. New outer shell OK
BTV-2	—	—	—	—	—	VCO test only, OK	—	½ battery failed after discharge (7 days)	—	Normal impact, 174 ft/sec. Good limiter	New shell design good. Valve seal OK
DPT-3	OK	9 deg	System OK. One penetrator failed (not from qualified lot)	OK	OK	Capacitor broke loose	OK	Diodes separated. Parallel halves were bad	Insulation good structure but no thermal data	Airplane drop 32-deg angle, 220 ft/sec. Good limiter	All structural elements sound
DPT-4	—	—	OK	Mating technique test only, OK	Capacitor leakage	—	OK (no RF test)	Failed	Heat rate slightly high after impact and immersion	Normal impact, 166 ft/sec. Good limiter	Leaking brazed joint after impact and venting
DPT-5[a]	OK	OK	OK	OK	OK	—	—	Failed. Six v section had a short but sufficient power after impact to conduct test	Good insulation prior to impact: Little loss in perforation after impact	—	—

[a] Flight configuration.

Table 16. Lunar capsule weight summary[a]

Component	Expected RA-3 weight, lb	Previous capsule weight, lb[b]
Retrorocket payload		
Survival sphere		
Electronics, antenna, batteries and wiring	24.0	24.3
Structure, insulation devices	13.5	12.7
Water	3.6	3.7
Seismometer	7.8	7.8
Flotation fluid and outer shell	8.2	8.2
Survival sphere total	57.1	56.7
Impact limiter	32.2	37.1
Vibration dampers and clamp	1.0	1.3
Balance weights	0.3	—
Control timer, batteries, and wiring	1.2	1.4
Motor heat shield	0.2	—
Total retromotor payload	92.0	96.5
Motors		
Retrorocket motor and igniter	214.4	213.3
Spin motor, igniter and attachment	2.4	2.3
Total separate weight	308.8	312.1
Bus mounted equipment		
Altimeter and antenna	6.6	6.6
Altimeter support and deployment	2.1	2.0
Motor support structure and separation	3.8	3.6
Bus interface J-box and connectors	1.0	0.8
Heat shield	3.4	3.0
Total lunar capsule	325.7	328.1

[a] As of December 15, 1961.
[b] Expected weight as reported in *SPS 37-12*.

Table 17. Operational schedule of weight, center of gravity and inertia

Configuration	Weight, lb	CG-(Z), in.	Inertia		
			Roll	Pitch	Yaw
Launch	325.7	449.2	3.25	11.37	11.15
After separation	308.8	448.2	2.51	9.35	9.34
At burnout	111.9	437.7	0.82	3.43	3.43
At impact	89.3	432.7	0.67	0.66	0.66

b. Spin motor.

Motor production. All motor grains were cast in a continuous production run between October 18 and November 10, 1961. Propellant for the motors was mixed and cast in 1-lb lots, using single lots of constituents except for the oxidizer. Because of equipment limitations in lot size for oxidizer grinding, 4 different oxidizer grind lots were used. Qualification test firings used samples from each of the grinds.

Table 18. Dispersion estimate

Subsystem	Contribution to burnout dispersion, rms		
	Transverse velocity, ft/sec	Axial velocity, ft/sec	Slant range to surface, ft
Bus	56.6	20.0	240
Mechanical alinement	10.6	—	—
Altimeter	—	—	78
Separation clamp	11.0	—	—
Spin motor	53.0	0.2	2.0
Power and sequencing assembly	—	—	87
Retromotor	40.5	16.0	235
Root Sum Square	89	25.6	356

The manifolds were treated as a separate subassembly. At the present time, all but 3 of the qualification and flight motor manifolds have been completed. The last 3 are in final stages of assembly.

Final assembly has been specified on 7 motors. Of these, the last 5 were assembled with the sterile technique.

Qualification tests. Five qualification tests have been conducted. The general specifications and results are tabulated below. All firings were conducted at ambient conditions. Firing results normal indicate no unusual characteristics of ignition, thrust buildup, torque level, total torque impulse, or thrust unbalance.

Test number	104	114	118	127	130
Test date, 1961	11-17	11-21	11-27	12-4	12-11
Cast date	11-10	10-26	11-2	11-1	10-26
Oxidizer grind	43	42	43	42	41
Motor conditioning	Special	None	Vibration	Complete	Complete
Results	Normal	Normal	Normal	Normal	Data not reduced

Motor installation. A number of tests were conducted to determine the load deflection characteristics of the retromotor closure plug and the spin motor under installation loads. It was determined that a preload of 40 lb on the spin motor will prevent rattling during vibration and will not cause excessive loads on the closure plug.

Velocity increment due to z-axis component. Total torque impulse imparted by the spin motor is computed from the results of qualification firing, for which accurate computer results are available.

Total thrust impulse in vacuum

$$T_{i\infty} = \frac{28.34 \times 2.51}{6.65/12} \times \frac{1.56}{1.40} = 142.5 \text{ lb-sec}$$

Thrust impulse on z-axis = 142.5 tan 10 deg = 25.1 lb-sec.

Velocity increment

$$V_i = \frac{25.1}{308.4/32.2} = 2.62 \text{ ft/sec}$$

At separation, the capsule weight = 308.4 lb, and the I_{roll} = 2.51 slug-ft$_2$.

The spin motor characteristics are:

Area ratio ε = 3.4

γ = 1.25

Nozzle angle = 10 deg

Nozzle radius = 6.65 in.

$C_{F_{SL}}$ = 1.4 (sea level)

$C_{F\infty}$ = 1.56 (in vacuum)

c. Retrorocket. During the period November 20 through 30, 1961, lunar capsule retromotor acceptance tests were accomplished at the Arnold Engineering and Development Center (AEDC) test facility. The following report is a brief analysis of results of these tests, and a summary of capabilities of the 5 flight motors for various lunar impact trajectories. More detailed information may be obtained from Reference 3.

The data presented indicates that performance is consistent with predictions of the early analysis. Some degree of deterioration of the aft 1 in. of the nozzle cone was observed in later stages of burning (Fig 4). This deterioration demonstrably does not affect axial performance or reproducibility to a significant degree. Analysis has shown the effect on cross axis dispersion to be within acceptable limits. A relatively minor effort could result in a fix for this problem, but it is not considered feasible or necessary for the immediate missions.

Eleven unfired motors remain in the program. Five are designated for flight missions, 2 for surveillance firings later in the program, and the remaining 4 are the result of not being able to obtain schedule time in AEDC to fire 12 motors in the acceptance tests.

The 6th in the series of 8 acceptance tests was destroyed at 6.1 sec of burning due to an obturation failure associated with the pressure measurement system. It is considered most likely that the failure started in 1 of the pressure fittings; however, the data was such that the exact start point could not be isolated. All indications were, however, that the failure was not motor induced and the firing was considered *no test* of the motor.

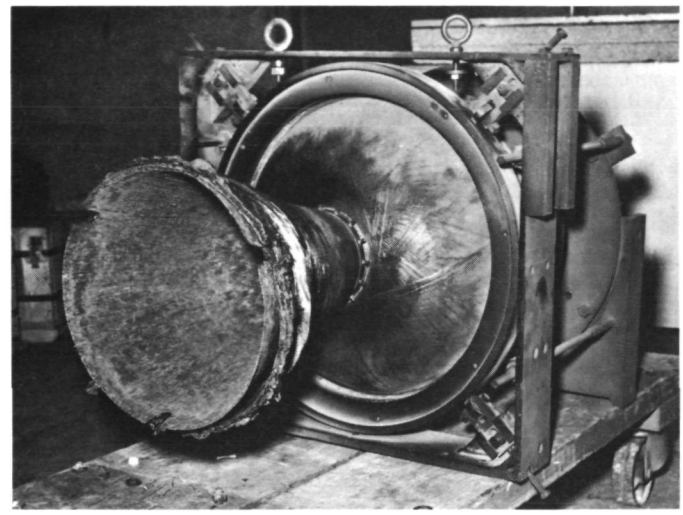

Figure 4. Postfire view of retrorocket Motor 45

Photographic records of the acceptance tests show that the nozzle exit cone aft of the spin motor index notches suffered deterioration in the later stages of burning. The deterioration is characterized by flaring of the portion of the nozzle aft of the notches and subsequent visible breaking up of the aft edge of the nozzle. The flaring starts nominally at 60% of burning, and visible deterioration of the aft edge commences at about 80% of burning. No visible asymmetries were detectable either in the flaring or subsequent breakup.

The 9th and 10th firings of the series contained a strengthening member of aluminum on the exterior of the nozzle cone. The fix worked well on the 9th test and held the geometry throughout burning. The aluminum support slipped forward on the 10th firing and allowed flaring of the nozzle at about 90% of burning. Neither the 9th or 10th firing showed any significant difference in axial performance. The data will be discussed later in this report.

Indications are that the tipoff is acceptably small; no steps were taken to reinforce the nozzle for the flight missions. Since tipoff was not measured in the acceptance tests, no further treatment will be accorded it in this report.

With the above exceptions, testing proceeded satisfactorily and the motors performed as expected.

Velocity decrement and payload. The unbraked velocities for *Rangers* RA-3, -4,and -5 differ slightly and depend

on the firing date. The payloads will be adjusted to provide braking to 0 velocity for each. It is necessary to adjust the unbraked velocity to account for lunar gravity effects during braking. The incremental velocity correction is:

$$\delta V = \left(\tau_B - \frac{h}{V_1}\right) g_m \qquad (1)$$

where

τ_B = motor burn time

h = distance above lunar surface at motor ignition

g_m = lunar gravity (5.3 ft/sec^2)

V_1 = average velocity of unbraked capsule

Motor burn time for this computation is the total action time and differs from burn time as defined later in this report. The demonstrated total action time at 70°F is 9.90 sec. Adjusting to the expected temperature at ignition of 67°F the action time would be 9.96 sec.

Four trajectories are selected. The quoted values and corrections to include Moon gravity are given in Table 19.

Table 19. Quoted values and corrections

Firing date, 1962	Unbraked impact velocity, ft/sec	Lunar gravity correction, ft/sec	Retro velocity required, ft/sec
January	8816	23	8839
April	8694	23	8717
June	8570	21	8591
July	8537	21	8558

Decremental velocity imparted to the capsule is obtained from

$$V_B = V_e \ln (W_o/W_B) + V_s \qquad (2)$$

where

V_B = velocity decrement

V_e = motor exhaust velocity = $(I_{se} \times g)$

W_o = initial weight

W_B = weight at burnout

V_s = velocity imparted by the spin motor

Table 20 is a summary tabulation of parameters derived from the acceptance test firings. The statistical summary

Table 20. Summary of retromotor performance from the acceptance tests

Run	Motor	Total weight, lb	Propellant weight, lb	Expelled weight, lb	Postfire weight, lb	Burn time, sec	Ignition time, sec	Specific impulse I_s, sec	Specific impulse I_{sc}, sec	Distance X, ft	Exhaust velocity V_e, ft/sec
37	03	213.68	191.26	194.62	19.06	9.490	0.043	275.67	270.92	48,490	8707
38	04	214.51	191.24	194.49	20.02	9.584	0.055	275.75	271.14	49,080	8714
39	05	213.96	191.26	194.88	19.08	9.633	0.055	275.88	270.75	49,002	8702
42	06	214.48	191.06	194.70	19.78	9.694	0.050	276.42	271.25	49,423	8718
40	07	213.68	191.20	194.34	19.34	9.524	0.075	275.62	271.16	48,876	8715
	08	No Test—pressure lost at 0.2 sec and flame-out at >6 sec									
43	09[a]	213.34	190.03	193.18	20.16	9.470	0.048	275.94	271.44	48,632	8724
45	10	214.65	190.78	194.78	19.87	9.552	0.045	276.10	270.43	48,572	8692

Statistics

Parameter	Mean	Deviation, 1 σ	Maximum deviation
I_s, sec	275.91	0.28	0.51
I_{sc}, sec	271.04	0.34	0.58
V_e (g = 32.140 ft/sec^2), ft/sec	8711	10	19
i, sec	0.053	0.011	0.022
b, sec	9.564	0.08	0.130
X, ft	48,868	250	555

Note: V_B = 8816 ft/sec; T_o = 70°F; weights at g = 32.146 ft/sec^2. Reduction of 0.01% necessary to adjust for g = 32.140.

[a]Stem potted, no pressure readout.

in Table 20 shows the uncertainty in exhaust velocity to be 10 ft/sec. To obtain the uncertainty in velocity decrement, Equation (2) is repeated.

$$\sigma^2_{V_B} = (\ln \lambda_B)^2 \sigma^2_{V_e} + \left(\frac{V_e}{\lambda_B}\right)^2 \sigma^2_{\lambda_B} \tag{3}$$

Two additional terms are required in Equation (3) to represent the uncertainty in measurement of V_e and the uncertainty in V_s.

The measurement error contains not only the instrumentation uncertainty, but also some error in grain temperature. The absolute instrumentation error is 0.12%/1 σ. An estimated value of grain temperature error in the tests of 1°C 1 σ will be used. The early estimates of mass ratio uncertainty are consistent with weighing methods and observed expelled weights and will be used here. Velocity uncertainty due to mass ratio uncertainty is 8 ft/sec. A breakdown of the contributions is:

Source	1 σ, ft/sec
Mass ratio	8
Grain temperature (1°C)	4
Exhaust velocity	9
Instrumentation	10
Total (rms)	16

The effects of grain temperature and the exhaust velocity are included in data in Table 20. The contribution of instrumentation error, while very small, represents the largest uncertainty in the system; without it the rms value would be 13 ft/sec.

Distance traveled during burning. The retromotor mission requires knowledge of the distance traveled during the braking operation. A mathematical model was used to predict the distance and its expected deviations. Equations for a vertical approach are

$$X(t) = X_0 + V_0 t - \int_0^t V_R(\phi)\, d\phi + \tfrac{1}{2} g_m t^2 \tag{4}$$

$$V_R(\phi) = \int_0^{\phi} \frac{F(\zeta)}{M(\zeta)}\, d\gamma \tag{5}$$

where

X = distance traveled

X_0 = initial value of distance

V_0 = initial velocity

t = time

ψ, ζ = dummy variables

Equation (4) is not amenable to analytical solution so a simplified neutral burning model was assumed.

$$\int_0^{\tau_B} V_R(\phi)\, d\phi = \tau_B V_e \left[1 + \frac{1}{1 - \lambda_B} \ln \lambda_B\right] \tag{6}$$

In order to obtain the true value of exhaust velocity, it is necessary to take into account the effect of air buoyancy and gravity variation on weights and the calibration system at AEDC. The above model, while useful for predicting performance, is not adequate for flight missions.

The thrust data taken at AEDC was used in conjunction with a calculated mass versus time to perform a numerical integration of the thrust-to-weight ratio.

$$X(\tau_B) = V_R \tau_B - g \int_0^{\tau_B} \int_0^{\phi} \frac{F_v(\phi)}{W(\phi)}\, d\zeta\, d\phi \tag{7}$$

The system weight was computed as follows:

$$\dot{W}(t) = -K F_v(t) \tag{8}$$

$$K = \frac{W_{exp}}{\int_0^{\tau_B} F_v(t)\, dt} = \frac{W_{exp}}{I_v} \tag{9}$$

$$W(t) = W_0 - K I_v(t) \tag{10}$$

where

$\dot{W}(t)$ = rate of weight expulsion

K = constant

W_{exp} = expelled weight

I_v = vacuum impulse

F_v = vacuum thrust

$W(t)$ = system weight

W_0 = initial system weight

These weight computations assume a constant thrust coefficient, exhaust gas composition, and combustion temperature. A similar function of motor chamber pressure could be used; however, in this case, the thrust data is considerably more accurate.

Trapezoidal integration of the vacuum thrust divided by weight was performed at 0.1-sec intervals for each of the acceptance tests. Table 20 contains a tabulation of the results with a computation of deviation. In each case, the inert weight, or payload, was adjusted to obtain a velocity decrement of 8816 ft/sec. Minor variations in propellant existed from motor to motor. It was expected

that the calculated distance traveled would vary accordingly; however, the data available was not sufficient to establish a trend. Very likely the change is so small as to be obscured by other uncertainties.

An effort was made to condition each motor to a temperature of 70°F prior to firing. It is felt the conditioning was no better than 70 ± 2°F, however, and an additional uncertainty existed due to dwell times in the test cell ranging from 2 to 4 hours at temperatures ranging from 65 to 75°F. Distance and burn time for Run 6 are sufficiently different from the mean to suspect a temperature problem. A temperature difference of 5°F would place this point on the mean.

Motor burn time and ignition time. Effects of these parameters are included in distance data shown in Table 20 because distance integration was performed from receipt of the ignition pulse to complete burnout of the motor. It may be of some interest to discuss their values since both figured in the early predictions of distance deviations.

Burn time, τ_B, is defined as the time from receipt of ignition current to the time when 99.5% of total impulse is delivered. This definition is taken to avoid some of the instrumentation uncertainty in defining the time of 0 thrust. Burn time then includes the ignition time. A grain temperature uncertainty of 1°C 1 σ (1.8°F) and an ignition delay uncertainty of 3.3 times 10^{-3} sec 1 σ were assumed in the predictions. It is expected that temperature uncertainty in the AEDC tests was consistent with that estimate; however, the ignition uncertainty was observed to be 0.011 sec 1 σ.

Observed deviation in burn time is shown in Table 20 to be 0.08 sec 1 σ. This value gives a value of distance uncertainty about twice as large as that obtained from the acceptance tests.

Flight mission parameters. It is necessary for the flight mission that payload capability for the mission be specified to obtain correct decremental velocity and that the distance traveled while burning be specified.

Payload and velocity decrement. The data in Table 20 gives exhaust velocity as 8711 ft/sec. This value must be corrected to conditions expected in flight. The corrections consist of (1) weight, (2) gravity, (3) grain temperature, and (4) expelled weight.

(1) *Weight.* As discussed previously, the total weight correction is −0.02 lb for the total unit weights taken at Bacchus. The postfire weights were taken at AEDC and the gravity value at AEDC is used.

(2) *Gravity.* Gravity to be used in V_e calculation must be consistent with that used in the thrust measurement calibrations. This value is the AEDC local gravity 32.140 ft/sec.

(3) *Grain temperature.* All units in the acceptance test program were fired at a nominal grain temperature of 70°F. The nominal grain temperature at ignition for the flight missions is expected to be 67°F. The sensitivity of V_e to grain temperature is 0.012%/°C; hence,a correction of −0.02% is required to compensate for the lower expected temperature.

(4) *Expelled weights.* The average expelled insert weight from Table 20 is 3.56 lb. However, the 9th and 10th firings were made with a nozzle reinforcement which altered the expelled weight values. It is believed more accurate to use the values of the remaining tests only for an average of 3.41 lb.

The flight motors will contain a spin support and ignition system which is ejected at first chamber pressure rise. This weight is not considered a retro weight.

Utilizing the above corrections the observed 8711 ft/sec, the corrected exhaust velocity for the expected flight conditions is 8710 ft/sec.

Five motors are available for flight missions. Physical parameters of these motors are shown in Table 21. Table 22 shows payload capability for each of the 4 selected trajectories.

Distance traveled during braking. In order to specify distance traveled during the braking operation it is necessary to know both motor grain temperature and the velocity decrement.

The mean grain temperature at liftoff is expected to be 72.5°F; at ignition it is expected to be 67°F. The distance sensitivity to grain temperature is:

$$\frac{\partial x}{\partial T_g} = -220 \text{ ft/°C} = -122 \text{ ft/°F} \qquad (11)$$

Table 21. Flight motors

Grain	Case	Total weight, lb	Nozzle closure and spin ignition assembly weight, lb	Propellant weight, lb
48	201	214.95	0.36	191.41
49	203	213.80	0.36	190.97
50	204	213.90	0.36	191.29
52	208	214.27	0.36	191.32
54	200	214.54	0.36	191.60

Table 22. Flight motor performance

Grain	V_B (ft/sec)			
	8839	8717	8591	8558
	Payload, lb			
48	91.08	93.58	96.18	96.89
49	91.53	94.03	96.63	97.33
50	91.94	94.44	97.04	97.74
52	91.62	94.11	96.72	97.42
54	91.79	94.29	96.90	97.60
Distance traveled, ft				
48	49,380	48,611	47,818	47,610

Note: $T_g = 67°F$; $g = 32.140$ ft/sec^2.

Figure 6 shows this result. The mean value of distance taken from the acceptance tests would have to be increased by 366 ft to allow for a grain temperature of 67°F. During flight, a thermistor circuit will be used to bias the ignition signal to provide for grain temperatures other than predicted. This thermistor circuit will utilize the slope in Equation (11).

A typical motor configuration was used to run the distance integrations for each of the 4 trajectory velocities discussed previously. Table 22 contains a list of the nominal distance traveled for each of the available flight motors at each of the 4 selected trajectories.

The 1 σ deviation in distance shown in Table 20 includes the effect of grain temperature uncertainty in the tests. This value is believed to be about 1°C 1 σ and coincides with the uncertainty expected in flight. Further contribution to uncertainty will occur as a result of exhaust velocity uncertainty, introduced by the thrust measurement system. As discussed previously, this value is 10 ft/sec. Multiplying by the partial derivative of distance with velocity, $6.3 \times 10 = 63$ ft from this source. The resultant uncertainty is:

$$\sigma_x = \sqrt{250^2 + 63} \qquad (12)$$
$$= 256 \text{ ft}$$

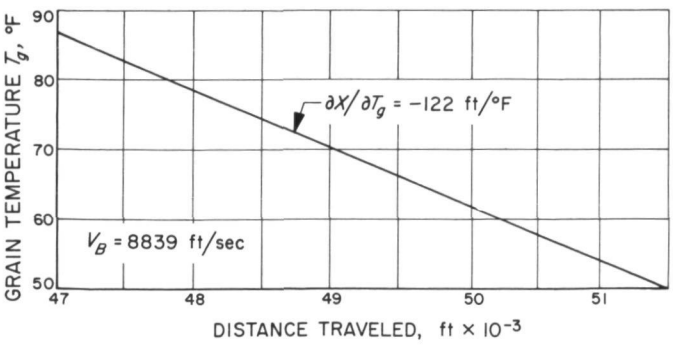

Figure 5. Grain temperature vs distance traveled

d. Landing spheres.

Survival sphere assembly. Most of the survival sphere hardware has been fabricated for *Rangers* RA-4 and -5. The majority of subcomponents is in an advanced state of assembly (Fig 6) to support the expected launch dates.

Most of the survival sphere hardware has been fabricated for *Rangers* RA-4 and -5. The majority of subcomponents is in an advanced state of assembly (Fig 6) to support the expected launch dates.

Capsule batteries. Considerable difficulty persisted in producing satisfactory batteries. Two difficulties were extant in the design previously tested: electrolyte leakage, either external or cell-to-cell; and breakdown of the separator material, resulting in decreased shelf life. Additional batteries were prepared incorporating design modifications, and battery performance is now adequate. A long-term discharge test is being conducted on 1 of the batteries to more accurately predict performance of the flight units already incorporated in landing spheres. Because of the lack of test data on batteries incorporating all the design modifications, there is a possibility

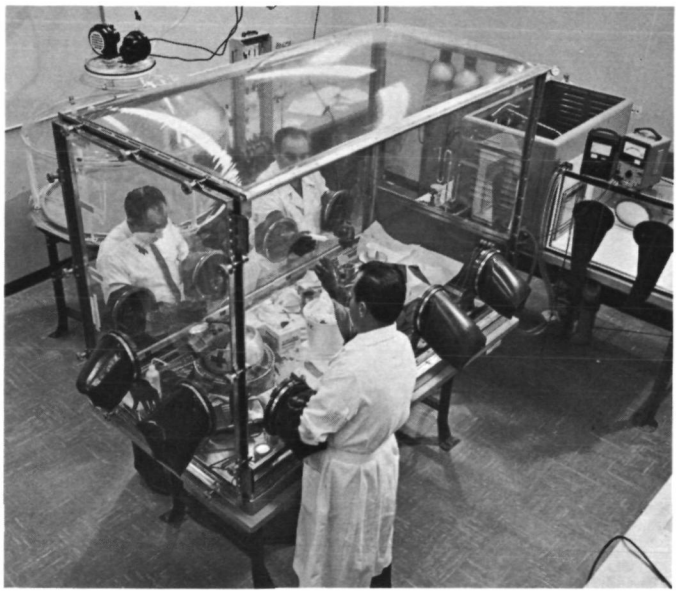

Figure 6. Potting and foaming electronic circuit boards in glove box

that the batteries used may not yield the total w-hr capacity inherent in the design.

e. External equipment. Basically, all the equipment, other than propulsion or landing spheres, has been completed for the 1st launch operation. In some cases, equipments to be used on subsequent launches have also been produced.

Altimeters. Successful completion of the design proof tests on 2 units of the Wiley altimeter was accomplished with final tests at ADF. These tests consisted of a low frequency vibration test and a deep-space vacuum test. One of the 2 units has been delivered to JPL for use on system tests in the field. The other is being used in further evaluation and as a control on the test equipment.

Delivery of the first 2 flight units was made to ADF; 1 was shipped to AMR for systems tests with the spacecraft and was used on the *Ranger* RA-3.

Support structures. Both spares and flight units of the altimeter support and erection structure and of the motor support structure have been acceptance tested and are ready for flight. The separation clamps and external wiring are completed with these structures and are being shipped to support launch operations.

Power and sequencing assembly. Problems were encountered in sealing a battery to withstand the centrifugal and vacuum environments. These difficulties have been overcome and satisfactory assemblies produced for design proof test and for flight.

Thermal radiation shield. A successful demonstration of the thermal radiation shield has been accomplished. A previous test had demonstrated the thermal performance of the basic design. This configuration was tested in the launch (design proof) vibration environment and was again tested functionally for retraction in the deep space tank. Figure 7 shows the capsule assembly with Marman clamp guard in place. The guard serves to ensure the Mylar thermal shield does not catch on the Marman clamp during retraction. Figure 8 shows the shield in launch configuration for the design proof vibration test.

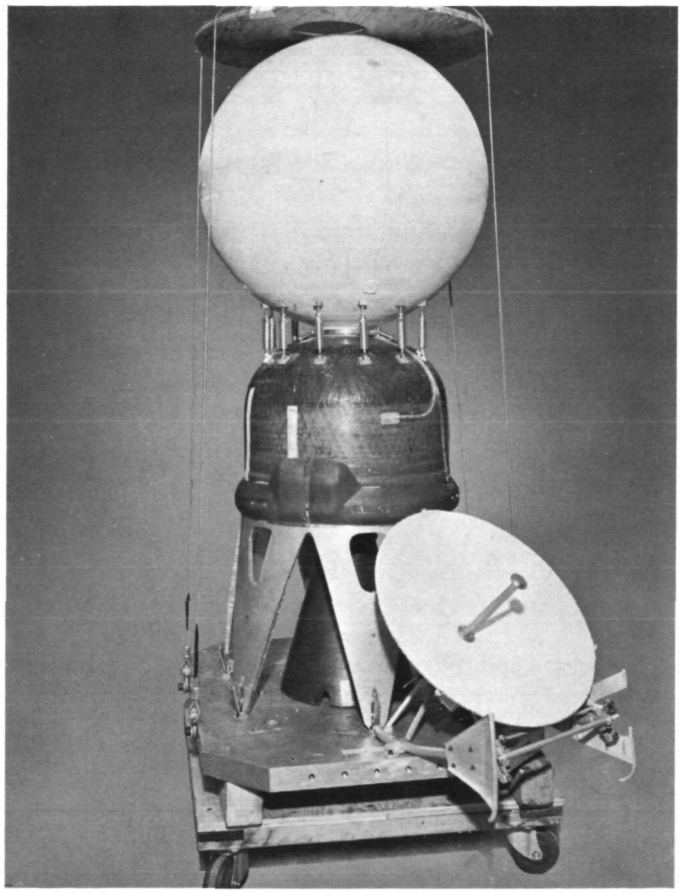

Figure 7. Capsule assembly showing clamp guard

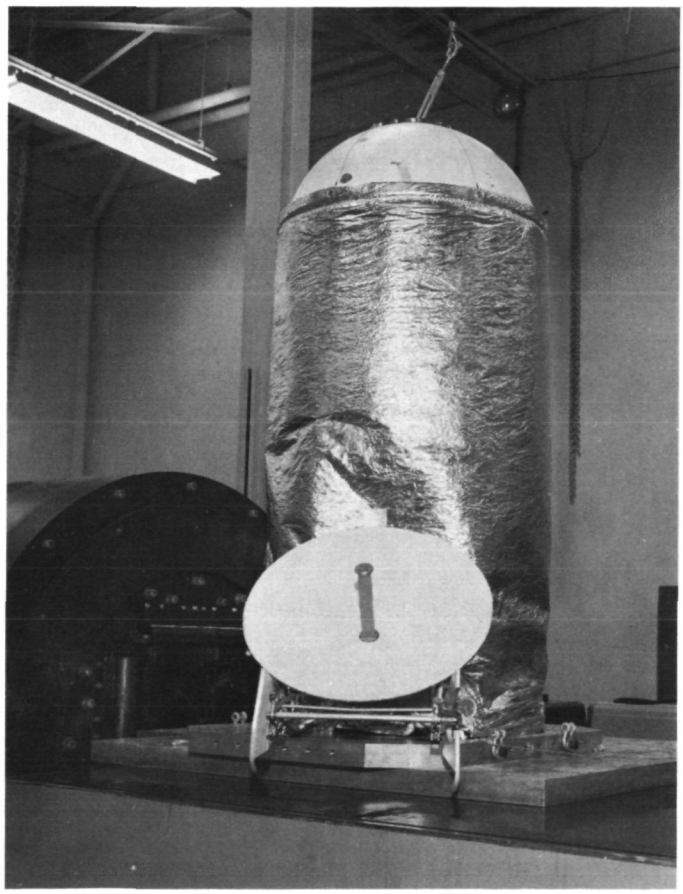

Figure 8. Thermal radiation shield

E. High Resolution TV Experiment

In support of the manned lunar program, one of the missions required is a high resolution TV experiment to be incorporated early in the *Ranger* project.

Considerable work had already been done between Radio Corporation of America (RCA) and JPL on the vidicon equipment developed for *Rangers* RA-3, -4 and -5. Examination of the problem, relating to rapid implementation of a more sophisticated TV mission on *Ranger*, indicated that an extrapolated development program with RCA could result in a TV subsystem at an early date. The proposed system would provide a picture of sufficient resolution to meet requirements of the manned program. Accordingly, a contract was initiated with RCA to provide a primary experiment TV subsystem to mate with the JPL-produced bus; this bus is to be essentially unchanged from the seismometer capsule series. *Rangers* RA-6, -7, -8 and -9 were selected for the high resolution TV mission.

1. Mission

The establishment of design requirements for vehicles that land and operate on the surface of the Moon is dependent upon an understanding of the details of lunar topography. The lack of scientific knowledge collected in the lunar environment has handicapped development and acceptance of a theory for the origin and composition of lunar surface features. Because of the disturbing influences of the atmosphere, the best photographs of the lunar surface obtained from Earth are limited in resolution to no more than about 600 m. Thus, it is difficult to evaluate the nature of the lunar surface environment on the basis of measurements made from the Earth.

Thus, the primary objective of an advanced *Ranger* mission will be to obtain high-quality pictures of the lunar surface at a resolution that is sufficiently high to enable an evaluation of the nature of the detailed lunar surface features. Resolution performance goal for this advanced mission shall be in the range of 0.1 to 0.5 m, providing the capability to identify small surface features that will comprise the interface with lunar surface vehicles. Data obtained from these pictures can then be used to improve understanding of origin and composition of the lunar surface, and to determine the effects of the surface on lunar landing vehicle requirements.

2. System Description

In order to accomplish this primary mission within the constraints of the existing *Ranger* spacecraft system and supporting facilities, a TV subsystem is to be developed that will be fully compatible with the present *Ranger* spacecraft mechanical, thermal, and electrical interface requirements. The major elements of *Ranger* TV payload will consist of optics, television cameras, controls, sequencers, telemetry, and transmitters needed to acquire and transform the energy reflected from the lunar scene into a video signal for transmission to Earth. This equipment will be combined with a space frame and a passive thermal control design to form a fully integrated payload that is dependent upon the *Ranger* spacecraft only for the receipt of instructions through the spacecraft command receiver, and transmission of the video signal over the spacecraft high gain antenna and stabilization. The TV payload will remain structurally attached to the *Ranger* spacecraft throughout the entire mission duration, and will impact on the lunar surface with the spacecraft at conclusion of the mission.

The *Ranger* TV subsystem will be supported on the ground by special equipment at the Goldstone Space Communications Station, which will be used to receive, store, and reconstitute the TV data transmitted from the TV subsystem. Additional ground support equipment will be required at JPL, Cape Canaveral, and RCA.

a. Design. For reasons of mechanical simplicity, it is desirable to use a fixed focal length optical system with the television cameras. With a fixed focal length optical system, it is possible to trade area coverage for resolution as the spacecraft approaches the Moon's surface. In light of environmental requirements for the payload, weight constraints, and problems of packaging and mechanical integration, it is desirable to employ the shortest focal length, dioptric lens system consistent with mission resolution goal. Moreover, the use of high speed optics to minimize the effects of uncompensated image motion by shortening the television camera exposure time is also proposed. The combination of these factors suggests the desirability of obtaining a final sequence of pictures at a minimum altitude above the lunar surface to satisfy the high resolution of the TV mission. Then, pictures taken at all prior altitudes will encompass a greater surface area at a correspondingly reduced resolution. The minimum altitude for the final pictures is determined by the time required to read out the video data from the television camera, and the spacecraft terminal velocity. The minimum altitude, and thus the highest resolution with a given optical system and

CONFIDENTIAL

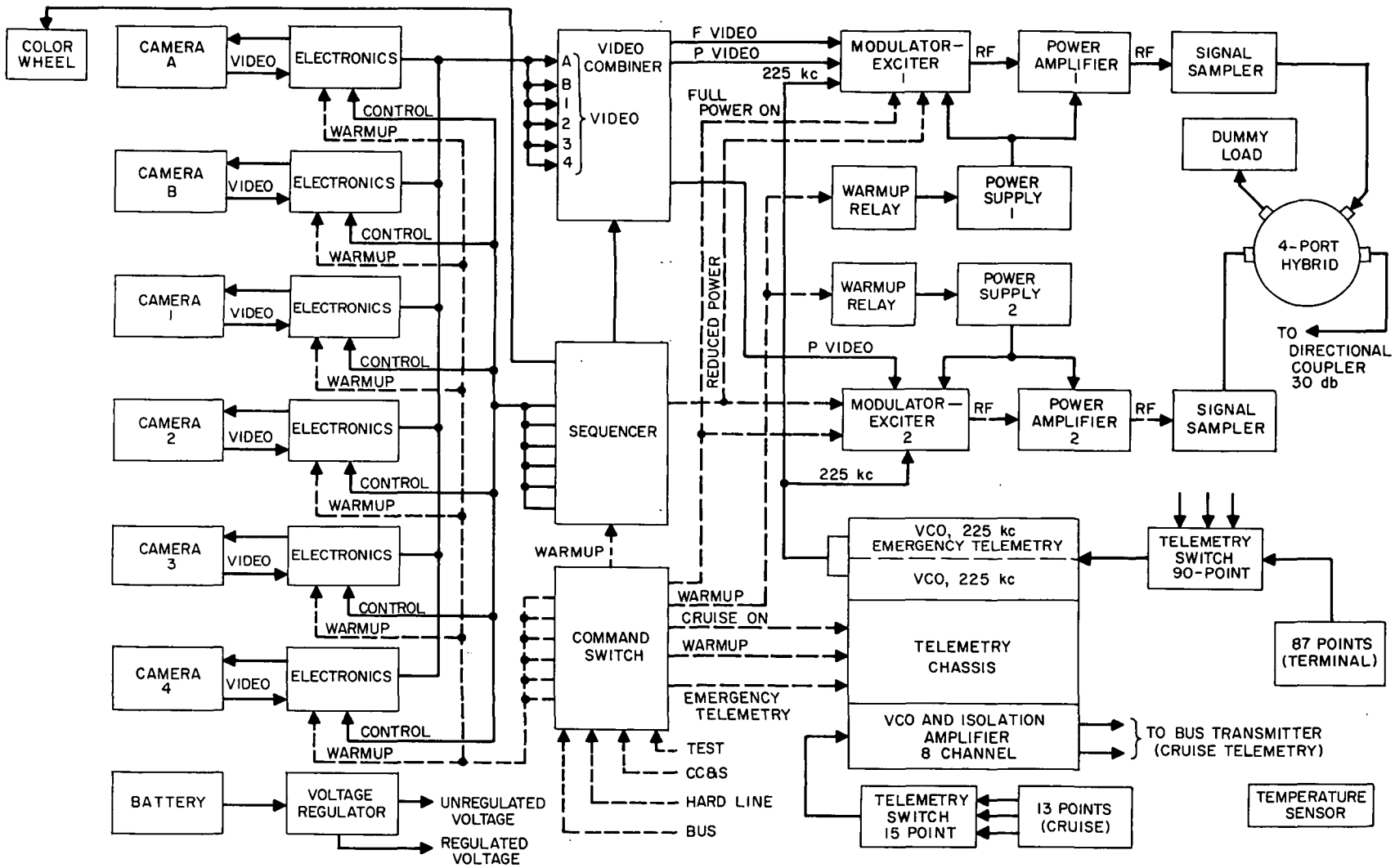

Figure 9. TV Subsystem

CONFIDENTIAL

camera design, will be obtained by minimizing the camera readout time. However, the minimum readout time is also constrained by the number of scanning lines (or line density) required to provide the desired camera resolution, and by the maximum permissible system video bandwidth. In the *Ranger* TV payload, the simultaneous goals of high line density and minimum readout time are achieved by the use of a special method of raster formation with a high resolution, 1-inch vidicon TV camera. Minimum readout time is achieved in camera by reading only the central 200 lines of a nominal 800 television line raster.

The spacecraft TV subsystem functional block diagram is shown in Figure 9. The TV subsystem consists of 6 slow-scan vidicon cameras, a control programmer and camera sequencer, a telemetry system, a 2 channel transmitting system, and a battery power supply with associated voltage regulators. The camera parameters and the system interconnections reflect the system design goals of (1) obtaining a high-quality television picture of the lunar surface at a resolution of about 0.2 m per optical line pair; (2) obtaining reasonable nesting of a sequence of television pictures, starting from a resolution of approximately 350 m per line pair; and (3) obtaining wide area coverage of the lunar surface. Another desirable goal achieved by the system design is to obtain a color image of the lunar surface.

The communication system is designed to make optimum use of a 2-mc bandwidth allocation centered at 960.0 mc, within which a channel allocation of 80 kc centered at 960.05 mc is required for the beacon transmitter. The allocation (Fig 10) thus consists of 2 bands of approximately 1 mc each, utilized by 2 transmitters: 1 centered at 959.5 mc and the other at 960.5 mc.

The first design goal, of obtaining high resolution pictures, is achieved by a system of 4 television cameras operating at a frame rate of 5 cps, and having a usable resolution of 35 optical line pairs per mm. The cameras are exposed sequentially and while 1 camera is being read out, the remaining 3 are being erased and prepared for

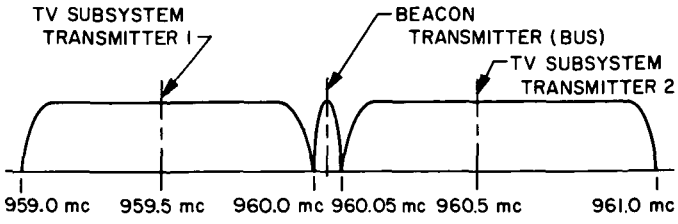

Figure 10. System bandwidth allocation

the next sequence of exposures. At the impacting velocity of 2700 m/sec, and with a proposed 76-mm camera lens, the system has good probability of obtaining a full television picture at a resolution of 0.2 m per line pair. The last sequence of 4 pictures will have resolutions varying from 0.8 to 0.2 m per line pair and will include a 16-to-1 variation in area coverage. Cameras 1 through 4, the partially-scanned cameras (Type P), provide these last 4 television pictures, which are scanned out and transmitted in real time within an RF bandwidth of about 1 mc. Cameras 1 through 4 are permanently connected to Transmitter 2. These highest resolution pictures are considered to be most important to the total Lunar Program; therefore, redundant transmission of the pictures from these 4 cameras through the additional channel of Transmitter 1 is provided during the final minute of the terminal mode of operation. This is achieved by a preprogrammed switching command.

The design goal for the nesting feature is to obtain a final set of pictures which can be located on present-day lunar maps. The initial pictures will be taken at 10 min from impact at an altitude of about 1300 kilometers. Their resolution will be of the order of 350 m per line pair and will enable the photointerpreters to locate these images on the available lunar maps. Each subsequent set will increase the resolution and will permit location by reference to the previous set. This technique of picture location will proceed to the final set where the highest resolution television pictures will then be located, permitting a more meaningful interpretation to be made of these images. A set of 2 fully-scanned cameras (A and B) is included to ensure that this technique of nesting is achieved. These cameras have a frame time of 2.56 sec, and the same line density as the partially-scanned cameras. Using the proposed 76-mm lens, they can account for a larger area coverage of 16-to-1 over that of the partially-scanned cameras. Thus, both nesting and wide-area coverage are achieved with this arrangement.

The arrangement of the fields of view of Cameras 1 through 4 and of Camera A is shown in Figure 11. These overlapping fields ensure that the 4 partially-scanned cameras are centered on the velocity vector. Moreover, the overlap between the fully-scanned camera and the partially-scanned cameras will help locate each frame in the previous nest of pictures. Camera A and B (Type F) are alternately scanned and erased, and their real-time readout is contained in the 1-mc RF bandwidth of Transmitter 1. Camera B is pointed at an angle of 30° from Camera A. It is presently located on the Y axis, but its field of view could be changed to plus or minus angles from this axis, as required. The purpose of this high

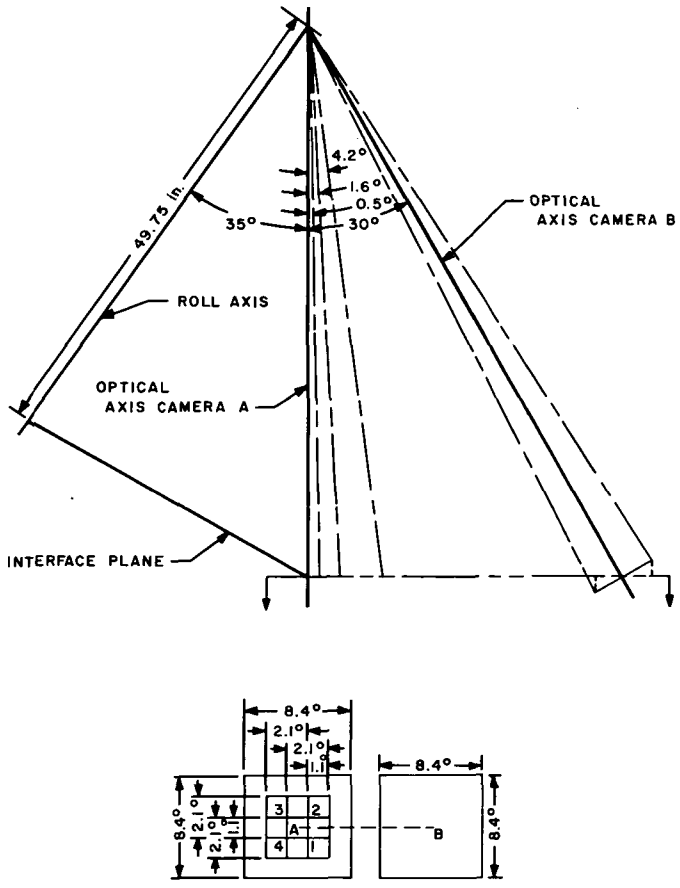

Figure 11. Terminal phase optical geometry

oblique field of view is to accomplish the wide area coverage shown in Figure 12.

In the early phases of the terminal mode, the picture scale changes by a small percentage between exposures of the fully-scanned cameras. To obtain additional lunar data during this largely redundant picture-taking phase, it is planned to equip Camera A with a set of color filters. Sequential exposures made through a blue, a green, and a red filter will permit a color photograph to be produced on the ground from an overlay of these 3 images.

The system block diagram (Fig 9) shows the signal flow as well as the equipment packaging. Cameras 1 through 4 have identical vidicon assemblies. Attached to each assembly is a preamplifier, a 1.0-ms shutter, and a 76-mm lens. Each vidicon assembly is driven by circuitry including the deflection amplifiers, video amplifiers, and the vidicon power supply (contained in the camera electronics box). Cameras A and B have similar vidicon assemblies, preamplifiers, and lens systems. The shutters are larger to accommodate the larger image format and have exposures of 5-ms duration. Their camera electronics are physically similar, with circuits modified to accommodate the fully-scanned camera parameters.

The 6 cameras are provided with raster-forming synchronizing signals and are sequenced through exposure, read, and erase cycles by the camera sequencer. The sequencer derives its time base from a crystal-controlled 18-kc oscillator, utilizing binary counters and gates to provide interlocked horizontal and vertical synchronizing, read and erase cycles, and shutter pulses. The clock countdown provides a convenient way to establish the preprogrammed power amplifier turn-on and the commands for switching between Cameras A and B. The sequencer contains a backup crystal-controlled oscillator which can substitute for the primary oscillator and which has separate counting chains and power supplies for Cameras A and B and Cameras 1, 2, 3, and 4.

The general system philosophy of using repetitive camera units and dual transmission channels to achieve a high probability of equipment operation is further served by including a free-running capability in Camera 1. This capability is provided by a programmer which can supply all synchronizing and sequencing signals to Camera 1 in the event of a sequencer failure. Limiting this circuit to only 1 camera is necessary because of the additional component weight and circuit complexity involved. The intent of this feature is to provide marginal system operation in the event of sequencer failure.

The video outputs of the 6 cameras are fed to the video combiners, where tones, video, and synchronizing signals are composed into the system standard after the appropriate amount of emphasis has been exacted. The command switch connects the system commands received

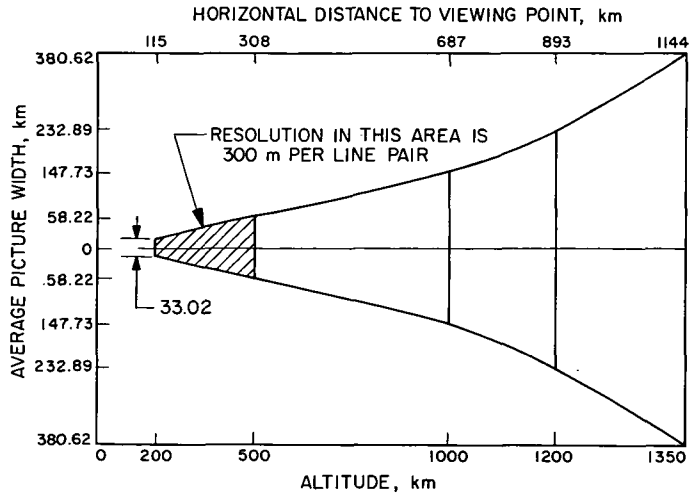

Figure 12. Coverage of Camera B

through the spacecraft interface to the appropriate system elements. The first position of the command switch is used for the warmup command, which is sent 15 min prior to impact. This command is stored as a backup command in the central computer and sequencer (CC&S). An emergency telemetry command occupies the 2nd position of the command switch and can be sent any time required after a warmup command has been sent. The emergency telemetry command is followed by a return-to-camera-video command in the 3rd position of the switch.

Other system sequences are derived from stored preprogrammed commands. The cruise-mode telemetry command originates in the CC&S. The power-amplifier-on command is supplied after the proper count from the camera sequencer, with a backup from the CC&S. The camera switchover command is derived from the sequencer.

Provision is made to permit system testing with or without a spacecraft, as well as for tests on the launch pad with a hard line to the TV subsystem. Small electric lamps will be incorporated in the Lockheed shroud, each one so positioned that it lies along the optical axis of 1 of the 6 TV cameras. These lamps would be physically located between the inner and outer walls of the shroud with small holes in the inner wall to allow light from each source to shine on a TV camera. The power source will be the externally supplied 28 v to the spacecraft allowing the lights to be energized at the same time as the spacecraft is on for test purposes. This departure from normal prelaunch test philosophy (calling out minimal tests only) was deemed advisable, since the TV subsystem is the prime purpose of the mission and a light source for each camera gives a rather comprehensive check on cameras, amplifiers, sweep circuits, and sync circuits. In this case a light source will permit a better TV subsystem evaluation than would many hard lines for stimulating and monitoring.

The telemetry subsystem consists of cruise mode telemetry elements as well as more detailed diagnostic telemetry elements for the terminal phase of the mission. A 15-point sampling switch, operating at a rate of 1 point per sec, samples critical temperatures and voltages. The output of this switch is used to drive a Channel 8, IRIG subcarrier oscillator. An ac amplifier and a transformer connect the output across the spacecraft interface, where it is mixed with other telemetry for transmission over the bus beacon transmitter.

During the terminal mode, a 90-point sampling switch, operating at a rate of 3 points per sec, samples the TV subsystem parameters. The switch output is used to drive 2 voltage-controlled oscillators (225-kc) connected in parallel. These 2 outputs are connected so that 1 VCO is mixed with the video at Modulator 1 and the other at Modulator 2. The VCO frequency was chosen so that it is located above the highest video frequency in the base band of the system.

In emergency mode, the video signals are switched out and the 90-point telemetry is used to modulate each of the transmitters directly. A possible condition requiring emergency telemetry would occur if video transmission were interrupted, and it became necessary to determine whether the TV subsystem was nonoperational or the high gain antenna was not locked to the Earth. A reduction of 40 db at the ground receiver would suffice to accommodate the telemetry bandwidth and would compensate for signal loss possible if reception were from the back lobe of the spacecraft antenna. The result would be a usable signal-to-noise ratio for the telemetry information.

The temperature sensor in Figure 9 is part of the telemetry system. Several spacecraft and subassembly temperatures are measured by thermistor circuits and are connected to the proper analog voltage for the telemetry sampling switch.

The communication system consists of two 60-w L-band, FM transmitters. The modulating signal consists of the camera video and the telemetry subcarrier. The transmissions of the 2 systems combined in a 4-port hybrid combiner with the beacon output of the transmitters are beamed toward the Earth from the spacecraft high gain antenna. Reception at Goldstone is effected with an 85-ft parabolic antenna equipped with an L-band maser preamplifier. Within the parameters of this system, the 60-w transmitters provide a substantial power margin above the receiver threshold; the resulting video signal-to-noise ratio will produce a high quality TV picture. Design of the communication system will permit reception at an alternate antenna site at Goldstone, which is equipped with an L-band parametric amplifier. The power margin at this alternate site will be reduced by 3 to 4 db, but will be usable.

b. Flight sequence. The nominal trajectories for the *Ranger* TV flights will employ a nearly vertical descent to the lunar surface. In transit from the Earth to the vicinity of the Moon, the *Ranger* will fly in a Sun oriented attitude, with the spacecraft solar cell panels perpendicular to the rays of the Sun. Thus, the optical axis of the television cameras will be fixed in vehicle body coordinate system. When the spacecraft reaches the vicinity of the Moon, it will undergo a commanded

terminal maneuver to aline the optical axis of the television cameras with the spacecraft velocity vector for descent to the lunar surface.

The initial command to the TV subsystem will occur 2.5 hr after the mid-course maneuver, 18.5 hr after launch. This command will originate in the CC&S, and will turn on the cruise mode (Channel 8) telemetry. At a time corresponding to 15 min before impact, the complete TV subsystem will be turned on in a warmup mode by a real-time command from the DSIF. Provision will be made for a CC&S backup command to support the real-time command for warmup of the payload. The TV subsystem will be turned on in a full power mode 10 min before impact by an internally generated command from the RCA control programmer. This internally generated full-power-on command will be supported by a backup command from the spacecraft CC&S. At 1 min before impact, the video data from the Type-F cameras will be switched out, and the data from the 4 Type-P cameras will be transmitted over both channels. This camera switchover will be accomplished by an internally generated command from the control programmer. In the event of loss of spacecraft stabilization or high gain antenna lock, a real-time command will be used to switch the TV subsystem into an emergency telemetry mode. In the emergency telemetry mode, the TV subsystem terminal telemetry data is transmitted over the high gain antenna using full transmitter power.

3. Test and Operations Schedule

Based on the assumption that RA-5 may be the 1st of the high resolution TV experiments, RA-5 is scheduled to begin assembly on March 19, with test operations scheduled to start April 23. This assumption places the most stringent time requirements on the program scheduling.

RCA will deliver 2 sets of their system test GSE to JPL. The 3rd set that will be needed for AMR operations will be utilized by RCA during checkout of flight hardware at their Astro-Electronics Division (AED), and will be shipped to AMR in time to participate in test operations of RA-5. Though this is in contradiction to normal requirements that all portions of the system test complex be checked out and utilized together at JPL, more is to be gained by having the equipment available to RCA for checkout of flight units over a longer period of time than having the GSE participate in JPL test operations. The RCA equipment has a minimum of electrical interface with the rest of the system test complex and, as such, compatibility with the TV subsystem is of more consequence than test complex operation.

It is planned to use the engineering test model (ETM) to system test the checkout equipment as well as to prove, under continuing operating conditions, the design concept of the TV subsystem itself. Upon completion of checkout equipment integration at AED, the ETM will be available for a period of time to expedite the installation and checkout of checkout Unit 2 at JPL. Availability of the model at that time would materially shorten the period required to start testing of the PTM.

In an effort to expedite the delivery of qualified subassemblies, some departure from the initial ETM–PTM flight units concept has been permitted. Although this new concept will mean quicker delivery of qualified components, it is achieved at some expense in the time required to arrive at full integration of the ETM, as originally planned. At present, it is planned to use breadboards in the ETM to as great an extent as possible. This plan will permit construction of an electrical model for use in evaluating the ground checkout system, in perfecting testing techniques, and in generating test procedures reflecting these techniques.

The system test complex will be set up in a manner similar to that utilized on *Rangers* RA-3 and -4. The addition of 13 racks of RCA equipment will consist of: 7 racks for final picture recovery and recording; 2 racks for TV subsystem simulation, monitoring, and control (hard line); and 4 racks for receiving equipment.

Since the flight TV subsystems for the 1st spacecraft, and partial equipment for the 2nd spacecraft, will not arrive until well along in the spacecraft test phase, the RCA electronic mockup and proof test model (PTM) subsystems will not arrive in time for the 1st few weeks of RA-5 at JPL, and for the initial test operations of RA-6. The PTM subsystem will have to handle initial testing of the following spacecraft also as the flight TV subsystems will not arrive in time for the 1st few weeks of testing. It is planned that the RCA temperature test mockup together with a temperature test spacecraft be utilized in the 25-ft space simulator in March 1962. It is considered mandatory that this test be made sometime before an actual flight *Ranger* spacecraft is subjected to this environment.

4. Basic Structure

The mechanical design of the TV subsystem basic structure has been established to the extent that assembly and detail drawings have been prepared for the structure.

These drawings reflect some changes in design brought about by a rearrangement of the 6 cameras, and relocation and method of inserting the batteries onto the structure. Final drawings for the complete structure were released to Lavelle Aircraft Corporation, the structure subcontractor, November 1961.

A full-scale plastic model of the structure has been fabricated. The full-scale model will be used to verify location of equipment on the structure and as a guide in the assembly of the actual structures. A preliminary stress analysis has been completed for the central box column, the thermal shield, and the TV subsystem mounting attachments.

A drawing of the structure is shown in Figure 13. The batteries are located in the lower bays, and inside the rectangular box frame. Except for the batteries and camera electronics, the equipment subassemblies are mounted between the thermal shroud and the box structure exterior. Removable panels in the rectangular box structure are not required with this arrangement, thus providing a more rigid box structure.

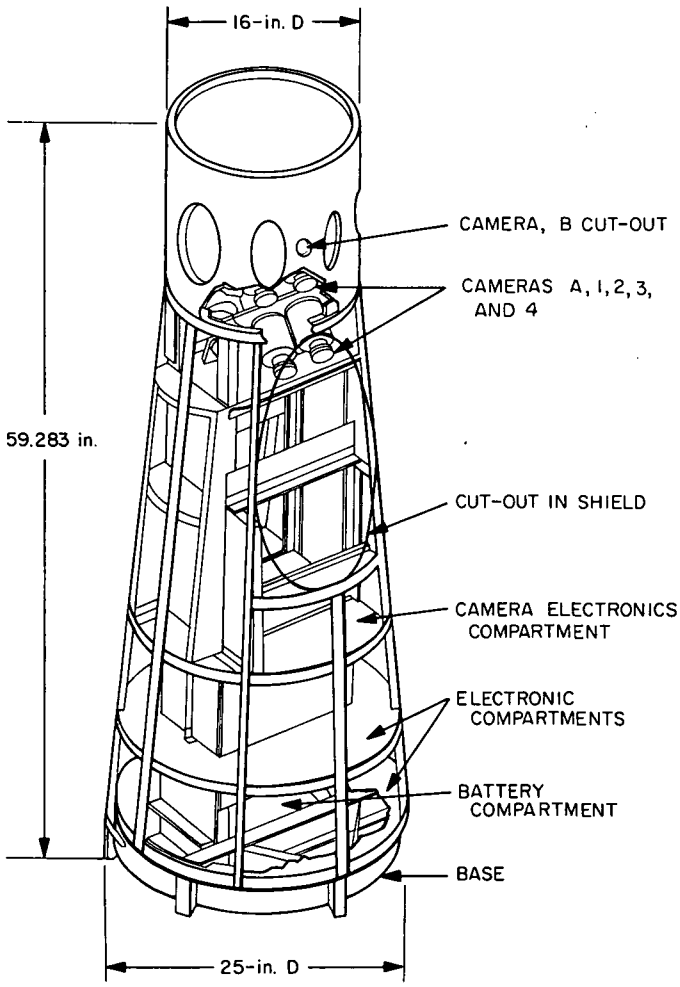

Figure 13. Basic structure

The thermal shroud is a 0.032-in. thick, and is designed to carry part of the structural load. The shroud is fabricated in 4 quadrants. Of the quadrants, 2 are permanently fastened to the assembly; the other diagonally opposite quadrants are removable for access to the interior for inspection, removal, and replacement of equipment.

A detailed weight analysis of the structure was completed using the final assembly drawings. Results of the analysis indicate a weight of approximately 75 lb for the structure and thermal shield. Design efforts aimed at reducing the weight of the structure and thermal shield have been initiated on a noninterference basis with the structure delivery schedule.

The initial structure and thermal shield will be used in the mechanical test model. In order to expedite delivery, Lavelle has been instructed to deliver this structure and thermal shield without any special surface treatment. The third structure and thermal shield will be used in the engineering model, and all aluminum alloy parts will be anodized. The thermal shield for the 2nd unit (thermal test model), 4th unit (proof test model), and Units 5, 6, 7, and 8 (flight models) will be cleaned, polished, and buffed on both sides to provide a bright, mirror-like, reflective surface. The remaining parts of these structures will be anodized.

A preliminary stress analysis has been completed for the critical elements of the structure. Results of the analysis verify that the design is structurally sound; however, a detailed stress analysis is being made.

5. Electronic Subsystems

a. TV cameras. In order to ensure meeting the required delivery schedule, the original camera design was based on previous operating systems. However, as the design study has progressed, it has become evident that more changes than were originally planned would be necessary in order to meet the requirements of the *Ranger* TV subsystem. Additional personnel have been assigned to the camera electronics in the RCA Camden facility. This group will complete the design of the circuits and their packaging, and fabricate the units.

Layout and fabrication of breadboard models for the engineering model are essentially completed. As soon as these boards are tested, they will be operated with a yoke–vidicon assembly. This operation should furnish redesign information for the proof test model.

After the fabrication and testing of the first 3 cameras, subsequent layout and fabrication (incorporating the necessary changes) will be made using printed circuits with the printing on the component side.

The television equipment consists of six 1-in. vidicon cameras. Of these cameras, 2 are fully scanned producing a resolution of 800 TV lines over a tube format of 0.44 by 0.44 in. with a side field coverage of 8.4 deg. A reduced raster is utilized by 4 of the 6 cameras scanning a 0.11- by 0.11-in. central portion of the tube at approximately the same line density to produce a resolution of 200 TV lines. The side field of view is 2.1 deg and is achieved with the same focal length lens as specified for the fully-scanned cameras. This leads to a natural designation, Type-F cameras for fully scanned and Type-P for partially scanned. The Type-F cameras are used as Cameras A and B in the system configuration and Type-P cameras are used as Cameras 1, 2, 3, and 4. The Type-F and Type-P cameras use the same imaging transducers and optical equipments and differ only in the detail of their electronic circuitry. The image transducer is an electromagnetically focused, 1-in. deflection vidicon photoconductor with a resolving capability in excess of 800 lines per picture height.

The Type-F or fully-scanned camera utilizes 1152 active horizontal scan lines over the 0.44 by 0.44-in. faceplate area. The horizontal scan rate is 450 cps with 0.22 ms appropriated to horizontal blanking. The active scan lines plus 46.6 ms for vertical blanking add up to the 2.56-sec frame period. At the end of its active scan the Type-F camera enters an erase phase which occupies an equal amount of time. In the *Ranger* television system 2 Type-F cameras are alternately scanned and erased in such a manner that 1 is being scanned while the other is being erased. This timing sequencer is illustrated in Figure 14.

Table 23. Camera performance summary

Parameter	Camera designation	
	A, B	1, 2, 3, 4
Frame time, sec	2.56	0.2
Vertical blanking, ms	40	6.6
Horizontal line rate, cps	450	1500
Horizontal line time	2.22 ms	666.6 μsec
Horizontal blanking	0.22 ms	111.1 μsec
Real resolution TV lines	800	200
Format, in.	0.44 by 0.44	0.11 by 0.11
Video bandwidth, kc	187	187

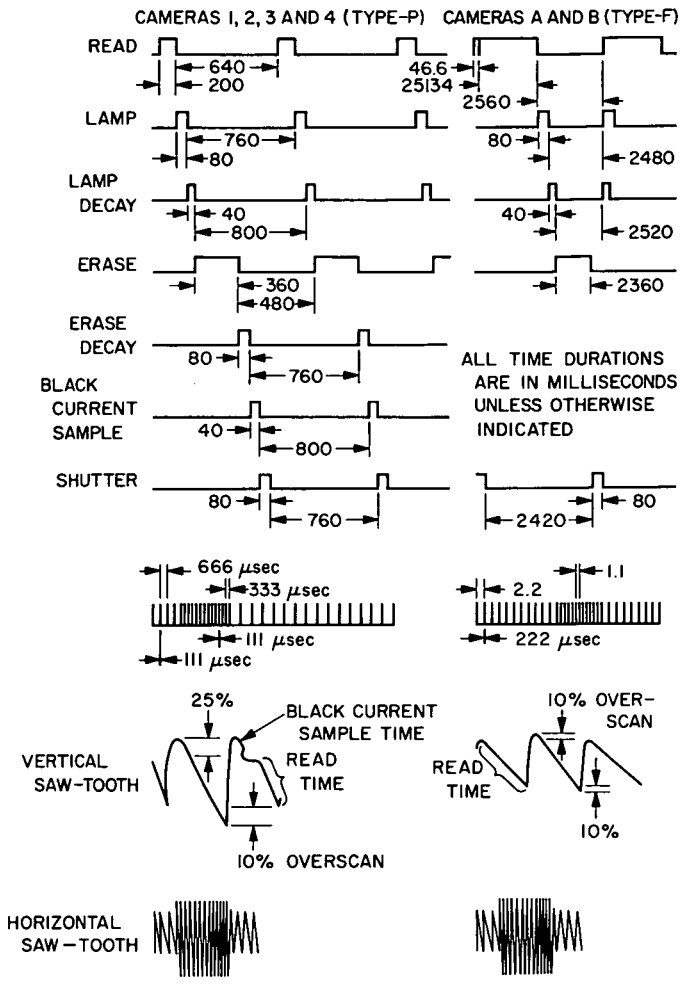

Figure 14. Camera timing and waveforms

The Type-P or partially-scanned camera utilizes 300 horizontal scan lines over a 0.11- by 0.11-in. faceplate area. The horizontal line rate is 1500 cps with 111.1 μsec allocated for horizontal blanking. The vertical scan plus a 6.6-ms blanking period occupies 0.2 sec. At the end of the vertical scan an erase procedure is initiated which occupies 0.64 sec. In the system, 4 Type-P cameras are sequentially scanned; while 1 is being scanned the remaining 3 are in various portions of their erase cycles. A 40-ms pulse is used to separate each sequence of 4 Type-P camera exposures. The total period per sequence is then 0.84 sec. Figure 14 illustrates the basic camera timing as well as the relationship of the 4 cameras in the system.

Each of the Type-F and -P cameras will derive their scan synchronization from the control sequencer. Of the Type-P cameras in a system, 3 will have their deflection amplifiers driven directly from the control sequencer. One of the 4 Type-P cameras will have free running horizontal

and vertical sync generators which can either be kept in step from the control sequencer or can supply sync without external excitation. This is an additional measure of safety intended as an emergency mode of operation in the event of failure of sync.

The cameras will each contain a preamplifier and video amplifier. There will be 2 designs breadboarded and evaluated. Design 1 utilizes a nuvistor preamplifier and a transistorized amplifier with a frequency pass band from near dc (about 5 cps) to 187 kc. The lower limit is to prevent unwanted shading and the upper limit contains the frequencies corresponding to the 800 TV lines and 200 TV line resolutions, respectively. The 2nd design to be breadboarded will use a tuned band pass amplifier. A high frequency signal injected on the vidicon grid causes the beam current to vary at this carrier rate and to modulate the video information. This carrier and the lower side band can be amplified by a band pass amplifier followed by a phase detector. The decision as to which circuit design will be used will be based on a comparison of the resulting signal-to-noise ratios.

The camera circuitry will also include a control grid current regulator, a focus current regulator, shutter drive circuits, dark current compensation, fast erasure circuits, and dc-to-dc converters for both high and low voltages.

The optics for Type-F and Type-P cameras will be identical lenses with a 76-mm focal length and an $f/2$ aperture ratio. Responses to preliminary specifications have been received from 4 vendors and sample lenses have been received from 2 vendors. Optical tests were performed on the samples utilizing the sine wave response technique and equipment of the applied research group of RCA Camden.

The shutter for Type-P cameras will be a *Tiros* type, linearly-actuated slit shutter. The slit will be adjusted to provide a 1-ms exposure and the traverse time of the slit over the 0.11 in. will be about 2 ms. If an exposure is made 0.2 sec before impact, the resolution will approach 0.2 m per line pair. The 1-ms exposure will prevent image smear for a 2.5-deg misalinement of optical axis with respect to the velocity vector. This will provide a high assurance of eliminating any smear from the last picture. It may also be traded off for additional exposure of the vidicon if necessary.

The shutter for the Type-F cameras will be a scaled up version of the *Tiros* shutter. It will be designed to cover the 0.44-in. fully-scanned format. Its slit will cause a 5-ms exposure which is sufficient to prevent image smear prior to the 1-min switchover signal. In the event the switchover is missed, the Type-F camera can continue to supply useful pictures down to 2.5 sec before impact. The additional exposure time will be useful in correctly exposing Camera A through the various color filters and, in general, will erase the difficulty of the shutter design.

The Type-P shutter is being fabricated at AED and shutters for the Type-F camera are being designed and fabricated in Camden.

A color wheel containing 3 color filters and a single neutral density will be supplied with Camera A. The wheel will be caused to sequentially position a different filter in the optical path for each exposure of Camera A. It will feed a coded signal to the control sequencer, which will be used to gate on the appropriate tone signals during the vertical blanking signifying the color filter being used. The specification of the spectral responses and transmission factors for the blue, green, red, and neutral filters will proceed early in the breadboard phase.

Work on the filter wheel is being done at AED. At present, the mechanical portion of the wheel is designed, and engineering releases have been issued for 4 assemblies. Spectral response tests have been conducted on vidicons for the color system. These tests will continue. Final selection of the filters for use on the wheel has not yet been made.

Six Bausch and Lomb lenses and 6 Elgeet backup lenses have been received, and testing of the lenses has begun. If the Bausch and Lomb lenses meet all requirements, the backup lenses will be used in breadboards and test setups. The specification for the collimator has been written, and vendor quotations are being received at present.

Five Type-P camera housings have been released to the model shop. The housings will incorporate the mechanical focusing and centering of the vidicon yoke assembly with respect to the optics.

The 1st vidicon has been delivered for evaluation and test; more complete specifications for the vidicons are being written.

b. Camera sequencer and control programmer.

Camera sequencer. Work on the camera sequencer has been subcontracted and has been directed toward finalizing the logic design and testing the basic logic circuits. The addition of new inputs, and difficulties encountered in adhering to the -10 to $+65°C$ temperature range, make it necessary to increase the number of circuits over the number originally planned. Most of the preliminary

design has been completed and the major effort in all areas is at present being expended on circuit packaging.

A complete block diagram of the control programmer and camera sequencer is shown in Figure 15. The blocks enclosed by the dashed lines represent the digital portions of the camera sequencer; the flow relationships with the video combiners, camera subsystems, transmitters, and test functions are indicated.

A primary and a standby 18-kc master timing reference generator provide the base for all pulse generation. A peak-to-peak detector serves as an inhibit monitor for the standby clock and also provides a telemetry signal indicating whether the oscillator is operating or nonoperating. This circuit has been temperature-qualified as a breadboard using 0.2-μsec (nominal) clock pulses.

The remaining circuits of the camera sequencer have been designed around 2 standard logic circuits: a flip-flop multivibrator and a *nor* gate.

The clock reference frequency is subdivided by a series of counter circuits in both the F and the P chains. Figure 16 shows the F-division chain and Figure 17 shows

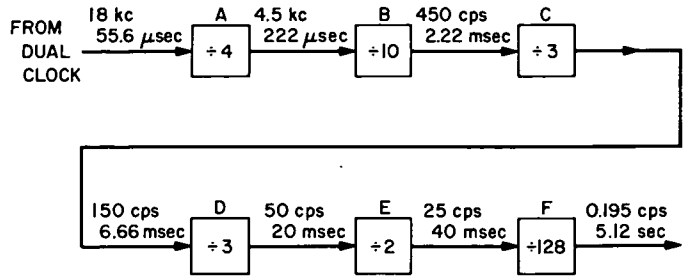

Figure 16. F-division chain

the P-division chain. The pulse widths and time durations required by the system are decoded by the F- and P-logic decoders. An example of this method of obtaining timing and synchronizing signals is the generation of horizontal synchronizing pulses. As shown in Figure 18, a pulse decoder gate is used, which recognizes 1 particular combination of flip-flops B, C, and D. The output will recur cyclically and the pulse width is determined by the number of inputs to the gate. The configuration requires no controls, has no time constant to take into consideration, and is not susceptible to system complexity.

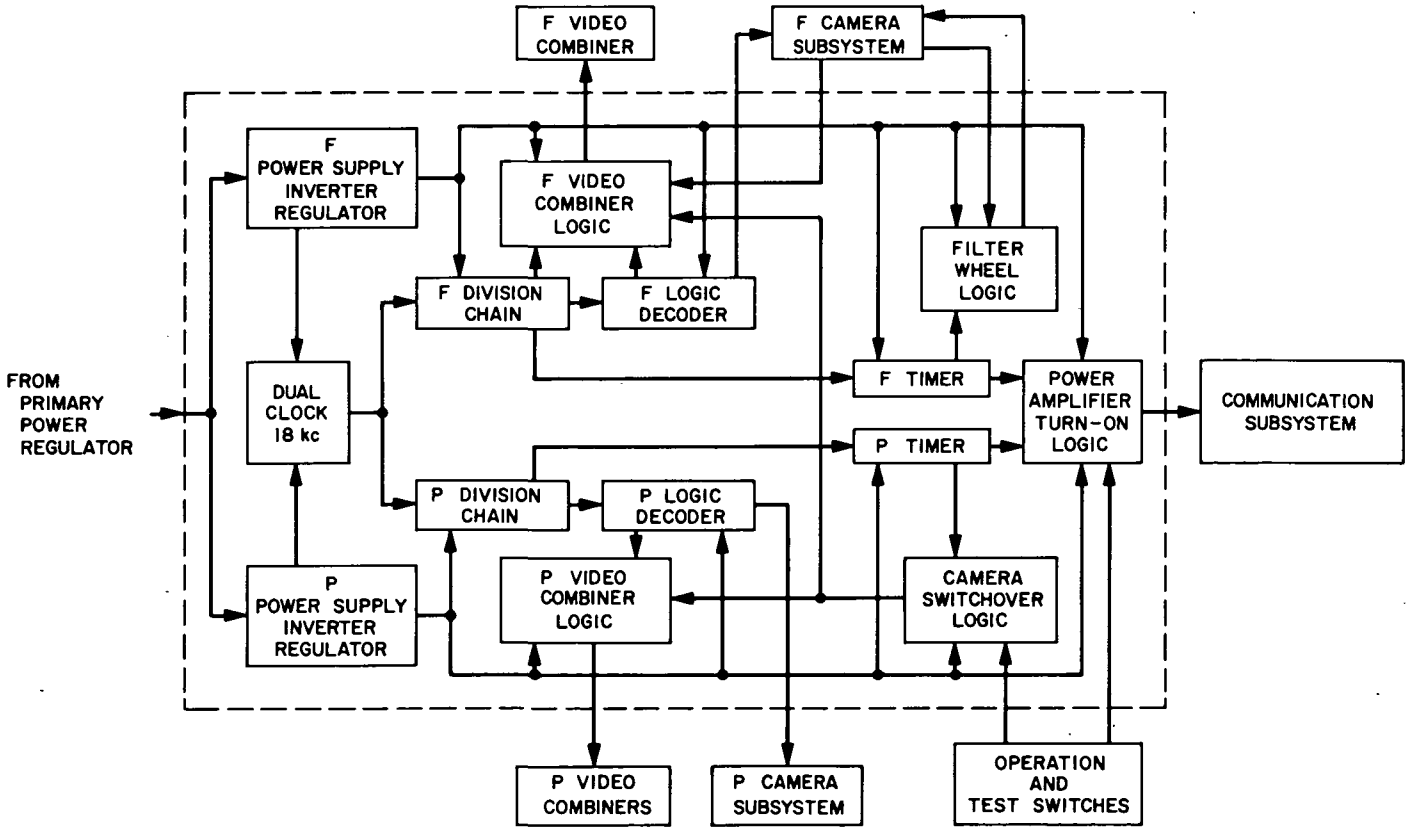

Figure 15. Control programmer and camera sequencer

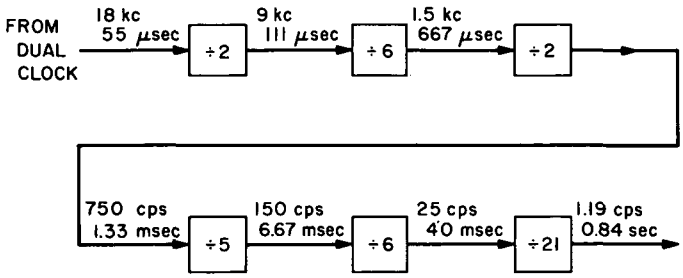

Figure 17. P-division chain

Figures 19 and 20 show times of occurrence and time relationships for the interface signals required for the camera control and summing amplifier. The camera sequencer controls the positioning of the Camera A filter wheel as shown in Figure 21. The first 2 stages of the F-division chain 5-min timer provide a 4:1 count of the Camera A fields. Each of the 4 filter wheel positions (red, green, blue, and neutral) is assigned to 1 of the 4 possible combinations of Counters A and B. An analog voltage representing wheel position is taken from a potentiometer arm linked mechanically to the filter wheel drive. This analog voltage is converted to a 2-bit digital representation for comparison with the A and B bits. During operation, when the A and B combination changes, the comparison circuit produces an output to the motor which drives the filter wheel until the input from the analog-to-digital converter is the same as the new A and B combination. Preliminary observations indicate that the changeover time from 1 filter to the next is less than 1 sec.

Video outputs from the 2 cameras of a set are summed by a video summing-mixing amplifier to provide modulation to the transmitter modulator. Video from each camera is applied to a summing amplifier through the analog gate. The gates are programmed by the sequencer. The analog gate preserves the dc level of the video signals and causes less amplitude distortion of the signals than would be caused by single-ended switches operating near cutoff. Preservation of the dc level is necessary because

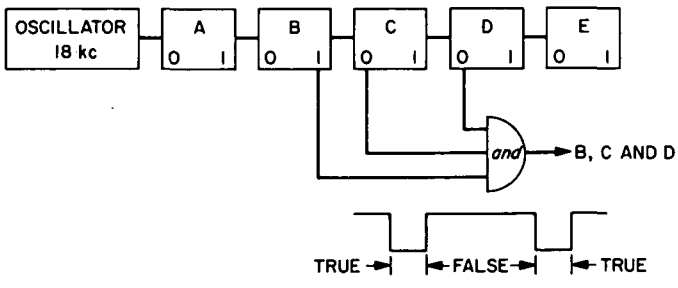

Figure 18. Horizontal synchronizing pulse derivation

any offset of the dc level introduced between the camera and the modulator alters the transmitter center frequency. Switching transients observed with this type of video switch are of the order of 30 to 50 mv at the diode bridge. Analog gates, having greater dynamic range, produce transients of the order of several volts, which could cause over-modulation, video spikes, false synchronizing pulses, and other spurious effects. The amplitude and frequency of transients measured in this circuit are of the order of 1% of the synchronizing pulse tip-to-peak white amplitude, and can be tolerated without difficulty. The switches have been operated over the full temperature range with less than 20-mv level change observed.

The basic summing amplifier consists of a medium gain differential amplifier with feedback for amplitude linearity and pass band control for FM pre-emphasis. Open-loop gain measurements indicate adequate gain stability over the temperature range; measurement of closed loop gain shows no measurable change from 10 to +65°C. The pre-emphasis characteristic of the amplifier is shown in Figure 22.

Use of a level control has resulted from the need for an optimum synchronizing pulse shape for best pre-emphasis utilization and the need for balance of the differential amplifiers. As it is now planned, this will be the only adjustment in the control programmer and the camera sequencer subsystem.

Three crystal-controlled oscillators are planned as the tone generator frequency sources. Tests of breadboards have indicated more than adequate frequency stability to satisfy the 0.1% accuracy required. However, final measurement cannot be made until crystals of the correct frequency are available. The 3 oscillators individually, and a fixed combination of all 3, give various summing amplifier inputs and allow the use of summing amplifiers that are nearly identical.

Design of the command switch has been accomplished by the electrical integration group, and a description of the operation of the command switch and associated relays is included in the electrical integration discussion of this report.

Relays are used at present in the control circuits of many of the *Ranger* TV subsystem assemblies. These relays control application of power applied to the assemblies. In some cases, 2 relays are used to accomplish power application.

Since electromechanical relays are considered inferior to solid state devices with respect to reliability, weight, and space consumption, the use of switching diodes to

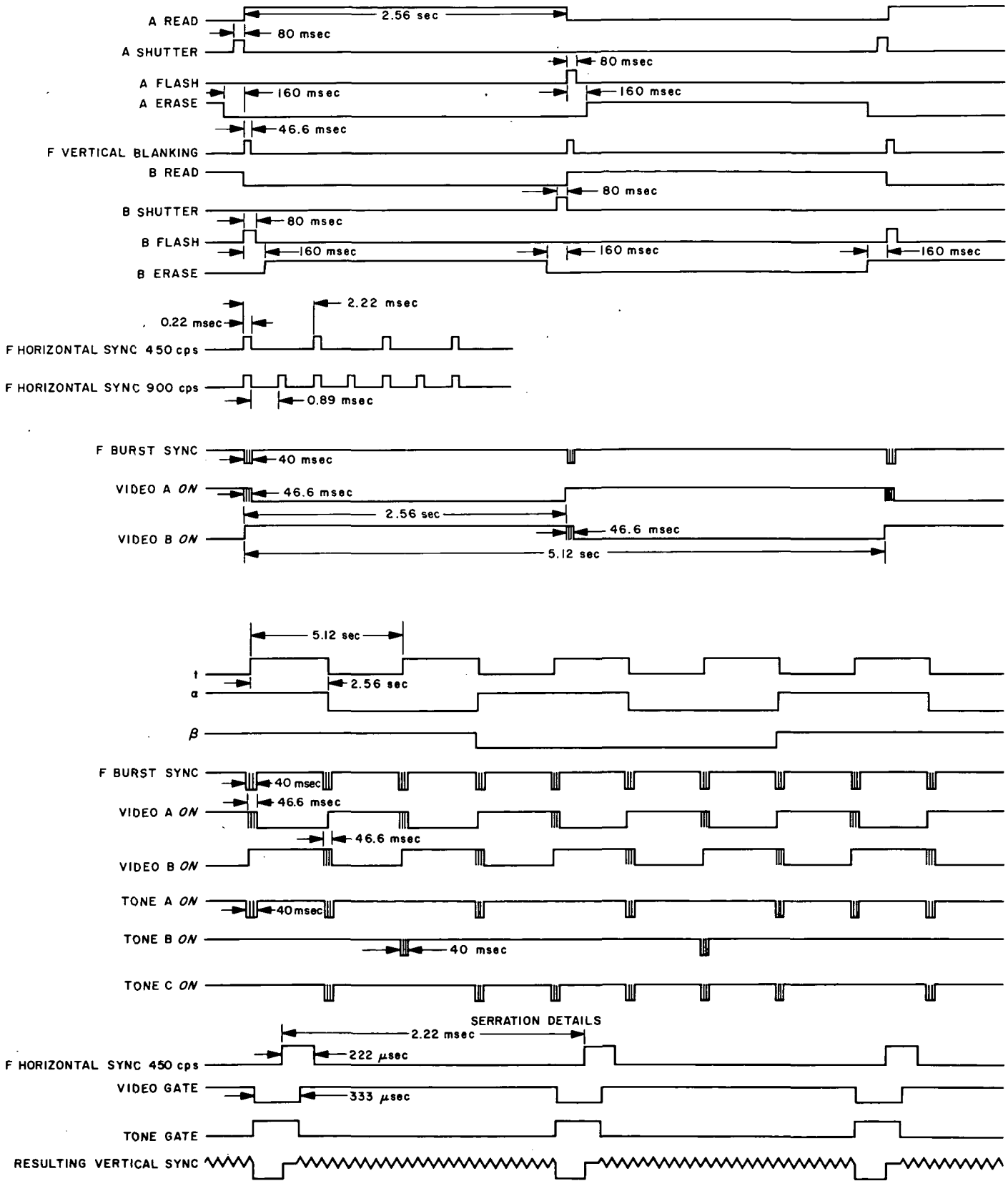

Figure 19. Type-F camera interface signals

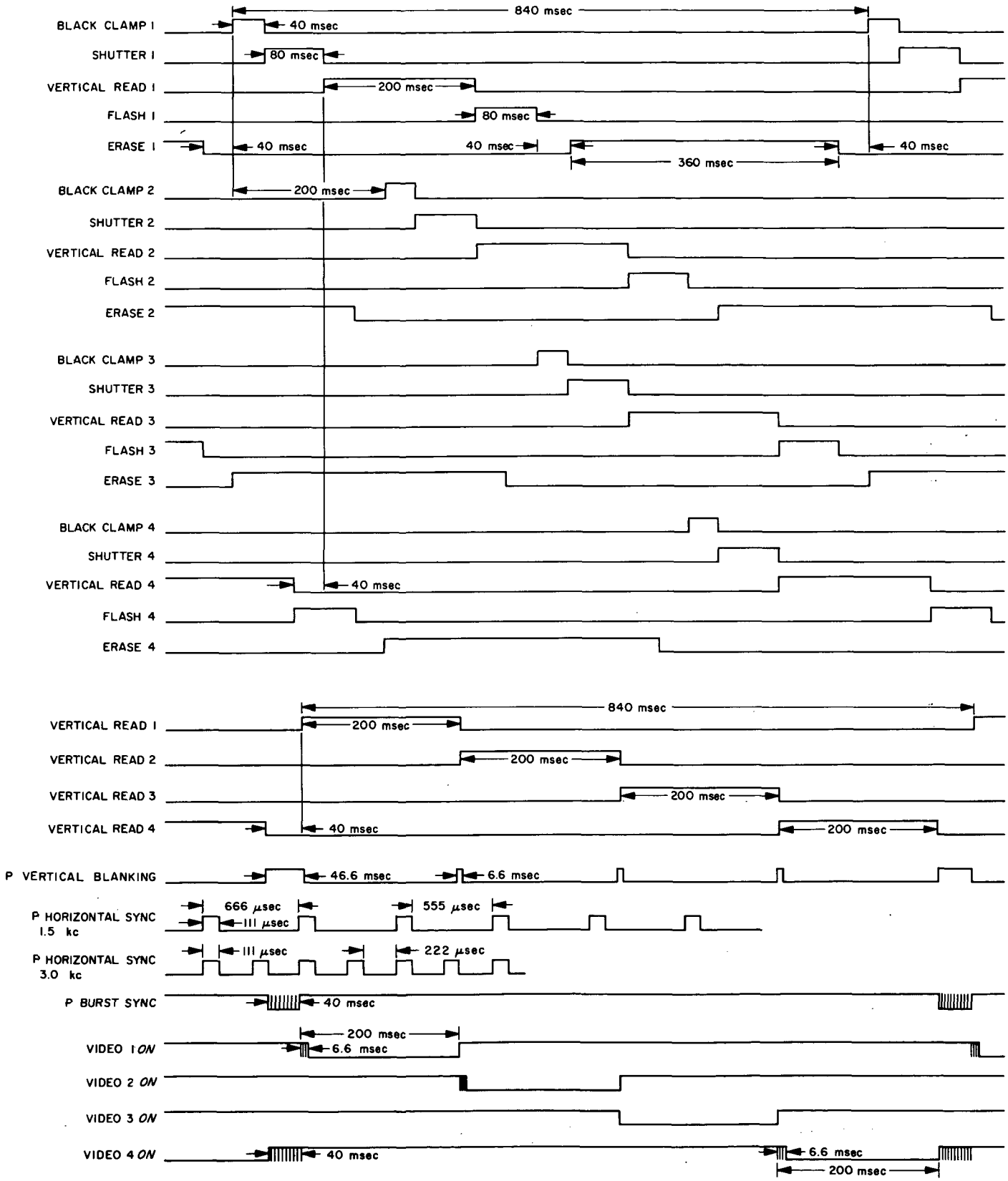

Figure 20. Type-P camera interface signals

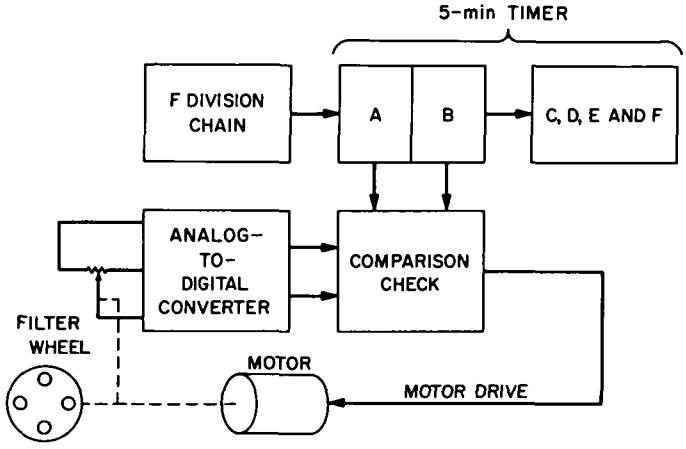

Figure 21. Filter wheel positioning circuit

replace certain of these relays is being investigated. A preliminary design is underway at present incorporating the diodes.

c. Communications and telemetry. The design approach to the *Ranger* television communications is to provide communication subsystem components for the transmission and reception of the multiplexed TV data and telemetry data. Specifically, these components consist of the following:

(1) Spacecraft telemetry components consisting of a 3-kc subcarrier oscillator (SCO), two commutators, two 235-kc SCO's, an ac amplifier, and a dc-to-dc converter.

(2) Spacecraft transmitter.

(3) Spacecraft power supply.

(4) Spacecraft communication system integration components such as junction boxes, control panels, etc.

(5) Ground telemetry components.

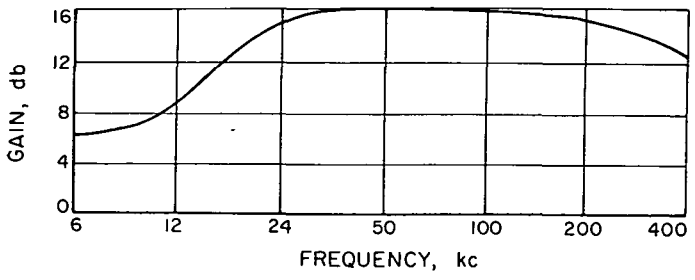

Figure 22. Summing amplifier pre-emphasis characteristic

(6) Ground receiver components including a 30-mc mixer, two 5.0-mc IF amplifiers, and two 0.5-mc IF amplifiers with automatic frequency control.

The current spacecraft and ground configurations are shown in Figures 9 and 23.

Modulator-exciters. The modulator-exciter schematic diagrams are shown in Figure 24. The design reflects the reliability requirements of design simplicity and the utilization of the minimum number of circuit components.

The frequency stability measurement on the 1st uncompensated breadboard of the circuit have been within ±0.003% for the 0 to 50°C range. This employed the use of a series resonant 20.819444-mc crystal. The order has been placed for 20-mc crystals having ±0.0005% stability under temperature.

Temperature compensation is being performed on the oscillator circuits and it appears that the 0.001% requirement may be met without the use of a crystal oven.

Frequency deviation requirements for the modulator have been met with less than 2% distortion of the modulating signal. With the transmitter operating frequency in the vicinity of 960 mc and the base exciter frequency at 20 mc, a total frequency multiplication of 960/20 = 48 must be accomplished in the multiplier chain. Thus for a total frequency deviation of 400 kc at 960 mc, the deviation requirement of the 20-mc oscillator is 400/48 kc = 8.33 kc or approximately ±4.2 kc around the center frequency.

The curve of Figure 25 shows the total deviation capability of the circuit and Figure 26 shows an expansion of the curve around the proposed bias point. Figure 26 points out the linear relationship between frequency and modulating signal which has a total permissible distortion of less than 2% for modulating signal (sine wave up to 600 kc with flat response) magnitudes which produce total deviations up to 9.5 kc.

The distortion measurements were made by ac coupling an audio signal into the varicap circuit at Test Point A. Modulation frequency response was measured from 2 to 600 kc with less than 1-db change in total deviation, for a modulating signal strength which produced a total deviation of 9.5 kc.

The establishment of the modulator amplifier interface with the video and telemetry inputs has not yet been completed. As such, design effort in this area is limited. The RF section is shown in Figure 27. The output signals from the modulator-exciters at 240 mc are fed to the ×4

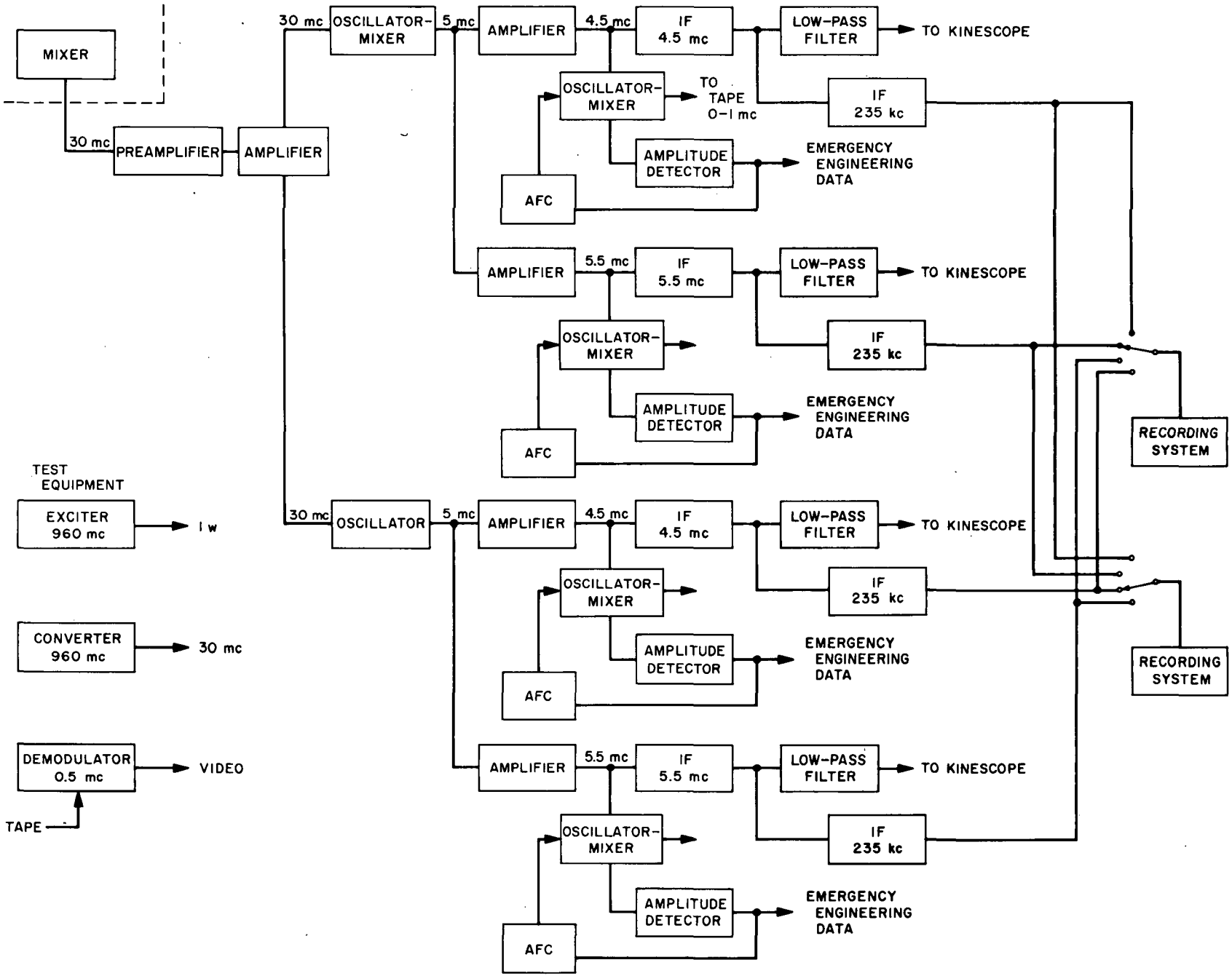

Figure 23. Goldstone receiving setup

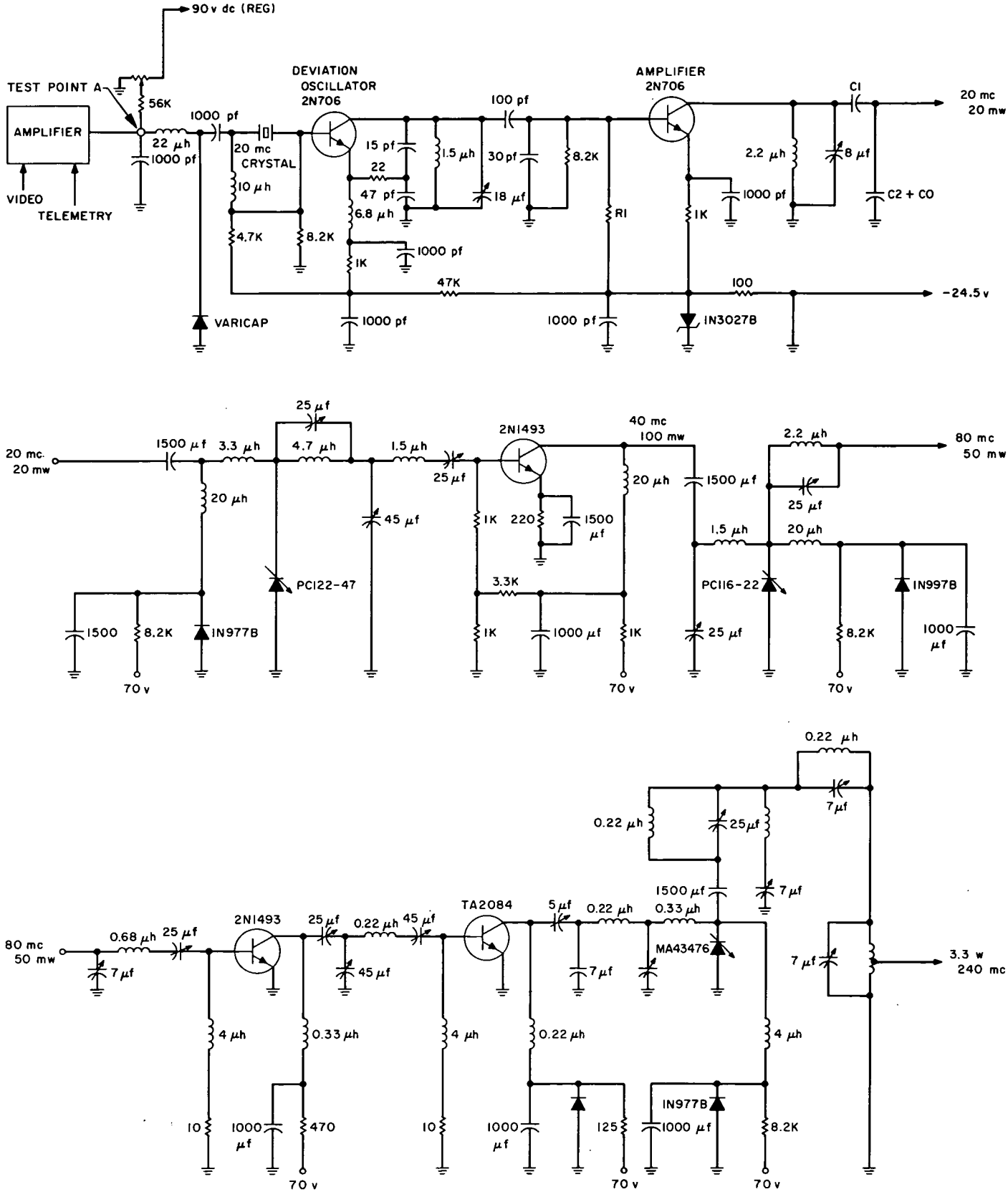

Figure 24. Modulator–exciter

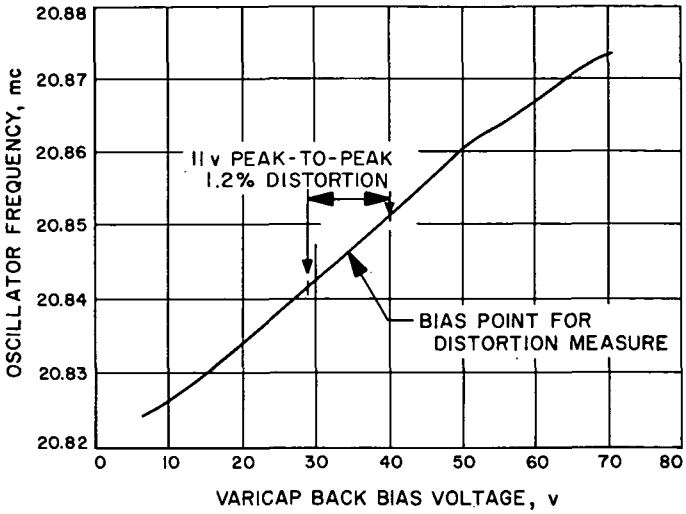

Figure 25. Modulator deviation characteristic

varactor multipliers. The 960-mc output of the multipliers drives the vacuum tube intermediate power amplifier (IPA). The 7-w output of the IPA drives the 60-w power amplifier.

At this point, the signals from the 2 chains are combined in a 4-port coaxial hybrid ring, which provides 20-db isolation between the 2 chains with an insertion loss of 3 db. This loss, 30 w per chain, is absorbed in a dummy load. The output from the hybrid ring is combined in the directional coupler with the 3-w signal from the bus transmitter.

The directional coupler provides 30-db isolation between the 2 signals with insertion losses of 10 db for bus transmitter inputs and 0.5 db for the TV. The RF signal then enters a 3-port ferrite circulator from which (at a 0.5-db insertion loss) the power is fed to the directional antenna. Reverse power, as a result of antenna mismatch, will be dissipated in the dummy load associated with the ferrite circulator. The total insertion loss from power amplifiers to antenna (assuming an antenna VSWR of 1.0) is 4.0 db, providing 24 w per transmitter at the antenna.

The over-all chassis drawings for the modulator-exciter have been completed. Connectors for the modulator-exciter have been ordered and fabrication of the chassis is in process.

Minor changes have been made in the ×12 multiplier because of packaging requirements in the modulator–exciter chassis. Drawings for the ×12 multiplier, the ×4 multiplier, and the 7-w amplifier have been released to the model shop, and fabrication of all 3 units is proceeding.

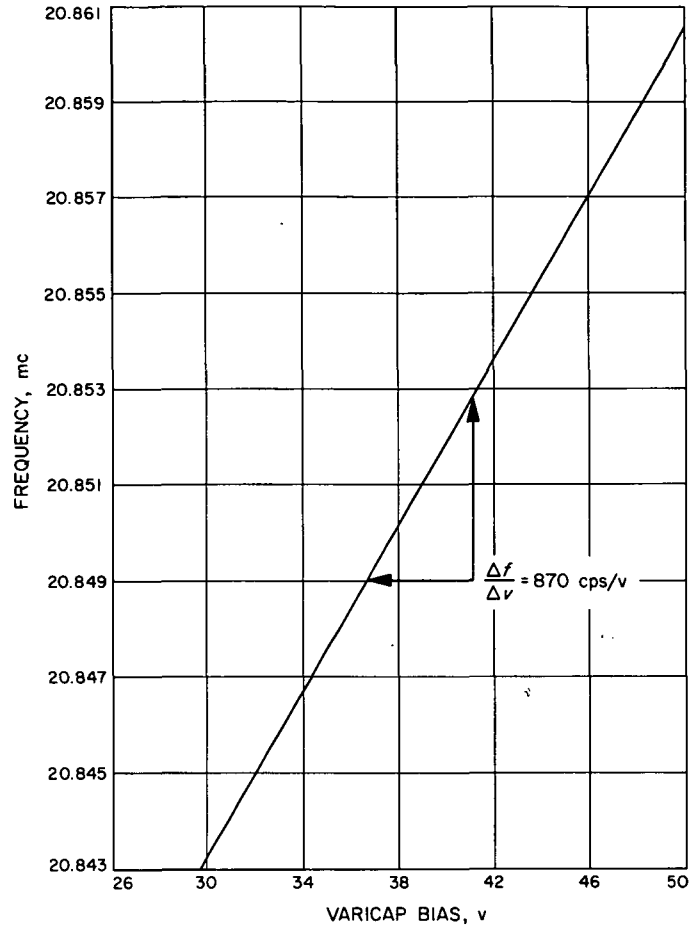

Figure 26. Modulator deviation expanded plot

Temperature and vacuum tests have been conducted on the 60-w power amplifier with favorable results.

Power supplies. The preliminary design on 2 power supplies, a 150-w unit and a 15-w unit, has been completed. However, changes in the over-all TV payload design have imposed significant changes in the 150-w unit. This unit was to have supplied 1000, 250, and 100 v outputs from a double-transformer, solid state converter operating from −27.5 v.

The changes to both voltage and current requirements require replacement of the 150-w unit by 2 units of 190- and 390-w, each with an operating frequency of approximately 2 kc. The 190-w unit will supply 500 v at 100 ma, 300 v at 50 ma, 100 v at 300 ma, 6.3 v ac at 1 amp, and 6.3 v ac at 8 amp. The 390-w unit will supply 1250/1000 v at 250 ma. These 2 power supplies will be housed in a single case and shielded to reduce effects of stray magnetic fields.

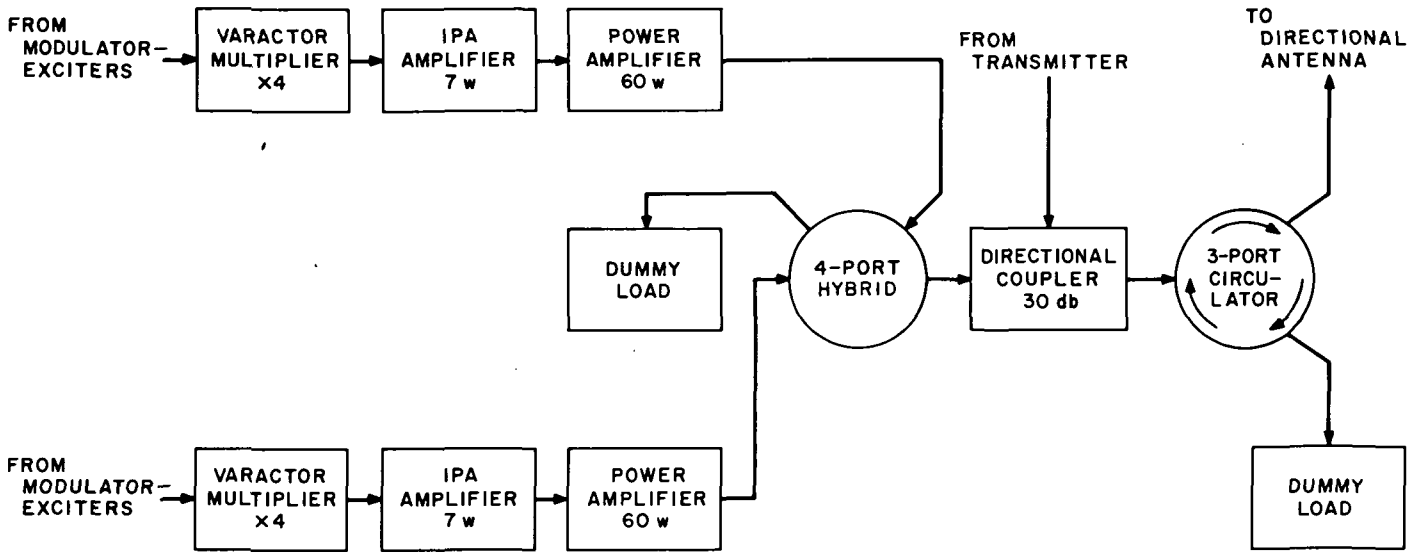

Figure 27. RF section

The 15-w unit will be housed in a separate shielded case. This unit is to supply 27 v regulated at 500 ma. This is a single transformer, solid state converter design, with an operating frequency of 2 kc. It operates from −27.5-v dc primary power. Preliminary design on the larger 2 unit power supply has been started. Mechanical design of the 15-w unit is underway.

Telemetry. The spacecraft and ground telemetry components are presented in Figures 28 and 29.

The communications system analysis has been made for the carrier-to-noise ratio, picture signal-to-noise ratio, and tone code signal-to-noise ratio. An analysis of the effects of using pre-emphasis to gain an improvement in signal-to-noise ratio for video transmission has been made.

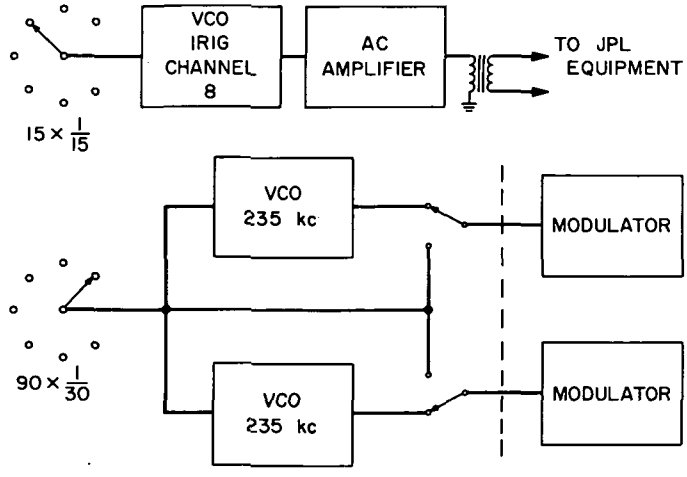

Figure 28. Telemetry flight equipment

d. Primary power.

Batteries. The *Ranger* TV subsystem power supply will consist of 2 silver–zinc storage battery units which will feed a common series-type voltage regulator and furnish a regulated output of 27.5±0.5 v. Each of the individual battery packages will be capable of furnishing the total payload energy requirements as determined by the mission power profile, improving the over-all reliability of the system. In addition to the batteries and voltage regulators required for the payload power supply subsystem, battery chargers and external power supply units will be required for the development, testing, and checkout of the payloads.

Each battery unit will consist of 22 series-connected, silver–zinc, electric storage cells. The batteries will be hermetically sealed; each 22 cell unit will be mounted in a stainless steel or anodic magnesium case. The individual cells will be matched for voltage and current characteristics, and will be constructed to minimize battery degradation due to electrolyte evaporation, separator deterioration, internal short circuits, and heat dissipation. The battery units will be rechargeable for ground payload operation and testing, but will operate in a single-shot mode during the actual mission. Weight of the battery unit, consisting of the 22 cells and the mounting case, will be approximately 43 lb. Each unit will occupy a volume of about 1000 in.^{2}. There will be 2 parallel battery units incorporated in each payload. The 2 units will feed a common voltage regulator, and will be separated by diode isolators to prevent a malfunction in 1 battery unit from affecting the performance of the other unit.

A systems test set of batteries and a flight set of batteries will be provided with each payload. The systems test set of batteries will be used to furnish internal power during the integration and testing of the payload, and will be recharged as required during testing. The flight set of batteries will be inserted after the completion of the final systems tests, and before the payload is mated with the *Ranger* spacecraft, in order to minimize the accumulated test time on the flight units. Each battery unit will have a rated nominal capacity of greater than 1800 w-hr with a 200-w-hr margin of safety, and will be capable of furnishing the total energy requirements for the payload mission.

The problem of assuring the internal and external sterility of the battery units will be considered in design of the batteries and selection of the battery mounting locations in the payload structure. The feasibility of thermally sterilizing the dry batteries as a part of the complete payload, and subsequently inserting a sterile electrolyte will be investigated. If design of the batteries precludes thermal sterilization, it is planned to thermally sterilize the payload without batteries, and subsequently insert the batteries in a sterilizing gas environment to ensure sterilization of the mating surfaces between the battery container and the structure. However, the use of liquid surface sterilants may be applied to the battery mating surfaces and the process of attaching the batteries to the structure in a sterilizing gas environment will be avoided.

The Electric Storage Battery Company (ESB), Missile Battery Division, Raleigh, N. C. was selected to supply the batteries. ESB conducted tests on *Ranger* cells to determine the design requirements. Figure 30 shows a plot of current density vs cell voltage at 50°F. The points for the curve were obtained during the final 20% of cell

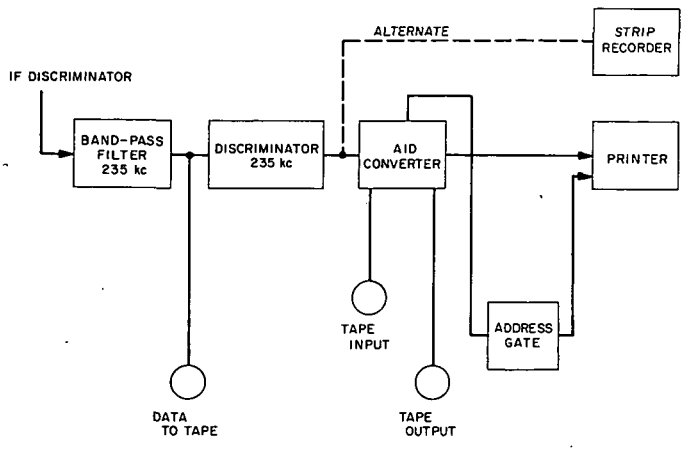

Figure 29. Ground station engineering telemetry

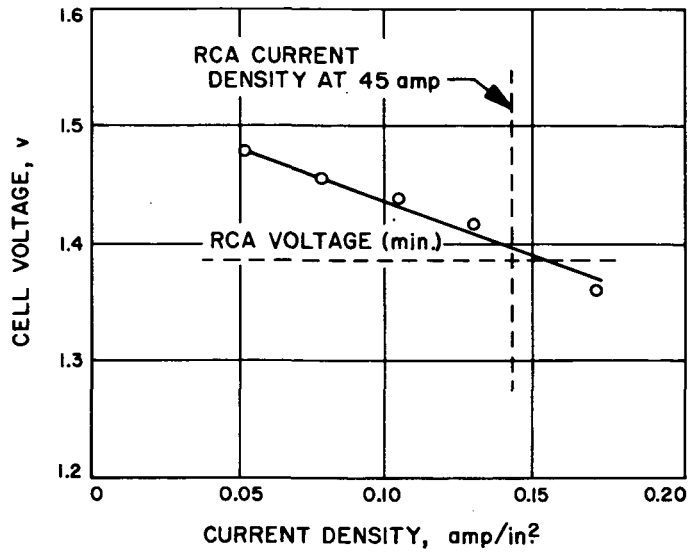

Figure 30. Voltage vs current density for battery cells

capacity. A preliminary design by ESB (based on an RCA spec) indicated that 21 cells could not supply the required terminal voltage. The design has been changed from 21 to 22 cells.

A sensitive differential amplifier will be used as the error detector. One input to the differential amplifier will be provided by a temperature stabilized voltage reference zener diode driven by the constant current generator. The other input to the differential amplifier will be derived from the unregulated bus voltage error applied through a resistive voltage divider network. The series regulating power transistor circuit will consist of several matched transistors. These transistors will operate in parallel in order to ensure proper load sharing and adequate maximum power transfer.

The external power supply and battery charger units will be adaptations of existing commercially available equipments.

Voltage regulator. A series-type voltage regulator will be used to provide -27.5 ± 0.5 v. There will be 2 batteries supplying the unregulated power and the power to the regulators. The maximum battery terminal-voltage variation that can be expected is from -41.5 to -30.5 v dc. The TV transmitters and camera shutters will operate from unregulated battery voltage to reduce the current drain on the regulator. A reduced current drain will result in reduced size and weight of the regulator.

The battery-regulator interconnection diagram is shown in Figure 31. Diodes D1 and D2 will become reverse biased if either battery develops an internal short, and

CONFIDENTIAL

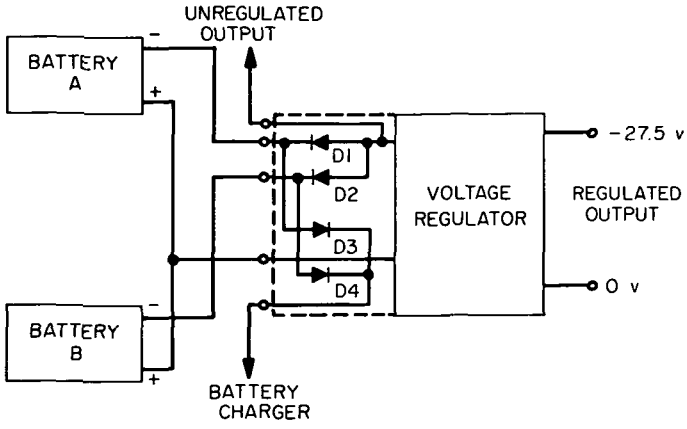

Figure 31. Battery regulator interconnection

will thus prevent the other battery from discharging into the shorted battery. Diodes D3 and D4 are used in the battery charging circuit of the umbilical cord. This circuit will be used to charge the batteries at the time the batteries are mounted in the payload, and again when the payload is on the mounting pad. If the umbilical cord or its connector to the payload should be shorted, diodes D3 and D4 would become reverse biased and prevent discharging of the batteries.

The breadboard circuit is shown in Figure 32. The low power Transistors Q1 through Q4 are mounted on the terminal board, and the driver Transistor Q5 and series-regulating Transistors Q6 and Q7 are mounted on the heat sink.

Transistors Q1 and Q2 are connected as a differential amplifier to perform the function of error detector. One input to the error detector is a reference voltage of −8.4 v obtained from the reference zener Diode D1. The other input is a fraction of the regulated output voltage obtained from the R1, R2, and R3 voltage divider. R3 is used to adjust the output voltage to exactly −27.5 v dc. Any variation of the output voltage resulting from load changes or input voltage changes will cause the error detector to amplify the difference between the reference voltage and the changed fraction of the output voltage.

The error detector output is a differential signal which is connected to another differential amplifier stage consisting of Transistors Q3 and Q4. This stage amplifies the output of the error detector and, in turn, drives the driver Transistor Q5.

The connection of the driver Transistor Q5 and the parallel-output series-regulating Transistors Q6 and Q7 has the advantages of high gain and no shunt current to ground. By reducing the shunt current to ground to a minimum, a high efficiency is maintained for the regulator when the output load current is low. Capacitors C1 and C2 are used to control the high frequency gain and phase shift of the error amplifier to prevent high frequency oscillations.

The regulation characteristic of the breadboard circuit is shown in Table 24. The input voltage was varied from −30 to −40 v dc, and the load current was varied from 0 to 5.0 amp. Also given is the variation in millivolts of the regulated output voltage from −27.500 v dc. The performance of the regulator with respect to regulation is more than adequate to meet the specified output-voltage variation of ±0.5 v dc.

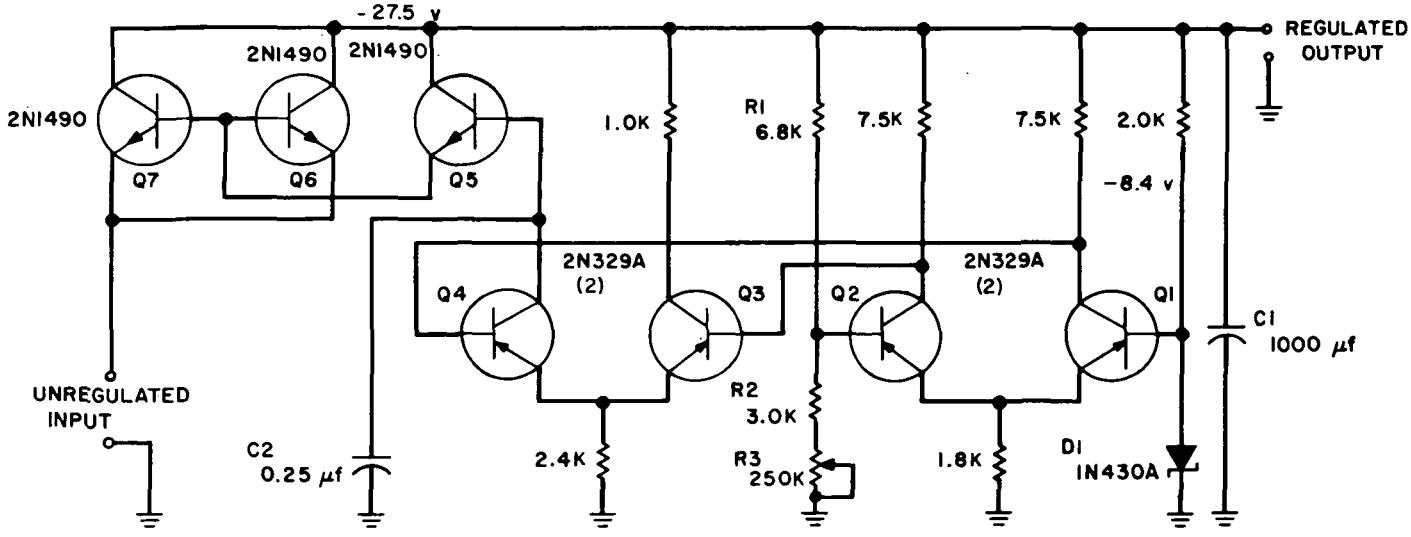

Figure 32. Voltage regulator breadboard circuit

CONFIDENTIAL

The regulator circuit breadboard was placed in a temperature chamber and performance was measured at temperatures from 0 to 72°C. Data obtained from this temperature run is shown in Table 25. The input voltage to the regulator was maintained constant at −33 v dc, and the load current was varied from 0.0 to 5.0 amp. Table 25 lists the regulated output voltages for the different load and temperature conditions. A total change in the output voltage of 0.25 v dc, which is well within the regulator specification requirement, was obtained on this temperature run.

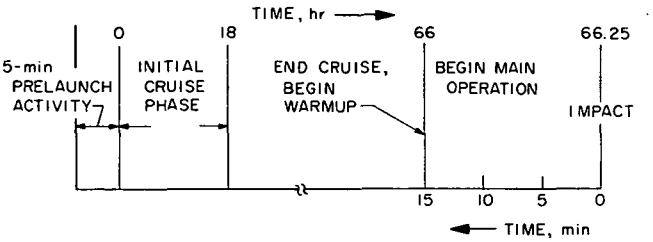

Figure 33. Major power draining periods

Table 24. Regulator output variations for different input and load conditions

Input voltage, v	Load current, amp					
	0.0	0.13	0.5	2.2	4.0	5.0
	Regulator output, mv					
−30	9.5	4.5	3.0	2.0	−2.0	−5.0
−32	9.5	4.5	3.0	2.0	−2.0	−5.0
−36	10.0	5.0	3.0	2.5	−1.5	−5.0
−40	9.5	5.5	4.5	3.0	−1.0	−4.0

Table 25. Regulator output voltage for different load and temperature conditions

Temperature, °C	Load current, amp				
	0.0	0.15	0.55	2.3	4.0
	Regulator output, v				
0	25.5	25.5	25.5	25.5	25.5
10	25.5	25.5	25.5	25.5	25.5
25	25.5	25.5	25.5	25.5	25.5
51	25.6	25.6	25.6	25.6	25.6
60	25.7	25.7	25.7	25.7	25.7
72	25.75	25.75	25.75	25.75	25.75

Mechanical design work has begun on a package for the regulator and blocking diodes. It is planned to keep the weight of the regulator to less than 1.5 lb, and to fit the regulator into a space 1.5 in. high by 3 in. wide by 5 in. long. Measurements will continue on the breadboard to further prove its performance.

Power profile. The total power-drain profile for the *Ranger* TV subsystem has been modified in accordance with the new payload operational sequence and subsystem requirements. Figure 33 shows the major power-draining periods for the new sequence.

The new total energy required is approximately 896 w-hr. This is based on the requirements of the clock and sequencer, voltage regulator, cameras, communications, and telemetry units for the entire mission. Regulated and unregulated power required by individual units during each of the major periods of the mission is given in Table 26. The total power profile is shown in Figure 34.

Ground battery-charger and monitor (launching-pad area). The purpose of the ground battery-charger and monitor of the launching-pad area (Fig 35) will be to maintain the full-charge capacity of the flight batteries when power drain during prelaunch test is continued for

Table 26. Power drain breakdown in watts

Subsystem	Prelaunch		Cruise				Warmup		Operation	
	5 min		0 to 18 hr		18 to 66 hr		15 to 10 min		10 to 0 min	
	R[a]	U/R[b]	R[a]	U/R[b]	R[a]	U/R[b]	R[a]	U/R[b]	R[a]	U/R[b]
Communications and telemetry	33	362.5	0	0	9.2	0	33	273.6	33	599
Clock and sequencer	45	0	0	0	0	0	45	0	45	0
Voltage regulator	0	0.7	0	0.7	0	0.7	0	0.7	0	0.7
Camera	60	0	0	0	0	0	60	0	60	0
Totals	138	363.2	0	0.7	9.2	0.7	138	274.3	138	599.7

[a]R = regulated.
[b]U/R = unregulated.

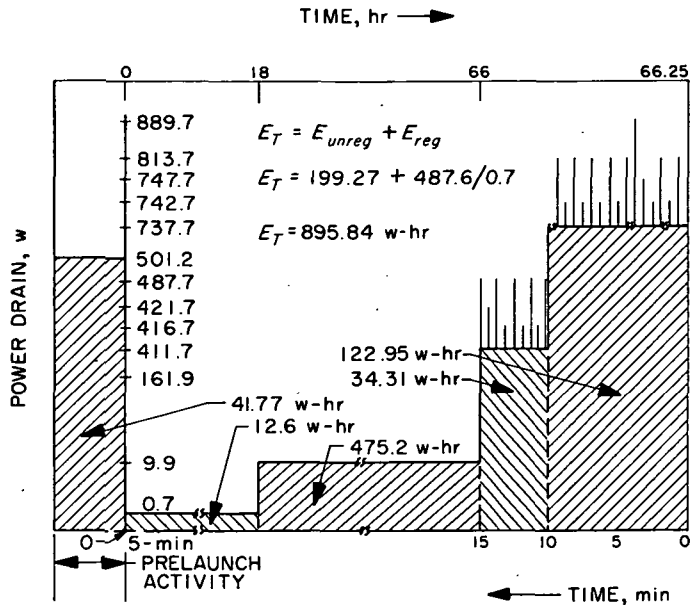

Figure 34. Total power-drain profile

an appreciable time. Since battery charging should not take place while the payload equipment is operating from the battery, the test procedure will make provisions to prevent charging during the prelaunch tests.

Ground power supply charger and monitor (service area). The ground power supply charger and monitor of the service area (Fig 36) will have a threefold purpose:

(1) To monitor the terminal voltage of each battery and to regulate battery charging by means of voltage sensing.

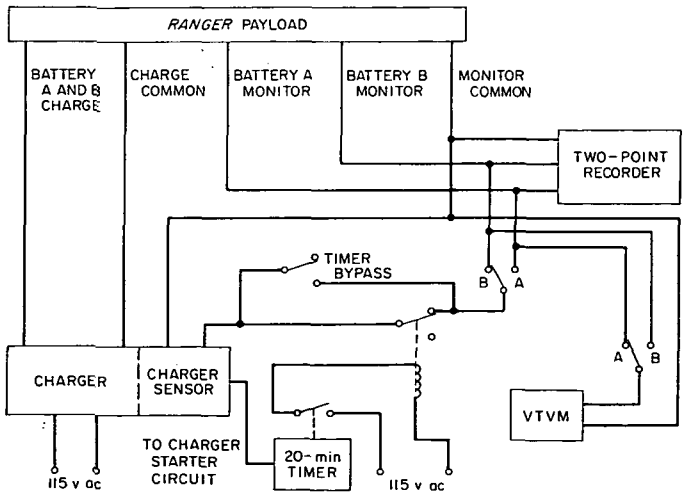

Figure 35. Ground battery charger and monitor, *launching pad area*

(2) To monitor individual cell voltages by selection and to also indicate continuously the temperature of each battery.

(3) To supply external power for payload equipment when desired.

An external power supply will supply 0 to 40 v for powering the payload equipment when it is not desirable to use battery power. An external–internal power relay will select either battery power or power from the external power supply for powering the payload equipment. This relay will be part of the test cable and will not be flown. The relay will be actuated by manually operating an external–internal power-select-switch. The same switch acts as a safety feature by turning off the charger when internal battery power is selected. The 27.5-v supply will power the thermistor circuitry and the external–internal power relay.

All connections for battery charging and sensing will be made through the payload umbilical cord; all connections for measuring cell voltages and battery temperatures will be made through two 25-wire plugs.

Battery and voltage-regulator bench test load. In order to test the battery and voltage regulator power capabilities, a test load was designed. The bench test load (Fig 37) will enable any flight power profile to be simulated. This will be done by means of 4 continuously-variable load ranges: (1) 0.06 to 0.55 amp, (2) 0.55 to 2.8 amp, (3) 2.5 to 10.0 amp, and (4) 8.2 to 47.0 amp. A panel-mounted current meter will be supplied for each load branch; battery terminal voltage will be continuously measured by an external meter.

6. Thermal Control

A detailed thermal analysis, to determine a continuous temperature–time history of the electronic modules throughout the mission, was initiated and is continuing. There are 3 separate computer programs being used to analyze configuration, radiation-coupling factors, and mission temperature–time histories.

Thermal analysis directed toward a passive thermal control technique is being made. The primary design parameters of such a system are:

(1) Location of the electronic modules within the spacecraft.

(2) Emissivity and solar absorptivity of all exposed surfaces.

(3) Mass available for thermal heat sinks.

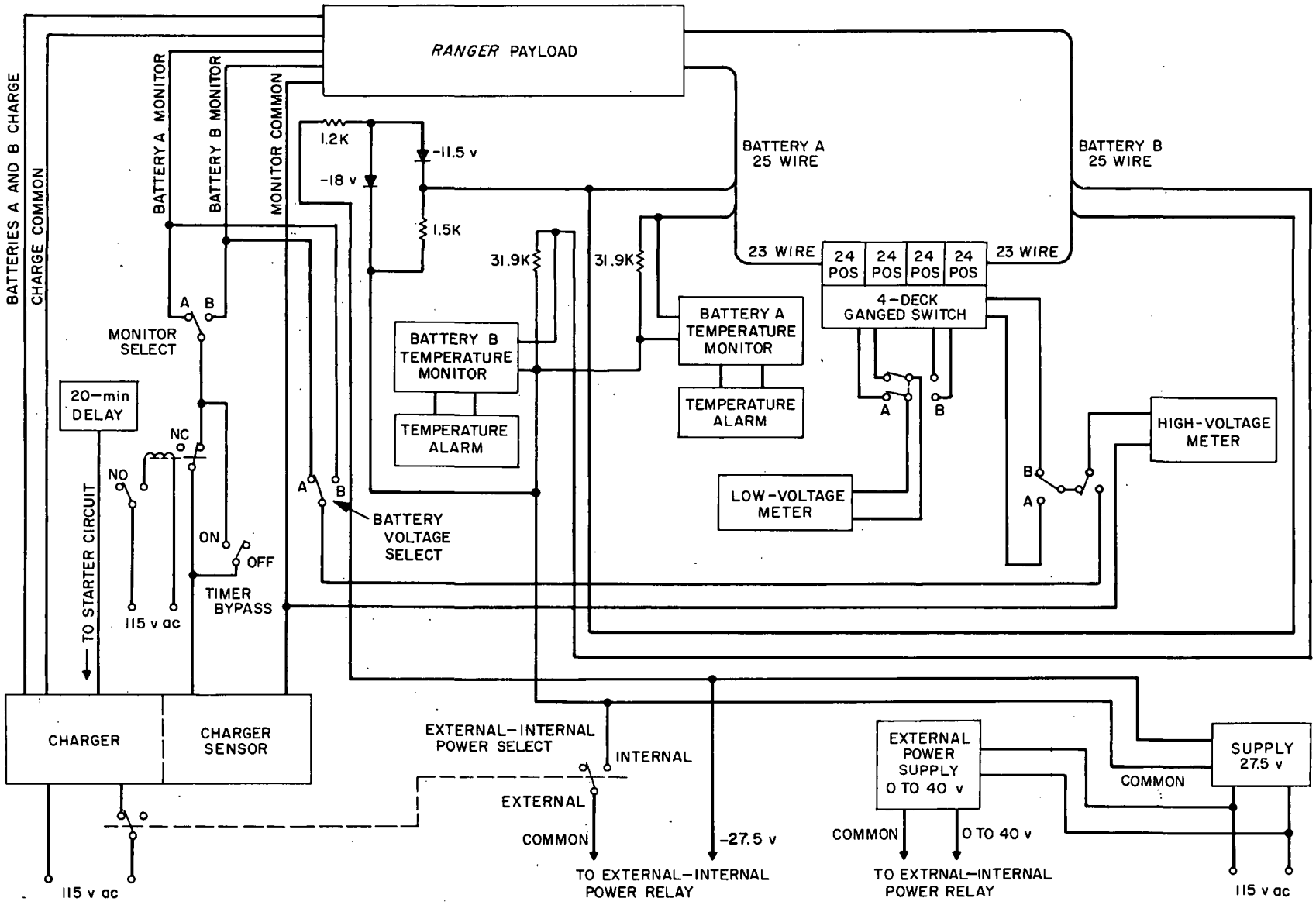

Figure 36. Ground power supply and monitor, service area

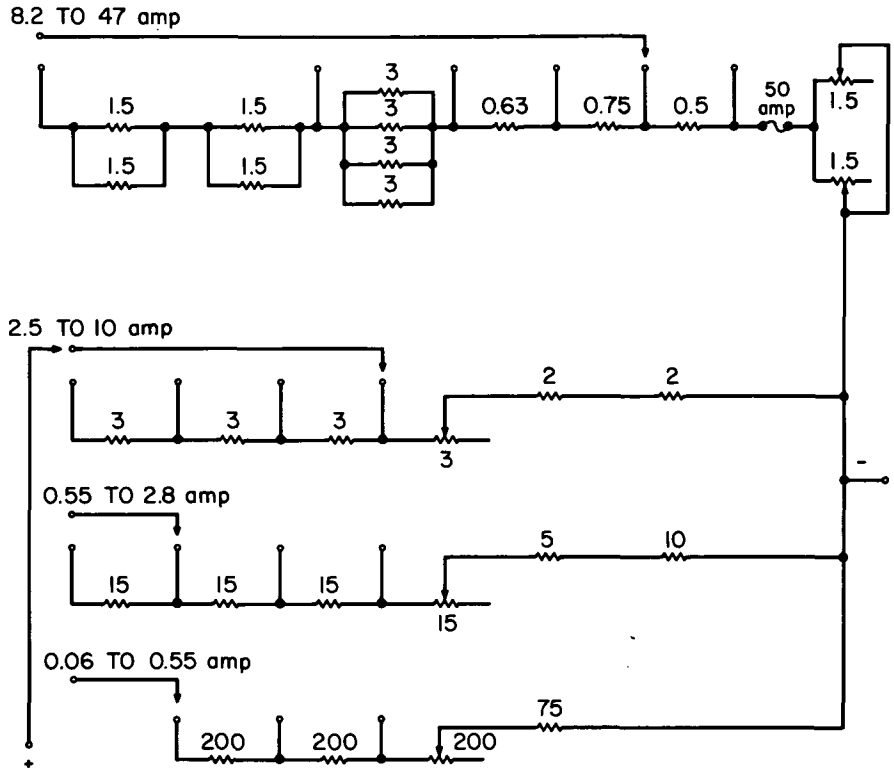

Figure 37. Battery bench test load

The *Ranger* TV subsystem consists of electronic modules that are in operation during limited time periods. Detailed examination of the modules indicates that there will be high thermal dissipation in some modules and little thermal dissipation in others. For this reason, the modules cannot be treated as a gross isothermal body, but must be treated as individual units, and a temperature–time history predicted for each unit. Temperature–time histories will be predicted for the following modes of flight:

(1) 100-nm parking orbit.

(2) Passage through the Earth's shadow.

(3) Solar-oriented cruise (1st phase).

(4) Mid-course maneuver.

(5) Solar-oriented cruise (2nd phase).

(6) Terminal camera orientation mode (1-hr duration).

(7) Terminal equipment warmup mode (5-min duration).

(8) Terminal operational mode (10-min duration).

The over-all result of the thermal analysis will be a continuous temperature–time history of appropriate electronic modules from launch to impact on the Moon.

Three machine programs are being used to analyze the system. A program has been developed for the IBM-709 computer to evaluate configuration factors using the principle of contour integration. The 2nd program, for analog computing equipment, evaluates radiation-coupling factors, which are a function of surface emissivities, module areas, and configuration factors. An RCA-501 computer will be used to compute temperature–time histories of the modules. The program for this computer is designed for solution of the temperature–time dependence of a 30-day body system, with each body exchanging energy with all other bodies by radiation and conduction.

Considerable design effort is required to evaluate the radiation-coupling factors, conduction-coupling factors, and effective thermal mass for each module. The temperature–time forecast is dependent on the accuracies of these factors, and in view of the complex geometry of the capsule, effective evaluation of these factors can only be obtained from testing of a thermal model. A detailed thermal model is being constructed for testing. The model will closely approximate a flight payload. It will be struc-

turally accurate and contain modules that simulate the electronic modules in size, weight, placement, and thermal dissipation. The model will be placed in a vacuum chamber capable of simulating external energy flux by infrared radiation at pressures of 1×10^{-4} mm Hg or lower. After necessary design information has been obtained, a solar-simulation test should reveal any thermal design problems that might exist, in time to permit solutions for the proof test model.

A problem associated with thermal design is the evaluation of contact conductance between mating surfaces. Contact conductance between electronic modules and structural mounting areas approaching that of solid metal is desirable in order to minimize thermal gradients. A literature search was initiated to determine what materials might be applicable. The conclusion was reached that all mating areas should have specified flatness deviation and surface roughness characteristics. If a particular module must be removable from the structure, either a soft aluminum shim, silicon grease, or other appropriate materials will be used between the interfaces. For fixed modules, thermally conducting epoxies will be applied to form a solid mechanical bond. Mechanical attachments for the modules will be designed to provide a high, uniform contact pressure at the interfaces for removable units.

A study has been conducted to determine an analytical expression for conduction coupling. The first model investigated consisted of 2 heat-dissipating bodies, mounted to an infinite, insulated plane. The model configuration was mapped, by means of complex variables, to a plane where the boundaries of the bodies appear as concentric rings, a situation for which the conduction equation can be easily written. By using the appropriate complex mapping function, the conduction equation was written for the model, and an effective conduction coupling factor was obtained. The model was extended to include many bodies on a plane, with radiation exchange from the surface. It is anticipated that the results of this study will provide realistic conduction-coupling factors for the machine program.

Design of the thermal model and proof test model test facility was initiated. It is planned to use lamps to simulate incident solar energy on the capsule. A test fixture is under development to provide a variable, uniform intensity on appropriate surfaces.

Results are listed in Table 27 of the preliminary calculations to determine magnitudes of thermal mass needed to minimize terminal temperature rise. The results indicate that many modules are sufficiently massive to require no additional heat sink. However, a few units are low in weight and have high dissipation densities; additional heat sink material is required for these units. Change-of-state materials with favorable thermal properties (wax in particular) are being investigated for use as additional lightweight heat sinks.

Temperature sensors for the spacecraft have been designed using the following system parameters:

(1) Supply voltage, 27.5 v.

(2) Output voltage range, 0 to −5 v.

Table 27. Preliminary estimate of effective heat sink weight required to hold impact temperature below 60°C[a]

Component	Size, in.	Power dissipation, w			Component weight, lb	Additional heat sink weight required[a]	Cruise temperatures, °C		Temperature at impact, °C
		Cruise	Warmup	Operation			Before cruise, power on	With power on	
A26 telemetry	12×5¾×5¾	5	12	12	10	0	0	6	27
A16 power supply	8×6×4	0	10	75	11	0	0	6	30
A14 transmitter	8.76×5.75×2.5	0	0	90	4	0	0	6	52
A15 amplifier	5⅛×2¾×2½	0	7	70	1.1	0	0	6	108
						1.9	0	6	53
A24 4-port hybrid	6½ D×1¾	0	0	5	1.5	0	0	6	31
A25 dummy load	1×1×14	0	0	60	2.5	0	0	6	53
A17 power relay	3×3×2.7	0	14	14	0.9	0	0	6	58
A10 battery	7.33×16.7×6	2	30	120	44.2	0	0	6	24
A12 regulator	3×5×1.5	5	73	84	3	0	0	6	73
						1.0		6	60

[a]Based on weight of aluminum.

(3) Subcarrier oscillator input impedance
Cruise, 500 K.
Terminal, 1 megohm.

It was determined that 2 temperature ranges would be adequate for monitoring all of the desired temperature test points. The ranges chosen are −10 to 65°C, and −10 to 100°C.

7. Subsystems Integration

Electrical. The design concept has been established for command switching of the TV subsystem by real time command (RTC) signals from the spacecraft bus. The purpose of this switching is to set the TV subsystem into different modes of operation required by the mission sequence of events.

Figure 38 shows the circuits and interconnections used for mode switching. Switching is accomplished by means of a rotary stepping switch that advances 1 position for each RTC signal received, and relays that are energized or de-energized depending on the rotary switch position. The 3 RTC signals which operate the command switch are:

(1) Warmup signal.

(2) Emergency mode signal.

(3) Emergency mode-off signal.

When the warmup signal is received, the command switch advances from Position 0 to Position 1. This action energizes Relay K6 in the command switch, Relays K3 and K4 in the transmitters, and Relay K5 in the telemetry section.

When Relay K6 is energized, a regulated −27.5-v dc power line is closed, applying −27.5 v to the sequencer and camera assemblies. The camera sequencer and camera assemblies do not have power switches; the applied −27.5 v starts the operation of these assemblies. Relays K3 and K4 apply unregulated −39 v dc to the transmitter power supplies. Relay K5 in the telemetry section closes contacts to −27.5-v regulated power to initiate terminal telemetry operation.

The warmup signal has a backup from the CC&S in the bus. This equipment provides a 100-ma contact closure for the backup signal. Total current required by the relay coils is 410 ma. Therefore, the CC&S signal must be amplified to operate the relays in the absence of the RTC warmup signal.

The emergency mode signal is the next RTC mission sequence. When the emergency mode signal is received, the command switch advances from Position 1 to Position 2, energizing Relays K10 and K11 in both transmitters. When these relays energize, the cameras become disconnected from the transmitters and the terminal telemetry signals are connected directly to the transmitters. In this position of the command switch, the warmup signal is still applied to the warmup relays to keep the TV subsystem in operation.

The final signal received from the bus is the emergency mode-off signal. This signal advances the command switch to Position 3, causing Relays K10 and K11 to de-energize. With Relays K10 and K11 de-energized, the cameras are again connected to the transmitters, and the TV subsystem performs in the normal operating mode. The warmup signal is applied to the appropriate relays as in the other modes.

Position 3 is the final position to which the command switch will be advanced during the mission.

It is not planned to use the switch during subsystems tests, except to test operation of the switch itself; therefore, no provisions are made to operate the switch from any other source except the RTC command contact in the bus. All TV subsystem signals generated by the switch will be simulated on the test panel.

Mechanical. Mechanical design developments and refinements of subassembly packaging have made it necessary to revise the initial component arrangement. The revised arrangement is shown in Figure 39.

The new arrangement concept complies with the requirement to keep the batteries as low as possible in the structure, yet accessible for ease of installation and sterilization. The batteries are located within the structural box, formed by the vertical longerons and side plates, and are assembled from the bottom of the payload. This method of assembly eliminates the need for cutouts in the plates forming the structural box and access doors in the thermal shroud. More efficient use is made of the remaining space and mounting surfaces for control of the center of gravity, of moments, and of thermal and electrical requirements.

A specific camera layout has been completed and a structural mounting bracket for accommodation of all 6 cameras has been designed and is being fabricated. The bracket is a single unit with provisions for alining all cameras in the proper angular relationship to one another without further adjustment. The bracket and camera assembly is installed within the structure on adjustable mounts for alinement of the entire camera array as a unit to the desired angle, representing the terminal velocity

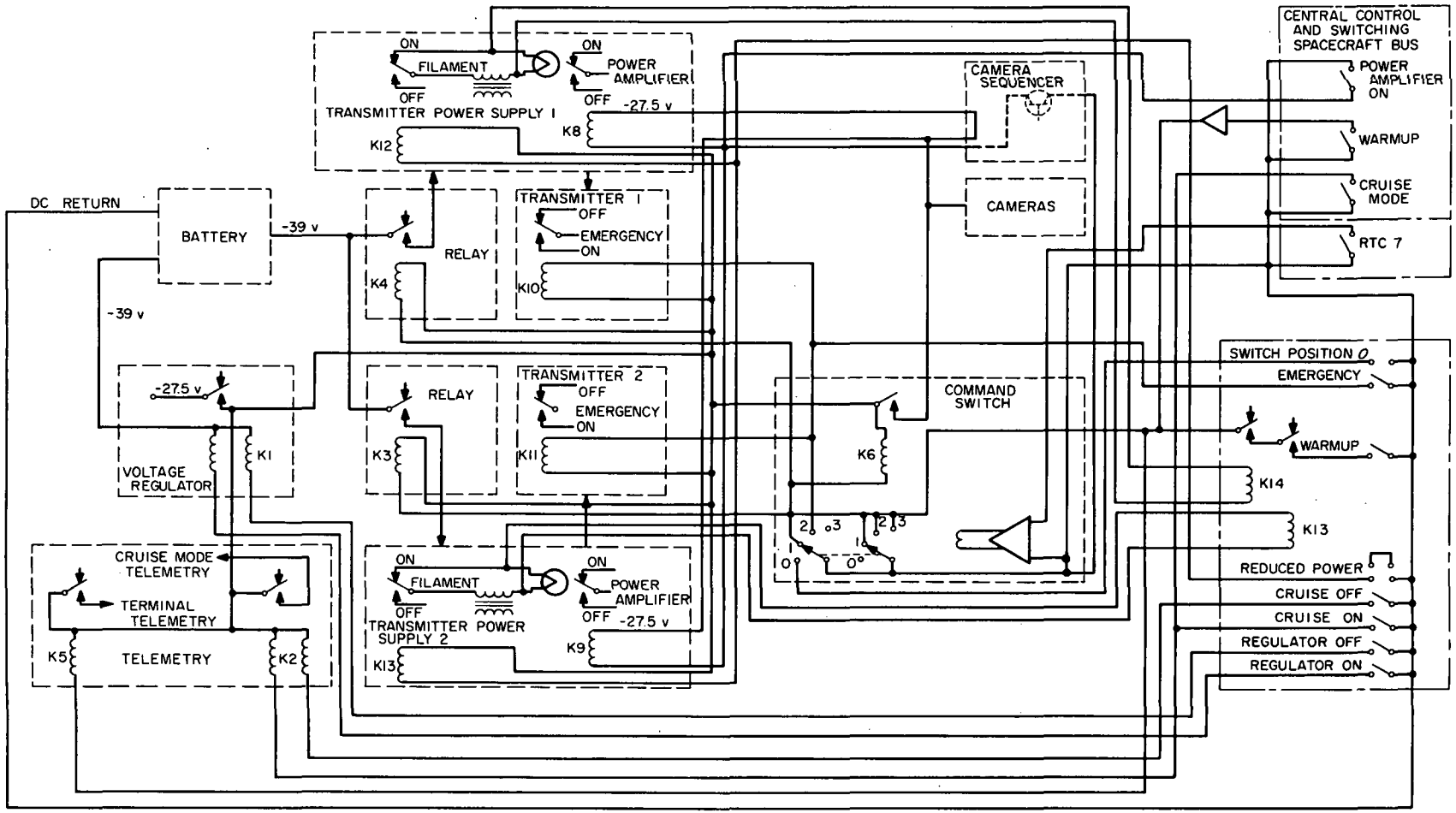

Figure 38. Preliminary control circuits showing command switch and mode switching relays

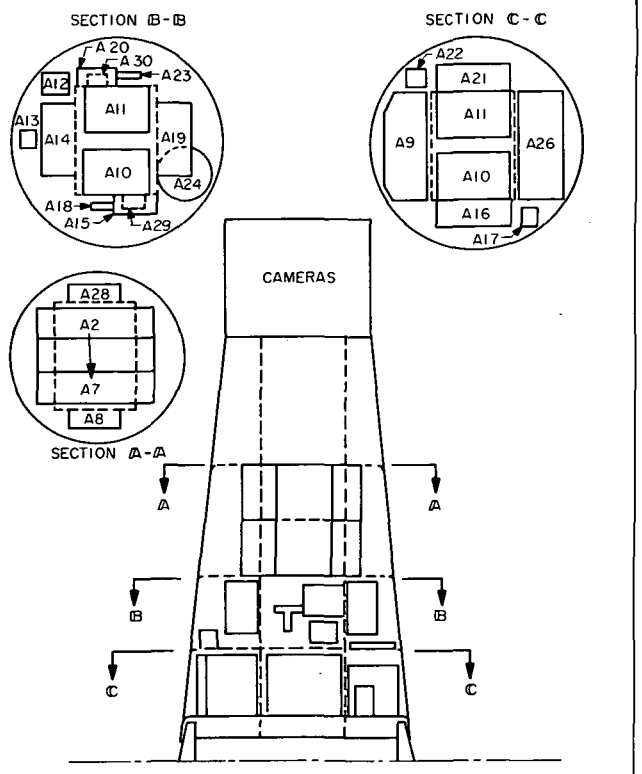

Unit weights and dimensions

Reference designation	Unit	Weight, lb
A1	Cameras (6 cameras and filter wheel on single bracket)	60.0
A2 through A7	Camera electronics (6)	43.8
A8	Video combiner	1.0
A9	Sequencer	9.0
A10 and A11	Batteries (2)	88.4
A12	Regulator	3.0
A13	Command switch	2.0
A14 and A19	Transmitter modulator (2)	8.0
A15 and A20	Amplifier, 60 w (2)	2.2
A16 and A21	Power supply (2)	22.0
A17 and A22	Power relay (2)	1.8
A18 and A23	Signal samplers (2)	0.4
A24	4-port hybrid	1.5
A25	Dummy load	2.5
A26	Telemetry	10.0
A27	Temperature sensor	1.5
A28	Sequencer power supply	4.6
A29 and A30	Telemetry processing (2)	0.5
—	Structure, thermal shield	70.0
—	Electrical harness	15.0
	Total weight	347.2

Figure 39. Arrangement of components in basic structure

vector. The camera arrangement within the structure is shown in Figure 40.

The revised moment values are tabulated in Table 28. The revised computation of the center of gravity is

$$\overline{Z} = \frac{\Sigma WZ}{\Sigma W} = \frac{6966.3}{347.2} = 20.05$$

$$\overline{Z}_{payload} = 477.60 - 20.05 = 457.55 \text{ in.}$$

$$\overline{Y} = \frac{\Sigma WY}{\Sigma W} = \frac{-39.7}{347.2} = -0.114$$

$$\overline{Y}_{payload} = -0.114 \text{ in.}$$

$$\overline{X} = \frac{\Sigma WX}{\Sigma W} = \frac{-14.5}{347.2} = -0.042$$

$$\overline{X}_{payload} = -0.042 \text{ in.}$$

Total payload weight is 347.2 lb, and the center of gravity location for the spacecraft–payload combination satisfies the JPL requirements.

8. Ground Support Equipment

The designs for the *Ranger* TV subsystem ground receiving equipment and ground checkout equipment have been finalized. Plans for the Goldstone equipment call for a 30-mc, caged preamplifier to be located on the antenna. The design provides for redundant receivers and tape recorders. Included also are 2 Kine-recorders which can be used for direct on-line or off-line photographic recording. The Channel 8 telemetry is selected, by means of an appropriate filter, from the wide band telemetry. After demodulation, the telemetry data can be presented as a printout.

Signal processing and interconnection switching have also been finalized, providing a versatile operational equipment. A 2 channel test transmitter is also planned. This test transmitter can be modulated either by signals from the video and sync simulator or by a prerecorded test tape.

Designs for a *Ranger* TV subsystem panel and a single-channel test transmitter for the ground checkout equipment have been finalized. The *Ranger* TV subsystem panel will permit exercising the spacecraft equipment by simulating command signals as well as making the correct connection to the checkout equipment. A single channel transmitter, which can be switched to either of the 2 frequencies, is provided for test purposes. The Goldstone receiver is replaced with a 960-mc front end for the tests.

The checkout panel to be included in the block house equipment is being designed. This panel will permit a

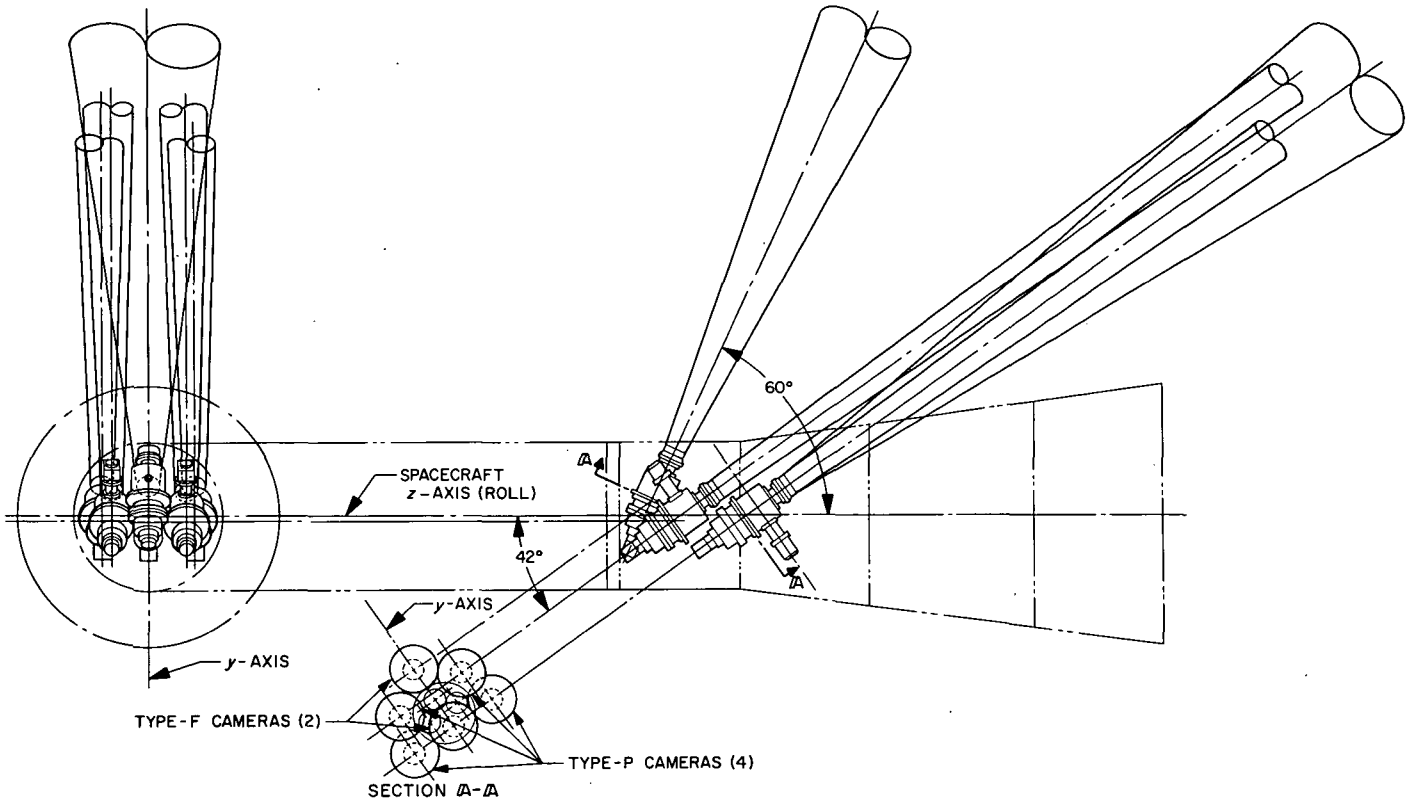

Figure 40. Camera array

brief exercise of the spacecraft through hard-line connections while it is emplaced on the launching pad. A receiving antenna and tower will be provided to receive the reduced power transmissions from the spacecraft during the countdown checks.

All primary power requirements for the GSE have been established and equipment layouts for the various installations have been reviewed. In addition, the interface between the RCA equipment and the ground support equipment at Goldstone was established.

The operational ground station comprises 2 major ground equipments: the TV data recording and display equipment, and the ground communications equipment.

a. Data recording and display.

Subsystem description. The *Ranger* TV ground support equipment (GSE: TV data recording and display subsystem) provides 3 primary functions:

(1) Data recording (telemetry and TV information).

(2) Data reduction (TV information).

(3) Control of checkout and exercising of the subsystem.

Data recording will provide interim as well as archival storage of events on a multi-channel, continuous-tape, magnetic recorder. Data reduction of information in the form of television signals will be recorded by a 35-mm film camera. GSE subsystems, intended for checking and exercising the system, will be provided by 1 kinescope and film-camera combination capable of recording either slow-scan or fast-scan video channels individually. Control of the subsystem will be manual and will include control of power, operate-test mode, CRT display designation (in test mode), and film camera. Monitoring of on-line or off-line video signals will be displayed by an A-scope which will receive appropriate sync and video signals. The A-scope will also be capable of displaying waveforms from other parts of the subsystem.

Figures 41 and 42 are block diagram and equipment layout, respectively, of the TV data recording and display ground checkout equipment.

Tape recorder. The tape recorder is a 4-channel, wide band, continuous linear magnetic-tape system which will record and play back the composite video and telemetry signals received from the subsystem interface equipment. Mincom tape recorders will be used in GSE Units 1 and

Table 28. Center of gravity computation

Reference designation	Unit	Weight, lb	X, in.	WX, in.-lb	Y, in.	WY, in.-lb	Z, in.	WZ, in.-lb	WZ^2, lb-in.^{2}
A1	Cameras 6 (cameras and filter wheel)	60.0	0	0	0	0		2561.0	137,800
A2 through A7	Camera electronics	43.8	0	0	0	0	25.70	1129.7	29,000
A8	Video combiner	1.0	7.0	7.0	0	0	22.70	22.7	774
A9	Sequencer	9.0	0	0	6.8	61.2	7.00	63.0	294
A10 and A11	Batteries	88.4	0	0	0	0	12.35	1090.0	14,350
A12	Regulator	3.0	−8.0	−24.0	−6.0	−18.0	14.00	42.0	588
A13	Command switch	2.0	0	0	−10.0	−20.0	14.00	28.0	392
A14 and A19	Transmitter modulator	8.0	0	0	0	0	14.25	114.0	1,625
A15 and A20	Amplifiers, 60 w	2.2	0	0	0	0	12.50	27.5	344
A16 and A21	Power supply	22.0	0	0	0	0	7.0	154.0	1,030
A17 and A22	Power relay	1.8	0	0	0	0	5.3	9.6	51
A18 and A23	Signal samplers	0.4	0	0	−8.5	−3.4	12.0	4.8	57
A24	4-port hybrid	1.5	−6.5	−9.75	0	0	14.50	21.8	316
A25	Dummy load	2.5	7.0	17.5	0	0	19.0	47.5	704
A26	Telemetry	10.0	0	0	−7.3	−73.0	6.8	68.0	462
A27	Temperature sensor	1.5	0	0	9.0	13.5	12.0	18.0	288
A28	Sequencer power supply	4.6	−7.0	−32.2	0	0	22.6	104.0	1,750
A29 and A30	Telemetry processor	0.5	0	0	0	0	13.0	6.5	85
	Structure and thermal shield	70.0	0	0	0	0	16.16	1454.0	32,000
	Harness, electrical	15.0	—	—	—	—	—	—	—
	Totals	347.2		−14.5		−39.7		6966.3	221,910

2; Ampex tape recorders will be used in GSE Units 3 and 4.

Sync and video simulator. The sync and video simulator contains the test-pattern control, sync generator, and video-simulator circuits. These circuits produce the function necessary to perform a comprehensive subsystem test to determine equipment operability. The test-pattern control panel enables selection of the various test signals which the simulator is capable of generating. The sync generator produces the timing waveforms required to operate the video simulator. The video simulator develops composite video signals which produce test patterns within subsystem operating ranges so that kinescope operating parameters can be determined.

The generated video test signals are selectable by a rotary switch on the simulator unit. These signals (Fig 43) comprise:

(1) Vertical bars (2 raster lines wide).

(2) Horizontal bars (2 raster lines wide).

(3) Grating pattern (horizontal and vertical bars).

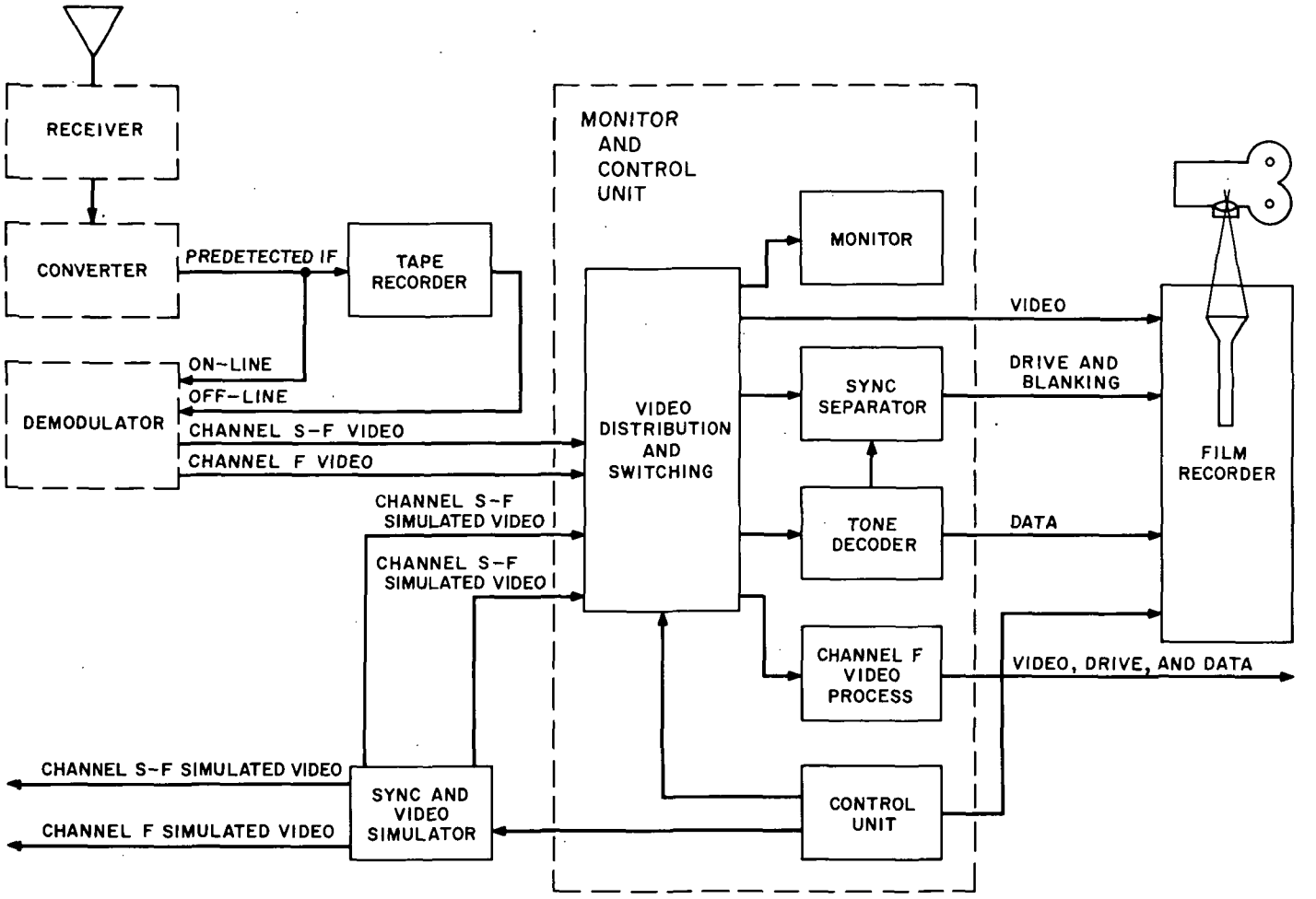

Figure 41. TV data recording and display ground checkout equipment

(4) Gray scale.

(5) Resolution bars (5 bursts of sine waves).

(6) Composite test pattern (grating, resolution bars, and gray scale).

The sync tips carry tone signals in accordance with the *Ranger* TV GSE subsystem specification, except that the tones carried by the Camera A–B rate composite video will be selectable by a test-pattern control-panel rotary switch.

The sync generator unit consists of an 18-kc, crystal-controlled, master oscillator and *and* gate logic circuits that perform frequency division to the line and frame rates, and intermediate divisions to provide for triggering of the video generator.

The 18-kc, crystal-controlled oscillator circuit is shown in Figure 44. This circuit provides a positive-going pulse varying from 8 to 0 v at an 18-kc rate. The pulse rise time (measured between the 10 and 90% points) is less than 0.22 μsec. Pulse width is not critical but is approximately 35 μsec. The circuit consists of 2 transistor amplifiers in series, with positive feedback from the 2nd to the 1st through a quartz crystal in the series-resonant mode. A clipped 18-kc sine wave is produced at the output of the 2nd amplifier, and is then fed through an inverter to provide the required rise time. Fabrication of the improved 18-kc oscillator has started.

The video generator unit consists of *and* gate logic, shift registers, 1-shot multivibrators, gated oscillators, a register matrix, and a video-processing amplifier. The video-processing amplifier breadboard has been completed, finishing the task of breadboarding circuits.

The *and* gate logic and the 1-shot multivibrators generate horizontal and vertical bars and a grating pattern determined by the line and frame sync rate. One shift

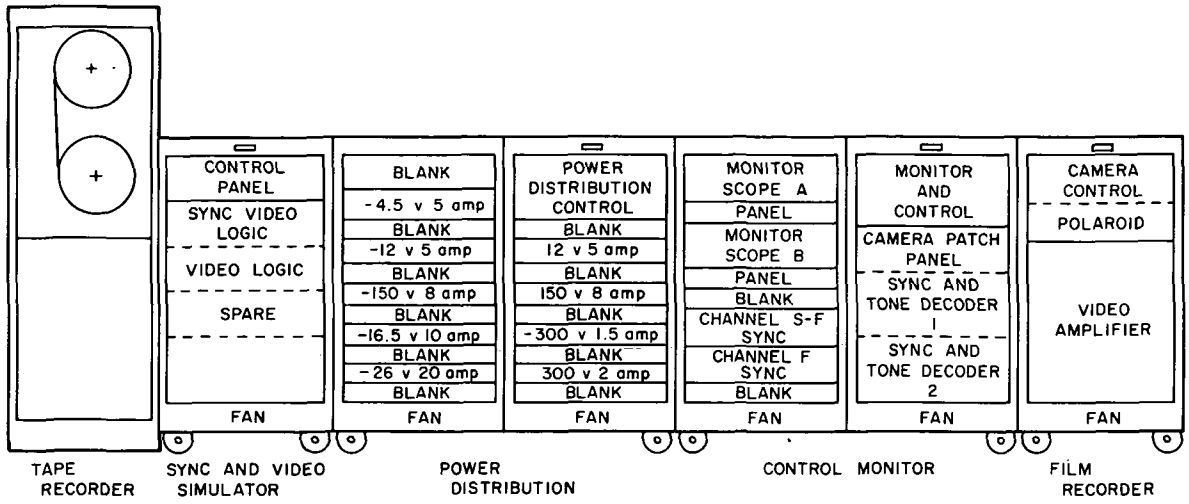

Figure 42. TV data recording and display ground checkout equipment

register drives the resistor matrix to generate the gray tone signal with a gamma factor of 0.5. Another shift register drives the high-stability gated Colpitts oscillators to produce multi-burst resolution bars, at the line sync rate. A gated oscillator module, controlled by a vertical-sync-rate-gate pulse, generates the coded tone signal. The video-processing amplifiers contain 2 resistor–diode video and sync mixer circuits and a line driving amplifier.

The mechanical configuration has been changed to accommodate the gated oscillators. The original design stipulated that each gated oscillator board would contain 5 tank circuits (only 3 of which would be used) of different center frequencies. When the board layout was being designed, it was found that 5 tank circuits could not be fitted on 1 board. It was necessary to provide a 2nd type of module to provide gated oscillators in the required quantity and frequencies. The same board and parts are being used in both modules. The only difference is the

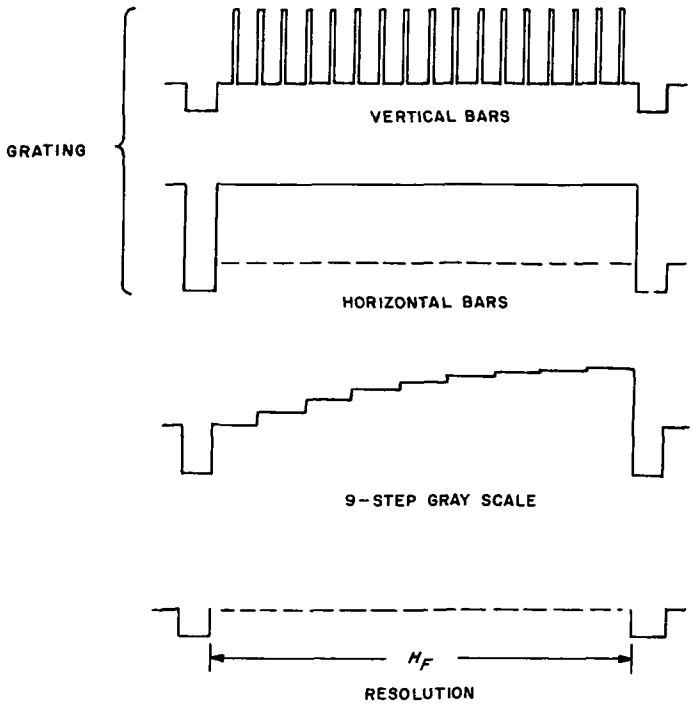

Figure 43. Video test signals

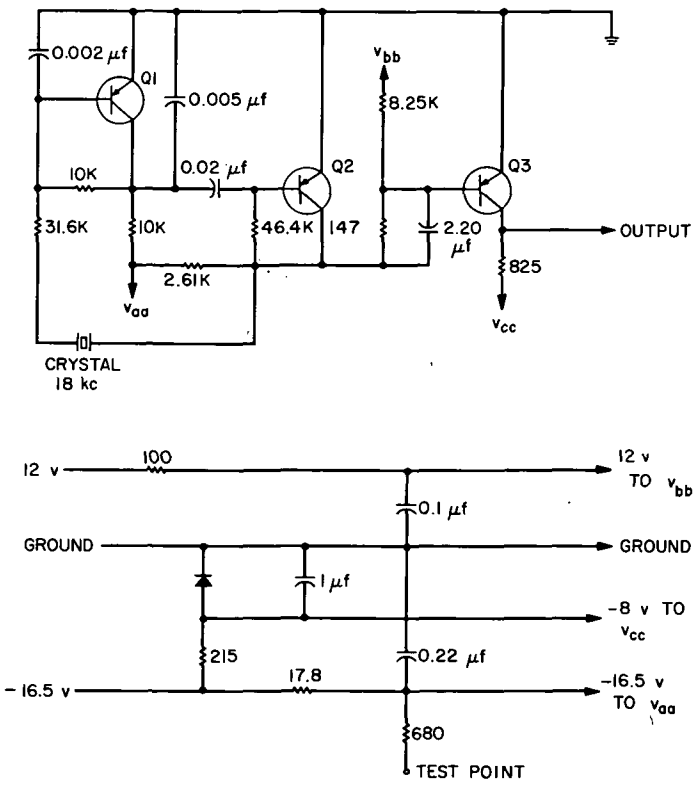

Figure 44. Schematic of 18-kc oscillator

resonant frequency of the tuned circuits being incorporated into the module.

Power supplies. The power distribution unit consists of a control panel, blower, and 9 individual dc voltage power supplies. This unit provides control of the ac and dc voltage requirements of the TV data recording and display subsystem. A blower, located at the bottom of the cabinet, provides ventilation that maintains safe operating temperatures for the power supplies. The individual power supply voltage, current, and voltage limit ratings are listed in Table 29.

Monitor and control unit. The monitor and control unit contains a monitor and control panel, camera patch panel, monitor scope (1 in the checkout configuration, 2 in the operational configuration), Channel S–F sync chassis, Channel F sync and tone-decoder chassis, 2 sync and tone decoder-module nests, and a communication panel. This unit provides a central point from which the subsystem can be operated. The monitor and control panel contains switches, indicators, counters, and a clock. The switches provide selection of operating commands for a subsystem during test or operate modes. Lights in switches and indicators provide monitoring information of system status and operation conditions. The counters indicate the film-recorder camera operation by counting the frame exposures of the 35-mm camera, and the clock displays a 24-hr GMT. The monitor or scopes (depending upon the subsystem configuration) monitor the video signals being applied to the kinescope display circuits.

Table 29. Power supply voltage and current ratings

Nominal voltage, v	Current, amp	Voltage limits, v
−4.5	5.0	−4.4 to −4.6
−12.0	5.0	−11.75 to −12.25
−16.5	10.0	−16.1 to −16.9
−26.0	20.0	−25.5 to −26.5
−150.0	0.8	−147 to −153
−300.0	1.5	−294 to −306
12.0	5.0	11.75 to 12.25
150.0	0.8	147 to 153
300.0	3.0	294 to 306

The Channel S–F sync chassis and the Channel F sync-tone decoder chassis separate and develop signals to produce the picture presentation and select the proper color filter indicator lamp at the film recorder. The sync and tone-decoder Nests 1 and 2 contain the modules which provide the sync and tone-decoder logic required by the film recorder.

Tones are separated from the composite video signals by 2 identical tone strippers. The tone strippers are shown in Figure 45. Each stripper consists of 3 decoders that are identical except for the frequency of the input filter. The filter possessing frequency characteristics similar to the tone frequency will pass the tone to the tone decoder. The tone is amplified by Q1, Q2, Q3, and Q4. The amplified tone is detected, integrated, and applied to the

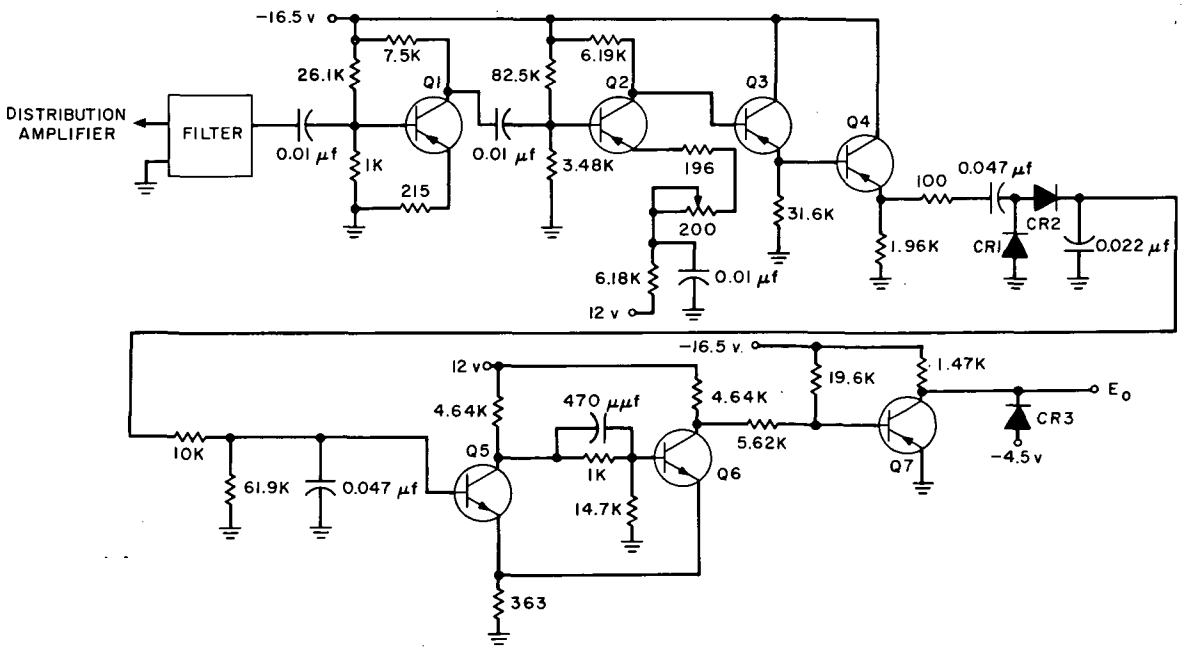

Figure 45. Tone decoder

Schmitt trigger, consisting of Q5 and Q6. The Schmitt trigger output is amplified and clamped to −4.5 v. Tone decoder outputs are used to indicate absence of tone and to indicate the color of the filter used in the TV camera.

Input to the tone stripper is from the video-distribution amplifier, shown in Figure 46. The video-distribution amplifier is an impedance-matching device, accepting video signals from a 91-ohm impedance and driving 91-ohm lines. The input signals are nominal 1-v peak-to-peak positive-going wave forms from a −1-v reference level. The module comprises 4 identical but separate circuits, each having unity gain. Terminal connections are such that maximum usage flexibility is provided.

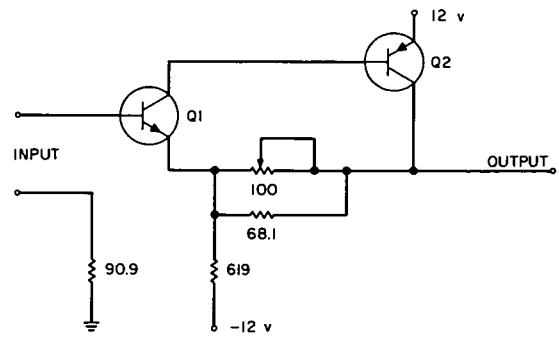

Figure 46. Video distribution amplifier

Film recorder unit. The film recorder consists of a 35-mm camera, Polaroid-Land camera, high voltage power supply, camera control, kinescope, kinescope-control circuits, and deflection amplifier. Figure 47 is a block diagram of the film-recorder unit. The primary purpose of this unit is to provide a film record of the kinescope display. The kinescope display is transmitted from TV cameras on the payload, and a 35-mm camera photographs the picture produced on the face of the kinescope. Adjacent to the TV picture on each 35-mm frame is a picture of a data box, consisting of a 24-hr clock, frame counter, tone-code notation, and a write-in block for other pertinent information. The Polaroid camera provides a means of monitoring the display operation of the film-recorder unit by rapidly furnishing a print of the kinescope display. Also provided with the Polaroid picture is a data-block display with information nearly identical to that photographed by the 35-mm camera. The kinescope electronics, deflection amplifier, high voltage power supply, and camera-control subassemblies provide the necessary functions for the kinescope to produce a quality picture and control the action of the 35-mm camera.

The 35-mm camera lens was selected on the basis of extensive tests performed by RCA Applied Research in Camden. Five lenses were tested (Taylor-Taylor and Hobson, Bausch and Lomb, E. Leitz, Canon, and Nikkor). On the basis of tests performed, the Canon 100-mm $f/3.5$ lens was selected. The sine-wave response of this

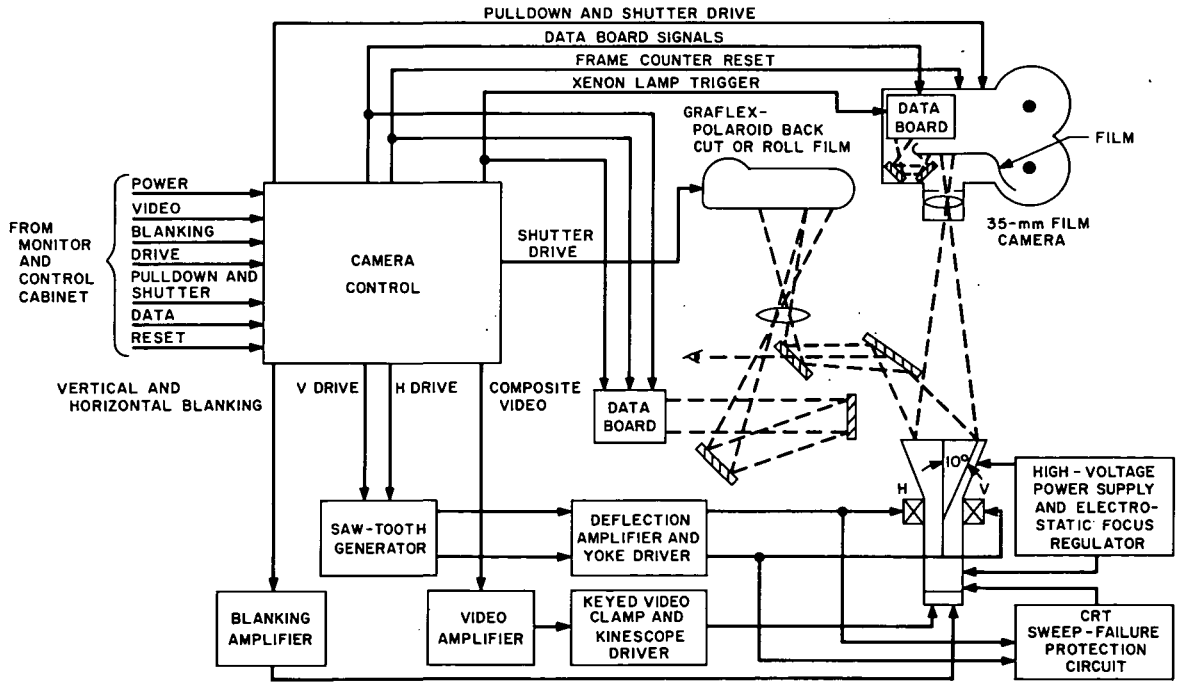

Figure 47. Film recorder unit

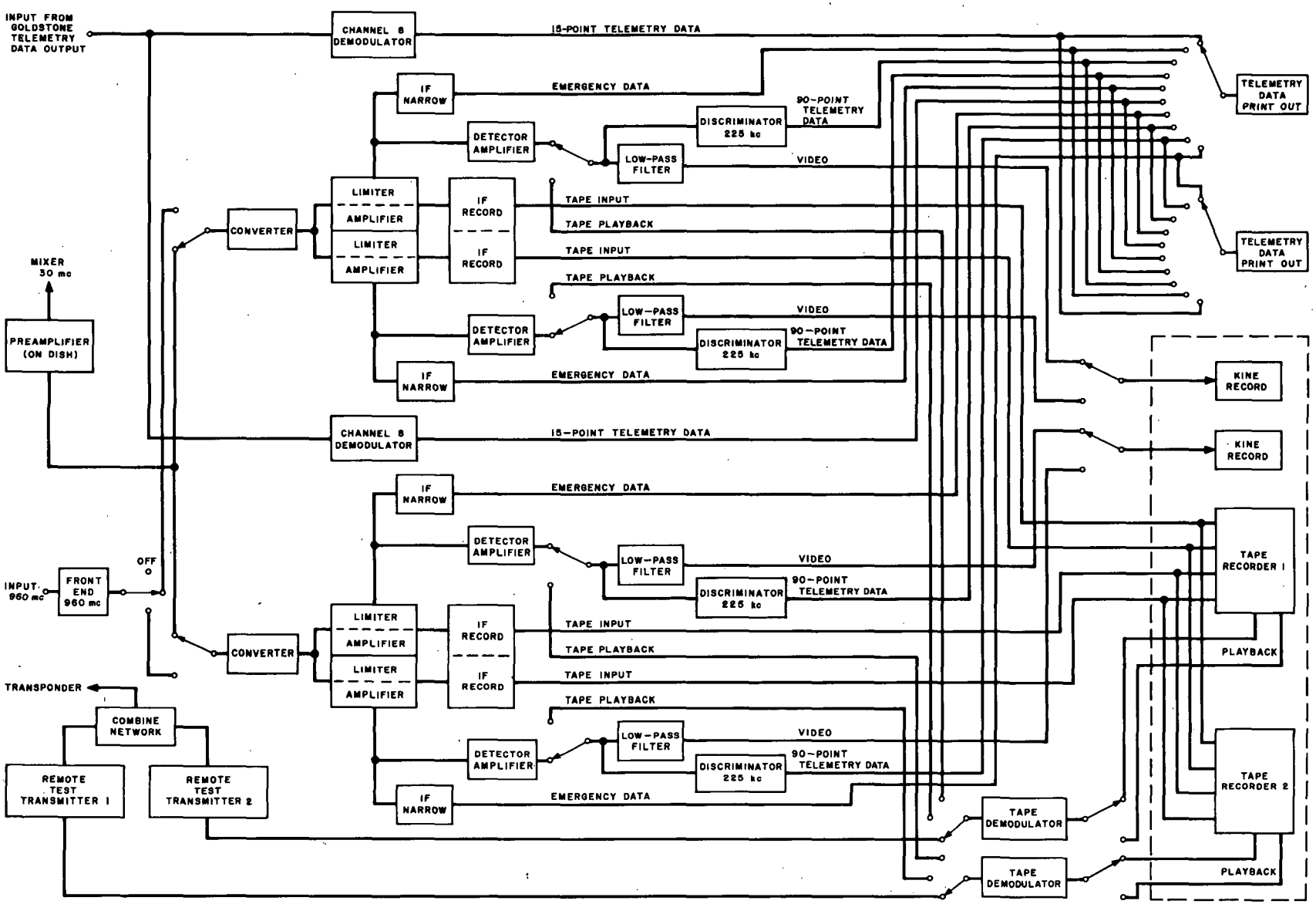

Figure 48. Goldstone ground receiving equipment

CONFIDENTIAL

lens (800 TV lines per picture height) at $f/4.5$ was 84%; at $f/8$, it was 90%. Calculations to establish the required exposure indicate that the lens opening will be between $f/4.5$ and $f/8$.

Eastman Kodak film 5374 was tentatively selected. Resolution figures were obtained from Eastman. On the basis of sine-wave response testing of 5302 film and the comparison obtained from Eastman between 5302 and 5374 (5374 has approximately 15% better resolution than 5302), the aperture response of 5374 film with an 800 TV-line raster has been calculated to be between 75 and 80%.

A process has been established and tested for developing the 5374 film which will result in a transparency having a gamma factor of 1.

b. Ground communications. The purpose of the communication portion of GSE being supplied to the DSIF Goldstone facility is to reduce the composite 960-mc signal into 2 separate video signals and a print-out of the telemetry information. In order to accomplish this with maximum reliability, a completely redundant system is used (Fig 48).

960-mc information is received and translated into a 30-mc IF signal. To assure a flat 2-mc bandwidth, a separate 30-mc IF preamplifier is mounted on the antenna. This composite signal is coupled to the RCA equipment located in the operations building. At this point, the 2 channels are separated: 1 is processed by a 4.5-mc IF, the other by a 5.5-mc IF. After limiting, the signal is detected and the telemetry information separated for further processing. The video signal then goes through a low pass filter to suppress the telemetry channel, followed by a deemphasis network to restore the flat video spectrum. This signal is then fed to the kinescope recorders for real time display.

Tape recorders are used for predetection storage of received signals. For this purpose, the 5-mc IF is translated to a 500-kc carrier, recorded on 2 channels of a tape recorder. For playback, the outputs of the 2 channels are combined and fed to a 500-kc demodulator. This composite signal is then coupled (in place of the 5-mc demodulator output) through filter networks to the kinescope and telemetry reduction system.

The telemetry-reduction system has an analog-to-digital converter with print out. Analog information may be received in 3 ways:

(1) Cruise telemetry: Channel 8 over the bus transmitter. An IRIG demodulator is used to reduce the Channel 8 FM signal to an analog voltage.

(2) Terminal telemetry. A 225-kc subcarrier on the TV transmitter is demodulated to obtain the analog telemetry signal.

(3) Emergency telemetry. The 5-mc signal is fed to a narrow-band phase-locked loop. The output of the phase-locked loop is coupled to the Adcon unit.

The Adcon unit provides a synchronizing signal to the print-out. The telemetry information is printed out using a 2-digit format (from 00 to 99).

To test the ground system, a TV simulator will be incorporated. To check the communication portion of the ground station, the signals from the simulator are preemphasized and fed to the test transmitter located in the collimation tower. At the collimation tower, the flight transmitters are simulated at a 1-mw level, combined with the bus signal, and radiated to the Goldstone dish. Power levels of the test transmitters are calibrated so that the DSIF equipment may be checked at a threshold signal level.

Vendor sources for the low noise preamplifier for the Goldstone installation are being investigated.

References

1. "Thirty-five Day Report," *Ranger I System Test Evaluation and Performance Analysis Report, L.M.S.C.-448617-01;* Lockheed Missile Systems Company, Sunnyvale, Calif. September 27, 1961.

2. "Launch Report for Atlas 117D/Agena-B 10205-6002 Ranger Spacecraft RA-2," *L.M.S.C.-271410, SSN-T61-102;* Lockheed Missiles and Space Company Space Systems; AFMTC Test Operation, Florida. December 2, 1961.

3. "Summary of the Retromotor Qualification Tests," *LC(b)-332;* Aeronutronic Division, Ford Motor Company; Newport Beach, Calif. December 26, 1961.

II. *Surveyor*

The objective of the *Surveyor* project is to soft-land a series of spacecraft on the Moon. The Hughes Aircraft Company, under contract coverage from the Jet Propulsion Laboratory, has the responsibility for the design and development of the spacecraft, ground support and data handling equipment, primary documentation, and mission operations.

A *Surveyor* spacecraft design for the first two missions has been released and placed under formal change control. A number of improvements have been incorporated in the general spacecraft arrangement, as well as in subsystem design. Improvements in the flight control system include converting from an open-loop vernier thrust command channel to a closed-loop acceleration command servo; in addition, the bang-bang solenoid actuator in the thrust-phase roll control system has been replaced by a proportional positioning servo.

Calculations of vernier propellant consumption have been refined; one significant result was a reduction of main retro-engine propellant weight. The descent trajectory conditions under which blind zones for doppler radar operation can occur have been studied, and it appears desirable to modify the radar logic circuitry to minimize blind zone effects. A more refined analysis of touchdown dynamics, based on latest weight and center-of-gravity locations and on actual (rather than rigid-body) loads, has been completed. Lateral vibration testing of a spaceframe with simulated components was completed and design improvements incorporated as a result. A prototype thermally controlled compartment is being tested in a high-vacuum chamber to evaluate effectiveness of the multiple-layer radiation insulation.

Coupling coefficients have been measured on slot patterns for the planar array antenna to determine slot spacing for desired phase corrections. A complete functioning breadboard of the altitude marking radar is being tested in a roof-house installation. Some components for the radar altimeter and doppler velocity sensor have completed breadboard tests.

Testing of flight-type components for the vernier propulsion system has started. Vernier thrust chamber performance has been below specification limits, but modifications now being tested show considerable improvement. Two spaceframes have been delivered to Thiokol for use in tests of the vernier system. Grain cracking took place in the second main retro-rocket engine fired; stress relief boots were added in the third engine fired and cracking did not occur.

Developmental extension booms and test fixtures have been fabricated for cold gas actuation tests, and wiring harnesses of various types for the booms are being tested. A design improvement in the solar panel/antenna positioner will give a substantial weight reduction. Generally satisfactory results were obtained in tests of the subsurface sampler in a high-vacuum chamber.

The Atlantic Missile Range spacecraft test procedure has been revised in accordance with the decision to perform terminal sterilization of the spacecraft before mounting it on the *Centaur*. Fabrication of components for the command and data handling console has started. A specification for the *Surveyor* spacecraft simulator has been prepared.

A. System Design Summary

1. System Description

The spacecraft configuration, incorporating all scientific instruments designated for the first two missions, P-42 and P-43, has been released and is under formal change control. The general arrangement for the stowed, mid-course, and post-landing conditions is shown in Figure 1. Additional views of the post-landed configuration are shown in Section J. The significant configuration changes since last reporting are also described in Section J.

Two important design changes have been made in the flight control system during the reporting period. First, the thrust control system has been converted from an open-loop thrust command channel to a closed-loop acceleration command servo. This has been accomplished by extending the use of the accelerometer in the mid-course velocity control system to the terminal phase. The second important modification involves a change in the thrust phase roll control system. The bang-bang solenoid actuator originally planned for use in a limit cycle control system has been replaced by a proportional positioning servo employing a conventional 400-cps servo motor.

2. Weight Summary

Current weight status is summarized in Table 1 and broken down in detail in Table 2. The weight reporting format has been expanded to include columns for maximum allowable weight, current design weight, and predicted flight weight. The previously reported "current weight" column was intended to show current predictions of flight weight, and has been renamed "predicted flight weight." The newly added column, "current design weight," shows weights associated with current hardware designs; these weights are obtained by estimate, by calculation from drawings, or by actual weight measurement, depending upon the state of development of the hardware involved. Predicted flight weights are shown to be less than current design weights only when means for weight reduction are known and are in process of incorporation; these weight reductions will result in lower current design weights in future reports. Additional means for weight reduction that are under study, but are not presently being incorporated, are not included in predicted flight weights.

The total separated flight weight reported in *SPS 37-12* was 2527.5 pounds (based on 345 pounds of scientific payload weight), compared the present predicted flight weight of 2537.6 pounds. The greatest increase has been in the spacecraft vehicle subsystem, for which the weight reported was 161.6 pounds, compared with a present current design weight of 182.1 pounds. This increase results from computer stress analyses and test data from spaceframe S-1 that indicate a need for stronger attachment fittings, additional truss bracing, and increased wall thickness in certain of the tubular members of the structure. At the same time, there have been reductions in the antenna/solar panel positioner and main retro-engine weights. A 15-pound saving in the retro-engine has been achieved by further trajectory optimization studies.

Table 1. Spacecraft weight summary

Item	Maximum allowable weight, lb	Current design weight, lb	Predicted flight weight, lb
Total separated weight	2500.0	2574.7	2537.6
Basic bus	553.0	618.1	596.8
Usable propellant	1602.0	1605.0	1590.0
Scientific payload	345.0	351.6	350.8

3. Electrical Energy

An electrical energy summary is shown in Table 3. This summary assumes launch on the eighth day of the launch window in August 1963; for this launch condition, solar energy will be available to the spacecraft for 163 hours from touchdown until crossing of the first day/night terminator. The current estimated energy requirements are based upon the payload specified for Missions P-42 and P-43.

The total available daytime energy, 7628 watt-hours, represents a significant increase over the available 5180 watt-hours reported in September 1961. This increase results primarily from a redesign of the battery charging circuitry to make more of the total incident energy available to the electrical power system. In addition, more energy is predicted available as a result of re-estimating the post-landing remainder of the first lunar day to be 163 hours instead of the 150 hours assumed previously. Portions of the increase in available energy have been made available to the basic bus, the scientific payload, and the reserve. Nighttime energy is supplied by batteries that are charged to their full capacity of 5300 watt-hours prior to passing of the day/night terminator.

4. Command and Data Channels

Command and data channels now being provided in the spacecraft are summarized in Table 4. In the table, the channels are divided between those required for the

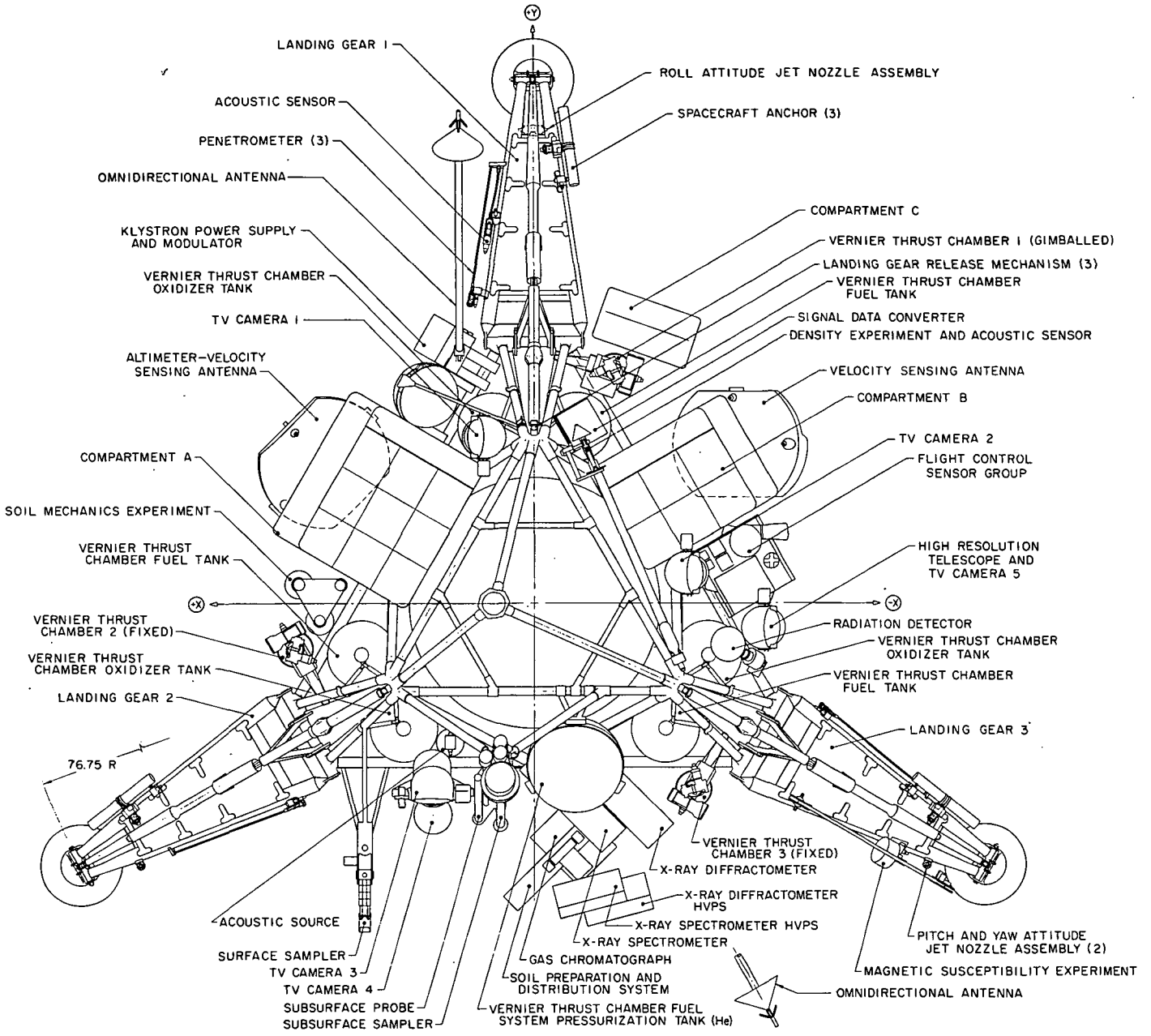

PLANAR ARRAY ANTENNA AND SOLAR PANEL HAVE BEEN OMITTED FROM THIS VIEW FOR CLARITY

Figure 1. Spacecraft general arrangement

basic bus and those required for the scientific payload. Command and data channels listed for the scientific payload include those required by the Hughes-supplied instrument auxiliaries, both mechanisms and electronics, in addition to the specific instrument requirements. The figures indicated in this summary are based upon the scientific payload specified for the first two missions, P-42 and P-43.

Table 2. Weight breakdown

Item	Maximum allowable weight, lb	Current design weight, lb	Predicted flight weight, lb
1.0 BASIC BUS (total)	553.0	618.1	596.8
1.1 Flight control		46.4	46.4
Sensor group			
Secondary sun sensor			
Attitude control system			
1.2 Electronics		93.9	93.9
Data Link (antennas, RF switches, transmitter and diplexer, command receiver and transponder)			
Central command decoder			
Central signal processor			
Altitude marking radar			
Doppler velocity sensor and altimeter			
Power control system			
TV camera No. 4			
Engineering data processing			
Mechanisms auxiliaries			
1.3 Electrical power		38.5	38.5
Solar panel			
Batteries			
1.4 Mechanisms		31.4	27.8
Positioner, planar antenna/solar panel			
Antenna mechanisms, omnidirectional			
Safety and arming provisions			
Separation sensing device			
1.5 Spacecraft vehicle		188.9	182.1
Spacecraft structure			
Landing gear installation			
Equipment attaching hardware			
Equipment compartments A, B, and C			
Electrical wiring			
Pneumatic lines, attitude control			
Release mechanism, retro-rocket engine			
Engineering measurements sensors			
1.6 Spacecraft propulsion (not including usable propellant)		219.0	208.1
Rocket engine, main retro			
Vernier propulsion system			
Unusable vernier propellant			
Helium			

Item	Maximum allowable weight, lb	Current design weight, lb	Predicted flight weight, lb
2.0 USABLE PROPELLANT (total)	1,602.0	1,605.0	1,590.0
2.1 Retro-rocket propellant		1,444.4	1,429.4
2.2 Vernier propellant		160.0	160.0
2.3 Pyrogen propellant (igniter)		0.6	0.6
3.0 SCIENTIFIC PAYLOAD (Missions P-42, P-43) (total)	345.0	351.6	350.8
3.1 TV cameras Nos. 1, 2 and 3, and mirrors		44.8	44.8
3.2 TV decoder and processor		1.3	1.3
3.3 High-resolution telescope and camera		14.9	14.9
3.4 Subsurface sampler		43.3	42.8
3.5 Surface sampler		10.0	10.0
3.6 Spacecraft anchoring device		10.9	10.9
3.7 Sample processor		13.5	13.5
3.8 X-ray spectrometer		28.9	28.9
3.9 X-ray diffractometer		21.1	21.1
3.10 Gas chromatograph		13.5	13.5
3.11 Surface geophysical subsystem		38.5	38.4
Density background counter			
Surface density instrument and acoustic sensor			
Surface thermal diffusivity instrument			
Surface magnetic susceptibility instrument			
Acoustic sensor			
Acoustic source			
Soil mechanics instruments			
Resistivity instruments			
Radiation pyrometer			
Penetrometers			
Subsurface geophysical auxiliaries			
3.12 Subsurface logging sonde		4.5	4.5
3.13 Acoustic velocity auxiliaries		3.0	3.0
3.14 Tape recorder		10.6	10.6
3.15 Ionization chamber assembly		5.6	5.4
3.16 Scientific instrument mechanisms auxiliaries		2.9	2.9
3.17 Scientific instrument thermal auxiliaries		5.3	5.3
3.18 Scientific payload batteries		62.0	62.0
3.19 Electrical wiring		17.0	17.0

Table 3. Electrical system energy summary

Energy	Daytime, 163 hours		Nighttime, 350 hours	
	Allowable watt-hours	Current estimated watt-hours	Allowable watt-hours	Current estimated watt-hours
Total available energy	7628	7628	5300	5300
Scientific payload operation	5355	5320	4128	4128
Basic bus operation	745	734	827	886
Energy reserve	1528	1574	345	286

Table 4. Spacecraft command and data channels

Item	Commands	Data Channels
Basic bus		
Data link and TV camera No. 4	29	20
Signal processing	29	—
Mechanisms, propulsion, and vehicle	21	47
Electrical power and radar	14	15
Flight control	25	64
	118	146
Scientific payload		
Tape recorder	10	—
Surface geophysical	29	9
Subsurface geophysical	12	7
Geophysical thermal	5	9
Acoustic velocity	4	9
Subsurface sampler and processing	21	17
Surface sampler	9	4
Gas chromatograph	12	9
X-ray diffractometer	11	5
X-ray spectrometer	13	5
Radiation detector	7	5
Television system	32	12
	165	91
TOTAL	283	237

B. Scientific Instrument Payload

In addition to accomplishing the functional integration of the scientific instruments into the spacecraft, Hughes Aircraft Company has provided technical assistance to JPL in the development of the prototype instruments. As a part of that assistance a number of instrument changes have been evolved. The major changes are reviewed below:

1. Gas Chromatograph

The development of the prototype gas chromatograph is being carried out by a new vendor, Beckman Instruments, Inc. Beckman Instruments did not carry out the original breadboard development, and in the prototype development some changes in design approach which affect the instrument/spacecraft integration have therefore been made.

The breadboard design of the column detectors used a tritium foil radiation source, which ionized the gases passing through the columns, so that gases other than the carrier gas (helium) could be detected. The Beckman design uses a Karmen detector, which is a voltage regulating device, for performing this function. The Karmen detector employs a corona discharge effect for detecting unknown gases passing through the columns. As an unknown gas passes through the detector, the voltage regulating characteristics of the detector change. Thus the presence of a gas other than the carrier gas may be detected by changes in the detector anode-cathode voltage. The effect of this change in type of column detector is to require that the spacecraft provide different forms of power for the chromatograph.

A change has also been made in the number of data channels required. Originally the variation in column temperature was monitored to a tolerance of $\pm 0.5°$ C. It is now felt that $\pm 0.25°$ C is required. To attain this accuracy would require an additional amplifier, resulting in a significant weight increase. To avoid using these additional electronics, the following indirect method of measuring this parameter is being pursued. Since it is the variation in column temperature rather than its absolute value that is important, the absolute temperature will be measured to the larger tolerance of $\pm 1°$ C. The temperature variation during a run will be determined by monitoring the voltage of the column temperature controller and also the battery voltage. These two additional measurements will provide the measurement accuracy required. A study is being made to determine the effect on the spacecraft of the change in the form of power required and the additional data channels required.

2. X-Ray Diffractometer

In *SPS 37-12* a proposed reduction in the diffractometer data transmission bandwidth was discussed. All of the technical problems associated with this change have been resolved, and a change in the diffractometer interface description is being prepared. This change allows the diffractometer data to be transmitted on the low-power transmitter, rather than the high-power transmitter, with a resultant saving in power. The data bandwidth does require the entire capability of the low-power

transmitter, however, and no other experiments can be operated during transmission of diffractometer data.

The scan range of the goniometer has been increased from 50 to 83 deg in order to detect additional minerals. This increase will increase the time required to scan the range. As part of this change, Hughes Aircraft Company is conducting a study, at JPL's request, of the feasibility of allowing real time decisions during the scan.

The high-voltage power supplies for both the diffractometer and spectrometer have been moved from the thermally controlled compartment and packaged as part of the soil analysis instrument group. This change has been made (1) to reduce the length of the 25-kv high-voltage cable from the power supplies to the measuring heads, and (2) to eliminate a possible thermal dissipation problem within the compartment where the high-voltage power supplies were previously mounted. This change of location places a new requirement on the power supply designs. Since they are not now thermally protected by the compartment, they must be designed to survive the very low temperatures of the lunar night. This requirement is being included in the present design.

3. Physical Parameters Package

Three of the four temperature measuring devices in the physical parameters package are now interferometer spectrometer radiometers, rather than total radiation pyrometers as previously used. The fourth device is a thermopile. The change to the interferometer was made because it had become apparent that the development of the total radiation pyrometer could not be accomplished in the time span of this program. The selection of the interferometer spectrometer allows the use of a slightly modified off-the-shelf item although it does impose more difficult interface problems on the spacecraft. It requires increased power and additional volume in the temperature-controlled compartment and may present a problem in the accuracy of transmission. These problems are now being investigated at Hughes Aircraft Company.

C. System Analysis

1. Guidance and Trajectory

a. Vernier propellant consumption. A careful recalculation of the vernier propellant consumption has been made. Except for the mid-course correction, where the full 26-pound allotment is regarded as a nominal condition, the dispersions during the terminal descent phase are statistically combined to obtain a more realistic picture of the maximum propellant requirement. Table 5 summarizes the results of this calculation. The initial conditions for the vernier phase are those for which the sum of the maximum terminal descent propellant requirement (nominal 3σ dispersion), plus the maximum mid-course requirement, just equals 161 pounds; this amount, except for ullage, represents the present tank capacity. The nominal conditions are 375 ft/sec in velocity and 31,000 feet in altitude.

The importance of this type of propellant analysis is that it determines the upper limit of the starting velocity and altitude conditions within the capability of the system. The lower limit is determined by sensor constraints discussed in detail later in this section. The difference between the two velocity limits represents the unbraked impact speed window capability, which has a direct effect on the hourly and daily launch window as was discussed in detail in *SPS 37-12*.

Table 5. Vernier propellant consumption

Operational phase	Nominal consumption, lb	3σ dispersion, lb
Mid-course correction (full allowance)	26	—
Main retro phase		
Pre-main retro ignition	0.4	Negligible
Control during thrusting	30.0	3.5
Thrust tail-off and separation	7.2	0.9
Vernier phase		
Guided descent (minimum and maximum thrust)	82.0	9.0
Allowance for segmental approximation of descent parabola	3.0	—
Touchdown	2.3	2.6
Total	150.9	10.1

b. Main retro propellant. Several changes in the ground rules for calculating requirements for main retro and vernier propellant have been made. The design spacecraft weight at start of servoed vernier descent is now lighter, corresponding to full consumption at mid-course of the 26-pound mid-course correction allowance, in place of only 17 pounds consumed. In addition, the propellant consumed during the most severe dispersions encountered during the powered descent were previously added algebraically to the nominal propellant required. In the present calculations, the propellant consumed because of these worst dispersions is added to nominal

propellant in a statistical (rms) manner. Under these conditions, a servoed descent from a nominal velocity of 375 ft/sec after main retro case separation brings the total vernier propellant required to the existing useful tank capacity of 161 pounds. Included in this 161 pounds is 7.2 pounds for an 8-second main case separation period, during which the vernier thrust is at maximum in order to optimize separation dynamics. During this separation period, the vehicle is slowed 35 ft/sec. The nominal speed at main retro burnout is thus 410 ft/sec. For this weight vehicle, and with unbraked impact speed of 8810 ft/sec, or 2686 meters/sec (a slight change from the value used formerly), a burnout speed of 410 ft/sec requires 1428 pounds of main retro propellant when the vernier engine is acting at its mid-thrust level of 200 pounds. This new figure for main retro propellant weight is 17 pounds below the former weight (1445 pounds).

With 1428 pounds of main retro propellant, if no vernier propellant is used during mid-course, the resulting nominal speeds for this heavier vehicle are 550 ft/sec at main retro burnout and 515 ft/sec after main case separation. At this higher speed at start of servoed vernier descent, the additional 26 pounds of unused mid-course vernier propellant is more than adequate for the ensuing successful descent to a soft landing.

2. Limitations on Spacecraft Attitude Control Imposed by Doppler Radars

a. General. The current spacecraft descent trajectory design is based on the assumption that the doppler velocity and altitude radars cannot be reliably used while the main retro-engine is burning. Thus the spacecraft attitude will be held fixed inertially throughout the main retro burning phase and, due to main retro thrust misalignments, large lateral velocity components may build up during this time. If the longitudinal velocity at main retro burnout is small, large angles between the spacecraft roll axis and the velocity vector may result. Immediately after burnout, the doppler velocity radar will then control the spacecraft attitude and cause the roll axis to align itself with the velocity vector (by servoing the lateral velocity components to zero). Thus at acquisition, large angles between the spacecraft roll axis and the velocity vector can result in a near-zero component of velocity along any one (or even two) of the radar beams (Fig 2). Under this condition, the beam will not operate properly for reasons described later in this section. Thus there is a velocity-angle region about the spacecraft (hereafter referred to as the "blind" zone) in which radar performance is compromised. The extent of this zone is indicated in Figure 3.

Since it is desirable to keep operation out of this blind zone whenever possible, the burnout velocities should be as large as possible. On the other hand, vernier fuel considerations tend to require the burnout velocity to be low. The present spacecraft design does not provide a sufficient spread between the limits imposed by these two requirements to provide the necessary launch window.

Several possible solutions are under study. The most attractive of these is to allow low burnout velocities and provide logic circuitry in the radar which will minimize the effects of this restriction. This can be done by switching in a zero velocity signal for that beam which is near zero and thus inoperative, and computing the velocity components on that basis.

b. Radar limitations. Due to the current mechanization of the doppler velocity and altitude (ranging) radars, there are several restrictions imposed on the spacecraft attitude and velocity vector. These are described briefly below.

Attitude relative to lunar vertical. As shown in Figure 2, the doppler velocity antenna beams are tilted 25 de-

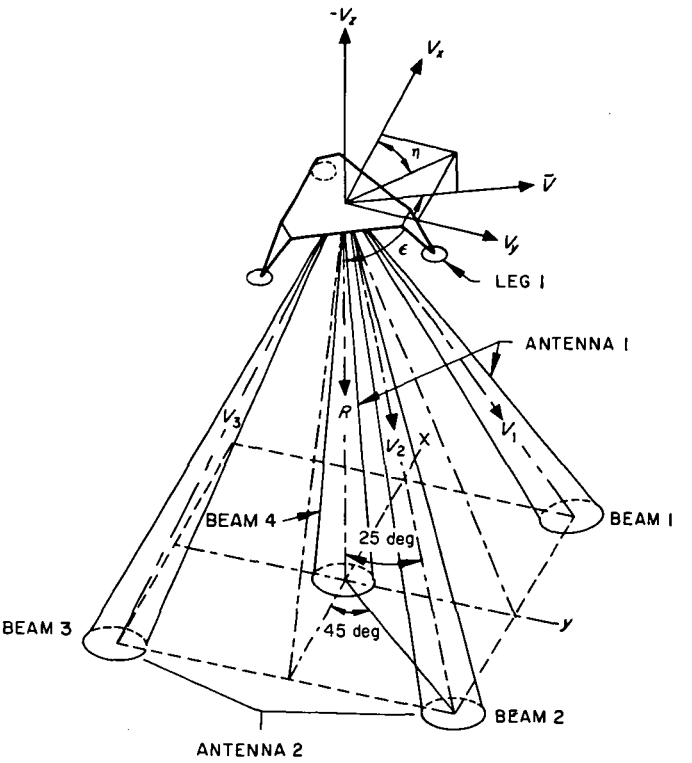

Figure 2. Spacecraft radar beam geometry

grees relative to the spacecraft roll axis. Thus to assure that all three beams hit the lunar surface, the spacecraft attitude angle relative to the local lunar vertical can at no time exceed 57 degrees(82 degrees between the beam and local vertical) at an altitude of 50,000 feet (assuming a smooth, round Moon). Further, to provide the required signal-to-noise ratio (under the assumption of a Lambert scattering law for the lunar surface at the radar frequencies), this attitude angle shall be limited to 45 degrees.

Negative longitudinal velocity limitation. The current doppler extraction circuitry in the radars does not include equipment necessary for operation when the component of velocity along the spacecraft roll axis is negative (that is, in an upward or rising direction). Thus the angle between the spacecraft roll axis and the velocity vector has an absolute maximum of 90 degrees. It should be noted here that the radar design has been maintained such that the addition of this negative V_z capability is a relatively easy matter in case it is desired in future systems.

Angle between spacecraft roll axis and velocity vector. The component of velocity along any of the radar beams (V_b) is given by

$$V_b = V_t \cos\gamma$$

where V_t is the total velocity magnitude and γ is the angle between the velocity vector and the radar beam. Two considerations restrict operation when this component of velocity, V_b, approaches zero: the signal-to-noise ratio decreases due to an increasing noise density from the crystal mixers at the low frequencies; and the tracking bandpass filter cannot be swept close to zero doppler during the acquisition phase without having a high probability of locking on to the leakage signal. These two restrictions, defining a blind zone for acquisition, are shown in Figure 3 for the case where the velocity vector, the spacecraft roll axis, and one of the doppler velocity beams all lie in the same plane. That is, if the spacecraft falls in that region at main retro burnout, one of the radar trackers will not be able to acquire the reflected signal and thus a measurement of velocity cannot be made. The position and extent of this blind zone may be observed in another way in Figure 4. Here the blind zone is shown

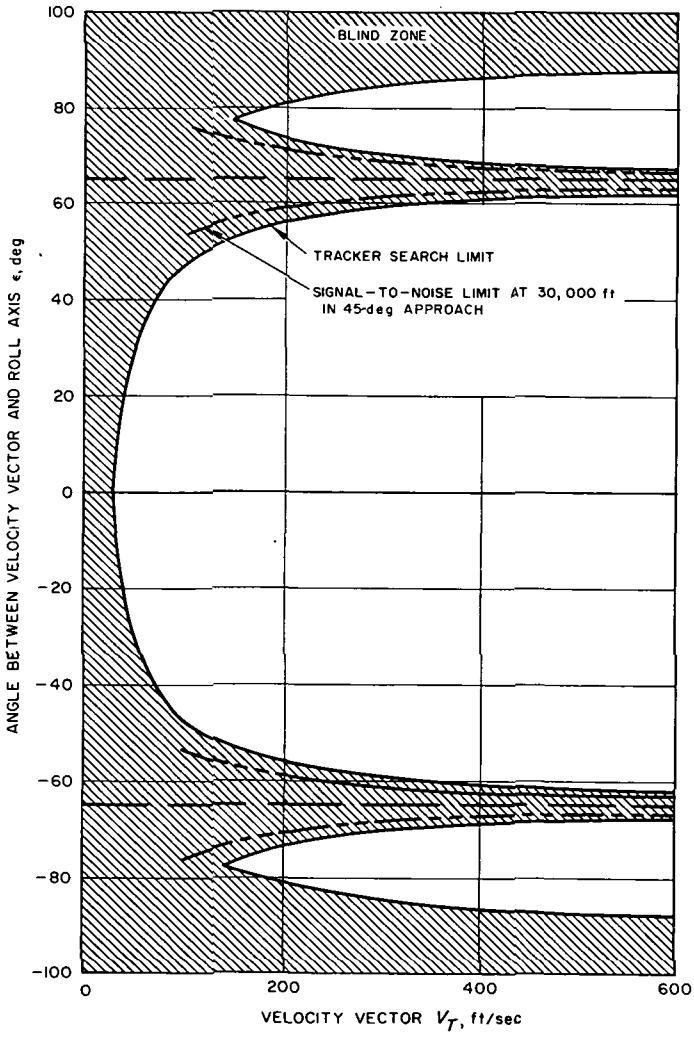

Figure 3. Blind zone for radar acquisition

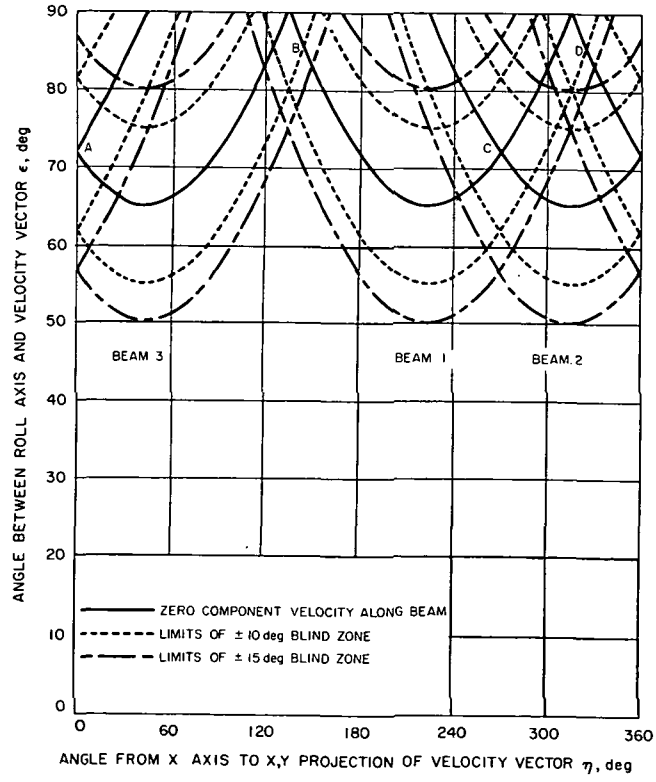

Figure 4. Blind zone as function of ϵ and η

as a function of ϵ (the angle between the velocity vector and the roll axis) and η (the angle between the projection of the velocity vector into the spacecraft X — Y plane and the spacecraft X axis). Two widths of the blind zone are shown; one for a ±10-degree width and the other for a ± 15-degree width. The solid line indicates those angles for which the component of velocity along each of the beams (1, 2, and 3) is exactly zero. From this figure, it may be seen that if the angle between the spacecraft roll axis and the velocity vector is allowed to exceed 65 degrees, there are large regions in which at least one of the three radar beams sees zero or near-zero velocity, several regions (marked A, B, C, and D) in which two of the beams simultaneously have near-zero velocities and, if the blind zone is large enough (greater than 12.5 degrees), one region in which the blind zone of all three beams will coincide. A rough analysis has shown that the probability of the velocity vector falling into the blind zone is approximately 0.12 for a ±10 degree blind zone, subject to the following assumptions:

(1) η is uniformly distributed between 0 and 360 degrees.

(2) ϵ is Rayleigh distributed with $\sigma = 30$ degrees (applies to the 45 degree landing approach case).

(This is grossly oversimplified and is included here only to indicate that if ϵ is allowed to reach 90 degrees the problem of blind zones is a real one.)

c. Vehicle design limitations. As a result of a previous decision not to use the doppler radar outputs to control the vehicle attitude until after the main retro-engine has burned out, large angles between the spacecraft roll axis and the velocity vector at burnout may exist. This is due to misalignments between the initial velocity vector and the thrust axis during burning, discussed in detail in Reference 2. During the entire retro-engine burning phase, the vehicle attitude control is in an inertial mode. Thus any initial misalignment between the thrust axis and the velocity vector will persist throughout the burning and will build up a lateral velocity component at the same time that the longitudinal velocity is being decreased. For the design tolerances involved, this lateral velocity component may be as much as 150 ft/sec (3σ). Thus trajectories with longitudinal burnout velocities of this magnitude will result in large angles between the roll axis and the velocity vector at burnout.

The main retro-engine burnout conditions are influenced (among other factors) by the lunar approach velocity, the total impulse supplied by the main retro, the amount of vernier engine propellant allotted for the post-retro descent, the landing approach angle, and the ignition altitude, as well as the angular considerations described above. In order to provide the required Goldstone visibility at landing for all conditions of lunar declination, Earth-Moon distance, and permissible launch azimuths, variations in the time of flight and thus in lunar approach velocity must be provided. This was discussed in detail in *SPS 37-12*. To accommodate these variations in approach velocity while maintaining a fixed total impulse retro-engine requires a variation in retro-engine burnout velocity of at least 218 ft/sec, and preferably 238 ft/sec, assuming the full 90 to 114 degree launch azimuth capability. (If this launch azimuth capability is not available, even greater velocity variations are required.) Other considerations (primarily the vernier engine propellant limitations) limit the maximum allowable nominal burnout velocity to approximately 375 ft/sec. Thus a minimum nominal burnout velocity of about 375 — 218 = 157 ft/sec (137 ft/sec desired) would be required to provide the desired launch windows. This, in conjunction with the dispersions on the burnout velocity (±125 ft/sec —3σ), would result in a minimum burnout velocity of nearly 32 ft/sec, which is much too low.

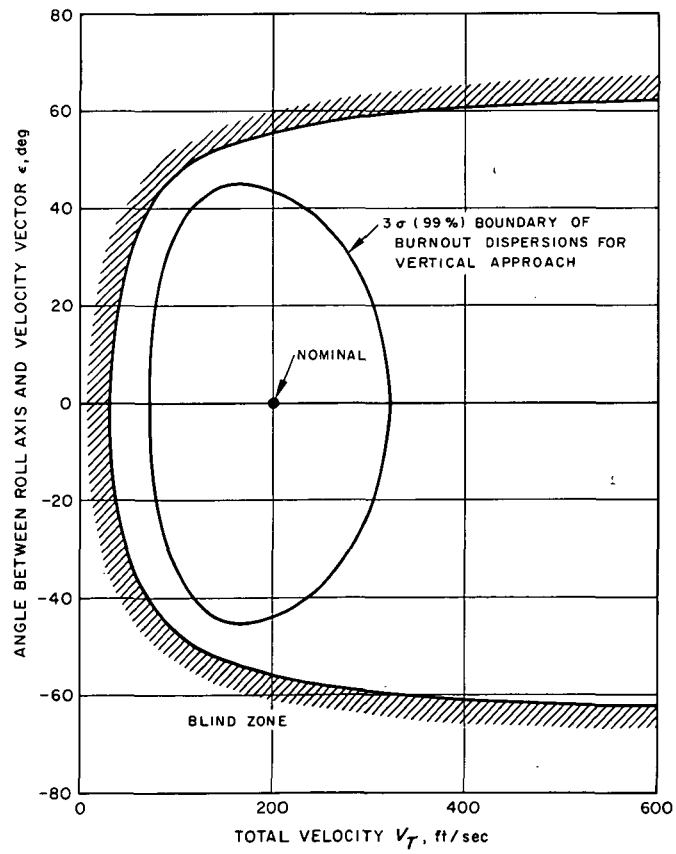

Figure 5. Blind zone and burnout dispersion

This problem may be considered in another way. Shown in Figure 5 are the doppler velocity acquisition limits replotted from Figure 3. Also shown in Figure 5 is the burnout dispersion ellipse (3σ) for the minimum allowed nominal burnout velocity for a vertical approach (197 ft/sec) that will provide no burnout conditions that fall in the radar blind region and no angle greater than 45 degrees with the vertical. This condition would provide a variation in approach speed of only 375 — 197 = 178 ft/sec, which is considerably under the 218 ft/sec velocity increment required.

The situation is somewhat more complicated for oblique landing conditions, and the burnout conditions for the maximum landing approach angle case (45 degrees) is being worked on currently. It has already become evident that for a 45-degree landing condition, angles between the roll axis and the velocity vector greater than 65 degrees will be required to meet the desired launch window conditions. In fact, it is highly desirable to operate with this angle up to its absolute maximum of 90 degrees. Thus burnout conditions extending into the blind zones are required.

d. Possible solutions. Several solutions to the doppler radar limitation problem are possible and are considered briefly in the following paragraphs. The currently most attractive solution (Item 2 below) is then discussed in more detail.

(1) Further tests of radio propagation in the highly ionized gases of a rocket exhaust may show that performance of the doppler radar will not be seriously degraded by the main retro-rocket exhaust. In this case, doppler radar operation could commence before the velocity errors grow large, and the problem would be eliminated. This is the hoped-for solution for subsequent flights, but it cannot be counted on for the first flights.

(2) The radars can be modified to eliminate the blind zone restriction. This could be accomplished by providing logic circuitry in the radars such that, should one or more of the beams have a reliable-operation signal[a] present and burnout has occurred, a zero doppler signal is switched in place of the normal output of the beam (or beams) that does not have a reliable-operation signal. The V_x and V_y outputs are then computed on this basis and used to control the vehicle attitude. Study has shown that even though these measured velocity terms will be in error, the amount of the error is not so large as to prohibit proper alignment of the spacecraft attitude if the width of the blind zone is approximately ±10 degrees or less.

(3) Raise the minimum main retro burnout velocity high enough so that operation in the blind zone is never required. This can, conceptually at least, be done in several ways:
(a) Eliminate from the permissible launch window those days in which the lowest lunar approach velocities are required.
(b) Permit landings at times when visibility from Goldstone is not available.
(c) Increase maximum allowed burnout velocity (and thus the minimum, as well, for a constant approach velocity increment) by increasing either the amount of vernier fuel or the maximum thrust level of the vernier engines. Both of these approaches are very costly and time-consuming at this stage in the development. Also the maximum operating altitude for the radars would have to be increased.
(d) Decrease the total velocity increment added during the main retro burning phase for those cases in which the lunar approach velocity is low. This could be done by off-loading main retro propellant, by reducing the vernier thrust level during the main retro burning, or by adding ballast to the spacecraft.
(e) Some combination of the above.

Of these solutions (1) is most desirable but cannot be counted on at the present time; (2) appears to be feasible and is described further in the following section; (3a) and (3b) are most undesirable from an operations point of view; (3c) requires an increase in weight and an appreciable schedule delay; and (3d) also appears feasible especially in conjunction with (2).

e. Study of attitude control in the presence of large velocity errors. To investigate the effect on spacecraft attitude correction of selecting zero for the component of velocity along any radar beam, consider the following expressions for the velocity components in spacecraft coordinates (V_x, V_y, V_z) in terms of the components of velocity along each radar beam (V_1, V_2, V_3)

$$V_x = \frac{V_1 - V_2}{2B_x}$$

$$V_y = \frac{V_2 - V_3}{2B_y}$$

$$V_z = \frac{V_1 + V_3}{2B_z}$$

[a] This is a signal that currently exists in each radar beam circuitry and indicates that there is a signal in that velocity tracker bandwidth.

where B_x, B_y, and B_z are the direction cosines of the beams. Setting one or more of the components V_1, V_2, and V_3 equal to zero for those velocity directions η (refer to Figure 2), where the velocity would be in the blind zone of the corresponding radar beam, and solving the above expressions for V_x, V_y, and V_z gives the components of velocity in spacecraft coordinates measured by the radar when the velocity is in the blind zone of the corresponding radar beam or beams. The V_x and V_y signals go to the flight control system causing the spacecraft to pitch and yaw in such a direction as to bring them to zero, thus aligning the Z axis of the spacecraft parallel to the velocity vector. Because V and/or V_y are not correct under these conditions, the flight control system will initially change the attitude of the spacecraft in the wrong direction. This angular error α in the direction of the attitude correction is

$$\alpha = tan^{-1}\frac{V_y}{V_x} - \eta$$

where η is the true maneuver direction.

The angular error α has been plotted as a function of ϵ, the angle from the spacecraft roll axis to the velocity vector as shown in Figure 2 with η as a parameter in Figures 6, 7, and 8. The curves in Figure 6 were computed assuming that $V_3 = 0$ for all ϵ. Similarly, the curves in Figures 7 and 8 were computed assuming V_1 and V_2, respectively, equal to zero. Since the radar blind zone is not as large as the range of ϵ on the abscissa of the graphs, the angular error α will not actually reach the maximum values represented here. To find the actual angular error, consider only that portion of the curve, centered about the point where α equals zero, where values of ϵ on either side of that point are equal to the width of the radar blind zone. For values of ϵ outside these bounds, the angular error is actually zero unless the velocity is in the blind zone of another beam. The curves in Figure 4 indicate most conveniently which beams are in a near zero velocity condition for all η and for ϵ from 0 to 90 degrees. For some values of η and ϵ, it is possible for the velocity to be in a blind zone of two beams simultaneously as indicated in Figure 4. For these cases, the angular error α is computed in the same manner as before, and these results are included in the boundary curves shown in Figure 9. It can also be seen from Figure 4 that, for a ± 15 degree blind zone, the velocity is in the blind zone of all three beams at $\eta = 315$ degrees and $\epsilon = 78$ degrees. Thus V_x, V_y, and V_z would all be equal to zero and the flight control system would receive zero signal resulting in no change in the spacecraft attitude. Therefore, a blind zone of $\pm$ 15 degrees

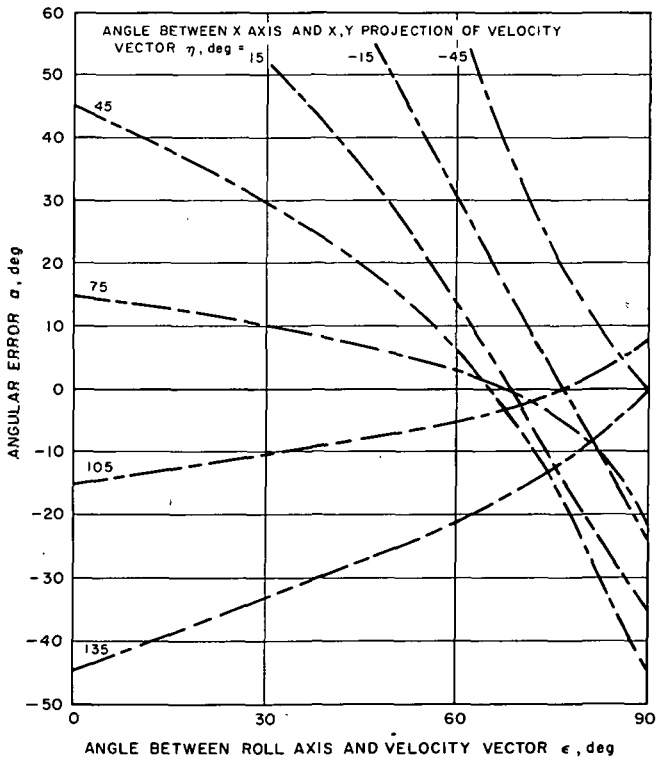

Figure 6. Angular error (α) vs ϵ Velocity along Beam 3 = 0

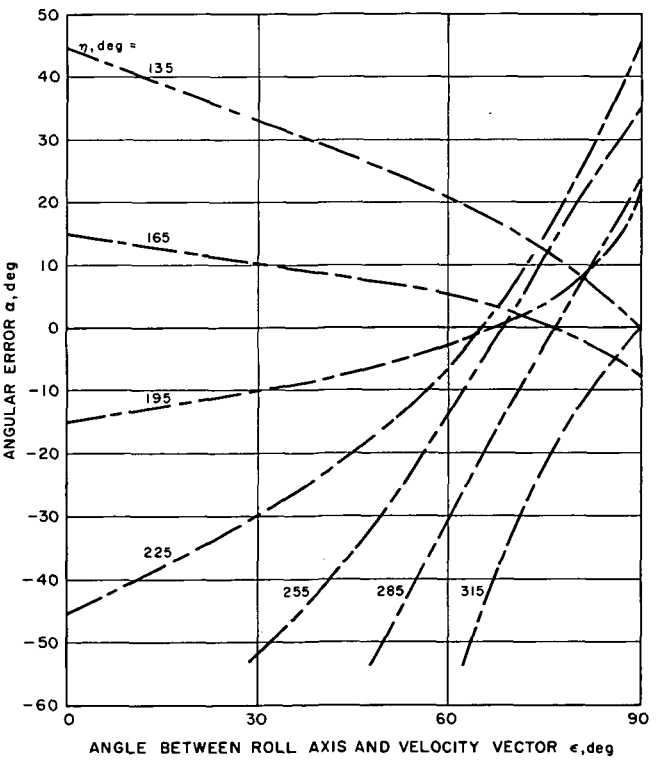

Figure 7. Angular error (α) vs ϵ Velocity along Beam 1 = 0

width is not tolerable and, in fact, ± 12.5 degrees is the widest blind zone possible if the condition described above is to be avoided.

The results of these calculations are summarized in Figure 9, which shows the bounds (within the shaded area) of the angular error (α) as a function of η subject to the following conditions:

(1) ϵ between 0 and 90 degrees.

(2) Width of blind zone is ± 10 degrees.

From this curve, it may be seen that the maximum angular error is 35 degrees. It should be noted here that this angle α is the error in the direction in which the spacecraft begins to maneuver immediately upon radar acquisition. Since this error is small, the maneuver will always be in the proper direction to reduce ϵ, thus bringing the spacecraft out of the blind zone.

f. Conclusions. From this study to date, the following conclusions may be drawn:

(1) A change is required to the present spacecraft design in order to provide landing visibility at Goldstone over all the desired launch windows.

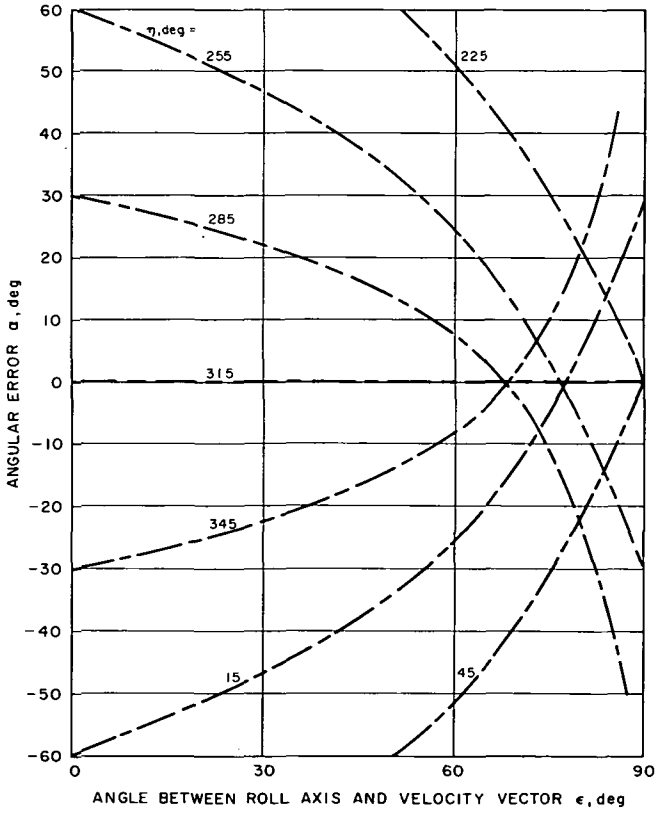

Figure 8. Angular error (α) vs ϵ Velocity along Beam 2 = 0

(2) To accomplish this change, there is a region of required operation (where the angle between the spacecraft roll axis and the velocity vector are greater than 65 degrees) in which the doppler velocity sensor does not perform properly.

(3) The spacecraft attitude control can work through this region if certain logic changes are made in the radar and if this blind zone is constrained to ± 10 degrees in width.

(4) With this change to the radar (and possibly the reduction of the vernier thrust level during main retro burning, and for the addition of ballast where necessary), the total launch window requirements can be met.

3. Design Mission Sequence for List II Payload

The following design mission sequence (Figs 10 through 17) illustrates an order of experiments which may be performed within the currently known system, operational, and DSIF constraints for an August 6, 1963, launch (last day of the August launch window), with touchdown at 5 hours before the end of Goldstone visibility and 163 hours before the lunar day/night terminator.

An increase in the total energy available to the scientific payload, a decrease in the expected power consumption of some instruments, and the ability to transmit the X-ray diffractometer data in the low-power transmitter mode will now essentially enable all soil analysis and noncontinuous geophysical experiments to be completed

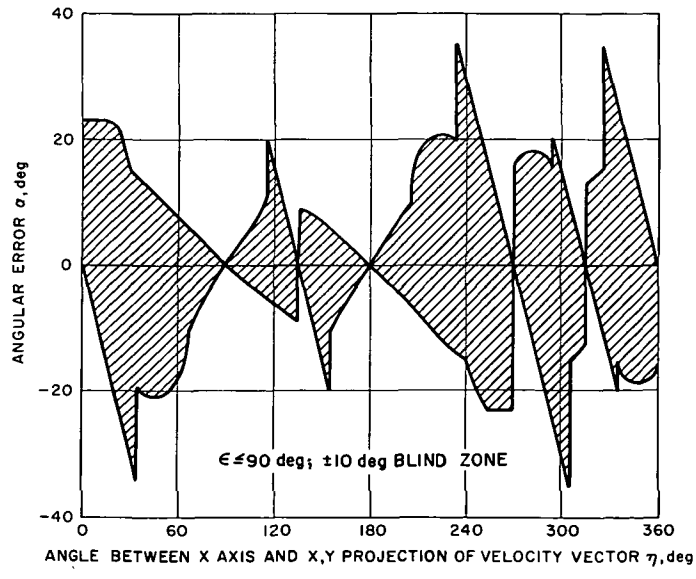

Figure 9. Angular error boundaries vs η

on the first lunar day. However, since the energy available to the scientific payload (5470 watt-hr for a 163-hour day) and the energy required to perform the experiments (5500 watt-hr) are presently approximately equal, further variation in either could necessitate a later rescheduling of some experiments to the second lunar day.

a. Mission constraints. This design mission sequence is based upon the following principal constraints:

(1) The scientific payload will be the List II complement of instruments and auxiliaries, which consists of the following:

(a) Surface geophysical experiments.
(b) Subsurface geophysical probe.
(c) Subsurface sampler.
(d) Surface sampler.
(e) Gas chromatograph.
(f) X-ray spectrometer.
(g) X-ray diffractometer.
(h) Radiation detector.
(i) Television.
(j) Tape recorder.
(k) Auxiliaries (mechanism, thermal, battery, wiring).

(2) The total energy available to the scientific payload during the first lunar day will be 5470 watt-hr, based on a 163-hour period of daylight. The energy consumed by the scientific payload during the lunar night will be 4128 watt-hr.

(3) A standard trajectory is selected which represents the worst case in terms of time from touchdown to the first day/night terminator:

(a) Launch date: August 6, 1963.
(b) Launch azimuth: 114 degrees.
(c) Touchdown at 35.5 degrees west longitude.
(d) Time from touchdown to dusk: 6.8 days (based on zero degree horizon).

(4) Utilization of the DSIF will conform to the following guidelines:

(a) Injection to 48 hours following lunar nightfall; 24 hr/day DSIF coverage.
(b) Remainder of first lunar night: daily tracking missions alternating between Woomera and Johannesburg stations.
(c) Just before lunar dawn to 24 hours after sunrise: 24 hr/day coverage.
(d) Remainder of second day: Goldstone tracking missions on second, fourth, sixth, and eighth days, Woomera and Johannesburg each having two tracking missions.
(e) Second lunar night: Woomera and Johannesburg, each three tracking missions.
(f) Third lunar day: Goldstone two tracking missions.
(g) Repeat (e) and (f) for remainder of mission.

b. Sequence. The experiments of the first lunar day are summarized in Figure 10, and experiments for each of the seven periods of Goldstone visibility after touchdown are detailed in Figures 11 through 17. With the exception of the continuous experiments (scientific temperature and the radiation detector) and thermal diffusivity, all experiments in this sequence are shown conducted under Goldstone control, since ample Goldstone visibility time is available. In addition to the experiments shown, engineering data will normally be sampled hourly, and more often during many operations. Experiments to be conducted during the first lunar night will be the scientific temperature and radiation detector, plus the nighttime portion of the surface thermal diffusivity. During periods where the DSIF is not scheduled for *Surveyor* tracking, data from the continuous experiments will be recorded (to a maximum of 18 hours per recording period, as limited by the recorder capacity).

D. Flight Control

1. Introduction

The flight control subsystem consists of those elements of the spacecraft which provide velocity control and attitude control during the transit phase of the *Surveyor* mission. Functionally, the lunar radar and propulsion elements are part of this subsystem although they are covered in other sections of this report. Elements of the flight control subsystem that are treated in this section include optical sensors, inertial instruments, attitude controls, and flight control electronics.

2. System Design

a. Summary. Two important design changes have been made in the flight control system during the reporting period. First, the thrust control system has been converted from an open-loop thrust command channel to a closed-loop acceleration command servo. This has been accomplished by extending the use of the accelerometer in the mid-course velocity control system to the terminal

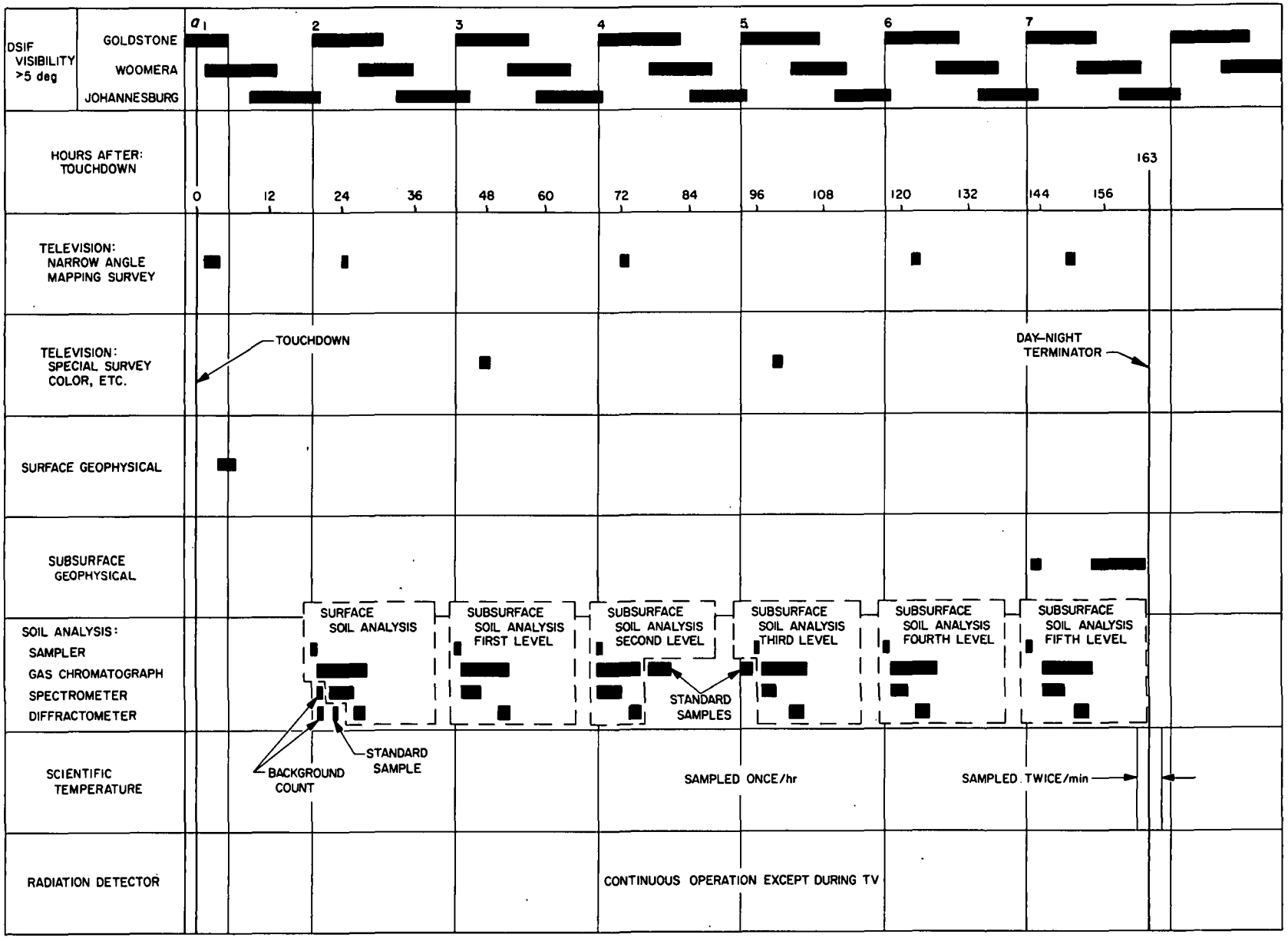

a PERIOD OF POST-TOUCHDOWN GOLDSTONE VISIBILITY

Figure 10. *Surveyor* design mission sequence

CONFIDENTIAL

CONFIDENTIAL

CONFIDENTIAL

CONFIDENTIAL

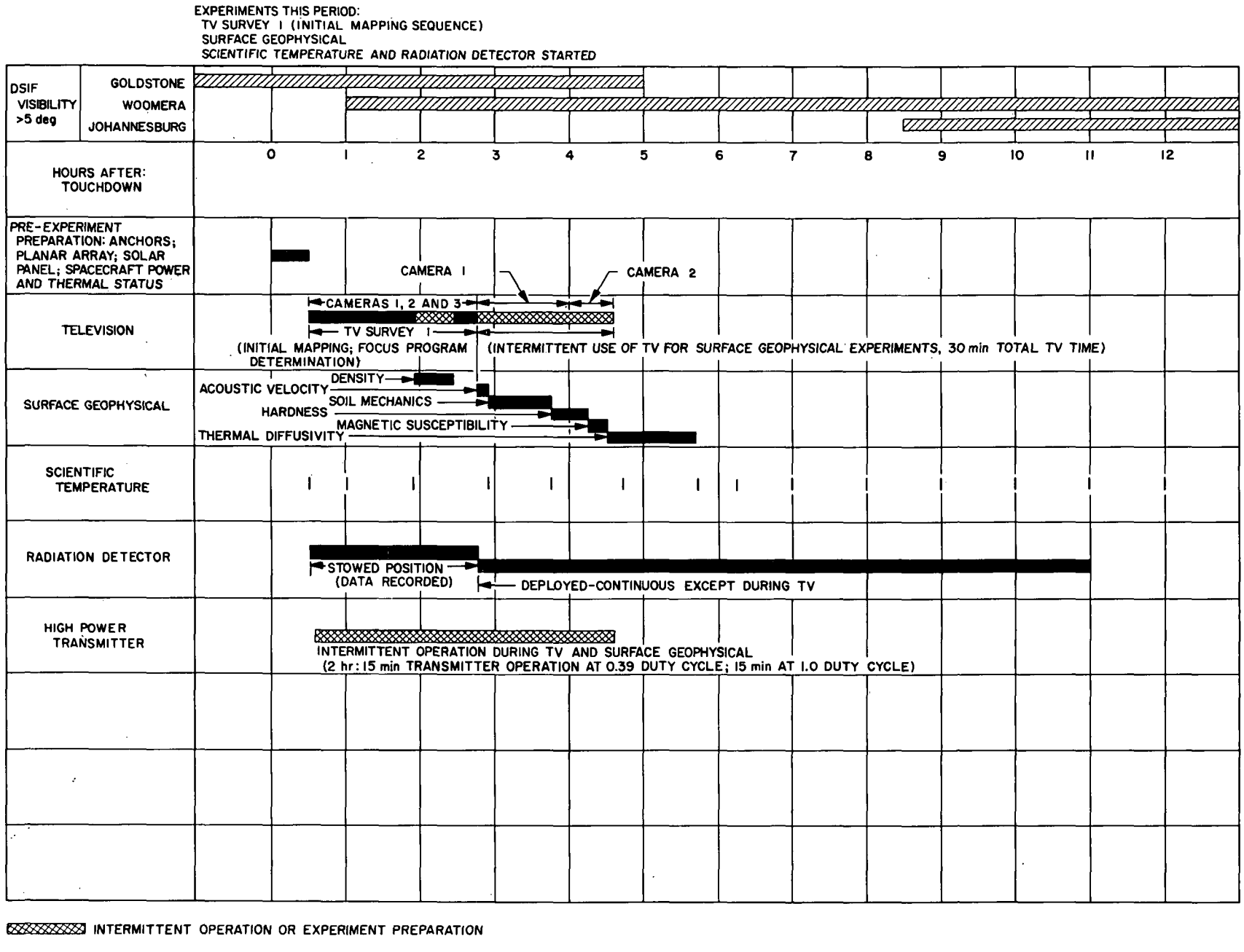

Figure 11. First period of Goldstone visibility

CONFIDENTIAL

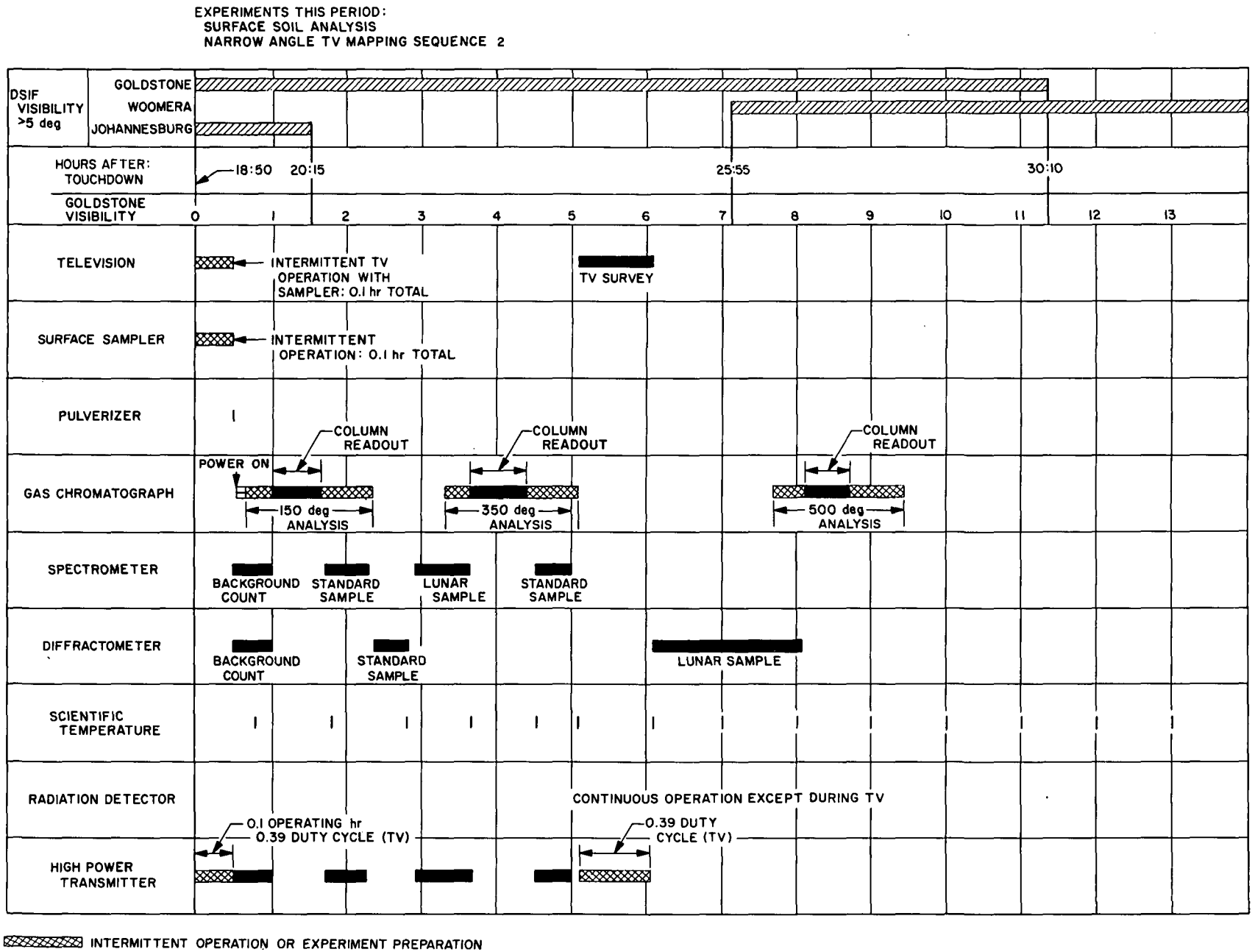

Figure 12. Second period of Goldstone visibility

CONFIDENTIAL

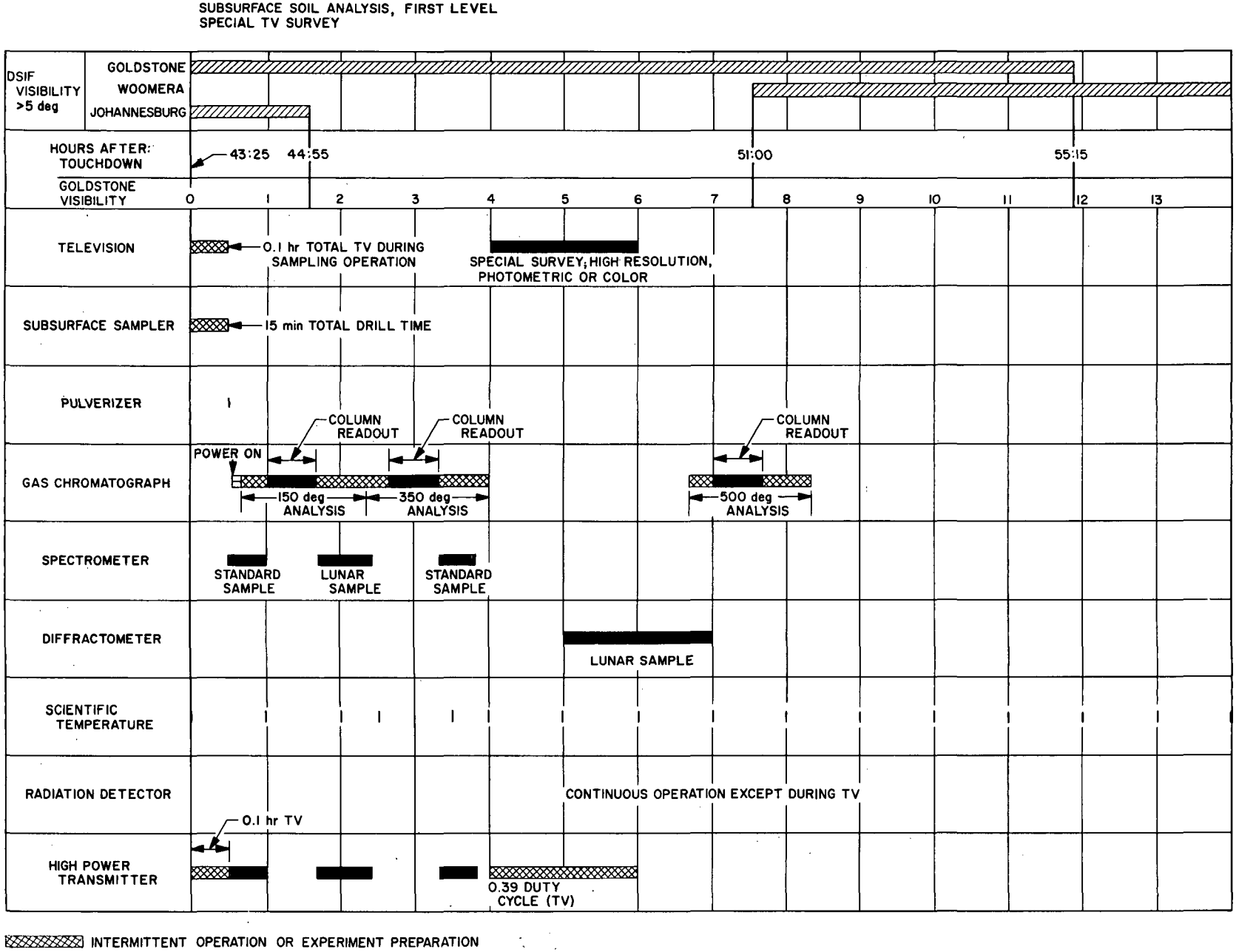

Figure 13. Third period of Goldstone visibility

CONFIDENTIAL

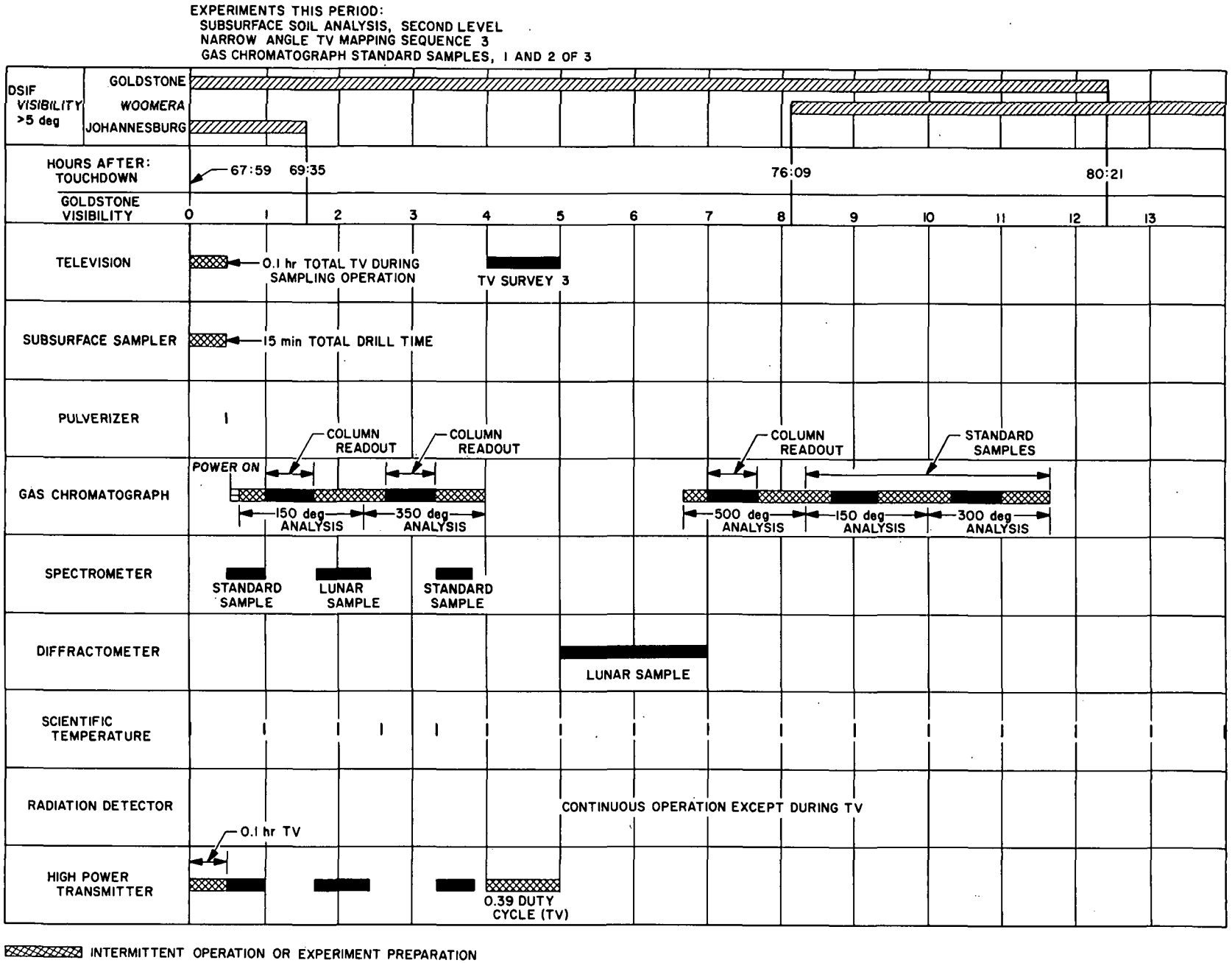

Figure 14. Fourth period of Goldstone visibility

CONFIDENTIAL

CONFIDENTIAL

CONFIDENTIAL

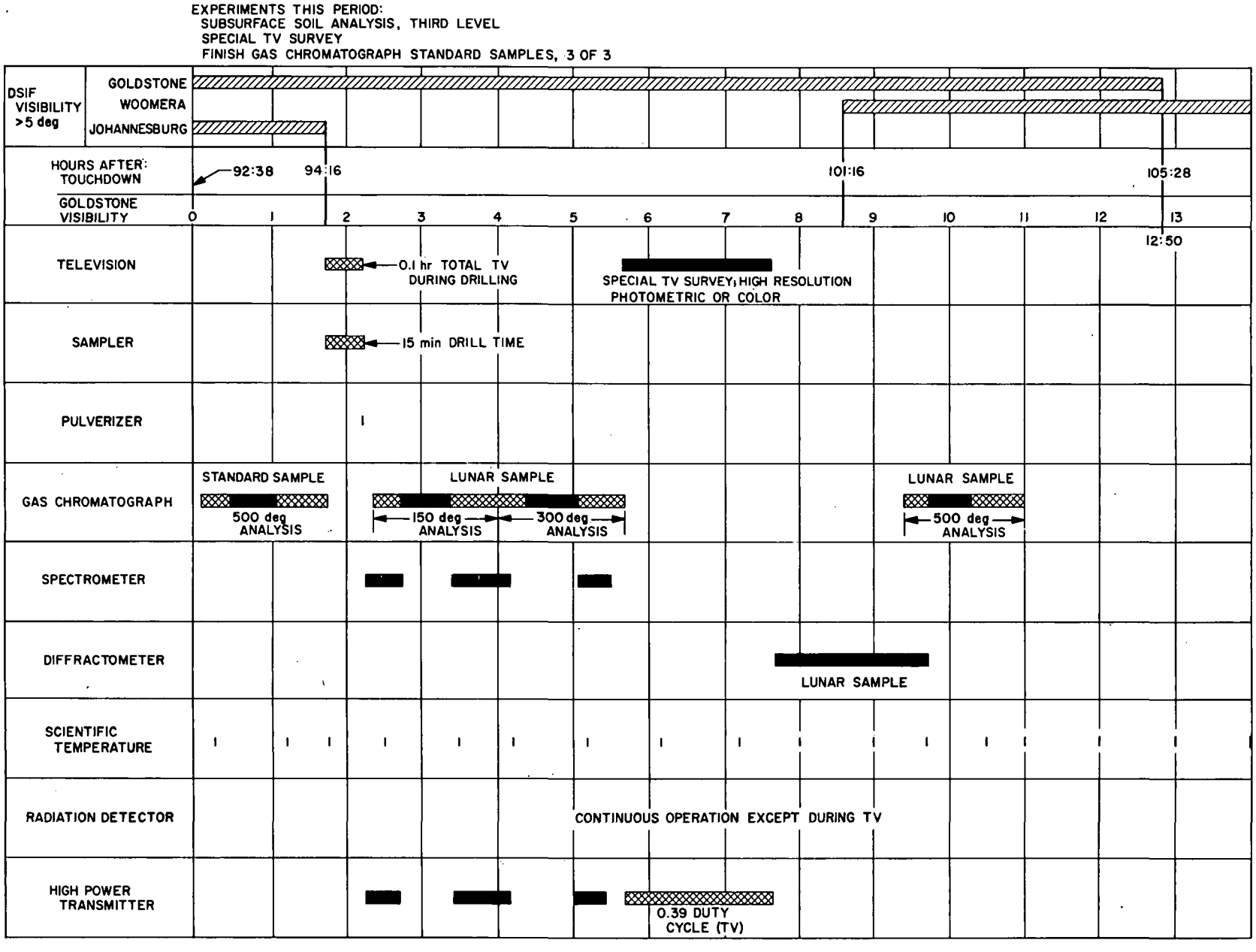

Figure 15. Fifth period of Goldstone visibility

CONFIDENTIAL

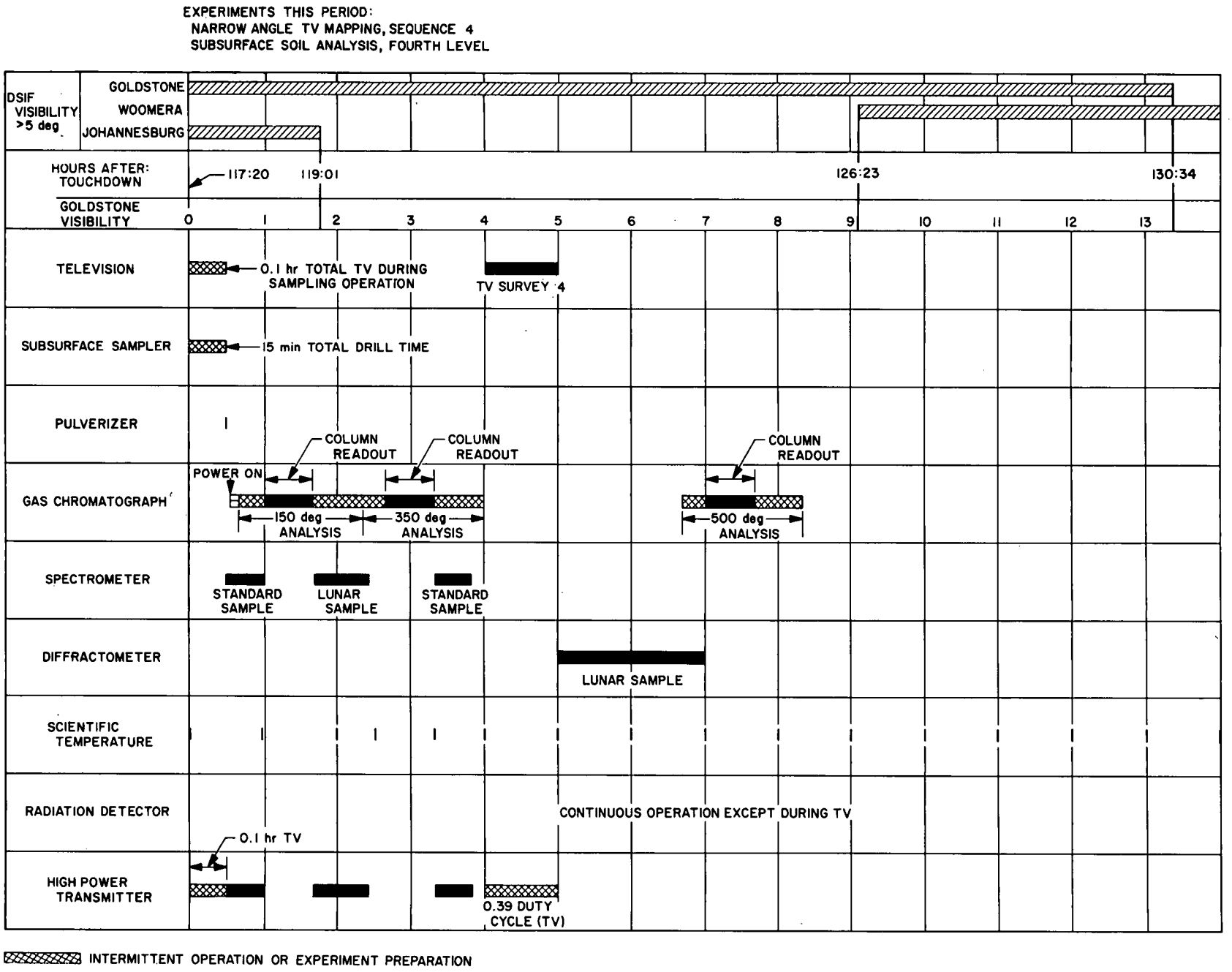

Figure 16. Sixth period of Goldstone visibility

CONFIDENTIAL

CONFIDENTIAL

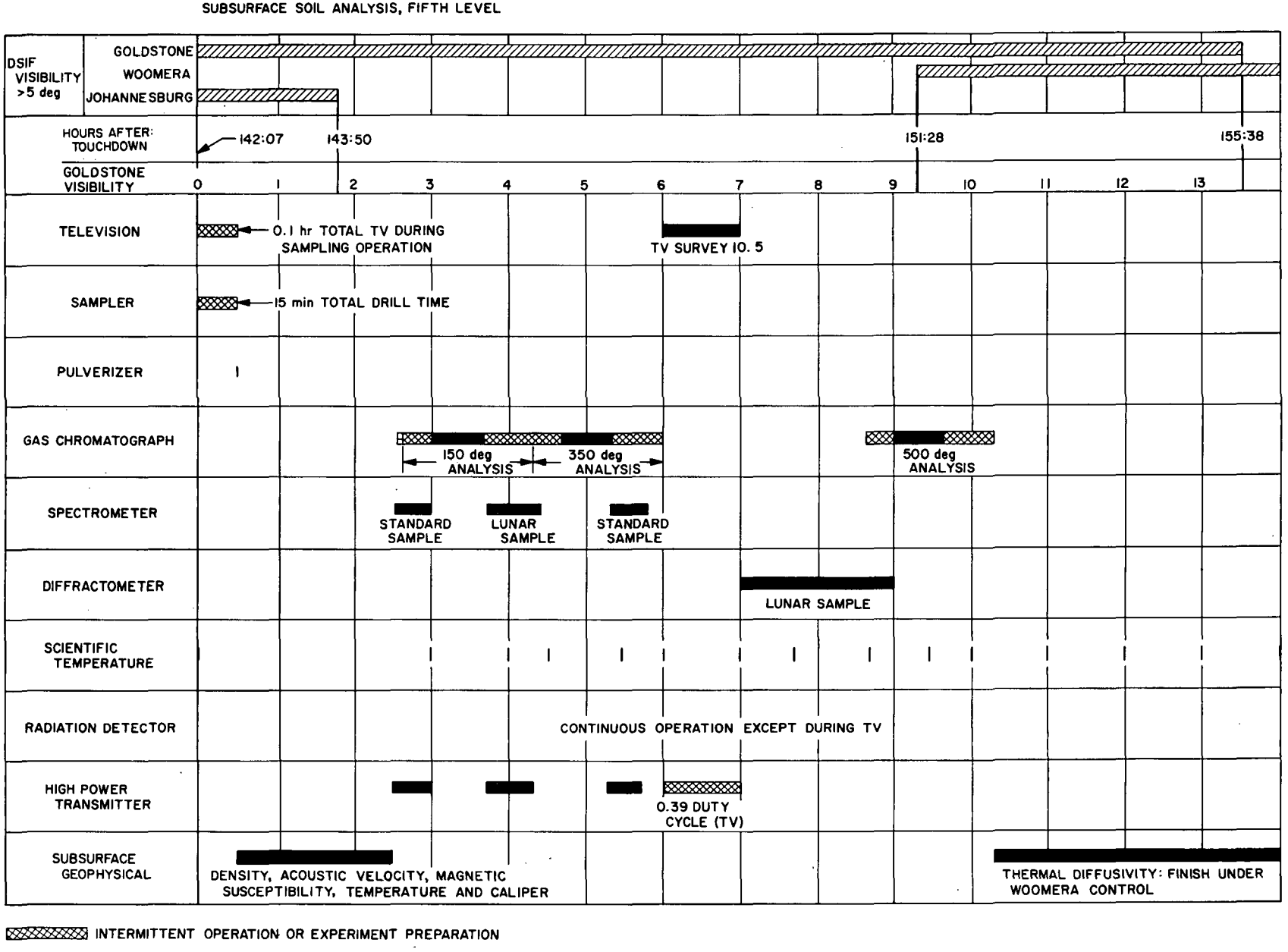

Figure 17. Seventh period of Goldstone visibility

phase. Since the maximum acceleration encountered in the terminal phase is about 0.41 *g*, it has been necessary to increase the accelerometer range from 0.25 to 0.5 *g*. The principal reason for the design change is to achieve a more efficient use of vernier engine fuel by operating the engines nearer their maximum thrust levels during the vernier descent phase. The large dispersion in thrust versus command in the open loop configuration, due mainly to the engines themselves, prevented operation on an efficient altitude-velocity control law, i.e., near maximum thrust. The precision accelerometer provides the means of accurately controlling thrust, independent of engine dispersions.

The second important modification involves a change in the thrust phase roll control system. The bang-bang solenoid actuator originally planned for use in a limit cycle control system has been replaced by a proportional positioning servo employing a conventional 400-cps servo motor. Two factors are involved in this decision. The inertia and center of gravity offset of the vernier engine have increased appreciably since the original design concept was established. Due to the resulting increase in force level and weight required, the solenoid is no longer considered competitive with a more complex but lighter weight servo. In addition, RMD (Thiokol) has expressed serious concern over the shock level experienced by the engine nozzle when the solenoid actuator hits the stops. The proportional servo, besides providing a net saving in spacecraft weight, will not constitute a degrading factor in television coverage, as was true of the bang-bang solenoid system.

The functional design of the coast and thrust phase control system has been refined through the use of both analog and digital computer studies. The coast phase gas jet attitude control system design has undergone changes principally with regard to loop gains in order to obtain optimum vehicle response and also has been modified to include changes in optical sensor signal characteristics.

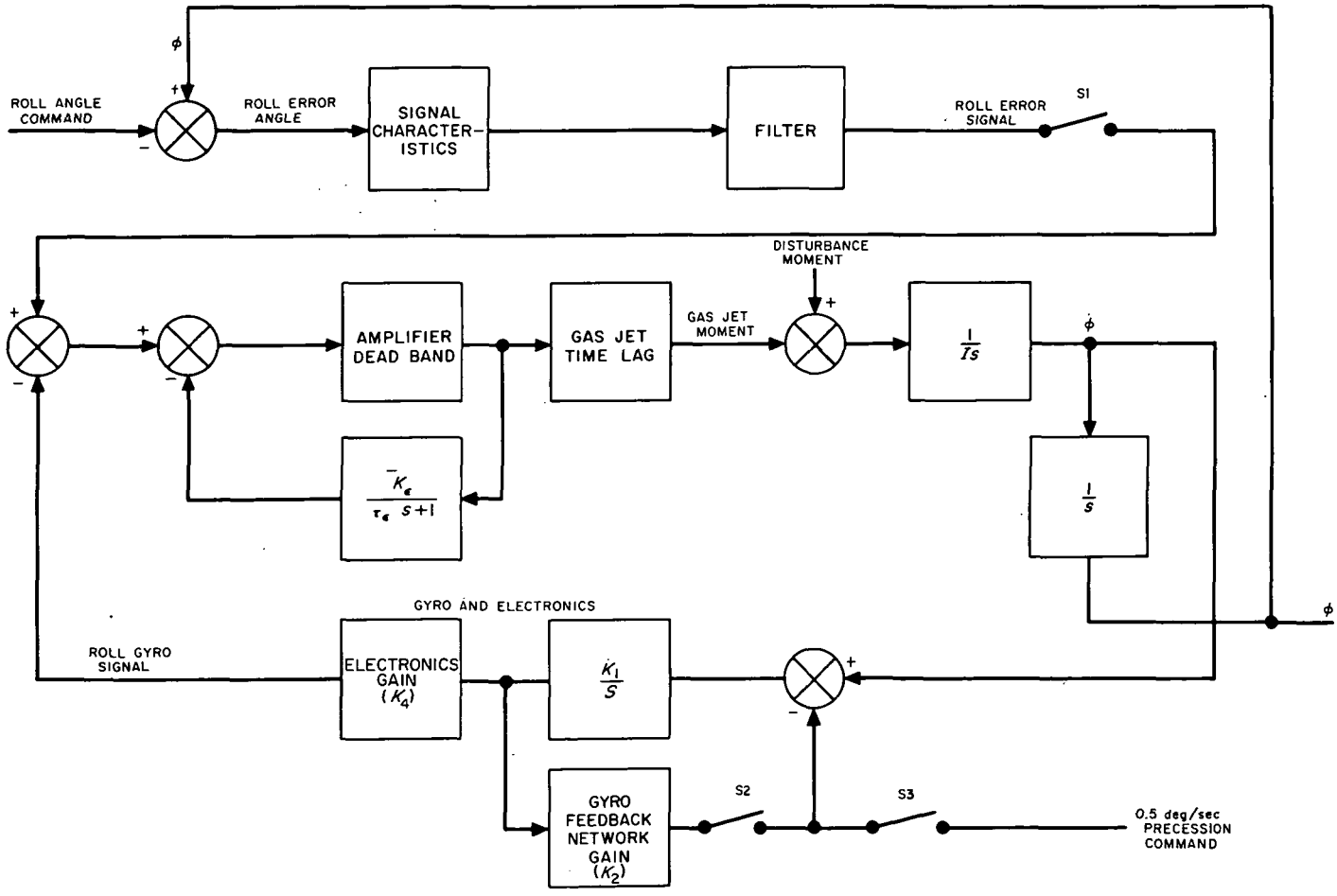

Figure 18. Roll attitude control system

The thrust phase vernier engine control system design has been affected by the aforementioned inclusion of the mid-course accelerometer during terminal descent. Digital computer studies have indicated the desirability of going to a four-segment control law trajectory which results in a fuel saving of approximately 6 pounds.

b. Coast phase attitude control. The coast phase attitude control system remains basically unchanged from that described in previous reports. Several parameter values have been altered as a result of updated information on the optical sensors, the physical characteristics of the vehicle, and revised criteria for determining optimum vehicle-control system performance. A block diagram of the roll-axis attitude control system is shown in Figure 18.

The primary objective of the three-degree-of-freedom analog computer simulation during this period was to determine an optimum set of loop gain and shaping network characteristics for both the inertial and optical modes of operation. The three criteria used in evaluating system performance were (1) system settling time, (2) impulse required, and (3) the integral squared error.

These measures of system performance in the inertial mode are shown in Figures 19, 20, and 21 for all three axes. The optimum values of $K_\epsilon = 6$ and $\tau_\epsilon = 3.2$ seconds were arrived at by a comparison of system responses using the foregoing three criteria. The gain K_1K_4 was adjusted to prevent the angular error from exceeding its maximum allowable value of 0.2 degree for the yaw channel, 0.136 degree for the pitch channel, and 0.121 degree for the roll channel.

The settling time and impulse required for the pitch and yaw optical channels are shown in Figures 22 and 23. The optimum rate loop gain (K_4/K_2) was determined based on initial conditions of a yaw angle of 9 degrees and a yaw rate of 0.5 deg/sec with a pitch axis rate of zero. The mechanics of Sun acquisition make such initial conditions highly probable, since the approach of the

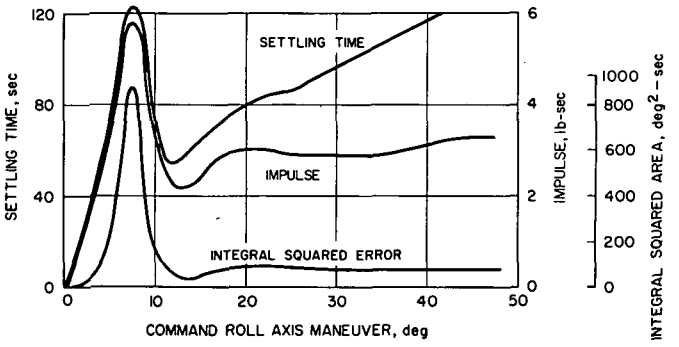

Figure 19. Optimum roll control in inertial mode

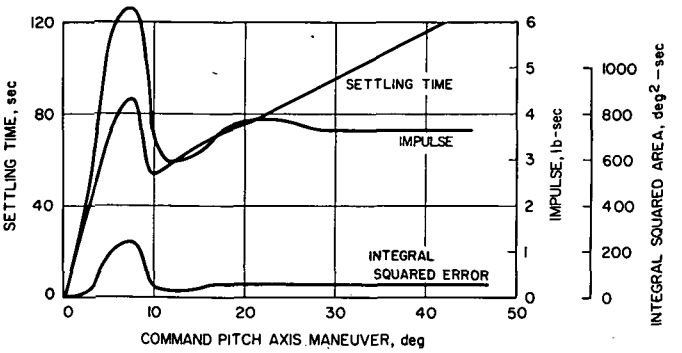

Figure 20. Optimum pitch control in inertial mode

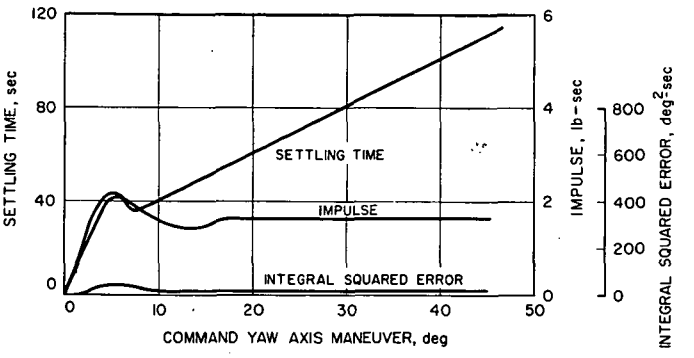

Figure 21. Optimum yaw control in inertial mode

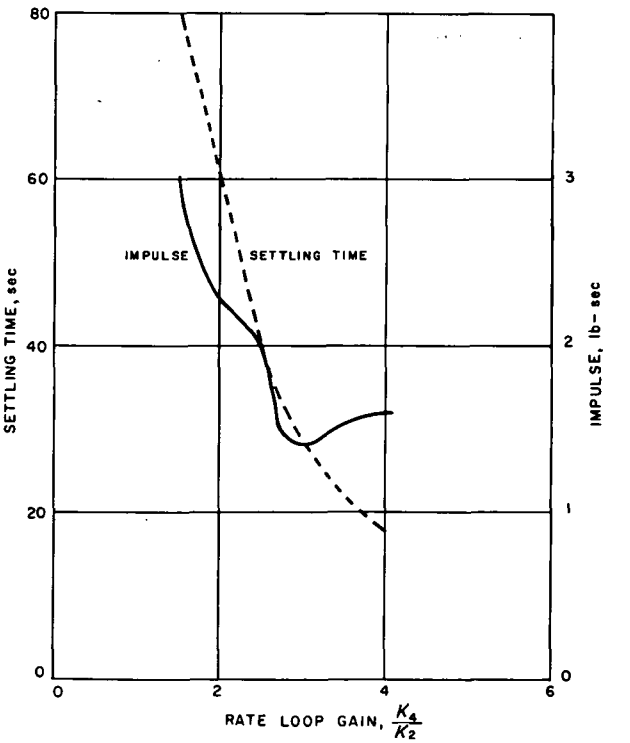

Figure 22. Optimum performance of pitch optical control

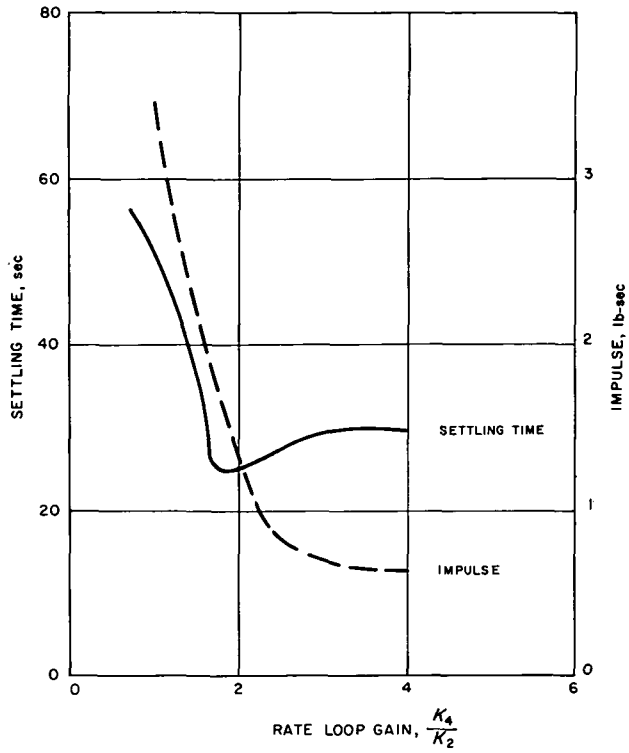

Figure 23. Optimum performance of yaw optical control

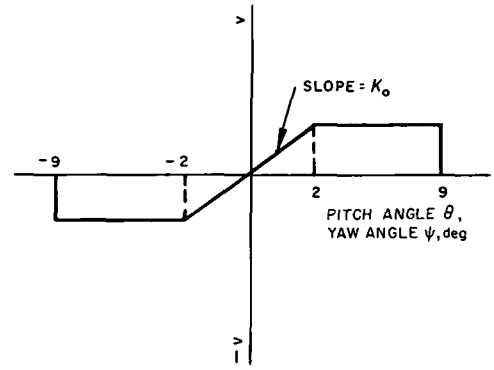

Figure 24. Primary Sun sensor signal characteristics

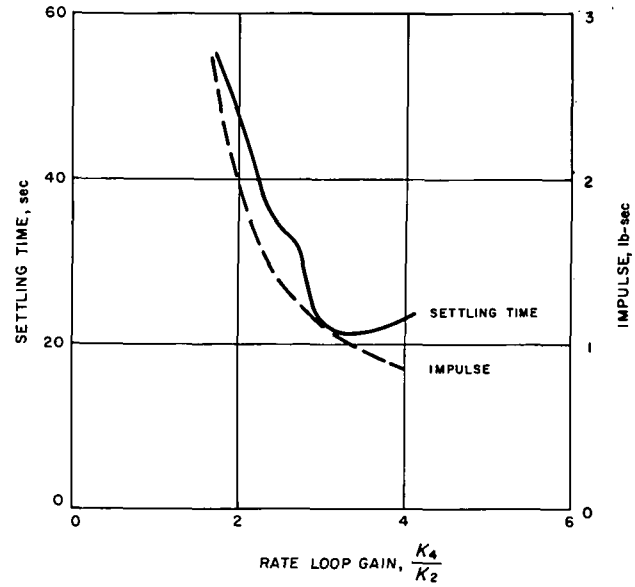

Figure 25. Optimum performance of roll optical control

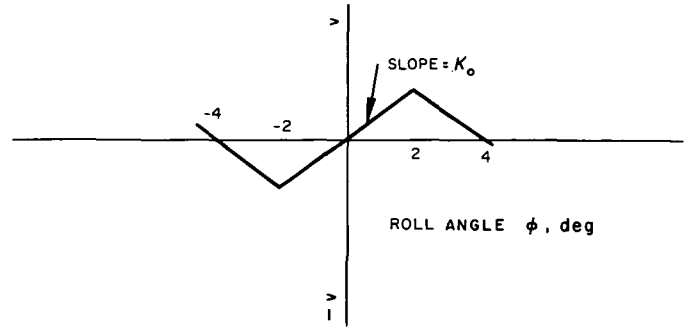

Figure 26. Canopus sensor signal characteristic

Sun line to the primary Sun sensor field of view will generally be in the pitch-roll plane, requiring a yaw maneuver. Constraints which operate in the attitude control system at this time include (1) the signal characteristics of the primary Sun sensor as shown in Figure 24 where the gain K_0 was chosen so that the maximum allowable error would cause the gas jets to fire, and (2) the gyro gain K_1K_2 which was chosen so that separation-induced rates will not cause gyro saturation.

The settling time and impulse required for the roll optical channel are shown in Figure 25. The optimum roll rate loop gain (K_4/K_2) was determined using an initial roll angle of 4 degrees and a roll axis rate of 0.5 deg/sec. The signal characteristics of the Canopus sensor are shown in Figure 26.

The rate loop gain (K_4/K_2) for optimum optical mode performance, the rate loop gain (K_1K_4) for minimum error angles about each axis during inertial mode of operation, and the closed-loop gyro gain (K_1K_2) cannot be realized simultaneously with the control system configuration represented in Figure 18. Various means of achieving all of these optimum parameters are under study. Two approaches appear promising. The first consists in adding a switch to change gains when going from the inertial to the optical mode of operation. The second approach is one of compromise in that optimum values of K_4/K_2 and K_1K_2 can be realized at the expense of a larger value of K_1K_4. In effect this would decrease the limit cycle deadband in the inertial mode by a factor of three, but would result in increased fuel consumption.

c. Vernier retro descent phase. The efficiency of the vernier retro maneuver is strongly dependent on the

average thrust level of the vernier engines during the maximum thrust phase. For each pound of thrust below the maximum available 312 pounds, a penalty of about 0.3 pound of vernier fuel is incurred. The open-loop thrust command system originally planned suffers in efficiency because of the large uncertainty in thrust versus command. This is due primarily to the dispersion of the vernier engines (approximately 10%). To avoid a pitch-yaw limit cycle oscillation and to ensure a safe margin for soft landing, the range-velocity profile would have to be set for a thrust level about 60 pounds below the maximum of 312 pounds.

In order to obtain greater fuel efficiency, the thrust channel has been modified to an acceleration command servo. This can readily be accomplished by using the precision accelerometer in the inertial reference unit (IRU) as the feedback sensor. The range of the instrument must be increased to 0.5 g, because of the higher acceleration involved in the vernier phase. The new design provides the means of accurately controlling the thrust-to-mass ratio. Since the spacecraft mass will be known to within a few percent, at the start of the maximum thrust phase, a considerable improvement in thrust control can be realized. The new configuration is shown in Figure 27.

The variation in spacecraft mass during the maximum thrust phase is accurately known. It is possible therefore to vary the acceleration command limiter in a way to compensate for the mass variation and thus maintain a constant maximum thrust level. Because of the simplicity of mechanization, however, it is planned to use a two-level limiter. By resetting the limiter when half the mass variation has occurred, only a small fuel penalty is involved. The total variation in mass during the maximum thrust phase will be about 10%. The two-level limiter will provide an average thrust 2.5% less than the peak. The improvement in a three-level limiter is not considered to justify the additional complexity. Even if a continuously variable limiter were used, the range-velocity profile could not be set to correspond to 312 pounds thrust level. Allowance must be made for several factors, the more important being

(1) Altimeter and doppler radar errors.

(2) Uncertainty in mass at the start of the maximum thrust phase.

(3) Residual for linear moment control range.

These factors total about 7.5% (3_σ). The average thrust level will therefore be about 10% below the maximum engine capability of 312 pounds. In comparison to the original open-loop design, an improvement of about 29 pounds in average thrust level can be realized. This is equivalent to a saving of about 8.7 pounds of vernier fuel.

A digital computer study recently completed indicates that a saving of about 6 pounds of vernier fuel can be realized by using a four-segment approximation to the reference parabola rather than the three-segment approximation originally planned. Provisions have therefore been made in the electronic circuits to add the fourth segment.

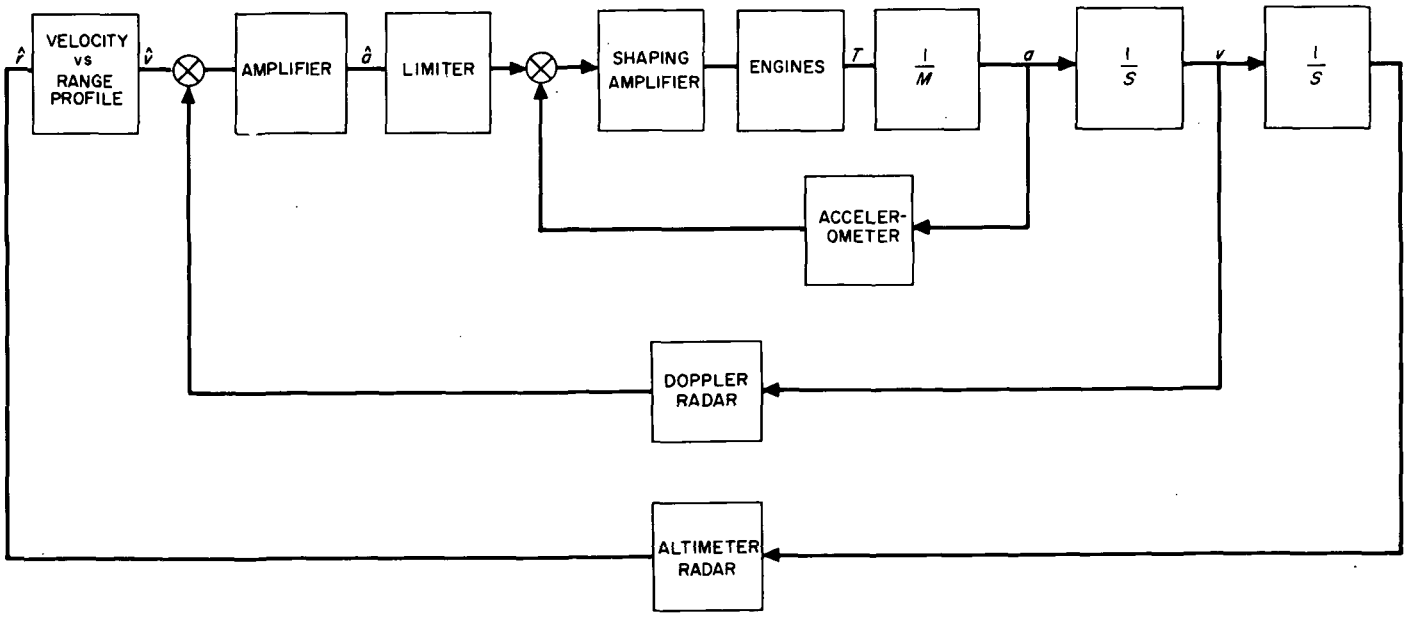

Figure 27. Velocity control system with acceleration servo

The gain in the pitch and yaw attitude control loop has been increased by a factor of two in order to limit the steady-state attitude error to 0.1 degree in the presence of the expected 3_σ main engine misalignment moment of 1100 inch-pounds.

3. Subsystem Tests

a. Single-axis air bearing table. Single-axis table tests are currently scheduled to start about February 15, 1962. Completion of the test facility is awaiting the receipt and installation of various pieces of associated hardware, including telemetering equipment, recorders, test consoles, and portions of the flight control subsystem. When completely assembled, the table inertia will be measured with the table forming a part of a torsional pendulum. The single-axis table will be required to provide the major portion of the design verification of the gas jet coast-phase attitude control system, because plans to run tests on the three-axis air bearing table at the JPL facility have been cancelled.

b. Flight acceptance test program. A preliminary subsystem flight acceptance test specification has been written for the flight control subsystem. The complete subsystem flight acceptance test will consist of a pre-environmental functional check, the environmental test, and a post-environmental functional check, which will be a duplication of the pre-environmental functional check for the most part. The single-axis air bearing table will be used to make the closed-loop functional check of the gas jet attitude control system with simulated Sun and star sources. A test facility with a single-axis dividing head and simulated Sun and star sources will be used to measure the alignment of the flight control sensors relative to the flight control sensor group mounting surface. The same facility will be used to determine the scale factor and null fixed drift of each integrating gyro as part of the entire sensor group. A rate table will be used to measure the alignment error of each gyro in the inertial reference unit relative to the flight control sensor group mounting surface.

c. T-2 test program. Additional T-2 trajectory analysis has been completed using a one-degree-of-freedom digital computer simulation. The program considered only the vertical force relationships and included variable mass due to fuel consumption. The thrust control loops

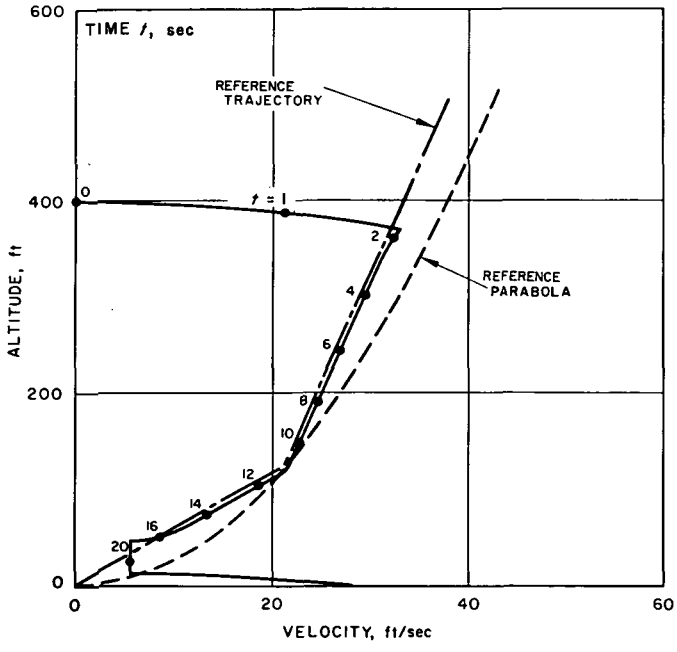

Figure 28. T-2 reference trajectory

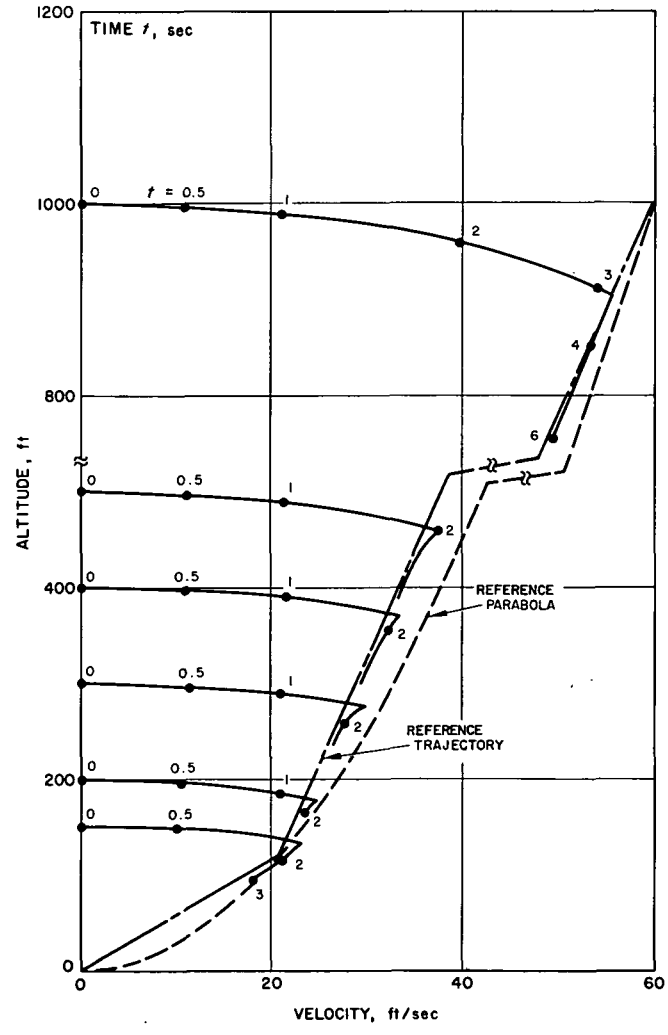

Figure 29. T-2 trajectories from various initial altitudes

were simulated except for the vernier engine and valve lag times. The purpose of the analysis was to determine (1) the initial drop altitude which provides adequate capture of the commanded trajectory, (2) the effect of thrust control system gain on system performance, and (3) a suitable reference parabola and associated straight-line segments.

In order to facilitate comparison of trajectory performance, the reference trajectory shown in Figure 28 was chosen, based on an arbitrary set of reference parameters. Trajectories were obtained for initial altitudes of 1000, 500, 400, 300, 200, and 150 feet as shown in Figure 29. Only the first portion of these trajectories is shown, since the remaining portion is similar to the reference trajectory. For all cases, it is apparent that initial altitude has little effect on vehicle performance. If the present 20 pounds of fuel carried by the T-2 vehicle is completely used, the maximum drop altitude is limited to about 460 feet. However, this does not take into consideration the fuel required for moment control.

The thrust system gain was varied from 16.2 to 81.0 lb/ft/sec with consequent vehicle trajectory performance as shown in Figure 30. These values of thrust system gain correspond to spacecraft values of 50 and 250 lb/ft/sec. As expected, the higher gain produced a tighter control response. The higher gain descent required approximately 3 pounds more fuel than the low gain descent.

All of the preceding trajectories were based on line segments fitted to a 1.79 ft/sec² acceleration parabola. Vehicle trajectory responses were determined for both a 0.870 ft/sec² acceleration parabola (Fig 31) and a 3.785 ft/sec² parabola (Fig 32) for various values of weight-to-thrust ratio. The results are based on the parameters listed on the next page.

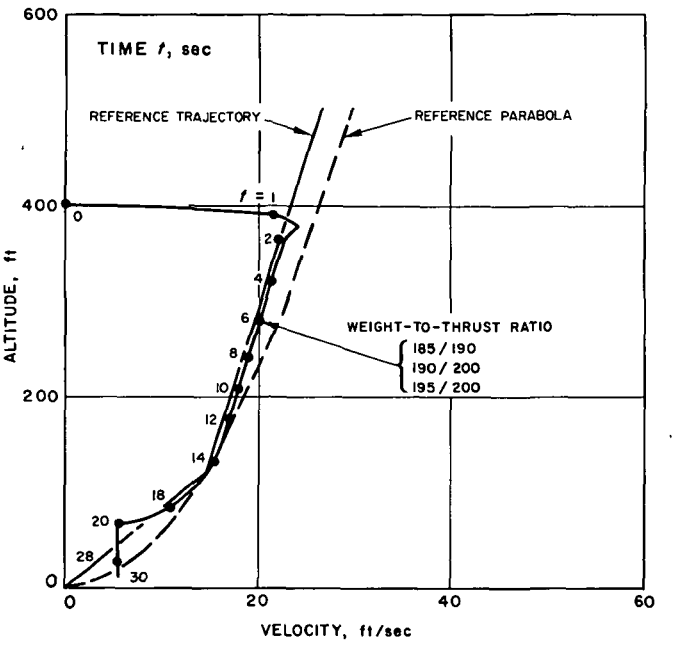

Figure 31. T-2 trajectory response for 0.870 ft/sec² parabola

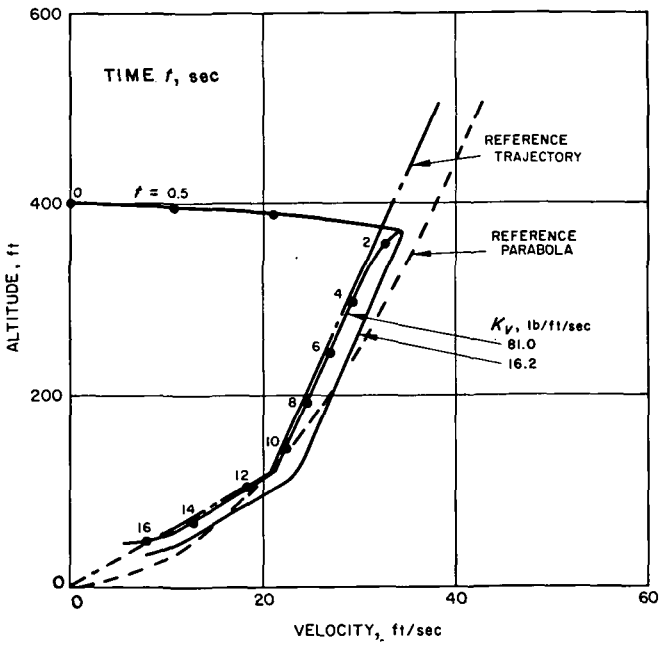

Figure 30. Effect of thrust system gain (K_v) on T-2 trajectory

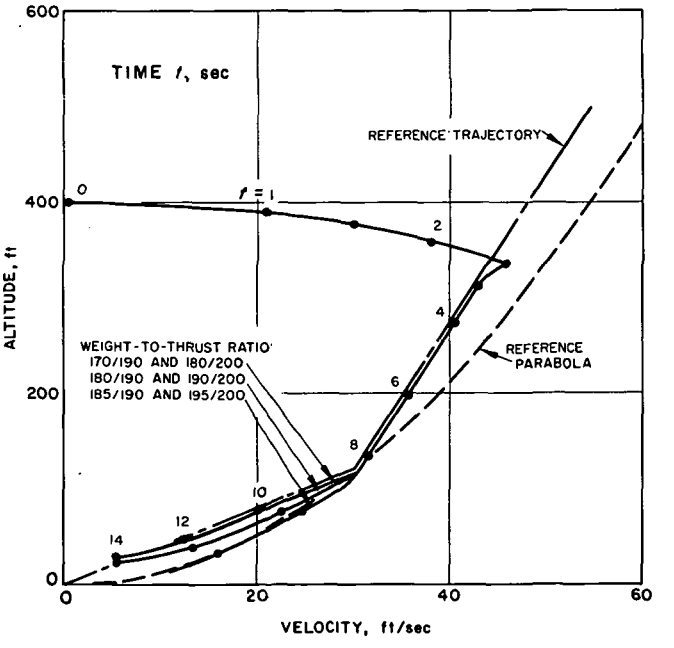

Figure 32. T-2 trajectory response for 3.785 ft/sec² parabola

Minimum programmed thrust, T_{mp} ..... 60 lb
Thrust system gain, K_v ..... 81 lb/ft/sec
Vernier propellant specific impulse, I_{sp} ..... 198 lb-sec/lb
Drag coefficient – area product, CdS ..... 14 ft²
Air density ..... 0.0025 slug/ft³

The vehicle performance on the low acceleration parabola compares favorably with the reference trajectory, while the vehicle performance relative to the high acceleration trajectory varied depending on the weight-to-thrust ratio. Satisfactory performance is obtained when the weight-to-thrust ratio corresponds to the constant acceleration from which the line segments are derived; that is, 170/190 and 180/200 for a = 3.785 ft/sec². The intermediate weights (180/190 and 190/200) produced marginal performance in that these trajectories had more error along the last line segment and barely stabilized at the commanded 5 ft/sec. The highest weights (185/190 and 195/200) trajectories are unsatisfactory because they appear to be diverging from the last line segment and are unable to stabilize at the constant velocity since they reached the 13-foot engine cut-off altitude before they attained a velocity of 10 ft/sec.

Final selection of the initial drop altitude, thrust system gain, and control law trajectory for T-2 tests is awaiting more extensive analysis, which will include moment control and better defined spacecraft trajectory performance and parameters.

4. Sensor Group Assembly

The flight control sensor group has undergone rearrangement as illustrated in Figure 33. The support, previously a space truss, is now conceptually a platform with three mounting lugs so spaced around its perimeter as to intersect the center of gravity of the sensor group. The support is made from aluminum and will be a brazed assembly consisting of an outer frame with stiffening elements and unit mounting bosses placed as required. A substantial weight saving in the support is realized with this simplified design. Increase in volumetric packaging efficiency allows the sensor group to be located closer to the roll axis of the spacecraft. Use of shorter mounting brackets on the vehicle will represent some weight saving, as well as providing a more rigid coupling to the sensor group.

In the new design, the inertial reference unit (IRU) has been moved from a position beside the electronics package to a position above it, causing a relocation of the IRU radiating surface. The flight control electronics unit is more rigidly attached to the sensor group support

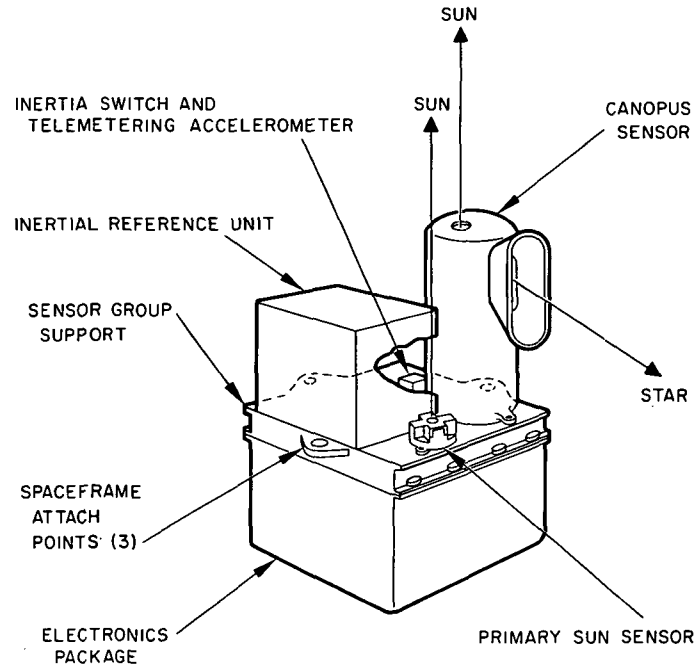

Figure 33. Flight control sensor group

in the new design and allows some simplification in the internal arrangement. The problem of stray light reflecting into the Canopus sensor has not changed appreciably with the new sensor group configuration. It is at present geometrically possible to pick up a multiple bounce light reflection from the extended vehicle landing legs. The light shield on the Canopus sensor may have to be altered to eliminate this possibility. The Moon detector has been eliminated from the assembly. Verification of the position of the star Canopus will be achieved by means of a star map constructed from telemetered star intensity signals.

Engineering effort has stopped on the original truss-type support, and will now be directed toward preparation of a test model of the new configuration.

5. Optical Sensors

a. Canopus sensor. Figure 34 shows a mechanical breadboard of the sensor which is similar in appearance to the first engineering model. During this report period, a working breadboard model of the Canopus sensor was completed and satisfactorily demonstrated. Temperature compensation has been added to the developmental circuits and a preamplifier included to provide additional gain for the photomultiplier tube.

As a result of initial lateral vibration tests on the mechanical breadboard model, the base of the sensor has been altered to attach more rigidly to the sensor group

assembly. The more rigid attachment alters a previous concept of thermal isolation and a thermal analysis of the combined sensor group and Canopus sensor is now being performed.

Although the first Sun-star simulator has been completed, additional circuitry is being added for calibration purposes to compensate for the high amplitude of star scintillation encountered during the breadboard model field tests.

Qualification test procedures have been written for the component parts of the sensor and qualification testing of critical items (phototube, motor and gear train, magnetic pickup, etc.) is continuing.

A decision was made to delete the Moon detector as an auxiliary indicator of Canopus position. Verification of Canopus position will be obtained by construction of a strip star map by means of telemetered data from a separate star intensity channel in the Canopus sensor.

b. Sun sensors. The developmental model of the primary Sun sensor (Fig 35) has been completed and preliminary tests have been run at the Sun sensor test

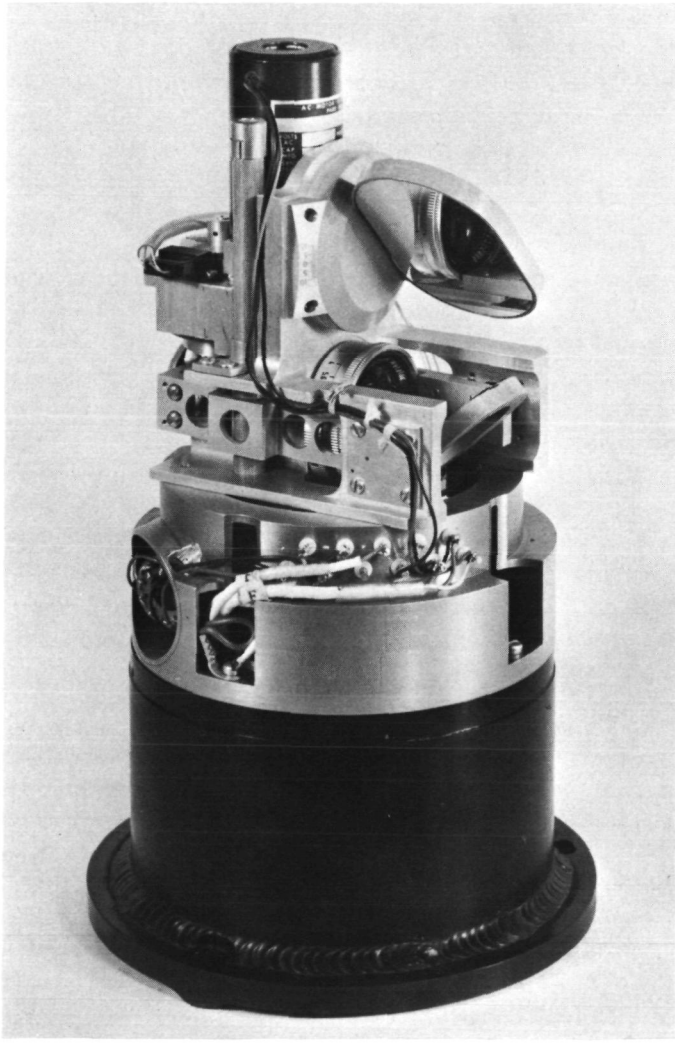

Figure 34. Mechanical breadboard of Canopus sensor

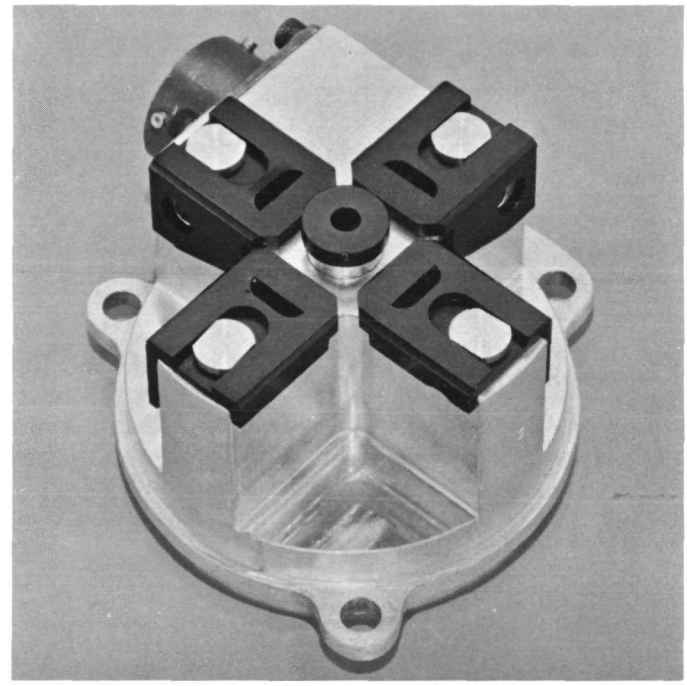

Figure 35. Primary Sun sensor

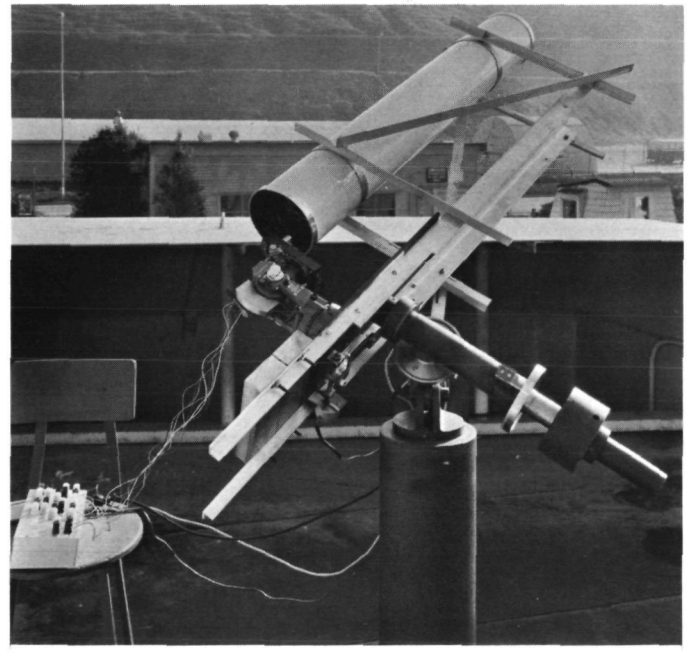

Figure 36. Sun sensor test facility

facility (Fig 36) at Hughes Aircraft Company in Culver City. The facility consists of an equatorial mount to track the Sun and a precision Kern, 1-second, theodolite attached to the mount to accurately position the sensor with respect to the Sun. The sensors are mounted on a special adapter plate attached to the theodolite. A 4-foot long fiberglass tube and light-tight enclosure are used to keep stray skylight from affecting measurements.

The intensity level on days when tests have been performed (in November) has ranged from 73 mw/cm^2 to 96 mw/cm^2 as measured with a silicon solar cell calibrated with an Eppley pyrheliometer. These levels are sufficient for most testing and are obtainable at Culver City because of the use of direct solar viewing instead of a mirror system. The facility will have provisions for battery operation, and measurements at a high-altitude location can be made if necessary. It is planned to correlate calibration of a Sun sensor with measurements made at the JPL test facility.

Tests on Clairex photoconductive cells are being continued with no serious problem areas yet uncovered. Illuminated cell resistance versus temperature, ultraviolet exposure, high-temperature soaks, and power dissipation tests have been performed.

The behavior of the illuminated cell resistance with temperature indicates that cells for the primary sensor will have to be roughly matched with regard to the slope of the temperature-versus-resistance characteristic. The effect of temperature on the cadmium sulfide cells at high levels of illumination is small, but matching is desirable for maximum null stability.

Cells were exposed to ultraviolet energy in the band from 2200 to 3150 Å for a period roughly equivalent to 1000 hours in space with no measurable degradation. The tests indicate that ultraviolet damage will not be a problem for either the secondary or primary Sun sensor. Exposure of cells to sterilization temperatures of 125° C for 24 hours also had no measurable effect on their behavior.

Short-term power dissipation tests at elevated temperatures have been conducted and indicate that operation at expected power dissipation levels presents no problem. Long-term tests are in progress to further check this point.

6. Inertial Reference Unit

a. Instruments. The final selection of a gyro which fully satisfies *Surveyor* flight control subsystem requirements was completed on November 3, 1961, with the release of a purchase order to the Kearfott Company for 26 gyros. Latest information from Kearfott indicates that parts for all 26 units are in work and on schedule. Delivery of the first unit is expected on January 30, 1962.

Additional phases of gyro procurement which are under continuing study are as follows:

(1) The establishment of a gyro environmental testing program compatible with *Surveyor* spacecraft requirements will be negotiated with Kearfott under an amendment to the contract.

(2) The establishment of incoming test procedures for gyro performance will be mutually agreed upon by Hughes Aircraft Company and Kearfott in order to achieve compatibility of testing techniques and to provide test data which can be properly correlated.

The accelerometer evaluation program is nearing completion. Two evaluation units, one from Donner and one from Palomar, were purchased to (1) determine the adequacy of this class of instrument for the *Surveyor* mission, and (2) assess the relative performance characteristics of units from two possible vendors. Both units have demonstrated the potential capability of meeting the accuracy and repeatability requirements, though results are still somewhat inconclusive because of minor functional difficulties encountered. Sticking around zero g was observed in the Palomar unit and after limited tests it was returned to the vendor for rework. The Donner unit exhibited an intermittent behavior at the normal operating temperature of 180° F, which is believed to be due to a faulty electrical component. Performance at room temperature was generally satisfactory. Additional tests are being performed on the Donner unit to determine its repeatability after environmental exposures. Similar tests on the reworked Palomar unit are planned.

b. Unit design. In mid-November all design and test efforts were stopped on the original T-mounting structure, and redesign was immediately started to conform to a space envelope compatible with the reconfigured flight control sensor group structure. The general reasons underlying this change were given above under *4, sensor group assembly.*

A portion of the analysis and design effort previously expended is directly applicable to the new design and was utilized in the establishment of the preliminary configuration shown in Figure 37. A general change to the original temperature control concept was necessitated by the reduced space view factor due to the new IRU mounting orientation. The temperature of each gyro will be maintained by individual controllers rather than the common controller of the original design. Excess heat will be conducted to a common space radiator, which

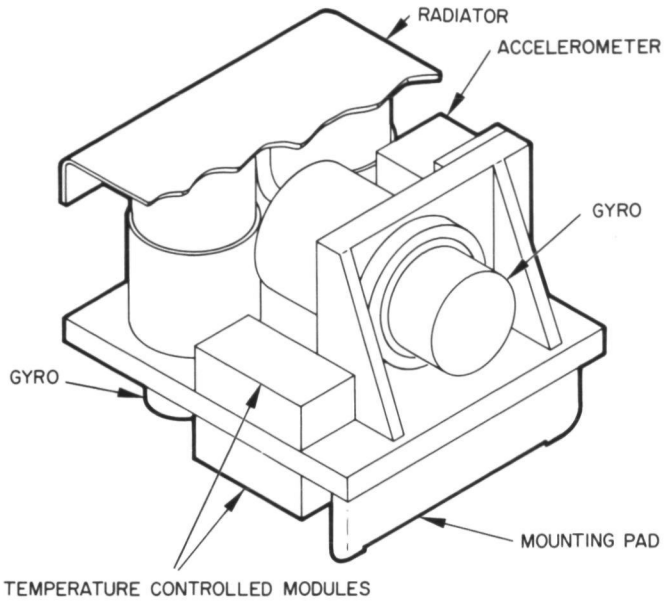

Figure 37. Inertial reference unit

will be oriented facing the Sun during transit phase to make maximum utilization of solar energy, thereby minimizing the average heater power which must be applied to maintain gyro operating temperature.

Preliminary analysis is in process to determine the control power and radiator temperature during the mid-course maneuver when solar energy to the radiation panel will vary. A parametric study has been run on the IBM 7090 computer to determine mid-course control power and radiator temperature for variations in the ratio:

$$\frac{\alpha F_1}{\epsilon F_2}$$

where F_1 is the view factor of the Sun and F_2 is the view factor of space; α and ϵ are absorptance and emittance of the radiator panel. The results indicated that in order not to exceed a peak heater power of 30 watts, the $\alpha F_1/\epsilon F_2$ ratio should not exceed 0.4.

The analysis of the transient thermal response of the gyro temperature when the heat source is the gyro heaters rather than solar energy is in process.

7. Attitude Control

a. Gas jet subsystem. Evaluation of gas tank vendor proposals indicated that the weight requirement of 7.2 pounds would be exceeded by approximately 0.7 pound with tanks made of 6AL-4V titanium alloy. Menasco Manufacturing Company proposed using 7AL-4Mo which would meet the weight requirements, and was therefore selected as the vendor.

After release of the procurement specification for the squib-operated valves, a design change was made. The requirements of one normally closed valve for gas release and one normally open valve for gas shutoff were changed to two normally closed valves. This will permit the release of residual tank pressure during vernier descent rather than storage, to minimize the possibility of gas tank rupture. Four vendors submitted proposals on the original concept, of which two, Conax and Thiokol, were considered acceptable. A revised procurement specification, statement of work, and drawings will be resubmitted to these two vendors for proposals.

The pressure transducer has been changed from a Bourns Model 304 to a Model 737 with modifications in mounting and electrical connections to obtain a hermetically sealed unit and also obtain increased overpressure capability.

Two jet valve pairs have been assembled and are now being subjected to environmental operation tests. Figure 38 is a photograph of the preliminary design. Other parts are in process which will reflect a close coupled AN-type pressure connection to satisfy the *Surveyor* gas plumbing requirements.

An engineering model of the pressure control, comprising the pressure regulator, pressure relief, and solenoid shut-off valve, is shown in Figure 39. Tests are

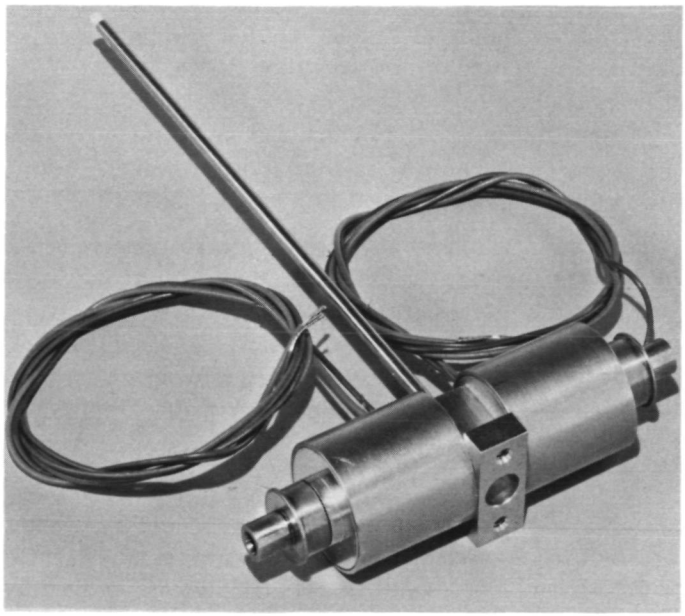

Figure 38. Gas jet valves

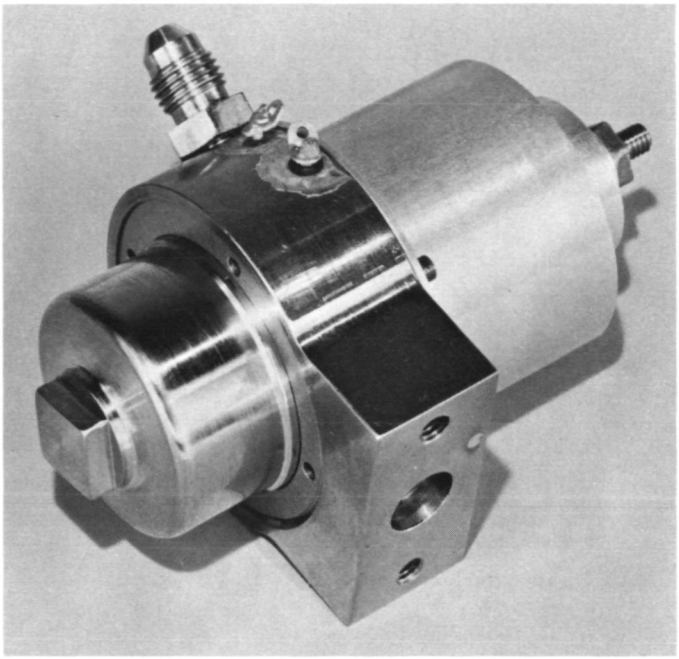

Figure 39. Pressure control for gas jet system

now in progress. Additional units are being fabricated which reflect minor design and fabrication changes.

b. Roll actuator. The vernier roll actuator provides roll moment control during mid-course and terminal maneuver phases by positioning the No. 1 vernier engine thrust axis. The actuator design previously under development was a double-acting electromagnet which pivoted the trunnion-mounted vernier engine through a lever arm linkage. The design concept for the roll actuator has been altered considerably in the present reporting period. The new design is a proportional positioning system using a conventional servo-motor and gear reduction unit and inductive pickoff sealed in a single housing.

The primary reason for the design change was the increase in the vernier engine weight, inertia, and location of center of gravity as seen from the pivot axis. In order to continue to meet performance requirements, the output force of the two-position solenoid would have had to increase to 7.5 pounds. The increase in output force caused a significant increase in solenoid design weight due to the increase in plunger size to carry additional flux.

In addition, concern over the effects of the bang-bang solenoid characteristics on the vernier engine nozzle structure had been expressed by RMD. An effort was under way to develop "soft" stops to limit engine motion. Unfortunately, the design requirements were somewhat conflicting since a soft stop implies delayed motion which tends to violate an initial requirement for rapid engine positioning. A bang-bang solenoid design which would meet the system requirements would result in an increase in spacecraft weight of 2 to 3 pounds. As a result, a thorough study was made of alternate techniques and the proportional system using an ac motor-gear and pickoff was selected.

The proportional system chosen will allow a decrease in power requirements and a slight decrease in spacecraft weight. Preliminary requirements for the actuator are:

Weight	< 1.2 lb
Power	< 8 watts, 400 cps
No-load speed	0.13 rad/sec
Stall torque	52 in.-lb

The new design of the roll actuator will be subcontracted. A detailed procurement specification and statement of work are presently being prepared.

8. Control Circuitry

a. Summary. Detailed evaluation and optimization of the control circuitry is continuing by means of breadboard testing. Circuit parameters are being adjusted where necessary to compensate for the varying ambient temperatures and power supply voltages.

The thrust control circuitry has changed as a result of using the mid-course accelerometer to provide acceleration feedback signals during the vernier descent mode. The revised thrust control circuitry is shown in Figure 40. The mid-course command signal is applied only during mid-course thrust control, providing, after summation with the accelerometer feedback signal, a thrust command proportional to the acceleration error. The acceleration loop during mid-course has not changed basically. However, use of the accelerometer during vernier descent has necessitated increasing its output range as well as decreasing its scale factor. During vernier descent the summation of the descent acceleration command and the accelerometer signal provides a thrust command to the vernier mixing network. The descent acceleration command is the amplified difference between the thrust axis velocity measured by the doppler radar and the altimeter signal that has been shaped by the nonlinear circuitry. The descent acceleration command is limited prior to summation with the accelerometer signal to prevent saturation of the vernier engines, in accordance with Figure 41. A low (but not minimum) thrust command results whenever the descent acceleration command is less than or equal to 0.11 g. Commands rising above this lower

limit will produce proportional increases in thrust until the maximum thrust command of 0.42 g results. At a certain point along the trajectory (approximately 2500 feet range), the limit imposed on the descent acceleration command is increased by approximately 6% to compensate for the decreasing spacecraft mass. The switches shown in Figure 40 are functional representations of standard flight control solid-state switches.

The roll actuator servoamplifier design has changed as a result of the decision to use a proportional actuator. Figure 42 is a block diagram of the proportional roll actuator and associated circuitry. The actuator consists of a two-phase servo motor which with associated gearing and position pickoff is mounted such that vernier engine No. 1 may be swiveled through a small angle. As before, the roll attitude error is obtained from the gyro

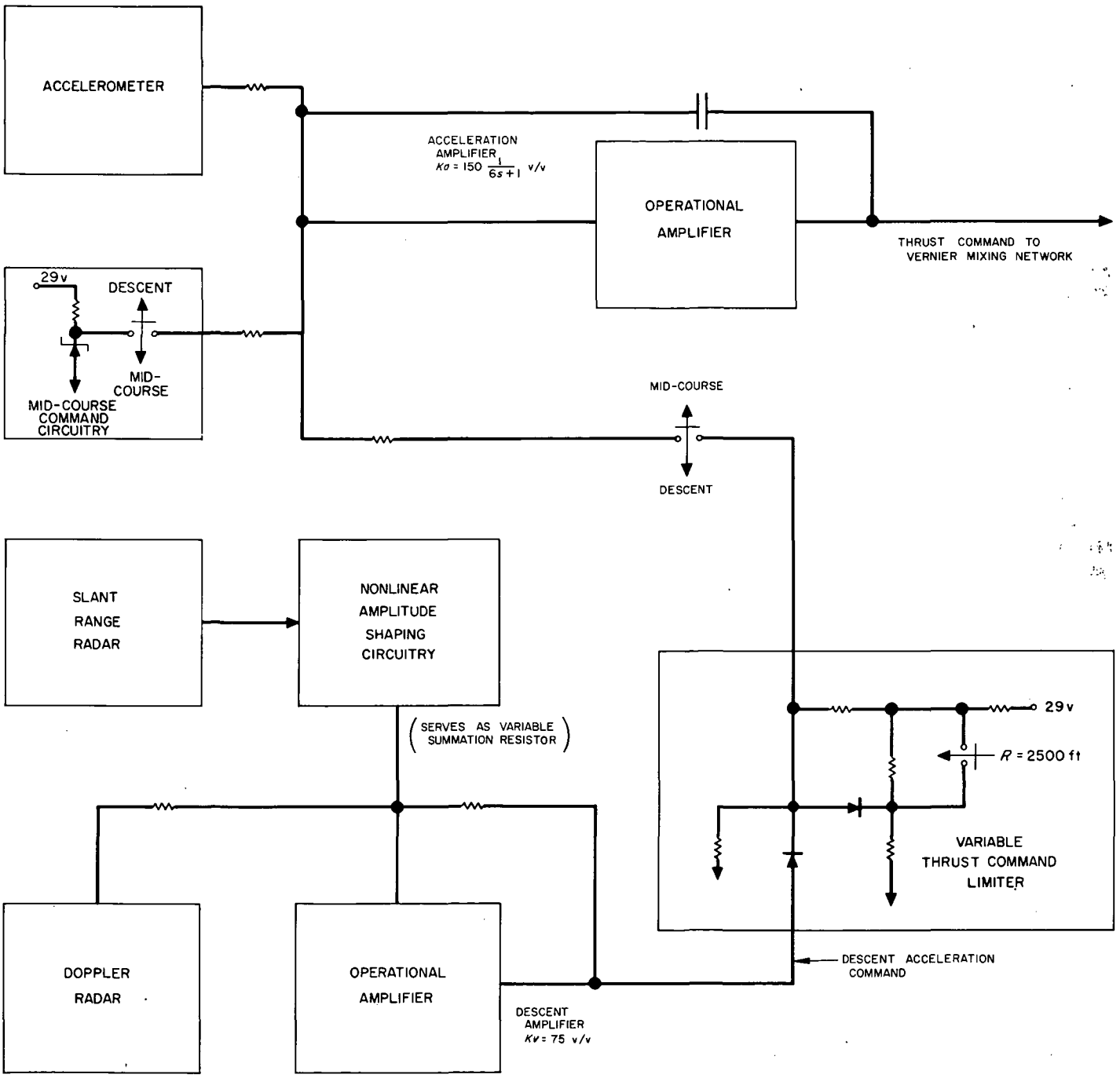

Figure 40. Thrust control circuitry

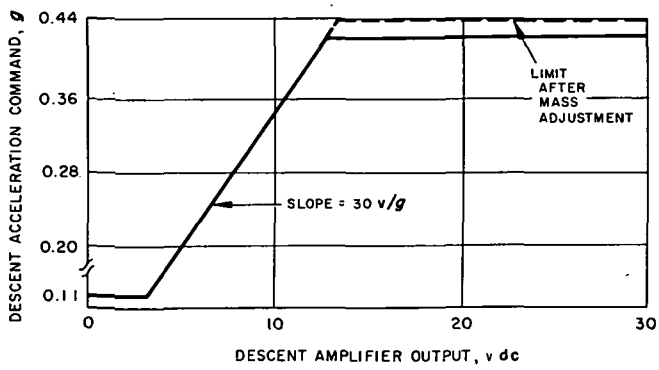

Figure 41. Descent thrust command limiting

and is amplified and frequency-shaped. This signal, which is a position command, is summed with the position feedback, to create a motor drive proportional to the position error. Upon separation of the retro-rocket case from the craft, a gain change is made in the attitude loop to compensate for the decreased moment of inertia that results. A Class B power amplifier is used to drive the servo motor, and is composed of the same type of power transistors that were used in the previous bistable version. The demand of the Class B amplifier from the power supply is now proportional to the position error. In the solenoid design there was a constant drain on the power supply. At maximum output the proportional circuit demand is smaller than that of the previous bistable version.

E. Electronics

1. Introduction

This section covers the various systems involved in telecommunications (including the demodulator circuits for the deep space station), the television system, and the radar systems. The spacecraft power management and the flight control electronics are discussed in Sections F and D, respectively.

2. Planar Array (High-Gain) Antenna

The planar array antenna concentrates the energy of the television transmitter in the direction of the Earth.

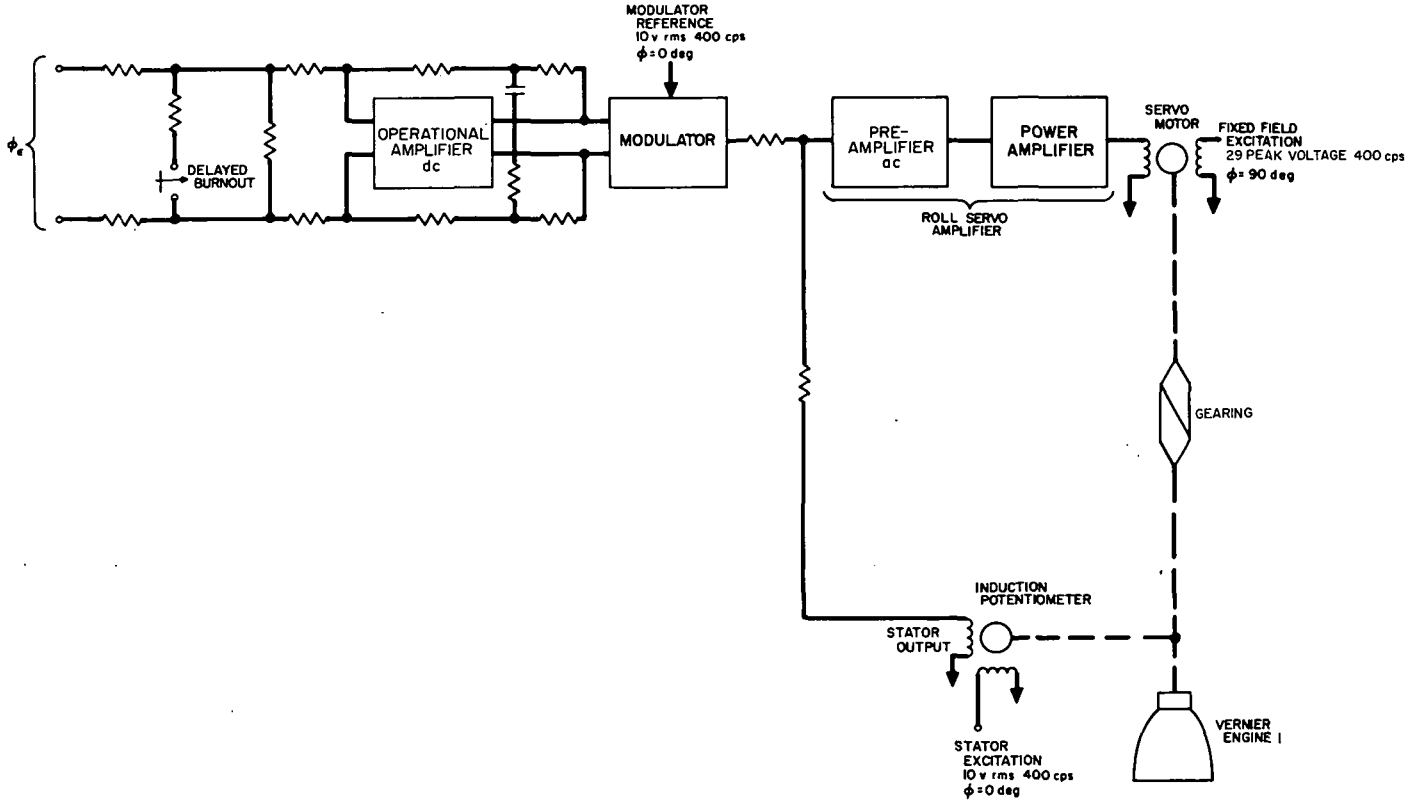

Figure 42. Proportional roll actuator

This high-gain antenna is a slotted waveguide planar array. Circular polarization is accomplished by utilizing crossed slots and simple slots in a manner that produces two orthogonal linearly polarized planar arrays in a given aperture. These two interlaced arrays are fed in time quadrature. Higher-order beams characteristic of large slot spacings are eliminated through the use of waveguide with wave-slowing corrugations which in turn allows reduced slot spacings.

Extensive coupling coefficient measurements were made on both the crossed slots and singular slots. These slots are generally nonresonant since the coupling value is controlled by the slot length. Figure 43 shows curves of coupling coefficient versus slot length for both types of slots. Tests show that the phase shifts associated with these nonresonant slots were much larger in the corrugated guide than in standard guide. Therefore, phase measurements have been made on both the radiated wave and the driving wave. These data were used to determine the adjustments in the slot spacing which effect the desired phase corrections.

A linear array test fixture has been built to accommodate removable aperture plates. The planar array slot configuration requires two slightly different slot patterns in its component linear arrays. Hence linear array aperture plates are made in sets of two. Two such sets have been made. The first set did not have its slot spacings compensated for induced phase shifts. The second set did incorporate corrections for such errors based on phase shift data mentioned above and a study of patterns taken on the first set of aperture plates. A second set of plates, designated 1b and 2b, gave fairly good results. Voltage standing wave ratios (VSWR) as a function of frequency are shown in Figure 44. The measured power into the load was almost exactly as calculated, indicating that the slot coupling data are good. Typical patterns are shown in Figures 45 and 46. They were taken on a 38.5-inch square ground plane to simulate the planar array. The polarization ellipse has its major axis aligned with the longitudinal axis of the array. Hence the magnitudes of the two orthogonal components shown on the patterns give an accurate indication of the axial ratio (approx 1.8 db). The beam tilts are about 1½ degree larger than expected but this is easily corrected. Measured gains, with respect to the gain of a circularly polarized isotopic source, are 17.3 and 17.0 db, respectively, for arrays 1b and 2b. The large lobes noticeable in the region near $\theta = -90$ degrees for E_θ polarizations are the second-order beams expected in the linear array patterns. The combining of the linear arrays into a planar array will suppress these beams.

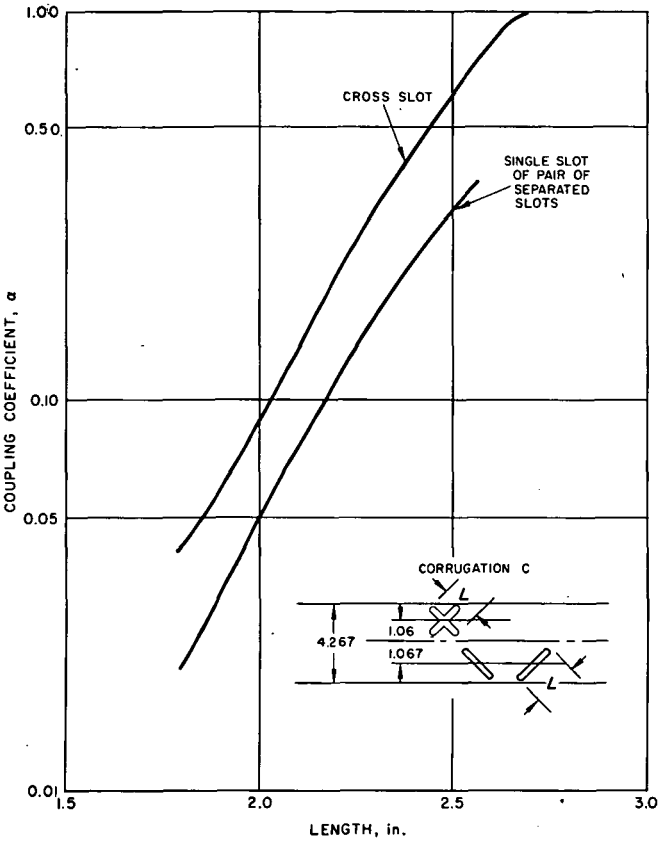

Figure 43. Coupling coefficient vs slot length

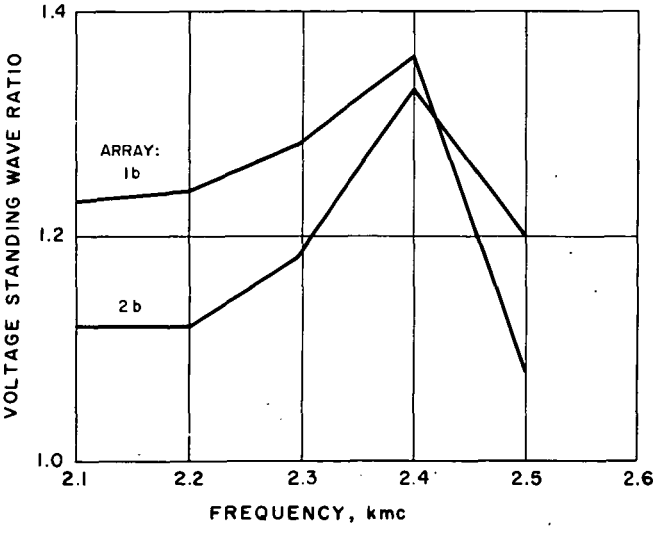

Figure 44. Voltage standing wave ratios of Linear Arrays 1b and 2b

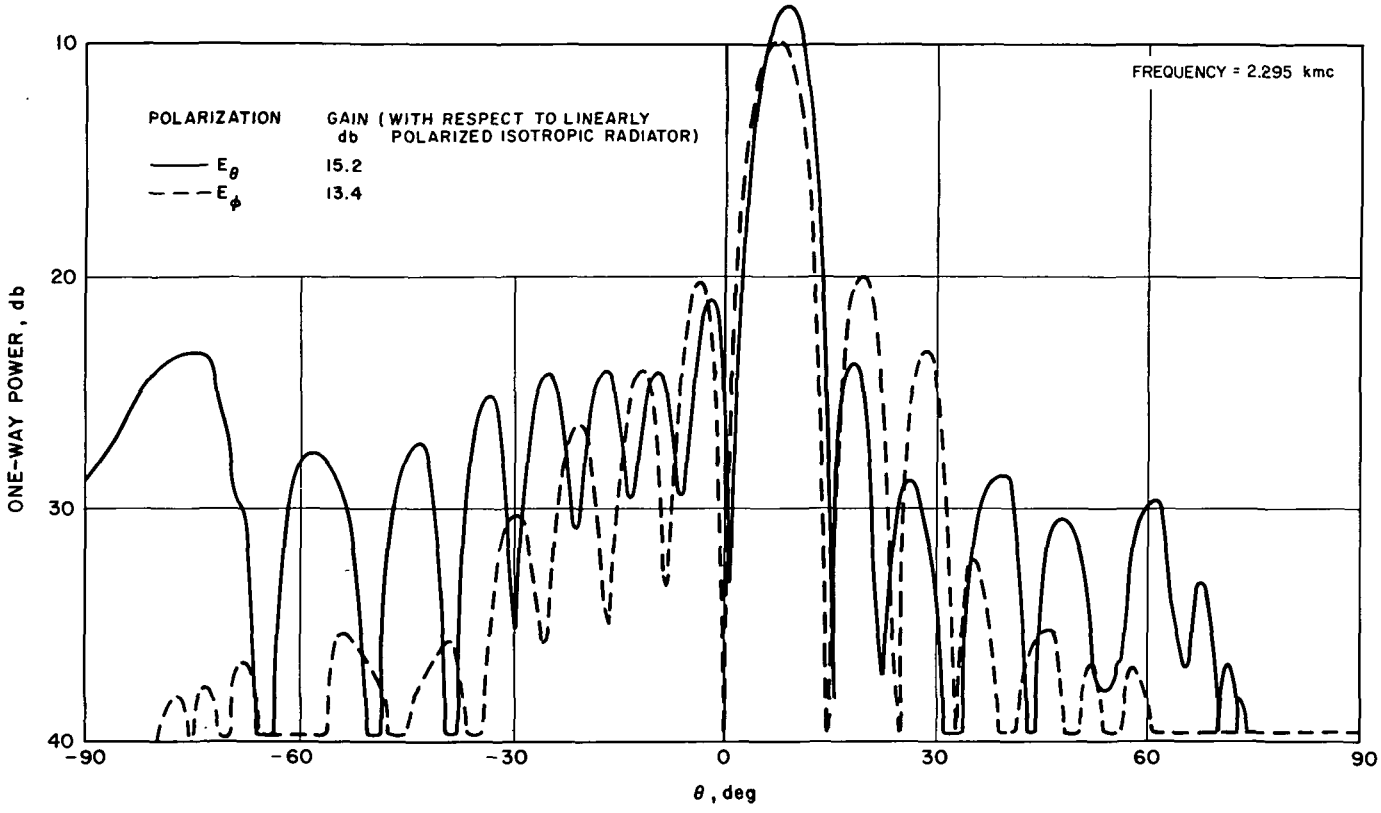

Figure 45. Antenna patterns of Linear Array 1b

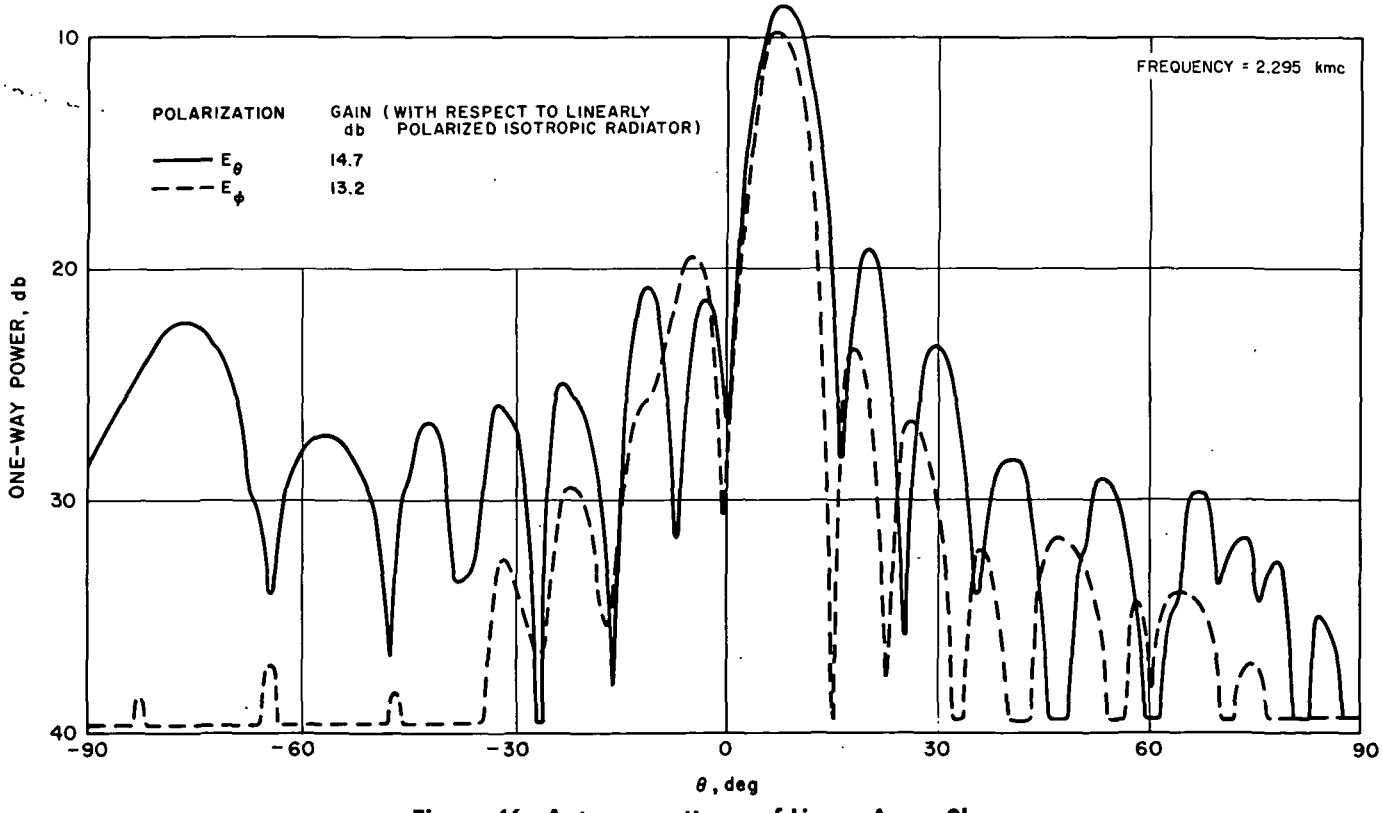

Figure 46. Antenna patterns of Linear Array 2b

Evidence of some phase error is still present in these patterns and the side lobes are higher than desired; therefore, an improved set of linear array aperture plates will be made before a full planar array aperture plate is designed.

A set of test fixtures for developing the full-size transition from the coaxial line connector to the feed guide were received, and measurements are now under way using a loop probe as a coupler. Preliminary data appear very promising and a VSWR of 1.2 has been obtained. This data is now being verified by newly designed loop probes. In addition, another fixture for taking feed line slot conductance measurements under conditions simulating the final configuration was received. Measurements on this fixture have also been started.

Fabrication of a breadboard planar array with a removable aperture plate has begun. The feed line for this model will be electrically identical to the feed to be used on flight units. Two mechanical prototypes are being built to prove out fabrication techniques. Delays in developing necessary tooling have held up production of a model welded by an ultrasonic welding technique. Several 8-inch square sections have been produced using this method. These sections appear functionally sound and the full-size model should be finished soon. The other mechanical prototype is being built as a backup to the ultrasonic welded model. This one uses an advanced resistance welding technique and is 75% complete. The results so far look as promising as the ultrasonic weld method.

3. *Omnidirectional Antennas*

The omnidirectional antenna system is used to pick up command signals from the Deep Space Instrumentation Facility (DSIF) and transmit telemetering data back to Earth. The omnidirectional antennas form part of the phase-locked loop between the spacecraft and the DSIF station which continuously measures doppler shift to determine spacecraft velocity. The antenna system consists of two turnstile antennas each of which is backed by a conical reflecting surface. The turnstile elements are oriented parallel to the ground plane (Fig 47).

The two turnstile antenna axes are to be oriented with respect to each other and to the spacecraft as indicated in Figure 48. It is believed that this orientation will give the best spherical coverage and still provide adequate operating characteristics in case a failure occurs resulting in a tumbling of the spacecraft about some axis.

A set of patterns was taken using two quarter-scale antennas and a quarter-scale model of the spacecraft oriented as shown in Figure 49 which also indicates the experimental setup used to make the patterns. The antennas were only approximately oriented to the optimum position indicated by Figure 48. This was due to the inadequate coverage of the particular turnstile antennas used for making these coverage patterns. A study is

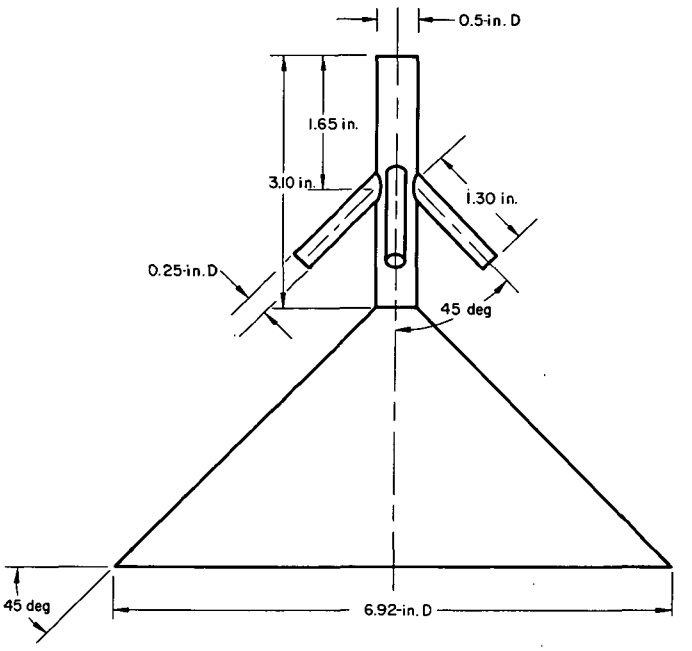

Figure 47. Omnidirectional antenna outline

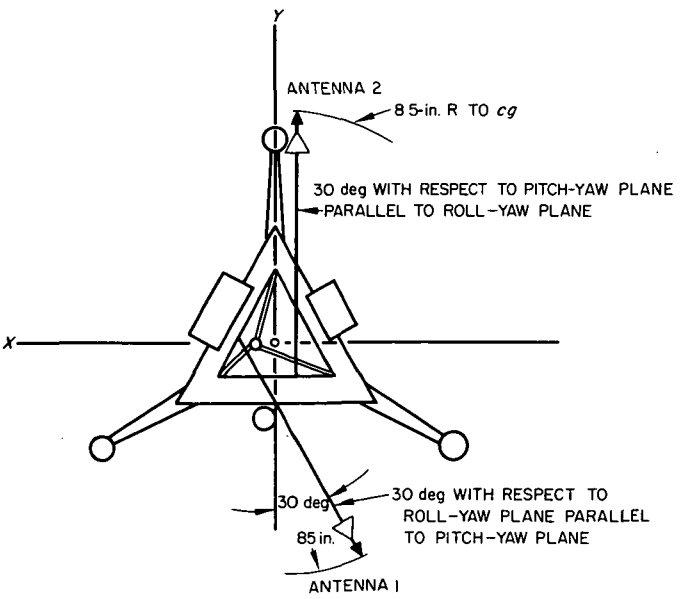

Figure 48. Omnidirectional antenna orientation

presently being directed toward increasing the angular coverage of the individual antennas.

Some of the patterns taken are shown in Figure 50. It should be noted that these patterns, taken with two turnstile antennas, provide 360-degree coverage (one antenna covers the null of the other) as opposed to the single antenna patterns of the last report.

The full-scale turnstile antenna is undergoing circuit development to obtain the proper phase relationships between radiating elements and to obtain the best impedance match over the band of operating frequencies being used. An alternate antenna design is under consideration in an effort to obtain the best pattern coverage as well as the mechanical advantages of light weight and structural rigidity. This antenna consists of a circular cavity radiating circular polarization at the apex of a cone. Figure 51 indicates the approximate configuration being considered.

Arrangements are being made to modify the antenna range to provide the facilities necessary to take antenna patterns using the full-scale antenna system with the full-scale model of the *Surveyor* spacecraft.

4. Command Display Console Demodulator

a. General. The command display console (CDC) demodulator serves as a frequency modulation and phase modulation detector for signals coming from the DSIF receiver. The CDC demodulator has four modes of operation which are described below.

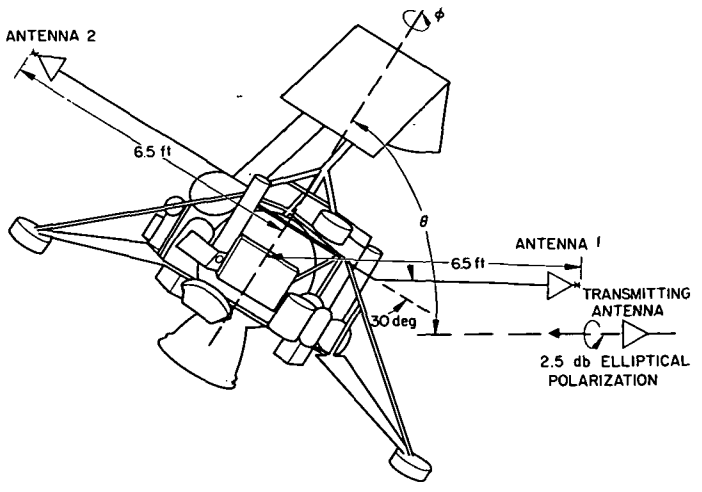

Figure 49. Test orientation of quarter-scale antennas

(1) *Wide band:* In the wide band mode of operation the demodulator detects the wide band television and telemetering data within a 3.3-mc intermediate frequency (IF) bandwidth.

(2) *Narrow band:* The narrow band mode of operation detects telemetering information within a 30-kc IF bandwidth.

(3) *Emergency mode:* The emergency mode of operation detects television information within a 4.4-kc IF bandwidth.

(4) *Phase lock mode:* The phase lock mode detects wide band phase modulation signal within a 3.3-mc IF bandwidth.

All detected signals are supplied to the CDC where they are processed.

As a result of the CDC demodulator circuit design review, certain modifications and additions to the present circuit are necessary or desirable:

(1) Wide band video filter.

(2) Emergency mode video filter.

(3) 2.4-megacycle IF channel to utilize existing narrow band IF signal from the DSIF receiver.

The wide band and emergency mode filters are required to realize the full signal-to-noise improvement gained by using wide band frequency modulation. The 2.4-mc IF channel was added to the demodulator for operation in the narrow band and emergency modes. The new channel takes advantage of a narrow band output signal from the DSIF receiver. The availability of this signal was just recently made known. The new IF channel reduces the complexity of the demodulator by replacing the third and fourth IF amplifiers formerly used for these modes of operation. The second and third conversion oscillators thus are also eliminated. The modification was desirable not only to simplify the demodulator, but to reduce the possibility of interfering signals being generated in the demodulator which would affect normal DSIF receiver operation. Especially serious was the existence of several conversion oscillators which could mix together and produce unpredicted signals.

b. Function description. A revised block diagram of the CDC demodulator is shown in Figure 52. The operation of the wide band discriminator and phase detector loop are the same as described previously (*SPS 37-12*),

with the exception that a low pass filter has been added to the wide band frequency discriminator output.

A 2.4-mc IF signal is supplied from the DSIF receiver to the input of the 2.4-mc amplifier. Provisions are also made in the DSIF receiver whereby a 10-, 20-, or 30-kc noise bandwidth for the 2.4-mc signal can be selected. The input signal is amplified and applied to a switch. In the narrow band position of the switch, the signal passes through a resistive pad which matches the crystal filter insertion loss. In the emergency position of the switch, the signal passes through a crystal filter with a 4.4-kc bandwidth. The amplified 2.4-mc signal is supplied

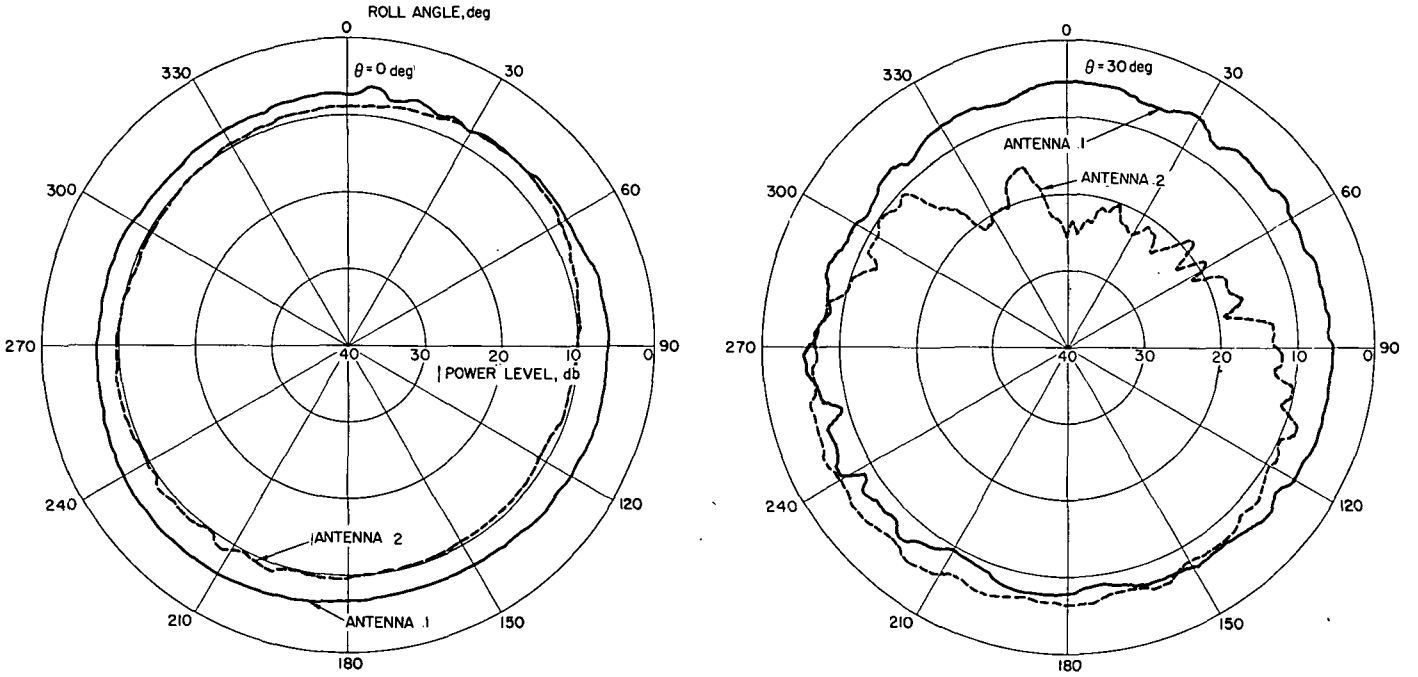

θ = angle between spacecraft roll axis and line of sight to transmitter, deg
Frequency = 9180 mc

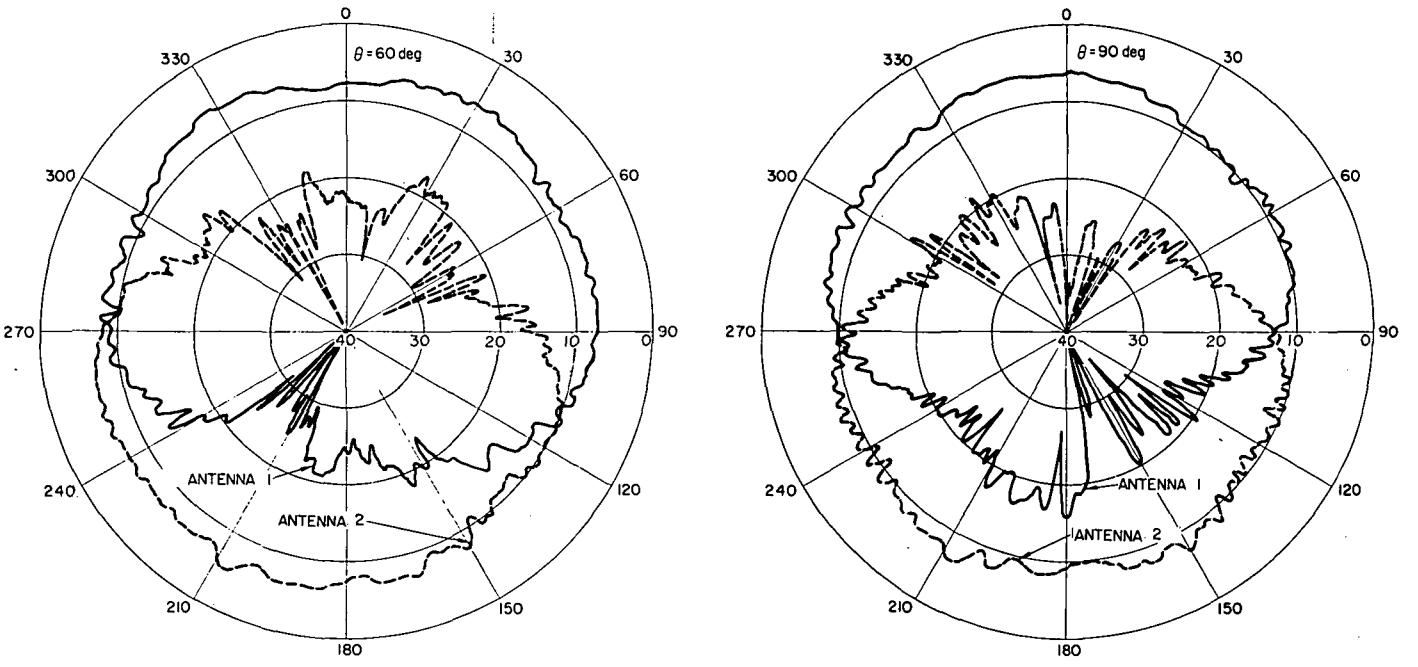

Figure 50. Antenna patterns with two turnstiles

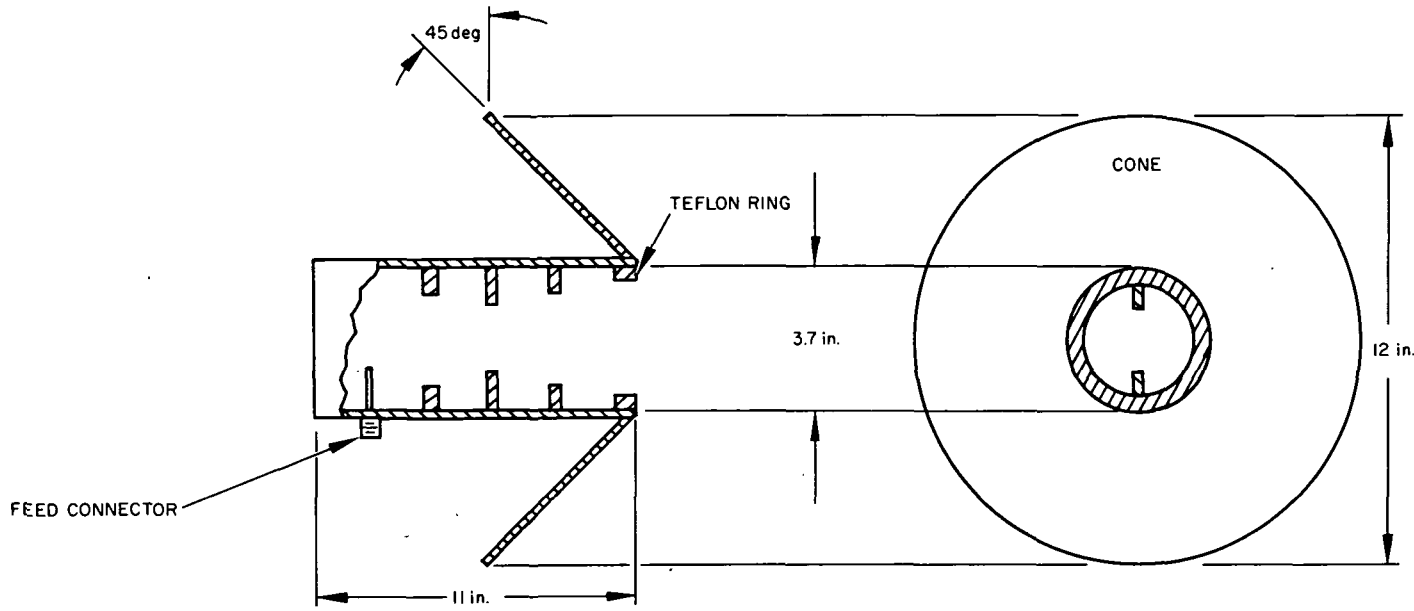

Figure 51. Cone-cavity antenna (design alternate)

to the limiter and the AGC detector. The AGC detector output signal is filtered and fed back to the 2.4-mc amplifier such that the input signal to the limiter is maintained constant for a 20-db variation of the input signal. The limiter removes amplitude modulation to which the AGC loop can not respond. The limiter output is fed to the narrow band frequency discriminator where the emergency television or telemetering subcarrier signals are detected. The telemetering subcarrier signals are applied to the summing network and they appear at the wide-band video output. The emergency television passes through a low pass filter and a video amplifier to the emergency television output terminal. The narrow band frequency discriminator dc output voltage is filtered and supplied for monitoring the frequency drift of the DSIF receiver. Tuning corrections to the receiver may be manually applied as necessary.

5. Signal Processing

The signal processing system in the *Surveyor* spacecraft processes the variety of signals from the scientific instruments and the many channels of engineering information into a form suitable for modulating the transmitter. The system consists of three major blocks: (1) the central signal processor, (2) the engineering signal processor, and (3) the scientific signal processor. One of the main objectives in the system design was to achieve as much independence between individual experiments and the processing of engineering information as is reasonable. This independence increases reliability and also allows changes to be incorporated into the system more readily.

a. Central signal processor. The central signal processor contains two analog-to-digital (A-D) converters, three subcarrier oscillators, six weighted summing amplifiers, eight power switches, and a subcarrier oscillator bypass gate. The block diagram of the analog circuit portion of the central signal processor is shown in Figure 53. Output signals from the A-D converter, scientific auxiliaries, and engineering signal processor are combined in the summing amplifiers and are then sent to either one of the two transmitters. The transmitters are either phase-modulated or frequency-modulated depending on which mode has been selected.

The method of summing the various signals has been changed since the last report. A redundant-type summing system has been selected in order to eliminate the possibility that failure in the "final' summing amplifier might prevent signals from modulating either of the transmitters. This system uses individual "final" summing amplifiers to provide signals for the four different modes: (1) frequency-modulated transmitter A, (2) frequency-modulated transmitter B, (3) phase-modulated transmitter A, and (4) phase-modulated transmitter B. Two additional summing amplifiers are used to "pre-sum" outputs of various scientific auxiliaries. This pre-summing reduces the number of inputs to the "final" summing amplifiers and therefore allows a reduction in the complexity of the summing amplifiers. In addition, changes can be incorporated into the system quite readily.

The analog circuitry for the central signal processor has been breadboarded and is undergoing performance tests. A design review of the circuit has been conducted and no serious problems were uncovered. Recommended modifications that were found to be valid were incorporated into the design. Final circuit release for productizing will be made when performance specifications are firmer.

The schematic diagram of the analog circuit portion of the central signal processor is shown in Figure 54. The signal summing is performed by operational-type summing amplifiers. Each of the six amplifiers uses two high-gain silicon planar transistors and they are identical except for minor variations that reflect different bandwidth and impedance requirements. Ground-out switches have been added at the inputs of the "final" summing amplifiers since the last report. The ground-out switch prevents signals from feeding through the input resistors of the "off" summing amplifier and affecting the channel gain of the "on" summing amplifier. The ground-out switch also prevents changes in channel gain from occurring if one of the summing amplifiers can not be turned off due to a failure in the power switch. The ground-out switches are activated by a 29-volt signal from the transmitters.

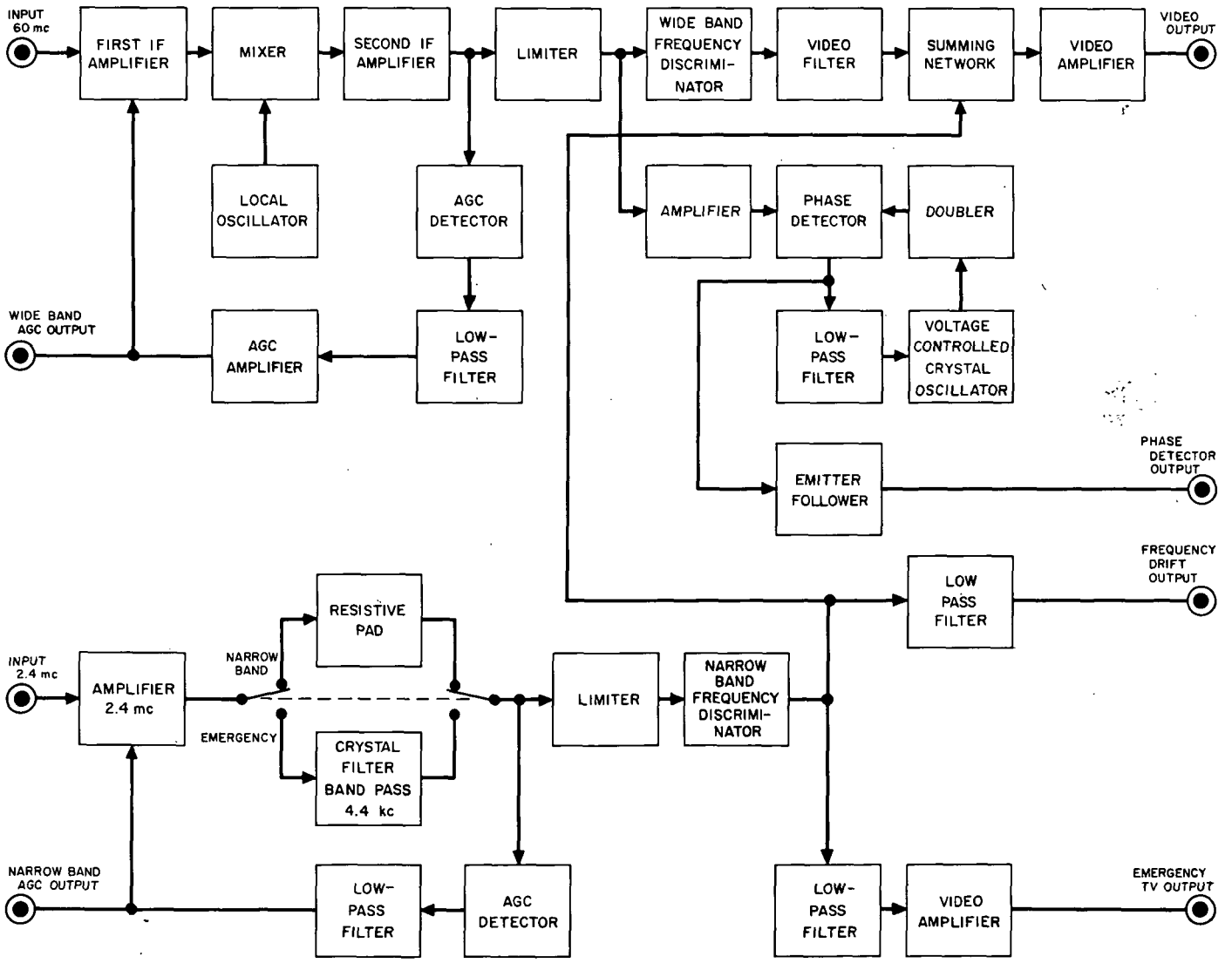

Figure 52. Command and data handling console demodulator block diagram

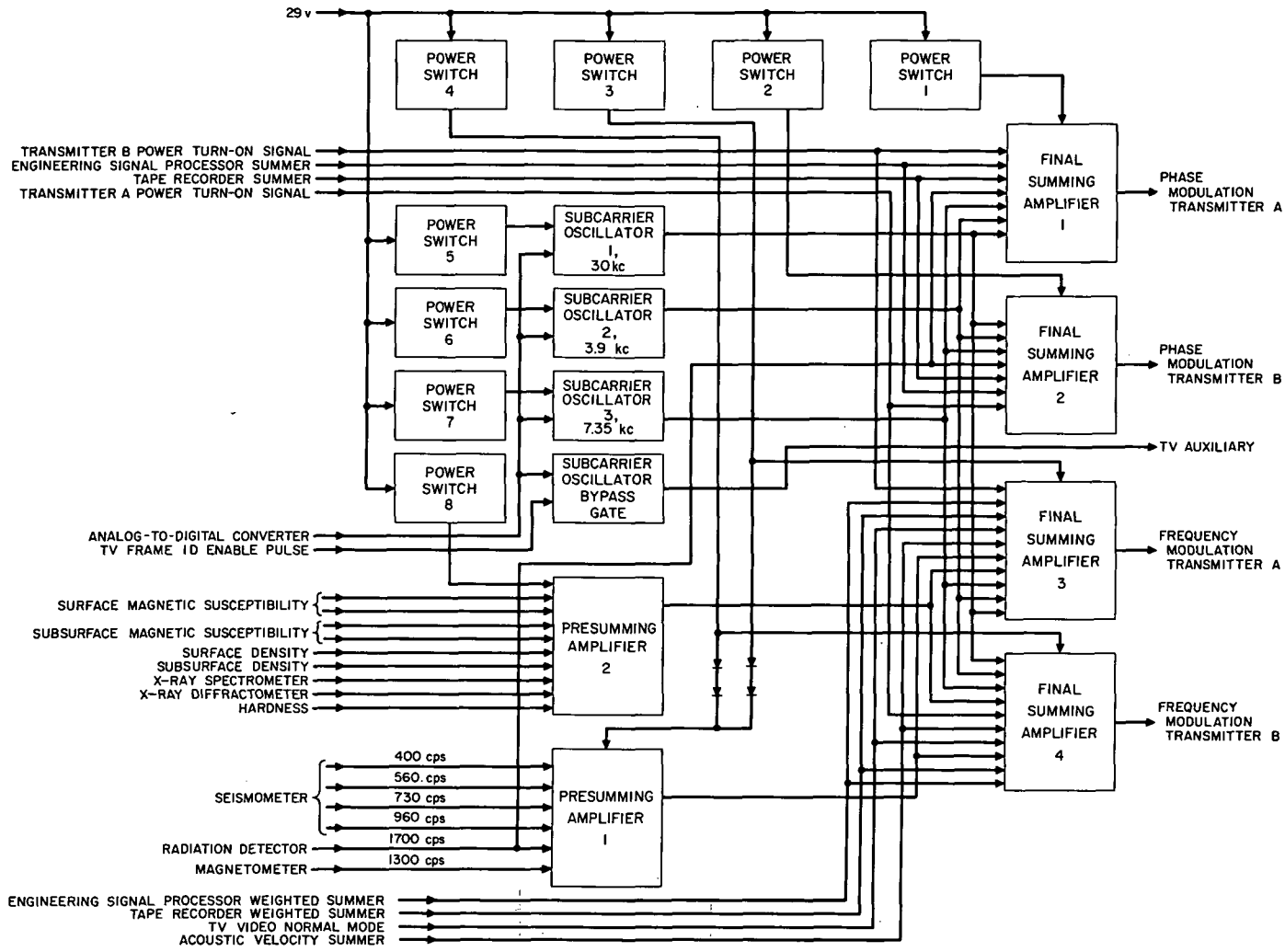

Figure 53. Central signal processor block diagram (analog circuits)

The subcarrier oscillator bypass gate has been added since the last report. The bypass gate allows the television frame identification signal from the A-D converter to frequency modulate the transmitter directly. The bypass gate is closed by an enable pulse generated in the TV auxiliary.

b. Engineering signal processor. A preliminary circuit release has been made for the engineering signal processor. A breadboard has been constructed and successfully tested. The breadboard incorporated the complete logic, electronic commutators, and a special commutator for the measurement of temperature. The engineering signal processor breadboard was then successfully integrated with a breadboard of the A-D converter. A recording of the output of the A-D converter was made to examine the various commutated inputs, and the desired accuracy was found to have been achieved.

c. Temperature measurement using resistive sensors. Temperature measurements in *Surveyor* will be accomplished by resistive temperature measuring sensors. The block diagram of the temperature measuring system is shown in Figure 55. The resistive sensors are excited from a constant current generator. An electronic commutator sequentially connects the constant current generator and the analog-to-digital converter to the various sensor resistors. Each position on the commutator contains two solid-state switches, labeled a and b. Switch a connects the constant current generator to the sensor resistor while Switch b connects the A-D converter to the sensor resistor. Switch b could be eliminated if the

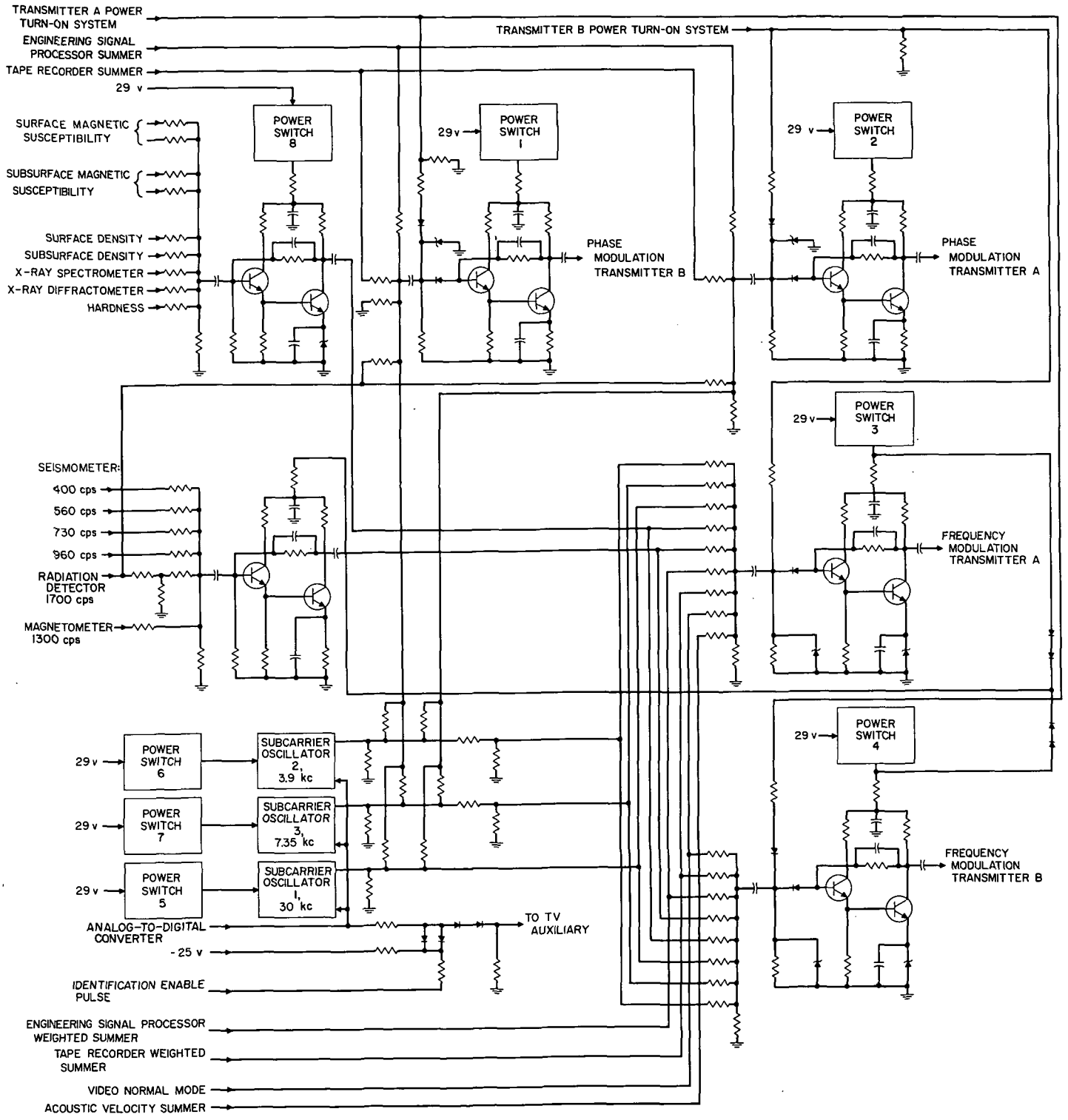

Figure 54. Central signal processor schematic (analog circuits)

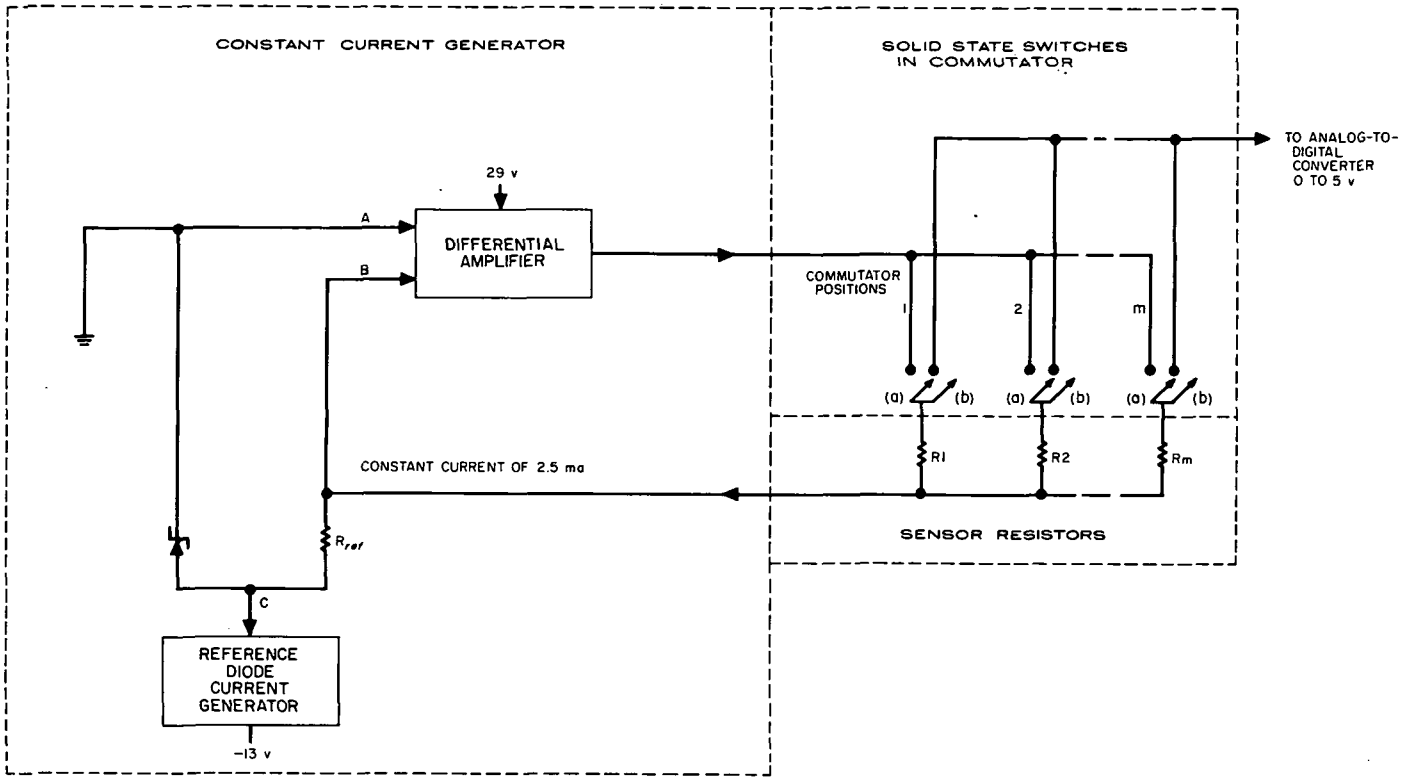

Figure 55. Temperature measuring system

A-D converter were connected directly to the output of the constant current generator. However, the offset voltage in Switch a has a relatively large variation since it must carry the sensor current. The variation is greater than the allowable reading error and this is intolerable. The current through Switch b is very small and therefore a much more accurate offset voltage can be maintained. The constant current generator maintains the sensor resistor common connection at a virtual dc ground (Point b). The reference resistor is connected from this virtual ground to a very stable negative voltage (Point c). The current flowing through the selected sensor resistor must pass through the reference resistor except for a very small percentage that flows into the high impedance differential amplifier. Therefore, a constant current can be supplied through the selected sensor resistor even if the closing of Switches a and/or b add or subtract current from the output of the differential amplifier.

Constant current generator. A constant current generator has been designed and tested that maintains the current constant to better than ± 0.1% for resistive loads between 0 and 2000 ohms and over a temperature range of −20 to 55°C. The nominal current is 2.5 milliamperes. The schematic diagram of the constant current generator is shown in Figure 56. The circuit maintains a constant current through the very stable reference resistor R11. A reference zener diode CR1 maintains a constant negative voltage at one end of R11. The voltage at the other end of R11 is maintained at zero volts by means of a five-transistor (Q1 through Q5) differential input amplifier. The input current to the amplifier causes less than ± 0.02% error in the current through R11. The current through the reference zener diode is controlled by a three-transistor (Q6, Q7, Q8) regulator circuit. This is necessary to maintain the required accuracy of the zener voltage.

6. Command Decoding

a. Central command decoder. In addition to minor changes in several other circuits, the receiver-decoder selector circuitry and the flip-flop circuit of the cental command decoder have been modified. A decision has also been made to include the basic bus subsystem decoders in the central decoder unit along with the redundant central command decoders and the receiver

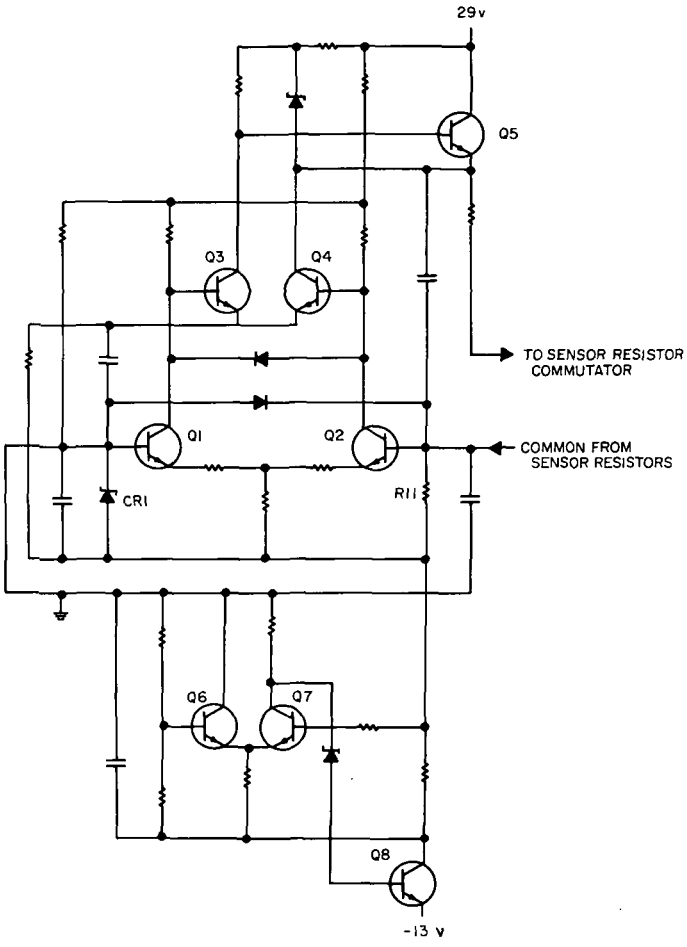

Figure 56. Constant current generator

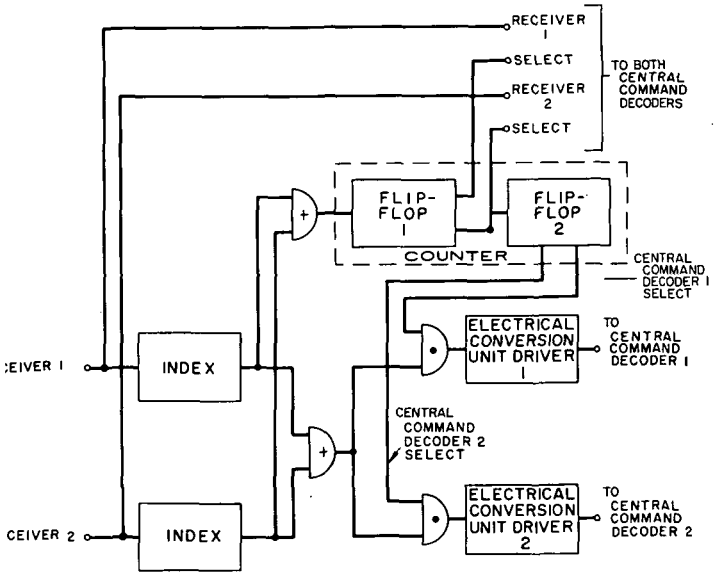

Figure 57. Receiver-decoder selector

decoder selector. Four subsystem decoders are included for the basic bus commands, excluding the flight control commands. The latter are handled by a flight control decoder in the flight control electronics unit.

A block diagram of the receiver-decoder selector is shown in Figure 57. The receiver-decoder selector determines which central command decoder and which receiver will be used. Which of the four possible combinations of central command decoder and receiver is used is remembered by a two-stage counter which is stepped each time transmission is terminated.

The index circuits consist of a resistor-capacitor network, a threshold recognizing circuit, and an amplifier. Transmission from the ground causes the index, after a short delay necessary to reject noise bursts, to put out a signal which turns on one of the electrical conversion unit drivers, which turns on the corresponding central command decoder. Flip-flop No. 2 of the counter determines which central command decoder is turned on. When transmission ceases, after a short delay, the index signal which operates the electrical conversion unit drivers turns off, resulting in changing the state of flip-flop No. 1 of the counter. Flip-flop No. 1 determines, by use of gating in each central command decoder, which receiver output will be used by the selected central command decoder. The state (off or on) of one central command decoder is telemetered via a yes/no commutator in the engineering signal processor. Since the sequence of the counter states is known, this signal is adequate to inform ground operators which receiver and which central command decoder are selected.

The central decoder unit flip-flop (and the central signal processor flip-flop) have been changed by the addition of four components to each flip-flop to reduce noise sensitivity and to allow simplification of the clock pulse circuitry. This added noise tolerance is of importance due to the low power level of the circuitry.

The old circuit is shown in Figure 58a. A sawtooth clock pulse was required. The new circuit, shown in Figure 58b, requires a simple rectangular clock pulse. More important, noise tolerance is greatly improved. The anti-noise bias, of approximately 1-volt amplitude, back biases the diodes connected to the transistor bases to protect against false triggering of the flip-flop by stray pulses on both the R and S input lines and on ground.

Modules for 60% of the command decoding circuitry have been designed. Six printed circuit boards will be used to mount approximately 66 modules, the number estimated for the command decoder unit.

Circuits have been assigned to modules, and a scratch pad "module-placement" layout is being drawn. The objectives of this layout are to minimize interconnections on and between cards and to uniformly place high-power-dissipating modules.

b. Flight control decoder and programmer.

Logic and organization. The flight control decoder and programmer (Fig 59) receives inputs from the flight control subsystem and from the flight control command decoder. Outputs from the programmer are used to control and actuate devices which effect initiation of the flight control action, angle maneuvers, mid-course velocity correction, and operations affecting final descent.

Preliminary logic equations for the programmer were released November 6, 1961. A block diagram of this design is given in Figure 60. The programmer in this

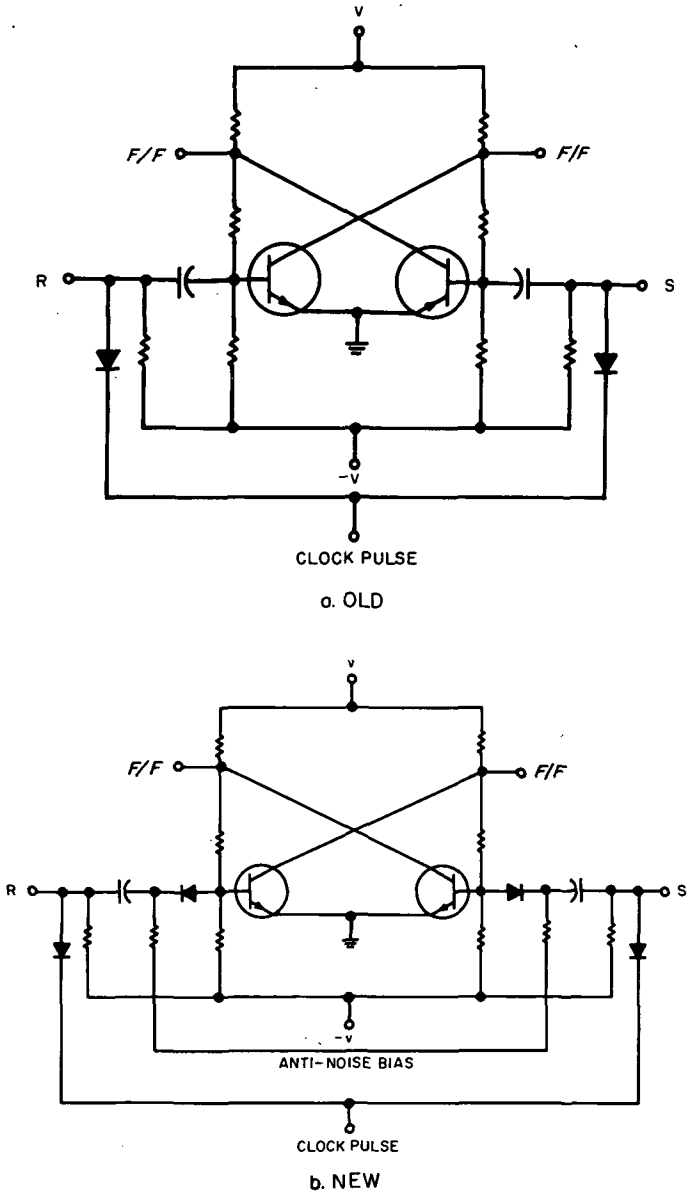

Figure 58. Central decoder unit flip-flops

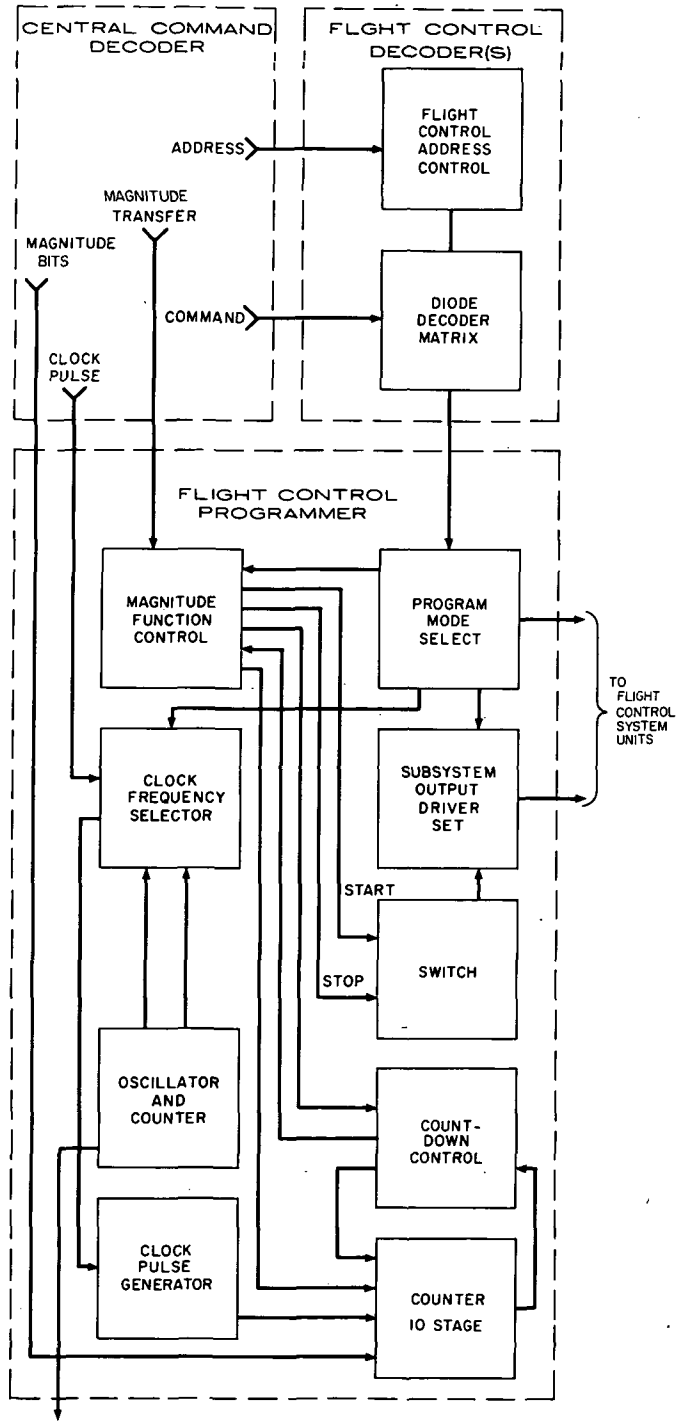

Figure 59. Flight control decoder and programmer

design is essentially a timing device operating in three modes according to signals from the flight control decoder and from the flight control system. The three modes are: (1) auto-external; (2) auto-internal; and (3) manual. In the auto-external mode, the time delays are automatically generated (after an appropriate "start" signal) according to magnitude bits generated externally on the ground and transmitted through the central command decoder. In the auto-internal mode, the time delays are generated automatically from magnitude bits generated by an internal number generator whose logic is wired to deliver preset magnitudes. In the manual mode the time delays are completely subservient to the start and stop commands generated at the ground station. In this mode, the time interval is defined by the interval between the start and stop signals.

The logic equations in this design call for 32 (reset-set) (R-S) flip-flops, 20 logic amplifiers, 15 output amplifiers, seven inverters, two clock pulse systems, one reference oscillator, and a set of countdown scalers. The need for two clock systems arose due to the asynchronous relation between the reference oscillator clock and the timing of signals originating in the command decoder. It was suggested that dc coupled flip-flops might be used to avoid a two-clock system. This technique was unable to solve the problem of resetting several flip-flops with the same pulse without a substantial increase in the number of flip-flops. The problem of synchronization was settled by using a gate-controlled relaxation oscillator driving a standard clock pulse output circuit. These clock pulses (called MCP) are produced whenever appropriate command pulses are present. The timing oscillator feeds scalers having two output frequencies, each of which is gate selectable and is capable of driving standard clock circuits. These circuits produce the timing clock pulses (TCP). The technique used here, of operating two sets of flip-flops each having separate clock timing, makes use of a single standard R-S flip-flop type.

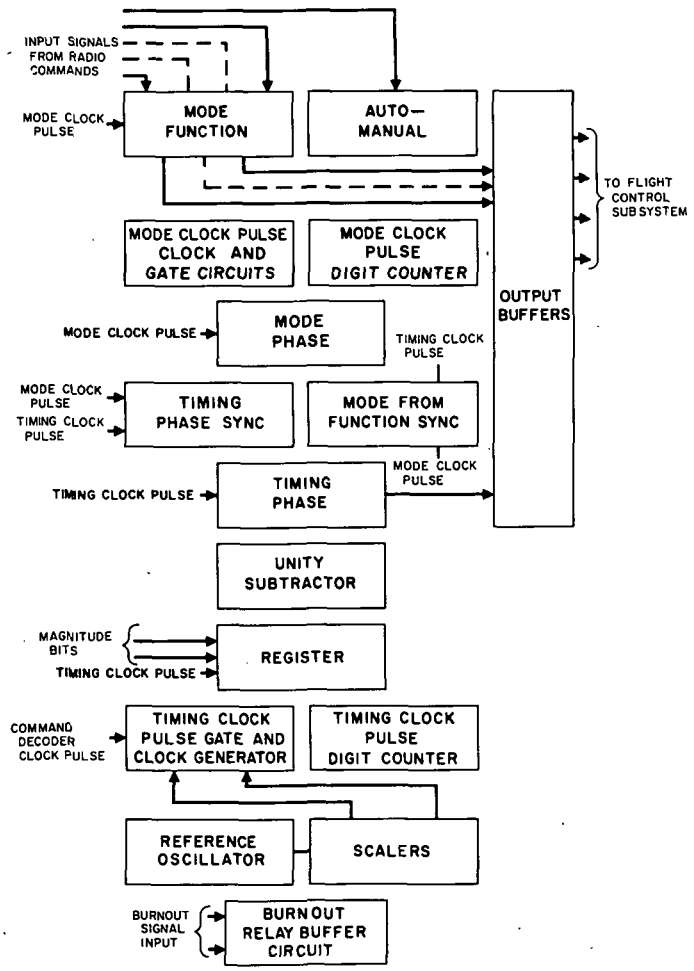

Figure 60. Flight control programmer

Oscillator circuit design. The long-term stability requirements of the frequency source circuits dictated the use of a resonator (crystal or tuning fork) to maintain the desired frequencies. An examination of crystals and tuning forks showed that, because of weight and relative insensitivity to mechanical vibration, the use of crystals would give superior performance. Crystals with a resonant mode below 10 kc have masses so large that their supporting leads do not stand up under mechanical vibration. Therefore, a decision was made to operate at a frequency of 12.8 kc and count down to the desired frequencies. Crystals of this frequency were purchased from two recommended vendors and were subjected to evaluation tests at environmental extremes. The results of these tests showed that excellent crystals could be purchased at this frequency. The frequency stability will be better than the 0.02% short term and the 0.1% long term stabilities required.

A study of single-transistor crystal oscillator circuits showed that the reactive elements required became excessively large and heavy. Therefore, a decision was made to use the circuit shown in Figure 61. Transistors Q1 and Q3 and associated biasing resistors form a two-stage amplifier. Positive feedback from the collector circuit of Q3 to the base of Q1 is provided by the crystal. The tank circuit attached to the collector of Q3 enables the circuit to be tuned to the exact frequency desired. Q4 and associated components form a buffer amplifier. Q1, Q3 and Q4 all operate Class A. Capacitor C6, Resistors R4 and R9, Diode CR1, and Transistor Q2 are

an AGC network which insures this Class A operation. Transistors Q5 and Q6 form a Schmitt trigger which shapes the sine wave output of Q4 into a square wave which is the input to the countdown stages.

In order to minimize the oscillator dissipation and provide an optimum design, a computer routine for use on the IBM 7090 has been written. Checkout and debugging of this routine is 90% complete.

Final design and checkout has been completed for the countdown stages. The 400-cps three-phase voltage requirement by inertial guidance components is derived from the same countdown circuits. Addition of one countdown stage provides a second 400-cps signal, 90 degrees out of phase with the first. The two 400-cps signals are used to generate the three-phase voltages.

Preliminary circuit development of the other programmer circuits is being carried out, and a preliminary circuit release will be made on or about December 15, 1961.

Breadboards. Three breadboards are currently being designed and constructed for flight control subsystem evaluation: (1) a 400-cps synchronization pulse generator which includes an oscillator and countdown circuitry to provide the two-phase 400-cps outputs; (2) a central command decoder simulator; (3) a complete breadboard of the programmer (which includes the 400-cps synchronization pulse generator) and a second central command decoder simulator.

Figure 62. Transmitter power amplifier and low power multiplier

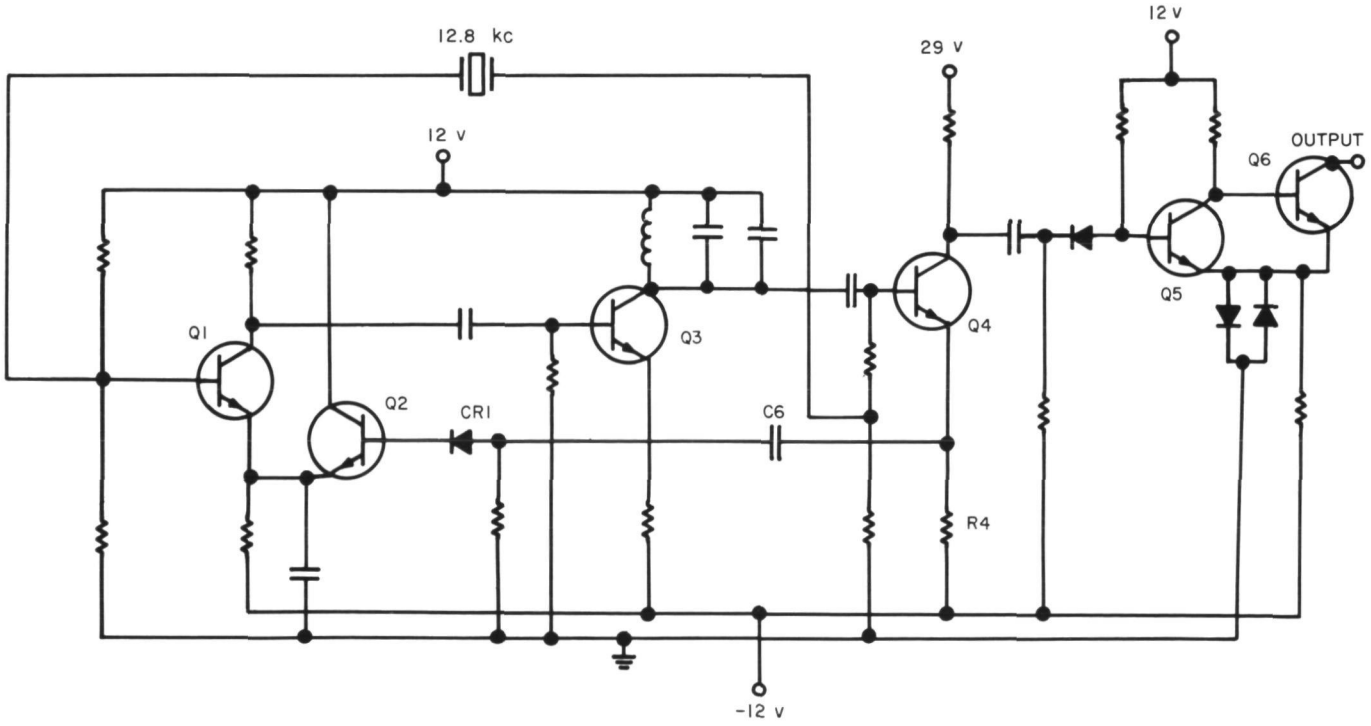

Figure 61. Flight control oscillator

7. Transmitter

Integration of the second set of development breadboards has been completed and temperature tests are now being made. Construction of the third breadboard model has begun in cooperation with the product engineer. The transmitter power amplifier and low-power multiplier, shown in Figure 62, is in the intended production configuration. Tests performed on it will reveal if any spurious effects can be expected as a result of the productized packaging.

a. Exciter. A block diagram of the transmitter exciter circuit is shown in Figure 63. Changes in this block diagram since the last report have occurred during development of the second exciter breadboard. The voltage controlled crystal oscillator (VCXO) signal now is fed through the phase modulator so that phase modulation can be used with the VCXO as a signal source. Resistive summing points are used wherever two RF signal sources join. This is necessary to achieve isolation from one signal source to the other. Since only one RF source will be on at any given time, mixing does not occur at the RF summing points. Amplifiers have been added to restore the output power level to 10 milliwatts to drive the transistor power amplifier.

Initial temperature tests have shown excessive frequency drift of the VCO and the VCXO over the operating temperature range. These circuits are being redesigned to achieve the required frequency stability.

b. Transistor power amplifier. The transistor power amplifier in the second breadboard model consists of two stages using 2N707A transistors and an output stage using a TA2084 transistor. Each stage operates Class C with the first stage saturated for power limiting.

c. Transmitter multiplier chain (lumped parameter). A varactor frequency quadrupler was built but never completely optimized. The circuit appeared quite critical and difficult to time. Two push-pull varactor doublers are being used to achieve higher efficiency and better filtering than the quadrupler could produce. Alignment requirements of the doublers have been reduced to one tuning capacitor per doubler.

d. Final development breadboards. Component layout for the final development breadboard model will be the same as the initial product version. This is being done to ensure satisfactory circuit operation in its final configuration. Fabrication of the final development breadboard model has begun under the joint direction of the development engineer and the product engineer.

e. X6 multiplier. Amplitude variation of power from the X3, X2 frequency multipliers was measured in a

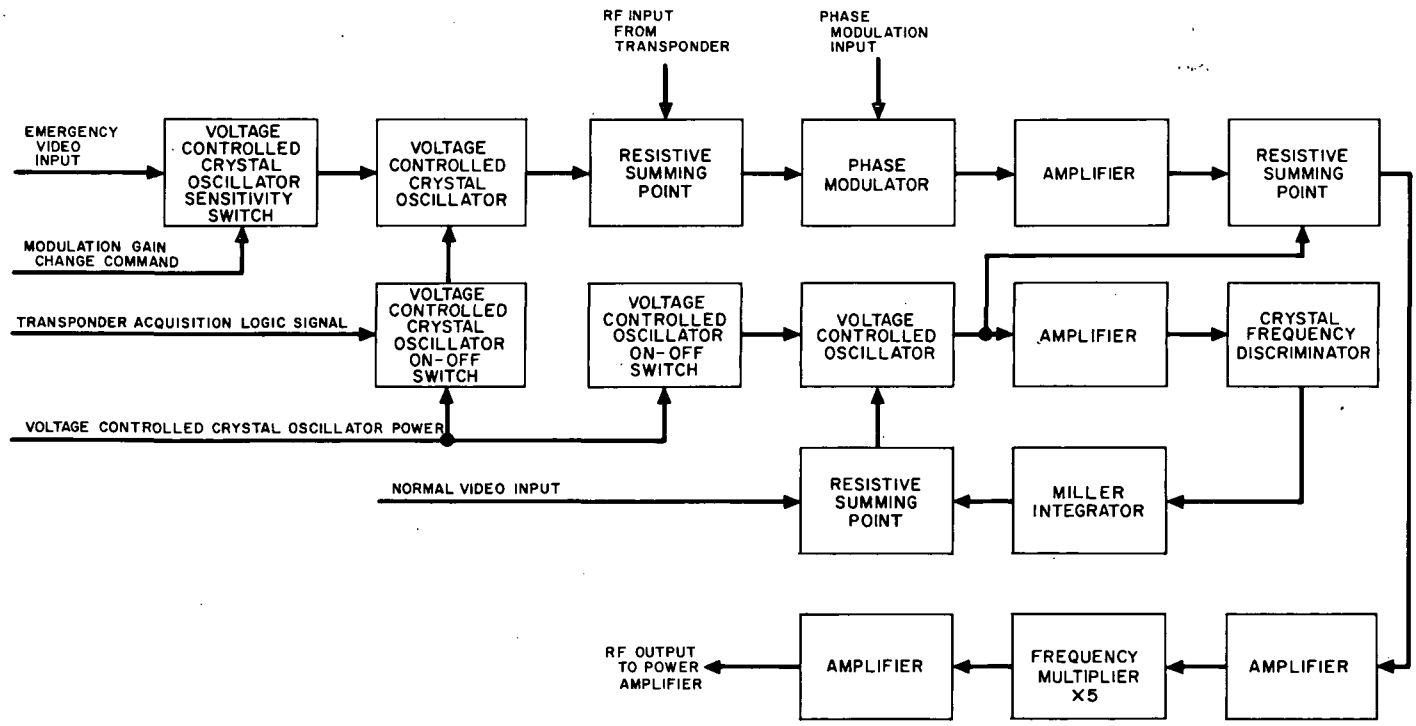

Figure 63. Transmitter exciter

temperature range from 0 to 125°F. The resultant curve, which varied 0.25 and −1.0 db from a nominal value at 70°F, is shown in Figure 64.

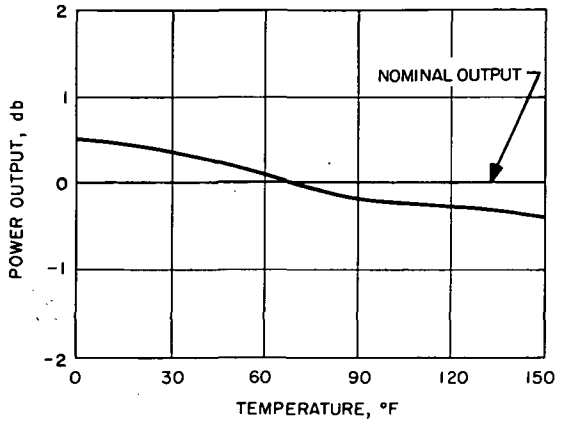

Figure 64. X6 multiplier power output vs temperature

The entire chain was again joined after redesign of the lower stages and the spurious lines previously seen at 96 and 192 mc from the central frequency were found to be suppressed 30 and 37 db below the desired frequency. This suppression is sufficient for proper operation of the transmitter and receiver in all modes.

The transmitter solid-state chain is required to function into each of several different types of loads. Although each load has an impedance close to 50 ohms at the transmitter frequency, the impedance curves across the spectrum have entirely dissimilar characteristics. A resonant line is now being added to the output doubler so that the diode sees the different loads through a narrow passband. In this way the loads will appear to be uniform.

f. TWT amplifier. The first few 10-watt tubes showed a degeneration with age. This has been traced to a deterioration of the attenuating material, which is sprayed on the helix supporting rods. The condition was corrected by using a pyrolytically deposited film of alumina. The tube is emitting 11 to 12 watts with 20% efficiency with no sign of change such as that observed in the previous tubes.

8. Command Receiver-Transponder Interconnections

The command receiver is a double conversion FM receiver. It must operate continuously throughout the life of the spacecraft. Reliability and power efficiency are the important factors in the design of the receiver since available power is severely limited.

The receiver also is able to operate in a phase-locked mode by energizing the transponder interconnection circuit. The reason for not operating as a phase-tracking receiver all the time is that the phase-locked mode requires significantly more power than the frequency tracking mode. Basically, the receiver has not changed

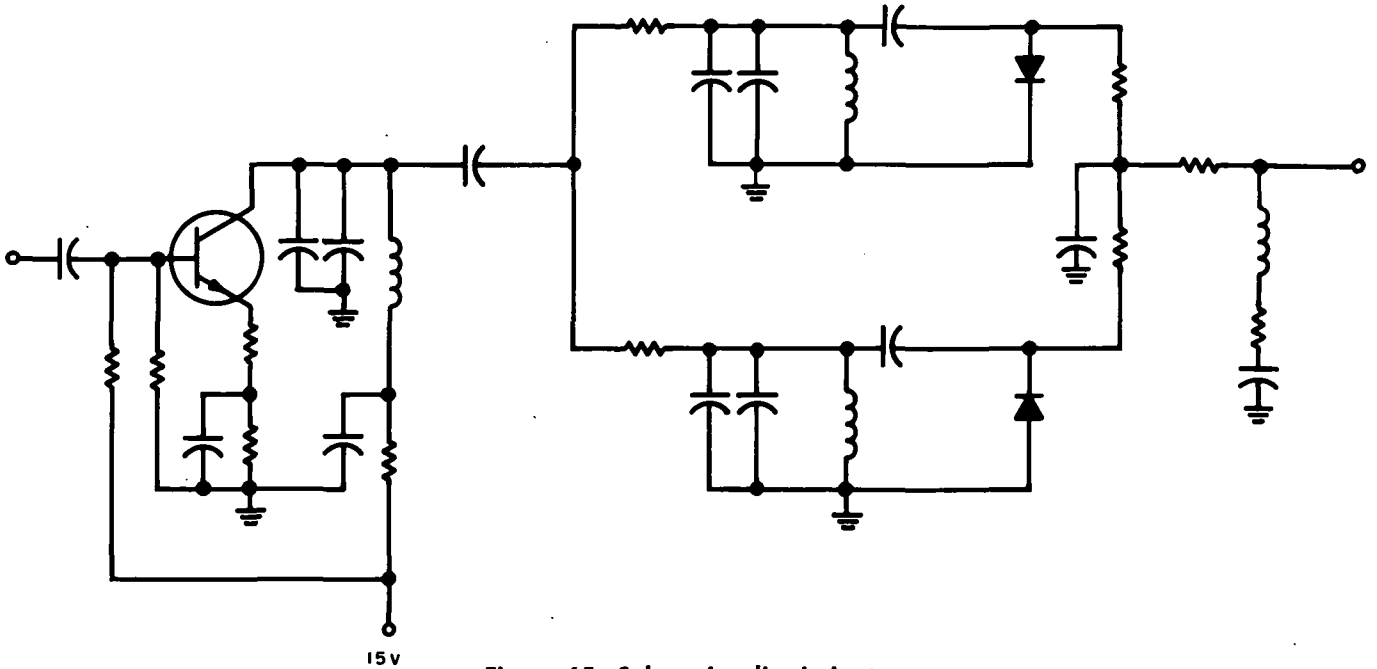

Figure 65. Subcarrier discriminator

much from that described in the previous progress report (*SPS 37-12*) and the block diagram remains valid.

a. Breadboard receiver-transponder interconnection system. Integration of the receiver-transponder interconnection system has been completed. All of the receiver and transponder interconnection circuits are operating satisfactorily and quantitative tests of the receiver performance are in progress. Spurious responses and interfering signals have been reduced to a tolerable level. All interfering signals are down to at least — 140 dbm. The interfering signal that caused the most trouble was the fifth harmonic of the frequency divider output signal which reflected back through the divider and caused modulation of the voltage-controlled oscillator. The interfering signals were reduced to a tolerable level by adding power supply decoupling, circuit isolation, and RF shielding.

b. Local oscillator. The second version of the local oscillator discussed in detail in Reference 1 has been incorporated into the receiver breadboard system. Operation of this local oscillator with the rest of the receiver was satisfactory. The output power is 1.5 milliwatts and all undesired sidebands were down by at least 30 db from the centerline.

c. 2.3-kilocycle subcarrier discriminator. A different subcarrier discriminator from that shown in the previous report has been incorporated into the receiver breadboard system. A schematic diagram of the subcarrier discriminator is shown in Figure 65. The discriminator consists of a tuned amplifier stage, two tuned detectors, summing network, and an output filter. One of the tuned detectors is a positive peak detector and is tuned above the center frequency, and the other is a negative peak detector and is tuned below the center frequency. The detector output signals are added together and filtered in the summing network. The series resonant circuit at the output rejects the 2.3-kc subcarrier signal. Figure 66 shows the output characteristics of the subcarrier discriminator circuit.

d. IF input stage. The 47-mc input stage has been redesigned to improve the noise figure. A schematic of the input stage is shown in Figure 67. A noise figure of 4 db was measured with this amplifier as compared with the 8.5-db noise figure of the previous input stage.

e. Breadboard construction. A different type of breadboard construction was used for the second receiver breadboard. This type construction was used in order to

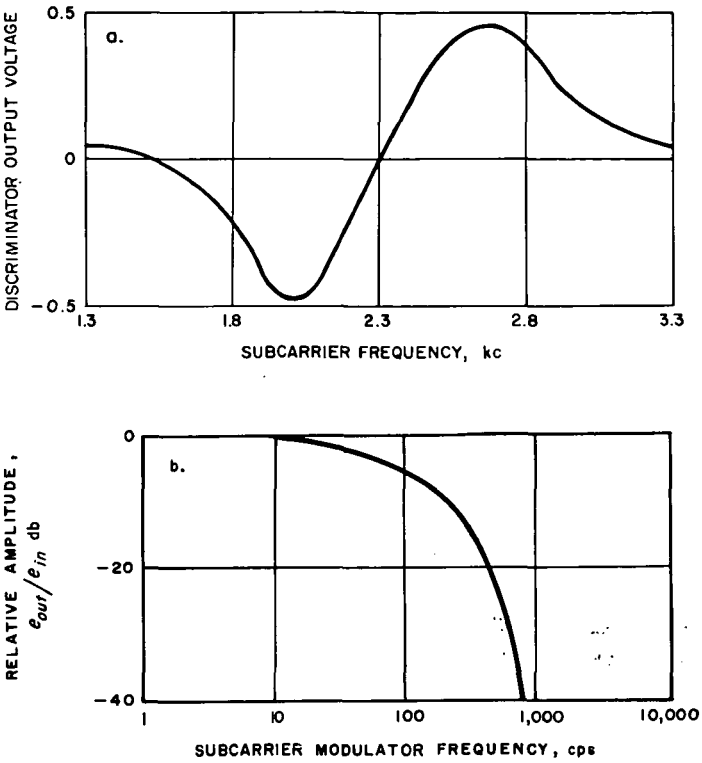

Figure 66. Subcarrier discriminator output characteristics

make the breadboard more compatible with the final packaged version. Also, this type of construction will provide much better RF shielding. The second receiver breadboard is shown in Figure 68. All of the RF circuitry is contained on the six "T" chassis. The subcarrier and electrical conversion unit will be constructed on a printed circuit which will be inserted into one end of

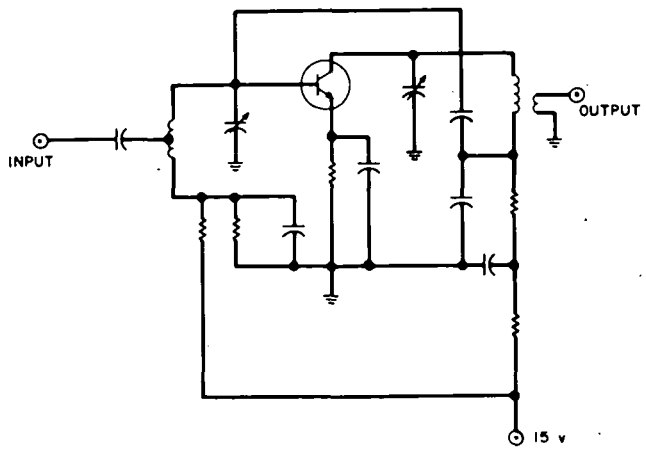

Figure 67. IF input circuit

the receiver package. The X6 cavity and RF mixer will be located at the other end of the receiver box.

f. X6 multiplier. A X6 cavity multiplier was subjected to a temperature variation from 0 to 125°F and the measured power output for a constant input is shown in Figure 69.

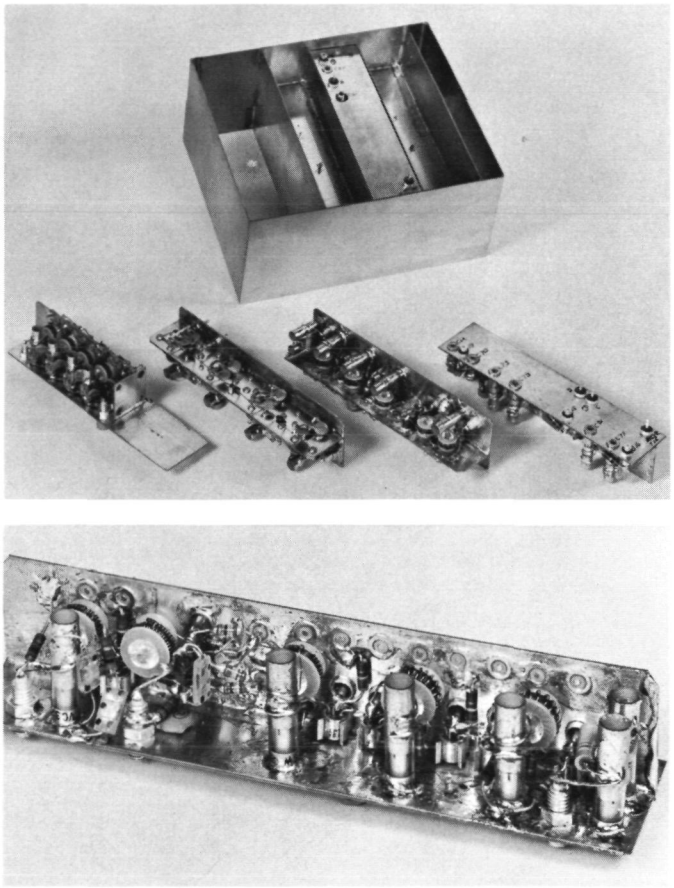

Figure 68. Second receiver breadboard

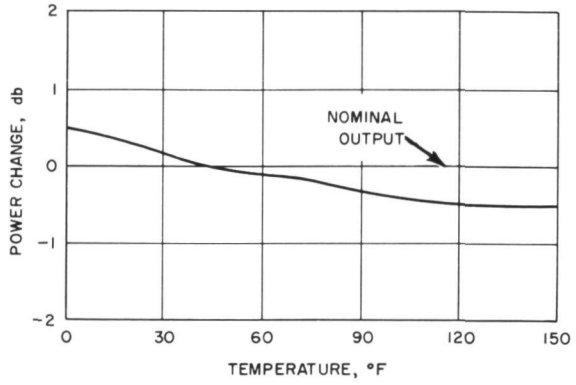

Figure 69. X6 cavity multiplier

Vibration tests on one model indicated a possible phase shift problem. Additional models will be tested to discover if the problem is inherent in the cavity or associated with the fabrication method.

g. Mixer. A lightweight mixer has been purchased from SAGE and initial noise figure measurements indicate that the noise figure is at the specified value; that is, less than 7.0 db if operated with a 1.50-db IF strip.

9. RF Switch

A latching transfer switch has been developed by Transco. After one million operations the switch was disassembled and there was no evidence of wear. A dc latching switch has been tested at 2295 mc and found to function with minor impedance matching. The switch, which weighs 0.6 ounce, has an inherent loss of

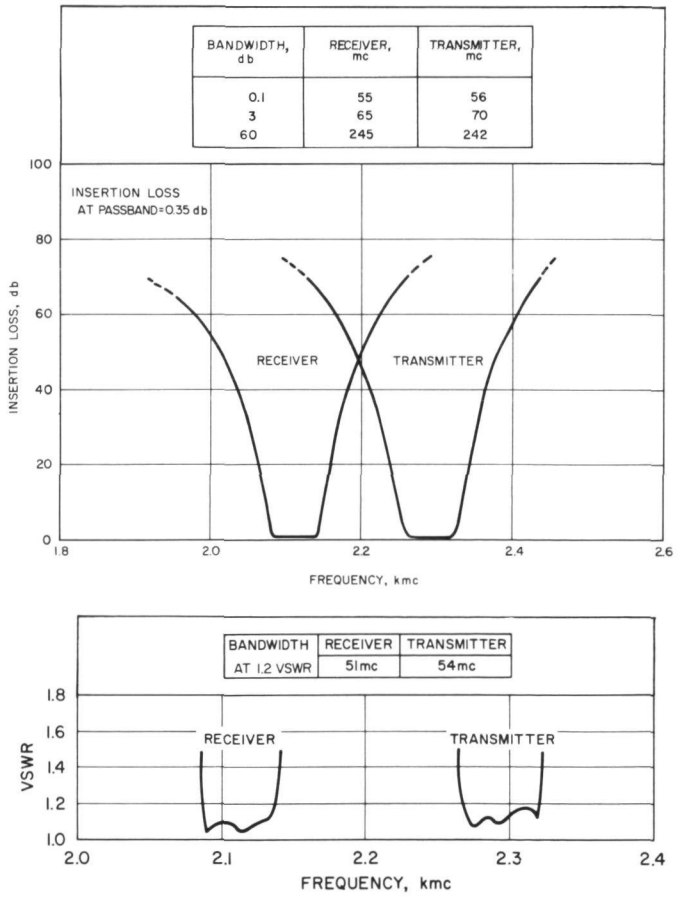

Figure 70. Electrical characteristics of diplexer

0.4 db. The manufacturer is being contacted to see if a different potting material and simple shielding could be incorporated to diminish the loss.

10. Diplexer

The RANTEC diplexer procured for engineering evaluation was delivered on schedule and the measured electrical characteristics, shown in Figure 70, surpassed the purchase order requirements described in Reference 1. The weight was 10 ounces instead of the 13 ounces originally estimated. No phase shift was discernible when the diplexer was subjected to sinusoidal vibration from 0 to 2000 cps with an 8.5 ± 1 g (peak to peak). The limitation of the measurement device was 0.25 degree.

11. Television

a. Sweep synchronization and blanking circuits, temperature testing. A series of temperature tests were made on the normal mode circuits. Performance was well inside specification limits on most circuits over the temperature range of -20 to 160°F. Outputs remaining within limits were as follows:

Horizontal frequency.

Horizontal amplitude.

Horizontal camera blanking pulse width.

Horizontal system blanking pulse width.

Vertical frequency.

Vertical blanking pulse width.

All blanking and synchronization pulse amplitudes remain well within $\pm$ 5%.

The anomalies observed were small. Vertical sweep yoke current exceeded specification limits at +160°F by 1.7% and horizontal synchronization pulse width exceeded specification limits by 1.2% at $-$ 20°F. Mil-Spec Characteristics B ($\pm$250 ppm/°C) resistors were used in constructing the breadboard circuitry, but Characteristic C ($\pm$25 ppm/°C) resistors are being specified for all critical applications in the prototype models. It is expected that this change will eliminate the minor difficulties noted. Further temperature testing will be done when these components are available.

b. Video logic circuit. The video logic circuitry has been modified to provide several new outputs. A "transmitter off" output has been added which will turn off the high-power transmitter at the conclusion of each bundle of TV data, thus providing a power saving. A "frame identification enable" gate is also provided to the signal processor which allows several frame identification groups to be transmitted at the end of video transmission. Frame identification had previously been transmitted continuously during absence of picture video, thus taking full advantage of the continuous transmitter "on" condition. Finally, a "shutter reset" pulse was provided which adds very little complexity to the video logic but greatly reduces the complexity of the shutter control circuit. The video logic block diagram and timing sequence are shown in Figure 71 and the schematic is shown in Figure 72.

c. Lens control circuits. Figure 73 presents the latest block diagram for the lens control circuits, excluding iris control. The system features a central control logic of the type described in the previous report. Use of one central logic circuit for focus, focal length, and filter position control rather than individual circuits provides a saving of at least 12 transistors. The system shown has been breadboarded and is presently being tested.

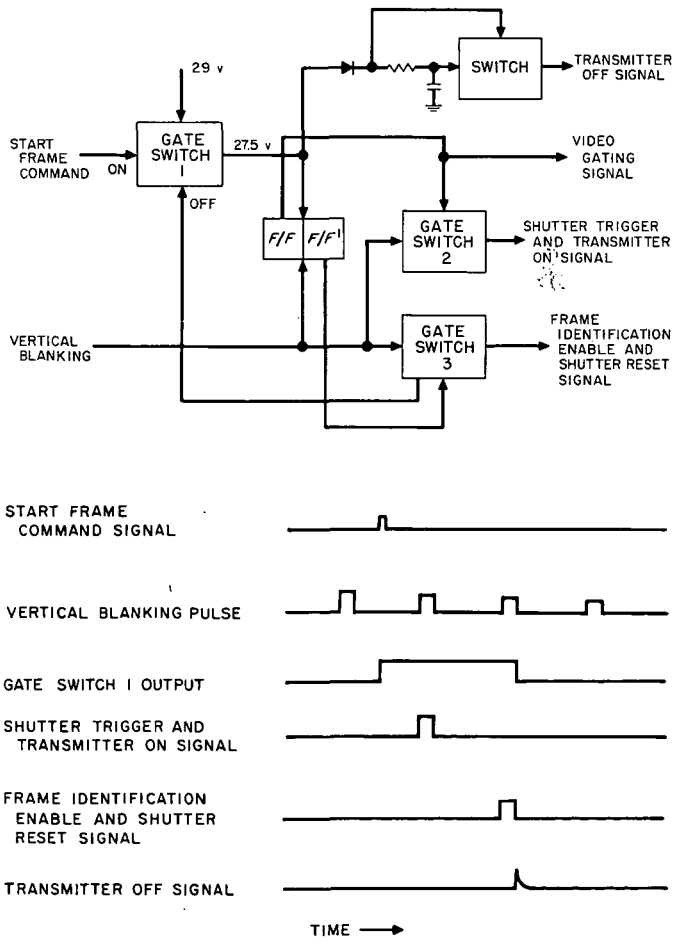

Figure 71. Video logic block and timing sequence

d. Shutter control logic and driver. The shutter control logic and driver circuit has been developed as shown in Figure 74. A photograph of the breadboard is illustrated in Figure 75. The circuitry (Fig 76) consists of four power switches (drivers), a monostable multivibrator to provide shutter timing, a bistable multivibrator, and inhibit gates.

The shutter trigger signal, a 200-millisecond-wide pulse from the video logic circuit is gated and fed to the No. 3 driver and the shutter timing circuit. The output of the timing circuit simultaneously energizes the No. 4 driver and inhibits the No. 3 driver for a duration of 150 milliseconds. No. 4 driver opens the shutter. At the end of this 150-millisecond period, driver No. 4 is de-energized and the inhibition signal is removed from driver No. 3, allowing it to close the shutter.

The shutter mechanism must be reset before another signal is applied to the timing circuit. The reset signal, which is the second vertical blanking signal, is applied to the No. 2 driver circuit to reset the shutter blades and complete the shutter cycle.

A second mode of operation, known as the time exposure mode, may also be used. In this mode of operation, the shutter can be commanded to remain in the open position. Time exposure on/off commands select the state of a bistable multivibrator. In the open shutter state, the bistable multivibrator inhibits the shutter trigger signal at gates No. 1 and 2. Shutter trigger signals pass through the "and" gates and energize drivers No. 1 and 4 to open the shutter. Between shutter triggers the shutter is latched. Normal operation returns when the bistable multivibrator is returned to the "off" state.

e. Vidicon thermal control. The vidicon thermal control circuit is designed to control the temperature of the faceplate of the television vidicon tube to $30 \pm 5°C$ over the ambient case temperature range of -20 to $125°F$. Because of possible picture anomalies introduced by the control system, heating or cooling power will be applied only during a 1.4-second period following picture readout during each picture frame. However, during the initial cooling process, the regulator will operate continuously.

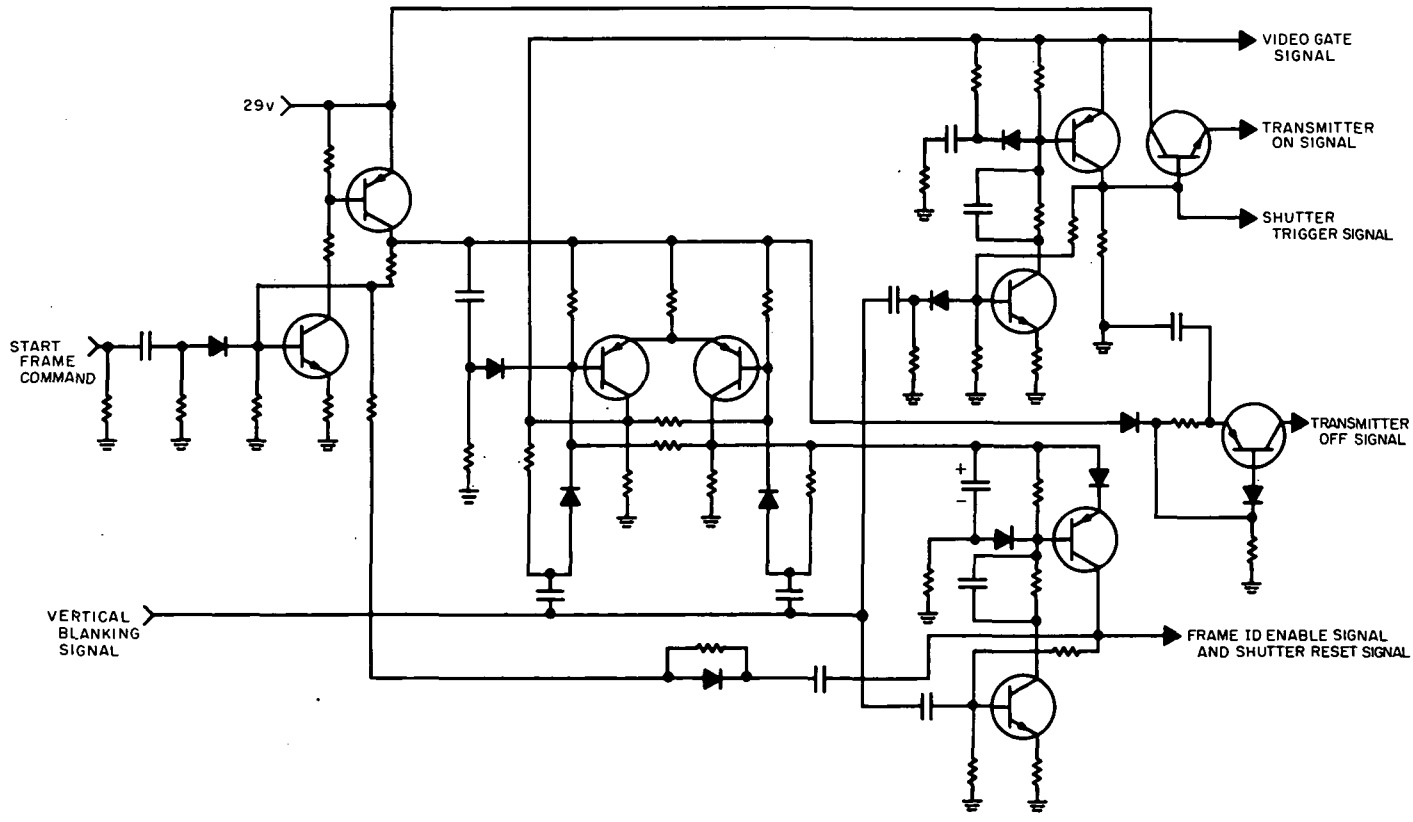

Figure 72. Video logic schematic

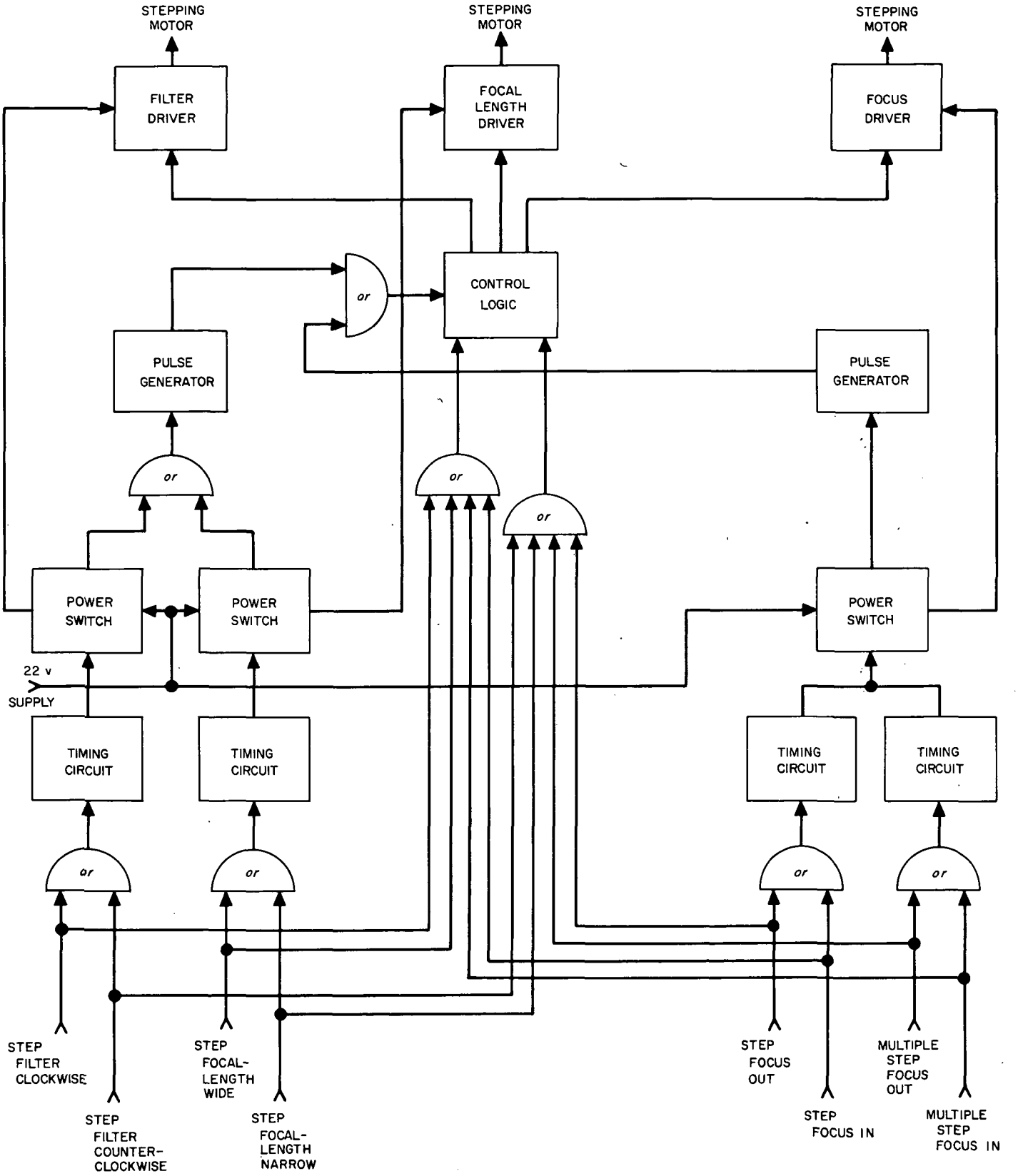

Figure 73. Lens control circuit

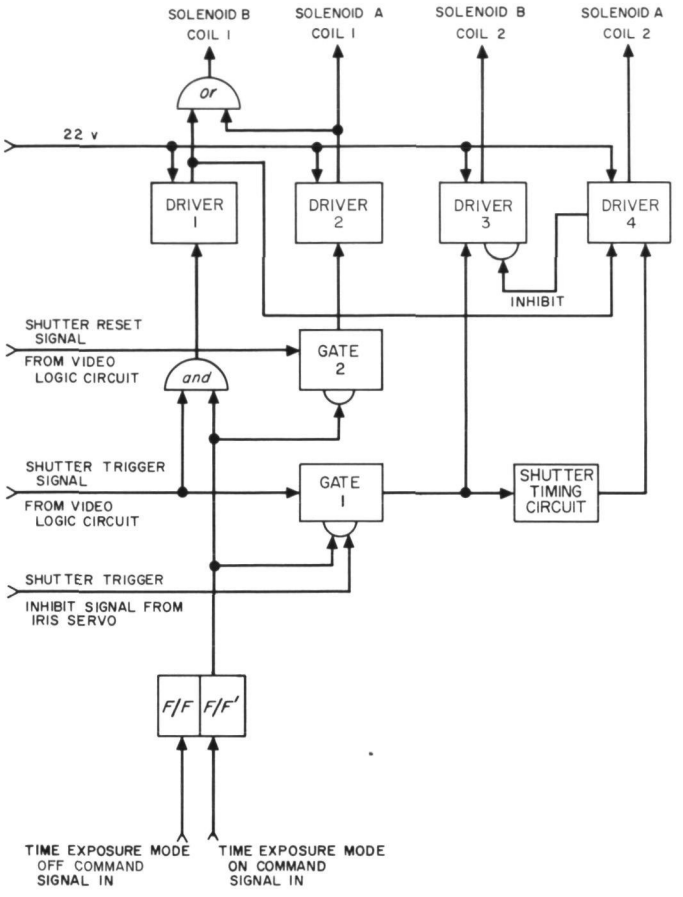

Figure 74. Shutter control and driver circuit

The present system is illustrated in the block diagram of Figure 77. Upon receipt of a "start vidicon thermal control" command, input power is applied to the control circuitry through a switch. This causes the regulator to start functioning. A planar-type diode is being employed as a temperature sensor. This device has a repeatable and consistent change of forward voltage-temperature characteristic of —1.8 millivolt/°C.

The output of the temperature sensor is amplified by the differential amplifier. The heating and cooling sensing circuits are threshold detectors which are biased to allow a dead zone between the active heating and cooling temperature regions. A temperature rise causes turn-on of the electrical conversion unit (ECU) which is a simple transformer coupled dc to dc converter which supplies current at 4 volts dc to the Peltier cooler. The Peltier cooler transfers heat from a collar around the vidicon tube to the case of the TV camera, thereby cooling the vidicon faceplate.

A temperature drop turns on heater power. The heater circuitry is cross-coupled to the ECU-off gate to ensure that the cooler is turned off whenever the heater is on.

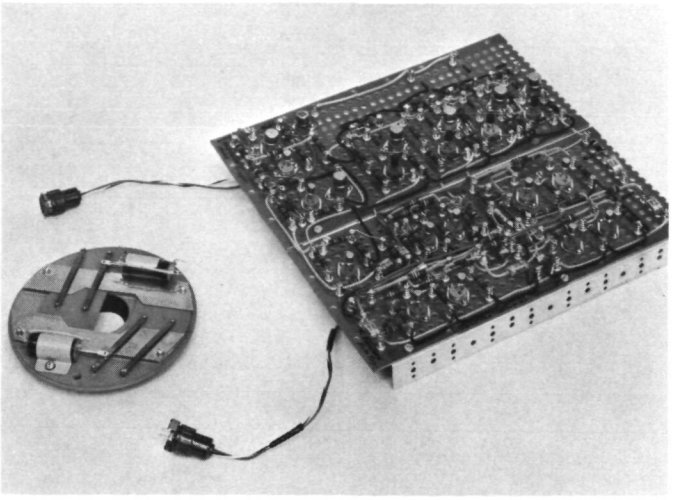

Figure 75. Shutter control breadboard

An inhibit gate turns off the heating and cooling during the video transmission period and during the second erase or vidicon priming period to prevent possible interference with the television picture quality.

A breadboard model of the vidicon thermal control including Peltier device and excepting the inhibit circuitry has been built and preliminary tests have been made. The breadboards are shown in Figure 78.

Present efforts are being directed toward optimization of the servo loop circuitry. The inhibit gating circuitry is being built, and upon completion of the breadboard, tests will be conducted to determine the feasibility of mounting the sensing diode directly on the vidicon face plate.

12. Packaging Concept

a. Unit installation. The units in Compartments A, B, and C will be bolted to a mounting plate within the compartments. Unit connectors will be accessible for harness connector attachment when the units are mounted in the compartment. Standardization of connectors, chassis, and other parts of units will exist where possible. The units will consist basically of a supporting framework, chassis, connectors, and special components not suitable for chassis mounting. The units will not have covers except where shielding is required.

The flight control electronic unit will be attached to a T-section frame which is part of the spacecraft structure. The front surface of the unit is a thermal radiator; heat generated within the unit is radiated from this surface. The other sides of the unit will be covered with a low-emissivity material to thermally isolate the flight

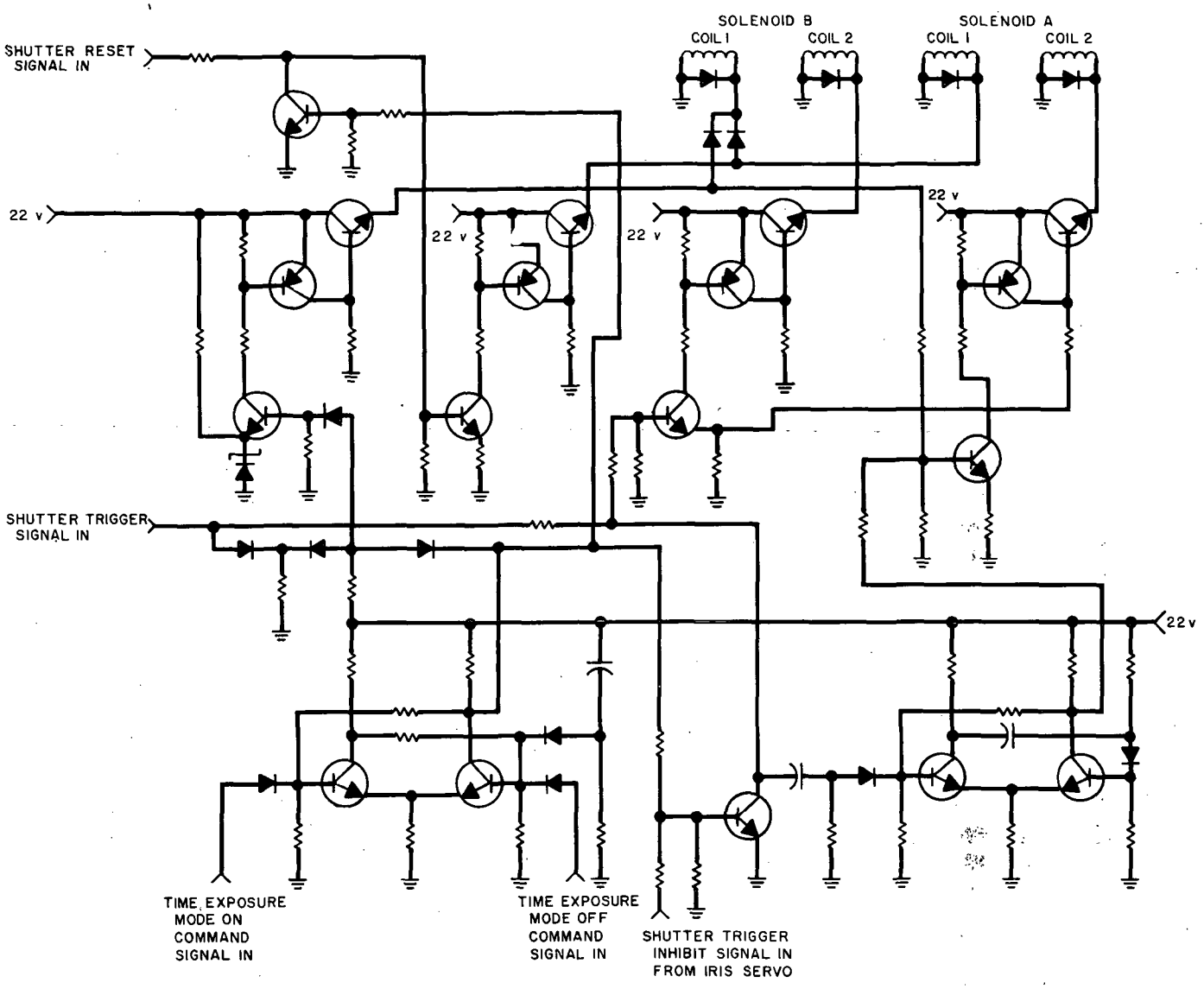

Figure 76. Shutter control and driver circuit schematic

control electronic unit from other parts of the spacecraft. The chassis within the unit will be attached to the unit frame and to the radiator.

The altitude marking radar is mounted on the exhaust end of the retrorocket nozzle. It consists of radar electronics rigidly mounted to a 15-inch-diameter platform which is the rear surface of a 30-inch-diameter antenna dish.

b. Chassis construction. Surveyor chassis are similar to those used in Hughes Aircraft Company missile receiver units. Typical chassis construction is shown in Figure 79. The modules mounted on chassis will be considered as individual components on the chassis, that is, removable and disposable in case of failure. Components are generally bonded to the plate and board sides.

The foam-sandwich-type chassis consists of a thin aluminum plate and a 0.032-inch epoxy glass etched-circuit board bonded to either side of a 0.1- to 0.125-inch sheet of polyurethane or epoxy foam. The chassis will be assembled by installing the board side components, bonding this board assembly and the chassis plate to either side of the sheet foam, and finally installing the plate side components.

The foam-sandwich type of construction using foam with a weight of 8 lb/ft^3 and a plate thickness of 0.030 inch will weigh approximately 0.0065 lb/in^2. In many

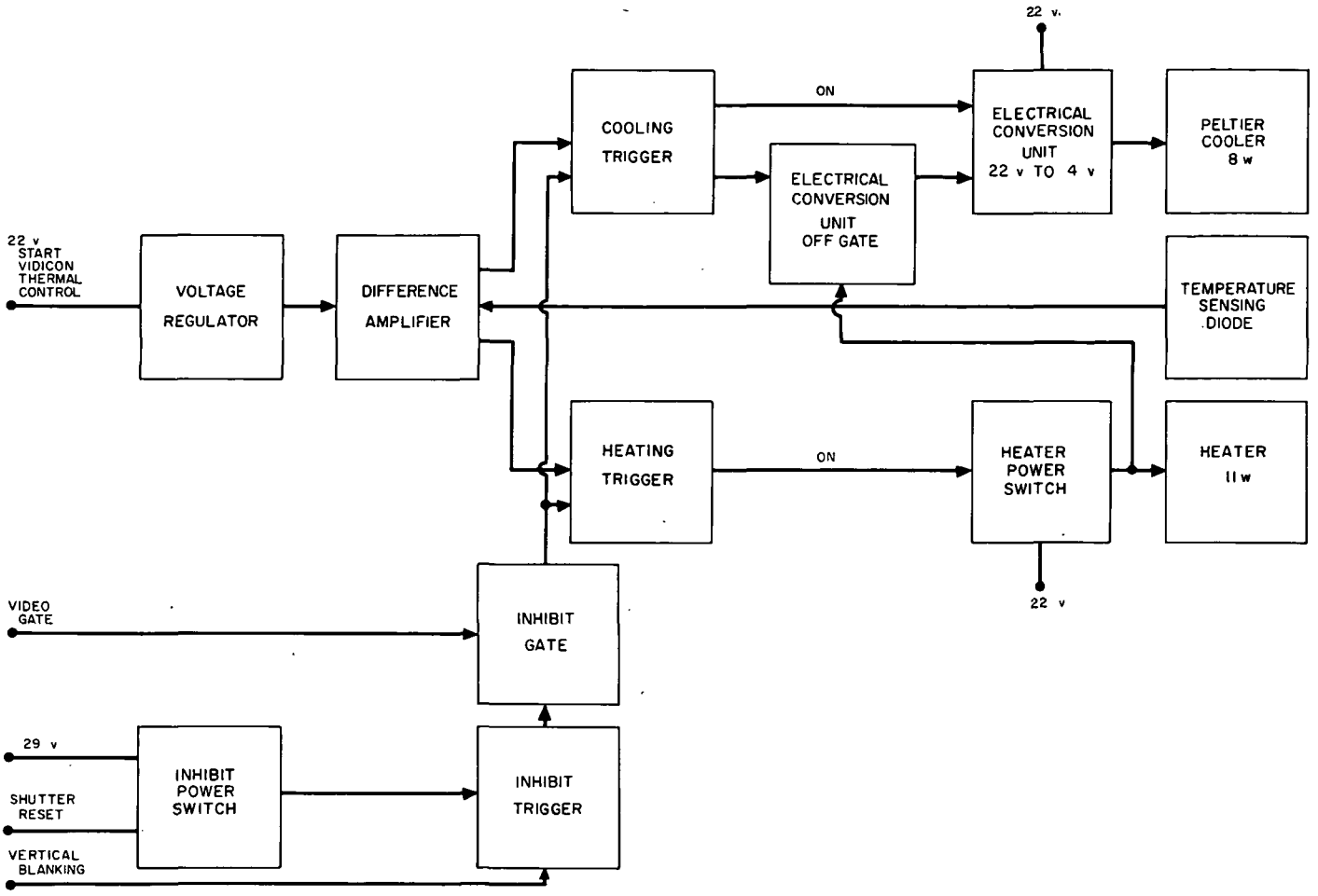

Figure 77. Vidicon thermal control

cases the thermal requirements permit the plate thickness to be reduced to 0.010 inch with the foam construction, yielding a weight of 0.0045 lb/in^2. There will be no restrictions to component layout due to stiffeners and board-to-plate ties. Fabrication and assembly time required to produce a complete chassis should be minimal.

The heat transfer path within the chassis is from components to the aluminum chassis plate. Plate-side components are mounted directly on the aluminum plate and good thermal tie is provided by the component mounting device. Most components will be attached by epoxy fillets, but provision will exist for clips, brackets, studs, and bolts for components requiring special mounting. Most components dissipating a significant amount of heat will be located on the plate side of the chassis. Board-side components will be attached with epoxy fillets. Heat transfer between board and plate will occur principally through copper leads. Another path for heat from board-side components will be by radiation between a chassis board and the plate of an adjacent chassis. The degree of thermal conductance required between the chassis plate and the mounting surface depends on the dissipation. Aluminum extrusion angle brackets may be used to provide heat paths between chassis and the heat sink. In Compartments A, B, and C the heat sink is the compartment surface to which units are mounted.

The same etched-board fabrication techniques will be used that have worked so successfully on Falcon missile chassis. The fabrication of chassis plates will be simplified considerably over missile chassis plates by the elimination of stiffeners and clips.

c. Module construction. Components are interconnected within modules by soldering the leads to circuit lines on 0.032 inch thick, epoxy-glass circuit boards containing circuitry on one side only. The modules have a height limitation of 0.5 inch, with lateral dimensions between 1.0 and 1.5 inches. The height is governed by

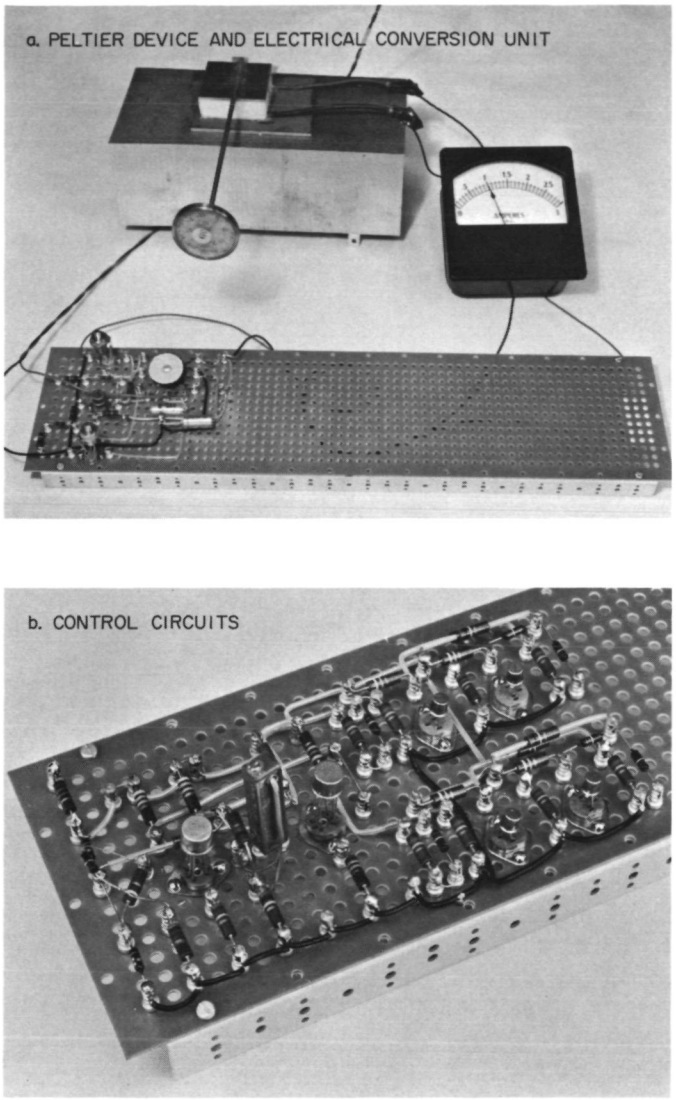

Figure 78. Vidicon thermal control breadboards

the maximum length (0.3 inch) of the high-usage components, i.e., glass jacket diodes and metal film resistors. The module height is made up as follows:

Maximum length of cordwise mounted components, in.	0.300
Spacing between ends of maximum length components and etched circuit boards, in.	0.076
Two etched circuit boards, in.	0.064
Solder balls each side, in.	0.050
Outer coating each side, in.	0.010
Total, in.	0.500

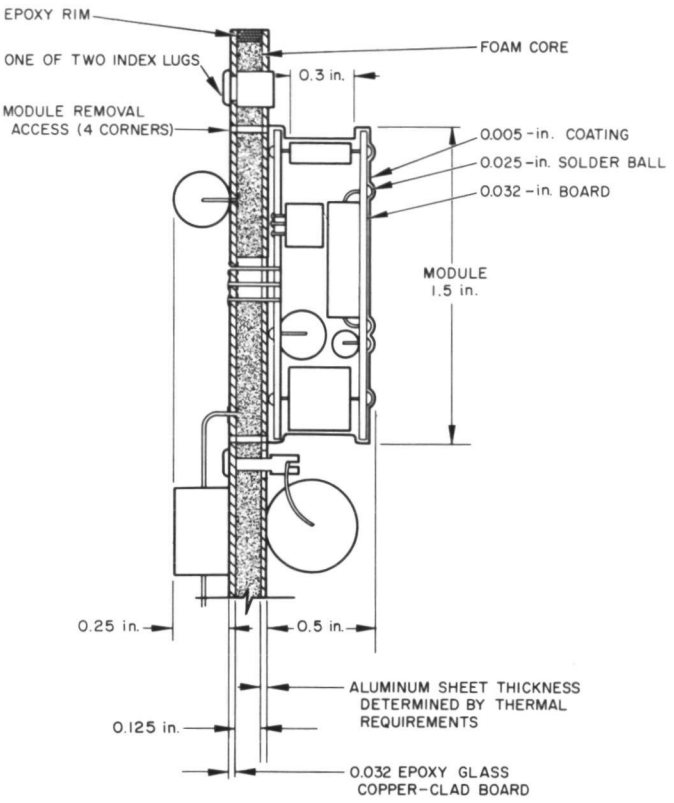

Figure 79. Typical chassis and module cross section

Other components are oriented as shown in Figures 80 and 81; e.g., transistors with leads exiting from one side and long components are mounted parallel to the etched-circuit boards. To minimize the weight of the module a "freeze coat" resin application or a foam encapsulant will be utilized. The "freeze coat" consists of thin webs (rather than a solid encapsulant) of resin between components to provide the necessary mechanical support.

Leads exit the modules in groups, in a close-spaced pattern. The grouping of leads will minimize the number of size of cutouts in the metal plate and also yield the minimum restriction on board-side-mounted components. Components will not be mounted over module leads to maintain access to the leads for module removal.

The module leads are soldered into plated-through holes in the chassis master etched-circuit board. A "solder-sucking" procedure has been developed for readily unsoldering individual module leads. An alternate procedure employs drawing of the solder out of the joint by capillary action onto a heater flux braid. The modules are fastened to the plate by resin bonding, possibly using a tape. Most chassis will contain both modules and indi-

vidual components. In areas such as command decoding where practically all chassis components will be modules there will probably not be any board-mounted components. The numerous restrictions imposed by module removal make the use of the board side rather inefficient in such cases.

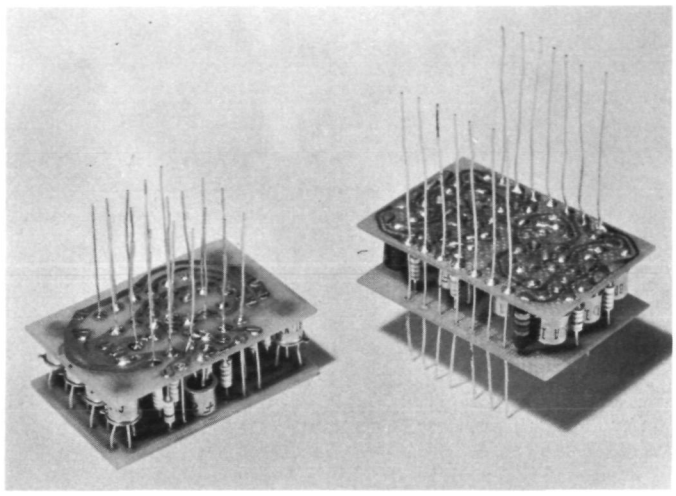

Figure 80. Component orientation, top view

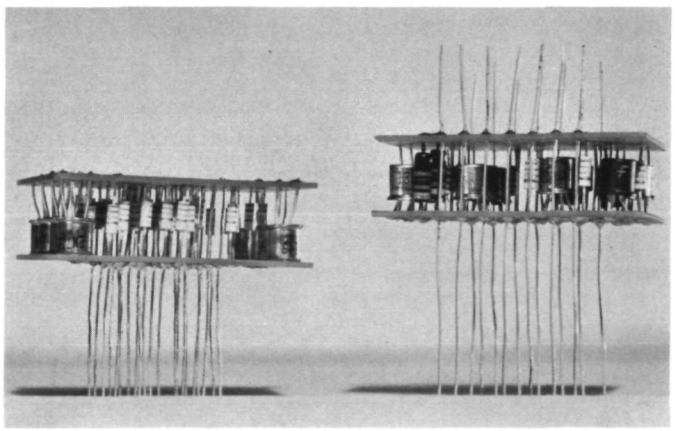

Figure 81. Component orientation, side view

d. Circuit grouping and arrangement. Where possible all components within a given unit will be grouped according to function. Similar circuits and/or entire functions will be placed on a common chassis or module. Redundant circuits, such as in the command decoding function, will be used in several different units or control items. The use of identical modules throughout the spacecraft system greatly facilitates the drafting and fabrication effort.

The type of packaging to be employed is also dictated by the type of circuits involved. In the case of flight control servos, it is anticipated that a large number of large components will be required, thus requiring the components to be individually mounted on chassis with only a small percentage of circuits permitting modular type of construction. On the other extreme, signal programming and decoding functions permit the use of small components wherein the majority of the functions will be packaged in modular construction.

Component layout is also dictated by the nature of the circuit. Flight control circuits as well as most of the decoding circuits, for instance, do not require a great deal of shielding. Therefore "open" chassis or modular construction can be employed. On the other extreme, however, are such units as the command receiver and transponder and the transmitter. For these units, shielded chassis type of construction will be employed.

As previously stated, it is believed that in most cases the modular type of construction will not require shielding. In those cases where shielding is required, a shield "coating" will be applied to the external surface of the module.

e. RF packaging concept. The concept for packaging the lumped constant RF circuits has been established. A 10-mil aluminum T-bar will be used, similar to that employed in JPL designs. RF circuits occupying one side of the T will be decoupled with feedthrough filters from the dc circuits occupying the other side of the T which in turn will be decoupled from the dc input leads. The T-bar will be enclosed by a 10-mil aluminum housing; the entire unused volume will be filled with foam and the base of the T-bar soldered to the enclosing housing. All tunable components will be accessible through the base of the T-bar to allow external tuning. Dry micro-balloons called "Eccospheres," which have the same dielectric constant as the polyurethane foam, will be used to test the effect of foaming on the prototype units while maintaining the ability to change components. This packaging concept is believed to satisfy the requirements of minimum weight while still meeting all spacecraft functional and environmental requirements. RF circuits using these packaging concepts have been employed in other Hughes Aircraft Company programs.

f. Environmental design. The equipment is designed to meet levels of shock and vibration which are based on Type Approval Test requirements. Levels are specified for chassis and components as well as for control items so that the ability to meet Type Approval Test requirements may be established for subassemblies prior to

testing the entire control item. The estimates are based on inputs to the rocket engine; certain transfer characteristics were assumed for the spaceframe structure and the unit structure. The vibration levels for assemblies such as those on the rear of the altitude marking radar dish, traveling-wave tubes, vidicon tubes, etc. must be determined on an individual basis.

g. Component selection. Issue II of the "Preferred Parts List for *Surveyor*" handbook has been issued by the Components and Materials Laboratory. The handbook has been reviewed by Product Engineering. Evaluation requests are being issued for special parts, such as chopper amplifiers, and those types of semiconductors which were not included in the handbook.

h. Test programs. A number of thermal, vibration, deflection, and other structural tests will be performed on the foam-sandwich chassis. Several vibration tests have been performed on prototype altitude marking antenna dishes. The dish design has been modified as a result of these tests to arrive at a minimum weight design with satisfactory structural requirements. Developmental structural tests will be performed on a prototype flight control unit and a prototype altitude marking radar.

Thermal tests will be conducted on chassis and other parts of units to obtain accurate thermal resistance values for use in computer studies. Computer studies are being utilized to predict component, chassis, and unit temperatures and to evaluate the adequacy of thermal design.

i. General project status.

(1) *Outline and mounting drawings:* Outline and mounting sketches have been issued for all control items other than those located in Compartment C which are presently under consideration. Final outline and mounting drawings, including weight, volume, center-of-gravity, and connector type and location, will be issued late in December.

(2) *Breadboard status:* Product engineers are cooperating with the circuit engineers in the fabrication of final breadboards. Final breadboards for the transmitter and the receiver and transponder lumped constant RF circuits are progressing. These breadboards approach the final productized design as much as feasible. "Productized" breadboards for other control items are slower in being realized.

(3) *Drafting status:* Layout drafting has started on the flight control electronics unit and will begin in the immediate future on the transmitter. Layout drafting will begin on the remaining control items as the circuit designs firm up.

13. Radars

a. Altitude marking radar. All breadboard units for the altitude marking radar have been assembled into a single package and mounted on the rear surface of the antenna. This equipment is shown in Figure 82. The components shown include the following: solid-state local oscillator,

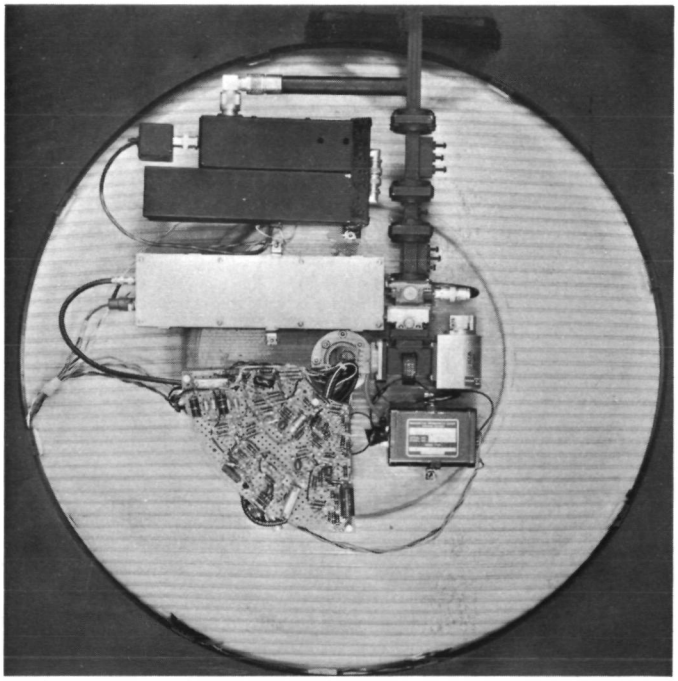

Figure 82. Altitude marking radar antenna, rear view

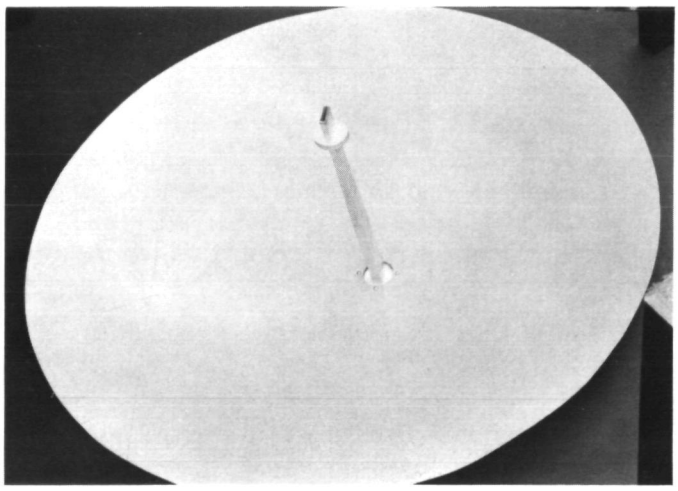

Figure 83. Altitude marking radar antenna, front view

upper left; IF amplifier, center left; RF unit, center right; synchronizer and video processing circuitry, lower left; and solid-state magnetron modulator, lower right. All elements of this breadboard are functioning and quantitative tests are being conducted in one of the roofhouses. Relative dimensions of the various components can be obtained with respect to the section of antenna shown; the diameter between mounting tabs is 24 inches. Figure 83 shows the reverse side of the complete 30-inch dish with breadboard feed attached.

Product engineering on the breadboard units shown will have considerable effect with respect to volume and weight. A revised solid-state local oscillator breadboard more nearly approaching the final circuitry and package has been constructed and is in unit test. The X16 multiplier is shown in Figure 84. This component will replace

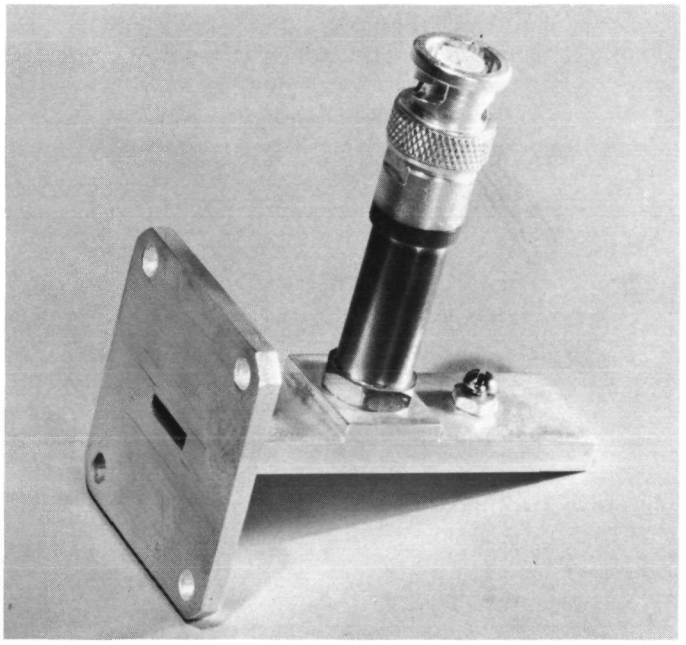

Figure 84. Frequency multiplier

all the waveguide and stub tuner components shown in Figure 82 which connect the lumped constant multiplier section (in the upper black box) to the mixer (directly at the right of the IF amplifier). The remainder of the revised local oscillator is packaged in a space slightly smaller than the upper of the two boxes now used.

The IF amplifier will be packaged approximately as shown in Figure 85; included in this package are the AGC amplifier and video circuitry. Other major packaging changes between the present breadboard and final unit, aside from modular packaging of the synchronizer

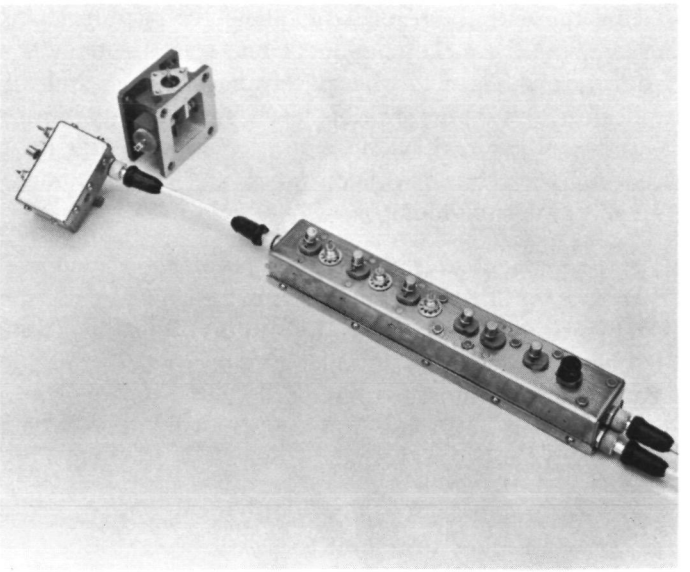

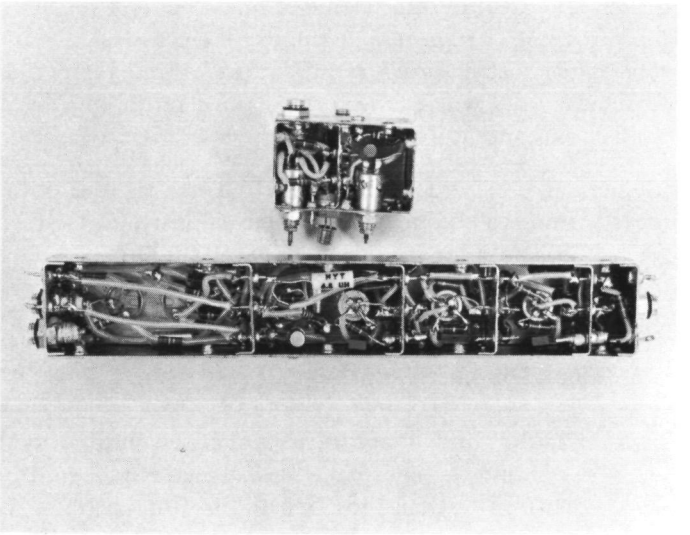

Figure 85. IF amplifier

and video circuitry, will be made in reducing flanges on the RF components and chemical milling of the feed.

Performance and environmental tests on the second set of breadboard units are being conducted on a unit basis simultaneously with the integration and test of the first breadboards as a system. The results of some of these tests on the X16 multiplier include the following: the spurious response due to the 15*th* and 17*th* harmonics and other harmonics are greater than 24 db below the desired 16*th* harmonic. Since an AFC is not employed, the only restraint on harmonics is due to efficiency or interference. A graph of the X16 multiplier output power versus input power at 582 mc is shown in Figure

86. The minimum power output of the lumped constant section will be 350 milliwatts at 582 mc. Noise figure corresponding to this value was given in the previous report. The bandwidth of the X16 multiplier is shown in Figure 87. Nominal −3-db bandwidth at 70°F is 41 mc. Temperature tests were also conducted on this multiplier; Figure 88 shows the results of power output measurements versus temperature. The data given are for a constant input at 582 mc. The bandwidth increases to 52 mc and center frequency decreases by approximately 5 mc between 70 and −40°F.

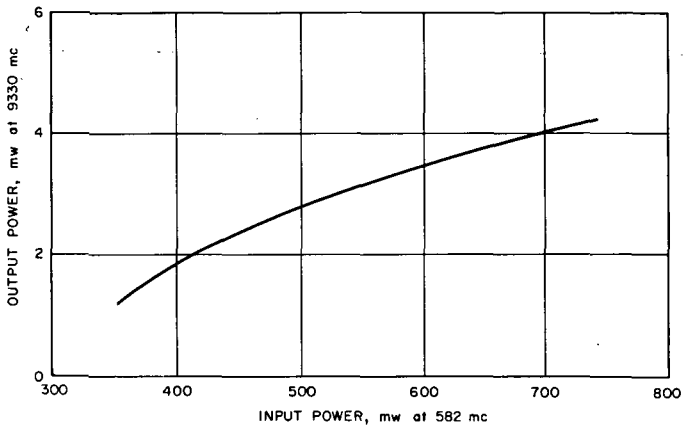

Figure 86. Multiplier output power vs input power

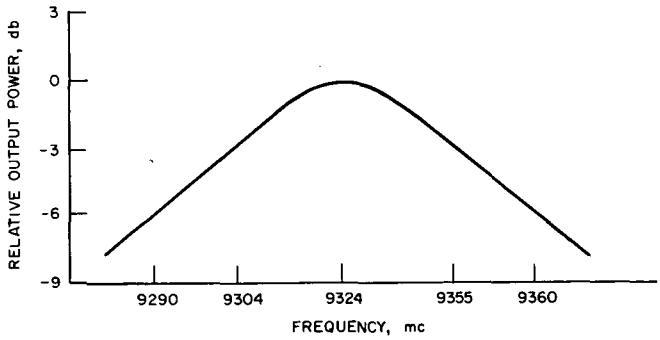

Figure 87. Multiplier bandwidth

A block diagram of the altitude marking radar synchronizer is given in Figure 89. The purpose of this circuitry is to generate the basic 350-pps repetition rate of the transmitted pulse and the precision delays for altitude marking. Two delayed range gates and one AGC gate are generated by this circuitry. The delayed gates correspond to 60 and 61 miles. A trigger to the solid-state magnetron modulator is also formed in the synchronizer. A sampled

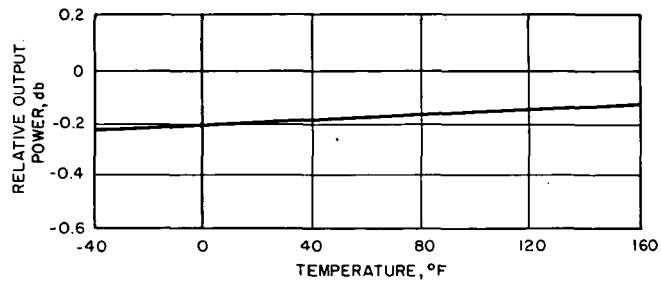

Figure 88. Multiplier power output vs temperature

output from the modulator triggers the delay generators to account for delays in pulsing of the magnetron for the 60-mile range measurement. The 1 to 60-mile AGC gate permits AGC control on noise only for low-level detection. The noise input to the video processor integrators is thus made independent of gain variation in the IF amplifier for low signal levels.

Measurement of the change in delay of the 60-mile range gate versus temperature changes from a nominal test temperature to expected temperature at lunar approach shows less than a ±0.08-mile change.

The video processor block diagram is shown in Figure 90. The video output from the IF amplifier is gated in the video processor and integrated to determine the presence of signal. Two channels of integration are provided, one each for 60- and 61-mile delays. If the threshold in the 61-mile channel is exceeded, and acceptance gate arms the firing circuit at the time the lunar return will be in the 60-mile gate. This dual-channel circuitry prohibits firing on an isolated noise burst. Arming of the firing circuit is also restrained by the absence of an enabling signal from command. The radar is turned on prior to this signal to permit warmup; however, marking is not possible until the enable signal is received. Marking on a second-go-around of the lunar signal is thus prohibited. The reset generator resets the integrator outputs to zero after a specified number of pulses (nominally ten). Temperature tests performed on the video processor included measurement of integrator gain, reliable triggering of the threshold amplifier (a Schmitt trigger), velocity prediction and acceptance generator delay changes, firing circuit trigger sensitivity, and reset generator trigger sensitivity. Preliminary analysis of the data indicates satisfactory operation over the temperature range expected.

Altitude marking radar antenna. The AMR antenna produces a narrow pencil beam for the altitude marking radar. Low sidelobes are required to keep the false alarm probability to an acceptable value, and relatively high

gain is required to provide assurance that the radar will give a firing signal to the main retro-rocket at the proper distance from the lunar surface.

The Hughes Aircraft Company designed feed mentioned previously has produced first sidelobes of approximately −30 db; however, it has never quite given the design goal of −30 db in both the E and H planes. Several modifications of this feed have been tried with some success. The sidelobes have been reduced a small amount and the gain has increased to 34.6 db.

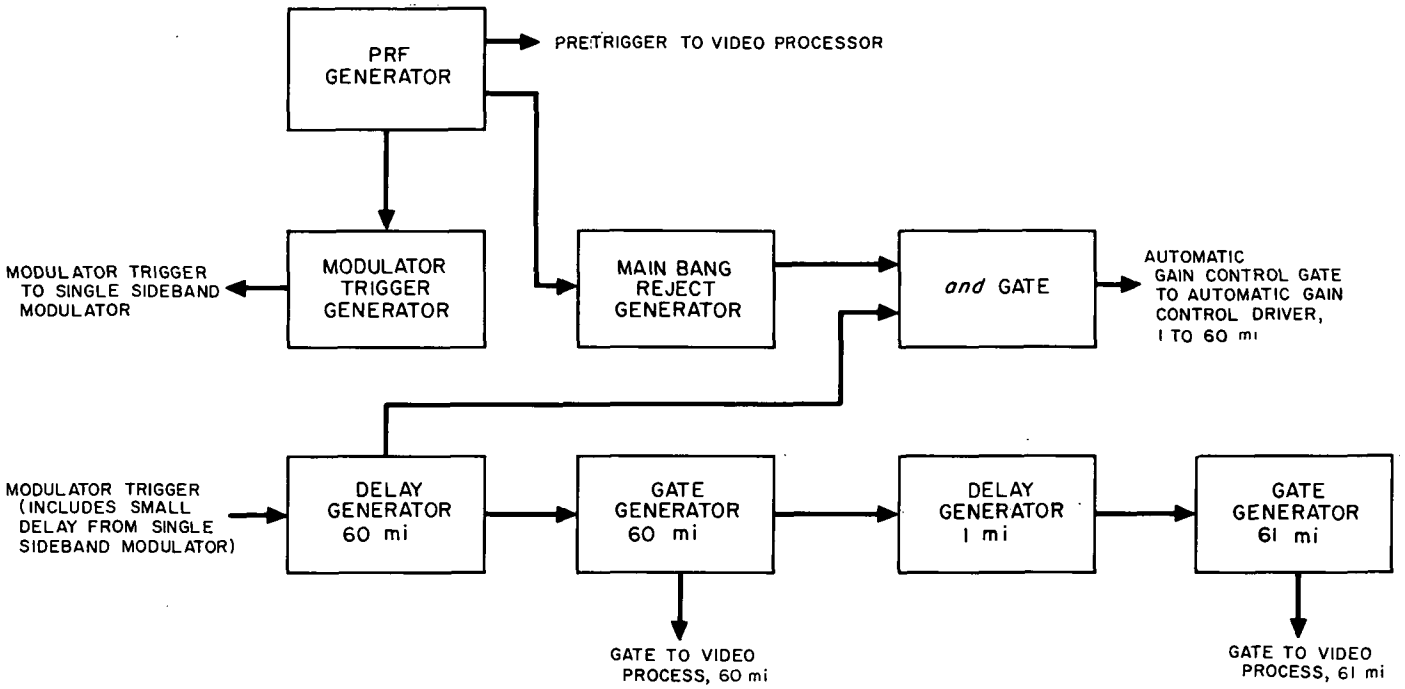

Figure 89. Altitude marking radar synchronizer

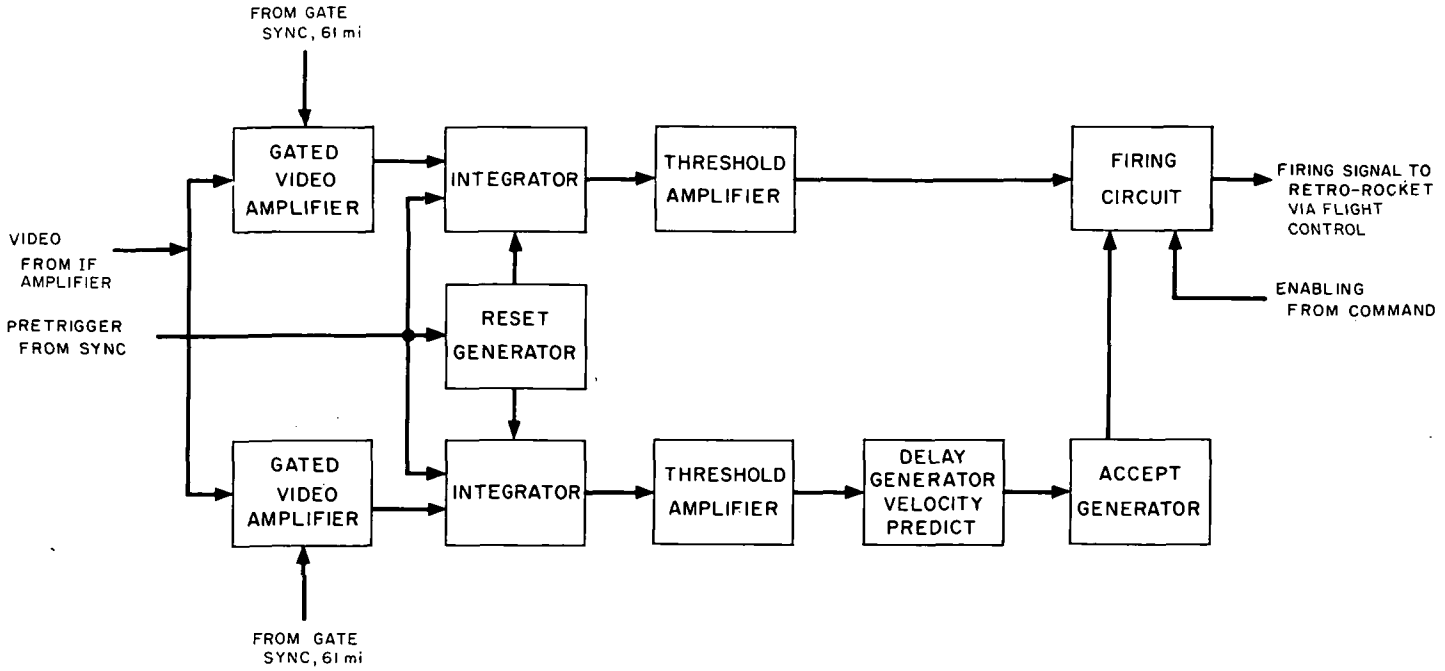

Figure 90. Altitude marking radar video processor

Improvements to the primary pattern range have allowed a more careful study of the primary patterns. The H-plane primary pattern shows evidence of shadowing on both sides of the feed. Efforts to reduce this shadowing are being made by tapering the sharp corners of the feed guide and by construction of fairings to fit along the narrow wall of the waveguide.

A modification of the ring source feed was built as a backup To-date, results from this feed are not as promising as results mentioned above. Further modifications of the ring source feed have been received from the shop but have not yet been tested.

Two more prototype dishes have been tested. Both produce patterns nearly equivalent to the spun aluminum dish used in the development phase.

b. Radar altimeter and doppler velocity sensors. The radar altimeter and doppler velocity sensor consists of four major units. The klystron power supply modulator (KPSM) includes the altimeter and doppler sensor klystron transmitter tubes and the high-voltage power supply for both klystrons. Two antennas are required to transmit and receive the four beams. Filter networks, isolators, microwave detectors and preamplifiers are mounted on the antennas as an integral unit.

The fourth unit, a signal data converter (SDC) includes the signal search and tracking functions, the arithmetic sections, frequency to dc converters, programming circuitry, range-marking functions, and the low-voltage power supply.

The state of development of these units has reached the breadboard evaluation and testing stage. The converter circuits have been completed except for the dc amplifier output stages which are still undergoing temperatures stability and drift tests. All portions of the tracker loops have been completed, but the voltage control oscillator, quadrature generator, and single sideband mixer (SSBM) remain to be completely evaluated. In order for the SSBM to function properly over the wide range of input signal levels, additional amplifier stages were recently added following the preamplifier. These amplifiers will be gated out in two steps as signal level increases.

Both low- and high-voltage power supplies have been designed and tests are currently being made on samples of the special transformers. The arithmetic circuits which generate dc signals proportional to the velocity components along the spacecraft axis are completed. Work is continuing on the programming, marking, and output stages. Physical outline and dimensions have been established as well as spacecraft mounting. Antennas for the developmental model are being fabricated.

A block diagram of the radar altimeter and the doppler velocity sensor (RADVS) is shown in Figure 91. A functional description of the major unit is given in the following discussion.

Radar altimeter. The *receiver-transmitter* operates at an undeviated carrier frequency of 12,900 mc with a 400-milliwatt continuous-wave power output. The transmitter output is frequency-modulated with low deviation at altitudes of 1000 feet and above, and high deviation at altitudes below 1000 feet. The frequency modulation consists of a negative linear sweep of 5 milliseconds. The FM sawtooth waveform has a fixed repetition rate of 182 cps at all altitudes. The signal return from the lunar terrain is delayed in time in proportion to slant range along the beam, and shifted in frequency in proportional to the component of spacecraft velocity along the beam. A small amount of transmitter power is coupled off the transmitting waveguide and applied as the coherent reference to the microwave detector. The microwave detector consists of a pair of balanced mixers producing two signal outputs to the two preamplifiers. The reference signal to each balanced mixer is applied in phase quadrature so that the two output signals to the preamplifiers are also in quadrature.

Due to range delay and doppler shift, the output signals from the balanced mixers contain signal spectrums which peak up in power at a frequency which is equal to the sum of a range proportional term, f_r, and a velocity proportional term, f_d. The center of power of the terrain signal spectrum into the preamplifier varies between 182 cps and 80 kc.

The *preamplifiers* raise the signal levels out of the balanced mixers to values suitable as inputs to the altimeter tracker, and shape the residual AM noise spectrum present.

The function of the *klystron power supply/modulator* is to supply beam, reflector, and filament power to the VA246 reflex klystron and to superimpose a sawtooth voltage waveform on the reflector voltage to the klystron for purposes of frequency modulation. The KPSM accepts an input from the 1000-foot marker in the programmer for purposes of changing the transmitter deviation from low to high.

The two quadrature signal inputs from the preamplifier and gated amplifier are applied to the *tracker.* The altimeter tracker is an electronic, self-tuning, frequency-

following loop which has as an output a signal of frequency equal to the center of power of the input signal spectrum to the tracker plus the tracker reference frequency, f_C. The quadrature input signals to the tracker are applied to a single-sideband mixer whose other pair of inputs are derived from a variable frequency quadrature signal generator operating at a frequency above the center of frequency of the input spectrum to the tracker by an amount equal to f_C. The single-sideband mixer translates the input signal spectrum from the preamplifiers to a frequency near the reference frequency of the tracker, that is, within the IF amplifier pass band. The single-sideband action is accomplished using phase cancellation of the upper sidebands of two quadrature carrier signals each of which is amplitude-modulated in quadrature with respect to the other.

Proceeding around the altimeter tracker frequency-following loop, the signal from the single sideband mixer is passed through the IF amplifier and then applied to the two mixers in phase quadrature. The difference frequency spectrums in the outputs of the two mixers are extracted using two low-pass filters. The signals out of the low-pass filters are applied to the phase detector. These two spectrums are in phase quadrature and produce, at the output of the phase detector, either a plus or minus voltage, depending on phase relationship of the two inputs. In the auto-tuning mode then, the tracker tunes to maintain the output of the single-sideband mixer centered at the IF frequency, the outputs of the low-pass filters at zero average frequency, and the output of the phase detector at zero volts on the average.

The mode of the altimeter tracker is controlled by the signal detector. When the signal detector has detected sufficient signal-to-noise ratio in the tracker low-pass filter, the altimeter tracker is placed automatically into the auto-tuning or tracking mode. When the signal-to-noise ratio in the low-pass filter is less than the signal threshold, the altimeter automatically goes into a frequency search mode, scanning the tracker search band on a continuous basis until a signal of sufficient strength is detected. The tracker frequency search is equivalent to an altitude search between about 1000 and 40,000 feet when the altimeter is in the low-deviation mode or 100 to 4000 feet when in the high-deviation mode. The signal detector circuit receives two inputs, one from the low-pass filter and the other from a band-pass filter. The band pass filter examines the mixer output signal in a frequency band adjacent to that of the low-pass filter.

The signal detector compares the narrow band signal plus noise out of the low-pass filter with the noise out of the band-pass filter. When this ratio exceeds the threshold for proper operation, the signal detector puts out the tracker signal lock, which stops the frequency search and the tracker then follows the frequency of the center of power of the detected signal.

The change in transmitter deviation from low to high changes the input frequency to the tracker by 14.6 kc. To prevent a tracker signal loss, the tuning position of the tracker variable frequency oscillator is raised by this same amount, which is accomplished by switching from No. 1 fixed frequency oscillator to No. 2 fixed frequency oscillator.

In the *altimeter artithmetic section and altitude converter,* the signal from the altimeter tracker is applied to the arithmetic section at a frequency equal to the sum of the signal frequency into the tracker and the tracker reference frequency f_C. The tracker output frequency is applied to a modulator and compared with the reference frequency. The difference frequency is extracted in the low-pass filter. The resulting signal frequency $(f_r + f_d)$ is scaled by a factor of two and by a factor of four, both scaled frequencies being applied to signal gates. The signal frequency from the arithmetic section is converted into a proportional dc voltage. At the same time, a signal with frequency proportional to the component of vehicle velocity along the roll axis, as computed in the velocity sensor arithmetic section, is applied to a scaling circuit in the altimeter arithmetic section and converted to a proportional dc analog in the signal processing chain. This dc voltage, with the proper scale factor, is combined with the converter signal from altimeter tracker signal for velocity, leaving a voltage proportional to range alone.

The change in range signal output scale from 1 to 20 mv/ft is accomplished by a change of 20 to 1 in frequency scale presented to the altitude converter input. This frequency scale change occurs as a result of changing the transmitter frequency deviation by a factor of ten at the 1000-foot range mark and scaling up the input signal frequency to the altitude converter by a factor of two at the same time.

The *programmer* contains the altimeter signal loss detectors and the 1000- and 13-foot range markers.

Velocity sensor. The velocity sensor is composed of functional units similar to those in the radar altimeter. Major differences are described below.

The *transmitter* operates at a carrier frequency of 13,300 mc with approximately 6 watts total con-

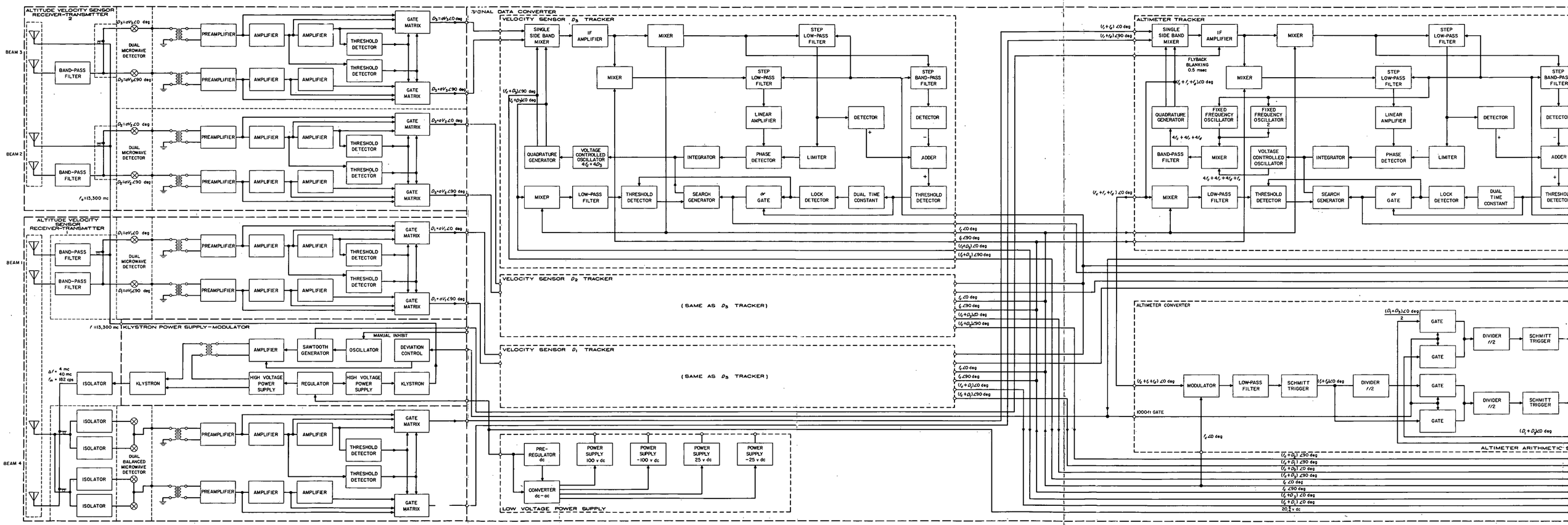

CONFIDENTIAL

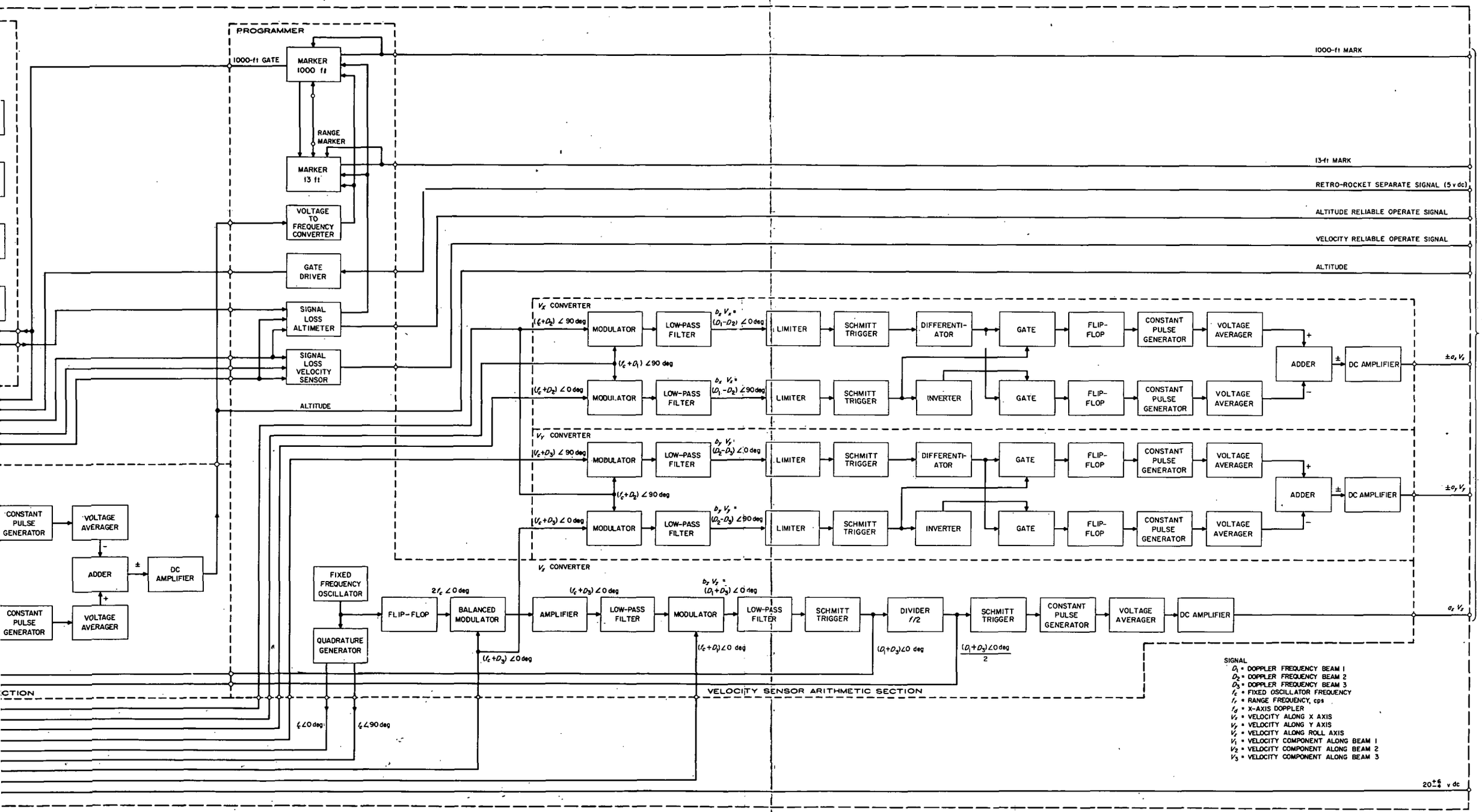

Figure 91. Radar altimeter and doppler velocity sensor

Page intentionally left blank

tinuous-wave power output. The microwave energy is divided equally among three antennas and is transmitted in three narrow beams displaced 25 degrees from the roll axis of the spacecraft. The doppler information from beams No. 1 and 3 is used to determine vertical velocity, V_z; beams No. 1 and 2 give lateral velocity, V_x, and beams No. 2 and 3 give lateral velocity, V_y. Considering a maximum velocity of 3000 ft/sec along any beam and a minimum velocity of zero, the center of power of the signal spectrums at the output of the microwave mixers can vary between 0 and 81 kc.

Velocity sensor *tracker* operation is essentially the same as altimeter tracker operation except the requirement for fixed frequency oscillators is not necessary for the doppler velocity sensor tracker due to the absence of scale change of tracking velocity.

The *arithmetic section* combines the three doppler frequencies to obtain frequencies proportional to the velocities along the spacecraft coordinates, (V_x, V_y, V_z).

The three velocity sensor frequency outputs are at carrier plus doppler frequency. Quadrature signals are also provided by each tracker. These outputs are applied to mixers and the difference frequencies are extracted through low-pass filters. Both lateral velocity converters, V_x andV_y, require the respective doppler difference frequencies and their quadrature signals for sign sense information.

The vertical velocity, V_z, is proportional to the sum of two doppler signals, whereas the lateral velocities are proportional to the differences of their respective doppler signals. Therefore, one tracker output is first mixed with twice the carrier frequency in balanced modulator and the difference frequency is extracted through a low-pass filter to obtain a signal frequency equal to the carrier minus the doppler frequency. This in turn is mixed with the other tracker output to obtain the difference frequency output equal to the sum of the two doppler frequencies. Vertical velocity sign sense is not required so that the quadrature signal is not obtained.

14. Tape Recorder

a. Introduction. Development of the tape recorder has been subcontracted to the Data Recorders Division of Consolidated Electrodynamics Corporation and has been in progress since August 21, 1961.

The tape recorder is to be capable of recording and reproducing data, on command, during two operational phases of the spacecraft. During the boost and landing phase, engineering data will be recorded on seven analog channels (5 to 1000 cps); record and reproduce will be at 20 in/sec. For lunar surface operation, 18 hours recording capability is provided at ⅓ in/sec. Playback is at 20 in/sec. Three analog channels, covering the range 1/60 to 5 cps and one analog channel for the range 1/20 to 20 cps, are provided for recording seismic activity. Two digital channels (550 bps NRZ and 180-200 bps NRZ) are provided for recording time-shared data from the plasma probe and the seismometer (tide data) and for the magnetometer. A unique feature of this lightweight (9 pounds maximum) recorder will be the low-power requirement, not to exceed 650 milliwatts during lunar record and 1.5 watts during playback.

b. Electronic development. To achieve the very low frequency analog response with good signal-to-noise ratio and amplitude accuracy, saturated FM recording is being used. The block diagram of the record portion of the system is shown in Figure 92. There will be four identical sections to accomplish the launch and lunar analog recording. There will also be three identical sections for the launch analog and the lunar digital recording. (The seventh lunar channel is reserved for recording a clock signal if desired for tape speed control in the reproduce mode.) In the analog channels, voltage-controlled oscillators (VCO) will provide center frequencies of 333 cps or 20 kc (lunar or launch) with deviation of ±50%. The driver amplifiers will amplify the frequency-modulated square wave signals and saturate the tape. In the digital channels, solid-state switches will feed input to the driver amplifiers for saturation recording of the digital signals.

Erase will be prior to record. Erasing will be accomplished by passing a dc current through a high-inductance head, thereby saturating the tape in one direction.

The block diagram for the reproduce circuits is shown in Figure 93. The operation is as follows:

The signal from the playback head is linearly amplified by a high-gain amplifier and fed through a level detector (Schmitt trigger) which shapes the signal. Each pulse of this signal then triggers a one-shot multivibrator, which is designed to have a constant area pulse regardless of frequency. The active filter integrates the signal to obtain its average area, which is proportional to the original intelligence signal. The integrated signal is amplified and capacitively coupled out. Since the lunar launch VCO's center frequencies will be designed for a 60-to-1 ratio (lunar playback/rewind speed ratio) the same reproduce amplifiers may be used for both lunar and launch

modes. The lunar digital signals can be obtained by simply tapping off from the level detector output.

Tape speed will be controlled by a closed-loop servo. A pickoff voltage from the motor drive will be fed to a discriminator; error voltages from the discriminator will drive a servoamplifier for motor speed control.

Electronic development has progressed to the establishment of the record, reproduce, and erase systems, and construction of operating breadboards of VCO's, driver amplifier, reproduce amplifier, Schmitt trigger, one-shot multivibrator, active filter, and servoamplifier. Tests are

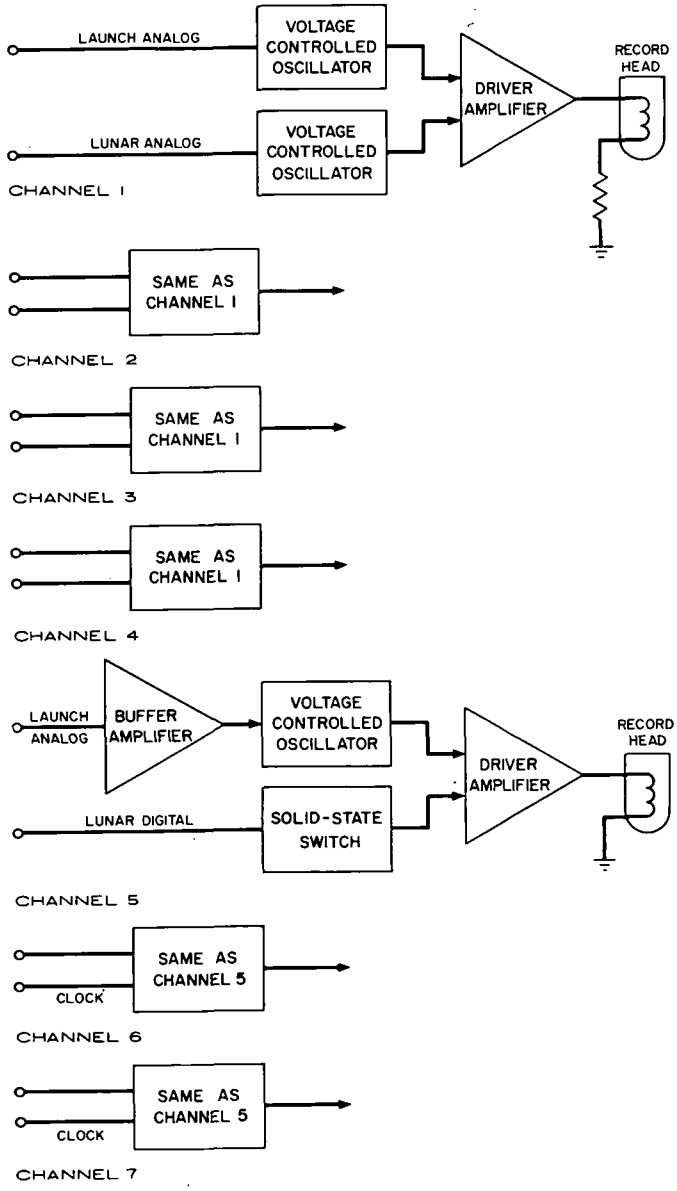

Figure 92. Tape recorder record section

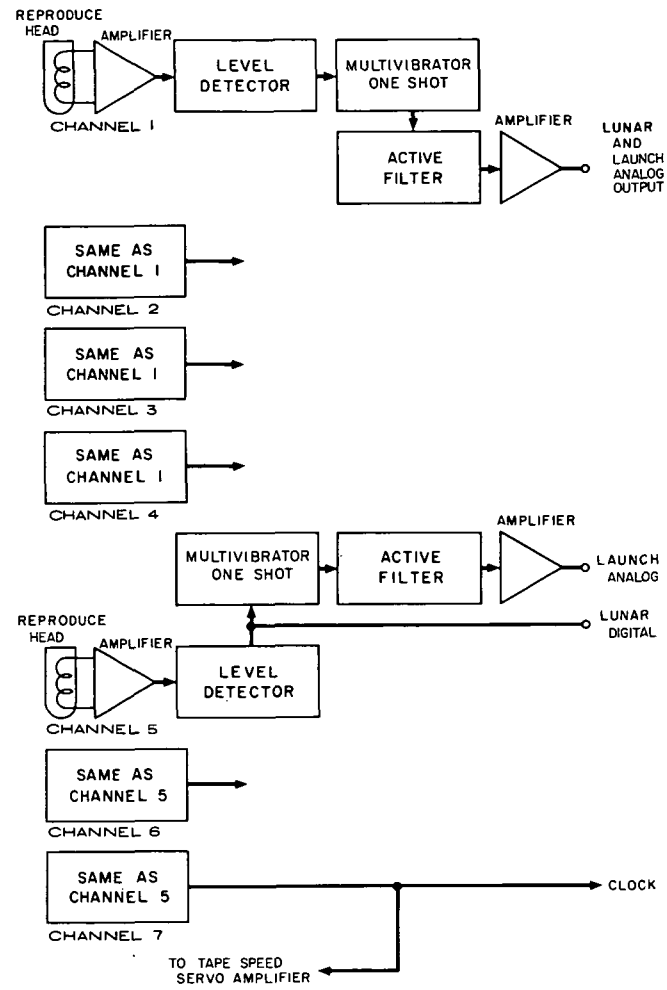

Figure 93. Tape recorder reproduce section

being conducted at room temperature and will be conducted over the expected temperature range. Specifications have been established and orders have been placed for the discriminators.

c. Electromechanical development. The tape recorder will be housed in an hermetically sealed drawn magnesium case filled with helium at one-half atmosphere. Size has been established as 8 by 9 by 5 inches. 1800 feet of ½ inch wide 1 mil Mylar tape will be used. The tape transport system is shown schematically in Figure 94. Reels are coaxially mounted. Tape tension will be maintained by a negator spring which applies relative torque between the takeup and supply reels through a differential. Tape tension varies with the radius of the tape on the reels. This system maintains tape tension and head contact at all times without need for a braking mechanism on the reels and minimizes power consumption for the reel drive mechanism by compensating the average load between forward and reverse tape drive. Two-speed

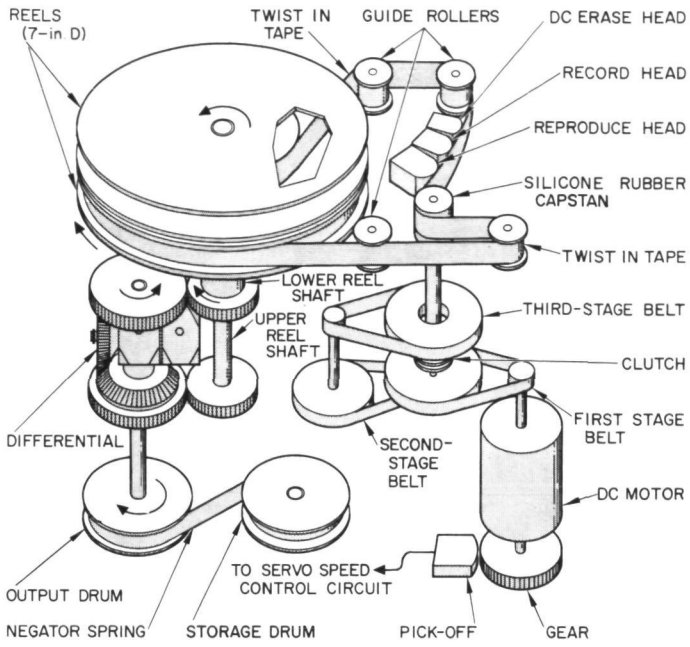

Figure 94. Tape transport system

operation will be achieved by use of a magnetic latching clutch with power used only during the speed change.

The motor which has been selected to drive the recorder is a miniature Japanese motor with unusually low brush friction and high efficiency (70%). Use of this motor is necessary to meet the requirements of low power drain during long periods of lunar recording.

Progress in the electromechanical area includes the following accomplishments:

(1) A preliminary packaging arrangement of the tape transport and electronic subassemblies has been completed; a preliminary outline and mounting drawing has been submitted.

(2) Procurement specifications have been established and orders have been placed for the negator spring assembly, the electromechanical clutch, and the differential.

(3) Samples of the special Japanese motors have been received. Similar motors have been previously environmentally tested by Consolidated Electrodynamics Corporation; the sample motors are special for 9-volt operation.

(4) A breadboard model of the capstan transmission has been made and has been used for preliminary flutter measurements.

(5) Specifications have been established and orders have been placed for record, reproduce, and erase heads.

(6) Reliability calculations have been made on the proposed circuitry, and a preliminary parts list has been submitted to Hughes Aircraft Company.

F. Electrical Power Supply

1. Summary

An oriented solar panel and a silver-zinc storage battery system are the primary and secondary sources of power, respectively, for operation of the *Surveyor* spacecraft. The Phase I solar-cell module development and type approval test program subcontract was awarded to two vendors on November 9, 1961, and will be completed in 2 months. Preliminary drawing release for the first development model solar panel has been accomplished, and fabrication of this panel is scheduled for completion in mid-December.

Final contract negotiations with Electric Storage Battery Company for the development and test of the silver-zinc battery have been completed, and the contract was awarded on December 4, 1961.

2. Solar Panel

The Phase I solar cell module subcontract has been awarded to two vendors, Hoffman Electronics of El Monte, California, and Heliotek Corporation of Sylmar, California. The solar cell subcontract consists of two phases. Phase I is a complete type approval test program to demonstrate the ability of the solar cell module to survive the severe lunar environment. Results of the Phase I subcontract will provide accurate solar cell design data for use in predicting solar panel performance on the lunar surface. The subcontract was awarded on November 9, 1961, and will be completed early in January, 1962.

Upon completion of the Phase I development and testing program, the Phase II subcontract for the production of approximately 10,000 modules will be placed with the successful vendor. Initial Phase I progress of both vendors has been satisfactory to date and is on schedule.

During this report period, primary design and development effort has been directed toward firming solar

panel design and fabricating the first development model solar panel. Preliminary drawings have been released for the development model and the necessary hardware has been received. Completion of fabrication is scheduled for December 15, 1961.

Figure 95 shows the solar panel substrate mounted in the fabrication fixture in preparation for assembly. Present panel substrate design utilizes 0.002 inch thick facing material and ⅜ inch thick aluminum honeycomb core with a ⅛ inch cell size. The titanium facing material is bonded to the core with FM-100 adhesive manufactured by Bloomingdale Rubber Company, Torrance, California. Measured panel substrate weight based on two substrates received to date is 2.60 pounds for the 9.2 square foot area. Maximum allowable substrate specification weight is 2.76 pounds.

The front surface of the solar panel will be coated with PT-401 epoxy insulating coating manufactured by Product Techniques, Incorporated, Los Angeles, California. Front and back surface thermal coatings are presently being evaluated for stability in the lunar environment. It is planned to employ a low-absorptivity coating ($\alpha = 0.25$) on the front panel surface not covered by solar cells, and a high emissivity ($\epsilon = 0.9$) on the panel back surface. Preliminary data obtained from the Phase I solar cell vendors indicates solar cell module absorptivity and emissivity values of approximately 0.82 and 0.83, respectively.

Initial vibration tests of solar panel substrates similar to those planned for final use have been completed with favorable results. Extensive environmental testing of the development panel is planned to verify results obtained to date. Solar cell modules for use on the development panel have been purchased from Heliotek Corporation and acceptance tests have been completed. A total of 106 modules assembled into a diode-isolated, parallel subgroup of four series strings will be used or the development panel. Average weight of the individual solar cell modules to be used on the development panel is 1.71 grams. Location and mounting of the secondary Sun sensor has been established, and a wooden dummy unit will be installed on the development panel.

Testing of the solar panel blocking diodes as installed in a panel substrate section has been initiated in vacuum of 10^{-6} mm Hg to determine thermal and electrical performance data. The diodes presently being evaluated are the Motorola IN3189 and the Unitrode Transistor Corporation UT234.

3. *Solar (Sunlight) Simulator*

Optical Coating Laboratory, Inc. (OCLI) has constructed a breadboard of the solar simulator to be used in testing solar cell modules. The present design is shown schematically in Figure 96. A tungsten lamp is used for energy wavelengths from 0.7 to 1.2 microns and a zenon lamp for energy wavelengths from 0.3 to 0.7 micron.

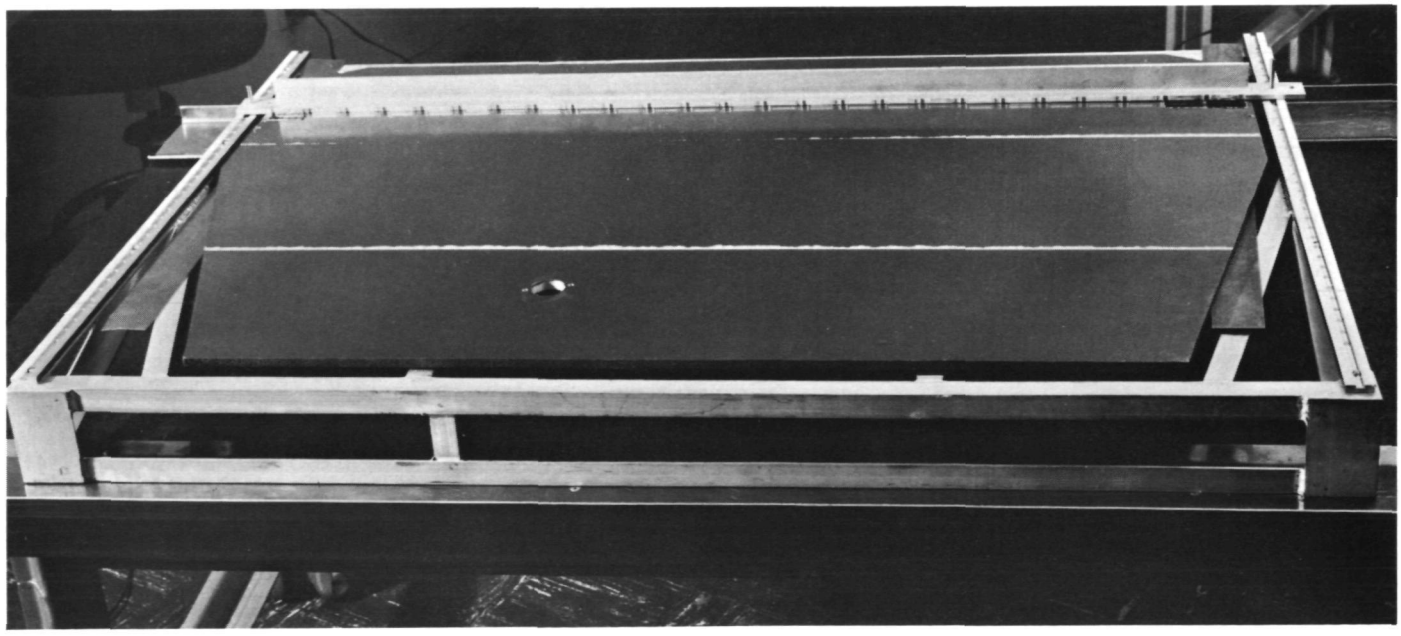

Figure 95. Solar panel substrate mounted in assembly fixture

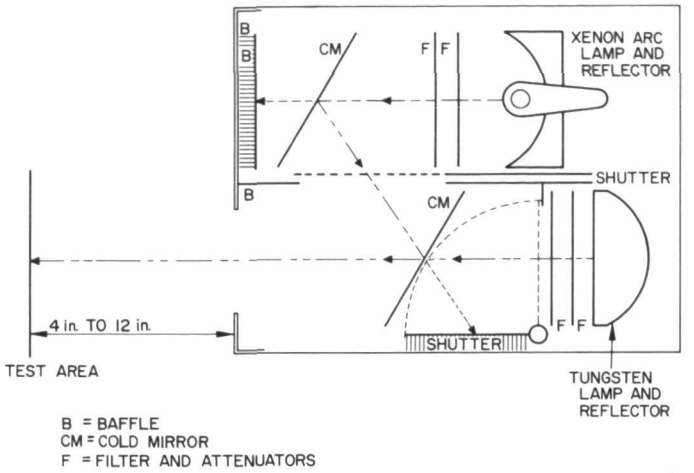

Figure 96. Solar simulator

The Sylvania "Sun Gun," a commercially available item, commonly used as a floodlight for home movies, is used as the tungsten lamp and reflector. The Sun Gun has a tungsten filament in an iodine vapor atmosphere to increase lamp life. To further increase life, the lamp will be operated at reduced voltage, although the color temperature will still be above 2800°K. A life test is presently in progress on this lamp. The OSRAM XBO-450W high-pressure zenon lamp, which requires 450 watts of dc power (20 volts at 22.5 amperes), is also used. The $f/0.2$ parabolic reflector gathers the output of this lamp with high efficiency.

Both lamps require high regulation of the power supplies to meet the performance requirements. Two cold mirrors are also employed to eliminate the Xenon energy above 0.7 micron more efficiently. This energy impinges on air-cooled baffle plates rather than heated optics. Several filters are used to further simplify the arrangement.

The simulator is planned for delivery in mid-January following performance verification at OCLI. Three weeks are allowed for acceptance testing at Hughes Aircraft Company during which time intensity, spectral output, and uniformity will be checked.

4. Battery

Charge-discharge cycle life tests of an Electric Storage Battery Company (ESB) three-cell, 25 amp-hr battery under simulated *Surveyor* operational electrical loads and temperature have been terminated. Performance of the battery to the end of the third lunar day (operating time in excess of 2 months) was within present *Surveyor* battery specification requirements, but the test was stopped due to the rupture of a second cell after a charge period of 7 days at 125°F. Earlier in the test of this battery one cell began to leak when nearly fully charged at a temperature of 125°F during operating conditions simulating the first lunar day. The leak was patched and the tests continued until the second cell ruptured. The battery is being returned to ESB for failure analysis and evaluation. Figure 97 shows the cells after completion of test. First and second lunar night discharge curves for the 25 amp-hr, three-cell battery are shown in Figure 98. Data obtained from tests of this battery indicate an average amp-hr efficiency of approximately 90%. It is noteworthy that although test results were excellent, this battery was a readily available development item and is not necessarily representative of future batteries procured to *Surveyor* specifications.

Figure 97. Silver-zinc cells after test

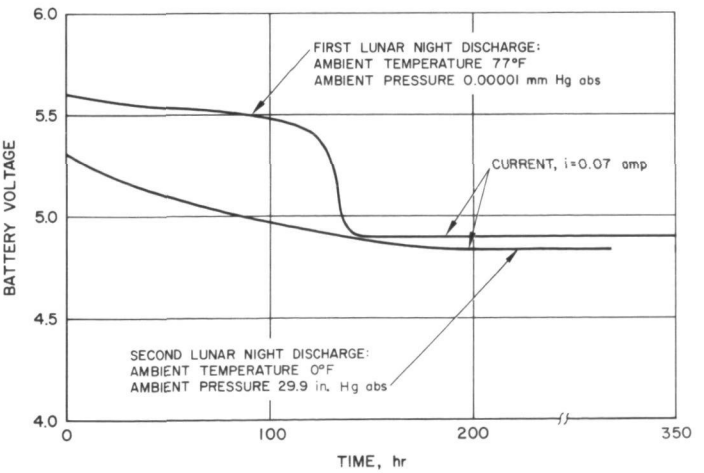

Figure 98. First and second lunar night discharge curves

A charging test on three new ESB 25 amp-hr cells has been initiated to determine the effect of various charge rates and temperatures on battery capacity (Fig 99). These data will be used to establish battery performance during the lunar day.

5. Power Management

a. Optimum charge regulator (OCR). This circuit (described in *SPS 37-10*) acts as a variable ratio, dc transformer. A control loop causes the effective ratio to be such as to obtain maximum power from the solar panel and deliver it to the battery system. The method of regulation used is a switching scheme in which the average current from the solar panel is that corresponding to the maximum power point on the solar panel output. However, the peak current is equal to the average current fed to the battery system, the pulses being supplied by a capacitor across the solar panel. A complete breadboard of the optimum charge regulator was fabricated and tested with satisfactory results during this report interval. As shown in Figure 100a, a transistor switch Q1 connects the input of an inductor L alternately between the solar panel and ground (by way of CR1). The current through the switch is a series of pulses with peak values equal to the OCR output current I_L. During the period that transistor switch Q1 is cut off, the collapsing field of inductor L holds I_L relatively constant, and CR1 provides the current return path from the load to L. Current relations in various parts of the circuit are shown in Figure 100b.

The switching drive is obtained from a low-power dc to dc converter in connection with a magnetic amplifier. The arrangement is such that the gating time of the magnetic amplifier determines the on-time of the switch. The slow response of the magnetic amplifier acts as an integrator such that the duty factor can be caused to increase or decrease linearly with time. As the duty factor (F_d) is thus varied, the output current I_L (Fig 101) varies from zero at zero duty factor to the optimum value corresponding to maximum I_L, and decreases to a lower value at 100% duty factor. The value at $F_d = 100\%$ is that value of current obtained by direct connection of the solar panel to the battery system. Figure 101 also shows the waveforms of duty factor and output current in closed-loop operation. The circuitry for discriminating the optimum point or the point of maximum current has been breadboarded and tested with the rest of the circuitry in a closed loop.

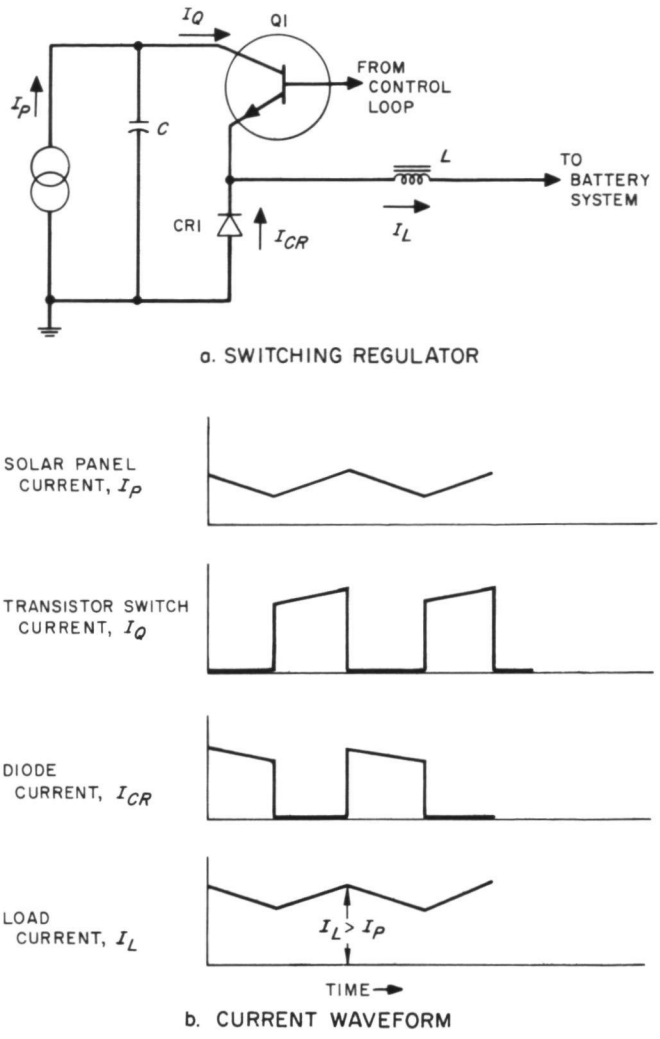

Figure 100. Variable dc transformer and current waveforms

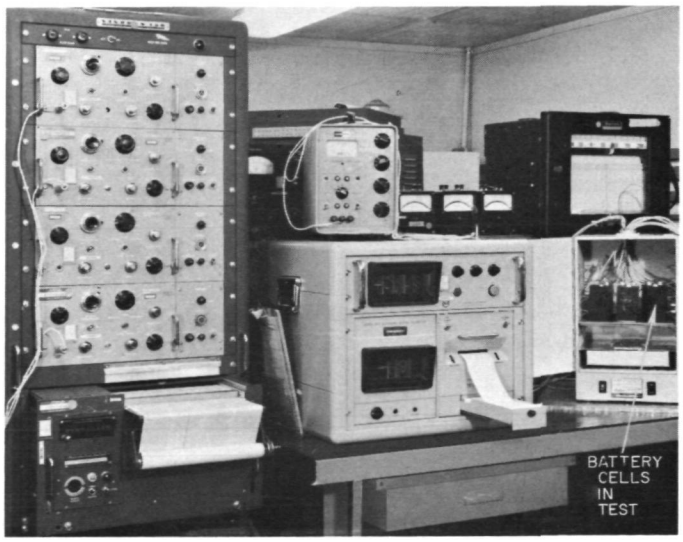

Figure 99. Setup for battery charging tests

b. Battery charging logic. Battery charge logic circuitry has been developed and breadboarded but no tests

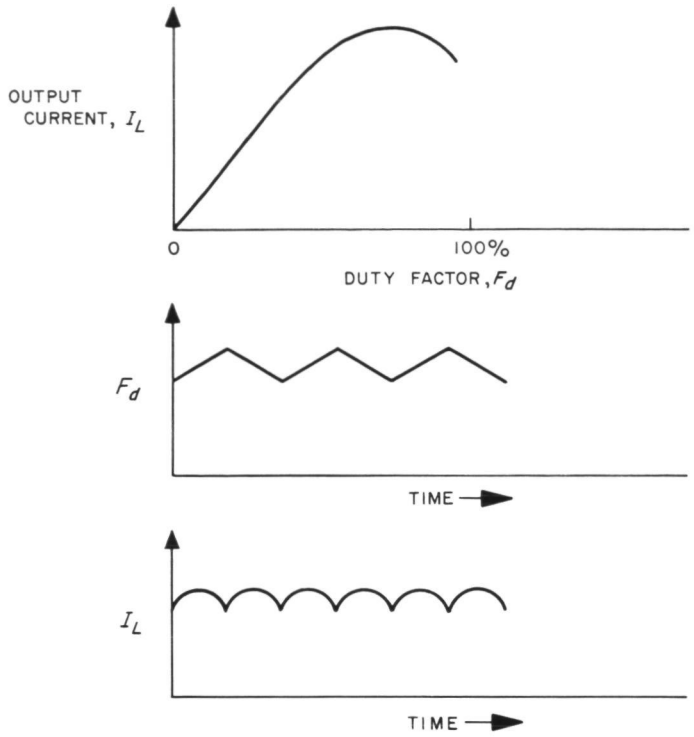

Figure 101. Duty factor and output current waveforms (closed loop)

have been performed. This circuitry will include all of the necessary logic to command charging of either or both batteries as well as to implement automatic charging.

In the latter case, each battery will be taken off charge when its terminal voltage reaches a preset amount. When the second battery is fully charged, a signal will be sent to the OCR commanding an output limitation of 28 volts dc after which the OCR will supply normal loads. If the load requirements exceed the capacity of the OCR, the batteries will deliver current to the load. This load current will cause the charge circuits to be actuated supplying charging current to the battery system as soon as excess solar panel output is available.

c. Main overload trip circuit. The main overload trip circuit has been designed and breadboarded. The breadboard has been subjected to environmental testing in the laboratory and operates satisfactorily. This circuit will sense the current and voltage on the main regulated bus. If the current exceeds a preset amount, or if the voltage drops below a preset level, the overload trip circuit will cause the main regulated bus voltage to drop to zero for about 20 milliseconds (except to the receivers and command decoders which bypass this unit). During this period of time, the individual load switches will drop out automatically and remain off. After 20 milliseconds the voltage will automatically recover, allowing loads to be commanded back on. This system saves the cabling which would be required if "off" signals were generated and distributed by separate wire to all the subsystem switches.

d. Electrical conversion units. The electrical conversion unit (ECU) program has developed to the extent

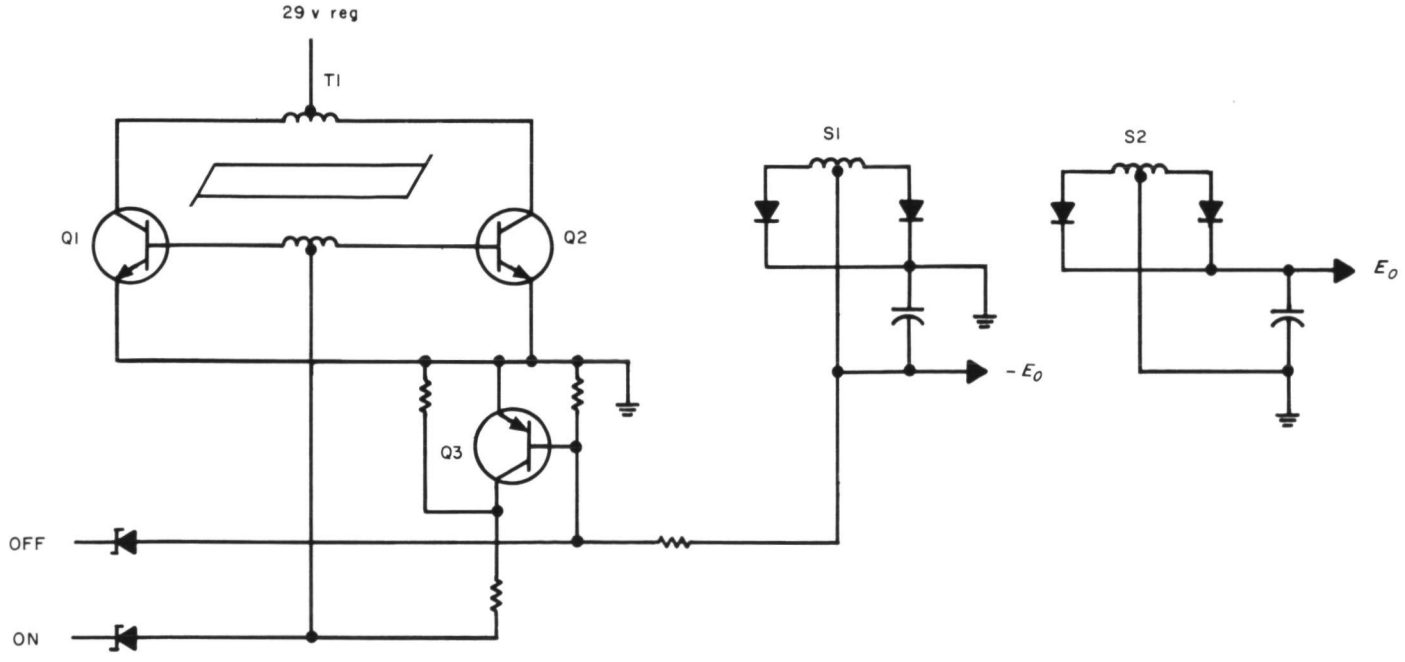

Figure 102. Typical electrical conversion circuit

that primary circuits have been released for several units and a number of breadboards have been built and tested. The efficiency of most of the converters is between 75 and 95%. Those converters with outputs less than 10 volts have low efficiencies as a result of rectifier voltage drop. The development of special inverters and converters for tight regulation, low ripple, or low distortion is under way. The breadboard of the three-phase, 400-cps inverter is now being tested with encouraging results.

Figure 102 shows a typical ECU circuit. Q1 and Q2 are part of a saturable-core oscillator with T1 being a saturating transformer. When a turn-on pulse is applied, Q1 and Q2 conduct and oscillation is produced by the feedback on T1. The secondary S1 produces a negative voltage which biases Q3 into saturation, completing the base return of Q1 and Q2 through R1. Outputs are taken as needed from secondaries S1, S2, etc. The regulation on a typical ECU is better than 1% for 50% load change. Turn-off is accomplished by supplying the standard positive command decoder pulse to the base of Q3. This absorbs the current being supplied to the base of Q3, holding it off for the duration of the command pulse. With Q3 off, the base circuit of Q1 and Q2 is open cutting the transistor off and causing oscillation to cease.

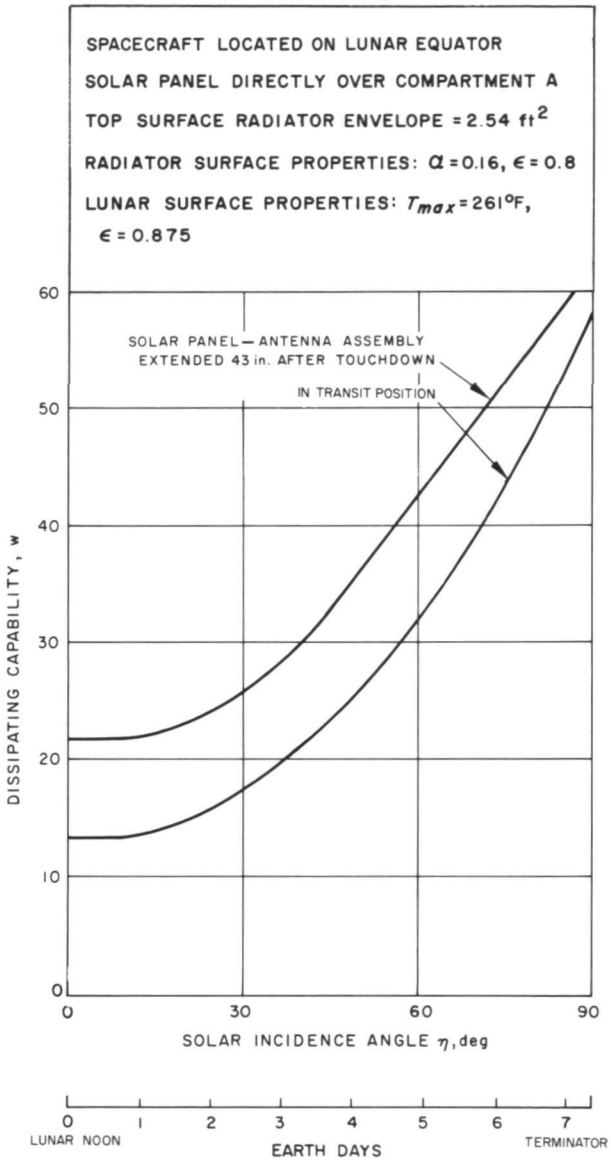

Figure 103. Compartment A dissipating capability

G. Thermal Control

1. Compartment Group

As previously reported (*SPS 37-12*) several modifications were made in Compartments A and B to optimize both lunar day and night thermal performance. Current lunar day performance characteristics for Compartments A and B are presented in Figures 103 and 104 in terms of steady-state internal power dissipating capability as a function of solar incidence angle. Also shown is the degradation in dissipating capability that would result if the solar panel-antenna assembly were to remain in its transit position. The performance indicated in Figures 103 and 104 is not entirely representative since most of the equipment in Compartments A and B operated intermittently, in some cases at peak power dissipations in excess of the steady-state performance. Under these conditions the resulting equipment temperatures will be transient in nature, and therefore a transient capability of Compartment A during the high-power transmitter mode of operation has been defined.

The next phase of compartment thermal design – detailed representation of the compartment and its surrounding environment to determine the temperature

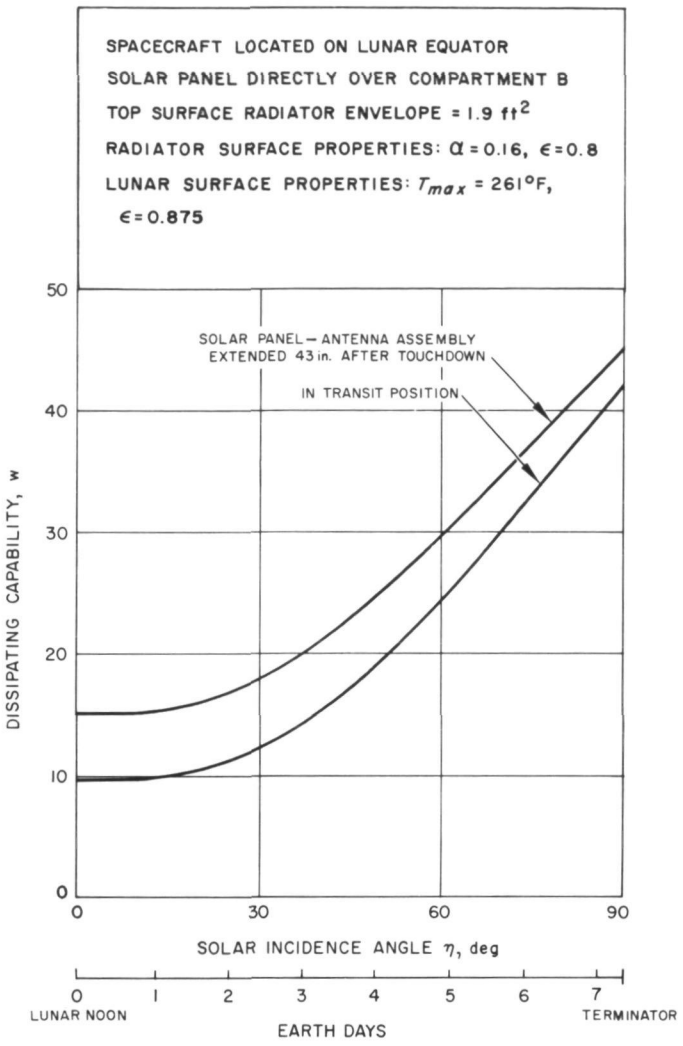

Figure 104. Compartment B dissipating capability

histories of specific units within the compartments and of the major heat paths – is under way. The complex radiation interchange between the external surfaces of the compartment – particularly the compartment radiators and other interacting surfaces (spacecraft, panels, Moon, and space) – will be accounted for by utilizing the network method (radiosity) developed by Oppenheim in conjunction with the IBM 7090 computer.

A preliminary study of the effect of local spacecraft equipment on the Compartment A dissipating capability indicated that the TV telescope and Camera No. 5 assembly (adjacent to Compartment A) would occupy an envelope equivalent to a 5% radiation view factor from the top of the compartment. This position would decrease the Compartment A dissipating capability at lunar noon from 22 to 15 watts, and therefore the assembly has been relocated. The new location, near the flight control group, will result in negligible effect on the compartments. The reduction in power dissipating capability illustrates the importance of maintaining an adequate view of space from the major radiating surfaces.

The current lunar night compartment power dissipation requirements for adequate thermal performance are 5.1 watts for Compartment A and 4.4 watts for Compartment B. These requirements currently exceed the heat available from normal equipment dissipation by 0.73 watt. An attempt is being made to meet this requirement by a revised sequencing of the Compartment A and B equipment operated during lunar night. An alternative method of assuring thermal compatibility involves the use of approximately 2.8 pounds of additional superinsulation to balance the existing heat deficit. Further study is required before the optimum tradeoff can be made.

In the previous report, it was indicated that several scientific instrument and mechanism auxiliaries not used during lunar night were removed from Compartments A and B to reduce wiring harness weight and lunar night compartment heat losses. This equipment (Table 6) has been packaged in a group designated Compartment C and will be designed to survive the lunar night; therefore, nightime thermal protection will not be required.

The thermal control of Compartment C will maintain the equipment between 0 and 125°F during the lunar day using passive radiation techniques to dispose of dissipated electrical power near lunar noon and supplemental heating near the terminator, where the combined environmental load and equipment dissipation will be insufficient to maintain 0°F equipment temperatures. The only units which dissipate significant power in this compartment are the subsurface sampler auxiliaries, which dissipate 37 watts during a 15-minute interval.

Table 6. Compartment C packaging

Item	Volume, in^3
Gas chromatograph auxiliaries	45
Subsurface sampler and processor auxiliaries	115
Surface sampler auxiliaries	29
Surface geophysical auxiliaries	133
Subsurface geophysical auxiliaries	92
Mechanism auxiliaries (partial)	164
Total volume	578

Current mission sequencing indicates approximately four such operating periods during the lunar day. A detailed thermal analysis of this compartment with the objective of minimizing the supplementary heating power required near terminator is currently under way.

A preliminary analysis was performed on the flight control compartment to determine if the Canopus sensor could be passively temperature-controlled to 32°F in the presence of conduction and radiation coupling from the inertial reference unit radiator at 160°F and from other local spacecraft surfaces. The results indicate that the Canopus sensor and inertial reference unit assembly temperature requirements are compatible and can be maintained by a surface treatment of absorptance, $\alpha = 0.16$ and emittance, $\epsilon = 0.8$ on the inertial reference unit radiator and Canopus package.

2. *Remote Subsystem Group*

Of the three main items of the doppler antenna subsystem – klystron box, signal data converter, and antenna dishes and equipment – the first two have been shown to be capable of passive control during transit. Due to their position (remote from the antenna dishes), the proper balance between solar energy received and infrared energy dissipated can be achieved on the surfaces of the boxes through selective surface coatings, and any desired temperature between the limits of approximately −100 and 100°F at the beginning of the descent phase may be obtained. The third item, however, cannot as readily be controlled. The antenna dishes in their original locations under Compartments A and B have been shown to reach a minimum temperature of −190°F at the end of transit. To avoid this low temperature, the antenna dishes have been moved slightly outboard to receive partial solar illumination. Thermal conduction will be relied on to provide heat distribution to the inboard sections of the dish. If it is found that thermal conduction is not sufficient to maintain the inboard portions of the antenna dishes at temperatures above −50°F, auxiliary heating may be required.

Figure 105 shows the results of one possible antenna configuration using aluminum facings and honeycomb construction with one-third of the antenna exposed to solar illumination. For this completely aluminum configuration, the minimum antenna temperatures are maintained well above the lower limit of −50°F.

An initial analysis to determine the degree of heating on the lower spaceframe tubes from the vernier engine exit nozzles has been completed. Thiokol, Reaction Motors Division, has indicated that a nozzle temperature of approximately 2800°F can be expected. The initial analyses are slightly conservative in that the 2800°F nozzle temperature was assumed to be a step function from the time of ignition. Figure 106 shows the lower spaceframe temperature as a function of time for a spaceframe emittance (ϵ) equal to 0.8 and a burning time of 214 seconds. An unprotected tube will approach 1200°F after approximately 200 seconds of vernier operation. Figure 106 indicates the cooldown characteristics after engine cutoff. The figure also indicates that heating is restricted to a localized region extending 12 to 15 inches from the engine attachment. Figure 107 illustrates the effect of a highly reflective tube coating ($\epsilon = 0.05$). It is concluded that the higher reflectance will reduce the tube temperatures to acceptable levels.

A tradeoff study to detrmine the vernier system fuel and oxidizer line heater power savings by using a high degree of insulation around the lines has been completed. Wrapping the lines with approximately 1 inch of ribbon aluminized mylar was found to be undesirable in view of the routing and attachment requirements. The lines will be thermally controlled using 2.5 watts of heating and a single low emittance aluminum foil outer covering. The foil will be spot-bonded, thus allowing volume for thermal expansion and outgassing of the bonding material.

An analysis to determine the thermal gradients throughout the spaceframe is nearly complete. Of prime

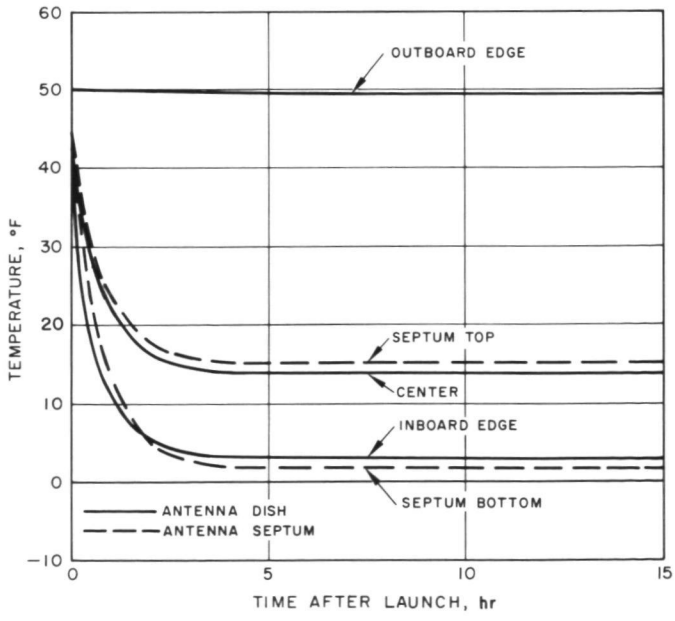

Figure 105. Doppler antenna temperatures in transit

importance will be gradients resulting from the nonsymmetric solar heating during transit. Such considerations must be included in certifying spaceframe structural integrity during the landing operation.

Figure 108 shows the result of a parametric study to determine the correct surface coating requirements on the shock absorber. As indicated, there are several combinations of solar absorptance and infrared emittance which would successfully maintain the shock absorber in the vicinity of 70°F. Initial selection has been for a shock absorber column coating of $\alpha = 0.8$, $\epsilon = 0.8$.

3. Scientific Instruments

Thermal analysis and coordination of the soil analysis group has progressed very satisfactorily. Coordination with the supplier of the X-ray instruments (Philips Electronics, Inc.) has resulted in the incorporation of compatible thermal design concepts in the package designs. Specified temperature limits have been negotiated and current thermal analyses indicate that, in general, the specified limits will be met. Emphasis has been placed on coordinating and assisting the vendor in the design of electronic circuitry and equipment capable of surviving the severe lunar night environment. Table 7 shows a comparison of former estimated lunar night heating requirements with the current design values.

An X-ray diffractometer thermal radiator has been designed for the dissipation of the 30 watts of heat generated in the X-ray tube. Several concepts have been considered and results of the recommended radiator in simulated lunar noon operation are shown in Figure 109. A final recommendation of a 6061-T6 aluminum radiator of 50 in^2 area with cross section tapered from ¼-inch at the root to ⅛-inch at the ends for weight savings has been made to Philips and will be incorporated in the X-ray diffractometer head package design.

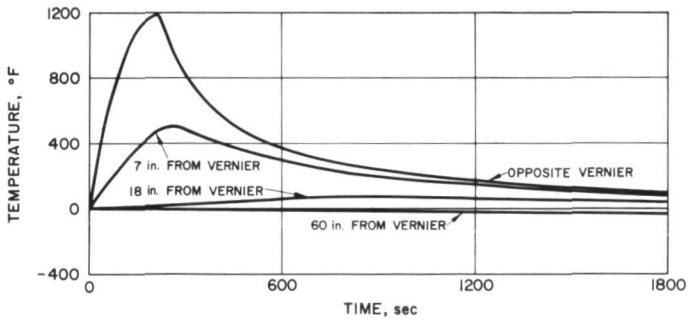

Figure 106. Spaceframe temperatures for ϵ = 0.8

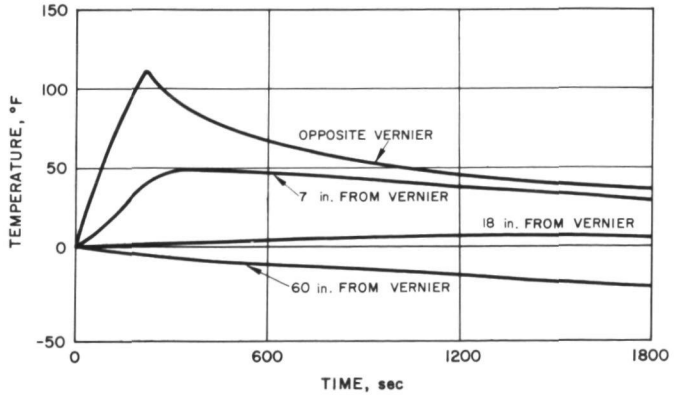

Figure 107. Spaceframe temperatures for ϵ = 0.05

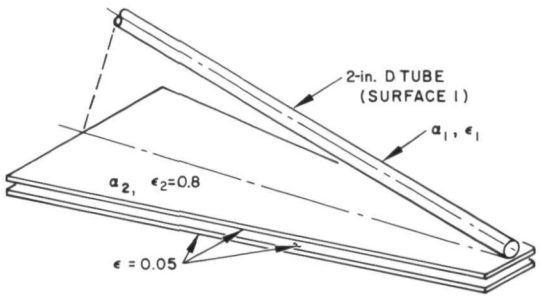

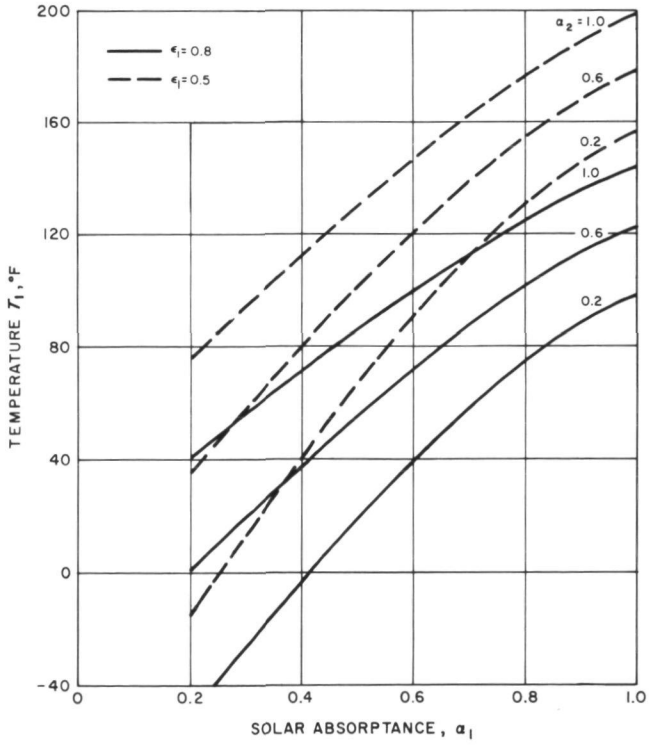

Figure 108. Shock absorber column temperatures

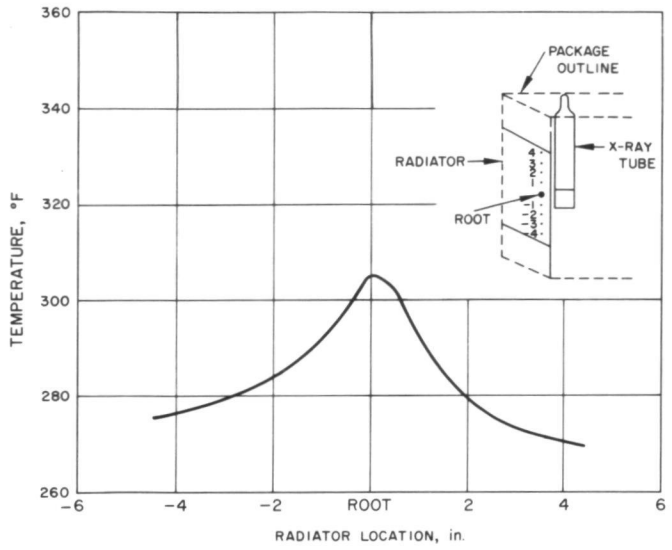

Figure 109. X-ray diffractometer radiator temperatures

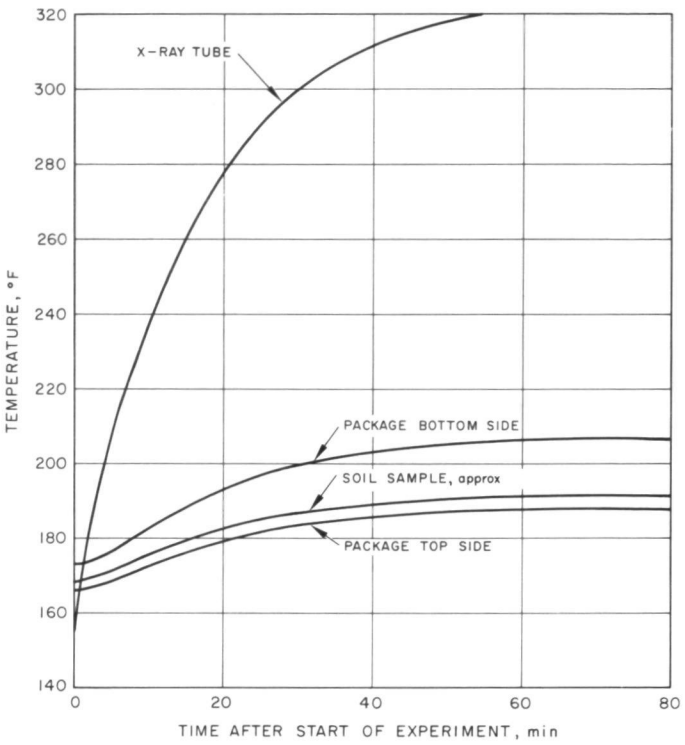

Figure 110. X-ray diffractometer head temperatures

With this design, the X-ray tube and diffractometer head will operate at temperatures within the specified tolerances. Figure 110 shows diffractometer head package temperatures resulting from this radiator concept. Proper surface treatments will be specified to the instrument supplier by mid-December.

The high voltage power supplies for the X-ray instruments are being developed to minimize lunar night survival requirements, as well as provide maximum heat dissipation during lunar daytime operation. The minimum allowable temperature has been lowered from — 148 to — 280°F, which reduces the heating requirements significantly (Table 7). The maximum allowable operating package temperature has been set at 210°F for both power supplies; thus it appears that an optimum thermal design will result.

The gas chromatograph thermal control design utilizes thermal isolation of the instrument components from the outside environment through the use of super-insulation. Very close temperature tolerances have been set on various components of the instrument. These tolerances will be maintained through the use of internal heating when required and external heat dissipation from the outside surfaces of the package. Surface treatments for the outer sides of the package are currently under analysis, the optimum coatings to be specified to the supplier (Beckman) when required. The lunar night heating requirement still stands at approximately 2.0 watts. An effort is currently being made to lower the minimum allowable non-operating temperature to reduce if not eliminate this heating requirement.

A preliminary thermal analysis of the thermal diffusivity portion of the Surface Geophysical Experiment has resulted in a recommendation to wrap the critical stepping motor with approximately 1/10 inch of super-insulation and provide a 35-watt heater for a 30-minute preheat in the event of lunar night operation. It has also been recommended that the heater wires be included in the motor wire bundle to provide preheating of the bundle which may be required to flex slightly during the experiment. This bundle will also be wrapped with about 1/10 inch of super-insulation.

The radiation detector thermal analysis has indicated that thermal isolation of the electronics package from the ionization chamber will result in a satisfactory design. The ionization chamber, filled with helium gas, will need no lunar night protection, while only fractional wattage is required to maintain the electronics at its minimum temperature during the night. Indications are that the electronics package may be designed to survive lunar night, in which case no auxiliary heating will be required.

Table 7. Soil analysis group night heating requirements

Instrument or package	Current minimum allowable temperature, °F	Original heating requirement, watts	Current heating estimate, watts	Net power saving, watts
X-ray diffractometer head	−320	0	0	0
Diffractometer high-voltage power supply	−280	1.59[a]	0.06	1.53
X-ray spectrometer head	−280	2.0	~0.05	1.95
Spectrometer high-voltage power supply	−280	1.17[a]	0.05	1.12
Gas chromatograph	−58	2.0	2.00	0
		Totals	2.16	4.60

[a]After removal of high-voltage power supply from Compartment A.

4. Thermal Switch

Table 8 is a synopsis of the pertinent thermal test results obtained to date on the lightweight aluminum design. As indicated by the low total switch conductance for the aluminum contact design, it does not appear that the design goal conductance of 0.7 Btu/hr °F can be achieved with aluminum contact surfaces. Empirical relationships indicate that the contact conductance is directly proportional to the contact material density, and therefore plating of the contact surfaces with both gold and copper is presently being examined. By plating the aluminum contacts, the better contact conductance performance of these heavier metals can be utilized without sacrificing the basic lightweight aluminum construction. Although gold is superior to copper as a contact material, both will continue to be examined since gold presents greater problems than copper in both plating and lapping.

Since the foil attachment in the switch used to evaluate the gold plated contacts was poor (evidenced by the conductance data in the table), the foil assemblies are presently being heliarc-welded at the tips and subsequently soldered to the inner ring and contact plug. The method is adequate; however, an inspection technique must be developed to ensure good joints prior to thermal testing of completely assembled switch units.

With the objective of fabricating the thermal switch case from a material capable of withstanding the 257°F heat sterilization temperature, the search for an alternative to polystyrene has continued. As previously indicated, one alternative is Ablatalite, manufactured by Thiokol. A case with a 15-mil wall thickness has been successfully machined from this material. The elastic modulus of Ablatalite has been measured and found to be 3×10^5 psi, which is adequate for this application. Materials testing will continue.

Rexolite is also under investigation. This material has structural properties similar to polystyrene but has a higher temperature capability.

5. Compartment A Super-Insulation Tests

The primary purpose of the Compartment A super-insulation tests will be to determine if the compartment thermal design as presently conceived is capable of maintaining the 0°F internal temperature during lunar night. The effectiveness of the multiple-layer radiation insulation will be of particular interest.

Figure 111 shows the basic thermal tray equipped with ten thermal switches. The outer compartment shell and its multiple-layer radiation insulation liner are also

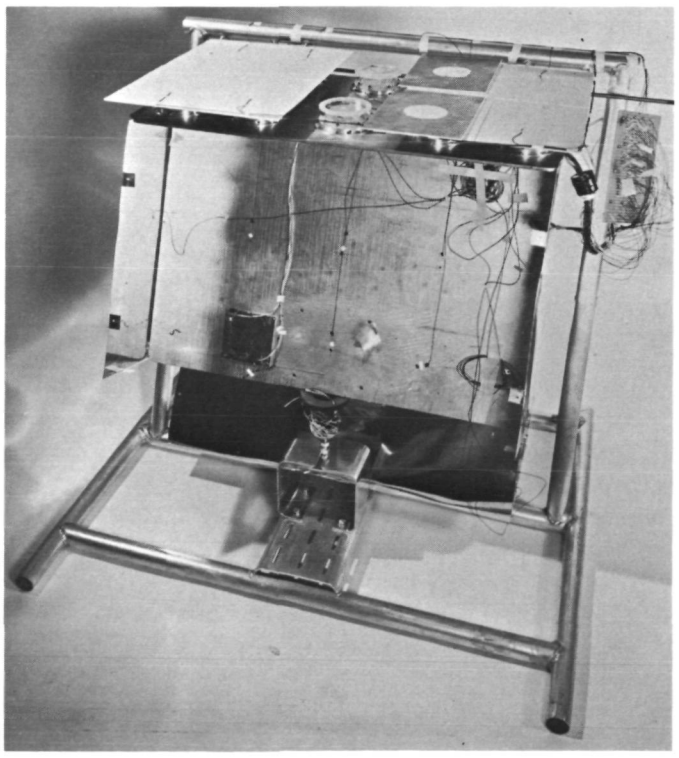

Figure 111. Basic thermal tray

Table 8. Thermal switch conductance data

Type of contact	Surface quality, micro-inches		Thermal conductances, btu/hr °F			
	Flatness	Roughness	Across contacts		Foil assembly	Total switch
Aluminum	10	10	Theory	0.17	2.22	0.15
			Test	0.30	2.0	0.24
Gold plate	20 - 30	*	Theory	0.94	2.22	0.55
			Test	0.82	1.0	0.40
Copper plate	5 - 10	5	Theory[a]	0.41	2.22	0.31
			Test	0.45	1.50	0.34

[a]Correlated vacuum-test data from Reference 1.
*Not measured.

included in the exploded view shown in Figure 112. This compartment thermal model has been completed and instrumented and is ready for test.

The structural supports are equivalent thermally to those of the final Compartment A design. Each support is equipped with a blocking heater on its external end so that the heat flux through any given support can be nulled during the test. The super-insulation consists of 100 separate sheets of aluminized mylar individually hand-wrinkled to minimize the contact area between sheets. All edges are interleaved so that no direct thermal connections exist between the inner and outer sheets. Ten thermal switches, less their contact closure mechanisms, are mounted on top of the thermal tray. The open switch conductance of the thermal switch is simulated in these units.

Subsystems that dissipate power within Compartment A during the lunar night are simulated in the test unit

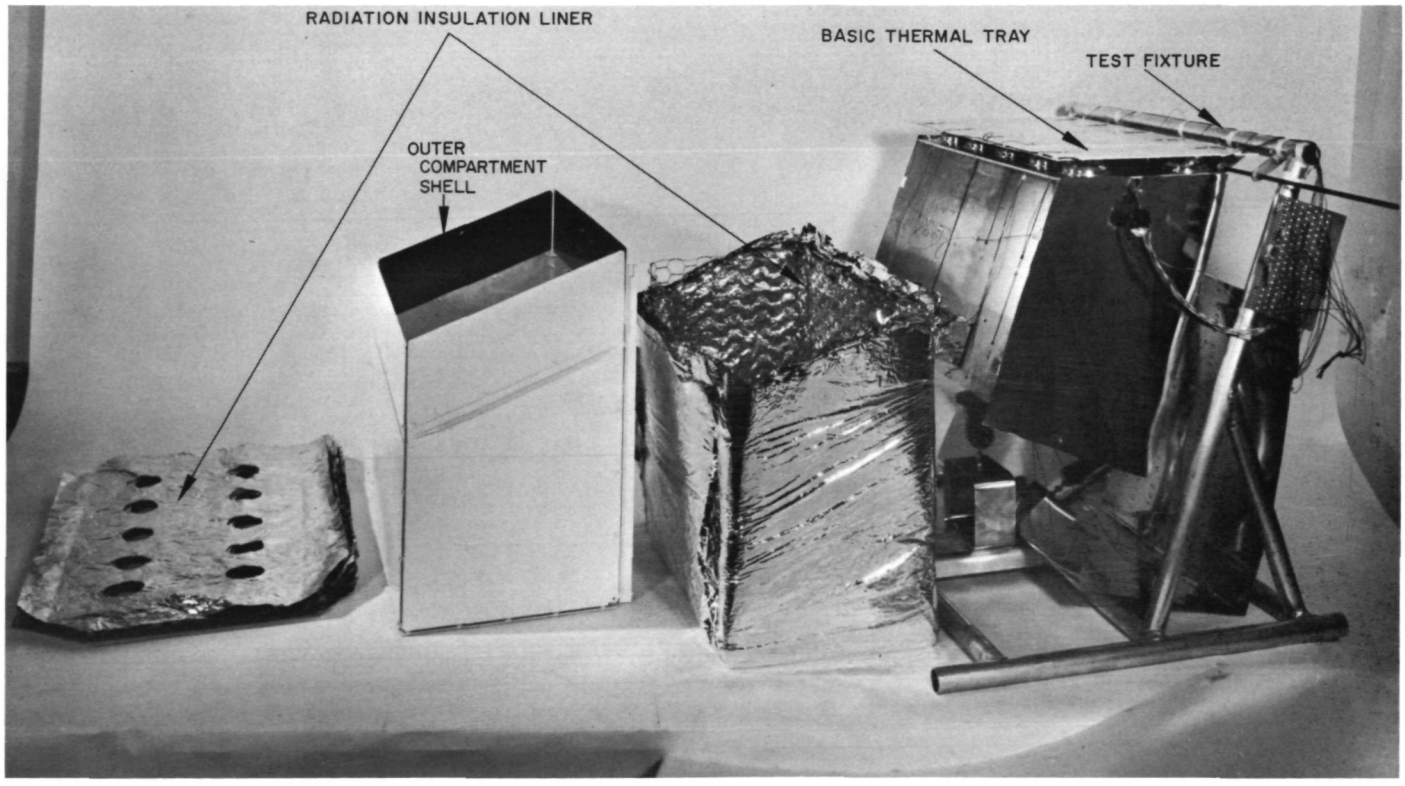

Figure 112. Compartment thermal model

by heater blankets bonded to the thermal tray. Thermocouples have been installed at 50 locations both inside and outside the compartment to enable a complete compilation of all heat loss contributions.

The cold-wall installation in Hi-Vac I has been delayed. Current planning calls for the tests to begin in mid-December.

6. Coatings

Table 9 summarizes the current status of the material testing being conducted for Hughes Aircraft Company at UCLA. The data for the aluminized Mylar and Tedlar are being repeated since the solar absorptance, α, should have been determined as a second surface mirror (looking through the film). It is anticipated that the Hughes Gier-Dunkle spectral reflectance equipment will be in operation in early 1962 and therefore will relieve the scheduling problems associated with routing samples through the UCLA laboratory.

Pending conclusion of an investigation of the proposed bonding material, a tentative decision to use second surface mirrors (Vycor) for the main radiating surfaces of MT-1 has been made. The mirrors must be bonded to the substructure with a high conductivity bond; therefore, two such techniques are currently being explored. The first involves a sweat solder joint using an indium alloy and the second, a silver-loaded epoxy resin.

Table 9. Coating properties data from UCLA

Material	Solar absorptance, α	Infrared emittance, ϵ	α/ϵ
Vycor No. 7910 — 1/16 inch thick, aluminized	0.122	0.856	0.14
Vycor No. 7910 — 1/8 inch thick, aluminized	0.114	0.854	0.13
Mylar — 0.010 inch thick, aluminized	0.095[a]	0.90[b]	—
Tedlar Type 200-A20 — 0.004 inch thick, aluminized	0.102[a]	0.832[b]	—
Ditzler white paint	0.244	0.910	0.26
Type 1199 foil — anodized			
0.2 mil film thickness	0.152	0.717	0.212
0.4 mil film thickness	0.164	0.768	0.214
0.6 mil film thickness	0.176	0.799	0.220
0.8 mil film thickness	0.185	0.818	0.226

[a]As first surface mirror.
[b]As second surface mirror.

Although confirming data have not been obtained, early indications are that a Hughes-developed inorganic white paint will prove useful for general spaceframe applications. This coating, while not as effective as the second surface mirrors, should have a solar absorptance between 0.20 and 0.22 and an infrared emittance between 0.8 and 0.9.

7. Thermal-Vacuum Tests

Three separate 120° sectors (designated MT-1) of the spacecraft structure complete with thermal mockups of the appropriate subsystems are to be tested under lunar day, lunar night, and transit environments. The Hughes cold-wall vacuum chambers to be used for this testing are expected to be ready in early March. Lunar night testing of all three sectors will be performed for several months. Lunar day and transit testing will begin in June, corresponding to delivery of the first solar simulation unit.

Because the chambers will have a maximum working height of 8.5 feet, the solar panel-antenna assembly cannot be extended to its postlanding position. In order to maintain the proper thermal radiation geometry during the lunar day testing, it will be necessary to scale down the MT-1 solar panel and planar array. Preliminary analysis indicates that the linear array dimensions can be scaled directly to the distance of the array above the compartments, with negligible errors resulting.

The design of the MT-1 spaceframe sectors is nearly complete. Thermal mockups of all subsystems are to be available for installation beginning in January.

H. Engineering Mechanics

1. Touchdown Dynamics

Recent studies of design data have shown that the ranges of center of gravity and radius of gyration are expected to be 16 to 18 inches and 28 to 32 inches, respectively. With use of these data, maximum landing gear loads, vehicle acceleration levels, and stability boundaries have been established. Load levels have been calculated, using $\Delta\ cg$ and k values of 16 and 28 inches, respectively, to give worst-condition loads. ($\Delta\ cg$ denotes the center of gravity height above spacecraft station 47.48, the plane of the landing gear pivot points.) Stability calculations were made with $\Delta\ cg = 18$ inches and $k = 32$ inches to give the worst stability conditions.

In previous bimonthly progress summaries, rigid body acceleration levels have been presented, since the order of magnitude of the amplification factor associated with these loads had not been determined. Subsequent analysis has indicated that shock amplification for the touchdown loads is approximately 2. Since rigid-body loads and those incorporating shock amplification may not have the same maxima as contributing parameters are varied, the examination of touchdown loads requires the use of the shock amplification factor to obtain a true indication of maximum loads. Therefore, the loads in this report are actual loads, rather than rigid-body loads.

A more precise definition of touchdown velocities and attitude has resulted from more rigid specifications on flight control parameters. Figure 113 shows the 3σ and 10σ dispersion ellipses for altitude and vertical descent-velocity at vernier cutoff. From this plot corresponding values of touchdown vertical velocity can be ascertained.

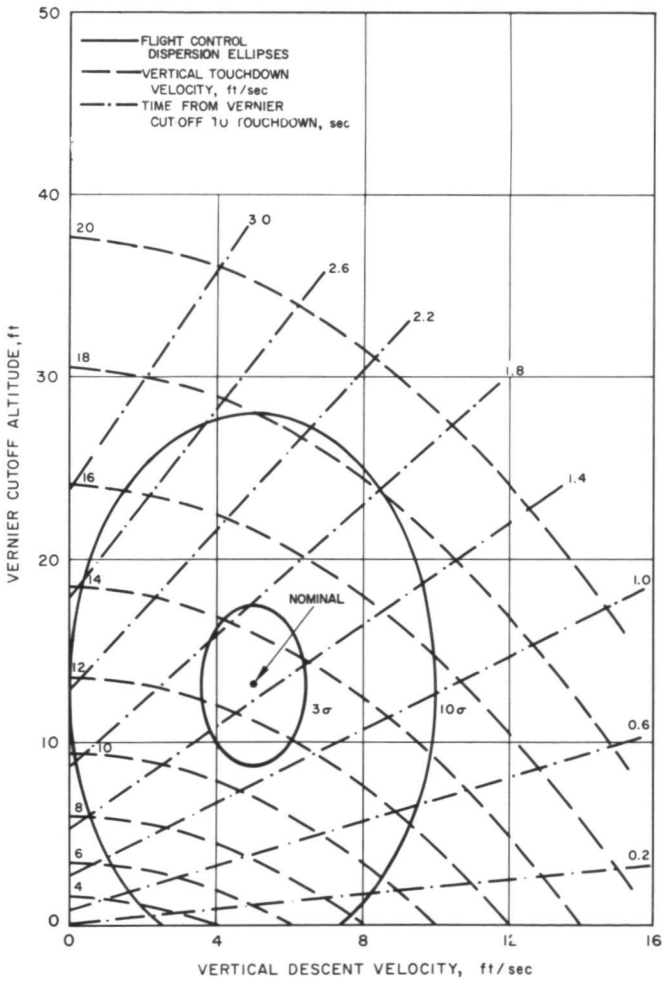

Figure 113. Effects of flight control dispersion on touchdown conditions

Figures 114 and 115 contain the 3σ and 10σ ellipses relating touchdown lateral velocity with touchdown attitude. These results, and those in Figure 116, are based on the following conditions:

Spacecraft weight	772 pounds
Radius of gyration	28 inches
Δ *cg*	16.05 inches
Site slope	15 degrees
Amplification factor	2

The effect of spacecraft-to-lunar surface friction coefficient (μ) on antenna lateral acceleration has been extensively investigated for $0 \leq \mu \leq 1.0$. Maximum lateral antenna loads occur at $\mu = 1.0$ (Fig 114), and

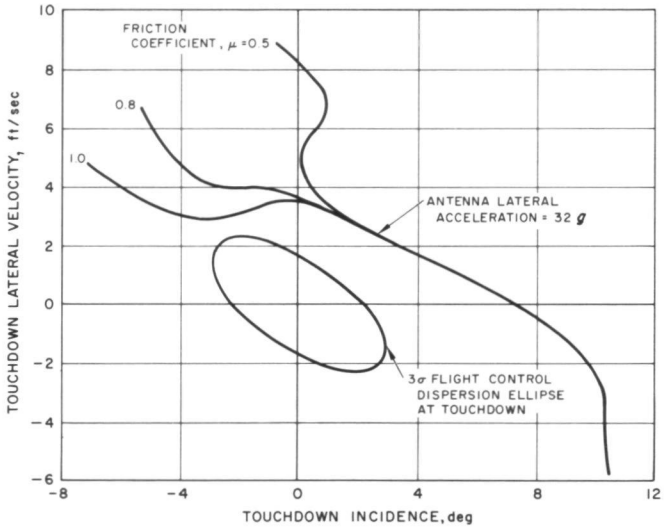

Figure 114. Antenna lateral acceleration 20 ft/sec touchdown vertical velocity

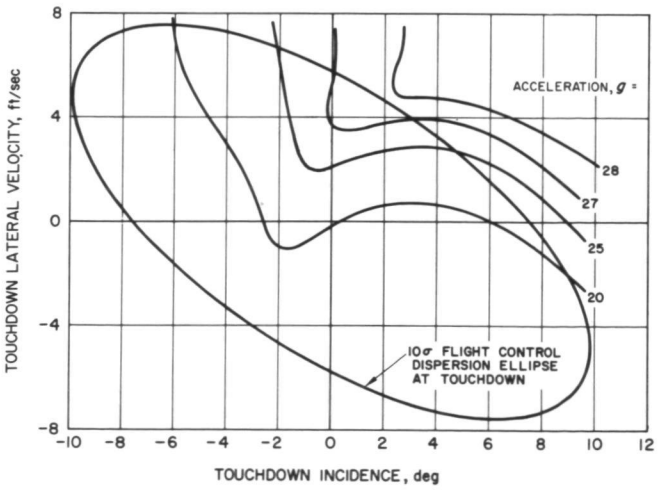

Figure 115. Antenna lateral acceleration 15 ft/sec touchdown vertical velocity; μ = 1.0

on the basis of the 3σ dispersion ellipse, a maximum acceleration level of 32 g has been established. This result corresponds to a touchdown vertical velocity of 20 ft/sec, which, from Figure 113, is outside the 10σ dispersion ellipse. A 15 ft/sec touchdown vertical velocity (corresponding to approximately 3σ) yields a level of only 28 g on the basis of a 10σ dispersion ellipse (Fig 115).

"Package" acceleration refers to the vertical acceleration of a point displaced laterally 30 inches from the center of gravity. It was determined that maximum package accelerations occur at low values of μ. Figure 116 shows the accelerations corresponding to $\mu = 0$. The established design value of $27g$ lies well outside the 3σ dispersion ellipse.

Another effect of the correlation between touchdown lateral velocity and incidence attitude has been to establish the maximum shock absorber compressive load at 8000 pounds. This load corresponds to vertical and lateral velocities of 20 and 5 ft/sec, respectively, with zero attitude and $\mu = 1.0$.

A more detailed investigation has been made of the landing gear foot pad. As the contact area of the foot pad increases, the moment arm of the resulting eccentric vertical force decreases, resulting in a limiting torque which can be applied to the rigid arm. Since this torque is a major contributor to the rigid arm design, every effort is being made to reduce it. The density of the foot pad has therefore been reduced from 6 to 3 lb/ft^3 in order to reduce the torque from 12,000 to 7500 lb-in.

Spacecraft touchdown stability, on site slope of 15 degrees, has been more thoroughly investigated for a higher center of gravity and larger radius of gyration. Parameters used in these studies are as follows:

Spacecraft weight	772 pounds
Radius of gyration	32 inches
Δ cg	18 inches
Initial spacecraft incidence	— 5 degrees
Spacecraft pitch rate	— 1 deg/sec
Shock absorber parameters	Nominal

As expected (*SPS 37-12*) the stability is lower with these parameters. Figure 117 shows the allowable lateral velocity as a function of site slope, as shown in *Space Programs Summary 37-12.*

If, regardless of vertical touchdown velocity, the smallest lateral velocity which results in toppling for a given site slope is denoted maximum allowable lateral velocity and is plotted versus site slope, the result is as shown in Figure 117. Actually, this value of lateral velocity occurs at a vertical velocity between 9.5 and 10.5 ft/sec for site slopes of 10 to 30 degrees. Consequently, at a nominal vertical touchdown velocity, there is in general more stability than is shown in Figure 117. Furthermore, the 32-inch radius of gyration is an absolute maximum, so that for the expected value of about 30 inches, the vehicle will be more stable.

The effect on stability of the variation of friction coefficient is being investigated for the same configuration

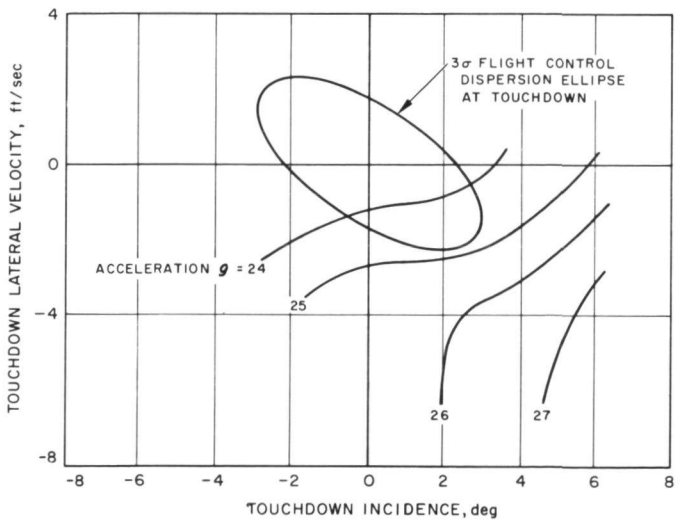

Figure 116. Package vertical acceleration 20 ft/sec touchdown vertical velocity; μ = 0

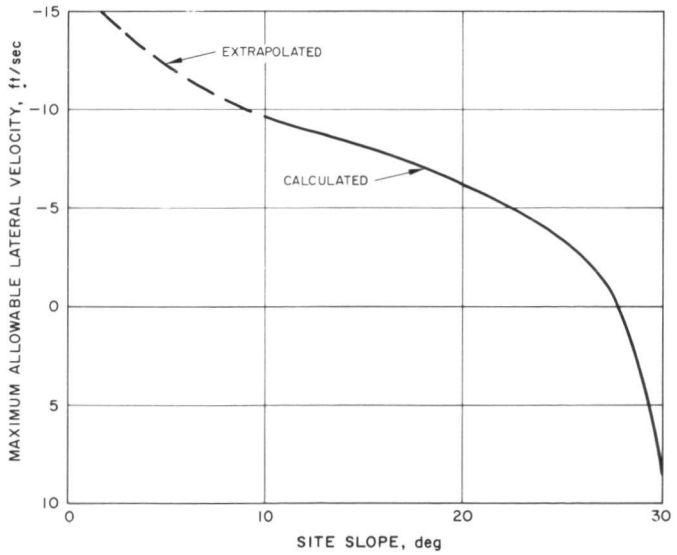

Figure 117. Allowable lateral velocity vs site slope μ = 1.0

($\Delta\, cg = 18$ inches and $k = 32$ inches). The results for a 15 degree site slope are indicated in Figure 118, which shows the instability region boundaries for various friction coefficients. The line denoted "abutment" corresponds to a stability boundary derived from a linearized solution for the case of rotation about the double leg contact point with no shock absorber action (gravity force being the only retardant to toppling). There is an indication that very large friction coefficients will give stability boundaries which approach this "abutment" curve. This high friction characteristic is especially significant for the case of penetration and lateral motion through an extremely soft surface. Although the force resisting lateral motion would be drag rather than surface friction for the soft surface, the large lateral force would be roughly synonymous in the case of stability.

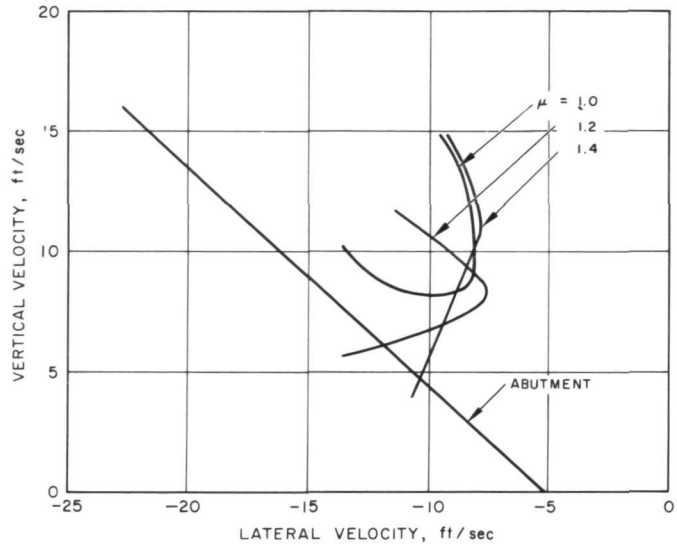

Figure 118. Effect of friction on stability boundaries 15 deg site slope

2. *Full-Scale Drop Tests (T-1)*

The scaffold for the simulated lunar landing drop tests of T-1 has been erected (Figure 119). The scaffold is 40 feet high, 20 feet wide, and 50 feet long. A track will be mounted in the center of the 20-foot span at the 40-foot height and will run the full length of 50 feet. The anti-gravity system will operate from this track and will follow the spacecraft as it travels down and/or parallel to the track exerting a constant vertical force of approximately $\frac{5}{6}$ Earth g on the test vehicle. The track itself is about two-thirds complete and ready for installation. The anti-gravity system has been tested successfully to full load capacity. The pistons and cylinders for the system have been built.

A search has begun for a landing surface material for the soft lunar surface that will offer a resistance of 10 lb/in.^{2} for 1 foot of deflection. Three materials have been screened: rubberized horsehair, wood shavings, and peat moss. The rubberized horsehair was too soft to be considered. Of the other two, peat moss appears the more promising.

A design for the hard surface landing platform has been formulated. The basic criteria for the design is that the platform shall absorb no more than 0.5% of the total energy available at T-1 impact. This criteria resulted in a requirement for extreme structural stiffness (about 900,000 lb/in.). Several construction schemes were considered and subjected to both analyses and test, including reinforced concrete designs, steel designs, various slabs supported by compacted earth, and similar schemes. The design that was finally selected on the basis of the comparative study is a platform constructed of 10 by 10 inch wooden timbers laid side by side to form a

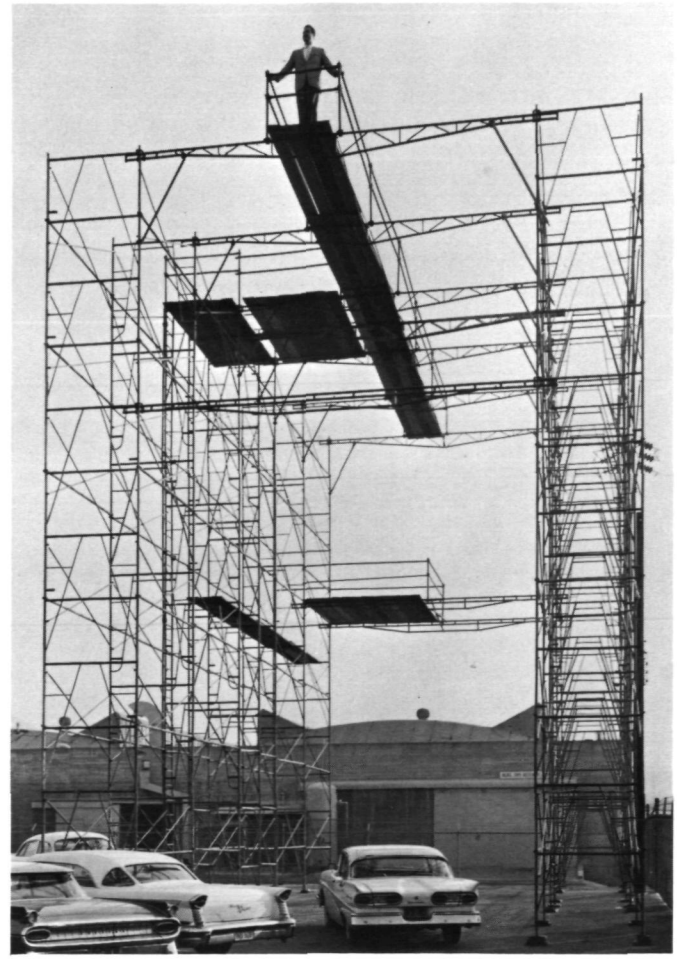

Figure 119. Scaffold for simulated lunar landing tests

solid surface. The surface will be supported on a framework utilizing 12 by 12 inch timbers as beams and columns.

a. Test facility checkout. A series of test drops of a test mass (not T-1) onto a 15 degree site slope surface will be made as a final check on the operation of the anti-gravity device. The test mass will be equipped with skids or wheels which will allow the mass to move freely down the slope. The anti-gravity cable force will be monitored and the ability of the cable to remain vertical during the motion will be observed. Final adjustments to the test apparatus will then be made as required.

b. Preliminary test plan. A preliminary test plan for the 25 scheduled drops of the T-1 vehicle has been formulated. The general categories of drops are described briefly in the following paragraphs.

Instrumentation checkout. The first drop with T-1 will be made onto a flat smooth surface to check the operation of the instrumentation and give the simplest means of a first comparison between the IBM program results and an actual drop.

Nominal landing verification. Two drops will be made at landing conditions corresponding to 3σ flight control conditions on a 15 degree site slope. These drops are for verification of expected landing stability and loads and will give situations other than extreme cases for correlation with IBM results.

Stability verification. Approximately five drops on a 15 degree rock-covered slope will be made to demonstrate toppling stability as a function of lateral and vertical velocity.

Center of gravity stability effect verification. Two drops will be made to show the change in stability resulting from a decrease in center of gravity height for the 15 degree rock-covered slope.

Soft surface stability. Approximately five drops will be made on a 15 degree slope with a very soft surface (attempting to meet the specified surface with a bearing stress of 0 psi). Since analytic solutions for this surface will be extremely difficult, the experimental investigation is felt to be necessary; the drops will also correspond to an apparent high friction coefficient.

High slope capability verification. Approximately four drops will be made onto a 25 degree rock-covered slope to show the steep slope capability compared with the drops on a 15 degree rock-covered slope.

Soft surface high velocity impact. Two drops will be made onto the 15 degree slope with a soft surface to show penetration and loading characteristics for a 20 ft/sec landing.

Maximum load verification. Two drops will be made onto the 15 degree rock-covered slope in order to verify the worst loading conditions.

Three-dimensional stability. Two drops will be made onto the 15 degree rock-covered slope with a cross-hill lateral velocity component to demonstrate three-dimensional stability.

3. Crushable Block Tests

At the present time, developmental tests are being performed on the aluminum honeycomb material to be used for the crushable blocks. Static crushing stress tests have been completed on a flat (0 degree) impact surface for a temperature range of −100 to 300° F. The results (Table 10) indicate a decrease in crushing stress with increasing temperature. Between −100°F and room temperature, the crushing stress is fairly constant; it then begins to drop off with temperature until at 200° F the stress is about 80% of maximum. The block material for these tests was 5052 aluminum with a 0.001 inch foil thickness and ⅜ inch cells.

From the results of these tests and other considerations, the present block configuration has been determined. The configuration is a modified hexagon, approximately

Table 10. Honeycomb block crushing test results

Specimen	Number of cells	Temperature, °F	Crushing Velocity, in./min	Average crushing load, lb
1	264	70	0.2	1760
2	264	70	0.2	1775
3	264	70	0.2	1750
16	264	70	20.	1750
17	264	300	20.	1210
18	264	300	20.	1350
19	248	200	20.	1550
20	264	200	20.	1550
21	264	200	20.	1450
22	264	300	20.	1375
23	264	−100	20.	1890
24	264	−100	20.	1950
25	264	−50	20.	1940
26	264	−50	20.	1960
27	409	70	20.	2770

8 inches across the faces, precrushed slightly to alleviate the very high initial crushing stress. On the precrushed surface there will be a thin sheet of corrugated aluminum designed to provide a large bearing surface for landing on a very soft surface, while still providing means for trapped air to escape from the cells during the boost phase.

Other testing in progress or planned includes dynamic crushing at impact velocities of 15 and 30 ft/sec on surfaces with the impact slope varying up to 40 degrees and tests to determine the effect of vacuum on the crushing stress, the variation of crushing stress with angle of applied load, and the effects of friction coefficient.

4. Shock Absorber Development

The definitive subcontract with the National Water Lift Company (NWL) of Kalamazoo, Michigan, has been finalized. The construction of the test modification prototype models to be used on T-1 and S-2 is near completion, and performance testing will start the latter part of December. Present indications are that the units will be delivered as scheduled early in January.

Extensive development has been carried out to date. Immediately on selection of basic shaft and seal dimensions, a seal leakage test device (Fig 120) was built. The silicon fluid in the cylinder is under specified preload conditions, and the seal is identical to that which will be used in flight models. This test duplicates storage conditions and will have been in progress for almost 2 years at the time of the SC-1 launch. The setup is kept in a temperature-controlled room, since temperature variation of the measuring tube will indicate a change in volume. After approximately 2 months, there has been no apparent leakage.

Evaluation of the cam detent is being performed on the development model shown in Figure 121. Minor modifications as a result of this test device have already improved the characteristics of this lock under repeated operation. The breakaway force necessary to overcome these locks has been shown to be very consistent.

A representative cylinder, piston, and metering pin assembly has been constructed for evaluation of spring and damping characteristics. Preliminary testing was conducted with the assembly unplated. It was found that plating was definitely required, so the unit has been plated and is ready for retest.

A representative seal fixture has been constructed which will be subjected to repeated heat sterilization

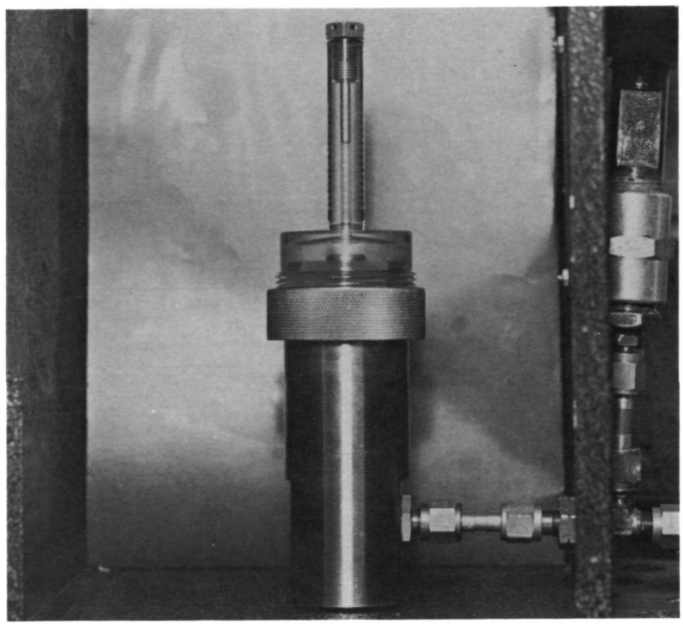

Figure 120. Leakage test of shock absorber seal

cycles to determine the degree of degradation of seals and silicon fluid from this process. This development test will be followed by sterilization type approval tests of prototype units.

Test fixtures necessary for the performance testing of the T-1 and S-2 shock absorbers are nearly completed. Hughes personnel will be present for the performance acceptance tests.

The spring-bellows temperature compensator shown in *Space Programs Summary No. 37-12* has been found to be undesirable. Pressurized gas is now planned as the means of maintaining a constant preload. A free-floating piston will be used to separate the gas and silicon fluid in the test modification prototype models. However, a light bellows will be used as a separating membrane on the flight models to eliminate the possibility of gas and fluid intermixing past elastomeric seals. The major design problem remaining is the construction of the tapered titanium tube. A tube which is rolled and fusion-welded prior to heat treatment is now undergoing development testing.

5. Structural Criteria and Loads

Several significant changes have been made in the structural design criteria since the issuance of the Preliminary Structural Criteria and Loads document described in *SPS 37-12*. Margins of safety for extremely rare landing conditions have been reduced from 0 on yield

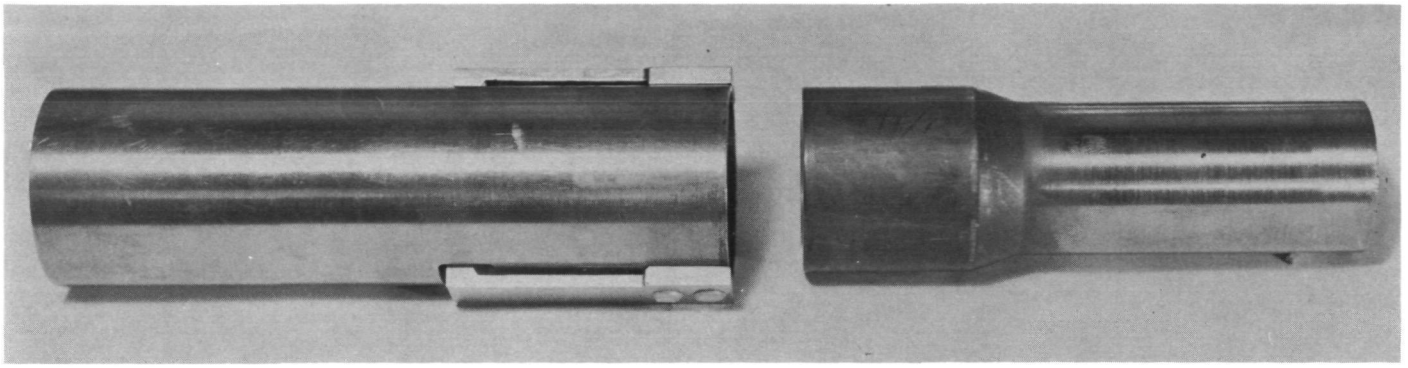

Figure 121. Testing of shock absorber cam detent

strength and 25% on ultimate strength to no requirement on yield and 10% on ultimate. Extremely rare conditions are those in which the probability of occurrence is less than the 5σ levels of normally distributed events. In addition, MIL-HDBK-5 "B" material strength values may be used in place of "A" values, inasmuch as "B" values lie close to the 3σ values with 90% confidence, the operating norm for *Surveyor* reliability analyses. Both these changes permit designs of lower weight than could be realized by the original requirements.

In order to avoid unnecessary weight penalties arising from uncertainties in internal or external load estimation or stress analysis, a policy was adopted to design the spaceframe and attachment bracketry for the structural type approval test vehicle to 85% of the loads presented in the criteria document. In order to prove the "low weight" spacecraft adequate for 100% of the loads, S-2 will be subjected to 100% of the externally applied loads. Should it prove adequate, dynamic response, internal loads, and stress analysis will be revised to show this adequacy. Should it prove inadequate, only the failing parts need be strengthened. In this way, unnecessary structural weight will be eliminated from flight spacecraft.

Computer Engineering Associates has satisfactorily completed Phase I of their analog computer studies of the dynamic response of the spacecraft. They are presently proceeding with Phase II according to a work statement which was modified to take account of the results of Phase I. The modifications involve the indirect measurement of dynamic stresses in the spaceframe, direct measurement having been found to be impossible because of the complexity of the spacecraft. The work is progressing on schedule, and should be completed by January 1, 1962.

6. *Acoustic Test Plans*

Plans are presently being formulated for subjecting the S-1 vehicle to the noise field generated by a rocket engine at the Rocketdyne test facility. The primary purpose of this test is to determine structural response to acoustic excitation (about 12 channels of acceleration and strain gage data will be taken). Current scheduling is for late January or early February 1962. Component suppliers have been invited to substitute compartment prototypes for the S-1 dummy units in order to determine on a go, no-go basis the structural adequacy of their compartment designs.

7. *Lateral Vibration Test (S-1)*

The S-1 lateral vibration test was completed on November 29, 1961. Data were obtained for all configurations and mounting directions included in the detailed test plan. The configurations tested were: (1) S-1 mounted rigidly to the vibration table; (2) S-1 mounted on the shell interconnect; and (3) S-1 mounted on the shell interconnect with damping tape applied to the inside of the interconnect. Figures 122 and 123 show the S-1 test setup for the first two test configurations. The hard mount simulates input described by JPL Specification 30240, which specifies only one value of acceleration in a given direction. All three supports therefore are subjected to the same input. The second test configuration was introduced to show flexibility effects of the interconnect. Input vibration level for most S-1 tests was ¼ g rms, corresponding to about one-third the JPL Specification 30240 requirement.

Data reduction has been begun and will be completed in late December, 1961. The following information is based on data analyzed to date.

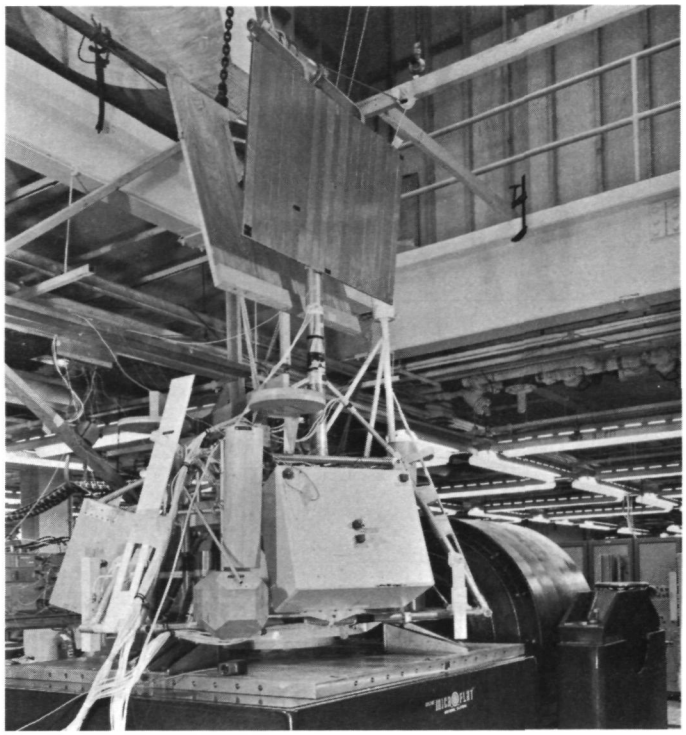

Figure 122. S-1 lateral vibration test (Configuration A-1)

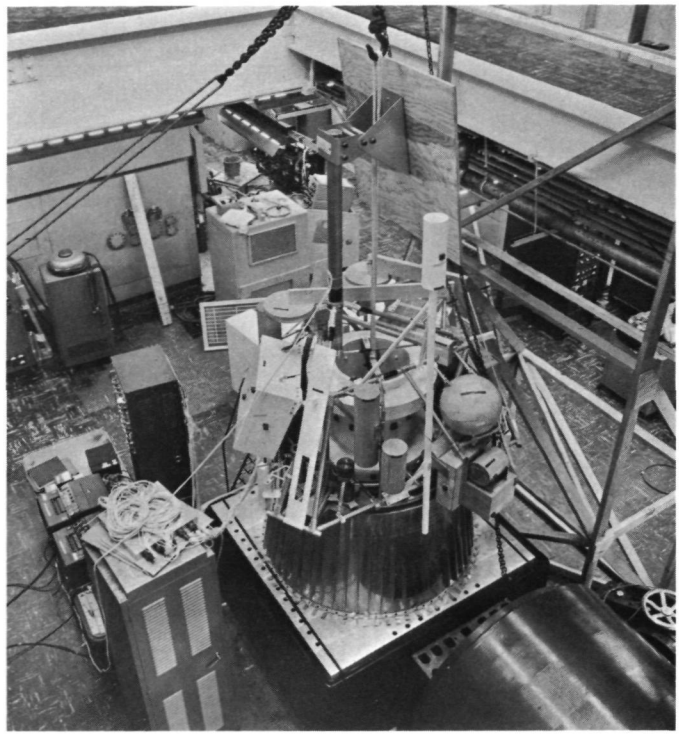

Figure 123. S-1 lateral vibration test (Configuration B-1)

Table 11 indicates the maximum amplification ratios which occurred during the hard mount tests and the frequencies at which these maxima occurred. The accelerometer locations and axis notation are defined in Figure 124.

Figure 125 shows maximum vibratory amplitude of the solar panel during resonance taken from a motion picture for the second test configuration. The panel motion has a double amplitude of 2.5 inches at the bottom and 1.8 inches at the top, for input vibration amplitude about one-third the specified value. The photograph also shows the characteristic collision between solar panel and mast. The white cylinder in the foreground is the simulated subsurface sampler. Although not of final flight design, the ballast solar panel (prototype model), antenna, and mast used for S-1 testing nevertheless provide a good simulation. The ballast hinge closely approximates the stiffness of a flight item, although motion of the hinge is restricted to one axis compared with four moving axes on the flight item. The shroud interference and mast collision condition has been eliminated by design changes made in the panel-antenna positioner assembly (see Section J).

During S-1 tests, a number of failures occurred. Welds in two mast support tubes failed early in the test program. These tubes were repaired and functioned satisfactorily thereafter. The mounting brackets for Cameras 1, 3, and 4 and an upper support tube for the helium tank also failed at welds.

The shell interconnect used in the second and third test configurations effectively eliminated all response above 40 cps. It caused some greater amplifications in the lower frequencies than appeared during tests of the first configuration.

The Scotchfoam damping tape does not seem to alter amplification at resonance. A preliminary examination of retro rocket and top of interconnect acceleration data at their resonant frequencies shows equal amplification ratios for both the second and third test configurations. These resonant frequencies occur at about 10 cps and 30 cps.

S-1 is now undergoing static structural tests, to be completed in mid-January 1962.

8. *Spaceframe Stress Analysis*

The matrix analysis program for the spaceframe has been completed and is being used currently. The solution yields axial forces, as well as bending moments and shear reactions, at the ends of the spaceframe tubes. Deflections and rotation of spaceframe joints are also obtained.

Table 11. Lateral vibration test results

Accelerometer location[a] number		Maximum magnification ratio	Frequency, cps	Direction
Retrorocket				
Center of gravity	(3)	3.0	80	A-2
Base	(4)	4.8	80	A-2
Compartment A				
Center of gravity	(6)	4.7	22	A-1
Center of gravity	(24)	4.2	22	A-5
Corner	(25)	5.9	22	A-5
Compartment B				
Center of gravity	(9)	4.4	22	A-5
Center of gravity	(26)	5.4	75	A-3
Corner	(27)	5.3	75	A-3
Antenna ring				
Parallel x axis	(12)	16.2	8	A-6
Parallel y axis	(13)	27.0	8	A-4
Drill motor				
Parallel x axis	(14)	12.5	12	A-2
Parallel y axis	(15)	10.9	9	A-1
Control sensor				
Center of gravity	(30)	6.3	19	A-1
Center of gravity	(29)	3.5	19	A-2
Corner	(28)	4.8	19	A-2
Soil analysis				
Center of gravity	(33)	1.7	85	A-2
Center of gravity (top)	(31)	6.9	100	A-1
Center of gravity (bottom)	(32)	11.6	100	A-1

[a]See Figure 124 for location and axis notation.

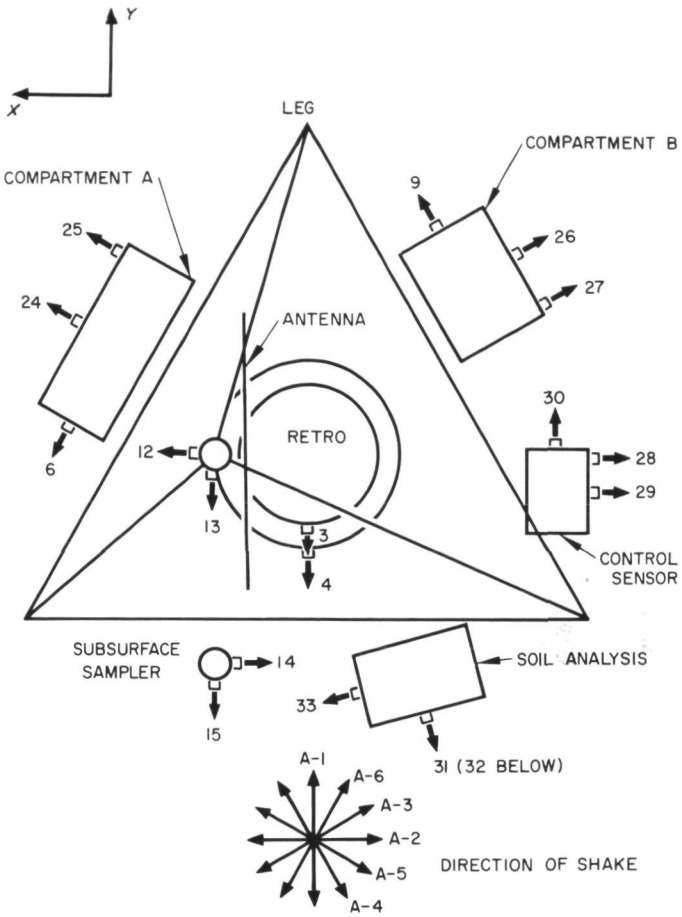

Figure 124. Axis notation and accelerometer locations (with channel numbers) for vibration testing

The design condition of lunar landing has been investigated, and some spaceframe tubes were found to be critical. In order to rectify this situation, two types of change are being investigated: (1) support bracket attach points for the heaviest units are being moved closer to spaceframe joints where possible in order to minimize beam-column bending stresses; (2) additional stiffening members are being added to reduce the effective column length of the longer spaceframe members. One portion of the matrix program is being streamlined to make the program more efficient in handling larger size problems.

In order to make the analysis more realistic, provision has been made to include beam-column effects by changing certain coefficients in the matrices. The solution also has been modified to account for variable moment of inertia of spaceframe members. The flexibility matrix is being computed for use in dynamic response studies.

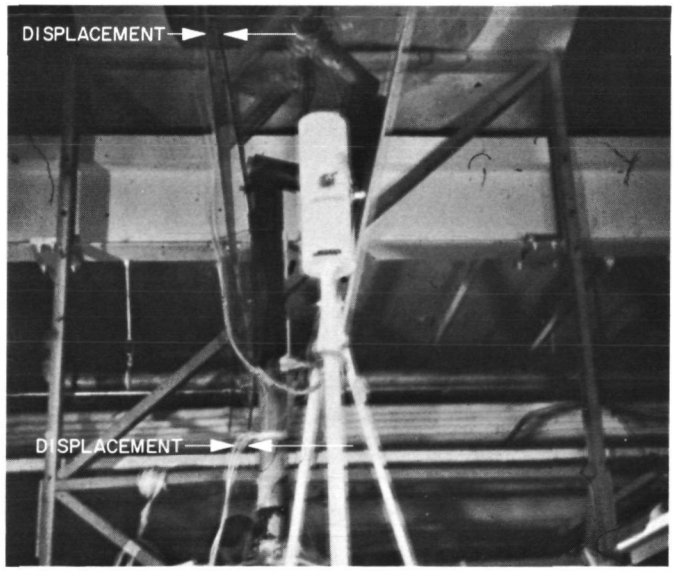

Figure 125. Maximum vibration excursion at 7 cps, shown by superposition of two motion picture frames

Table 12. Summary of tensile test results for 7178-T6 aluminum alloy sheet specimens

Group	Ultimate tensile stress, psi	Number of specimens	Test temperature, °F	Stress concentration	Exposure prior to test	
					257 °F for 24 Hours	10^{-4} mm Hg for 24 Hours
Sheet No. 1						
A	91100	6	−50	No		
B	89000	6	−50	Yes		
Sheet No. 2						
C	85900	3	68	Yes		
D	88200	3	−50	Yes		
E	86100	3	68	Yes		X
F	89400	3	−50	Yes		X
G	86900	3	68	Yes	X	
H	89100	3	−50	Yes	X	
I	87200	3	68	Yes	X	X
J	89700	3	−50	Yes	X	X

The problem as a whole can be formulated matrically as:

$$\begin{bmatrix} M_1 & M_{12}^T \\ M_{12} & M_2 \end{bmatrix} \begin{bmatrix} \delta \\ \theta \end{bmatrix} = \begin{bmatrix} P_{ext} \\ M_{ext} \end{bmatrix}$$

where M_1 is the stiffness matrix of framework assuming pinned ends, M_2 is stiffness matrix of the framework for fixed ends, and M_{12} and M_{12}^T are interaction matrices. However, each part can be treated separately and corrected for interaction. Thus,

$$M_1 \delta = P_{ext} + \Delta P_{ext}$$

$$M_2 \theta = M_{ext} + \Delta M_{ext}$$

The corrections are introduced as equivalent loads or moments.

9. Material Properties Tests

Table 12 summarizes the tensile strength values obtained from static strength tests of 36 specimens of 7178-T6 aluminum alloy, chosen as the primary structural material for the spaceframe. As indicated in the table, the specimens were exposed to various combinations of a hard vacuum and a simulated sterilization temperature prior to testing.

The test section of the specimens was 0.5 inch wide and 0.064 inch thick, and round holes were drilled in most of the specimens to simulate rivet holes. All specimens were then tested to failure at room temperature or at −50°F. Although addition of the hole caused a slight decrease in tensile strength at −50°F, all specimens tested at −50°F showed a greater ultimate strength than those tested at room temperature. Neither the exposure to a hard vacuum nor exposure to sterilization temperature had a measurable effect on strength. Elongation remained unchanged from room temperature to −50°F. Apparently the large static strength degradation in 7178-T6 referred to in a test report by General Dynamics, Astronautics Division, occurs only in the presence of large stress concentration factors, on the order of 6.

Impact tests of 7178-T6 specimens at −50°F are currently being prepared. On satisfactory completion of all static and impact tests at −50°F, full-scale tests of typical spaceframe tubes will be performed in order to obtain statistical strength information for 7178-T6 tubing, which will permit more refinement in design and analysis. These tests will encompass a range of loading including bending, torsion, column, combined beam-column, and fatigue of riveted joints.

I. Propulsion

1. Introduction

The spacecraft mid-course correction, attitude control during main retro operation, and incremental velocity corrections are accomplished by a liquid bipropellant

vernier propulsion system. Main spacecraft deceleration during the terminal phase of flight is performed by a spherical solid propellant retro-rocket engine. Development of the vernier system and the main retro-engine has been subcontracted to the Reaction Motors Division (RMD) and the Elkton Division, respectively, of Thiokol Chemical Corporation.

2. Progress Summary

Outline and mounting drawings for all propulsion components were released for integration into the spacecraft.

Design of the flight-type vernier system has been completed, and testing has started on flight components. Initial tests were completed on the vernier system throttle valve; it exhibited excellent repeatability and response characteristics. Performance of the thrust chamber has been below specification limits; however, recent testing of improved chambers has demonstrated considerable improvement in this area.

Two firings of the main retro-engine were made during the report period. In the first test cracking of the propellant grain produced an unacceptable pressure characteristic and nozzle erosion was excessive. For the second test, both head-end and aft-end stress relief boots were used to reduce thermal stresses in the grain, and this engine was temperature-cycled and fired with no evidence of grain cracking. A section of pyrolytic graphite was placed at the throat of the nozzle to reduce erosion. Portions of the insert were dislodged during the firing, but total failure of the insert did not occur until so late in the firing that ballistic performance was not adversely affected. Although the results of this most recent test firing were satisfactory from the viewpoint of the grain withstanding thermal stresses, the total experience from the five engines cast to date indicates that additional modification or environmental constraints may be required to achieve the desired reliability for the flight unit. The recent requirement for 17 pounds less propellant in the main retro-engine can be accomplished without hardware change, simply by loading less propellant (shortening the grain at the aft end), although the full 17-pound saving may not be realized because of possible need for increased insulation material.

3. Main Retro-Rocket Engine

Five main retro-rocket engines have now been cast as part of the "heavy-wall" phase of the development program. Since the initiation of testing on August 25, 1961, three engines have been fired, the most recent on December 6, 1961. Of the two remaining engines, one was thermocoupled for evaluating environmental temperature-time histories and the other was rejected because of excessive cracking during thermal cycling. Two of the three engines fired were defective in that either the propellant had cracked or separated from the rocket case. The third engine, having stress relieving boots in both the head and aft ends of the case, did not display these defects on temperature cycling. Further evaluation will be required to determine whether the design modifications incorporated in the third engine fired are entirely adequate. Design of the flight configuration rocket engine has been completed and fabrication of components initiated. Fabrication of the altitude test facility and the horizontal test stand is nearing completion.

a. Rocket engine testing. Engine No. 2 was conditioned to 20°F and fired at sea level conditions on October 16, 1961. This heavy-wall engine contained the 5.4-inch separation boot in the aft hemisphere as previously reported. The separation boot did not provide the desired stress relief to the propellant grain under 20° F temperature conditioning. The propellant cracked at a single point during conditioning at the junction of the star valley and the pyrogen port. The location of cracking in engine No. 2, as well as in engine No. 3, is shown in Figure 126. The propellant crack and the space between the separation boot and the case insulation were filled with an epoxy-polysulfide material at 70°F. The engine was conditioned to the 20°F and fired using only the graphite section of the attitude-type nozzle. The results, shown in Figure 127, indicated that additional propellant surface had been exposed. It was concluded that the increase in burning surface resulted from a propellant separation in the forward hemisphere. Analysis of the effect of such a separation on chamber pressure and the post-firing condition of the engine case (hot spots) substantiated the conclusion.

Based on the performance of the second engine, two additional engines, 3 and 3A, were cast using larger separation boots to relieve the stresses in the propellant grain. (Figure 128.) Both engines employed a larger aft separation boot and an additional boot was installed in the forward hemisphere of engine No. 3A. Each engine was subjected to temperature cycling between the limits of 110°F and 20°F. Propellant cracking occurred in engine No. 3 at the juncture of the star valley and the pyrogen port during the first conditioning cycle at 20°F. Cracking of the grain continued during the second temperature cycle. Engine No. 3 was therefore rejected without static testing. Engine No. 3A was successively conditioned to 70°F, 110°F, and 20°F prior to firing at

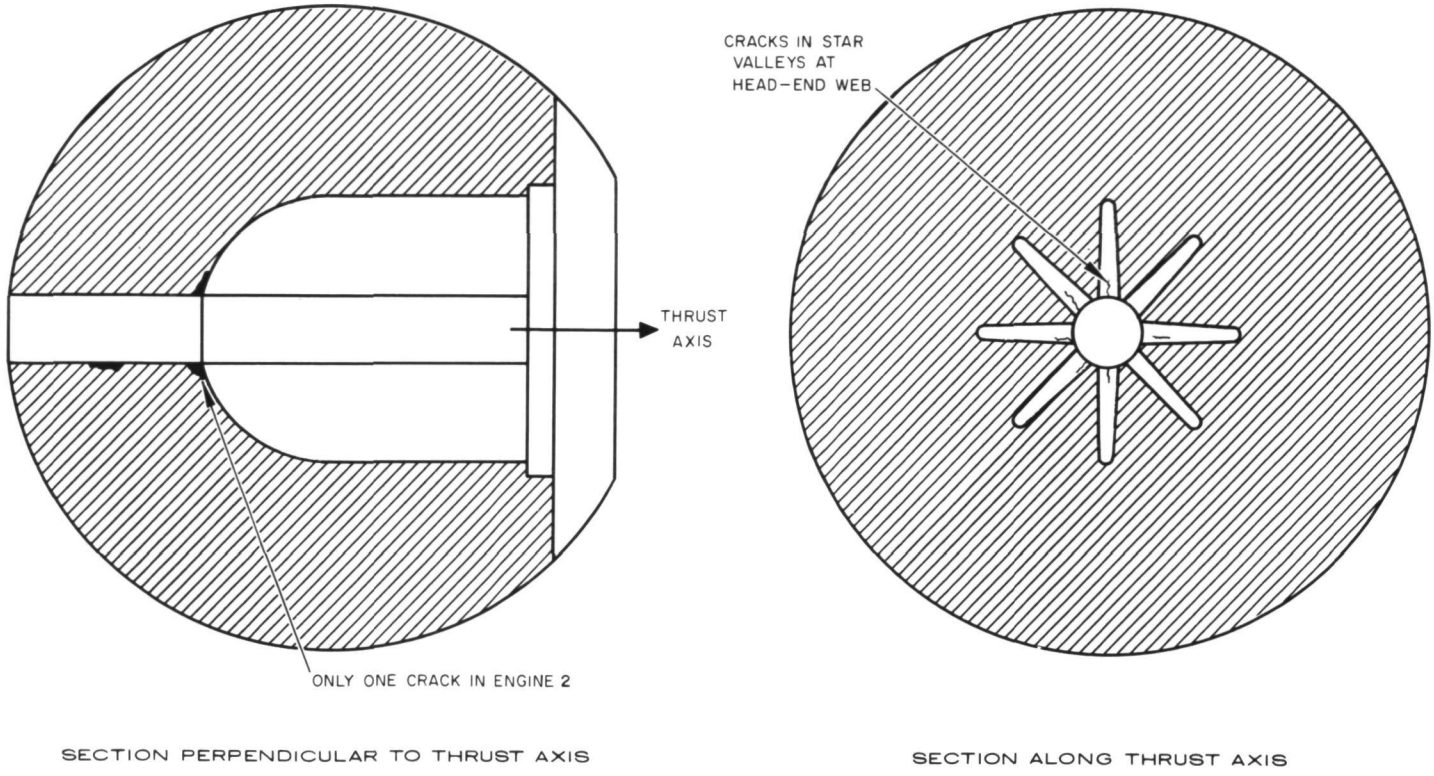

Figure 126. Propellant crack locations in Engines 2 and 3

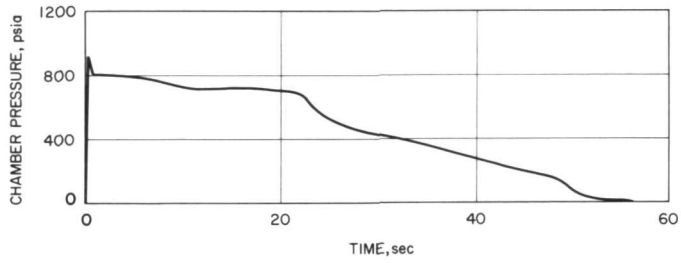

Figure 127. Performance of Engine 2

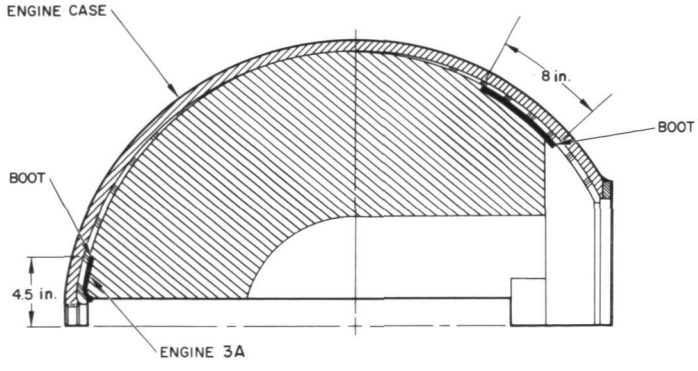

Figure 128. Stress relief boots in Engines 3 and 3A

70° on December 6, 1961. Based on preliminary test data, the operation of engine No. 3A was satisfactory.

Temperature cycling of the thermocoupled engine was instrumental in determining the extent of the propellant cracking problem. The engine was cast without a separation boot and was subjected to temperature cycling, primarily to obtain information for use in thermal analysis. The aft propellant surface separated from the insulation in a manner similar to that in engine No. 2. Subsequent conditioning to 20°F resulted in an increase in the separation to a depth of approximately 10 to 15 inches. The separation was filled with liner material and temperature cycling resumed. The temperature cycling program on the thermocoupled engine has been completed and now the engine is being subjected to the heat sterilization environment (257°F) to establish the temperature-time history required for thermal sterilization of flight engines.

b. Flight-weight case. Design of the flight-weight case and attachment fittings has been completed. Forgings for the case hemispheres have been received and the thin-wall spherical case is being fabricated. Completion of the first flight-weight case assembly is anticipated in early January.

c. Case insulation. An asbestos-filled buna-N rubber (Gen-Gard V-44) has been selected for use in the main retro-rocket engine for case insulation. The insulation material demonstrated acceptable performance with engine No. 3A and offers a distinct weight saving for the flight-type rocket engine.

d. Nozzle. The flight-type nozzle design has been completed. Fabrication is nearing completion on the initial nozzles for use in the altitude test program. Engine No. 3A was fired with the pyrolitic graphite throat insert shown in Figure 128. Although there was excessive spalling of the insert during the test, the pressure trace indicated that the required throat area was maintained throughout the firing. An alternate throat insert of tungsten-molybdenum has been designed and is also shown in Figure 129. The pyrolytic graphite insert offers a weight advantage over the tungsten insert, but selection of either configuration will depend on future test results.

e. Propellant development. Minor adjustments have been made to the PBAA propellant formulation to obtain optimum physical properties for the rocket engine. Samples of the propellant have been subjected to heat sterilization with negligible degradation of physical properties. Although present information is inconclusive, there is some evidence that the propellant is sterile in the cast and cured condition. A detailed investigation of self-sterilization capability is in progress.

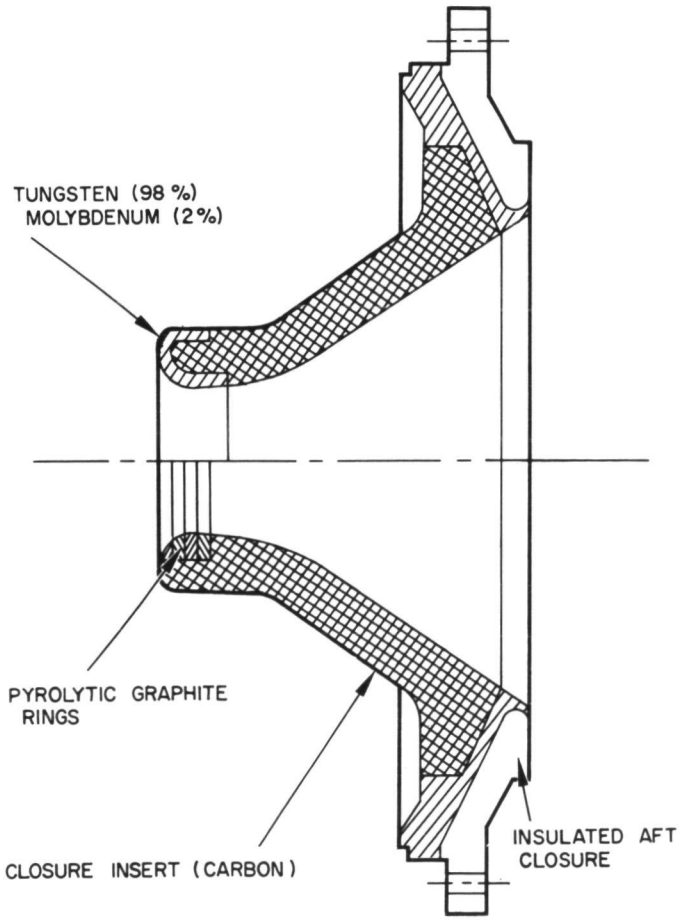

Figure 129. Alternate nozzle throat designs

f. Separation boot. Separation boots have been subjected to test in engine Nos. 2, 3, and 3A. The boot configurations employed in engine No. 3A provided adequate stress relief to the propellant grain and will be fully evaluated in future tests. The material used in the separation boot is similar to the material used for the case insulation.

g. Pyrogen ignition system. The propellant surface area has been reduced in pyrogen ignition system and the pyrogen throat area increased. High ignition pressure during the first firing prompted this change. Performance of the modified pyrogen was satisfactory in the test of engine No. 3A.

h. Test facility status. The altitude test facility and horizontal thrust stand design has been completed. The Reaction Motors Division of Thiokol Chemical Corporation will fabricate the test stand and altitude facility. The facility, shown in Figure 130, provides a vacuum capability for pressure-altitude simulation at 70,000 feet which yields a sufficiently low pressure to allow the nozzle to run full. The facility will be operational in late December, 1961, and will be used for testing engine No. 4 which will have the altitude nozzle configuration.

4. Vernier Propulsion System

The vernier propulsion system consists of three thrust chambers, each of which is capable of providing any thrust level between 30 and 104 pounds on command, and the associated liquid propellant tankage and helium pressurization system. The fuel, which is used to regeneratively cool the thrust chambers, is monomethyl hydrazine. The oxidizer is nitrogen tetroxide with 10% nitric oxide added as a freezing point depressant. The system is capable of providing approximately 50,000 pound-seconds of impulse.

The major accomplishments of the report period were:

(1) Completion of significant areas of propulsion system design integration with the flight model spaceframe.

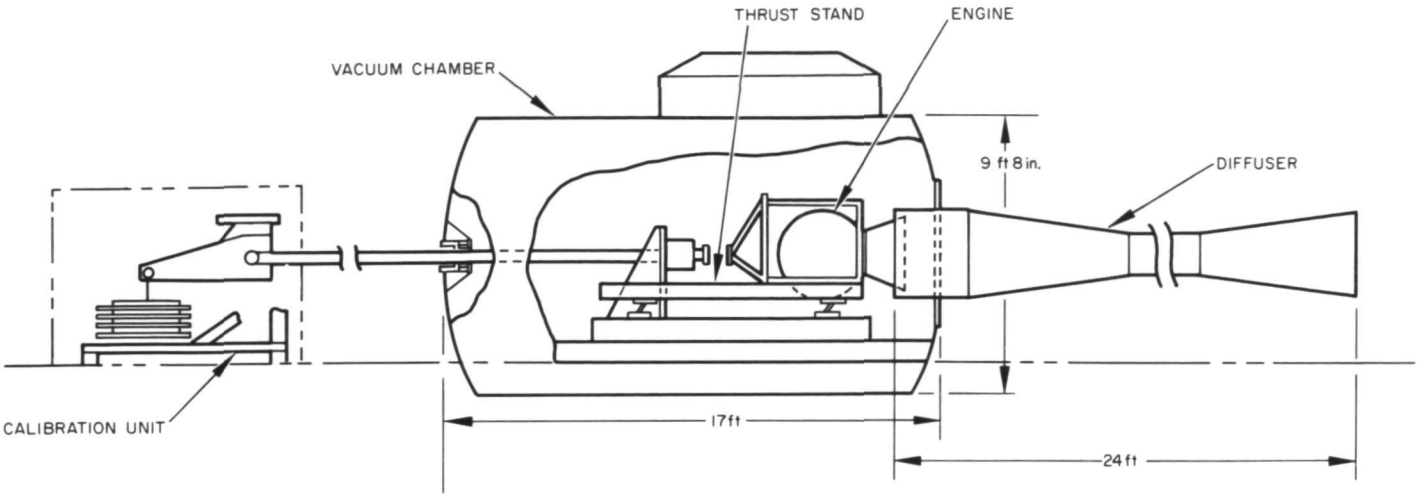

Figure 130. Altitude test facility for main retro-engine

(2) Initiation of type approval testing on the helium tank, the helium fill-release-dump valve, the throttle valve, and the propellant on-off valve.

(3) Assembly of the first complete vernier system on the test spaceframe. The following paragraphs present details of the more significant items of accomplishment.

a. Propulsion system design integration. Design of the propellant and pressurant-line routing and installation hardware, and the propellant and helium tank mounts was completed for the flight configuration spacecraft. Close coordination between the propulsion system subcontractor and Hughes Aircraft Company was maintained to derive the most efficient methods of routing and installation.

b. Thrust chamber development. Thrust chamber development in the RMD altitude test facility was initiated on September 8. Testing to date has included evaluation of the radiation-cooled flight nozzle extension, the test configuration of the flight injector, the flight nozzle throat, the test thrust chamber in conjunction with the flight throttle valve, and the flight thrust chamber assembly.

Early testing has indicated very satisfactory durability and performance of the nozzle extension. Earlier problems with the joint between the nozzle extension and the silicon carbide throat have been solved by flame-spraying molybdenum on the extension where the joint is made and grinding the deposited material to the correct dimensions.

Low performance data obtained during early testing has dictated a change in the angular relation between the oxidizer and fuel holes in the injector and a decrease in the size of the fuel holes to raise efficiency to the required value. The pressure budget has been maintained by reducing all operating chamber pressures, and the thrust has been maintained by enlarging the nozzle throat diameter. The reduction in chamber pressure was also necessitated by lack of nozzle durability at the maximum thrust level. Complete results from testing of modified thrust chambers are not yet available, but early indications show that the durability problem has been essentially solved and considerable improvements in performance have been indicated.

Testing of a heavy-duty thrust chamber in conjunction with a flight throttle valve has been accomplished with demonstration of excellent throttling response characteristics. In addition, testing has been initiated with the flight thrust chamber assembly, including the on-off valve and throttle valve, to determine response characteristics and the operating throttle range.

c. Component development. Component development progressed to the type approval phase for many of the units. The following paragraphs present the status of each component.

(1) Helium tank – Development testing has been completed and type approval testing is near completion.

(2) Helium fill-release-dump valve – Development testing has been completed and type approval testing is in progress. The valve is attached directly to the

BLADDER MATERIAL :									
TEFLON TYPE	TFE	TFE – FEP LAMINATE						FEP	
COATED (C) OR UNCOATED (U)	U	U	U	U	U	C	C	U	U
NOMINAL WALL THICKNESS, in.	0.014	0.014	0.014	0.014	0.008	0.006	0.008	0.014	0.014
SAMPLE (S) OR BLADDER (B)	S	S	S	B	B	S	B	S	S
HELIUM BACK PRESSURE, psig	37	37	57	1	300	37	300	37	57

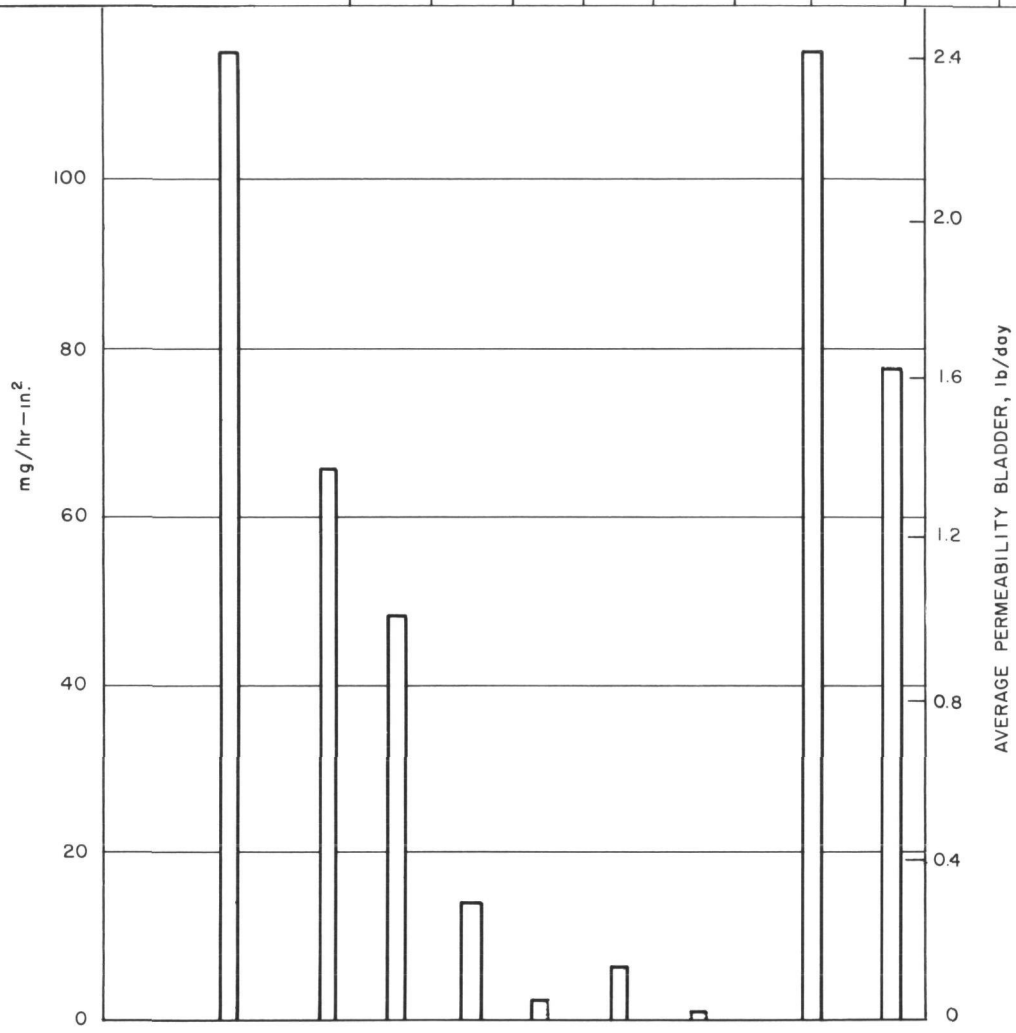

Figure 131. Permeability of propellant expulsion bladders

helium tank. Squib valves are used to activate release of helium to the propellant tankage or to dump helium overboard in case of emergency. Helium filling is accomplihed through a quick-disconnect which is integral with the helium valve.

(3) Helium-regulator-check valve-relief valve package – Development testing of the regulator section is continuing. The O-ring seal in the second stage of the regulator has been changed to a bellows seal to provide the required regulation when the entering helium gas is at a low temperature. Development has been completed on the check valve and relief valve sections and type approval testing is pending evaluation of the regulator changes noted above.

(4) Propellant tanks – Welding and X-ray inspection techniques are being finalized and type approval testing will be initiated in the next report period.

(5) Propellant expulsion bladders – An extensive program to determine permeability and durability of candidate bladder materials has been completed and evaluation of complete bladders is now in progress. Results of permeability testing to date are included in Figure 131. The tests employed the

N_2O_4/NO oxidizer in 72-hour runs at 100° F. The samples were 1.485 inch² in area. The bladders themselves have an area of 400 inch². The currently favored bladder material is FEP Teflon impregnated with a substance which reduced permeability to a very low value. The bladder is to have a wall thickness of 0.004 inch, and is expected to have a permeability of less than 0.2 pound of nitrogen tetroxide in 10 days.

(6) Propellant throttle valve — Development testing has been completed and type approval testing initiated. Results of testing to date show excellent repeatability and characteristics well within the *Surveyor* requirements (Figs 132 and 133). The throttle valve controls propellant flow by means of two

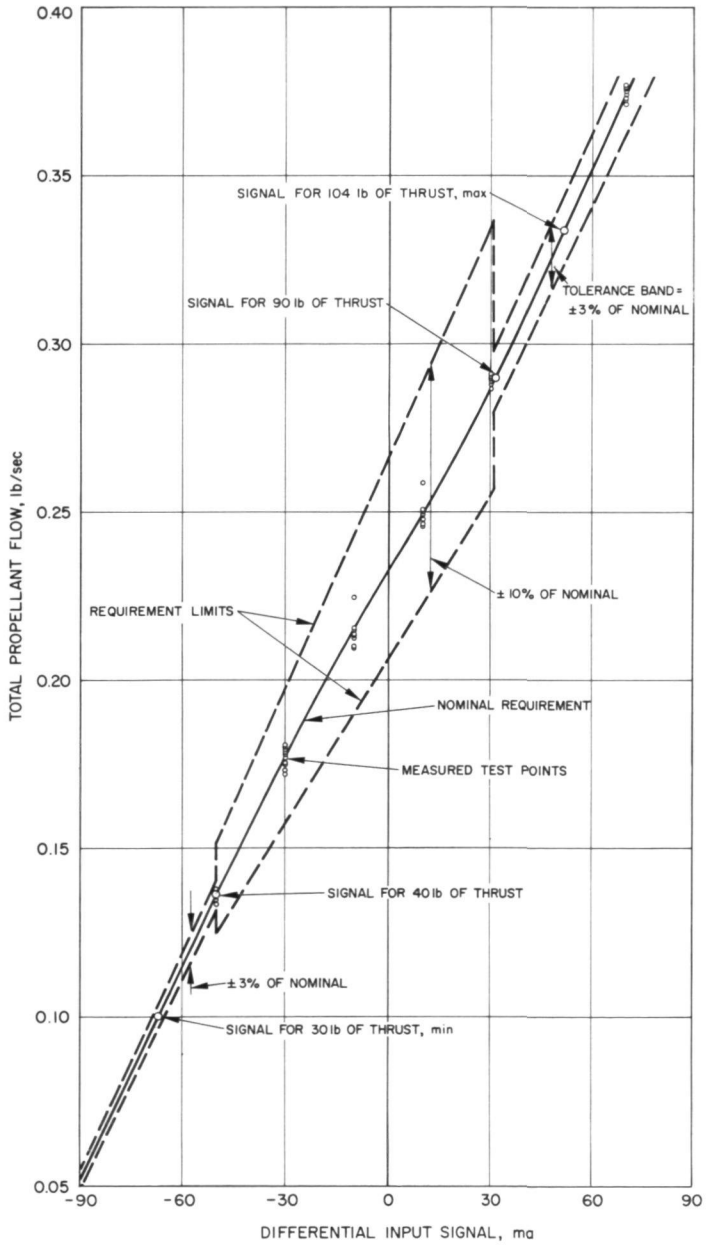

Figure 132. Propellant throttle valve flow

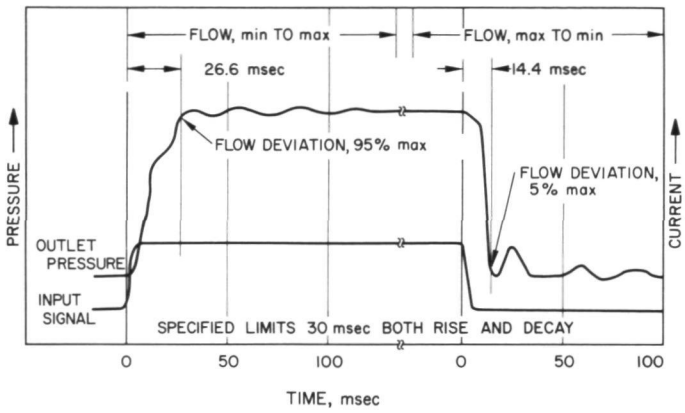

Figure 133. Propellant throttle valve response

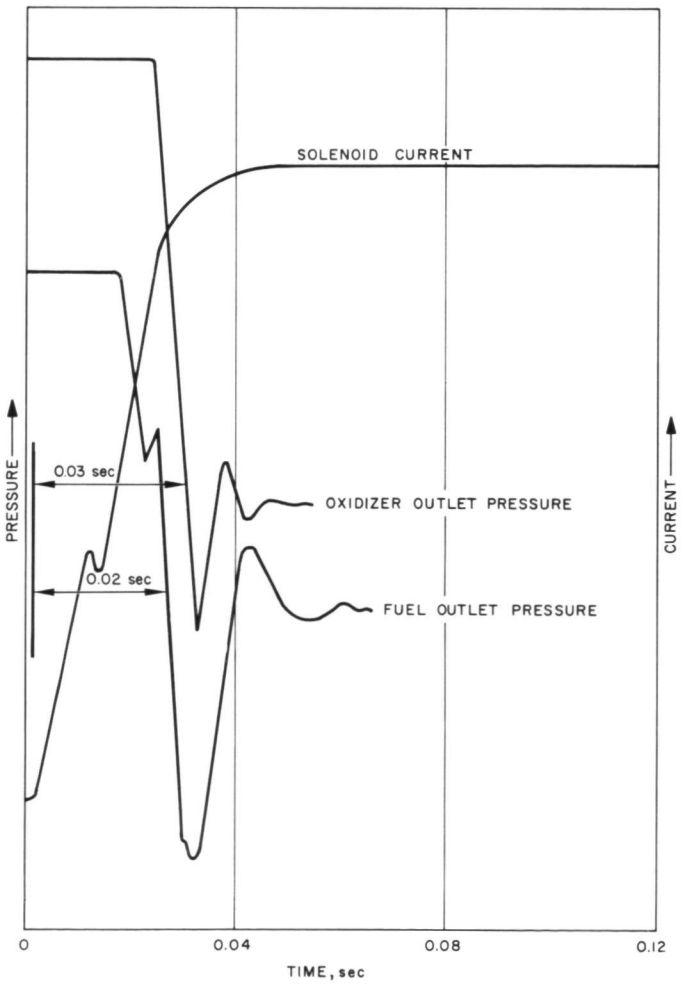

Figure 134. Propellant on-off valve opening response

reeds (operated by a single torque motor) which vary the effective orifice areas. Effects of pressure variations are controlled by spool valves, which are enclosed in the same body as the reeds and orifices.

(7) Propellant on-off valve – The on-off valve is a solenoid-piloted, helium-actuated unit which utilizes a linked-poppet arrangement to ensure proper propellant flow sequencing. Development testing has been completed and type approval testing has been initiated. Figures 134 and 135 present typical valve opening and closing response characteristics and indicate that the 75-millisecond response requirement for thrust initiation and shutdown will be met.

d. Complete system development. Assembly of the complete vernier propulsion system on the first development spaceframe has been completed and testing of this assembly is expected to begin early in the next report period. Firing tests will be accomplished in the RMD facility under pressure conditions simulating altitude in excess of 100,000 feet.

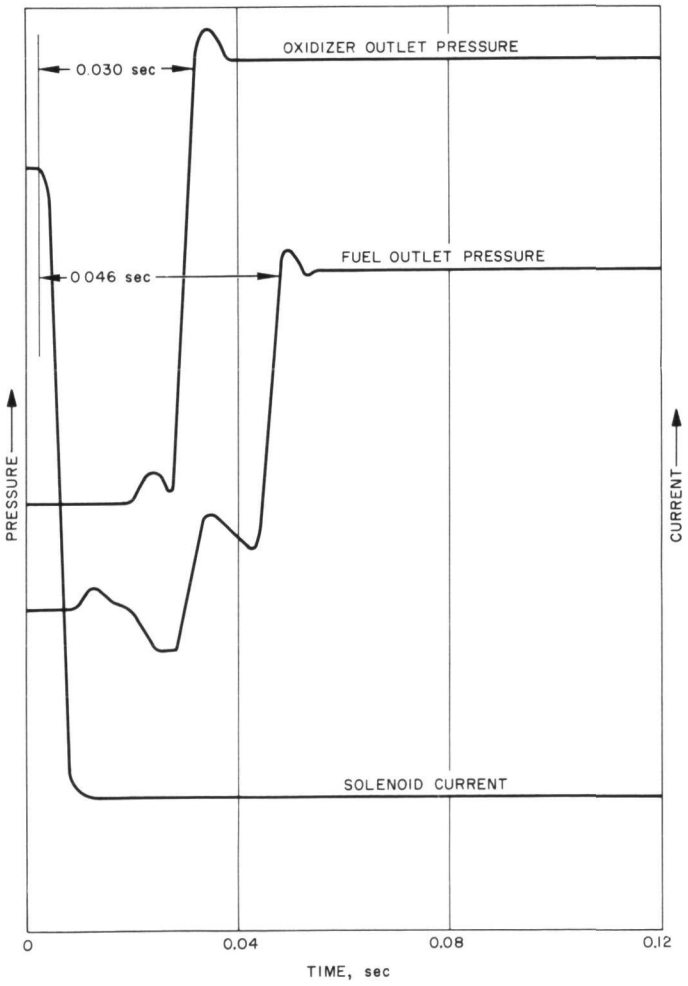

Figure 135. Propellant on-off valve closing response

e. Ground support equipment. Requirements for the ground support equipment have been finalized and negotiations for procurement are in the final stages. Approximately 20 weeks will be required for procurement and assembly of the equipment, a period which will permit sufficient time to develop the systems and train personnel in their use.

J. Spacecraft Vehicle and Mechanisms

1. Spacecraft Vehicle

a. Configuration. The final configuration of the T-4 and SC-1 spacecraft has been determined. The general arrangement is illustrated in Figure 1. Figures 136 and 137 represent this design pictorially. The significant changes which have been incorporated since the preceding report are as follows:

(1) To provide greater thermal isolation between the vernier engine and the high-resolution telescope and to facilitate the routing of the wiring harness to Compartment A, the telescope was moved to the space formerly occupied by the soil mechanics experiment.

(2) The soil mechanics experiment was then moved into the No. 1 sector near leg No. 2.

(3) Relocation of the high-resolution telescope permitted improvement in the configuration and installation of Compartment C, which houses those electronic components that are not required to operate during the lunar night. This change in turn improves thermal control of Compartments A and B.

(4) Television camera No. 3 was raised and canted outward 13½ degree to enable its use in observing the action of the surface sampler and the instruments on legs Nos. 2 and 3.

(5) The magnetic susceptibility experiment was relocated to a position on leg No. 3. This location eliminates the need for an extension boom and therefore reduces weight and complexity.

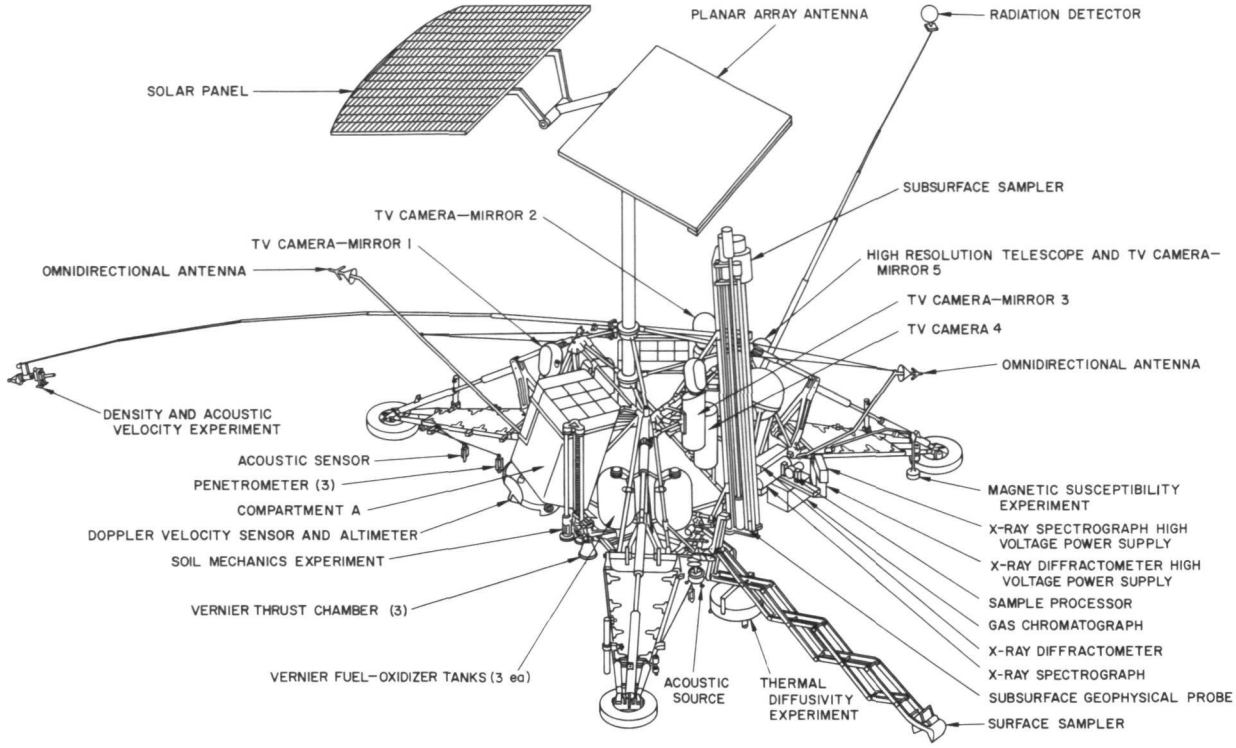

Figure 136. Spacecraft post-landing configuration

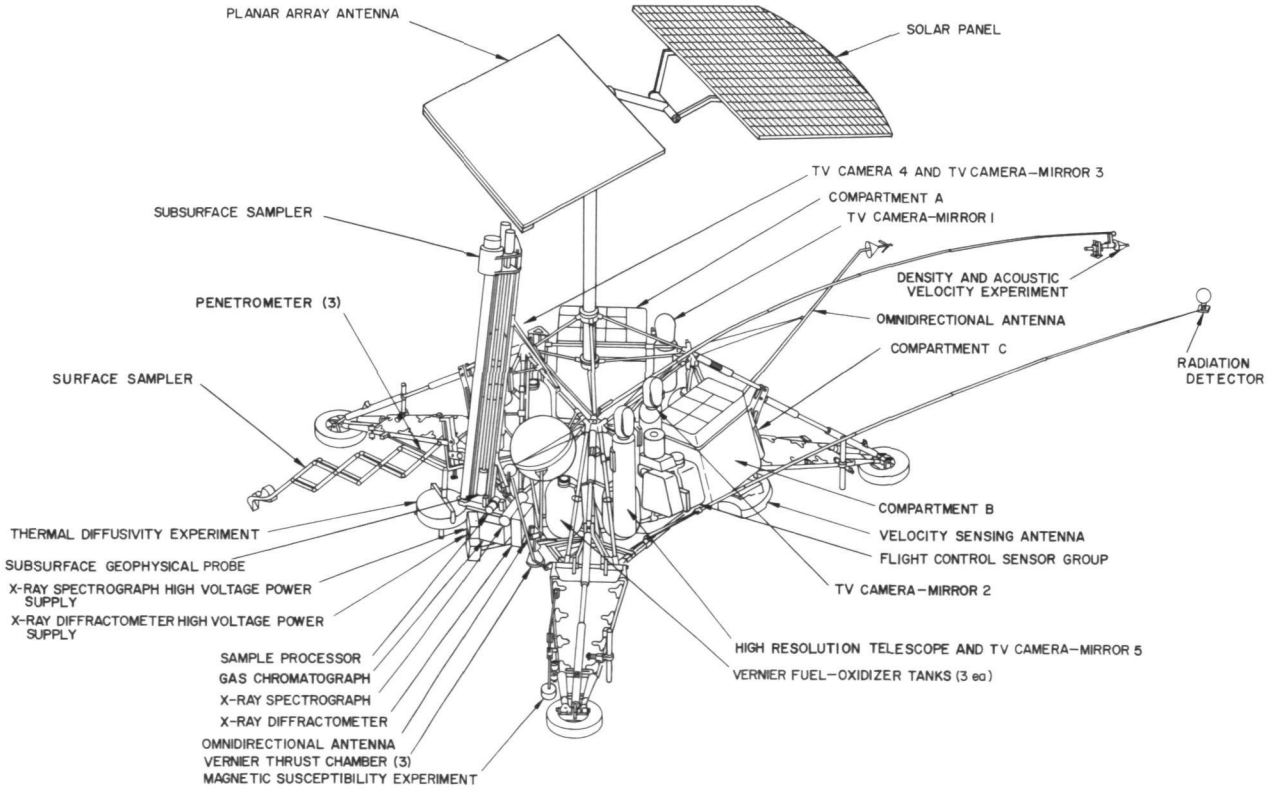

Figure 137. Spacecraft post-landing configuration

(6) Detailed results from omnidirectional antenna coverage tests on the quarter-scale model suggested an orientation change, and consequent repositioning of these antennas allows a change in the deployment method which reduces weight. The antennas are now mounted on rigid supports which swing out from the bottom member of the spaceframe (Fig 136).

(7) The previous configuration release reflected a reduction in planar array/solar panel interconnecting arm length and an attendent weight reduction of approximately 4 pounds. A new gimbal support system (described later in this section) which will further reduce weight has been adopted. This system results from modification of the previous one by motorizing the elevation motion and eliminating the declination motion. The new arrangement is shown in Figure 138.

The design of the thermally controlled Compartments A and B has now progressed sufficiently to allow release of the thermal test mockup MT-1 for fabrication. Figures 139, 140, and 141 illustrate the modular arrangement and structural details of the equipment compartments. Compartment B is smaller than Compartment A, but has the same type of construction.

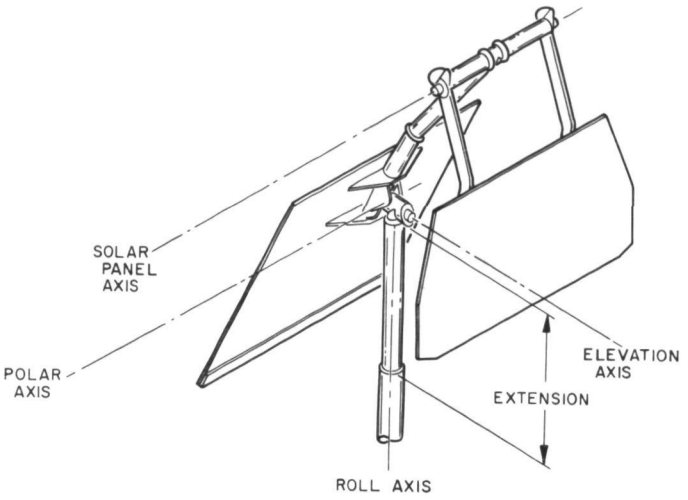

Figure 138. Planar array/solar panel assembly

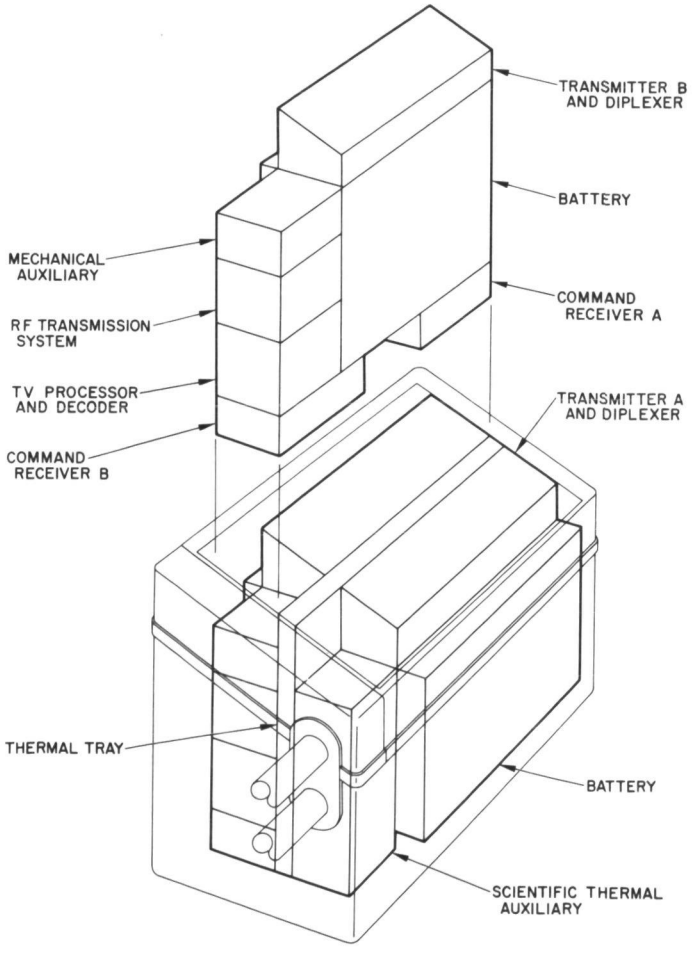

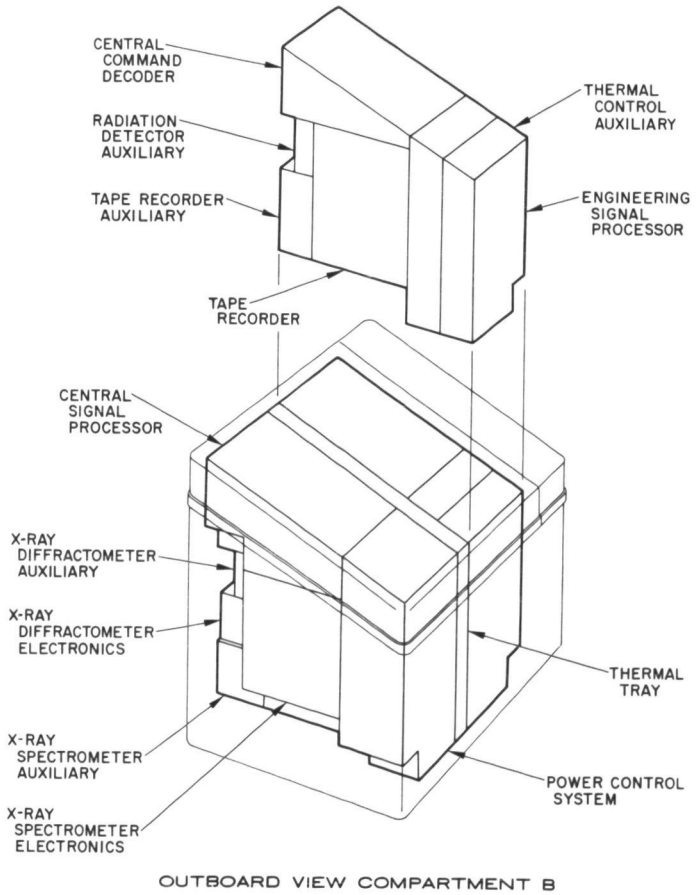

Figure 139. Compartments A and B

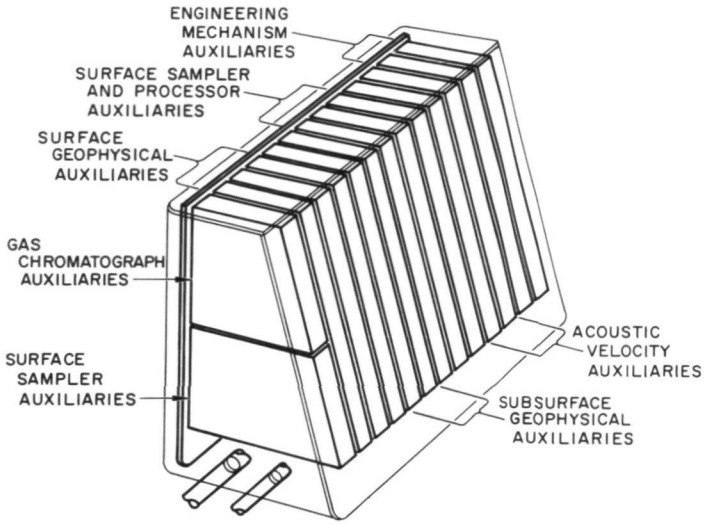

Figure 140. Compartment C

The central thermal tray on which the electronic components are mounted also constitutes the main load-carrying member. It consists of two 0.081 inch 7075 aluminum facing sheets bonded to a central honeycomb core for rigidity. The upper edge of this panel member is attached to the inner thermal switch support plate and is further stiffened by diagonal braces.

Side loads produced by the components under acceleration are carried through the upper switch support plate into the spaceframe through diagonal struts made of Fortisan-reinforced epoxy resin. These struts must serve as thermal insulators, since they bridge from the spaceframe across the mylar super-insulation (0° F inside to a — 300° F external ambient temperature during the lunar night). Vertical loads are transmitted into the lower spaceframe member through a thermal insulator pylon also made of Fortisan-reinforced epoxy resin.

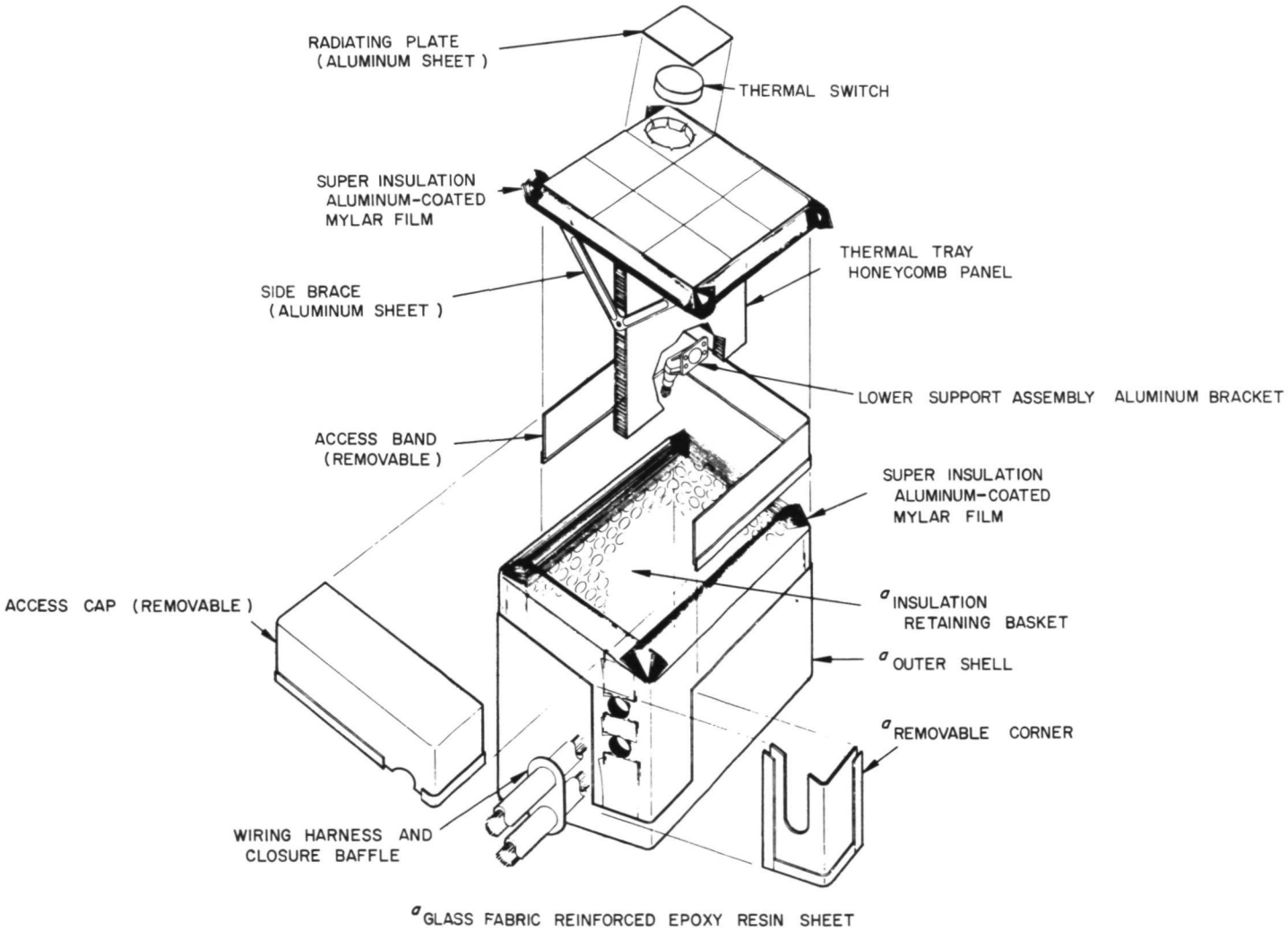

Figure 141. Construction of Compartment A

All internal heat is conducted through the thermal switches, each to its individual radiating plate.

Super-insulation consisting of layers of 0.00025 inch mylar sheet is provided between the lower thermal switch plate and the upper switch plates and in the space between the inner and outer glass-reinforced resin shells of the lower enclosure. Edges of the sheets over a reasonable length are accessible at all mating edges and at entry points for wiring and structural supports to allow for interleaving of the mylar during the assembly process. During assembly, the upper supports hold the unit while the lower cover is being installed. After assembly and interleaving, the access and retaining band is installed.

b. Wiring harness design. Additional testing of the wiring harness has included the special problem of serving the 15-foot telescoping booms. Three methods have been investigated.

One method involved the use of flat, accordion cable stowed in a magazine which allowed only one fold to be withdrawn at a time (Fig 142). Tests conducted using an actual boom which was pneumatically driven indicate that this method can be employed for instruments with electrical requirements allowing the use of flat cable. Tests are also in process on cables consisting of conventional wires for serving the booms. A third method uses flat tape cable, doubled end-to-end and wound on a reel (Fig 143). The reel is fixed to a central section of the boom. As the boom extends, the cable feeds out from the reel in opposite directions. This method appears to be highly practical, uses the minimum length and weight of cable, and employs a reel of very lightweight construction.

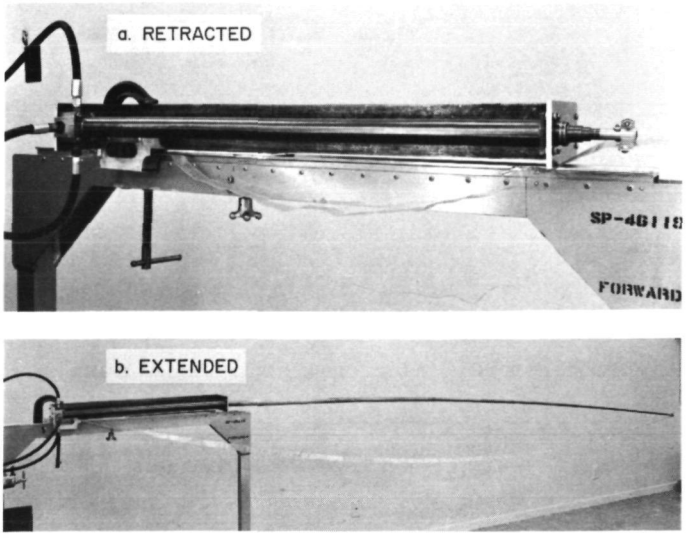

Figure 142. Tests of accordian-type boom cable

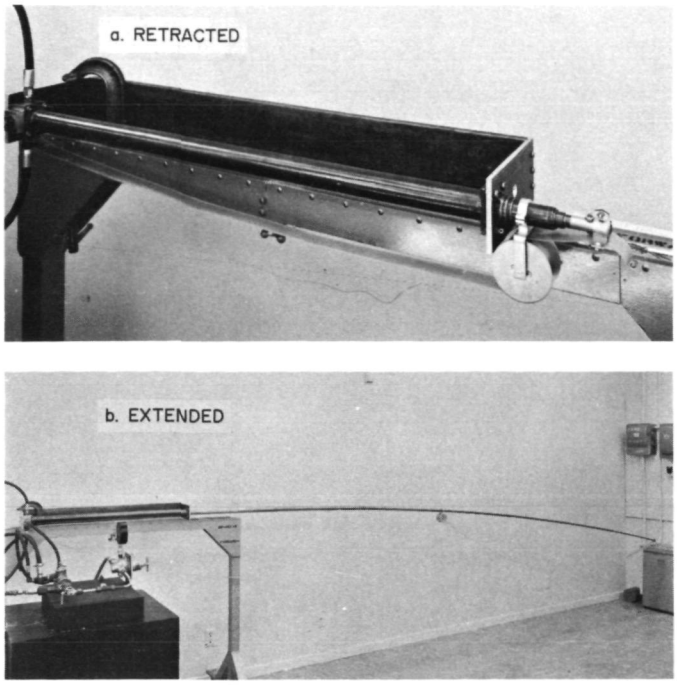

Figure 143. Tests of reel-wound boom cable

A wire type has been selected for harness use, based on a study of wire types which are compatible with the transit and lunar environment. The most promising type is a wire having conductors of Alloy 63, a thin-wall fluoroethylene propylene teflon primary insulation, and an outer coating of Surok (Dupont). Tests show that this wire (in 24-gage AWG) is superior in strength, flexing, abrasion resistance, and cold flow to 22-gage AWG copper wire with 600-volt teflon insulation. In cases where strength requirements determine the minimum wire gage (likely to be more than 50% of the total cabling), a wire weight saving of nearly 65% is estimated through use of the lighter gage wire.

c. Structures. The landing gear has been redesigned to reflect torsional load reductions at the foot joint. A weight saving of 5 pounds results from a reduction in foot pad foam density from 6 to 3 lb/ft^3.

Detailed design of scientific instrumentation attachments to the landing gear and the gear release mechanism has been completed (Figure 144).

The design of the crushable blocks, which are a part of the landing mechanical system, has been selected and is shown in Figure 145. The 5052 aluminum honeycomb block contains 409 individual $\frac{3}{8}$ inch hexagonal cells

divided by walls 0.001 inch thick. The block, which is 7 inches high by 7⅞ inches minimum distance across its hexagonal cross section, is bonded to a 5/16 inch thick aluminum honeycomb sandwich attached by six screws to the spaceframe. A phenolic-resin fiberglass cover will protect the crushable blocks from the heat of the vernier engines.

d. Special test vehicles. Spaceframes S-4 and S-5 (Fig 146) were shipped to Reaction Motors Division of Thiokol Chemical Corporation on October 11 and November 15, respectively, for vernier propulsion system tests. Drawings have been released for the fabrication of S-6, the third spaceframe, also for RMD use. Fabrication of the spaceframe for the drop test vehicle (T-1)

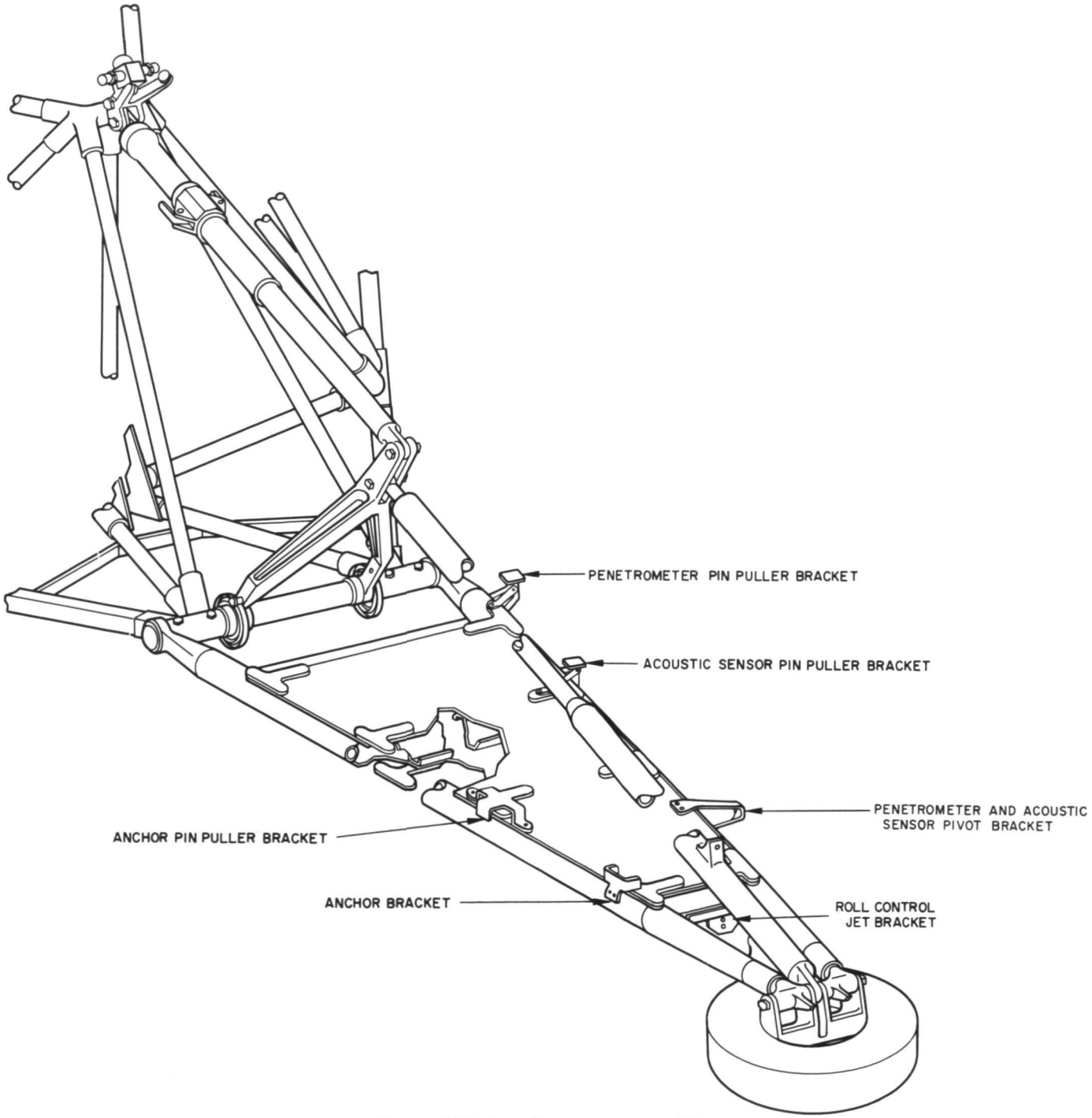

Figure 144. Landing gear assembly

is in process, and the drawings for its ballast (simulated subsystems) have been released.

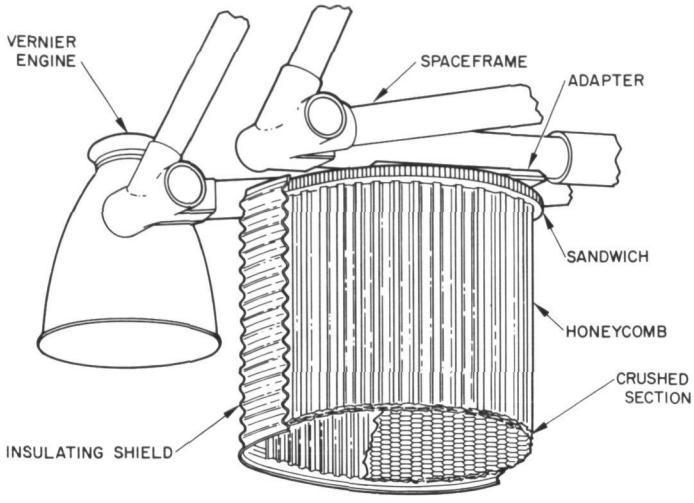

Figure 145. Crushable block in landing system

Northrop Corporation, Norair Division, has been awarded a subcontract to fabricate landing gear (exclusive of the shock strut) for test vehicles T-1, L-1, L-2, MT-1, and S-2. The full-scale antenna test model MA-2 (Fig 147) has been completed by Pacific Miniatures Company.

2. Mechanisms

a. Extension booms. Developmental models of the cold gas actuated extension booms for the omnidirectional antennas, radiation detector, and surface density experiments have been fabricated (Figs 148 through 156). A developmental test fixture for determining extension velocity, acceleration, and friction has been completed (Fig 157). 50,000 cycles of reciprocating motion of a representative boom section test specimens have been completed in a vacuum of 10^{-9} mm Hg without flaking of the molybdenum disulfide lubricant or galling of the metal surfaces. Vacuum testing to determine

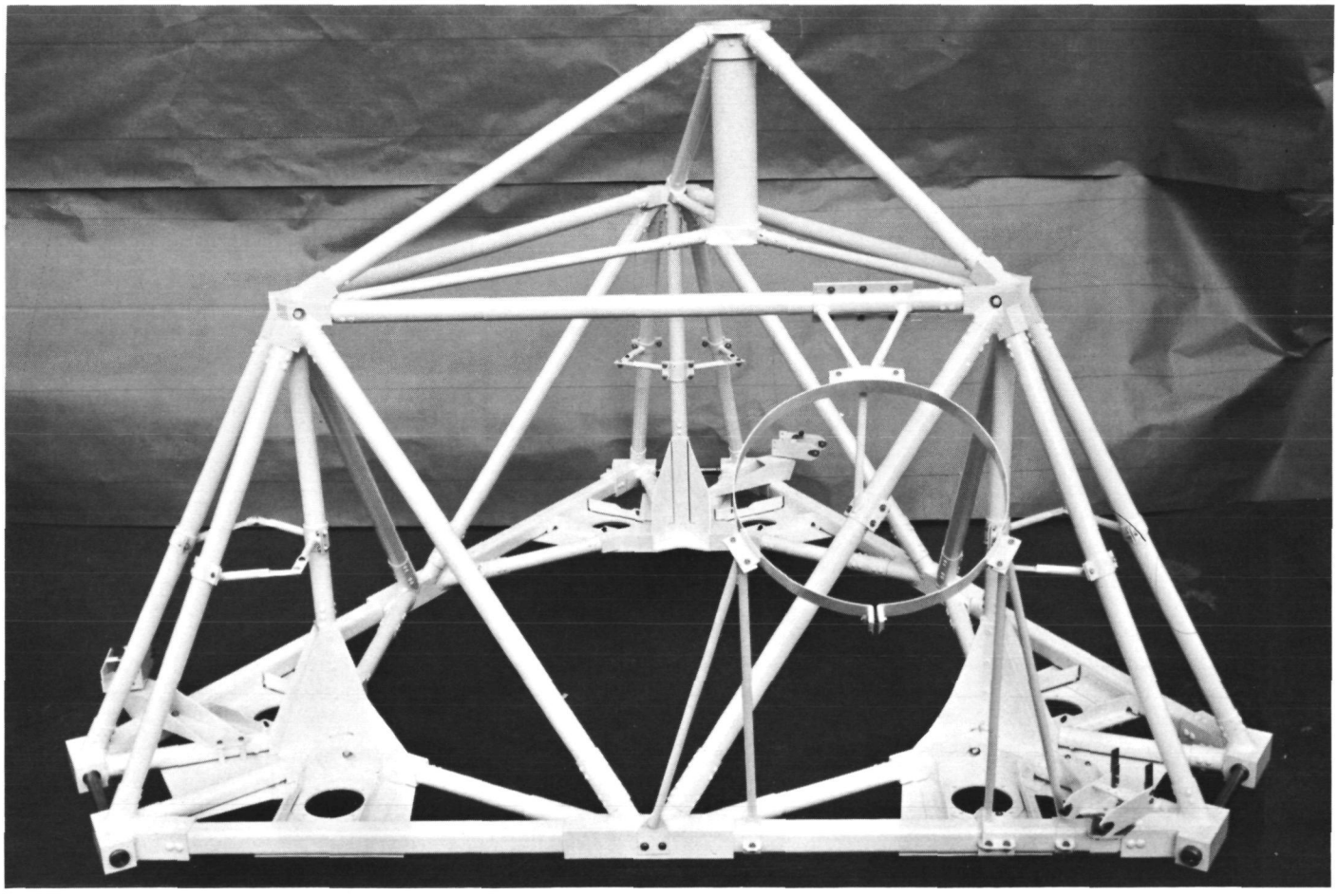

Figure 146. Test spaceframe S-5

quantitative frictional coefficient values is continuing on this dry film lubricant.

A simplified, nontelescoping boom arrangement for the omnidirectional antennas is being actively investigated in parallel with the present design. Some weight saving and reduction in complexity are offered by the new design.

b. Antenna/solar panel positioner. The high-gain antenna and solar panel positioner has been further redesigned with a substantial weight reduction. The number of controllable axes has been reduced from five to four by the elimination of the declination axis drive. The "one-shot" torsion spring drive in the elevation axis has been replaced by a controllable bidirectional drive mechanism. The geometry of the gimballing structure has also changed favorably with respect to weight and loading by lowering the solar panel hinge point, permitting a reduction in the length of the gimballed support structure. The prototype models will be built to the new design, while the developmental test model is being

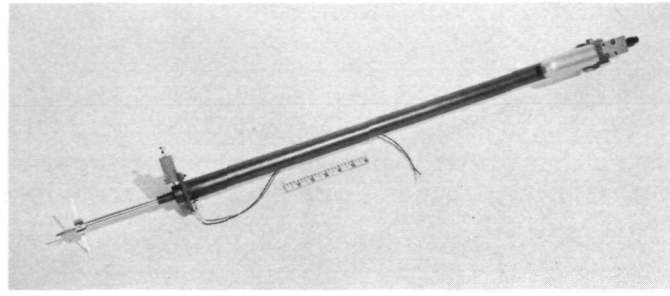

Figure 148. Omnidirectional antenna stowed

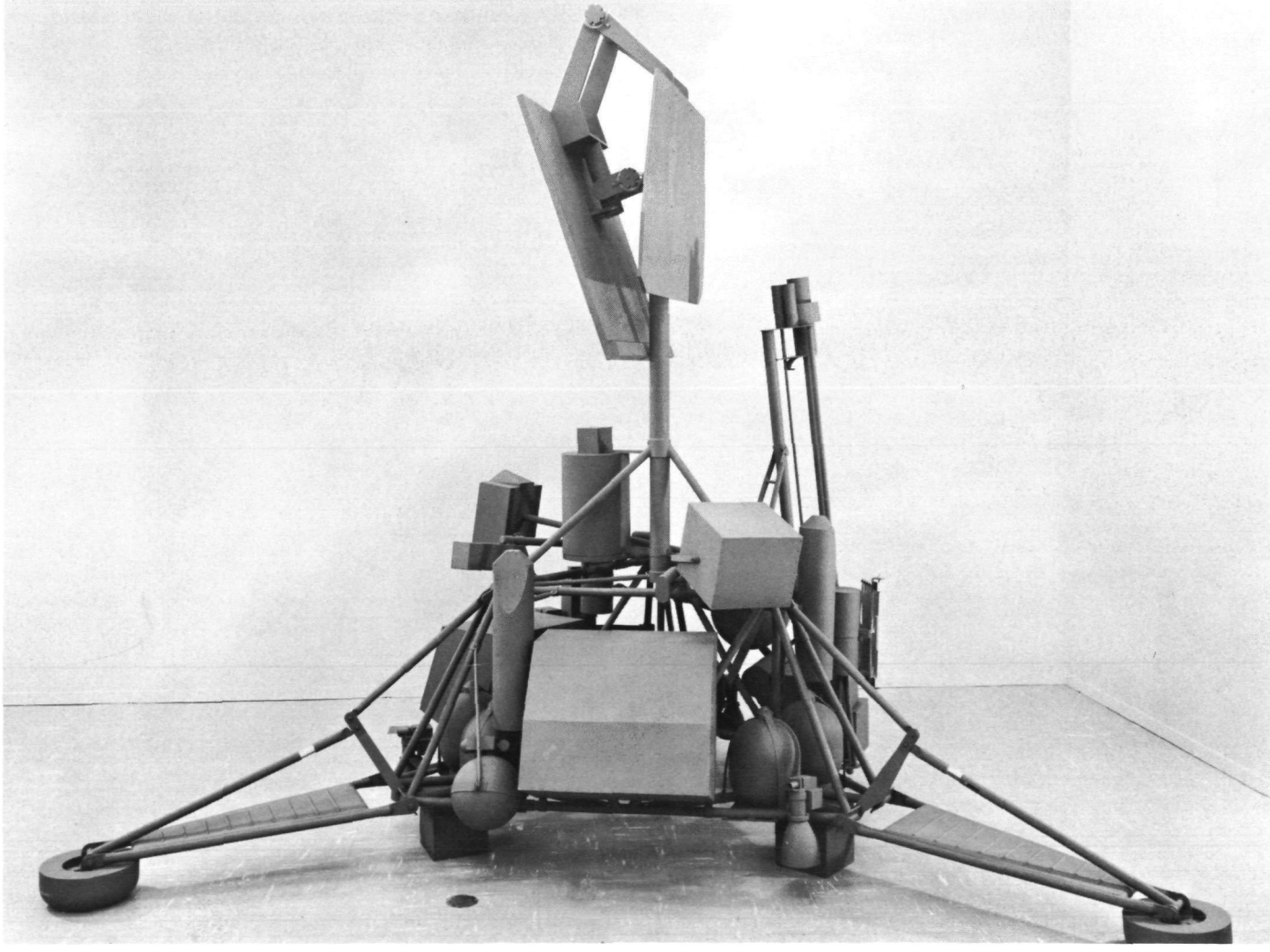

Figure 147. MA-2 full-scale antenna test model

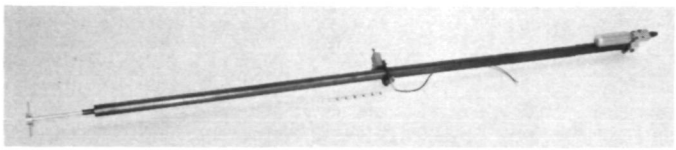

Figure 149. Omnidirectional antenna extended

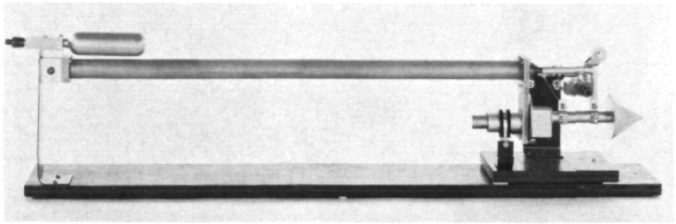

Figure 150. Surface geophysical experiment stowed

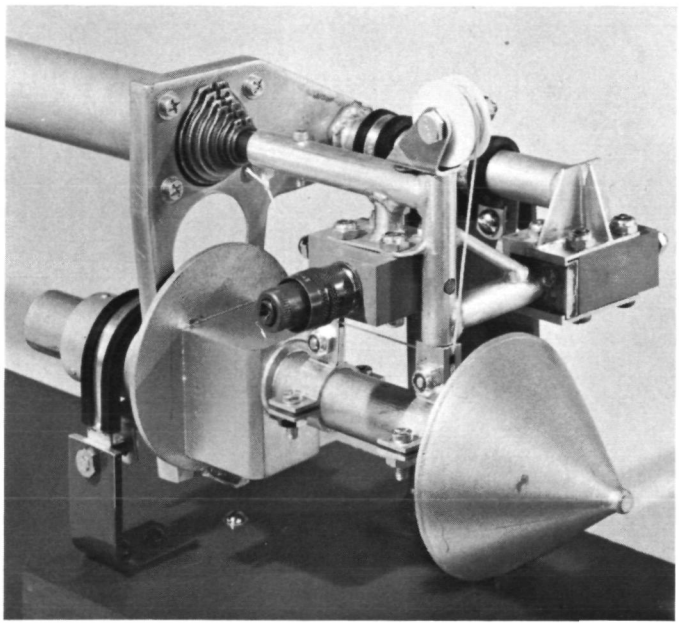

Figure 151. Surface geophysical experiment unlocked

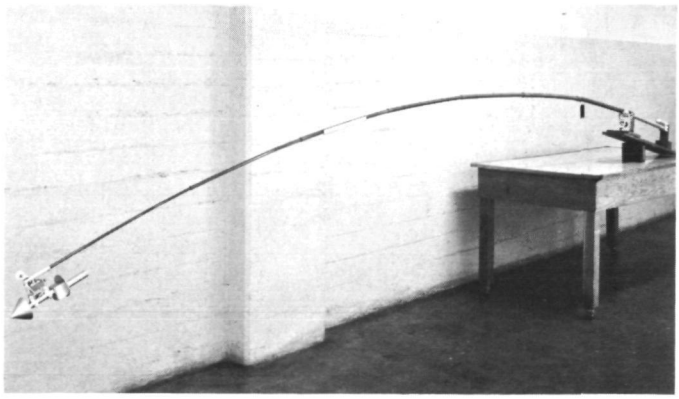

Figure 152. Surface geophysical experiment extended

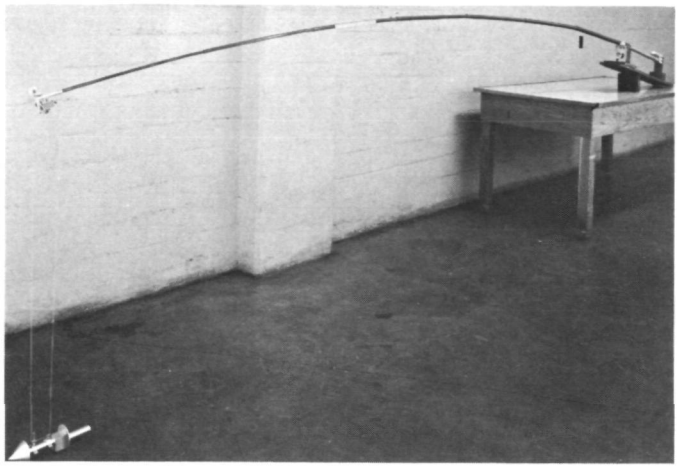

Figure 153. Surface geophysical experiment lowered

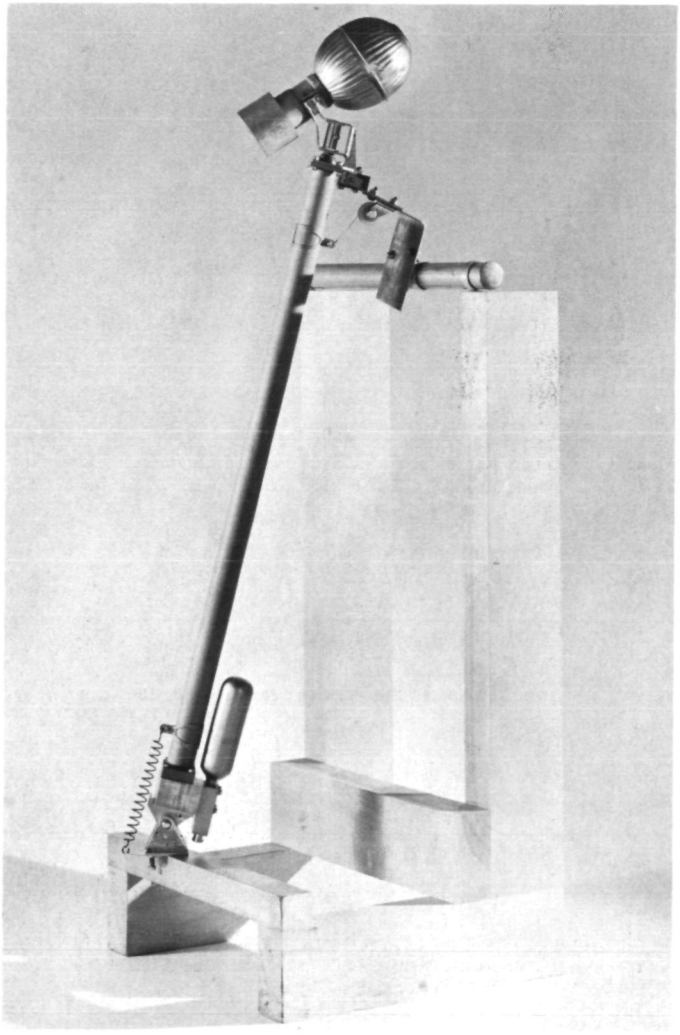

Figure 154. Radiation detector stowed

fabricated to the previous five-axis control design. Those details and subassemblies of the prototype design which are different from the developmental test model will be individually tested prior to final fabrication and test of the complete prototype model. The thermal test model positioner shown in Figure 158 is generally representative of the developmental model now being fabricated.

An early vibation test model of the positioner is shown in Figure 159. This model has undergone vibration tests on Vehicle S-1 which indicated that insufficient clearance

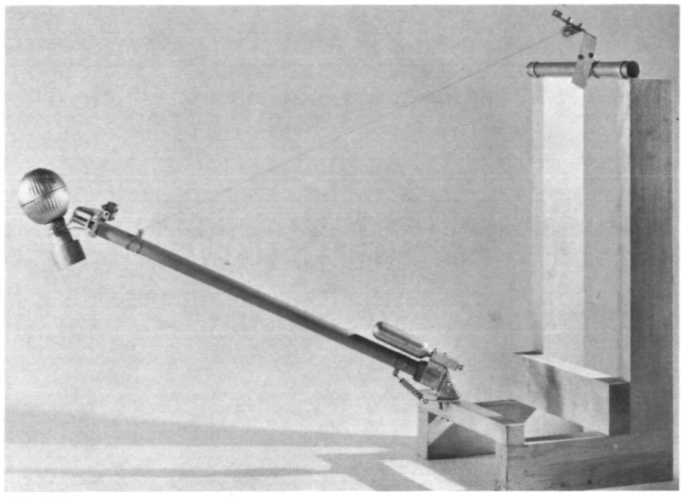

Figure 155. Radiation detector positioned

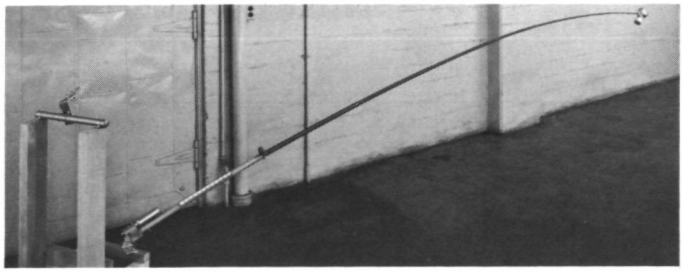

Figure 156. Radiation detector extended

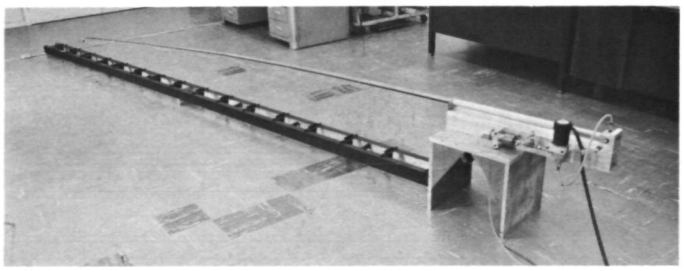

Figure 157. Extension boom test fixture

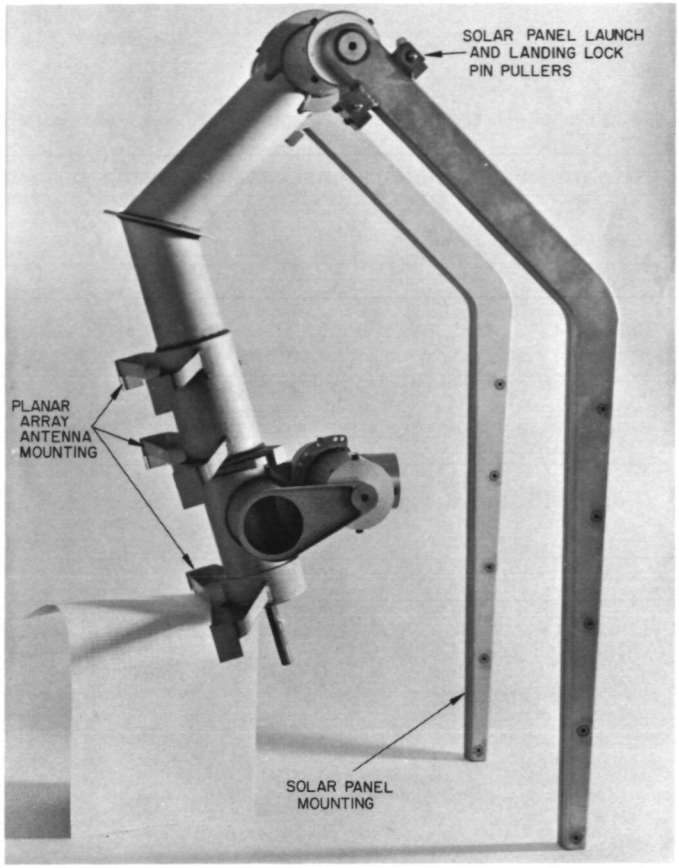

Figure 158. Antenna–solar panel positioner thermal test model

existed between the panels and the mast and shroud. These clearances have been increased in the new prototype design by the shift in the solar panel hingeline and a change in the high-gain antenna stowage angle. A structural test specimen of the solar panel hinge support was statically loaded as shown in Figure 160. The specimen was loaded to destruction and failed at 145% of design load (Fig 161) at the predicted location.

A test fixture has been fabricated to test the gas-operated elevating mechanism. Tests are being conducted to determine the magnitude of seal friction existing in the elevating mast sections. Preliminary results indicate that the design is compatible with the high-pressure gas source specified for this application when operated under ambient conditions.

Several motors have been tested for torque and response rates to determine the type of motor most suitable for operating the planar antenna and solar panel. As a result of these tests, an additional quantity of rotary solenoid motors, modified for vacuum operation, have been ordered.

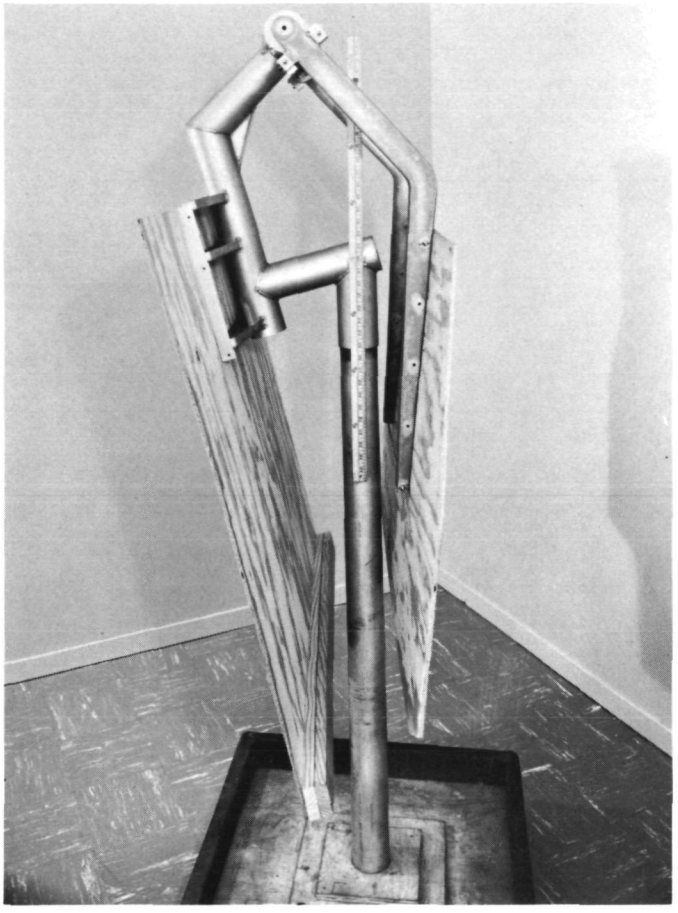

Figure 159. Antenna–solar panel positioner for Vehicle S-1 vibration test

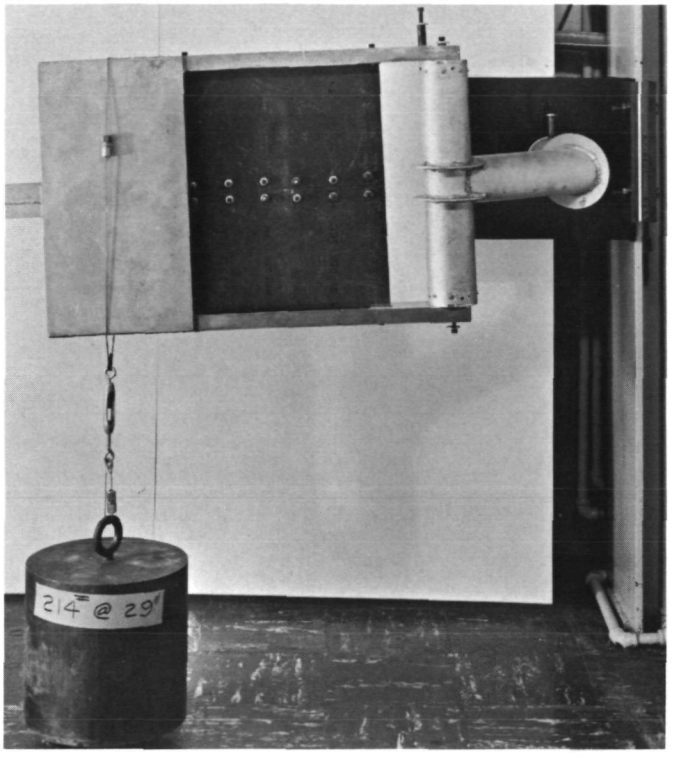

Figure 160. Static load test of solar panel hinge support

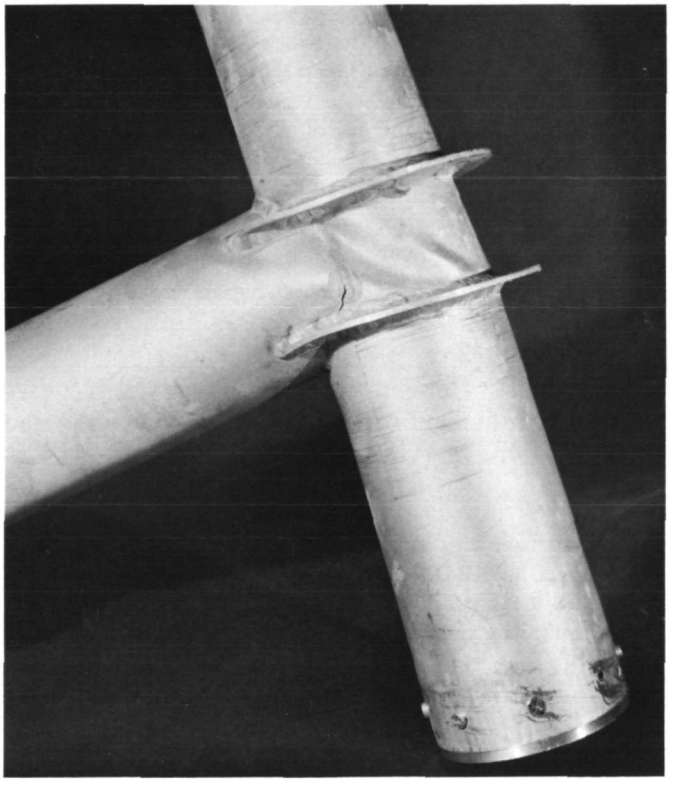

Figure 161. Failure of solar panel hinge support (145% load)

c. TV mirror assemblies. Fabrication of a developmental model TV mirror assembly, providing tilt and pan capability for the television cameras, has been completed (Figs 162 and 163). Preliminary testing revealed the need for a minor modification of the elevation drive unit. This has been accomplished and developmental testing will resume shortly.

The high-resolution telescope mirror assembly will be basically the same as that for the television cameras, with the exception of the gear reduction ratios on the drive units and the reduced size of the elliptical front surface mirror. Developmental testing of the complete television mirror assembly in conjunction with subassembly testing of the telescope mirror drive unit and telescope mirror mounting hardware will provide test data applicable to both the television and telescope mirror assemblies.

In order to check and calibrate the stepping accuracy of the TV mirror drive unit, a special test fixture

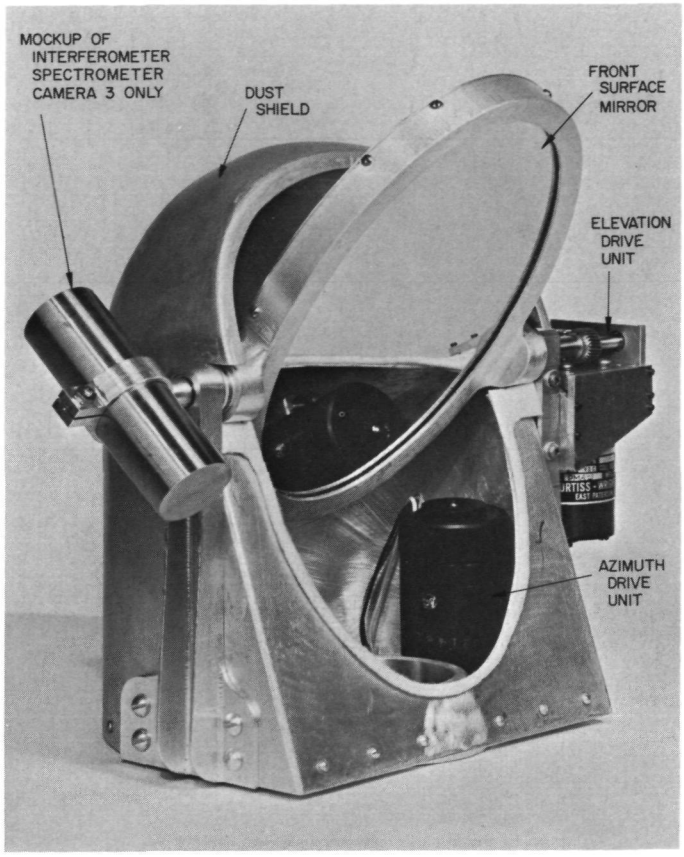

Figure 162. Developmental model of TV mirror drive in operating position

consisting of two precision rotary index heads and an autocollimator is being fabricated. High-vacuum environmental tests are scheduled for the worm and wheel antifriction coatings. The environmental evaluation of potentiometers for positioning indication is continuing. Tests have been completed on drive motor torque and response times at temperatures of 75 and 265°F at atmospheric pressure. (Figure 164 shows representative test data). These motors have been modified for vacuum operation and will be subjected to high-vacuum environmental operating tests.

d. Subsurface sampler. The subsurface sampler obtains samples from various depths down to 5 feet beneath the lunar surface and delivers the samples to the sample processing system. The sampler consists of a drill head, drill shank, bit, dump mechanism, vertical drill drives, supporting structure, subsurface geophysical probe lowering drive, and jettison device.

A full-scale breadboad model of the subsurface sampler has undergone simulated operational tests in a 5-foot diameter by 10-foot long ultrahigh vacuum test chamber (Fig 165). The tests were performed to verify the

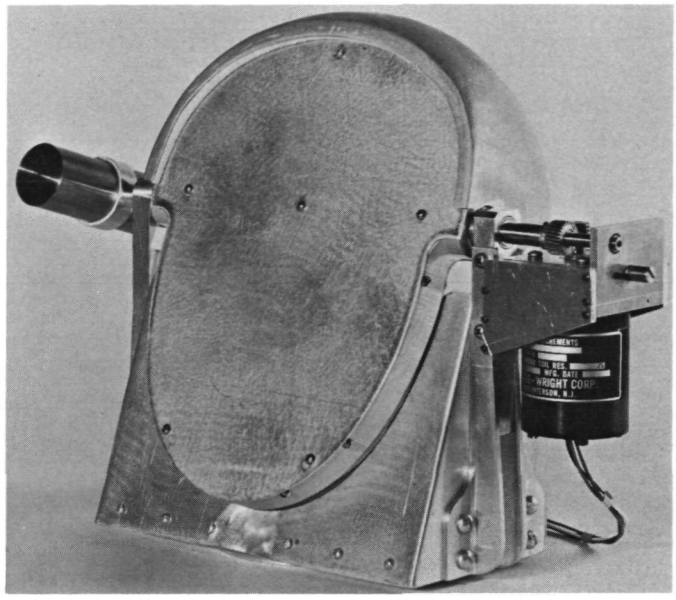

Figure 163. Developmental model of TV mirror drive in stowed position

performance of the developmental model. The entire mechanism was operated at an angle of 60 degrees from the vertical because of the limiting chamber dimensions (Fig 166). This arrangement had the advantage of reducing the gravity force acting to discharge the sample

TEMPERATURE, °F	TORQUE in.-oz	VOLTAGE, v			
		28	24	23	35
75	STALL	12.48	11.20	8.64	18.56
	CLOSING	2.88	2.56	1.92	4.16
265[b]	STALL	4.85	4.20	2.75	6.65
	CLOSING[a]	1.12	0.97	0.61	1.49

[a] EXTRAPOLATED VALUES
[b] COIL WOUND FOR 70°F OPERATION

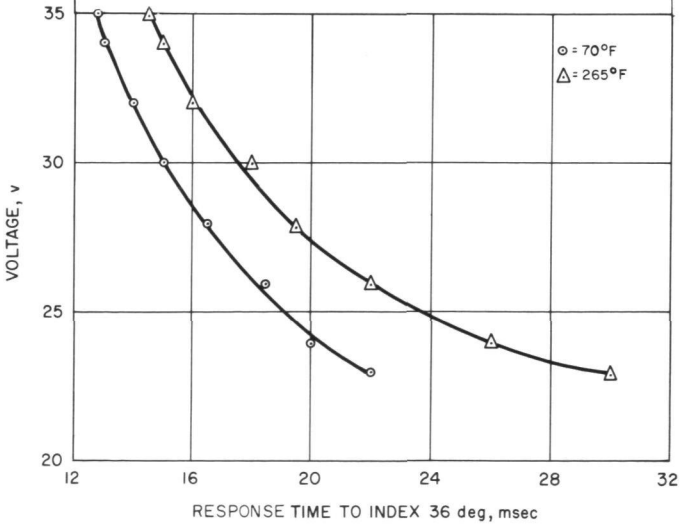

Figure 164. Typical stepper motor test data

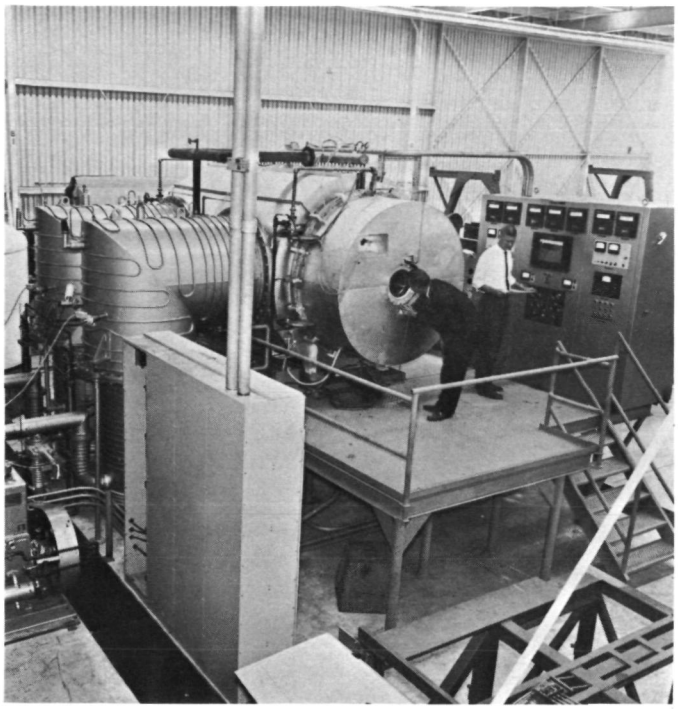

Figure 165. Convair high vacuum test facility

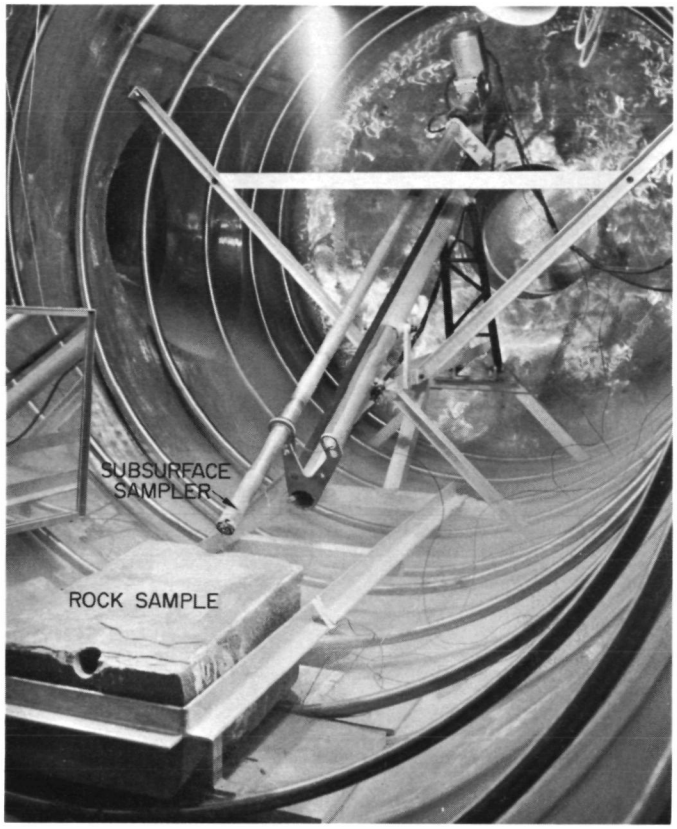

Figure 166. Subsurface sampler high vacuum test

from the drill magazine. In effect, it permitted a crude simulation of the lunar gravity force to determine whether or not the drill cuttings will flow properly in a hard vacuum. Both sandstone and granite were drilled.

The mechanism operated successfully in a vacuum ranging from 3 times 10^{-7}mm Hg to 6 times 10^{-4}mm Hg. The total operating time in the vacuum was 18.3 minutes and the nonoperating time was 54 hours.

Figure 167 shows the variation of vacuum chamber pressure with time for the sandstone test run. The test results were as follows: A 6¼ inch deep hole was drilled in Berea sandstone at an average rate of ⅞ in./min. The depth of the hole was limited by the size of the test rock. A 3.5-inch deep hole was drilled in Harris granite at an average rate of ¼ in./min (Fig 168). The test terminated when the impact hammer spring fractured. The temperature rise of the drill head, drill shank lower bearing, and drill sample during operation were within calculated values.

A geophone was attached to the rock near the hole and a record of the drill sound was recorded. In the dump position, the sample discharged freely. Some of the sample was lost from the entrance port in the drill bit as the drill was being moved from the drilling position to the dump position. During drilling, some dust was thrust upward, coating the drill head and the end

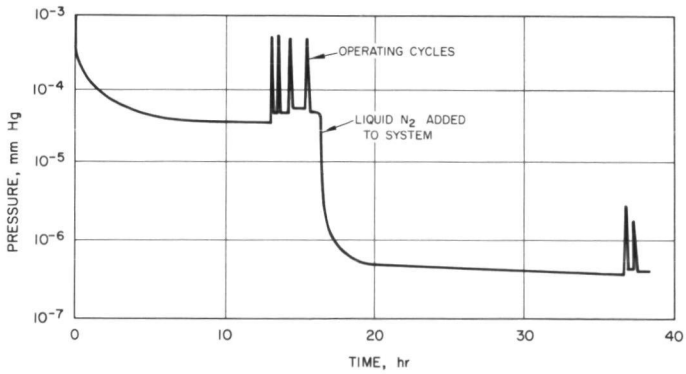

Figure 167. Vacuum chamber pressure in subsurface sampler test

of the vacuum chamber. A drill tooth fractured after 14 minutes of drilling in granite. The Teflon nut and screw assembly functioned properly as did the loading spring and thrust application limit switch.

The 1095 steel impact spring, which returns the impact mass from the anvil position to the pre-energized position, failed from fatigue. A change to 302 stainless steel is being made in the breadboard model. The drill head for the prototype and flight units will be developed

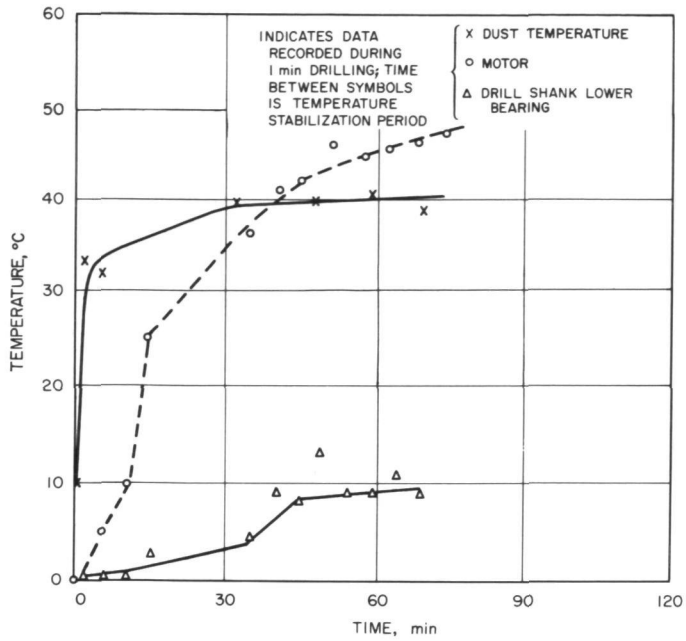

Figure 168. Temperatures in subsurface sampler test

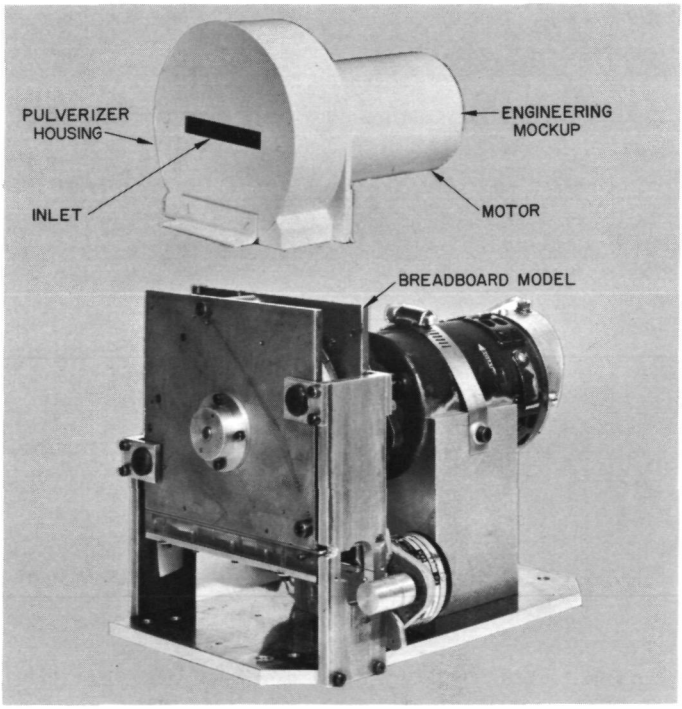

Figure 169. Pulverizer size comparison

by a subcontractor. A valve was added to the drill bit entrance port to prevent premature sample discharge.

A dust shield has been designed to prevent the dust from coating the drill and spacecraft during the drilling operation. Carboloy 55A was used for the drill bit tooth

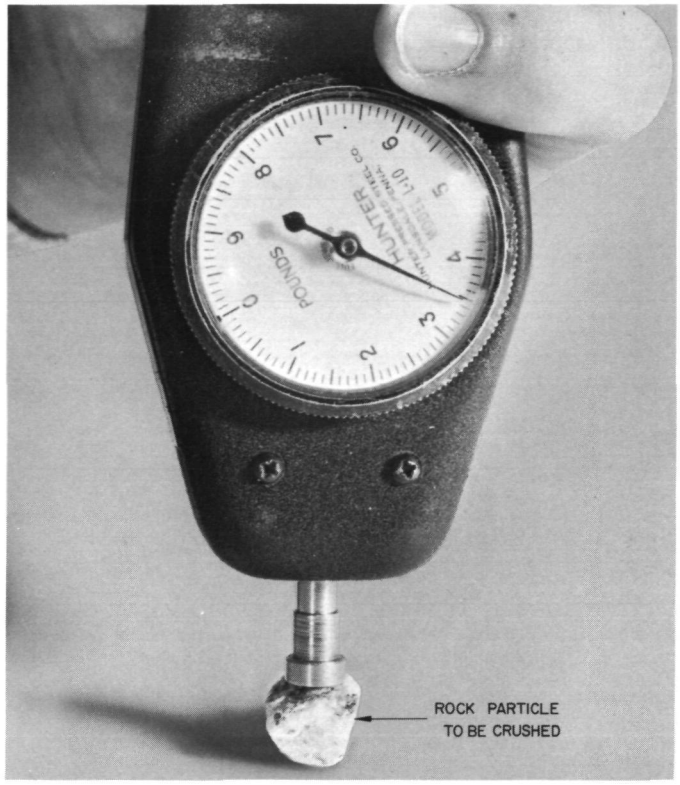

Figure 170. Crushing test of rock particle

material during the test because of its availability. Carboloy 44A, which is tougher and less brittle, is to be substituted for later models. Also, drill tooth impact pressure is being reduced by increasing the drill tooth radius from 0.015 to 0.030 inch. The developmental model, incorporating the design features described, is being fabricated and is scheduled to be completed by March 1, 1962.

e. Sample processing system. Pulverizer and sample transport breadboad tests are almost complete. Preliminary design information from these tests are being reflected in the developmental model, the fabrication of which has begun. A mockup of the flight pulverizer, which is very similar in shape to the developmental model, is compared with the breadboard in Figure 169.

The breadboard pulverizer tests, conducted in a 10^{-4} mm Hg vacuum, have shown that: (1) The pulverizer is capable of reducing 4 cc of Harris granite to less than 200 mesh in less than 45 seconds. (2) The simultaneous pulverizing and filling of the sample cup method using 200-mesh screen was successful.

To determine the effect of dust or crushed rock spilled on the rails of the sample transport system, tests were conducted with the transport breadboard in atmosphere

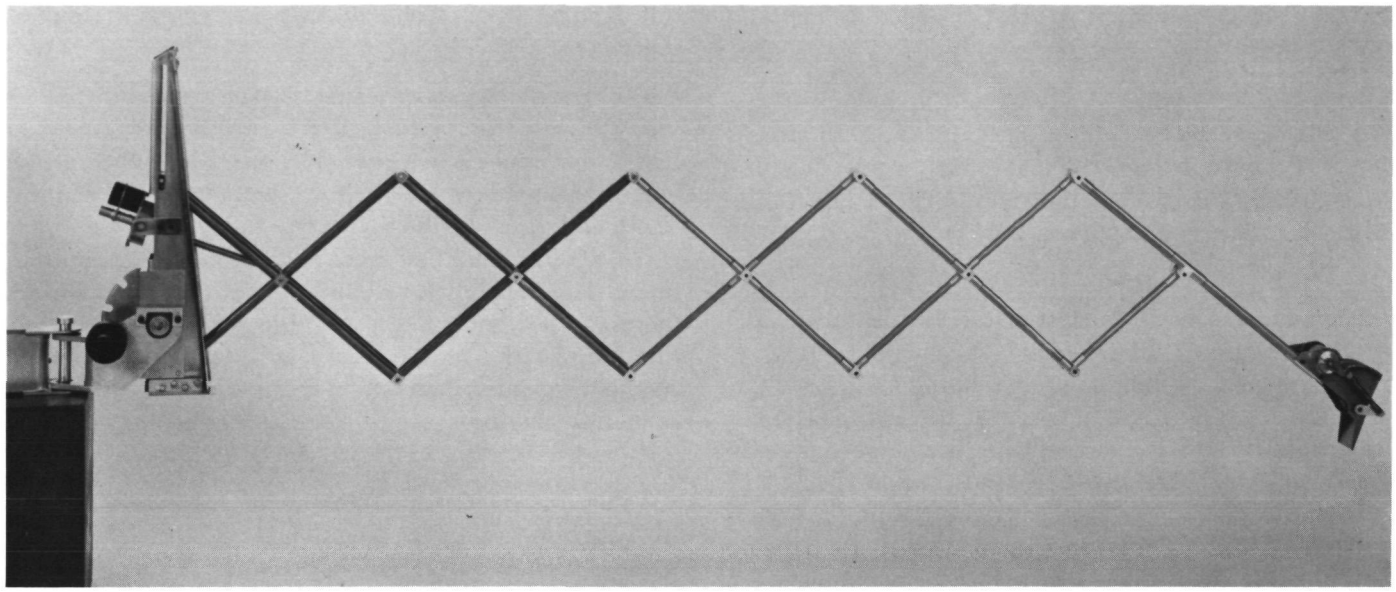

Figure 171. Surface sampler breadboard extended

and in 10^{-4}mm Hg vacuum. It was shown that for a given clearance between the sample cups and teflon rails, the cups would glide over small particles ($<$ 200 mesh), push along large particles ($>$ 20 mesh) and jam on intermediate size particles. The teflon rails were too soft and therefore applied too low a pressure to crush the intermediate size particles. Hard-coated aluminum rails and reduced contact area between the cups and rails are now being tested as solutions to this problem.

To determine the force required to crush particles, crushing tests have been performed (Fig 170). A force between 3 and 6 pounds was required to crush quartz particles varying between 0.032 to 0.016 inch in diameter and a force of 4 to 8 pounds was required to crush granite of the same size. Particles greater than 0.060 inch could not be crushed with a 20-pound load. Particles of this size, however, could be readily pushed away by the sample cups.

f. Surface sampler. The surface sampler consists of a scissors-type extension mechanism capable of being extended, elevated, and rotated with motor drives. A motor-operated clamshell is located at the end of the extension arm. The mechanism will be capable of obtaining a 25-cc sample of loose soil from the lunar surface by means of scraping, grasping, and depositing it either into the sample receiving measure or directly into the gas chromatograph.

A breadboard model of the surface sampler is shown in Figures 171 through 173. This model is complete except

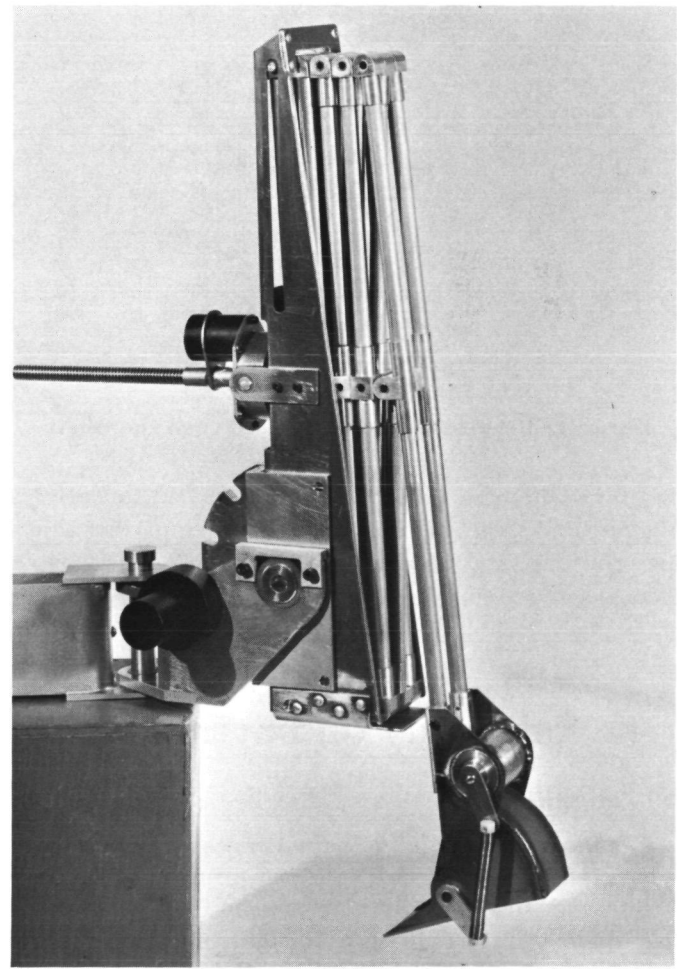

Figure 172. Surface sampler breadboard retracted

for operational motors and gearboxes which are mockup units.

Tests will be conducted on this unit in a high vacuum and will verify such engineering features as teflon-glass sleeve bearings, friction pinned joints, epoxy bonding of assemblies, and precision of allowable manufacturing tolerances. The effect of lunar dust on the bearings will also be checked.

The motors selected for test of this breadboard model are pulse operated, bidirectional, salient pole, programmed logic type stepping motors, rotating 15 degrees per step. The logic for these motors will be packaged separately from the motors and will be programmed for 450 steps per second. Tests will be conducted to check: (1) the design ratios of the gearheads and the power output of the motor drives; (2) the precision and manipulation ability of the device; (3) the ability to manipulate the unit on the basis of information from TV operation

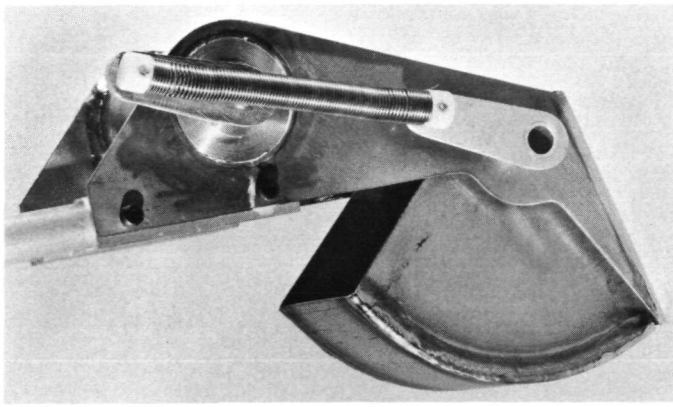

Figure 173. Surface sampler breadboard clamshell

and by positioning potentiometers; and (4) the manipulation time required to obtain a soil sample by scraping, grasping, and depositing the sample in the sample receiving measure.

K. Reliability and System Test

1. Reliability

a. Spacecraft reliability estimate: flight and landing phase. The following is the second estimate of the reliabilities of the spacecraft system and its subsystems. The spacecraft reliability for the flight and landing phase is defined as the probability that the spacecraft, after successful injection, will not malfunction to preclude soft landing successfully on the prescribed portion of the moon.

The functional requirements of each subsystem necessary for spacecraft system success have been synthesized into a system mathematical model into which the current values of subsystem reliability estimates have been entered and provide the basis for this prediction. It is currently estimated that there is an 80% probability that the system reliability will be greater than 0.69 during the flight and landing phase of the spacecraft. It is further estimated that there is a 20% probability that a reliability greater than 0.87 will be achieved. The mean reliability for the system calculation is estimated to be 0.78.

Table 13 contains an estimate of spacecraft reliability which is appraised according to responsible equipment design areas at Hughes Aircraft Company. The system estimate corresponds to that synthesized from the following system reliability equation for flight and landing:

$$P_L = P_{RF}\, P_{DE}\, P_{FCS}\, P_{PS}\, P_{ES}\, P_{DS}\, P_{TC}\, P_{LG}\, R_E$$

where:

P_L = probability of flight and landing
P_{RF} = RF communications
P_{DE} = decoding
P_{FCS} = flight controls
P_{PS} = electrical power
P_{ES} = propulsion engines
P_{DS} = essential data measuring and processing
P_{TC} = thermal control
P_{LG} = landing gear
R_E = interconnections, structure, separation mechanisms

One of the above terms, expanded and evaluated for the sake of illustration, is shown below. The other terms were similarly evaluated.

$$P_{FR} = f(P_{AO_1}, P_{AO_2}, P_{R_1}, P_{R_2}, P_{T_1}, P_{T_2}, P_{PA}, P_{S_1}, P_{S_2})$$

where:

P_{AO_i} = omnidirectional antenna = 0.9998
P_{R_i} = receiver = 0.9955
P_{T_i} = transmitter = 0.9918
P_{PA} = planer array = 0.9990
P_{S_i} = transponder circuitry = 0.9981
$i = 1, 2.$

Table 13. Reliability estimates for the flight and landing phase

Equipment	Reliability	
	Lower limit	Upper limit
	0.69	0.87
Flight control group Attitude reference sensors, control equipment, roll vernier actuator, retro burnout sensor, flight control accelerometer, attitude jet system	0.75	0.95
Propulsion group Vernier engine system, retro-rocket engine	0.83	0.96
Electrical power group Solar panels, batteries	0.999	0.999
Electronics group Power system control, command receivers, transponders, telemetering transmitters central command decoders, essential signal processing circuits, radars (altitude marking, doppler velocity, altimeter), television No. 4 electronics	0.979	0.997
Vehicle group Harness and interconnections, retro-rocket separation, vehicle structure, landing gear	0.97	0.98
Mechanics group Antenna and solar panel drive, vehicle anchoring, television No. 4, manipulating devices, optics	0.995	0.999
Thermal control group	0.99	0.999

There are 512 possible combinations of good and bad elements of the RF communication system. By considering all of the possible *effective* combinations and combining like terms, the following expression for P_{RF} is obtained (P means the probability of the function not occurring):

$$P_{RF} = P_{AO}^2 R_R^2 P_T^2 P_{PA} P_S^2 + 2 P_{AO}^2 P_R^2 P_T^2 P_{PA}^2 P_S P_S + 2 P_{AO} P_R^2 P_T^2 P_{PA} P_S^2 P_{AO} + 2 P_{AO}^2 P_R P_T^2 P_{PA} P_S^2 P_R + 2 P_{AO}^2 P_R^2 P_T P_{PA} P_S^2 P_T + 2 P_{AO} P_R^2 P_T^2 P_{PA} P_S P_{AO} P_S + 2 P_{AO}^2 P_R^2 P_T P_{PA} P_S P_T P_S + 2 P_{AO} P_R P_T P_{PA} P_S P_R + \cdots$$

$\cdots$ *higher orders* ≈ 0.998

When the above equation is evaluated it can be shown that the higher order terms are negligible (those containing more than one P) when the individual P values are higher than 0.99, which is the case for this system. The nonredundant term P_{PA} becomes the dominant one. However, further study of terms containing P_{PA} may be found to have some effectiveness which will cause an even closer approach of P_{RF} to unity.

The increased reliability shown in the propulsion group reflects the optimism of RMD in achieving their required reliability goal based on the more detailed analysis of the proposed vernier engine system. A typical failure mode analysis chart submitted by the vendor is given in Table 14. Each major item in this subsystem has been so analyzed by the vendor.

Reliability of the electronics group similarly shows increased capability because of new information on a vended system (Ryan altimeter and doppler radar). It was learned by more detailed analysis of potential failure modes that unreliability due to the radar on-off duty cycle was being weighted too heavily in the subsystem estimate. Appropriate changes in the calculations reflect the results of this reappraisal.

Data concerning the tradeoff of reliability versus weight are being accumulated to determine where reliability and weight can be optimized. By the calculus of variations, it can be shown that the $\partial R/\partial W$ values should be identical for all series elements in the optimum system. It will be approached by methods such as the use of redundancies and derating where such choices are still available.

b. Components and materials. An investigation has been made to obtain information for selection of wire types which have minimum weight and thermal conductivity and will function reliably in the lunar environment. The assumed environment is a hard vacuum ($< 10^{-5}$ mm Hg) with temperatures from —300 to 260°F. Conductors, insulation, and jacketing materials were examined.

A temperature of 260°F in a hard vacuum produces substantial outgassing in many compounds commonly used for wire insulation. Very few insulating materials have any flexibility at —300, while 260°F exceeds the maximum allowable operating temperature for many insulating materials. Consequently there are only a limited number of materials worth considering. Thus far, TFE Teflon, Surok, and irradiated polyethylene have been tested.

Conventional conductors would be expected to perform satisfactorily under lunar conditions. Thermal conductivity, weight, and flex life are therefore the determining factors in conductor selection. Jacketing compounds should be subject for the most part to the same limitations as the primary insulation materials.

To simulate lunar temperature and pressure, a preliminary 1-inch diameter glass test chamber was constructed and used to obtain initial temperature rise versus current data on candidate wire types. Subsequently a larger chamber capable of testing cable as-

Table 14. Typical failure mode analysis chart

Project 8701 Drawing Number 313702 C

DESIGN RELIABILITY AUDIT
FAILURE MODE ANALYSIS

Component Name: Dual Prop Valve Assembly

Failed Part	Description and/or reasons for assumed failure	Component failure mode	Influence on system	P (fi)	P (F/fi)	P (Ri)	Basis for estimate of probabilities and/or remarks	Possible methods to eliminate failure mode
(1) Solenoid Valve (Item 17)	(a) Coil burns out	Propellant valve cannot be opened.	Mission requirements may not be accomplished.	0.0001	1	0.9999	Manufacturer's estimate and engineering judgment.	
	(b) Open circuited connections on the electrical connector due to excessive shock and/or vibration.	Same as 1 (a).	Same as 1 (a).	0.0001	1	0.9999	Engineering judgment and estimate.	
	(c) Sticking of plunger and poppet assembly in body due to temperature extremes.	Erratic prop valve operation.	Same as 1 (a).	—	—	—	Temperature extremes encountered will not be great enough to cause this type of failure.	
	(d) Sticking of plunger and poppet assembly due to foreign matter.	Same as 1 (c).	Same as 1 (a).	0.0001	1	0.9999	Engineering estimate. The helium tank filter will aid in the minimization of this malfunction.	
	(e) Solenoid valve body damage (cracking, distortion, etc.) due to excessive vibration and/or shock.	Erratic propellant valve operation due to loss of He gas and/or sticking solenoid valve plunger assy.	Same as 1 (a).	0.0001	1	0.9999	Manufacturer's estimate and engineering judgment.	
	(f) Deterioration of solenoid valve body due to space environments (i.e., radiation, vacuum).	——	——	—	—	—	Exposure time to these environments is not long enough to detrimentally affect the part.	

ESTIMATED COMPONENT RELIABILITY = $R_C = \prod_{i=1}^{n} [1 - P\{f_i\}P\{F/f_i\}] = \prod_{i=1}^{n} [P\{R_i\}] =$ **0.9986**

$P\{f_i\}$ Probability of Occurrence of Failed Part

$P\{F/f_i\}$ Probability of Component Failure if Part Failure Occurs

$P\{R_i\} = 1 - P\{f_i\}\,P\{F/f_i\}$

semblies as well as single wires was built. This test chamber consists of six 6-inch diameter by 18-inch long pyrex pipe tees (Fig 174). Electrical leads are brought out through flange plates on the tee sidearms. Each section is wrapped with nichrome wire and asbestos insulation to provide the necessary elevated environmental temperature. A separate variac controls the power input to each 18-inch section. The pumping system consists of an NRC fore pump and an Eimac pyrex diffusion pump using DC 704 oil. A Veeco ionization gage is used for pressure measurements. Pressures of 2 times 10^{-5} mm Hg are readily achieved. Wire and environmental temperatures are monitored by thermocouples. For most tests the average-temperature deviation on the inside of the chamber wall was $\pm 3°F$.

Room temperature flex tests are being run to make a relative comparison of different conductor materials. These tests are performed on a motor-driven reciprocating device which moves the upper end of the wire

through a 180 degree arc while the lower end is constrained between two 0.103-inch diameter horizontal mandrels. The insulation is stripped off the lower end of the wire, starting just below the mandrels. A 200-gram weight hanging on the conductor maintains even tension and drops to the table when the conductor fails. Flex testing at —300°F will be conducted in a fixture presently being built. Preliminary tests have been conducted by simple immersion of the sample in a dewar flask filled with liquid nitrogen.

To assist designers in selection of wire, data have been obtained on temperature rise versus current for several wire types and are presented in Figure 175. Data on additional wires will be made available as tests are run. Both Alloy 63 and copper conductors appear to satisfactorily withstand the exposure to lunar environment as expected.

Rough estimates of the relative amount of outgassing from each type of insulation were made by observing the degree and duration of changes in the system pressure as wire temperature increased. Table 15 summarizes these observations. Surok is a trade name designating FEP teflon coated with a modified polyamide lacquer (made by Dupont) which provides greatly increased abrasion resistance, heat resistance, and cut-through strength, thus permitting the use of 300-volt, instead of 600-volt, insulation thickness. A comparison of the abrasion, heat, and cut-through resistance of Surok and FEP teflon is given in Table 16.

Table 15. Outgassing from wire insulation

Insulation type	Relative amount of outgassing	Temperature at which outgassing is substantial, °F	Temperature at which insulation fails, °F
TFE teflon	Slight	575	>700
Surok	Moderate	500	550
Irradiated polyethylene	Substantial	380	550

TFE teflon and Surok do not crack when flexed severely (180 degrees) at —300°F; irradiated polyethylene, however, will fracture with only slight (15 degrees) flexing at —300°F. Table 17 shows the relative weights of the

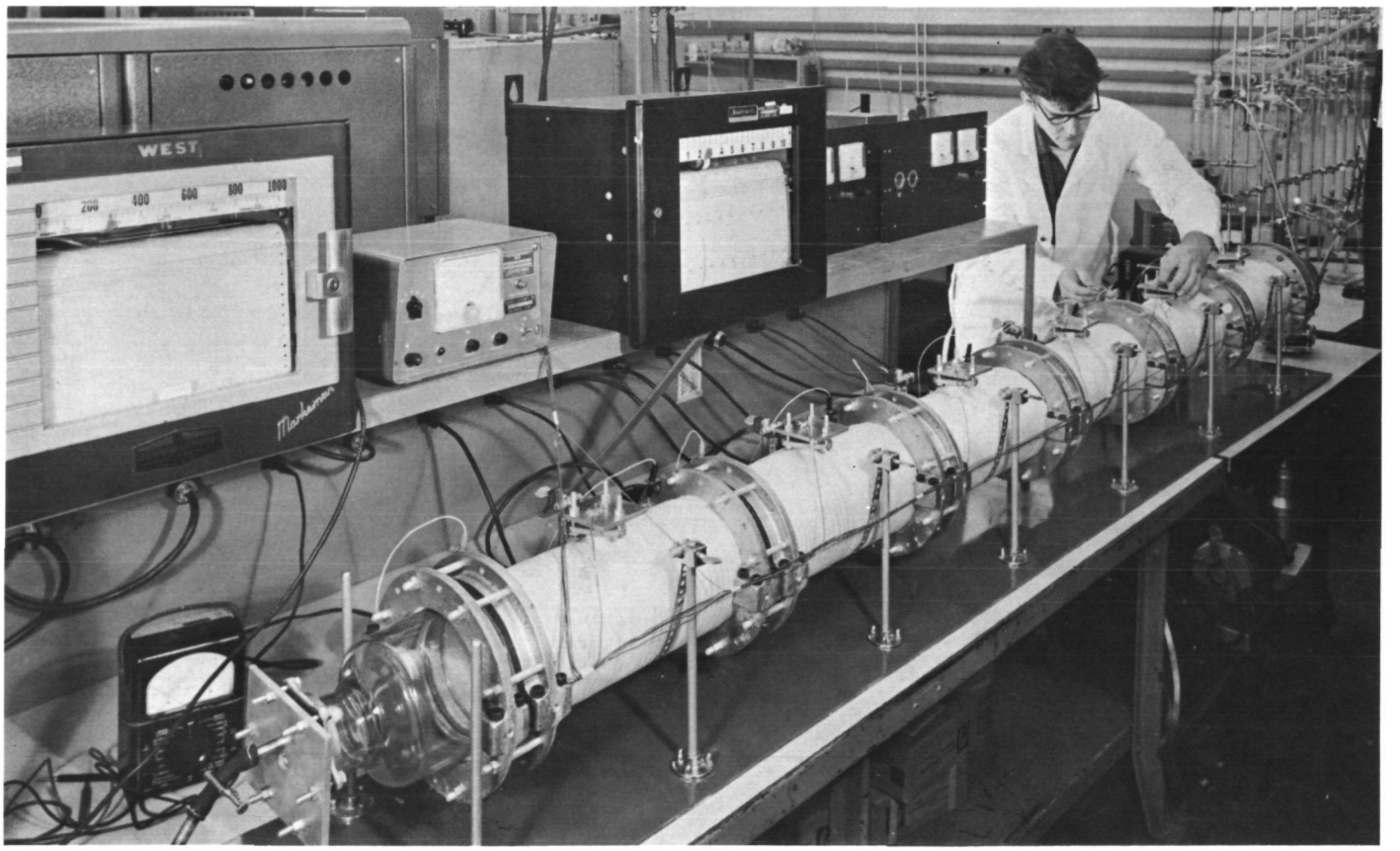

Figure 174. Temperature-vacuum testing of cable assemblies

various wire types tested. From this table, it is apparent that Surok offers a weight saving comparable to irradiated polyethylene.

Results of room temperature flex life tests are shown in Table 18. Thus far, samples of Alloy 63 have been available in 24 AWG only. Samples of 20 through 26 AWG are on order. Alloy 63 has approximately 80% of the conductivity of copper.

Based on the partial test data available, Surok insulated Alloy 63 is the preferred wire for *Surveyor*. Teflon insulated Alloy 63 is equally satisfactory except for its greater weight. Irradiated polyethylene is of questionable suitability due to its outgassing tendencies and its lack of flexibility at —300°F. 24 AWG ($^{19}/_{36}$) is the minimum recommended wire size for Alloy 63 wire. Copper is also a satisfactory conductor; however, to obtain the same flex life as any given size of Alloy 63, one gage size larger is required in copper. Studies are continuing and information will be provided as it becomes available.

2. System Test

a. System test equipment assembly (STEA) design. The functional requirements for the STEA UHF transmitter and receiver have been developed. This equipment will comprise four 7-inch rack panel assemblies and will be housed in the STEA transmitter and receiver test racks. The specific requirements of each are described below.

UHF receiver. The UHF receiver (Fig 176) is designed specifically to simulate the DSIF receiver functions during spacecraft testing. This unit will receive signals from the spacecraft transmitter and provide frequency conversion and selectivity such that output IF signals of 60 mc at bandwidths of 3.3 mc (3 db) and 2.4 mc at bandwidths of 10, 20, and

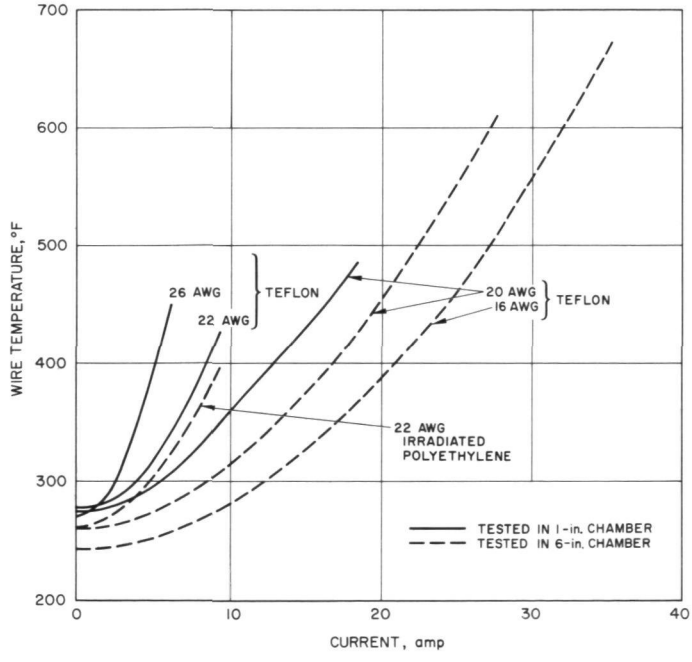

Figure 175. Temperature rise in various conductors

Table 16. Comparison of plain and coated teflon

Parameter	Uncoated FEP teflon	Surok
Abrasion resistance (test conducted per NAS-703)		
No. 20 solid conductor, inches of tape	17.7	36.6
No. 22 stranded conductor, inches of tape	24.7	42.7
Cut-through resistance (Underwriters Laboratories test)		
Slow compression test, pounds to cut through	40.5	99.1
Penetration test at room temperature, pounds to cut through	5.4	10.0
Hot soldering iron test	Melts through and shorts out in 2 to 3 sec when loaded with 1 lb weight	No cut through in 1 hr when loaded with 3 lb weight

Table 17. Wire weight comparison

Wire size	Total weight of conductor and insulation, lbs/1000 ft			Weight of Alloy 63 conductor only, lbs/1000 ft
	10-mil TFE teflon	6-mil Surok	12-mil irradiated poly-ethylene	
20 AWG (19/32 in.)	5.55	4.54	4.4	3.90
22 AWG (19/34 in.)	3.92	3.02	2.9	2.42
24 AWG (19/36 in.)	2.77	2.03	2.0	1.56
26 AWG (7/34 in.)	1.97	1.31	1.2	0.88
28 AWG (7/36 in.)	1.47	0.92	0.9	0.57

Table 18. Flex life test results

Conductor	Cycles to failure
Alloy 63, 24 AWG (19/36 in.)	830
Copper, 24 AWG (19/36 in.)	594

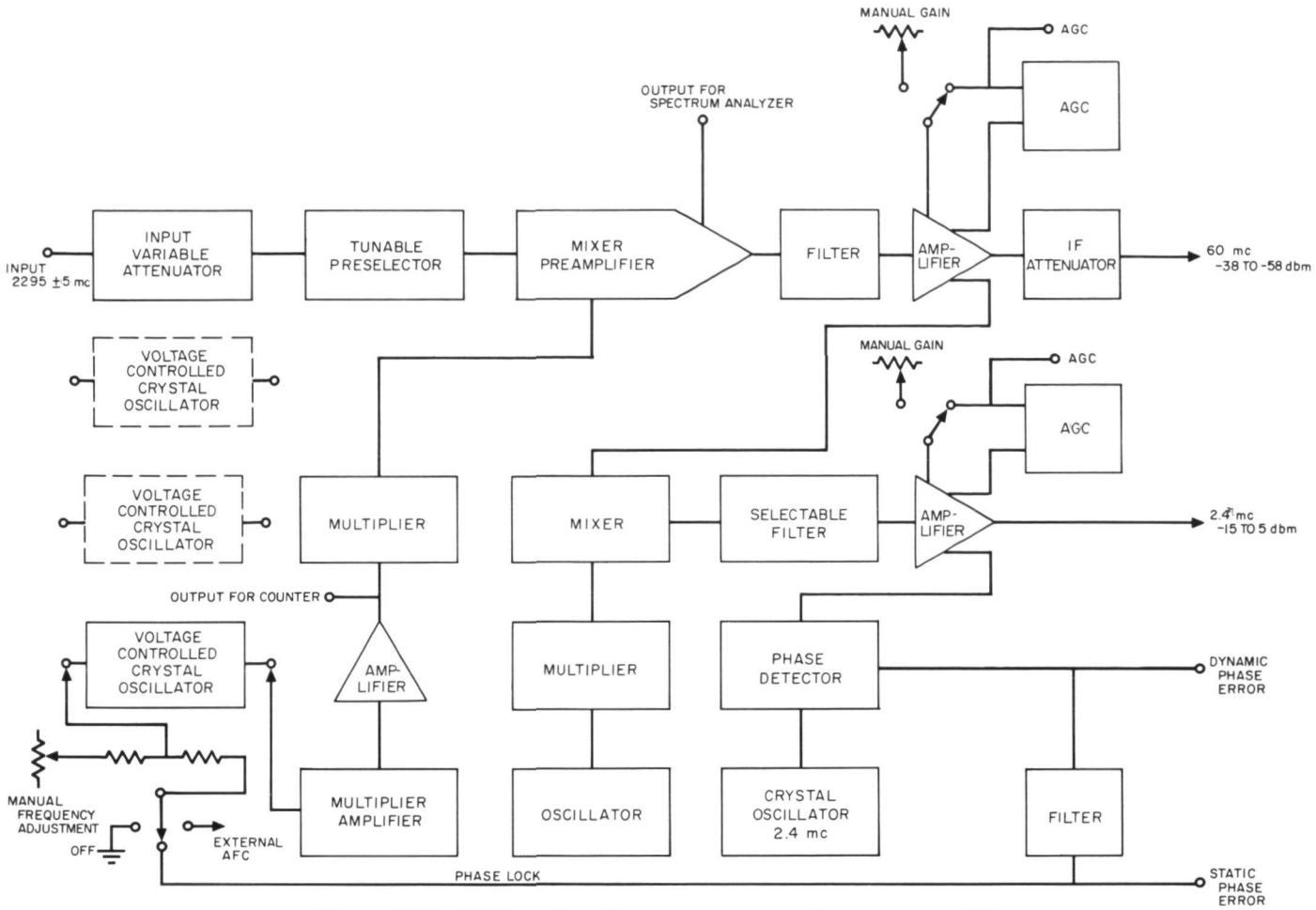

Figure 176. UHF receiver for system test equipment assembly

30 kc will be available at the command and data handling console input for demodulation. The receiver will provide phase-coherent detection of the spacecraft transmitter signal which will facilitate frequency stability measurements and transponder evaluation.

Among the requirements that have been established for the UHF receiver is a frequency range of 2200 to 2300 mc, providing flexibility to add frequency channels for possible program expansion. A choice of three crystal frequencies may be selected by front panel control. The local oscillator will be capable of external voltage tuning over a range of ±150 kc for the purpose of locking on to the receiver signal and manual control from the front panel for the purpose of searching a narrow spectrum for the spacecraft-transmitted signal. Frequency stability will be 1 part in 10^7 parts long term and 1 part in 10^9 parts short term. Phase stability will provide less than 3 degrees peak-to-peak phase error.

Phase lock circuitry will be provided such that the 2.4-mc IF signal will be phase-detected with reference to a 2.4-mc crystal oscillator to produce a signal which will be fed back to the local oscillator to produce a phase-locked loop. The output time constant of the phase detector will be adjusted so that the closed-loop noise bandwidth is 20 cps at the threshold.

Spurious responses will be at least 60 db below the desired signal response, and the over-all noise figure will be 11 db or less. An accurate input attenuator with a range of 0 to 60 decibels will be provided as an integral component of the UHF receiver. The IF passband characteristics for both 60 and 2.4 mc will duplicate those of the DSIF receiver which this unit is required to simulate. The 10, 20, and 30 kc IF filters will be of the crystal lattice type. Output levels of −58 to −38 dbm for 60 mc and −15 dbm to 5 dbm for 2.4 mc will be compatible with CDC requirements.

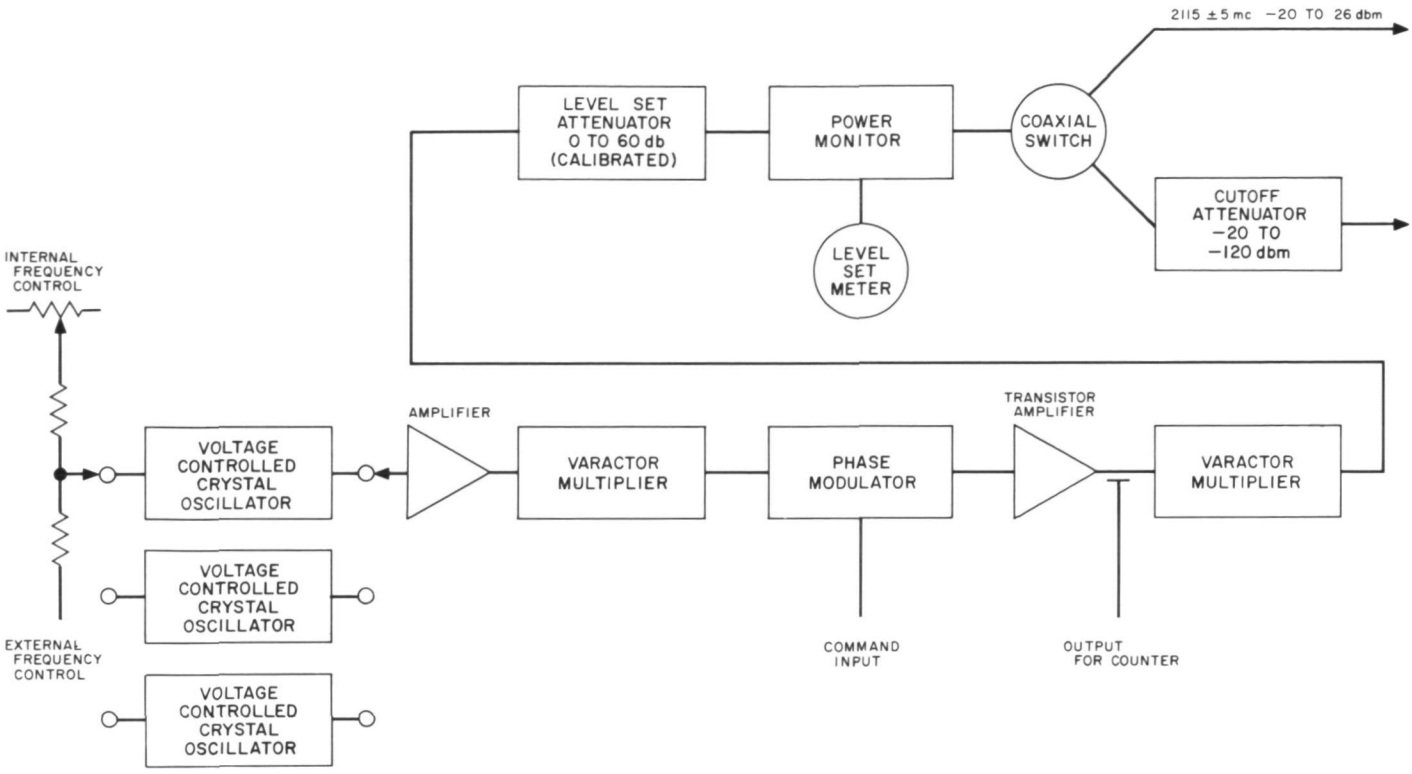

Figure 177. UHF transmitter for system test equipment assembly

UHF transmitter. The UHF transmitter (Figure 177) is designed specifically to simulate the DSIF transmitter functions during spacecraft testing. This unit will generate signals to provide a communication link with the spacecraft and subject it to various test sequences during the process of subsystem and system test which will check out the spacecraft receiver, as well as other portions of the spacecraft. For this purpose, commands originated in the CDC will modulate the transmitter. During prelaunch checkout on the launch stand at AMR, the transmitter will provide contact with the spacecraft over a 2-mile link.

Characteristics of the transmitter will include a frequency range of 2100 to 2200 mc, a choice of three crystal frequencies by panel selection, and a panel control for frequency variation over a range of ±150 kc for the purpose of tuning to spacecraft receive frequency. The local oscillator will be externally voltage tunable, ±150 kc, for the purpose of sweeping its frequency while testing the spacecraft transponder for tracking range, tracking rate, and lockon range. Frequency stability will be 1 part in 10^7 parts long term and 1 part in 10^9 parts short term. Spurious FM will be 1 part in 10^8 parts or less, and phase stability is to be such that there will be no more than 3 degrees peak-to-peak phase error. A front panel output, 1/16 of the output frequency, will feed a frequency counter for the purpose of measuring the transmitter output frequency and computing the spacecraft receiver input frequency, tracking range, and lockon range. The transmitter will be capable of phase modulating its carrier ±2.4 radians at the output frequency. Power output, variable from 26 to −20 dbm, is provided at one panel connector, and output variable from −20 to −120 dbm is provided at a second panel connector. A power level monitor is provided to ensure accurate output setting. RF leakage at the carrier frequency is required to be less than −120 dbm. Spurious output frequencies will be at least 60 decibels below the carrier level.

b. Magnetic testing. The search for a site for the magnetic testing facility is continuing. The Hughes Baldwin Hills site was checked and found to be too noisy (approximately 25 gammas rms ac noise). A site in El Segundo was found to have a low dc gradient (less than 1 gamma/ft) and a low ac level (approximately 8 gammas rms). However, it was decided not to

use this location because Hughes could not control the surrounding area which might become a source of magnetic interference. A site was offered on a 400-acre ranch 20 miles north of Malibu, but since this location is somewhat distant, a site closer to Malibu is being sought.

Preliminary procurement specifications and drawings have been drafted for the magnetic test facility. The major part of the test facility will be the coil array, a system of eight large coils located on three perpendicular axes and mounted in a cubical structure attached to the floor (Fig 178). Four Fauselau-Braunbeck coils will be mounted along the A axis, which will be aligned with the Earth's magnetic field. A Helmholtz pair of coils will be mounted along the C axis, which will be aligned with the magnetic east-west direction. A second Helmholtz pair will be mounted on the B axis, which will be perpendicular to the A and C axes. The largest coils will be 12 feet in diameter.

This hybrid design using Helmholtz and Fanselau-Braunbeck coils was chosen for the following reasons. For the given maximum coil size of 12 feet, the Helmholtz coils are spaced 6 feet apart. The Fanselau-Braunbeck coils are spaced 3 feet apart. If Fanselau-Braunbeck coils were used on all three axes there would be virtually no working accessibility at the magnetic field free zone at the center of the coils. By using Helmholtz coils on axes B and C, accessibility is much improved. Effectiveness of the Fanselau-Braunbeck coils is much greater than the Helmholtz coils. A three-axis Helmholtz array of similar size would result in a magnetic field free sphere (0 ± 10 gammas) of approximately 1.3 feet diameter. By using Fanselau-Braunbeck coils on one axis and approximately aligning that axis with the Earth field, the field free sphere at the center of the coils is expanded from approximately 1.3 to 3.3 feet in diameter. The preliminary specifications and drawings have been submitted to bidders for quotes.

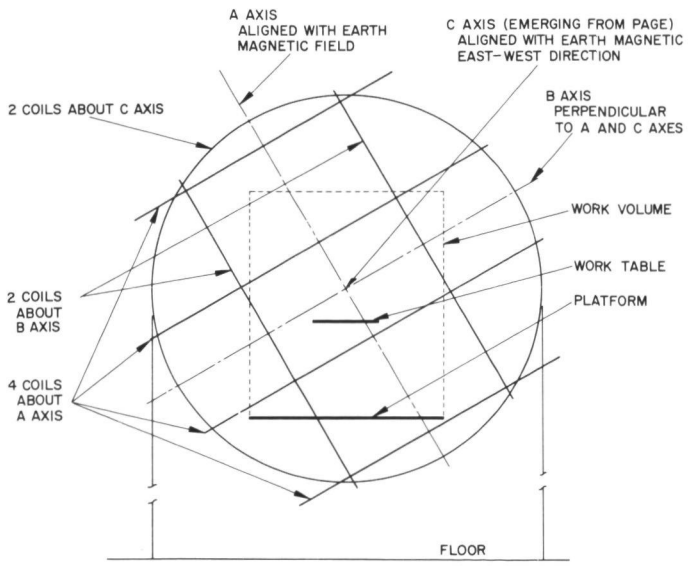

Figure 178. Magnetic test facility layout

Use was made of the Space Technology Laboratory Magnetic Test Facility at Malibu, California, to measure the permanent field of several components, with the following results:

Component	Maximum field at 1 foot
Traveling-wave tube	2000 gamma
Miniature relay	150 gamma
Digital motor	10 gamma
Magnetron	47,500 gamma

c. Sterilization. A continuing components and materials study is being conducted to evaluate the compatibility of the *Surveyor* components and materials to the sterilization requirements of exposure to heat (two cycles of 36 hours at 257°F) and gas (ethylene oxide and Freon 12 for 24 hours) processes. To date the heat and ethylene oxide terminal gas sterilization compatibility tests of materials are approximately 85% complete.

In an effort to remain consistent with the philosophy of sterilization by heat, efforts are being made to provide a heat-sterilizable spacecraft. Heat labile components, such as the photomultiplier tube of the Canopus sensor, are currently being evaluated for inclusion in a heat-sterilizable package. Similarly, gyros of the inertial reference unit, although heat-sterilizable, must be individually adjusted after heat sterilization prior to factory shipment, which is inconsistent with the sterilization philosophy. Satisfactory methods of installation and adjustment are being studied.

As revealed in the development of the thermal switches, the low thermal conductivity and high modulus of elasticity of the polystyrene switch case is not adaptable to heat sterilization. A material substitution program is being pursued to provide a material similar physically to polystyrene but with an adequate usable temperature range. Current results indicate at least three candidate materials. The properties of the candidate materials are shown in Table 19 in relation to polystyrene.

Ablatalite, whose constituents are based on a combination of polyurethane and epoxy resins with a suitable

Table 19. Switch materials

Properties	Polystyrene	Ablatalite	Rexolite 1422	Texolite 11546
Thermal conductivity, BTU/hr/ft²/°F/ft	0.058-0.080	0.060	0.085	0.18
Elastic modulus, psi	4-5 X 10^5	3-5 X 10^5	4 X 10^5	1 X 10^5
Tensile strength, psi	5-9 X 10^3	8 X 10^3	7-9 X 10^3	38-49 X 10^3
Maximum usable temperature, °F	170	300-500	300-400	266
Thickness obtainable, inch	0.010	0.015	[a]	[a]

[a] Currently under study.

filler, shows promising characteristics. Flexibility is afforded in that the strength characteristics can be varied by the concentration of filler with little variation in the coefficient of thermal conductivity. A program is under way with Reaction Motors Division of Thiokol (only present Ablatalite source) to provide samples of varying constituents to best approach the characteristics of polystyrene. A recent attempt at machining a thermal switch proved that Ablatalite was machinable to 0.015 inch. Machining to 0.010 inch was not completed prior to the reporting period. Simultaneous efforts are being made to evaluate Rexolite 1422, a cross-link polystyrene, and Texolite 11546, a glass epoxy, whose properties are also shown in Table 19.

Since the shelf life of the landing gear shock absorber is limited and repetitive heat sterilization imposes a most critical requirement on the design, an installation procedure of the shock absorber at the Atlantic Missile Range is being considered. The vendor, The National Water Lift Co., under Hughes Aircraft Company cog-

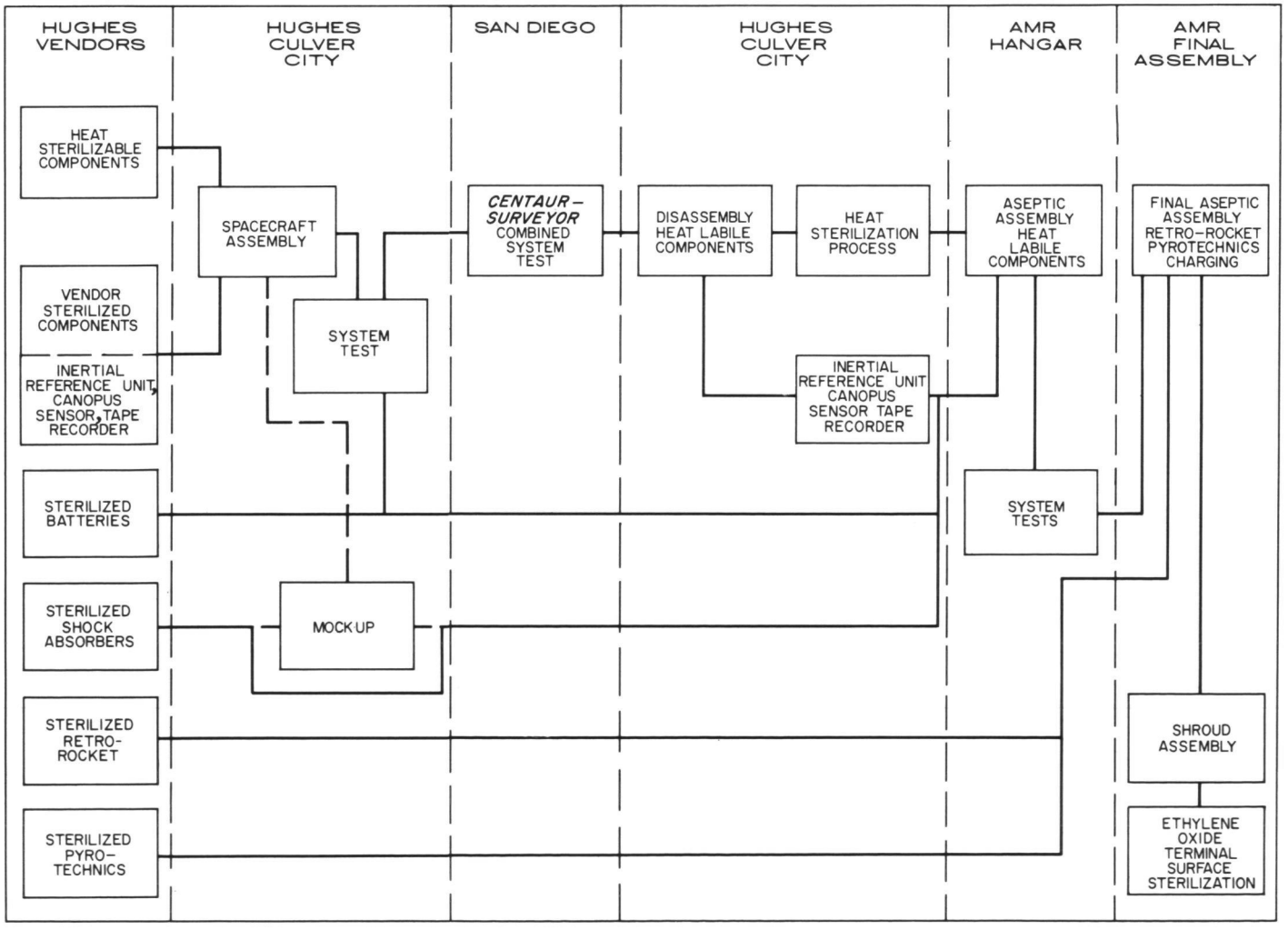

Figure 179. Master sterilization plan

nizance, would heat-sterilize the shock absorber column and conduct operational tests prior to shipment.

A tentative master sterilization plan in block form is shown in Figure 179. The heat labile components which are individually handled are being investigated for incorporation into one heat-sterilizable spacecraft package.

L. Mission Operations

1. Launch Operations

A number of changes in the basic Atlantic Missile Range (AMR) test philosophy have been made since the mission operation phasing chart was issued in the *Space Programs Summary No. 37-12*. Most of the changes are a result of the decision by JPL to perform the terminal surface sterilization off-stand, before mating the spacecraft to the *Centaur*. A general statement of the current AMR test philosophy is given below.

a. Spacecraft and STEA checkout at AMR. The spacecraft will be heat-sterilized at Culver City before being shipped to AMR. The present plan is to have the System Test Equipment Assembly (STEA) arrive simultaneously with the spacecraft. Since the first STEA delivered to AMR has been used previously to check out a spacecraft at Culver City, only minimum interface tests will be required to check out the STEA with the spacecraft.

The first flight spacecraft will arrive 8 weeks prior to the first launch window and will be assembled with special attention to items that may not be heat-sterilized, such as the inertial reference unit and Sun sensor of the flight control unit. An abbreviated functional check will be made at this time. These tasks will be performed at the checkout facility at AMR.

b. Proofing operations. The first flight spacecraft will be moved to the final assembly area where it will go through a series of proofing operations. The proofing operations are designed to confirm equipment, personnel, and procedures in the AMR environment.

c. Compatibility checks. Compatibility checks will be performed at the launch complex to verify that the spacecraft, the *Centaur*, the Atlas, and the launch complex are compatible.

d. Field acceptance test. The spacecraft will be demated from the *Centaur* and returned to the checkout facility. About 4 weeks are planned for each flight spacecraft for the field acceptance test which will afford a complete checkout of the spacecraft as near launch as possible. Although no environmental testing is anticipated at AMR, the tests performed during the period will be nearly identical to the acceptance test procedures at Culver City, modified to fit AMR testing requirements.

e. Flight preparation. The spacecraft will be moved to the final assembly area. Flight preparation will include installation of flight equipment, loading of liquid propellants, installation of main retro-rocket, and installation and checkout of marker radar. The helium and nitrogen tanks will be pressurized, and the igniters and squibs will be installed. The weight and balance and thrust alignment check will be performed. The General Dynamics, Astronautics Division, shroud will be installed and hermetically sealed. The terminal surface sterilization operation of approximately 12 hours duration will be performed at this time. Physical access to the spacecraft will not be possible after this time.

f. Launch countdown. The spacecraft will be moved to the launch complex and mated with the *Centaur*, after which as many systems and scientific instruments as possible will be checked via the RF link from the trailer-mounted Command and Data Handling Console. Only qualitative checks can be made on designated scientific instruments and spacecraft systems because of time and environmental restrictions. The objective will be to design spacecraft equipment so as to permit sealing within the shroud for a period of up to 10 days to allow for normal operations plus recycling operations necessitated by possible delays in firing or use of the backup spacecraft.

2. Command and Data Handling Console

Purchase orders have been placed for all subcontract items in the command and data handling console (CDC). Circuit designs have been completed for all Hughes-developed console units except the demodulator and the buffer unit. Completion of mechanical designs (with the same two exceptions) will allow prototype fabrication to begin by the end of December 1961. Demodulator and buffer unit fabrication will begin in January 1962.

a. Mockup. The physical configuration of the CDC has been established, and a mockup of this configuration has been completed (Figure 180). The present CDC design consists of a three-bay control console and seven standard 19-inch equipment racks in an L-shape plan.

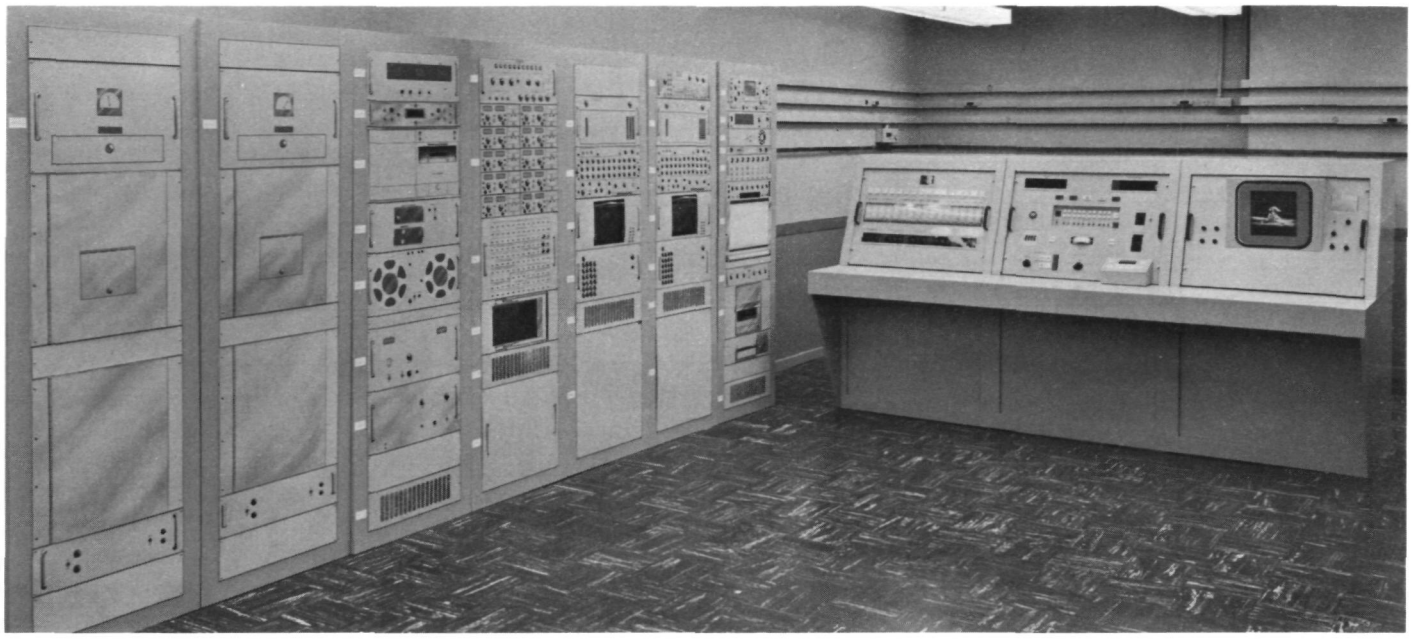

Figure 180. Command and data handling console mockup

The three-bay control console contains: (1) a center bay with command generator and command generator control panel, (2) a left bay with pulse code modulation (PCM) telemetry data display panel, and (3) a right bay with television monitor equipment. The individual panel configuration of each of these bays was described previously.

The seven equipment racks contain the remaining console equipment which falls into three general categories: (1) signal processing and control, which includes the demodulator, discriminators, PCM decommutator, patch panels, subcarrier oscillator, and buffer unit; (2) read-in and read-out, which includes the punched tape reader, command printer, TV photographic recorder, oscillographs, oscilloscope, events-per-unit-time meter; and (3) self-test, which includes the PCM simulator, FM calibrator, and TV test signal generator.

As shown in Figure 180, there are four patching centers on the equipment racks, two of which are identical (one on each of the decommutators). The patching centers – known as the decommutator patch panel, the low-density patch panel, and the high-density patch panel – are used to control the routing of signals and hence determine the data handling configuration of the console.

The decommutator patch panel controls the handling of PCM data and the displays associated with it. The panel accepts plug-in type patchboards previously wired and checked out to correspond to the several different data formats from the spacecraft. During operations, the data handling configuration can quickly be changed by removing one patchboard and installing another. The functions controlled by the decommutator patch panel are:

(1) Number of words (channels) per frame.

(2) Selection of the 16 channels to be converted to analog for display.

(3) Selection of the 5 of the 16 channels to be available in binary form.

(4) Selection of the 16 out of the 50 binary bits (10 bits per channel) selected in (3) to be displayed on the telemetry panel.

(5) Selection of the 5 channels to be converted to binary coded decimal (BCD) for decimal display.

(6) Selection of the 8 channel gates to be supplied to the telemetry-to-teletype encoder.

(7) Patch panel identification code.

The high density patch panel is used basically to switch from one decommutator to the other. All of the approximately 180 output leads from each decommutator are connected to this patch panel. By plugging in either one of two prewired patch boards, the outputs of either decommutator can be rapidly selected for routing to the appropriate destinations.

The low density patch panel is used primarily for checkout and calibration. Outputs, inputs, and test points of various units are routed to this panel. The panel is wired so that when a patch cord is plugged in to the jack, the normal connection of that function is disconnected and a new connection is made by the patch cord. By this method, in addition to checkout flexibility, some changes in system configuration can be made under abnormal circumstances.

In the CDC a number of on-line spares are provided to minimize station down-time due to console failure. These spares include a demodulator, three discriminators (minimum), decommutator, TV video processor, TV photographic recorder, punched tape reader, command generator, power supply, and subcarrier oscillator.

b. PCM decommutation system. Electro-Mechanical Research (EMR) was awarded the subcontract on November 3, 1961, for ten PCM decommutation systems, to be utilized in the command and data handling system. The proposed system is very similar to the EMR standard digital decommutation production line and will require only a minor design and development effort to meet *Surveyor* requirements. The PCM decommutation systems provide flexibility, accuracy, and outstanding synchronization performance.

Salient characteristics of the proposed system are as follows:

(1) Solid-state circuits and modular construction throughout.

(2) Bit rates of 45 to 80,000 serial PCM per second, word rates of 8 to 5500 per second, frame lengths of 5 to 128 channels, and up to 33 bits for frame synchronization codes.

(3) Binary and binary-coded-decimal digital outputs and analog outputs.

(4) Full use of digital circuits, affording high accuracy, synchronization flexibility, and rapid data acquisition.

(5) Patchboard control of digital and analog outputs (wired for expansion).

The first system is scheduled for delivery in February 1962. Environmental, acceptance, and reliability tests will be performed on the first system. The nine remaining systems will not undergo environmental tests but will be subjected to acceptance and reliability tests. The reliability test consists of 55 hours per system of system operation and will be performed after the completion of the acceptance tests. Monthly progress reports and biweekly PERT (Program Evaluation and Review Technique) charts will be provided to monitor production schedules.

c. TV recording and monitoring unit. A subcontract was awarded to Hallamore Electronics Corporation of Anaheim, California, to design and manufacture the CDC television monitoring and photographic recording system. The system to be supplied by Hallamore will consist of three major subunits: (1) a video processor sync separator which will acquire vertical and horizontal synchronization and provide synchronizing signals to the monitor and recorder as well as perform line to line clamping of the video, (2) a visual monitor which will utilize a long persistence cathode ray tube to enable the operator to perform a real-time evaluation of the received slow scan picture, and (3) a photographic unit which is basically a monitor with a short persistence blue phosphor, a 35 mm frame type camera which has a built-in "data box" to record the frame identification data pertaining to the received television picture as well as time. The limiting resolution of the ground system will be 720 lines on the photograph. Thus the estimated resolution of the ground unit with a 600 line by 600 element, noise-free input would be approximately 410 lines vertical and 460 lines horizontal resolution. Studies were made indicating that significantly higher display resolution could not be achieved within the development plan for *Surveyor*.

This system is very similar to the ground portion of the Hallamore-designed, slow scan television link used by Convair on the *Centaur* project. The system is used by Convair to monitor and record the condition of the liquid hydrogen in the *Centaur* fuel tanks under flight conditions. Only minor electronic and mechanical redesign is required to adapt this equipment to *Surveyor* requirements.

The prototype unit is to be delivered to Hughes by March 12, 1962. This unit will have completed all acceptance and environmental tests. After systems integration tests with the CDC, the prototype will be returned to Hallamore for any changes required to update it to the production configuration.

d. Demodulator. A design review was held on the circuits of the demodulator. It was felt that for narrow-band operation the original design resulted in more local oscillators and IF frequencies than was desirable from the standpoint of possible interference problems. It was learned that a 2.4 mc/sec signal output from the deep space station receiver which could be used for narrow band operation was available. Redesign of

the demodulator narrow band section using this 2.4 mc/sec input was therefore undertaken. The resulting circuitry (Fig 181) is considerably simpler than the original design since several local oscillators and one narrow-band discriminator were eliminated.

e. Discriminators. EMR Model 167 discriminators have been selected for the CDC. These discriminators are phase-locked loop, solid-state units in which the latest techniques are employed in determining optimum loop parameters. These techniques have been arrived at through empirical results as well as analytical considerations. The components affecting loop optimization are contained in the channel selector and output filter plug-in units. As a result, separate plug-in units, containing loops optimized for each of the various combinations of spacecraft information rates, waveforms, and deviations, will be required, and only a minimum of basic discriminator units will be needed. Ten of the basic discriminator units will be provided for each console. Since analysis of mission sequence indicates that a maximum of seven subcarrier channels will be utilized simultaneously, three discriminators can be considered spares.

Present spacecraft data requirements indicate a need for 20 channel-selector plug-in units and 17 output-filter plug-in units. CDC patching capabilities will allow any combination of discriminators and plug-in units dictated by data requirements, thus affording considerable flexibility. In addition, the discriminators chosen are well adapted to the requirement for console expansion capability, since additional data requirements or changes in present data channel configurations necessitate only additional plug-in units. Standard Inter-Range Instrumentation Group (IRIG) channel configurations can be obtained by use of proper plug-in units. While little or no threshold improvement will be obtained in some of the present spacecraft channels (compared with pulse counting discriminators), a substantial threshold improvement will be obtained in channels using higher modulation indexes.

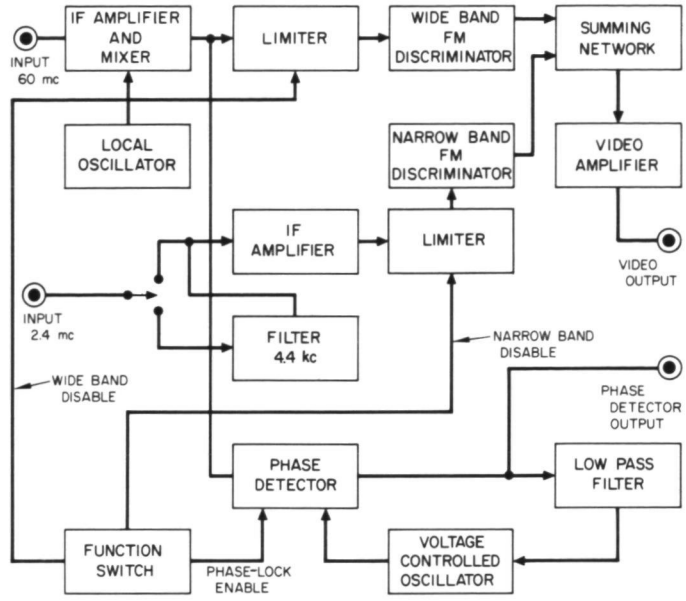

Figure 181. Demodulator block diagram

3. Surveyor Data Reduction and Processing Facility

The *Surveyor* data processing facility at the Hughes Culver City plant is designed to provide efficient handling of data required for final spacecraft performance analysis from a variety of magnetic tape formats, to allow means for data monitoring, and to generate tapes for computer reduction and analysis. A data processing facility functional arrangement has been established (Fig 182), consisting of tape reproducers interconnected through patchboards to decommutators and demodulators. The latter are in turn interconnected to direct recorders and the complex of equipment employed to generate two distinct computer formats. The type and quantity of units conform to the anticipated data flow generated by the *Surveyor* spacecraft instrumentation system with the additional data generated by the Deep Space Instrumentation Facility, command and data handling consoles, and range timing systems.

A detail specification has been prepared for a universal magnetic tape search system which will permit display, control, and translation of various range time formats needed for editing and data time identification. The unit will also provide means for rapidly extracting desired data from nonsequential portions of the magnetic tape. A second detail specification defines the format control buffer, a computer preparation subsystem consisting of analog and digital signal switching units, analog-to-digital converters, buffers, and buffer controls which will arrange data in formats for entry into the G-15 or IBM 7090 computers.

The manual and semiautomatic mode of data processing operations will be used to supplement the automatic magnetic tape processing complex. This mode is arranged functionally to support the *Surveyor* program, as shown in Figure 183.

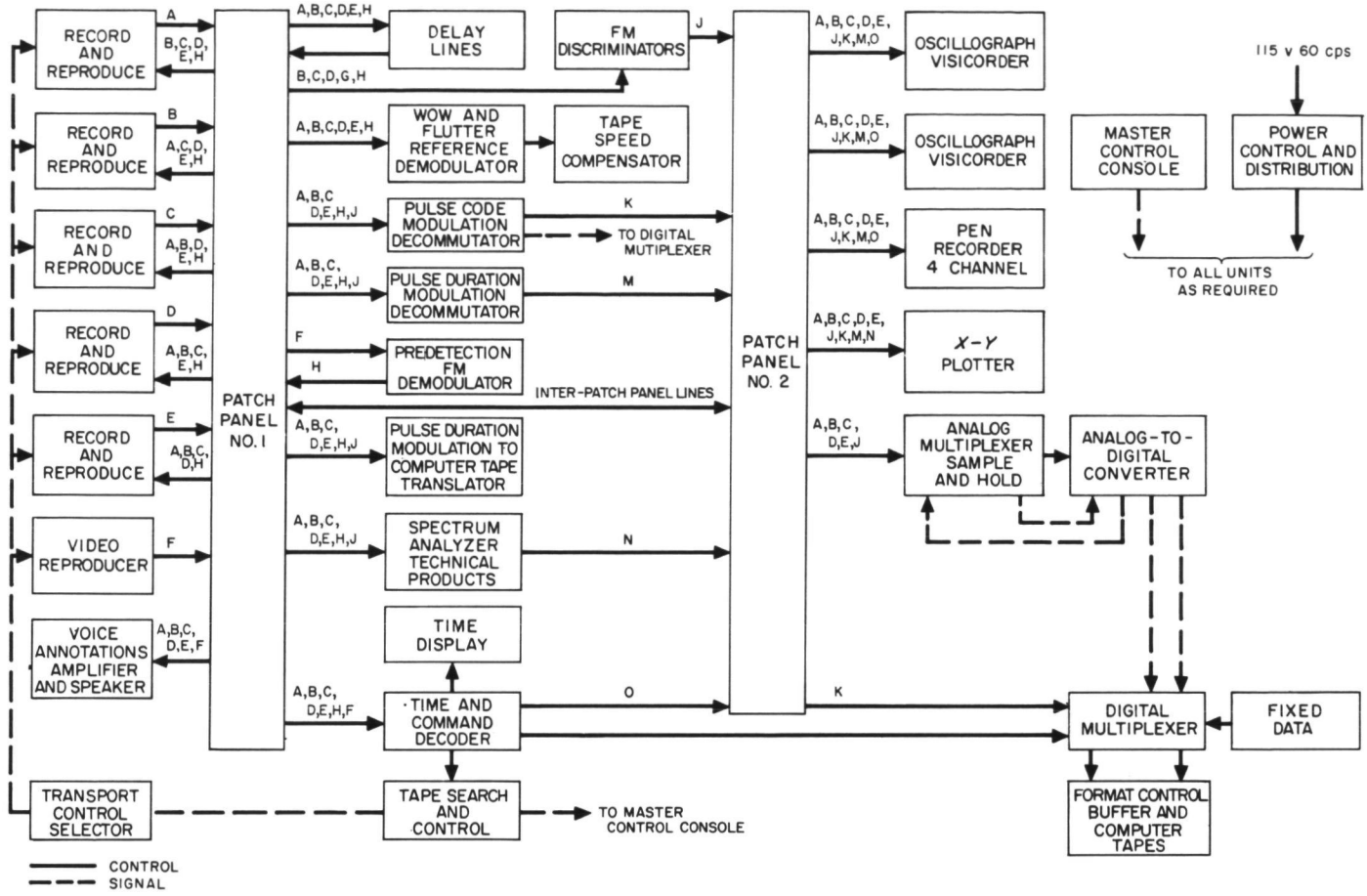

Figure 182. Data processing facility functional diagram

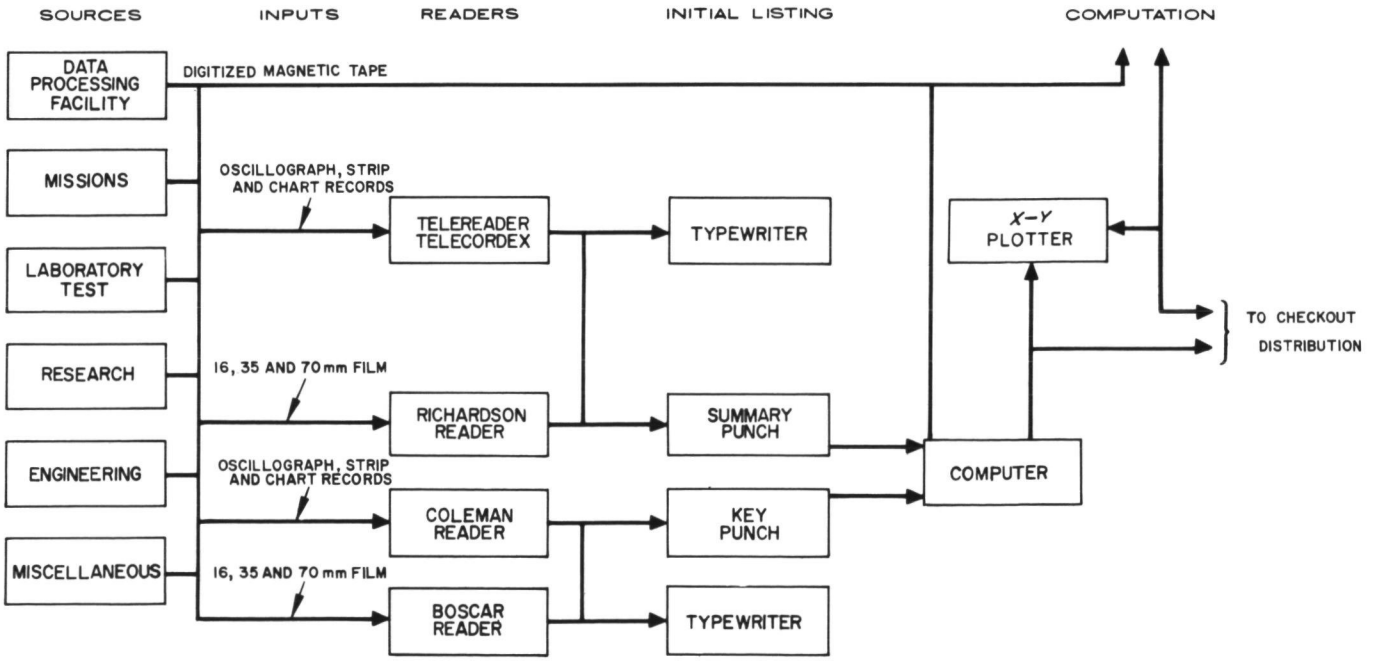

Figure 183. Data reduction functional diagram

4. *Surveyor* Spacecraft Simulator

A firm detail design specification for the *Surveyor* spacecraft simulator (Figs 184 and 185) has been released. This unit will be utilized at each station of the DSIF to provide CDC-DSIF spacecraft system checks as required.

A design criteria of the simulator is that it must provide the capability to transmit each subcarrier frequency complex which will be transmitted from the spacecraft. In many cases, the spacecraft signal processing subsystem provides redundant subcarrier oscillator frequencies for different experiments. This redundancy has been eliminated in the simulator. Since the preceding bimonthly summary, the surface geophysical package simulation has been eliminated, made possible by changes in the arrangement of spaceraft subcarrier oscillator frequencies.

The deep space stations are designed to provide a precision radio tracking system that includes the measurement of radial velocity utilizing a two-way doppler system. The advisability of including doppler simulation in the spacecraft simulator was carefully considered. However, provisions for a doppler simulation test will be incorporated in the DSIF doppler extraction subsystem. Therefore this capability will not be provided in the *Surveyor* spacecraft simulator. A digital readout capability has been added to facilitate checkout and fault isolation.

Existing spacecraft circuitry and packaging design will be utilized to the fullest extent possible in the simulator, but some changes must be made to provide for maintainability. Test points, circuit breakers, jack panels, etc., will be added to make all critical circuitry readily accessible for maintenance, fault isolation, or simulation of possible spacecraft malfunctions.

Two additional areas of simulator application are presently under study: (1) use of the simulator for checkout of the CDC when DSIF equipment is not available, and (2) possible use of a tape recorder or other means to simulate moon path time delay effects in spacecraft responses to earth commands.

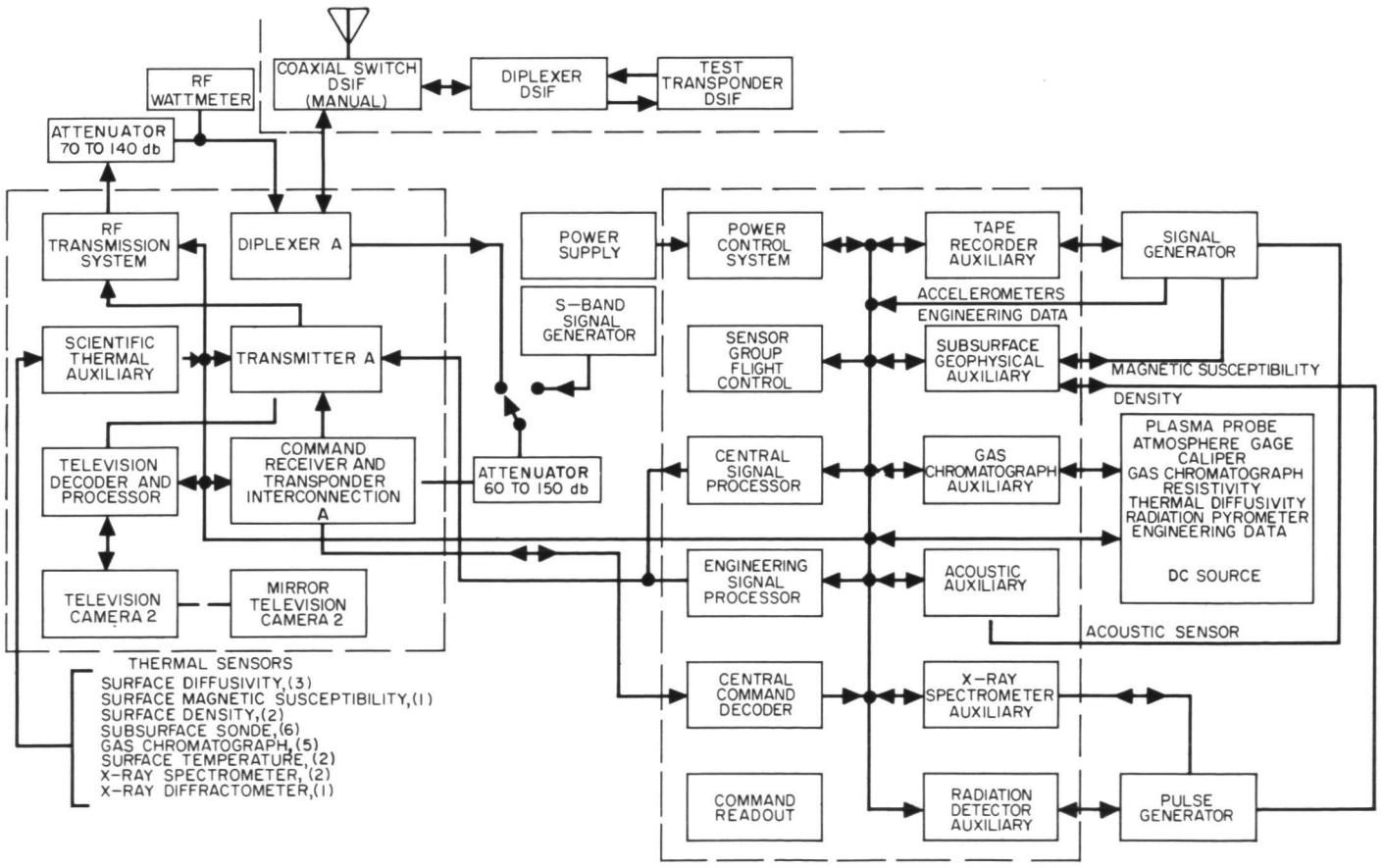

Figure 184. *Surveyor* spacecraft simulator

CONFIDENTIAL

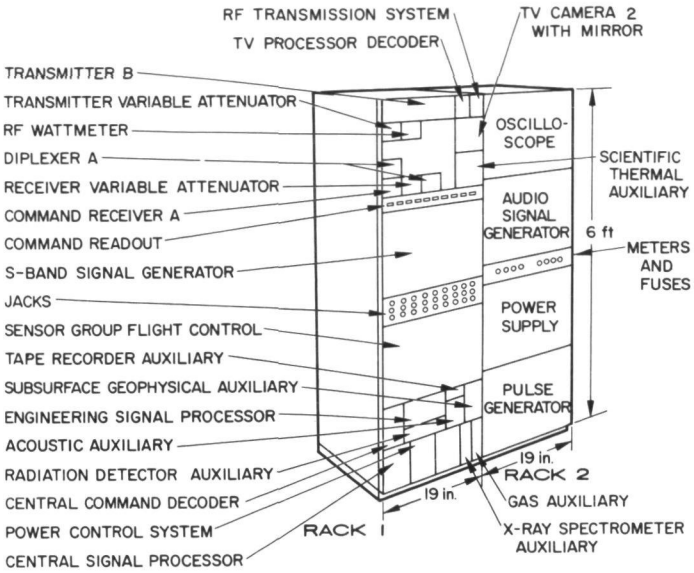

Figure 185. Simulator rack layout

The first may be accomplished by making the spacecraft simulator or portions of the system portable to permit removal to the main control building. The second would provide a more realistic operational simulation for maintaining operation proficiency and for developing new operational procedures.

5. Lunar Mission Sequencing Documentation

It is planned that documentation of the transit and lunar operations will be categorized into one of three possible levels depending on the purpose of the document, the ultimate user, and the amount of detail required. The first-level documents will include the information necessary to define facilities; establish operational requirements; and guide the Lunar Operations Director (LOD) and the Directors of the Data, Operations and Control Facility (DOC), DSIF, and Space Science in controlling the mission. Second-level documents will outline detail operating requirements and guides. Third-level documents will define detail operating procedures.

In each level of documentation, only as much detail on mission sequencing will be included as is required by the respective users in order for them to control their portion of the mission. Selected blocks of the mission sequence chosen to illustrate how the sequencing will be handled in the three levels of documentation are shown in Tables 20, 21, and 22. The sequencing shown is expected to change somewhat by the time the first SFOP (Space Flight Operation Plan) is published; the examples show format rather than actual sequencing details.

Table 20. First level sequence of events (SFOP)

Item No.	Time of event[a] Standard	Actual	Station[b]	Event
6	T + 115m		DSIF 3, DOC	Sample scientific temperatures.
7	T + 117m		DSIF 3, DOC	Conduct density experiment.
8	T + 147m		DSIF 3, DOC	Complete first TV survey.
9	T + 167m		DSIF 3, DOC	Begin radiation detector experiment with boom extended.
10	T + 168m		DSIF 3, DOC	Conduct acoustic velocity experiment.
11	T + 178m		DSIF 3, DOC	Sample scientific temperatures.
12	T + 179m		DSIF 3, DOC	Conduct soil mechanics experiment.
13	T + 230m		DSIF 3, DOC	Sample scientific temperatures.
14	T + 231m		DSIF 3, DOC	Conduct hardness experiment.
15	T + 261m		DSIF 3, DOC	Conduct magnetic susceptibility experiment.
16	T + 276m		DSIF 3, DOC	Sample scientific temperatures.
17	T + 277m		DSIF 3, DSIF 4, DOC	Transfer control to DSIF 4.
18	T + 278m		DSIF 4, DOC	Conduct thermal diffusivity experiment.
19	T + 290m		DSIF 4, DOC	Sample scientific temperatures.
20	T + 300m		DSIF 3	Loss of DSIF 3 visibility.

[a]T: lunar touchdown
[b]DSIF 3: Goldstone; DSIF : Woomera.

CONFIDENTIAL

Mission sequencing to be included in the standard sequence of events portion of the SFOP will consist of two types of presentations: a bar chart, similar to Figures 11 through 17, showing the order of events, their duration, and time the event should occur, as well as the visibility period of each deep space Station, which can be time-correlated with the sequence of events once the time of lunar touchdown has been established. This type of presentation will be used to quickly determine the planned activity during any given time period and the effect of deviations from the standard sequence.

The second presentation to be included in the SFOP (Table 20) shows each major function to be performed along with the time referenced to lunar touchdown. The functions are identified by an item number, also used as a reference for the second- and third-level documents. This table will be used by the LOD to control the mission and equate actual with planned events.

The SFOP information will be expanded for the DSS Operating Memo (Table 21). In this document, the items in the SFOP are broken down into various functional steps to be followed sequentially by operating personnel.

In the third-level document (Table 22), each significant event, all commands to be sent and their order of execution, telemetry data to be received at the DSS, evaluation of the data necessary to proceed to the next command, and the individual responsible for the evaluation are outlined for use of the operating personnel. The procedures shown are based on the assumption that the lunar phase has proceeded as planned and that the spacecraft configuration has not changed since completion of the last experiment. For example, with the acoustic velocity experiment, acoustic sensor No. 1 will have been deployed with the instrumentation used during the density experiment, and consequently separate commands for its deployment are not shown. However, in the case of nonstandard sequences, a separate set of documents will be prepared showing the required configuration of the spacecraft for conducting each given experiment. These documents will be used if the LOD should decide to change the order of conducting the experiments.

Since these three documents will all be correlated with a common referencing system, the LOD can closely control and monitor the progress of the mission. It is planned to duplicate this type of presentation for those nonstandard sequences that can be anticipated.

M. Scientific Experiments

1. Lunar Petrographic Microscope

The breadboard model of the lunar petrographic microscope, exclusive of the vidicon subsystem, is being constructed by Armour Research Foundation, Chicago,

Table 21. Second level sequence of events (DSS)

Item No.	Time of event[a] Standard	Actual	Event
6.1	T + 115m		Sample scientific temperatures.
7.1	T + 117m		Conduct TV survey of emplacement area for surface density experiment.
7.2	T + 124m		Emplace surface density instrument.
7.3	T + 125m		Conduct second TV survey of emplacement area.
7.4	T + 132m		Conduct surface density background count.
7.5	T + 137m		Begin surface density experiment.
7.6	T + 146m		Surface density experiment completed.
8.1	T + 147m		Complete first TV survey (more detail will be supplied when available).
9.1	T + 167m		Begin radiation detector experiment with boom extended.
10.1	T + 168m		Begin acoustic velocity experiment. Position acoustic velocity sensors and acoustic source.
10.2	T + 173m		Activate acoustic signal processing and conduct experiment.
10.3	T + 177m		Acoustic velocity experiment completed.

[a]T: lunar touchdown

Table 22. Third level detail procedure — acoustic velocity (CDC)

Item No.	Time of event[a] Standard	Time of event[a] Actual	Event	Command[b]	Incoming data to be evaluated	Required action	Responsible individual
10.1.1	T + 168m		Prepare for acoustic velocity experiment.			Insert patch panel No. 17.	CDC rack technician.
						Insert telemetry display overlay No. 17.	Telemetry monitor.
						Determine that acoustic sensor No. 1 has been displayed.	Telemetry monitor.
10.1.2			Display acoustic sensor No. 2.	Unlatch positioner.	Acoustic sensor No. 2 positioned.	Verify that acoustic sensor No. 2 is positioned.	Telemetry monitor.
10.1.3			Display acoustic source.	Unlatch acoustic source.	Acoustic source positioned.	Verify that acoustic source has been positioned.	Telemetry monitor.
10.2.1	T + 173		Activate acoustic signal processing and begin experiment.	Surface acoustic signal processing on.			
10.2.2				High-power transmitter on.	High-power transmitter on.	Verification.	Telemetry monitor.
10.2.3	T + 175m			Fire acoustic source No. 1.	Acoustic time reference signal No. 1.	No action required.	
					Acoustic geophone No. 1 output.		
					Acoustic geophone No. 2 output.		
10.2.4	T + 176m			Surface acoustic signal processing off.			
10.2.5				High-power transmitter off.	High-power transmitter off.		
10.3.1			Acoustic velocity experiment completed.			Verification.	Telemetry monitor.

[a]T: lunar touchdown
[b]Octal number associated with each command will also be shown when available.

Illinois. It will be completed and delivered the first week in January 1962. The slow-scan vidicon subsystem is being constructed by General Electrodynamics Corporation, Garland, Texas, and will be delivered in mid-January.

Twenty-four different plastic tapes have been tested by Armour for stability in vacuum. Further tests on stability of thermal, optical, and strength properties are being concluded as of this writing.

The vidicon subsystem to be used in testing the microscope breadboard will provide dc to 220-kc response and slow-scan monitoring. The line frequency is variable from 10 to 1000 cps; the frame frequency is independently variable from 0.02 to 2 cps. Resolution is 600 lines per in. and there are 8 grey scales. Sensitivity is 0.5-ft-candle faceplate illumination. The vidicon may be operated remotely from the central power supply by means of a 3- to 5-ft cable, and may thus be used on standard laboratory microscopes and other images as well as on the lunar breadboard model.

Sample preparations of several rock and mineral types have been made for testing the resolution and over-all optical performance of the breadboard against a standard laboratory microscope, with and without vidicon transmission. Figure 186 is a photomicrograph of crushed dunite particles in the 75 to 250 μ size range taken in

CONFIDENTIAL

plane-polarized white light. Significant characteristics of this sample are the: (1) high relief of olivine grains against the mounting medium ($n = 1.54$), (2) absence of cleavages, (3) rock grain size coarser than grain size of crushed sample, and (4) nearly monomineralic rock. All features necessary to identify the original rock type can be discerned at this magnification.

Figure 187 is a crushed bronzite pyroxenite viewed under the same conditions as the dunite in Figure 186. The good cleavages distinguish the grain from olivine, and their transparency at this grain size distinguishes them from hornblende.

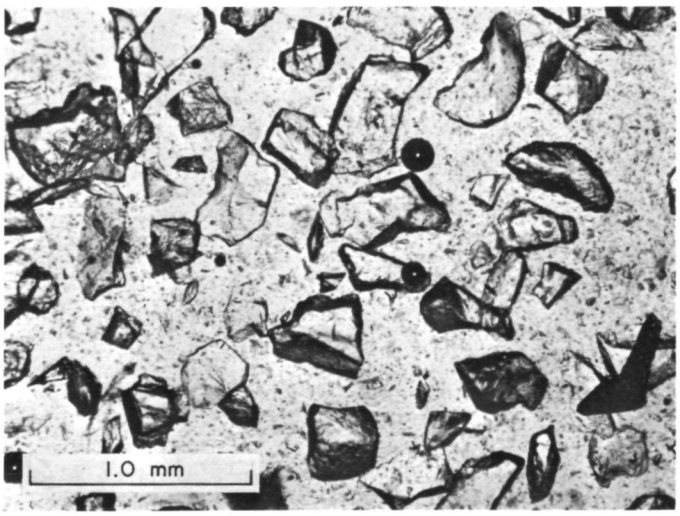

Figure 186. Crushed dunite, plane-polarized white light

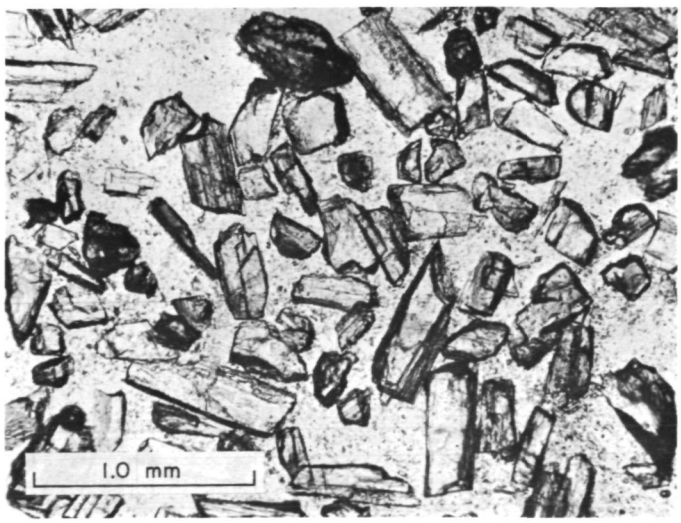

Figure 187. Crushed pyroxenite, plane-polarized white light

Figure 188 shows a typical basaltic volcanic texture in contrast to the plutonic textures of Figures 186 and 187. The phenocrysts are olivine and pyroxene (high relief), and plagioclase (low relief). The fine-grained particles contain glass with fine magnetite making them appear nearly opaque. They contain numerous subparallel plagioclase tablets (as in encircled grain). The edges of vesicles may be seen in some particles (arrows to cusps); the amount of vesiculation may be estimated from the number of cusps present in a field of many grains. The inequigranular texture, the mineralogy, the flow-oriented plagioclase crystals in the ground-mass, and the edges of vesicles all identify the rock as a basalt flow.

Figure 189 is a glassy rhyolite tuff showing the crushed pumice fragments (large particles), small particles of glass, and phenocrysts (quartz and sanidine) with low relief. Figure 190 is the same field of view in cross-polarized light; all particles except the few birefringent phenocrysts are glass and are isotropic.

2. *Sigma Plasma Detector*

The *Surveyor* plasma detector, now under development at JPL, will examine the solar wind and Moon interaction and is a second generation version of the solar plasma detector flown on *Rangers I* and *II*. It will be used to measure the charged particle energy spectra as a function of arrival direction. The principal purposes of these measurements are to determine the low energy particle

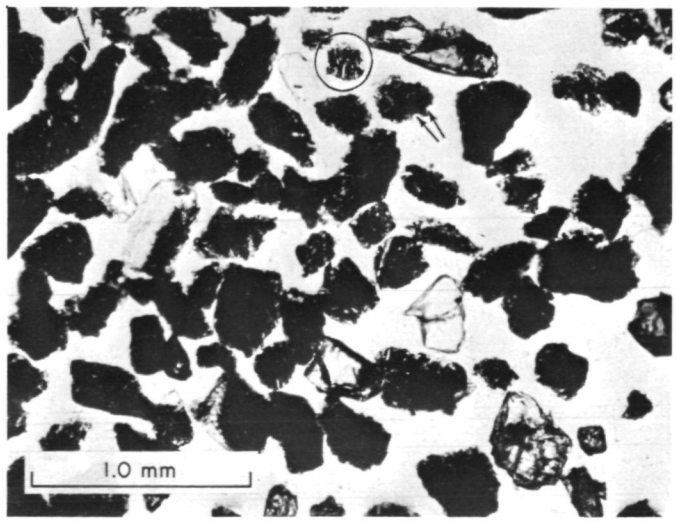

Figure 188. Crushed basalt, plane-polarized white light

CONFIDENTIAL

environment of the Moon and to aid in the interpretation of the magnetometer data. The charged particle measurements could be related to the magnetometer measurements as follows:

(1) From the measured magnetic field magnitude and direction, a 1st iteration field model is constructed. The 1st iteration field might be a magnetic dipole located at the center of the Moon with the necessary strength and orientation to produce the observed field at the spacecraft. The expected modulation of the motion of interplanetary particles in crossing this model field is then calculated.

(2) A comparison of the calculated and the measured distributions of particles as a function of angle of arrival and energy is made. The general features of any disagreement are then studied qualitatively to aid in the generation of a 2nd iteration model which might be something like a distorted dipole field which is greatly compressed on the Sun side by a solar wind. This process is repeated until 1 or more models are found for which the calculated and measured particle distributions are in reasonable agreement.

Direction of travel will be determined by 5 electrostatic analyzers (Fig 191), each with an acceptance angle of about 18 deg about the normal direction. The analyzers

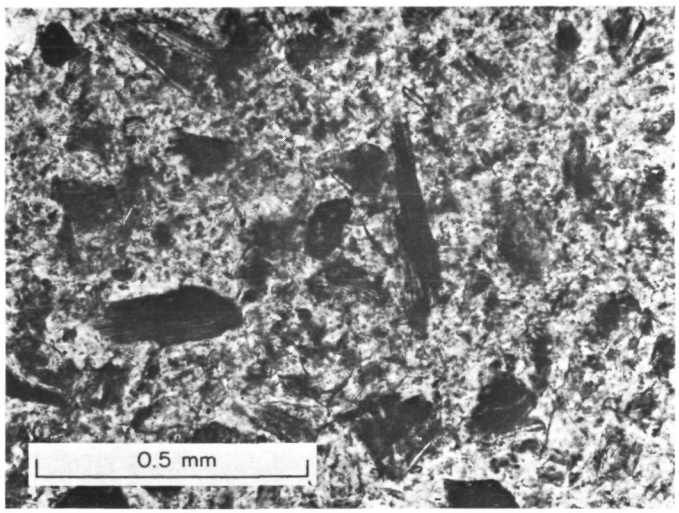

Figure 189. Crushed rhyolite tuff, plane-polarized white light

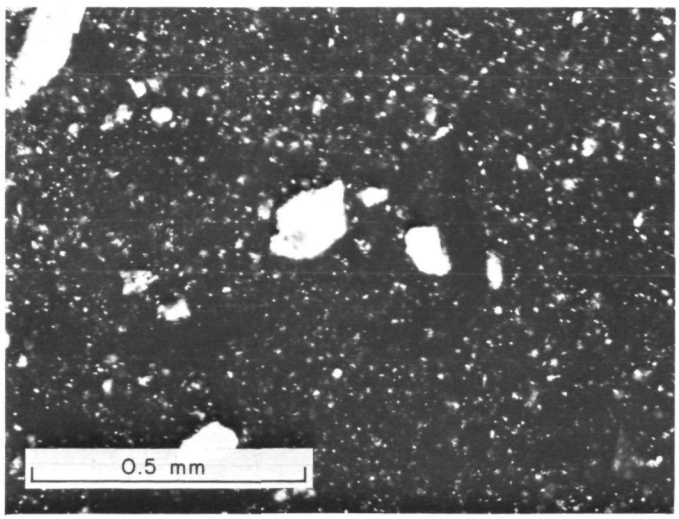

Figure 190. Crushed rhyolite tuff, cross-polarized light

a.

b.

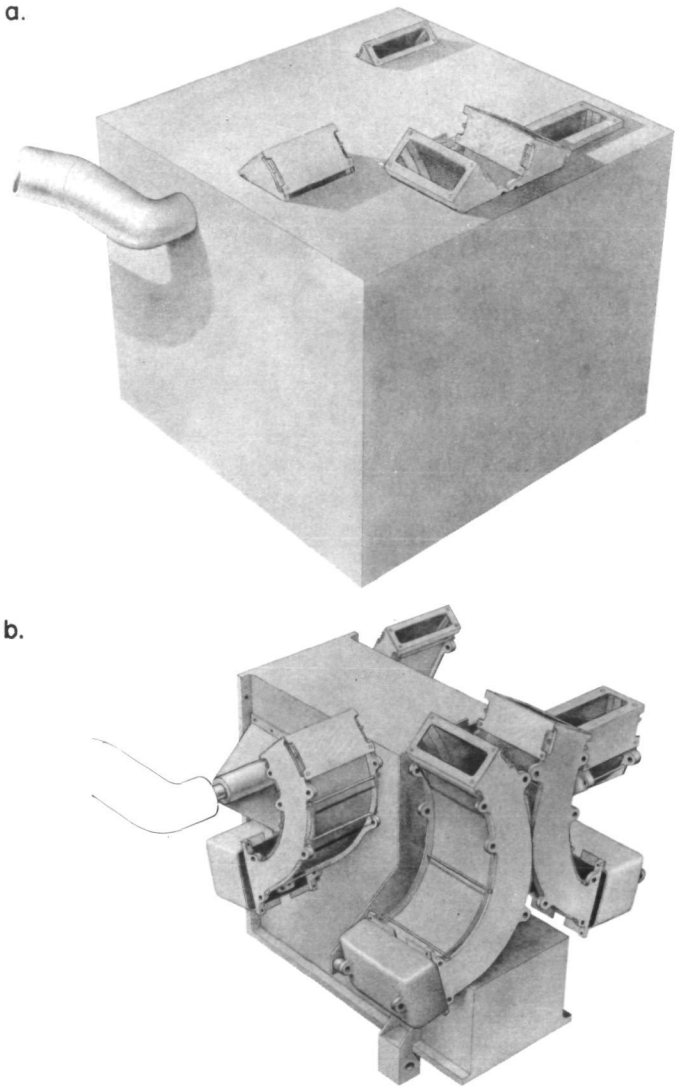

Figure 191. *Surveyor* sigma plasma detector (a) with and (b) without thermal shield

CONFIDENTIAL

are situated so that 1 detector analyzes particles incident from the local vertical, while the other 4 point at 45 deg to the vertical at 90-deg intervals. The package is to be extended from the spacecraft on a 12-ft telescopic boom and gimbaled on 2 axes to seek the local vertical for proper orientation of the analyzers.

Charged particles entering an electrostatic analyzer are deflected by an electric field which is approximately transverse to the particle velocity. Those particles with a particular charge sign, a certain range of energy per unit charge, and a certain angle of incidence are deflected onto the charge collector cup. Particles which enter the deflection plates with the wrong charge sign, energy per unit charge, or angle of incidence strike the deflection plates and are not recorded. The energy distributions of both positively and negatively charged particles entering the instrument can be determined by varying the sign and magnitude of the deflection voltage. The instrument is capable of analyzing positive ions or electrons with energies between 2 ev and 6 kev.

The 5 deflection plate systems are grouped around 1 box and, by means of special high resistance switches (open circuit resistance $>10^{16}$ ohms), time share a single electrometer amplifier and high-voltage sweep amplifier (Fig 192). This arrangement results in a significant saving in weight and power over a system in which each set of deflection plates has its own separate electronics. The *Surveyor* detector, with 5 analyzers, weighs 12 lb and uses 1 w, whereas the 6 analyzers on *Rangers I* and *II* weighed 33 lb and used 2.75 w.

a. Electrometer amplifier. The electrometer amplifier for the *Surveyor* detector is an improved version of the *Ranger I* and *II* models. A development contract was let to the Applied Physics Corporation in April 1961 to devise a piezoelectric pickoff on the vibrating reed dynamic capacitor, in order to control a reed resonance tracking oscillator on the *Surveyor* detector. This effort has been successful and the 1st version of this development will be implemented in the *Mariner* R plasma probe. Subsequent work on improved sealing methods of the reed capacitor container has led to a marked reduction in contact potential, and a temperature coefficient of contact potential of less than 70 μv/°C. Use of this improved modulator has resulted in an electrometer with increased sensitivity and a greater dynamic range over the temperature span anticipated in the lunar environment (−50 to +100°C). Several prototype reed modulators have been thoroughly evaluated over this range and have successfully passed the sterilization procedure.

Perhaps the most significant improvement in the *Surveyor* probe is the incorporation of an automatic scale factor device (Fig 193). The feedback element of the *Ranger* electrometer is the bipolar logarithmic compressor which has the approximate transfer function:

$$E_{out} = K \log I_{in}$$

This device, however, requires a well insulated battery to measure electron current (*SPS 37-11*); the stability of the electrometer can be no better than the long term stability of the thermionic compressor diodes. In order to more thoroughly exploit the advantages presented by the electrometer amplifier, an automatic gain system was devised which uses resistors as feedback elements and results in the transfer function:

$$E_{out} = -I_{in} R_f$$

Since the electrometer has a useful dynamic range of ± 10 mv to ± 10 v, circuits were designed to automatically change the feedback resistors as a function of the output voltage. The feedback resistors selected for the *Surveyor* instrument enable the amplifier to measure currents from $\pm 10^{-7}$ to $\pm 10^{-14}$ amp in 3 ranges with a decade overlap on each range. For the plate geometry selected this corresponds, respectively, to particle fluxes between 4×10^{10} and 4×10^{3} particles cm^{-2} sec^{-1} for each energy level. The device consists of a chopper input stage (in order to sample both positive and negative voltages) followed by suitably scaled amplifiers. After restoration and integration of the resultant square wave, amplitude discriminators examine the integrator outputs to determine whether the electrometer is within the range of ± 50 mv to ± 10 v. The discriminator outputs drive a reversible counter up or down, depending upon the appropriate limit crossing, and logic switching on the counter inserts the proper feedback resistor. An analog voltage proportional to the feedback resistor is resistively summed with a voltage proportional to the collector cup number, and this signal is fed to the data system for identification. The overlap between ranges was provided to prevent oscillation between resistors and to take advantage of the fast response of the electrometer with the smaller resistors in place. By increasing the sampling rate at the amplifier output to 10/sec, for example, rapid cyclic variations or waves may be observed in the plasma.

Evaluation is being made of a new low noise silicon input stage for the electrometer to replace the presently used germanium transistor. This will enable the electrometer to more reliably withstand the lunar temperature environment. It is also planned to evaluate field-effect transistors in this application. These units, by virtue of their high power gain, may well result in a significant

CONFIDENTIAL

CONFIDENTIAL

reduction in circuit components as well as improved performance.

b. Deflection voltage system. The deflection voltages for the analyzer plates are generated by 2 fully transistorized assemblies: the programmer and high voltage sweep amplifier (Fig 192). The programmer consists of a 4 by 13 diode matrix, driven by a 4-stage binary scaler, which consecutively gates a reference input voltage to 1 of the

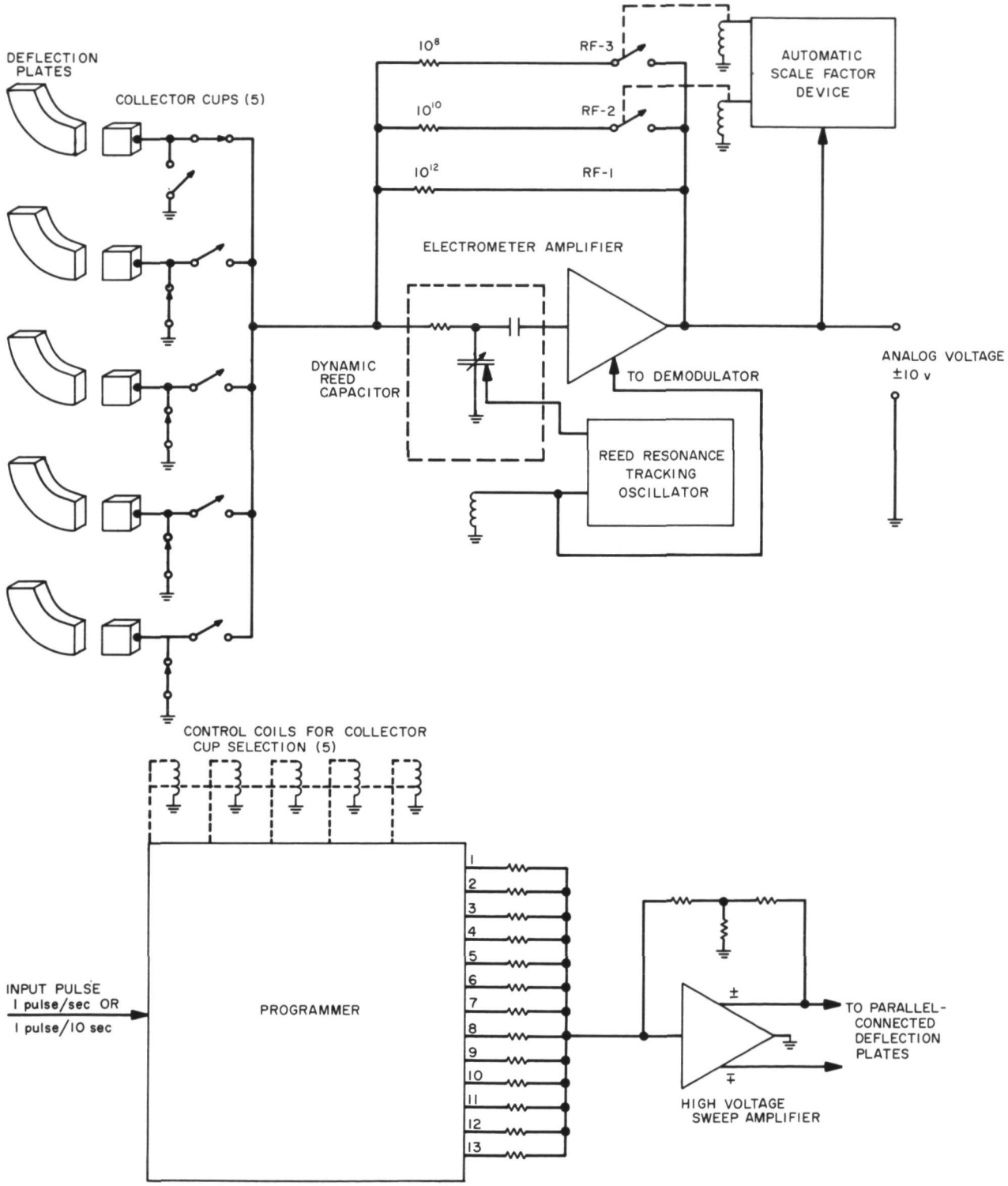

Figure 192. *Surveyor* sigma plasma detector circuit

CONFIDENTIAL

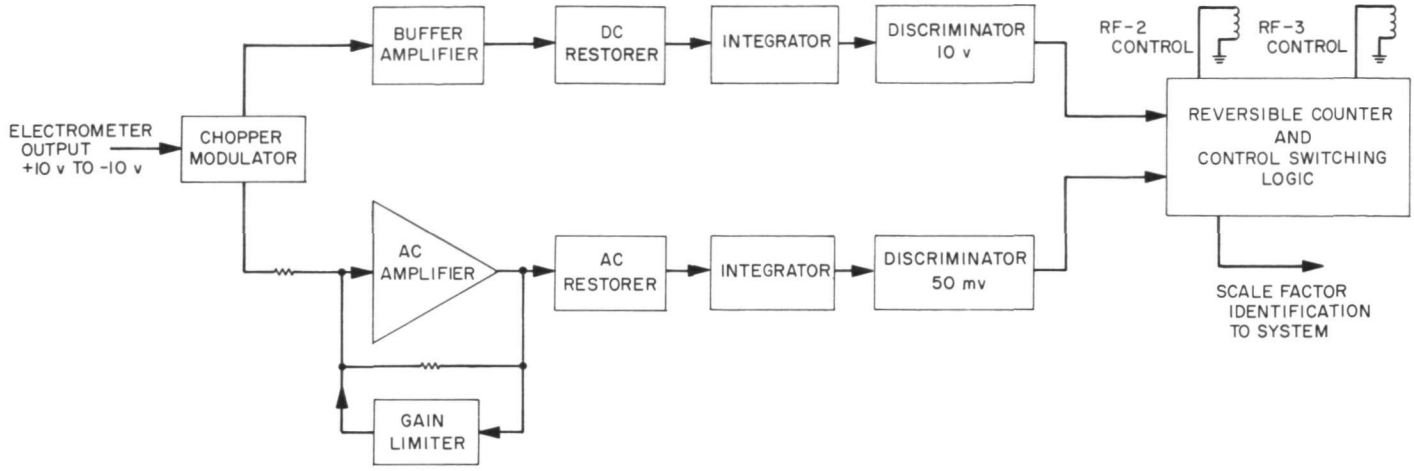

Figure 193. Automatic scale factor device

12 input resistors of the high voltage sweep amplifier. The rate at which the programmer steps is governed by the rate of the input timing pulse from the system. Upon receipt of the 13th pulse, logic steering resets the programmer to the first step, opens all collector cups, and injects a standard current into the electrometer. This self-generated reset pulse is also used to drive a 3-stage scaler and a 3 by 6 matrix that controls the collector cup selection switches. The programmer thus sequences the sweep amplifier through 12 energy levels, resets itself, and injects a standard current on the 13th step. It also steps to the next collector cup in the sequence on that step.

In addition, there are 3 values of standard current which are sampled alternately so that 3 complete cycles of the programmer and the 3 scale factor ranges of the electrometer amplifier are tested. This corroborative test procedure seems wise in light of the fact that:

(1) The lunar surface temperature environment is extremely severe by present flight hardware standards and is not fully understood.

(2) Methods of simulating these temperature and vacuum extremes are not fully adequate.

(3) The system must be designed to operate intermittently for a long period (30 days or more).

(4) Since the logic circuitry already exists, only a few components need be added for the task.

The instrument may operate in 1 of 2 modes upon ground command. When the largest resistor (10^{12} ohms) is in the feedback loop, the electrometer must settle out for a few seconds before a useful reading is obtained. The programmer is, therefore, sequenced only once every 10 sec. If the particle fluxes incident on 1 of the analyzers are large enough to sequence the electrometer to the 10^8 or 10^{10} ohm resistors, the timing pulse rate may be increased to 1/sec by ground command to take advantage of the rapid amplifier settling time.

The high voltage sweep amplifier is being redesigned as a carrier type dc operational amplifier in contrast to the direct coupled approach taken on the *Ranger* experiment. Chopper transistors have been made available recently which can ensure the null stability necessary in this application.

c. Temperature evaluation. A temperature control model of the instrument has been constructed. It consists of the outer chassis with the 5 electrostatic analyzers in place and a covering of insulation material surrounding the whole package. The heat of the electronics is simulated by resistors, and thermocouples are connected at various points around the box.

Reference

1. Graff, W. J., "Thermal Conductance Across Metal Joints," *Machine Design*, September, 1960.

PART THREE
PLANETARY–INTERPLANETARY PROGRAM

I. Program Status

A. Objectives

The primary long range objective of the NASA Planetary–Interplanetary Program is the development of automatic, unmanned, interplanetary spacecraft technology and the use of this technology in the form of space probes to gather fundamental scientific knowledge concerning the planetary and interplanetary environments, the planets themselves, and solar phenomena, both out of and within the plane of the ecliptic.

The secondary long range objective of the program is the development of technology and the collection of scientific data which will contribute to the successful manned exploration of the planets and interplanetary space.

The primary objective of the program by 1970 is to have rather completely demonstrated and, to some reasonable extent, exploited (in terms of acquired scientific data) spacecraft capable of (1) being put into orbit around and (2) landing on the surface of Mars and Venus.

A secondary objective during this period will be the initial effort toward extending the above capability toward the planets Mercury and Jupiter and space shots out of the plane of the ecliptic and in toward the Sun.

The immediate objective of the program is the initial probing of Mars and Venus.

B. Missions

The Planetary–Interplanetary Program at present consists of 3 projects: (1) *Mariner* R using the *Atlas–Agena* B vehicle, (2) *Mariner* B using the *Atlas–Centaur* vehicle, and (3) the *Voyager*, using the *Saturn* vehicle. The missions planned for these projects are defined below and are obviously subject to change because of such influences as new scientific discoveries or unexpected developments in vehicle availabilities.

1. Mariner R Project

The intent of the *Mariner* R project is to perform flyby missions to Venus in 1962 using the *Atlas–Agena* B vehicle. These missions are a replacement for the *Mariner* A project which was cancelled during September 1961 due to unavailability of *Centaur* launch vehicle.

The primary objective of the *Mariner* R project is to develop and launch 2 spacecraft to the near vicinity of the planet Venus in 1962, to receive communications from the spacecraft while in the vicinity of Venus, and to perform a radiometric temperature measurement of the planet. A secondary objective is to make interplanetary field and/or partial measurements on the way to Venus and in the vicinity of Venus.

CONFIDENTIAL

2. Mariner B Project

The primary purpose of the *Mariner* B project is to permit scientific investigations of the planets Venus and Mars during their periods of availability in 1964 through 1967. Secondary purposes in order of priority are (1) to make interplanetary scientific investigations in the regions between Earth and Mars, (2) to develop experience in the design of a spacecraft that has considerable flexibility with regard to the specific missions it is basically capable of covering, (3) to provide experience and knowledge which will permit a quality and efficient design of the later *Voyager* spacecraft. To these ends, the spacecraft will be designed for a precision flyby mission and will incorporate the capability of either carrying or not carrying a small landing capsule. The *Mariner* spacecraft will be injected by the *Centaur* launch vehicle and it is expected to launch 2 identical probes during each of the planet launching opportunities. Deep space probes, to be launched in between periods of Mars and Venus availability, are included in the *Mariner* B project.

3. Voyager Project

Voyager missions are envisioned to evolve to sophisticated orbiters and landing experiments beginning in 1966 or 1967 using *Saturn* vehicles. Planetary orbiters are a necessary part of the evolution and are a logical step in the development of spacecraft technology. Orbiters are probably required to permit sufficient observation of the planet to know how to proceed with the landing missions. Furthermore, orbiters may well constitute an important step in the actual landing experiments. The emphasis on planetary orbiters, therefore, will be to contribute to the successful accomplishment of the landing objective.

C. Program Activities

1. Mariner R

The design interfaces for *Mariner* R spacecraft were frozen in mid-October; since that time work has progressed in the finalization of design of all hardware with the final detail design freeze set for early January 1962.

This has been an active period with procurement of new *Mariner* R peculiar equipment and the modification of existing *Ranger* and *Mariner* A equipment. It also marked the beginning of flight acceptance testing of individual systems and subsystems, with the peak load of this testing occurring in late December 1961 and running through January 1962. Assembly of the spacecraft is scheduled to begin in early January with the first assembled spacecraft subsystem and system type tests to begin late in January.

The final version of the Project Development Plan has been prepared and is at Marshall Space Flight Center (MSFC) for review and approval. It is planned to submit the approved and signed copy to NASA Headquarters early in January.

2. Mariner B

Mission objectives and design criteria were generated and have been used for the preliminary design effort. This effort was initiated in October 1961, is proceeding on schedule, and will be completed on April 1, 1962. A Preliminary Project Development Plan has been prepared. One rough draft copy of this plan has been transmitted to NASA Headquarters. A final draft of this Preliminary Project Development Plan is being prepared and will be transmitted to MSFC and NASA Headquarters for review during January 1962.

3. Voyager

In addition to the technical preparation underway within the technical divisions, effort is being applied in the Planetary Program Office in the preparation of a set of mission objectives for the *Voyager* project. These objectives are intended to serve as a guide for a *Voyager* study committee to be formed early in 1962 for the purpose of generating design criteria for use in the preliminary design phase. The primary current problem is the determination of which launch vehicle will be assigned to the *Voyager*. Detailed project planning cannot proceed until this decision is made and announced.

CONFIDENTIAL

II. Mariner R

A. Systems

1. Launch Considerations

The *Mariner* R launch vehicle will be the *Atlas–Agena* B which will provide a spacecraft weight of approximately 446 lb for at least a 47-day launch window. Since a delay in launch time, if not compensated, causes an error at Venus encounter, it is necessary to alter both the launch azimuth and parking orbit coast time between *Agena* burning periods.

Figure 1 shows typical *Agena* 2nd burn period as a function of firing azimuth from 90 deg east of true north to 114 deg east of true north. The large hatched area indicates the area in which the 2nd burn could occur, dependent upon the trajectory. The top boundary line represents the earliest start of 2nd burn; the lower boundary line represents the latest end of 2nd burn; and the side boundaries are formed by the launch azimuths 114 and 90 deg. The launch azimuth will vary (between 90 and 114 deg) with the time of launch within the 2 hr and 40 min firing window.

Use of a parking orbit can allow injection to occur at any point over the Earth's surface. Figures 2 and 3 show the maximum injection locus for July 17 and September 15, 1962, respectively. The restrictions of azimuths to those indicated take into account postinjection tracking considerations and yield an approximate 2 hr 40 min firing window for all *Mariner* R launch days. Time errors at encounter can be minimized by the mid-course maneuver.

2. Orbit Characteristics

a. Geocentric phase. Launch azimuth, geocentric injection latitude, and longitude vary with launch time and

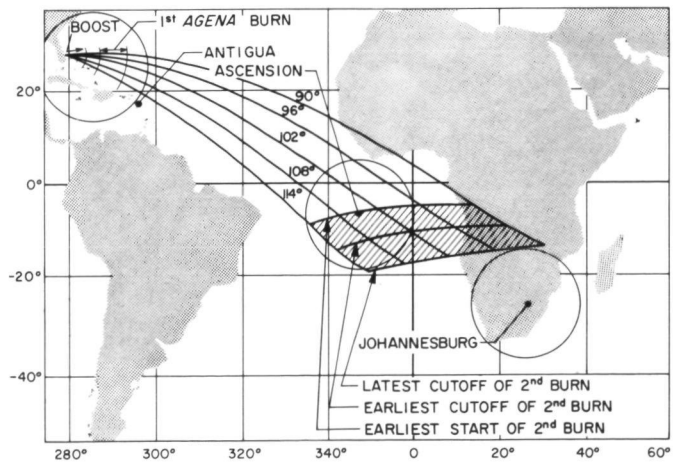

Figure 1. Typical *Agena* 2nd burn period as firing azimuth from east of true north to 114 deg east of true north

launch date. The time from launch to Goldstone radio horizon depends primarily on longitude of geocentric injection. As the launch date varies, the required geocentric energy (C_3) changes. This is clearly seen in Table 1

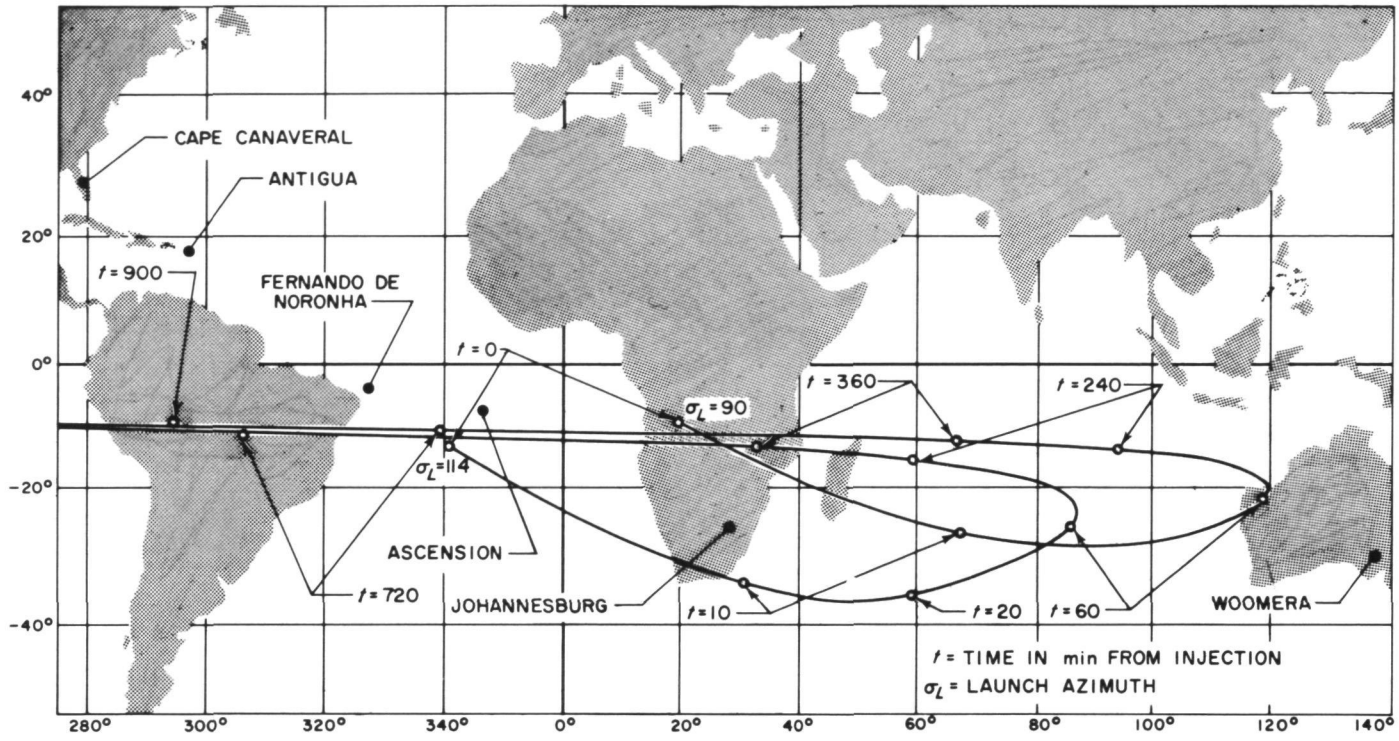

Figure 2. Maximum injection locus for July 17, 1962

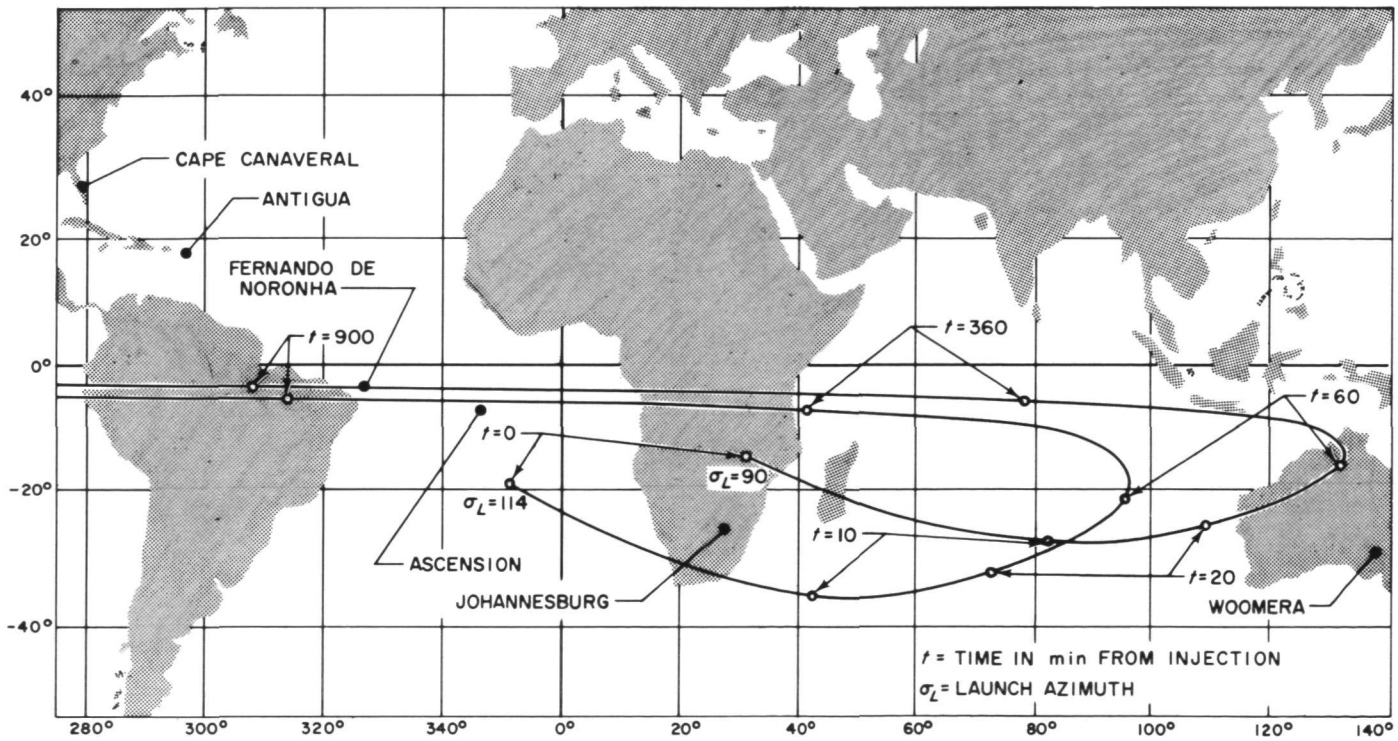

Figure 3. Maximum injection locus for September 15, 1962

CONFIDENTIAL

where C_3 decreases monotonically with launch date until August 23, and afterward increases monotonically until the final date of launch. The greater the energy, the greater the speed of injection. Table 1 also gives estimated injection locations for all days in the launch window for azimuths of 90, 96, 102, 108, and 114 deg.

b. Heliocentric phase. The probe moves in a nearly elliptical orbit primarily under the influence of the Sun (with the Sun at 1 of its foci). The true anomaly of heliocentric injection increases as launch date is delayed. Figure 4 is a plot of Earth–probe–Sun angle versus days from launch. In this figure, 4 specific launch days are referred to as Trajectories 1, 2, 3, and 4. Separate arrival dates, 2 days apart, have been selected for the *Mariner* R P37 and P38 trajectories varying from December 6 through 16, 1962. Figure 5 shows corresponding dates for the 67-day firing period. Note, for example, that for Trajectory 4 the maximum Earth–probe–Sun angle occurs at approximately 42½ days from launch and is then about 168 deg. The other trajectories have approximately the same Earth–probe–Sun angles for maxima. The reason that the maximum angle is not 180 deg is that the inclination of the probe's heliocentric orbit to the ecliptic varies from 1 to 2.5 deg depending on launch date. It is to be noted that the same curves may be used to determine the position of the probe as the Earth and Venus orbit the Sun.

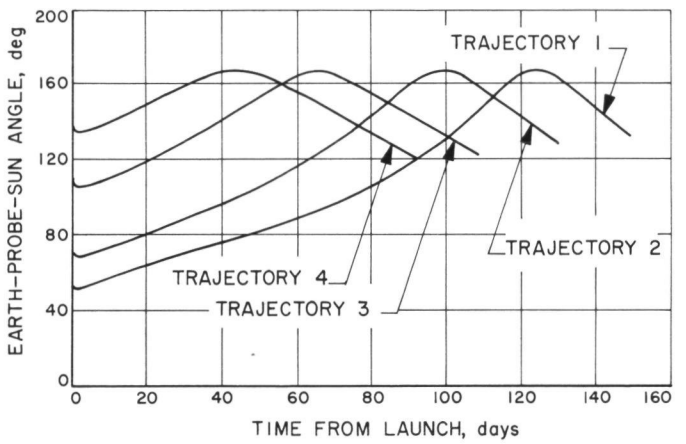

Figure 4. Plot of Earth–probe–Sun angle versus days from launch

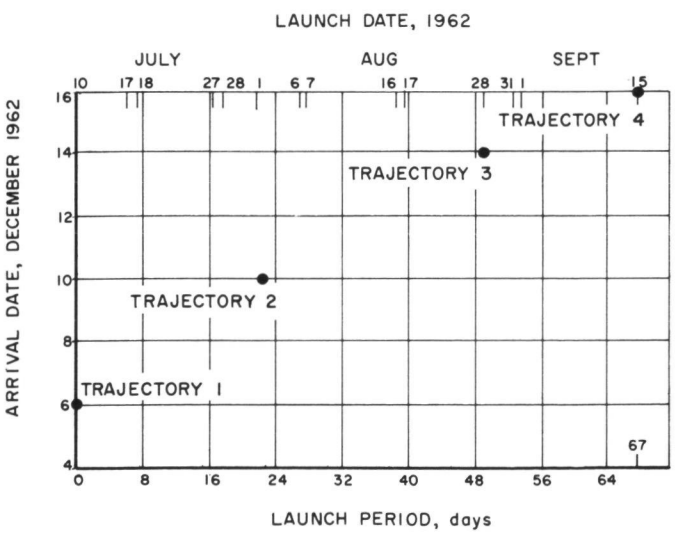

Figure 5. Arrival dates for 67-day firing period

c. Hyperbolic trajectory. For *Mariner* R the hyperbolic excess velocity of the probe with respect to Venus varies from 5.3 to 6.0 km/sec. To obtain the Cytherean aiming point it is necessary to make use of the expected dispersions and the spacecraft constraints. Because of the radiometer it is desirable to pass Venus when the angular diameter of the planet subtends angles of 10 to 45 deg, which implies a radius vector length of 16,000 to 71,000 km from probe to Venus, respectively. On the other hand, because of the magnetometer, it is desirable to pass close to Venus. In order to obtain better nominal aiming points, more calculations remain to be done. Figure 6 illustrates miss distance vectors and the components $B \cdot T$ and $B \cdot R$; current estimates of the miss

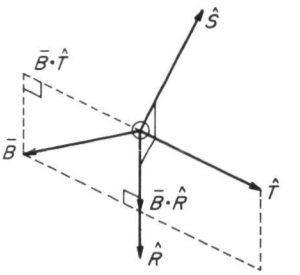

IMPACT PARAMETER COMPONENTS

$\hat{S}$ = A UNIT VECTOR IN THE DIRECTION OF THE INCOMING ASYMPTOTE

$\hat{T}$ = A UNIT VECTOR PERPENDICULAR TO $\hat{S}$ THAT LIES IN THE ECLIPTIC PLANE

$\hat{R}$ = A UNIT VECTOR WHICH FORMS A RIGHT-HANDED SYSTEM

$R = \hat{S} \times \hat{T}$

$\bar{B}\cdot\hat{T}$ = PROJECTION OF THE IMPACT PARAMETER B UPON THE UNIT VECTOR $\hat{T}$

$\bar{B}\cdot\hat{R}$ = PROJECTION OF THE IMPACT PARAMETER B UPON THE UNIT VECTOR $\hat{R}$

$$B^2 = \left[(\bar{B}\cdot\hat{T})^2 + (\bar{B}\cdot\hat{R})^2\right]^{\frac{1}{2}}$$

Figure 6. Miss distance vectors and components $B \cdot T$ and $B \cdot R$

CONFIDENTIAL

Table 1. *Mariner* R trajectory characteristics

Launch day	C_3 $\times 10^8$	$\sigma_L = 90$ deg			$\sigma_L = 96$ deg			$\sigma_L = 102$ deg			$\sigma_L = 108$ deg			$\sigma_L = 114$ deg		
		Latitude	Longitude	T_L[a], sec	Latitude	Longitude	T_L[a], sec	Latitude	Longitude	T_L[a], sec	Latitude	Longitude	T_L[a], sec	Latitude	Longitude	T_L[a], sec
7-10	0.14158	−15.259	31.281	31259.0	−15.604	19.433	34215.4	−16.590	8.291	36909.8	−18.099	358.248	39241.2	−19.983	349.332	41202.0
7-11	0.13905	−14.505	29.671	31406.9	−14.848	17.852	34355.4	−15.829	6.789	37028.5	−17.328	356.854	39330.8	−19.198	348.057	41259.8
7-12	0.13670	−13.800	28.198	31528.4	−14.141	16.407	34469.5	−15.117	5.417	37123.0	−16.608	355.582	39398.4	−18.465	346.895	41298.2
7-13	0.13450	−13.139	26.845	31626.0	−13.479	15.079	34560.4	−14.451	4.157	37159.6	−15.934	354.416	39446.2	−17.781	345.831	41318.9
7-14	0.13245	−12.518	25.595	31703.4	−12.857	13.853	34631.4	−13.826	2.994	37249.7	−15.303	353.340	39477.1	−17.140	344.850	41324.6
7-15	0.13043	−11.936	24.443	31754.6	−12.274	12.723	34676.8	−13.240	1.923	37279.4	−14.712	352.349	39485.4	−16.541	343.948	41309.8
7-16	0.12858	−11.386	23.367	31793.7	−11.723	11.667	34710.3	−12.687	0.923	37298.1	−14.154	351.426	39484.0	−15.976	343.107	41286.5
7-17	0.12680	−10.868	22.365	31814.2	−11.205	10.685	34725.7	−12.166	359.993	37299.6	−13.629	350.567	39466.7	−15.444	342.326	41248.9
7-18	0.12655	−15.378	31.540	29531.4	−15.710	19.659	32497.7	−16.660	8.431	35218.5	−18.114	358.274	37586.2	−19.929	349.243	39586.7
7-19	0.12430	−14.760	30.210	29591.3	−15.089	18.354	32551.3	−16.033	7.189	35255.3	−17.476	357.120	37599.9	−19.277	348.184	39575.1
7-20	0.12217	−14.176	28.979	29629.8	−14.504	17.145	32583.9	−15.442	6.039	35272.2	−16.875	356.052	37595.3	−18.663	347.206	39547.0
7-21	0.12017	−13.624	27.835	29649.5	−13.950	16.021	32598.2	−14.883	4.970	35271.8	−16.308	355.060	37574.8	−18.083	346.298	39504.7
7-22	0.11826	−13.101	26.768	29651.4	−13.426	14.973	32595.0	−14.354	3.975	35254.9	−15.771	354.136	37539.1	−17.536	345.454	39448.5
7-23	0.11645	−12.606	25.772	29636.3	−12.930	13.996	32575.1	−13.854	3.047	35222.1	−15.264	353.275	37488.8	−17.019	344.667	39379.1
7-24	0.11473	−12.138	24.840	29605.7	−12.460	13.081	32540.0	−13.381	2.178	35175.0	−14.784	352.469	37425.2	−16.530	343.931	39297.5
7-25	0.11309	−11.694	23.967	29560.1	−12.015	12.223	32490.2	−12.932	1.364	35113.8	−14.405	351.978	36990.6	−16.067	343.242	39204.0
7-26	0.11152	−11.273	23.147	29500.2	−11.593	11.419	32426.3	−13.507	0.600	35039.3	−13.899	351.007	37259.5	−15.628	342.596	39099.2
7-27	0.11001	−10.873	22.376	29426.9	−11.192	10.662	32349.2	−12.104	359.883	34952.1	−13.491	350.343	37158.6	−15.213	341.990	38983.5
7-28	0.10895	−14.760	30.210	27334.9	−15.075	18.323	30304.3	−15.977	7.078	33033.7	−17.356	358.905	35413.0	−19.077	347.864	37426.3
7-29	0.10721	−14.300	29.240	27278.5	−14.614	17.370	30243.5	−15.510	6.170	32960.9	−16.880	356.060	35323.9	−18.589	347.090	37319.3
7-30	0.10558	−13.865	28.332	27206.4	−14.176	16.478	30167.2	−15.068	5.322	32873.4	−16.429	355.271	35221.1	−18.127	346.366	37199.7
7-31	0.10403	−13.451	27.482	27119.2	−13.761	15.642	30076.1	−14.848	4.527	32771.8	−16.002	354.532	35105.1	−17.689	345.689	37068.0
8-1	0.10257	−13.060	26.684	27017.7	−13.368	14.859	29971.0	−14.251	3.782	32656.8	−15.597	353.840	34976.6	−17.275	345.055	36924.7
8-2	0.10119	−12.688	25.937	26902.5	−12.996	14.125	29852.3	−13.874	3.083	32528.9	−15.214	353.191	34835.9	−16.883	344.461	36770.1
8-3	0.09990	−12.337	25.235	26773.7	−12.643	13.436	29720.2	−13.518	2.428	32388.0	−14.852	352.583	34683.1	−16.513	343.905	36604.3
8-4	0.09867	−12.005	24.578	26631.8	−12.310	12.790	29575.3	−13.181	1.815	32234.9	−14.510	352.013	34518.7	−16.162	343.384	36427.6
8-5	0.09753	−11.691	23.961	26477.3	−11.994	12.185	29417.8	−12.863	1.239	32069.7	−14.188	351.479	34343.0	−15.832	342.896	36240.4
8-6	0.09645	−11.394	23.383	26310.2	−11.697	11.617	29248.1	−12.563	0.700	31892.7	−13.881	350.979	34156.0	−15.521	342.439	36042.6
8-7	0.09542	−14.859	30.423	24308.9	−15.161	18.502	27288.5	−16.023	7.168	30045.5	−17.341	356.878	32462.8	−18.986	347.719	34517.6
8-8	0.09426	−14.525	29.712	24146.9	−14.824	17.804	27123.3	−15.682	6.504	29871.6	−16.993	356.260	32277.0	−18.628	347.152	34318.8
8-9	0.09319	−14.209	29.048	23971.5	−14.507	17.151	26944.9	−15.361	5.883	29685.1	−16.665	355.683	32079.3	−18.292	346.624	34108.7
8-10	0.09221	−13.911	28.428	23782.8	−14.208	16.542	26753.3	−15.058	5.303	29485.8	−16.357	355.145	31869.4	−17.975	346.131	33887.4
8-11	0.09132	−13.631	27.849	23581.2	−13.927	15.974	26549.1	−14.773	4.763	29274.3	−16.067	354.643	31648.0	−17.678	345.673	33655.1
8-12	0.09051	−13.368	27.311	23367.1	−13.663	15.445	26332.5	−14.507	4.261	29050.9	−15.795	354.177	31415.3	−17.401	345.247	33412.2
8-13	0.08980	−13.122	26.810	23140.9	−13.416	14.953	26103.9	−14.257	3.794	28815.9	−15.541	353.744	31171.5	−17.141	344.852	33158.8
8-14	0.08917	−12.892	26.345	22902.9	−13.185	14.497	25863.6	−14.024	3.361	28569.6	−15.305	353.344	30917.0	−16.900	344.487	32895.2
8-15	0.08863	−12.678	25.915	22658.7	−12.971	14.076	25612.3	−13.808	2.961	28312.6	−15.086	352.974	30652.1	−16.677	344.151	32621.9

[a] T_L = time from launch.

CONFIDENTIAL

CONFIDENTIAL

Table 1. *Mariner* R trajectory characteristics (continued)

Launch day	C_3 $\times 10^8$	$\sigma_L = 90$ deg			$\sigma_L = 96$ deg			$\sigma_L = 102$ deg			$\sigma_L = 108$ deg			$\sigma_L = 114$ deg		
		Latitude	Longitude	T_L[a], sec	Latitude	Longitude	T_L[a], sec	Latitude	Longitude	T_L[a], sec	Latitude	Longitude	T_L[a], sec	Latitude	Longitude	T_L[a], sec
8-16	0.08819	−12.479	25.519	22393.8	−12.772	13.687	25350.4	−13.607	2.593	28045.3	−14.883	352.634	30377.6	−16.470	343.842	32339.3
8-17	0.08782	−15.575	31.969	20460.5	−15.869	19.998	23454.3	−16.710	8.530	26249.5	−17.996	358.059	28719.3	−19.600	348.707	30831.5
8-18	0.08742	−15.346	31.471	20203.7	−15.639	19.509	23195.1	−16.478	8.067	25983.5	−17.760	357.632	28444.0	−19.360	348.318	30546.1
8-19	0.08713	−15.133	31.010	19936.4	−15.426	19.058	22925.3	−16.262	7.640	25707.4	−17.542	357.238	28159.1	−19.138	347.961	30251.5
8-20	0.08695	−14.936	30.586	19658.8	−15.227	18.642	22645.6	−16.063	7.247	25421.5	−17.340	356.876	27864.8	−18.933	347.635	29948.0
8-21	0.08689	−14.753	30.196	19372.0	−15.044	18.260	22356.6	−15.879	6.887	25126.7	−17.155	356.546	27562.0	−18.746	347.338	29636.5
8-22	0.08095	−14.585	29.839	19076.4	−14.876	17.911	22058.9	−15.711	6.559	24823.4	−16.986	356.247	27251.1	−18.576	347.070	29317.2
8-23	0.08713	−14.431	29.515	18772.6	−14.723	17.594	21753.1	−15.557	6.262	24512.3	−16.833	355.977	26932.6	−18.423	346.829	28990.7
8-24	0.08744	−14.292	29.222	18461.7	−14.584	17.308	21440.3	−15.419	5.994	24194.4	−16.695	355.735	26607.7	−18.286	346.615	28658.1
8-25	0.08788	−14.166	28.960	18143.8	−14.459	17.052	21120.6	−15.215	5.756	23869.8	−16.573	355.521	26276.3	−18.166	346.427	28319.4
8-26	0.08846	−14.055	28.727	17819.8	−14.348	16.826	20794.8	−15.186	5.547	23539.2	−16.466	355.335	25939.3	−18.062	346.266	27975.2
8-27	0.08918	−13.957	28.523	17490.2	−14.250	16.628	20463.6	−15.091	5.368	23203.4	−16.374	355.175	25597.2	−17.974	346.129	27626.2
8-28	0.09005	−13.872	28.348	17155.9	−14.167	16.459	20127.6	−15.010	5.211	22863.0	−16.297	355.042	25250.7	−17.902	346.018	27273.1
8-29	0.09107	−13.801	28.200	16817.4	−14.096	16.316	19787.5	−14.943	5.084	22518.6	−16.235	354.934	24900.5	−17.846	345.931	26916.5
8-30	0.09225	−13.742	28.079	16475.6	−14.039	16.201	19444.2	−14.889	4.982	22171.1	−16.187	354.851	24547.3	−17.805	345.868	26557.0
8-31	0.09359	−13.697	27.985	16130.7	−13.995	16.112	19097.7	−14.849	4.907	21820.6	−16.154	354.794	24191.2	−17.780	345.830	26194.8
9-1	0.09485	−16.108	33.146	14459.7	−16.410	21.166	17455.1	−17.276	9.676	20254.5	−18.600	359.171	22729.9	−20.253	349.776	24848.4
9-2	0.09648	−16.027	32.965	14137.1	−16.331	20.993	17130.3	−17.201	9.522	19923.9	−18.532	359.044	22391.5	−20.193	349.677	24501.2
9-3	0.09829	−15.958	32.813	13813.3	−16.264	20.848	16804.4	−17.139	9.396	19592.3	−18.478	358.944	22052.1	−20.149	349.605	24153.3
9-4	0.10031	−15.902	32.688	13489.2	−16.210	20.730	16478.3	−17.090	9.298	19260.6	−18.438	358.870	21712.7	−20.120	349.557	23805.5
9-5	0.10254	−15.858	32.591	13164.9	−16.168	20.640	16151.9	−17.055	9.226	18928.7	−18.412	358.822	21373.3	−20.106	349.534	23457.9
9-6	0.10498	−15.826	32.521	12841.1	−16.138	20.577	15826.2	−17.032	9.180	18597.6	−18.400	358.800	21034.8	−20.107	349.536	23111.2
9-7	0.10766	−15.807	32.477	12518.5	−16.121	20.540	15501.6	−17.023	9.161	18267.7	−18.402	358.804	20697.5	−20.123	349.563	22765.9
9-8	0.11057	−15.799	32.460	12197.7	−16.116	20.529	15178.8	−17.026	9.166	17939.6	−18.417	358.832	20362.1	−20.154	349.613	22422.7
9-9	0.11374	−15.802	32.468	11878.6	−16.123	20.543	14857.8	−17.041	9.198	17613.4	−18.445	358.885	20028.8	−20.199	349.688	22081.5
9-10	0.11717	−15.818	32.502	11562.0	−16.142	20.584	14539.3	−17.099	9.254	17289.7	−18.487	358.962	19698.0	−20.259	349.787	21742.9
9-11	0.12088	−15.844	32.561	11248.2	−16.172	20.648	14223.6	−17.109	9.335	16968.9	−18.542	359.063	19370.2	−20.333	349.909	21407.4
9-12	0.12488	−15.882	32.644	10937.9	−16.213	20.737	13911.4	−17.160	9.439	16651.6	−18.600	359.188	19046.0	−20.420	350.54	21075.6
9-13	0.12919	−15.931	32.751	10631.0	−16.265	20.851	13602.6	−17.223	9.568	16337.8	−18.689	358.337	18725.2	−20.520	350.222	20747.3
9-14	0.13382	−15.990	32.883	10328.0	−16.328	20.988	13297.8	−17.298	9.720	16028.0	−18.781	359.508	18408.5	−20.634	350.412	20423.1
9-15	0.13878	−16.059	33.037	10029.3	−16.402	21.148	12997.2	−17.383	9.895	15722.4	−18.884	359.702	18096.1	−20.761	350.625	20103.2

[a] T_L = time from launch.

CONFIDENTIAL

components $B \cdot T$ and $B \cdot R$, based on Trajectories 1 and 4, give $-28{,}000$ km and 2000 km, respectively.

B. Engineering Mechanics

The first *Mariner* R spacecraft structure was delivered to the spacecraft assembly facility little more than 3 months after start of preliminary design. Prototype tests included both temperature and vibration tests, as well as functional tests.

A match-mate test has been completed between a spacecraft mockup and a prototype *Agena* B–spacecraft adapter. Despite the similarity of both spacecraft and adapter to *Ranger* items, many incompatibilities were found to exist. The early completion of the test allowed these incompatibilities to be corrected without schedule delay. A final verification of the mechanical interface was achieved when the structural prototype spacecraft was mated to a flight-type adapter in preparation for the combined vibration test.

Thermal tests on the basic hex portion of the spacecraft have been successfully completed in a cold walled vacuum chamber. Electrical resistance elements were used to simulate the heat dissipated in the various electronic assemblies of the hex and to heat the surface of the upper shield. A thermal balance was obtained for a number of the more critical flight modes.

The primary conclusion from these tests was that it is reasonable to expect that the temperature of the assemblies in the hex portion of the spacecraft can be controlled within the present flight acceptance limits. The exchange of heat within the hex portion was better than had been anticipated on the basis of calculations. The lowest measured temperature internal to the hex during any flight mode was 42°F on the servo ring; the highest measured temperature was 77°F on the science assembly. (These limits were exceeded exterior to the hex enclosure with a low of -58°F measured in the areas of the umbilical plugs and a high of 300°F imposed on the upper solar shield.) Primarily, as a result of this good thermal exchange, the louvers on the face of the science assembly were removed and a lighter weight thermal shield was substituted. Large thermal gradients across the face of some of the hex boxes due to an uneven distribution of power (as was experienced in previous tests performed with the individual boxes) were not found. The largest temperature difference in any 1 box was 6°F. It is probable that the reason for this small difference is that the ratio of the amount of heat transmitted internally within the hex to that transmitted externally to space is large.

Several predictions concerning the heat balance of the hex portion were partially confirmed. The average temperature of the hex is relatively independent of the solar heat of the upper thermal shield. With an upper shield surface temperature of 70°F (representing that at Earth) to that of 300°F (representing a case near Venus), the average temperature of the basic portion of the *Mariner* R experienced a rise of only 10°F. This was also the first series of tests employing a heat shield instead of polished or plated surfaces on the hex assemblies. Indications are that it is a good method of obtaining a low effective emissivity.

In general, the series of tests was felt to be valuable, verifying the design approach chosen and providing good preparation for more extensive tests. Future tests will involve increasingly complex prototypes and finally the flight units themselves.

Various vibration tests and modal surveys have been performed on portions of the structure and component parts. Prototype tests have verified the adequacy of the superstructure and the radiometer structure and their method of attachment. Type approval tests have verified the adequacy of the solar panel structure and high gain antenna when subjected to a greater than expected vibration environment. A modal survey of the entire spacecraft mounted on a rigid base has verified that frequencies and mode shapes of the structure as a whole and component parts are acceptable. The resonant frequencies of the structure as a whole and of component parts are significantly separated, resulting in a minimum of dynamic coupling. The entire structure looks adequate, the lowest resonant frequency being above the design goal of 30 cps.

Modal tests are now underway on the complete structure mounted on the *Agena* adapter. A composite vibration test of the prototype spacecraft and adapter is planned, as well as a test of the spacecraft on the adapter with the shroud installed.

C. Propulsion

The function of the *Mariner* R mid-course propulsion system is to remove or reduce *Agena* B injection disper-

CONFIDENTIAL

sion errors so that a Venus flyby with a sufficiently small miss distance can be reasonably assured. This function is performed during the single spacecraft mid-course maneuver (executed approximately 8 days after launch) at which time the spacecraft is directed to turn to a prescribed position in space and impart a corrective impulse via the mid-course propulsion system.

1. System Description

The *Mariner* R mid-course propulsion system is essentially the same 50-lb-thrust monopropellant hydrazine propulsion system developed for the *Ranger* RA-3, -4, and -5 spacecraft; primary variations to the *Ranger* system consist of the (1) utilization of nitrogen instead of helium as the pressurizing medium to accommodate better the 8-day launch-to-mid-course maneuver storage requirement, (2) painting and surface finish changes consistent with *Mariner* R thermal control requirements, and (3) the inclusion of dual-bridgewire, hermetically sealed squibs in place of the single-bridgewire *Ranger* squibs.

A schematic of the propulsion system is shown in Figure 7. The system utilizes a liquid monopropellant, anhydrous hydrazine, as the propellant. It is functionally a regulated-gas pressure-fed, constant-thrust rocket. Principal system components consist of a high pressure gas reservoir, a gas pressure regulator, a propellant tank, and a rocket engine. The rocket engine contains a quantity of catalyst to accelerate the decomposition of hydrazine. The engine nominally develops a vacuum thrust of 50 lb and a vacuum specific impulse of 235 lb-sec/lb (without jet vanes).

Explosively actuated valves are used throughout the system. Normally closed explosively actuated valves are fired to initiate nitrogen pressurization of the propellant tank, to initiate propellant flow to the rocket engine, and to release nitrogen tetroxide from the engine ignition cartridge. Normally open explosively actuated valves are fired to terminate nitrogen pressurization of the propellant tank and propellant flow to the rocket engine.

The design and operational philosophy of the system represented in Figure 4 is directed toward maximizing system reliability and reproducibility, minimizing preflight handling and spacecraft interactions, minimization of inflight electrical signals, and minimization of the number of system components. In order to avoid electrical or mechanical sequencing, the propellant tank is prepressurized with nitrogen during the preflight operation so that engine ignition and regulated nitrogen pressurization of the propellant tank can occur simultaneously through 1 signal from the central computer and sequencer (CC&S). Similarly, only 1 signal is necessary for thrust termination; therefore, a total of 2 signals are required by the mid-course propulsion system for impulse initiation and termination.

The propulsion system can be fueled and pressurized several weeks prior to launch and emplacement within the spacecraft. The system in the pressurized and fueled condition is safe for personnel to work around over the temperature extreme of 35 to 165°F. No spacecraft umbilicals or hard lines are required to maintain the propulsion system in the *ready* condition.

The firing of the mid-course propulsion system is controlled by the CC&S. For the mid-course maneuver, the CC&S receives the time, direction, and magnitude of the mid-course firing through the ground-to-spacecraft communication link. After the spacecraft has assumed the correct firing attitude, the mid-course propulsion system is ignited (at the prescribed time) through an electrical signal from the CC&S. Inasmuch as the propellant tank is prepressurized, the rocket engine ignition can occur concomitantly with the release of the high pressure nitrogen to the regulator without allowing time for the propellant tank pressure to build up to the normal operating level. Thrust termination is controlled by the CC&S via an electrical signal once the specified velocity increment has been realized as computed by the spacecraft integrating accelerometer. During the rocket engine firing, spacecraft attitude is maintained by the autopilot-controlled jet vane actuators.

The specific sequence of events for the propulsion system subsequent to spacecraft orientation and up to thrust termination is as follows:

(1) At the command signal from the CC&S to ignite the rocket, normally closed explosive valves ⟨15⟩ (Fig 7), ⟨8⟩ and ⟨4⟩ are fired allowing regulated nitrogen pressurization of the propellant tank, propellant flow to the rocket engine, and injection of a small quantity of nitrogen tetroxide to the rocket engine.

(2) Hypergolic ignition ensues, followed by continuous catalytic monopropellant decomposition of the anhydrous hydrazine.

(3) At the command signal from the CC&S to terminate rocket thrust, normally open explosively actuated valves ⟨7⟩ and ⟨21⟩ are fired, terminating propellant flow to the rocket engine and positively isolating the remaining pressure in the nitrogen sphere from the propellant tank.

COMPONENTS

1 ROCKET ENGINE
2 IGNITION CARTRIDGE GN_2 FILL VALVE
3 IGNITION CARTRIDGE GN_2 RESERVOIR
4 IGNITION CARTRIDGE ACTUATION VALVE
5 IGNITION CARTRIDGE OXIDIZER RESERVOIR
6 IGNITION CARTRIDGE BURST DIAPHRAGM
7 SHUTOFF PROPELLANT VALVE
8 START PROPELLANT VALVE
9 PROPELLANT TANK FILL VALVE
10 PROPELLANT TANK
11 PROPELLANT TANK BLADDER
12 PROPELLANT TANK PRESSURIZATION VALVE
13 HELIUM PRESSURE REGULATOR
14 HELIUM FILTER
15 HELIUM START VALVE
16 HELIUM TANK FILL VALVE
17 HELIUM TANK
18 VISUAL PRESSURE GAGE, 0-4000 psi
19 VISUAL PRESSURE GAGE, 0-500 psi
20 PROPELLANT FILL BLEED
21 HELIUM SHUTOFF VALVE (A)

INSTRUMENTATION

PRESSURE

(P_1) NITROGEN TANK
(P_2) PROPELLANT TANK

PRESSURE MONITORING GAGES

(G_1) NITROGEN TANK
(G_2) PROPELLANT TANK
(G_3) IGNITION CARTRIDGE RESERVOIR

TEMPERATURE

(T_1) PROPELLANT TANK
(T_2) NITROGEN TANK

SYMBOLS

(E) TWO-WAY VALVE, EXPLOSIVELY OPERATED
(M) ANGLE VALVE, MANUALLY OPERATED
BURST DIAPHRAGM
FILTER
PRESET REGULATOR
VISUAL PRESSURE GAGE
COMPONENT NUMBERS
INSTRUMENTATION NUMBERS
CAPPED TUBE END

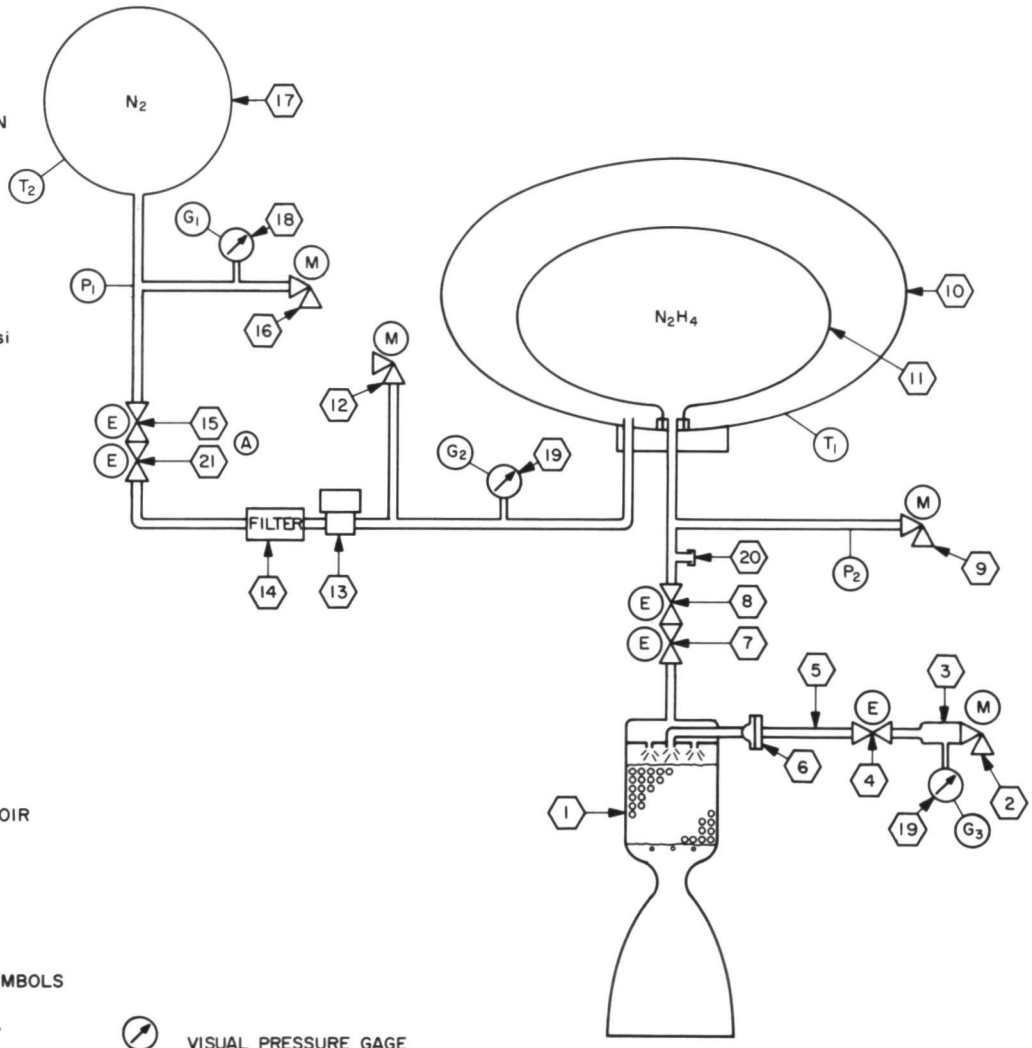

Figure 7. Propulsion system

2. Development Program

The chronological development program of the *Ranger* mid-course propulsion system was reported in *SPS 37-3* through *-11*.

In addition to the aforementioned reported work, a flightweight propulsion system with solenoid valves in place of the explosive valves and nitrogen in lieu of helium as the pressurizing medium was thoroughly tested at ambient test cell conditions over the *Mariner* R design limits. Figure 5 depicts the test cell setup. A 4-to-1 flightweight engine in lieu of a 44-to-1 flight engine was used for the ambient tests. A total of 10 hot firings were conducted with propellant tank prepressurization levels ranging from 0 to 550 psig, oxidizer start cartridge pressures ranging from 327 to 415 psig, and oxidizer (N_2O_4) injection quantities of 12 and 18 cc. Successful ignitions and steady-state operation were realized for all 10 firings. It is interesting to note that successful engine ignitions with simultaneous actuation of all valves (no sequencing) can be accommodated with propellant tank prepressurization levels as low as 0 psig and as high as 550 psig, and with injected oxidizer quantities of 12 and 18 cc. It appears that the bipropellant ignition scheme for the *Mariner* R and *Ranger* 50-lb thrust engine is not critically affected by N_2H_4 injection pressure, N_2O_4 injection pressure, and quantity of injected N_2O_4. System operation with the nitrogen pressurizing medium was wholly satisfactory during the course of system testing.

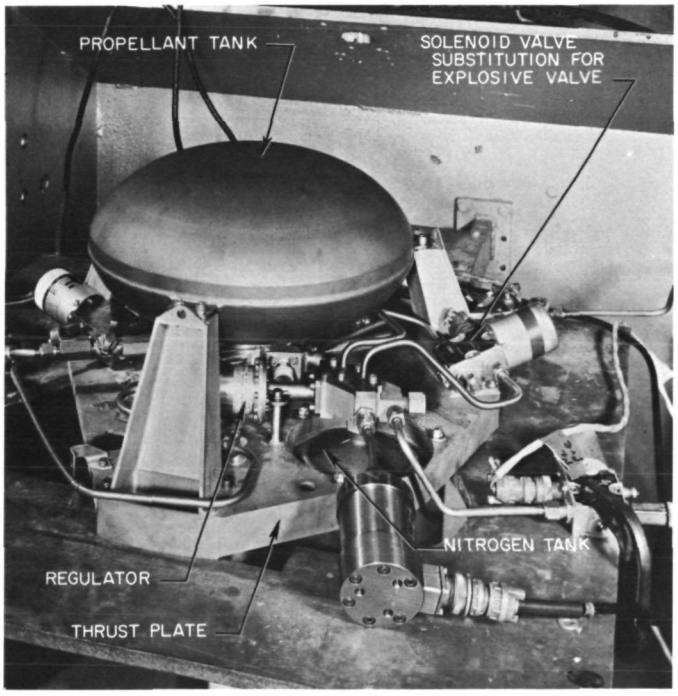

Figure 8. Flightweight system test cell setup

Ranger propulsion systems RA-5 and RA-5 spare were diverted from use on *Ranger* spacecraft RA-5 and will be used in *Mariner* spacecraft. The units have undergone modification consistent with *Mariner* R requirements. (In addition to the aforementioned 2 systems, a 3rd system for the *Ranger* RA-6, -7, -8, and -9 program will be used as a spare system for the *Mariner* R program.) The MR-1 flight system buildup has been completed except for the installation and alinement of the jet vanes. A January 8, 1962, delivery of MR-1 to the spacecraft assembly facility (SAF) is scheduled, and MR-2 buildup has commenced in support of the January 22, 1962, MR-2 SAF delivery requirement.

The flight-weight test system was then modified consistent with *Mariner* R requirements and turned over for temperature control tests in the temperature control model spacecraft. All flight thermal control features (surface finishes, etc) were duplicated on the test unit, and 9 lb of water were placed in the fuel tank to simulate the propellant thermal load.

The MR-1 flight system weights (actual) in pounds are summarized in the following:

Dry unserviced propulsion system weight	21.07
Nominal propellant load, N_2H_4 (including reserves)	9.40
Nitrogen (includes N_2 in the N_2 tank, propellant tank, and start cartridge)	0.85
Oxidizer, N_2O_4	0.04
Cabling	1.51
Jet vane actuators (4)	2.01
Pyrotechnics (estimated)	0.41
Total propulsion system weight	35.29

Page intentionally left blank

III. Mariner B

A. Spacecraft Design

1. Introduction

The preliminary design of *Mariner* B is in progress. A spacecraft working configuration has been chosen, the design characteristics and restraints have been written, and the various functional specifications can now be generated. Completion of the functional specifications will signify the completion of preliminary design.

Initial effort has centered around attempting to better understand the problems and to set forth design philosophies in the areas of structural design and dynamics, temperature control, instrument integration, pyrotechnics, and packaging. With this as a basis, it is intended that the functional specifications, including adequate design layouts for nearly complete interface definition, will be able to serve as a firm guide during the detail design and development periods.

Emphasis has been placed on maximizing the reliability of the basic bus within the weight and space limitations imposed. Such things as redundancy in the pyrotechnics system, minimization of interdependence of events, minimum reliance on active temperature control, and minimization of articulating members fall in this category. The dual planet capability and its effect on the configuration, especially in the areas of temperature control, sensor location, and the planetary horizontal platform, were also of major concern, as was the capsule carrying capability.

2. General Configuration and Mechanics

The *Mariner* B spacecraft is capable of performing scientific investigations at the planets Venus and Mars during their periods of availability in 1964 through 1967. It also has the capability of performing interplanetary scientific investigations in the regions between Venus and Mars.

In order to have this dual planet capability and be able to perform its required missions, the spacecraft consists of a hexagonal instrument compartment, referred to as the basic bus, and a 145 ft^2 solar cell array. This array is made up of 90 ft^2 of erectable solar panels and 55 ft^2 of fixed panel, the latter serving also as a solar shield to the basic bus. In this manner the spacecraft temperature control system can be made less sensitive to the large difference in the solar constant at Venus and Mars.

In order to perform the planet oriented experiments, the spacecraft configuration has the ability of carrying a 2-deg-of-freedom platform for planetary scientific instruments.

In satisfying the communication system requirements the spacecraft configuration includes a steerable high gain 4-ft parabolic antenna, with a fixed feed and a low gain, body fixed array.

The spacecraft attitude control system uses the Sun and Canopus as reference bodies. The spacecraft roll axis, normal to the plane of the solar panels, is pointed toward the Sun; its roll orientation is maintained by a Canopus seeker. (Canopus is roughly a south polar ecliptic star with an apparent visual magnitude of -0.73.)

The spacecraft propulsion system is an integral unit easily removed from the spacecraft. This unit consists of a 50-lb-thrust hydrazine engine, and a propellant tank, sized to impart a velocity increment of 200 m/sec to a 1500-lb spacecraft. Integral with this unit is its own pressurization system and all the associated valving and plumbing. The propulsion unit mechanically ties into the spacecraft at the bases of 3 of the 6-hex columns (Fig 1).

In addition, the spacecraft has the capability of carrying or not carrying a small capsule and certain capsule related items. For 1965 and subsequent missions, these items include a receiver in the spacecraft bus (capable of receiving the capsule transmissions and forwarding them to a data storage system) and planetary approach guidance equipment. If a capsule is flown on the Mars 1964 mission, the capsule shall communicate directly to Earth after separation from the spacecraft bus. The capsule–bus mechanical interface consists of an adapter section which contains a capsule separation joint and an adapter bus field joint. The field joint ties into the top of the basic hex, and carries across it the necessary electrical disconnects to support the separation release system and the capsule–adapter electrical interface. The capsule separation will be a spring ejection system with a pyrotechnic release mechanism. The capsule–adapter electrical disconnect will be a passive 0-engagement type quick disconnect.

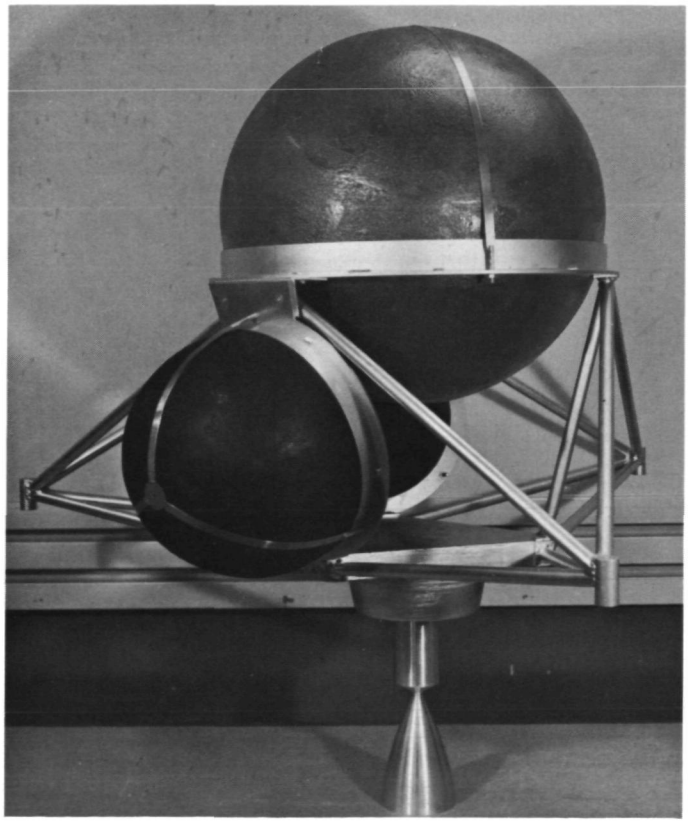

Figure 1. Propulsion unit mounting fixture

Due to uncertainty in the capsule size and weight at this time no extensive detail design effort will be devoted to the capsule–adapter or capsule–adapter separation joint. However, a structural bus interface will be established so that a capsule–adapter may be subsequently introduced.

The spacecraft, as now envisioned, incorporates 11 actuators to perform its necessary tracking, scanning, and articulating functions. This total can be divided into 2 groups: 1 of 6 passive actuators, the other of 5 servoactuators. The 6 passive actuators are used in the erection of the 4 solar panels, the antenna, and the PHP boom. Of the 5 servoactuators, 2 are used for the antenna track, 2 for the PHP track, and 1 for the planet scan.

The Canopus seeker requires 2 deg of freedom. One is mechanized by an all electronic system, and the other is provided by the spacecraft roll freedom, thus avoiding any mechanical actuators. Since the spacecraft roll control is provided by the Canopus seeker rather than an antenna-mounted Earth sensor, as on *Ranger* and *Mariner* R, the antenna tracking system becomes slightly more complicated. With the spacecraft assuming an inertial reference system (the Sun–probe–Canopus system) the antenna must be capable of tracking the Earth through 2 deg of freedom without masking the Earth by the spacecraft itself. To satisfy this requirement the antenna is provided with an azimuth–elevation type mount. This mount is erected a suitable distance away from the spacecraft to avoid masking the Earth. In this manner the view field of the antenna is somewhat greater than a hemisphere. In order to have the ability to track during the propulsion maneuvers, the antenna view must encompass an unobstructed hemisphere whose base is parallel to the thrust vector. The present scheme satisfies this condition.

The 2 actuators could be removed if an antenna-mounted Earth sensor were used for spacecraft roll control. These 2 actuators consist of 1 passive actuator for the antenna erection and 1 of the 2 servos, with the spacecraft roll affording 1 deg of freedom. On the other hand, the disadvantages in this scheme are numerous. To be considered are:

(1) The mechanization of such an Earth sensor to cope with the dynamic range of the Earth as seen from the spacecraft in going to both Mars and Venus.

(2) The compatibility with the Earth–probe–Sun angle going to 0.

(3) The complication of the planet track scheme at encounter.

(4) The inability to communicate during propulsion maneuvers.

The remaining 4 actuators are required for the PHP. This instrument has an azimuth–elevation mount erected suitably away from the spacecraft to satisfy the planet look angles. The sensitive axis of the PHP is servo-locked to the center of the planet disc by means of a planet horizon seeker and 2 servo actuators. The planet oriented experiments scan about this axis using a programmed scan actuator.

Figure 2 is a photograph of a full scale configuration mockup now under construction. A drawing of the spacecraft is shown in Figure 3.

3. Structural Design

A structural test model based on the proposed design configuration is nearing completion of fabrication. This model will be subjected to dynamic testing which is scheduled to start early in January 1962. Determination of normal-mode characteristics (i.e., frequencies, mode shapes, and structural damping coefficients) will be the prime goal of the tests. These results will then be compared to the computer analysis to ascertain the validity of certain assumptions made in the analysis. Upon completion of all modal survey work, it is planned to subject the test model to the structural type approval dynamic test.

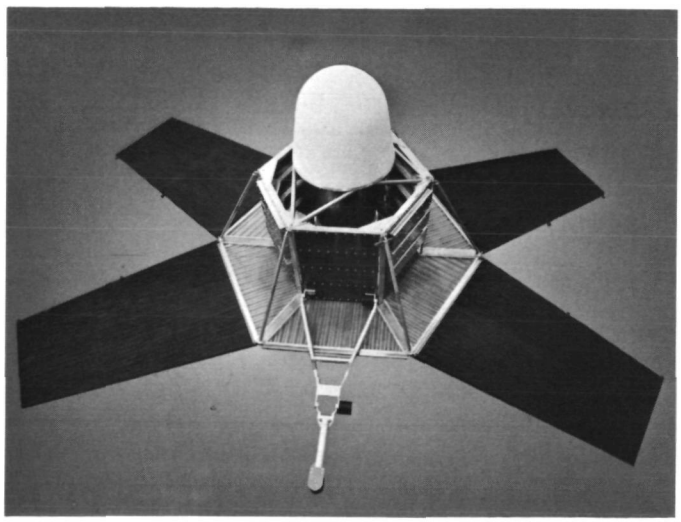

Figure 2. Full-scale configuration mockup

A solar panel optimization study has been initiated, utilizing a structural configuration similar to that used on *Mariners* A and R. The panel area required for the Mars mission (22.5 ft^2 per panel) is best achieved by using 2 longitudinal main beams with the typical corrugation structure spanning transversely. The advantage in this configuration comes from the corrugation stiffness requirement being dependent on panel width rather than length. Thus, longer solar panel lengths do not increase the weight nearly as rapidly as when corrugations span lengthwise. The beams, which are dependent on panel length, can be efficiently designed by taking advantage of increased depth to achieve stiffness. This construction is readily adaptable to panels which will ease the handling and cell installation problems. Structural splices between modules can be accomplished with but slight penalty in unusable panel area.

Preliminary study work has been completed on a solar concentrator structure as proposed by Boeing Airplane Company. This design consists of corrugation construction. This type of panel can be considered for use on the Mars vehicle only. It cannot be used at Venus because the cell operating temperature is too high.

Structural consideration of the antenna and PHP has been limited to configuration and location studies. The position of the antenna requires that the fixed feed intrude

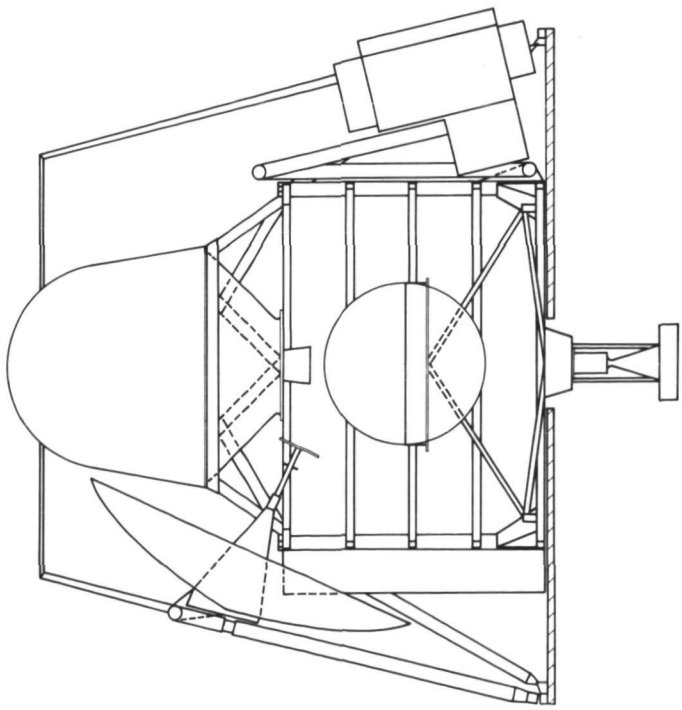

Figure 3. *Mariner* B spacecraft configuration

into the center of the basic hex and under the capsule. This requires that a 6-point truss be used to support the capsule.

Some structural improvements have been made in the mid-course propulsion system. The motor support structure has been lightened by more efficient structural use of the metal. The usual ring support for the propellant tank has been eliminated in favor of 3 local bosses on the tank to which the support truss is bolted.

4. Structural Dynamics

a. Environmental vibration criteria. As an interim measure, pending more detailed investigation, the spacecraft vibration environments to be used for structural design have been selected to be identical with those specified for the *Surveyor* spacecraft.

b. Modal vibration analysis. Modal vibration analysis of the *Mariner* B spacecraft makes use of an existing digital computer program applying to pin-jointed spaceframes having masses concentrated at the joints. Inasmuch as the basic bus is more characteristic of semimonocoque construction than truss construction, adequate elastic and inertial representation of the complete spacecraft (i.e., bus, fold-out solar panels, antenna boom, and PHP boom) is encumbered by limitations in conceptual translation from the actual to the fictitious structure, and in limitations in the number of degrees of freedom which can be accommodated in the computer program. Accordingly, supplementary-methods development has been initiated to permit modal-type analyses which employ normal modes of major components (e.g., bus, panel, or boom) as generalized coordinates in a Lagrangian treatment. By this building block technique, the number of degrees of freedom which need be treated in any one computer run may be substantially reduced and the structural representation of each component may be upgraded accordingly, as required.

Investigations show that this approach may be developed in a routine manner when each panel (or boom) is supported on the bus in a statically determinate manner (e.g., cantilevered or simply supported.) However, a solution for the case of statically indeterminate support has not been examined.

The currently proposed interlatching of adjacent solar panels, in conjunction with a link-type support from the bus near each panel free edge, introduces redundancies which may induce large loadings on panel hinges and latches during the boost phase. At the same time, the high shear stiffness of the interlocked solar panels has a marked effect on raising the natural frequencies of the 1st several oscillation modes of the spacecraft.

Further investigation of this structural configuration is planned by an integrated program of theoretical analysis and modal vibration tests.

c. Measurement of rigid-body mass parameters. The desirability of minimizing handling and reorientation of large spacecraft during the measuring of weight, cg coordinates, and centroidal moments of inertia in pitch, roll, and yaw is recognized. Accordingly, a test setup has been conceived which appears to permit adequate measurement of all of these properties with the spacecraft in its nominal vertical position. In particular, when the centroidal products of inertia about pitch–roll and yaw–roll axes are very small, analysis shows that accuracy requirements can be met.

The essential feature of the proposed method is utilization of a trifilar suspension. Weight and the cg location in the x-y plane are first determined by conventional static measurements. Subsequently, a helical spring of suitable stiffness is inserted in 1 of the 3 filaments, permitting determination of vertical cg position and a centroidal moment of inertia about an axis in the x-y plane as functions of setup parameters and measured frequencies of 2 natural oscillation modes. Repetition of this process with the spring placed, successively, in the other 2 filaments gives measurements of centroidal moments of inertia about other axes in the x-y plane. From the 3 moments of inertia so determined, centroidal pitch and yaw moments of inertia and the centroidal product of inertia about the pitch–yaw axes may be derived. The roll moment of inertia is obtainable by use of the suspension as a conventional trifilar pendulum.

The analysis is being extended to determine the influence of pitch–roll and yaw–roll products of inertia on the accuracy of the determinations and, moreover, on the practicability of measuring these products of inertia with meaningful accuracy.

5. Temperature Control

a. Basic hex. Since *SPS 37-12*, there has been a basic change in the temperature control philosophy. It was determined that the internal conducting plate can not be made in 1 piece; a multi-piece unit, with many more joints having indeterminate conductance values are necessary. The extra joints change the internal temperature gradient from 30°F to approximately 70°F. This gradient uses too much of the allowable temperature range of most

equipment to allow adequate margins for all unknown surface properties, conduction paths, view factors, etc.

Currently, the basic temperature control scheme utilizes the exterior surface of the spacecraft as the primary radiator, the heat path being radially outward from the electronics. Provision is made for the components to either attach directly to this radiator or to be physically separated from it (Fig 4). This allows control over the flux path, a direct path to the radiator when the heat flux is large, and an indirect path when the heat flux is low. Since the path lengths are shorter and there are less joints, the temperature variations due to the unknowns in the path lengths are lower than in the previous approach. The exterior shell of the spacecraft will be as smooth and unbroken as possible to allow each particular segment of the surface to have as large a view factor to space as possible. This minimizes interaction effects between various sections of the spacecraft.

As many components as practical will be included inside the outer shell of the spacecraft hex, giving each a more predictable environment than possible if they are mounted externally. The interior of the spacecraft hex will be as open as possible, linking, by radiation primarily, all of the subsystems into a more isothermal package. This allows more of the spacecraft hex than just the item concerned to react during power transients or solar heat loads during unoriented periods, thus reducing the accompanying temperature variations. Active controls, to modify the heat flux or the flux path, will be provided where operational temperature tolerances are small.

During cruise, the spacecraft is isolated from the solar heat load by the fixed solar panel array which is insulated on the back, or by an insulated shield. This is necessary due to the large changes in solar intensity between the Earth and either Venus or Mars. However, during maneuvers the spacecraft will be forced to endure solar input directly to certain radiator surfaces, causing large changes in the amount of heat to be rejected. Presently the only way to handle these large solar inputs is by thermal inertia and limiting the amount of time such conditions will be experienced. There is no way available within the present weight limits to effectively transfer these quantities of heat without large temperature differences from 1 side of the spacecraft to the other.

b. Capsule. As presently envisioned, the capsule will be flown in the shade below the spacecraft. The ablation shield utilized for planetary entrance protection will also provide a high resistance heat path during cruise allowing small electrical heaters to maintain the capsule interior temperature at a desirable level. If the ablation shield does not provide enough insulation and the capsule requires more power than can be allocated, additional lightweight insulation will be added to the capsule or the spacecraft will be inverted, placing the capsule in the Sun.

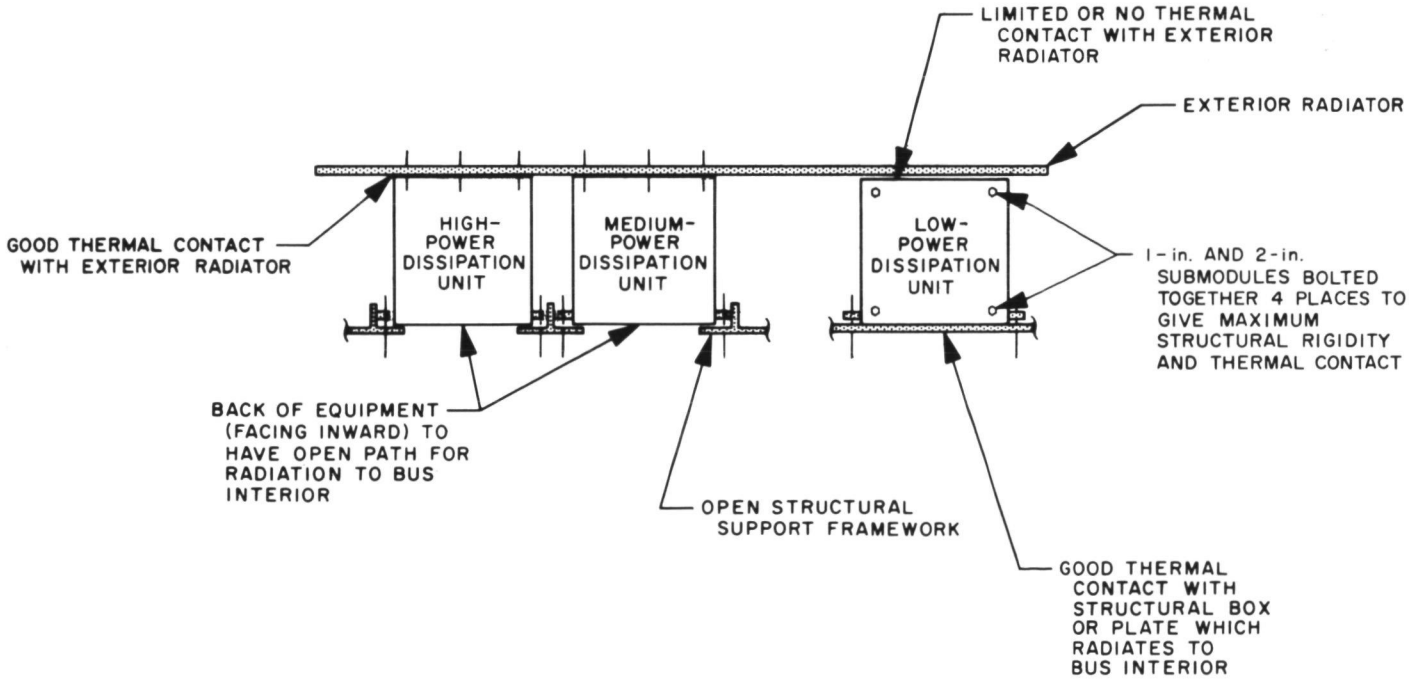

Figure 4. Thermal needs related to packaging mechanics

CONFIDENTIAL

In either case, temperature control of the capsule after separation will probably require a slow tumbling rate to equally distribute the solar heat input and minimize cross-capsule temperature gradients.

c. Components. The temperature control aspects of the external actuators, antennas, and external sensors are being investigated. However, based on past experience, these kinds of component must be able to operate over an extremely wide temperature range. Such things as unavoidable shading during maneuvers, variations in area exposed to sunlight during operation, low ratio of weight to surface area, and large variations in internal power introduce requirements for wide temperature tolerances.

Rough estimates of the ranges of temperatures to be expected by these components are listed in the following:

External actuators, −100 to 200°F.

Antennas, −100 to 250°F.

External sensors, −100 to 200°F.

d. Solar panels. Preliminary analysis has been completed on the solar panels, allowing a fairly representative picture of the operating temperatures of the fixed and folding solar panels. In the present configuration, Table 1 lists the operating temperatures for various points in the trajectory. The range in values for a fold-out panel include the effects of the electronic boxes, variations in surface properties, and various doublers and gussets on the back side.

6. Instrument Integration

In order to provide as ideal an environment as possible for the scientific instruments, it is desirable to mount them inside the protective external hexagonal cover. This desire sometimes conflicts with the requirement of the instrument to have a clear view (with a fairly large cone angle) free from interference by the spacecraft and its appendages. This problem is complicated, in many cases, by the requirement to view the Sun as well as space at various stipulated angles to the Sun. In the case of a spacecraft such as *Mariner* B, employing large solar panels, this requires either peering over the edge of the panels or through holes provided for that purpose. In order to minimize the conflict of these requirements, the initial effort in instrument integration has centered around defining the requirements more precisely:

(1) The size and weight of the unit.

(2) Its view direction(s) and cone angle(s).

(3) The ability to separate the sensor from the electronic equipment.

(4) The allowable thermal environment, particularly of critical components.

Much of this preliminary information is now available as a result of close liaison with the experimenters, and as soon as the cruise attitude of the spacecraft is determined, each of the spacecraft fixed instruments will be assigned a location.

The planet oriented experiments present special viewing problems during planetary encounter due to the

Table 1. Solar panel operating temperatures

Panel	Venus perihelion, °F	Earth perihelion, °F	Mars perihelion, °F	Mars aphelion, °F
Fold-out	213 to 227	111 to 124	20 to 33	−9 to −21
Fixed (insulated on back)	342	219	107	54

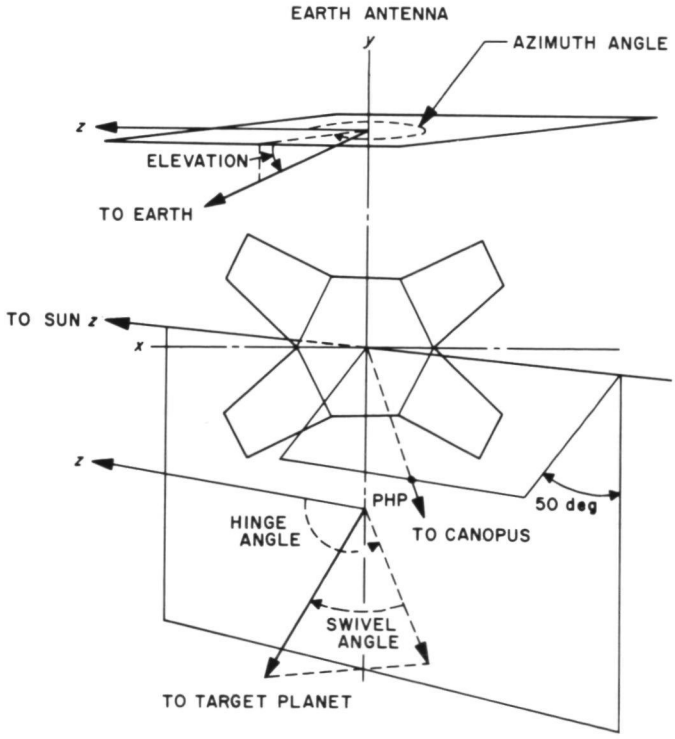

Figure 5. Coordinate system for 1964 launch opportunities

CONFIDENTIAL

requirement of tracking a moving target relative to the spacecraft. A planet oriented horizontal platform (PHP) with a superimposed 1-dimension scan movement fulfills this need. For the Mars and Venus missions of *Mariner* B the following problems must be considered:

(1) All spacecraft field of view constraints for the designed trajectory and planet pass for each target planet.

(2) Any modification to the spacecraft necessary to provide dual planet capability.

(3) Introduction by later year missions of any new constraints which might affect spacecraft design.

(4) Planet pass dispersion effects on PHP field of view.

Available information is insufficient to resolve all of these problems at this time. It is sufficient, however, for analyzing the 1964 opportunities. Figure 5 shows the coordinate system used for the analysis. Figures 6 and 7 show the Venus and Earth trajectories, respectively, relative to the spacecraft. These curves appear framed by the interference outline of the spacecraft. Figures 8 and 9 show similar plots for the 1964 Mars encounter. In order to achieve the clear fields of view indicated, it was necessary to roll orient the spacecraft relative to Canopus as shown in Figure 5. It is not clear that this same roll offset will satisfy the later missions. It may be that gyro control of roll orientation during encounter will be necessary in order to preclude relocation of the Canopus seeker for each mission.

An interesting effect of the 50-deg roll offset is the resultant scan pattern for the instruments. Figure 10 demonstrates a typical Venus scan with the scan axis parallel to the boom swivel axis. The chart is a mercator projection of the planet surface showing the trajectory path from right to left with the scan pattern above and below it at various times before and after closest approach.

7. Pyrotechnics

Exploding wire is being considered as the ignition approach for the pyrotechnics system on *Mariner* B. This

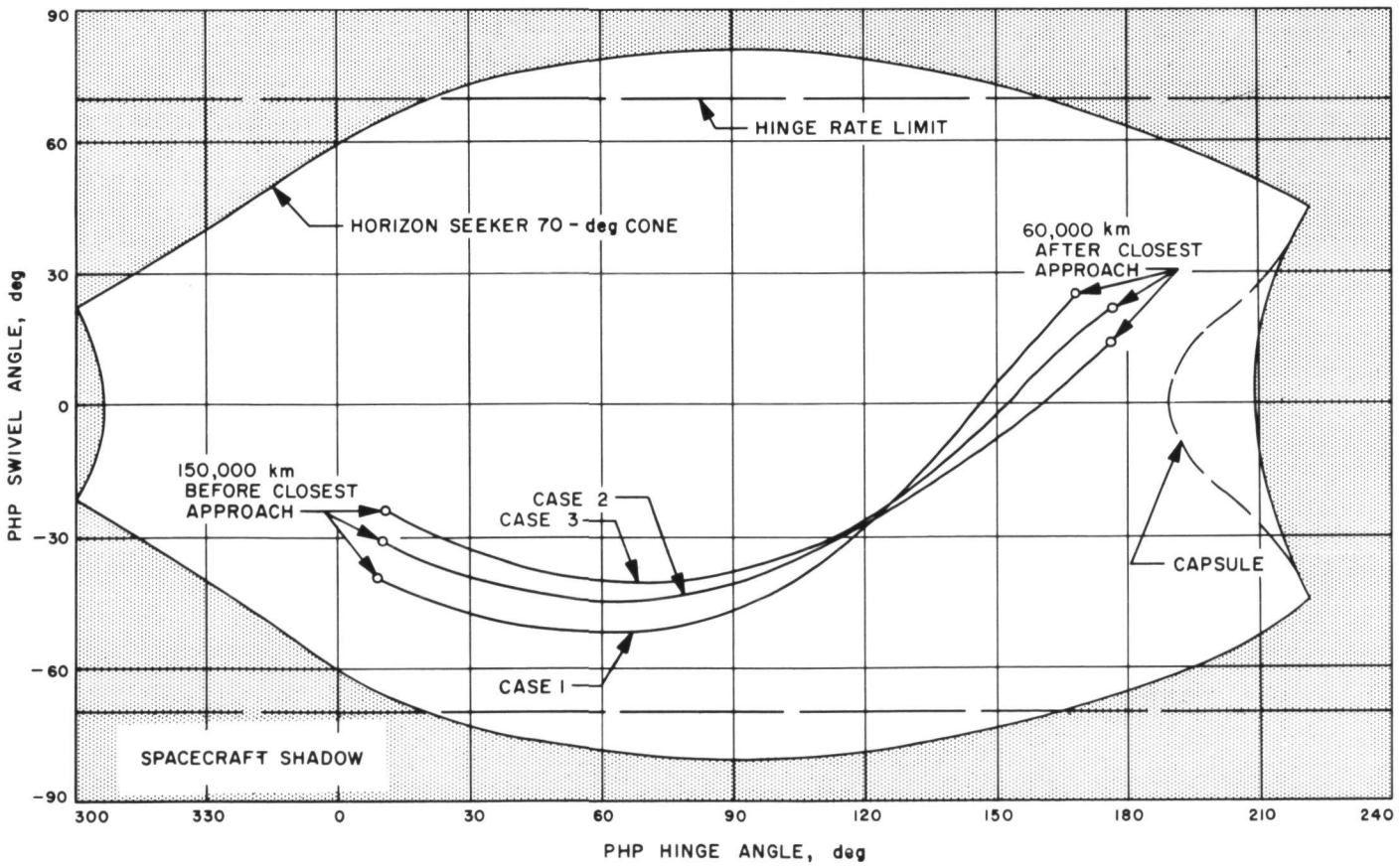

Figure 6. Venus trajectory relative to spacecraft

decision has been in part promoted by the recent attention focused upon conventional hot-wire pyrotechnics by the AMR Safety Committee. That office has issued a document requiring 1 amp, 1 w, no-fire squibs in all future operations at AMR. This requirement imposes stringent design constraints on the ignition system and indicates a trend which significantly reduces the desirability of hot-wire systems.

It is intended that a backup design be carried through the initial phases of the design, utilizing capacitive discharge ignition and 1 amp, 1 w, no-fire squibs.

The design criteria and requirements for the pyrotechnic system are as follows:

(1) There will be full redundancy in the command, control, cabling and explosive subsystems (i.e., 2 independent, commands, ignition channels, and bridgewires or squibs).

(2) Requirements imposed on the pyrotechnic system for close tolerances in firing 2 or more devices will be held to a minimum. Any requirement for any tolerance in this respect must be arbitrated at the earliest possible date.

(3) Ignition of all squibs will be performed by exploding wire techniques with a backup design being carried for conventional 1 amp, 1 w, no-fire squibs.

(4) The total number and description of required events is not yet available and will be necessary before the system can be completely defined.

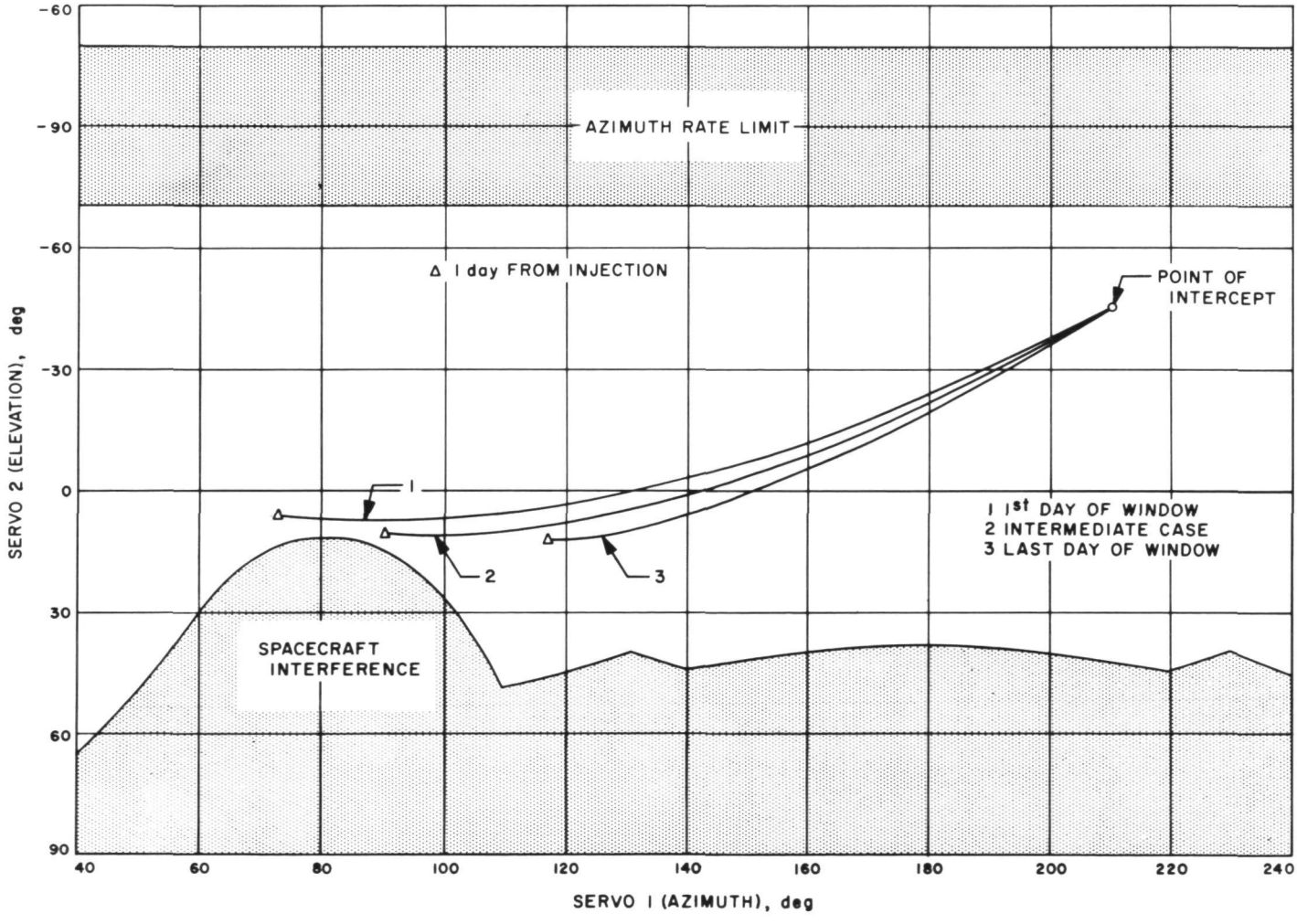

Figure 7. Earth trajectory relative to spacecraft, 1964 Venus encounter

(5) The weight of the ignition system and firing harness utilizing redundancy is estimated to be 10 lb.

(6) The pyrotechnics system will derive its power from the main spacecraft dc supply.

(7) Exploding bridgewire simulators are being developed for system test operations.

8. Packaging

The basic packaging concepts for *Mariner* B have not changed since the last reporting period. Some modifications have been made in the design to accommodate the change in philosophy for the temperature control of the spacecraft and as a consequence of further development of chassis and subchassis design. The original basic design philosophy for temperature control (that the heat flow would be inward and upward) has now been revised to provide for direct mounting of high heat dissipating subassemblies on the radiating surfaces and located as far from the solar panels as possible. The low power dissipating equipment would still conduct toward the interior of the spacecraft but with provisions for a thermal control shield to be mounted externally to the subassemblies on the outboard side.

The use of plug-in subassemblies for the low and medium powered assemblies is a design goal to provide better wiring between these subassemblies having a relatively high pin density. The use of a double width subassembly is contemplated for some assemblies with digital type circuitry to reduce the interconnecting wiring between subassemblies. For these double-width units it is presently planned to eliminate the center bulkhead ring of the structure.

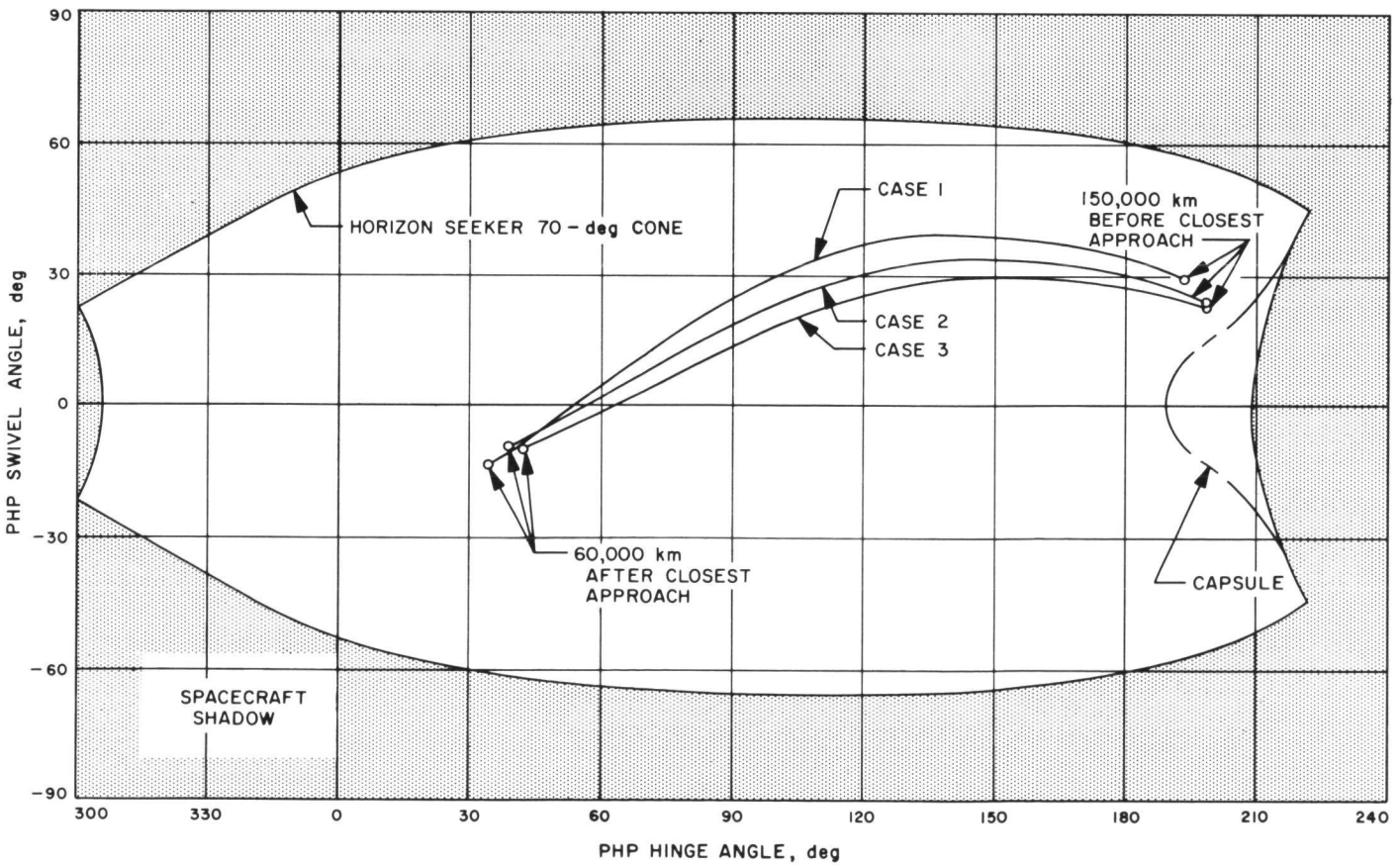

Figure 8. Mars trajectory relative to spacecraft

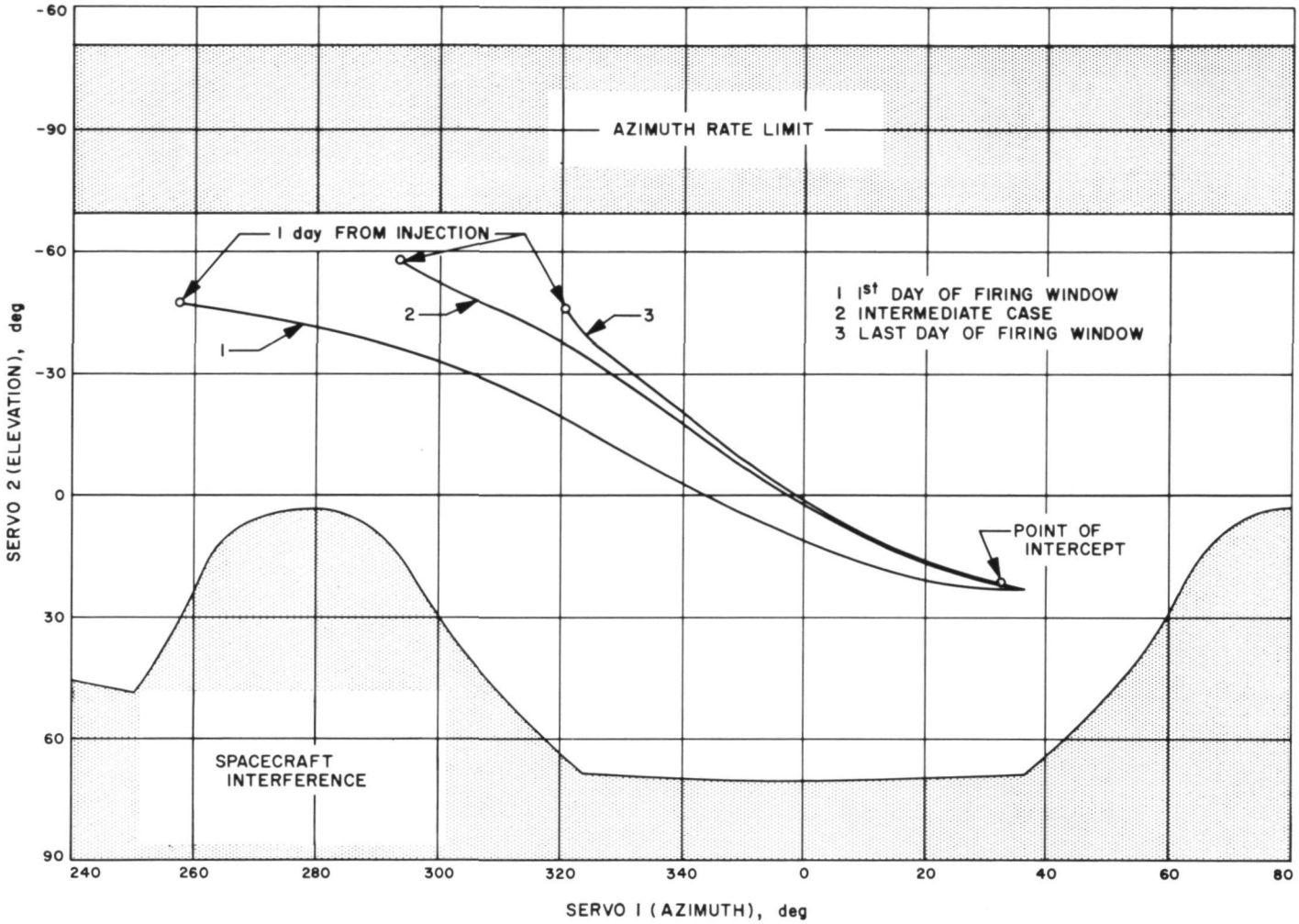

Figure 9. Earth trajectory relative to spacecraft, 1964 Mars encounter

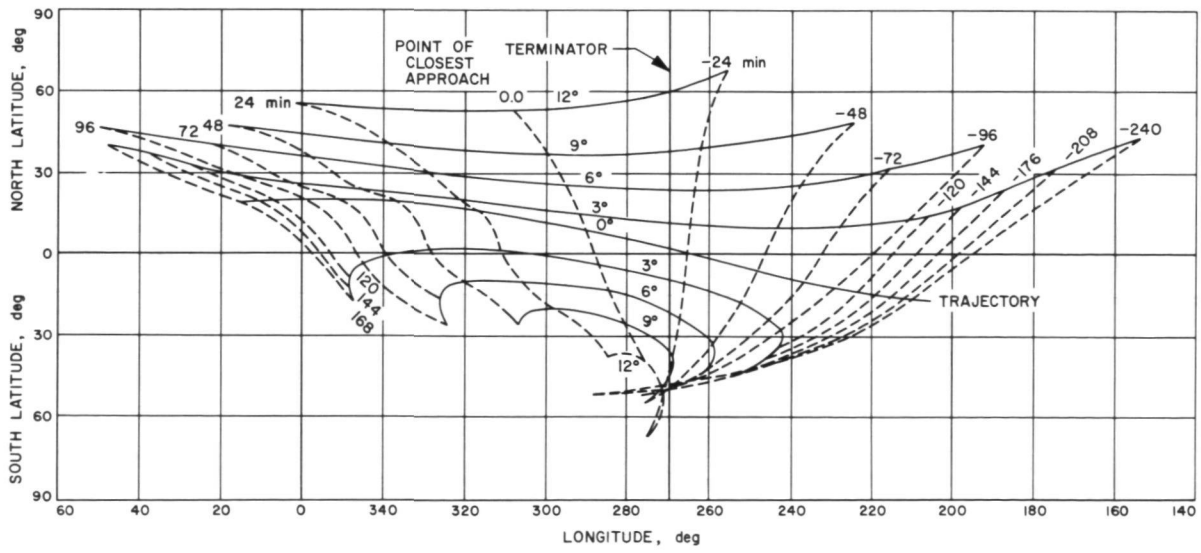

Figure 10. Typical Venus scan

IV. *Voyager*

A. Synopsis

Specific efforts directed to the accomplishment of the *Voyager* Project have been initiated. The Systems Division is participating with the technical divisions in the generation of mission objectives and the preparation of preliminary systems design specifications for interplanetary spacecraft to be used as planetary orbiters and landers, and out-of-the-plane-of-the-ecliptic probes, using the *Saturn* vehicle as the booster.

The Space Science Division is conducting *Voyager* scientific feasibility studies to establish the feasibility of meteorological, biological, and certain adaptions of geological experiments for the *Voyager,* and to refine the knowledge of the Mars and Venus environments as they may affect the experiments and spacecraft for these flights.

The Guidance and Control Division is continuing its studies of guidance and control requirements, methods, and techniques for advanced planetary missions, both those currently planned and those that become necessary or desirable as a result of discoveries on early planetary exploration missions that require further exploratory operations. The methods to be used include study of possible mission requirements to deduce the general requirements for guidance and control subsystem performance, evolution of subsystem configurations to accomplish the required tasks, and parametric and error analyses of typical missions and operating situations to determine the ranges of parameters and tolerances required.

The Engineering Mechanics Division is performing *Voyager* spacecraft studies, including analytical investigations of configuration, thermal control, entry and landing dynamics, postlanding and roving techniques, booster compatibility, multiple mission, or universal design concepts and compromises, and structural design problems.

Page intentionally left blank

PART FOUR
ADVANCED DEVELOPMENT

I. Lunar

The Lunar Advanced Development Program consists of those projects and efforts which will extend the state-of-the-art and will provide knowledge applicable to a specific problem or technical field of interest, thus leading to the development of hardware necessary to the planned Lunar Exploration Program. The Advanced Development Program also establishes a mechanism to ensure exploitation of advances in the state-of-the-art.

A. Ultra-High-Speed Optical System

A research and advanced development effort is being performed (by Optics Technology, Inc., Belmont, California, under contract to JPL) to demonstrate the feasibility of an optical system with a relative aperture of less than $f/1$ and whose complexity in component elements is simplified by the use of fiber optic constituents. Previous systems which have been developed with similar performance characteristics have been, in large, too complex, bulky, and unsuited for the space environment.

A large portion of the program is to conduct possible application studies of optical systems possessing the following characteristics:

(1) Low relative apertures (less than $f/1$).

(2) Wide field angles (20 to 40 deg).

(3) Capability of approaching the diffraction limitation of light in image quality.

(4) An optimum resulting image plane which will be flat and capable of using photographic plates for system testing.

(5) The capability of performing under severe environmental conditions.

(6) Utilization of fiber optics components to achieve simplicity in number of components and minimization of optical alinement difficulties.

(7) Capability of performance in ultraviolet, visible, and infrared regions of the spectrum.

The resultant system would possess the advantages of dynamic scanning and/or space filtering capabilities.

One system will then be selected, based on the study results. An optical system breadboard model for study, testing, and design will be constructed. The fiber optics components, as they are developed, will be subjected to complete space environmental testing.

An image synthesizer for comparing various image degrading effects using a variety of test objects has been constructed and is now in use. In initial 3rd order aberration analysis, spot diagrams were used that approximate the intensity distribution for primary spherical aberrations, zonal spherical aberrations, coma, and diffraction rings in an airy disk. A series of photographs was made where the size-to-spot diagram dimensions varied between ½ and 20. This analysis will be extended to take account of diffraction in the presence of aberration, and spot diagrams of the point spread function with degrees of spherical, coma astigmatism, and coma-astigmatism aberrations.

General expressions that define the 3rd order aberrations of simple 2- and 3-element reflecting and refracting systems are being generated and the effect of their dependence on the system parameters is being studied. Because field curvature and distortion may be ignored (due to the use of fiber optics) it is expected that a large number of simple systems exist for which the other 3 aberrations may be corrected.

Initial work has been undertaken to construct a breadboard model of a wide field, low *f*-ratio optical system, using a Sutton-type lens system and fiber optics image corrections. A design with an *f*/3.5, 4.5-in. system with a 120-deg total field angle is now under study. The lens was mounted in a viewing camera having a suitable aperture. The wide angle property of the lens was demonstrated by rotating the lens on its nodal point through a 100-deg angle. No appreciable change was found in the image quality viewed through a microscope. A fiber optics field flattener and conical condenser are nearing completion and will be used to completely evaluate this system.

A 2nd design with an *f*/2.8, 2-in. system and 120-deg field angle is being prepared. This lens will be incorporated with fiber optics image correctors and detailed tests on its photographic speed and resolution will be made.

B. Sun Simulator

A laboratory mockup of the Sun simulator (*SPS 37-12*) has been developed. The radiation source is a Hanovia 900-w Xenon arc lamp. An *f*/2 projector lens and an *f*/2 camera lens are used for condensing optics (Fig 1) and an *f*/1 camera lens is used for the collimating lens. The setup is limited to an *f*/2 system because of the slow condensing optics. The collimating lens has a 50-mm focal length, and provides a collimated energy bundle of approximately 1 in. diameter.

Tests conducted by energizing a silicon solar cell show its short-circuit current to be approximately ½ its output in incident sunlight extrapolated to 0 atm. This indicates that radiation intensity is approximately 30 mw/cm² throughout the spectrum produced by the Xenon lamp. A radiation intensity of 58 mw/cm² from the Xenon lamp should energize a silicon solar cell to the same degree incident sunlight (140 mw/cm²); this is an equivalent solar constant of 1.

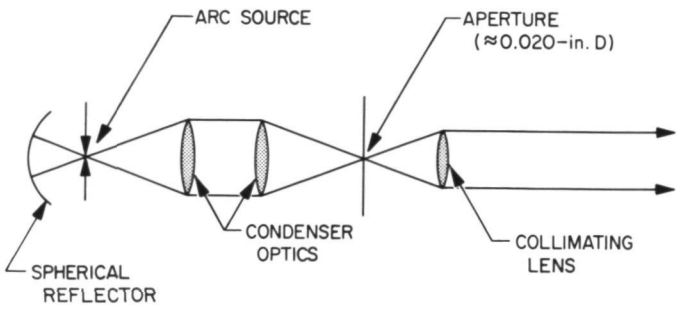

Figure 1. Sun simulator

II. Planetary–Interplanetary

A. Synopsis

The Planetary–Interplanetary Advanced Development effort during FY 62 includes the following long-term studies, analyses, and developments leading to feasibility demonstrations of advances in state-of-the-art techniques intended for application to future planetary–interplanetary projects beyond the first flight missions now scheduled.

The Systems Division is conducting system analysis studies related to trajectory and guidance problems associated with the return of a vehicle from a planet to Earth; trajectory and guidance analysis problems for missions to planets other than Venus and Mars; planetary entry and descent from planetary orbits; and extended trajectories to other planets. In addition, studies are being conducted to determine the values and effects of errors in the fundamental solar system constants.

The Space Science Division is developing an exobiology microscope and a companion microscope spectrophotometer. The exobiology microscope is a soil-sample-gathering-microscope vidicon system capable of performing visible analysis on soil samples which have been graded according to particulate size and density. The microscope spectrophotometer provides a spectral scan in the range 2000 to 5000 Å of a sample located on the stage of a microscope. Additional efforts are directed to developing sample handling systems for this equipment. Also under development are microwave receivers to provide research tools for the scientific study of lunar and planetary surfaces, atmospheres, and ionospheres; and instrumentation utilizing solid-state radiation techniques for making measurements of fluxes and energy spectra of charged particles in space. Studies are being made on the merits of the interferometer type of infrared spectrometer, and on wet chemical analysis techniques applicable to biochemical analysis and life detection.

The Telecommunications Division is pursuing development of a planet-based capsule communication system; study, design, fabrication, and testing of erectable large spacecraft antennas; investigation of the application of all magnetic logic circuitry to spacecraft time-multiplexing and programming subsystems; development of a high-capacity data storage system; evaluation of various methods of range acquisition; and analysis and development of various circuit techniques applicable to long range communications.

The Guidance and Control Division is conducting advanced development efforts in the area of logical designs for guidance computers; developing experimental models of 9-ft concentrators and a 500-w thermionic converter to provide techniques which may prove feasible as spacecraft power sources; and surveying and developing advanced attitude control system mechanization methods.

The Engineering Mechanics Division is performing advanced development of the use of crushable structures for entry capsules; a thermal stress plastic analysis of radiator structures; development of inflatable instrumentation booms for spacecraft application, studies of atmosphere entry and temperature control aspects of various spacecraft configurations; and development of techniques applicable to the environmental survival of equipment.

The Engineering Facilities Division is developing instrumentation components, equipment, and systems to support the advanced development efforts of the other divisions.

In the field of chemical propulsion, the Propulsion Division is conducting an industry-wide survey of high energy solid propellant development activities in order to select propellants for investigation and use with spacecraft. Efforts are also being expended in the evaluation of throat and nozzle materials.

In the field of electric propulsion, the Propulsion Division is keeping abreast of preliminary descriptions of the SNAP-VIII reactor system, its power conversion system, and its thrust units, and is evaluating the constraints they place on the spacecraft and/or constraints the spacecraft should place on these units. Supporting the electric propulsion are the following efforts being undertaken by other divisions: trajectory and guidance analysis; systems studies and preliminary analysis of spacecraft designs; communication analysis; analytical design of guidance and control subsystems; and studies and analyses in the areas of structural dynamics, structural configuration, shielding, and temperature control for electric propulsion spacecraft.

B. Space Sciences

1. Spectra of Venus and Jupiter

Some empirical data studies have been made on the intensity distribution in the spectra of Venus and Jupiter. Nitrous oxide absorption has been suggested as an interpretation of the low ultraviolet albedos of these 2 planets and Mars (Refs 1, 2, and 3), but the available data (Refs 4 and 5) does not seem to corroborate the hypothesis.

a. Venus. Both Kozyrev (Ref 6) and Heyden, Kiess, and Kiess (Ref 1) have pointed out that the Cytherean spectrum was considerably fainter in the near ultraviolet with respect to the visual region than were the observed comparison sources. Kozyrev compared the Venus spectrum directly to the solar spectrum, while Heyden, Kiess, and Kiess used the Moon for a spectrophotometric comparison.

The 3-color photoelectric measures of Harris (Ref 7) show that the U-B color of Venus is $0^m.55$ more red than the solar U-B value. In fact, *all* the planets and satellites observed by Harris have U-B greater than $0^m.14$, the value assumed for the Sun from observations of other G2V stars.

On the basis of a low ultraviolet albedo alone, there would seem little justification for the necessity of nitrogen tetroxide (N_2O_4) absorption in the blue and near-ultraviolet regions of the Venus spectrum, as suggested (Ref 1). Venus actually reflects relatively more ultraviolet ($\lambda_{eff} \approx 3500$ Å) light with respect to the visual ($\lambda_{eff} \approx 5500$ Å) than our Moon (Ref 7), in contradiction to the spectrophotometric result of Heyden, Kiess, and Kiess. Ganymede (J III) is an excellent match for Venus in both geometric albedo and color, yet N_2O_4 atmospheres are not observed on our Moon or Ganymede. Moreover, Kaplan (Ref 5) has noted a dissimilarity between the Venus spectrum and the absorption spectrum of nitrogen tetroxide.

In 1953 Kozyrev (Ref 6) found 2 discrete absorption bands in the violet region of the Cytherean spectrum at λ 4372 and λ 4120 Å. Neither Richardson (Ref 8) nor Heyden, Kiess, and Kiess were able to confirm the presence of these bands when they compared the Cytherean spectrum to that of the Moon. Therefore, a search through the Mount Wilson Observatory plate files was made and 8 suitably exposed and widened 100-inch coudé spectrograms were traced in the blue region near λ 4372 Å with the Mount Wilson microphotometer. The exposure dates and phase angles for the Venus plates are given in Table 1; lunar spectrograms coude 1004 and 896 were photometered as comparisons. The linear dispersion was about 3 Å/mm at Hγ, thus the resolution is an order of magnitude superior to Kozyrev's.

The tracings of Venus and the Moon are similar in the λ 4372 Å region; the absorption band found there by Kozyrev is not present on the 8 Venus spectrograms listed in Table 1. A dip of 5% would probably be detected on the tracings, and a band with a sharp head would have to be very shallow to avoid detection. It was con-

Table 1. Log of the Venus spectrograms

Coudé number	Date	Venus phase, deg
93	8-6-27	120
464	4-16-32	86
478	5-16-32	110
495	5-22-32	115
506	6-13-32	146
562	10-19-32	68
565	11-9-32	58
922	4-18-35	53

cluded that the λ 4372 Å band is absent from the Cytherean spectrum, at least for phases greater than 50 deg.

b. Jupiter. The faintness of the Jovian continuum in the blue and near-ultraviolet noted by Kiess, Corliss, and Kiess (Ref 2) and also observed by Heard (Ref 9) with lunar comparisons is probably not the usual case. The photoelectric colors of Jupiter quoted by Harris show that during his observations Jupiter reflected relatively more ultraviolet, with respect to the visual, than our Moon. Several calibrated medium-dispersion spectrograms were obtained of Jupiter and the Moon on April 28, 1961 at the Kitt Peak National Observatory. The blue and near-ultraviolet regions to about λ 3500 Å were not depressed compared to the lunar spectrum.

Photometric tracings were also made of a set of uncalibrated medium-dispersion Lick spectrograms of Jupiter and the Moon taken in 1936 and 1937 with the Crossley reflector. One spectrogram of Jupiter exposed on July 4, 1937 showed a broad, shallow absorption dip from about λ 3900 to 3500 Å; other Jovian spectra had slightly weakened ultraviolet continua compared to the Moon. The lunar spectrogram was taken at about the same air-mass as the Jovian spectrograms, but on another night. Since the spectrograms were not exposed simultaneously, these observations should be given low weight. Still it is possible that the atmosphere of Jupiter, or a portion of it, undergoes definite changes which affect the ultraviolet continuum; Harris' compilation of photometric observations of Jupiter (Ref 7) indicates a variability of the $V(1,0)$ value on a long time scale.

A systematic patrol program of ultraviolet, blue, yellow (UBV) photometry and photoelectric spectral scans seems necessary to clarify the possibility of Jovian variability.

2. Atmospheric Entry

Presently conceived spacecraft may incorporate a capsule that will enter the atmosphere of Mars and Venus. The instruments aboard this capsule will provide the first on-site data from these planets, and should answer some of the questions that now exist concerning the environment of those planets. Most of this information will be directly applicable to the design of future soft landing vehicles and contribute to a planned evolution of our exploration of Mars and Venus. Because more is known of Mars than Venus, the configuration of the scientific package is different for each.

a. Venus. The known facts regarding Venus are: (1) There is a large amount of CO_2 present in the atmosphere. (2) Atmospheric temperature extremes range from 200°K to greater than 600°K, the latter probably being at the planetary surface. The surface pressure is estimated to be as high as 100 atm. Thus the spacecraft environment may be extremely severe for even unmanned vehicles, and it is extremely important to know, as soon as possible, what precise design goals should be given for subsequent missions. The problem of location and origin of the high temperature is probably the most interesting problem of planetary science, exclusive of the problem of extraterrestrial life.

With these considerations, a Venus capsule would be worthwhile if it could measure the temperature and pressure profiles of the atmosphere. Preliminary studies of a Venus capsule capability indicate the following specifications for instruments: (1) pressure dynamic range (2 sensors)—0 to 20 atm and 0 to 1000 atm; (2) temperature dynamic range—200 to 700°K; (3) accuracy—both 5%; (4) data rate—less than 1 bit/sec total; and (5) weight of sensors—less than 2 lb total. Transducers to perform these measurements are readily available. The problem of height measurement is more difficult and has not been adequately solved. The capsule should also include devices to report on the behavior of the capsule during the re-entry phase from which upper atmospheric parameters could be deduced.

b. Mars. Knowledge of Mars is more extensive; therefore, many physical parameters of the atmosphere and surface are known well enough to permit predicting the performance of the capsule and instruments in the Martian environment. Here the primary problem is to collect data that answers the fundamental question of whether there is or is not extraterrestrial life.

Studies are being made of capsule instrumentation packages. At present, the experiments to be included on a capsule are:

(1) *Fields and particles.* Instrumentation to investigate the radiation belt and magnetic field of Mars may include a 3-axis fluxgate magnetometer and simple radiation detectors.

(2) *Upper atmosphere.* An attempt will be made to measure the scale height of the upper atmosphere. This will be done by using an accelerometer to measure the maximum deceleration of the capsule. Even from an aerodynamically calibrated capsule, it is uncertain whether it is possible to infer the scale height from this 1 measurement. Any measurement of upper atmospheric parameters is difficult because of the disturbance in capsule environment during the entry maneuver.

(3) *Atmospheric thermodynamics.* These measurements include pressure and temperature profile, specific gas constant, ratio of specific heats, and density of the atmosphere. Available instrumentation to accomplish these measurements are thermistors, barometers, and sound velocity tubes. To provide the necessary height information, the feasibility of incorporating an altimeter is being investigated to measure altitude to an accuracy of ± 250 ft at 30,000 ft.

(4) *Atmospheric composition.* Several instruments are under investigation to measure chemical composition of the atmosphere. These are the gas chromatograph, mass spectrometer, solar infrared or ultraviolet radiometer, and instruments designed to detect the amount of a single component.

(5) *Biology.* At present it seems impossible to instrument a meaningful biological experiment that will operate only prior to impact with the surface. This is because these experiments need a long operating time (growth experiments) and a soil sample. Specific experiments under consideration are growth experiments and a device that samples several biologically important characteristics of the Martian surface.

3. Ultraviolet Spectrometer

The following ultraviolet spectrometer design may have possible applications in future space projects. The original scientific mission intended to look at both the visible and the ultraviolet radiation from the planet Venus at intensities ranging from day-side cloud scatter down to night-side after-glow. The night-glow was made difficult to see by close proximity to day-side radiation 3 or 4 deg off axis.

Figure 1 and Table 2 show the aspects of Venus during approach. Spectral data is started at 4 hr before closest approach, when the spacecraft is approximately 100,000 km from Venus. The planet's angular radius is 3.5 deg; and the Sun is approximately 63 deg off the telescope axis. The telescope axis is offset 2 deg toward the dark side, and scans up and down a line tilted 15 deg to the terminator.

Under ordinary conditions a telescope is not subject to interference from light sources outside its field of view. However, spectral features of interest on the night side of Venus are as much as 10^5 less intense than the day-side visible light. When the telescope is pointed at the night side, the bright off-axis source scatters interference from every baffle blade and optical surface. Table 3 lists the expected brightness of various wavelengths of interest. Note that 5500 Å mid-visible green light from the day-glow has a brightness of 9×10^8 Rayleighs compared with night-glow brightness of 9×10^3 Rayleighs at 5500 Å, and 7×10^3 Rayleighs at 3000 Å (near ultraviolet).

Table 2. Range vs angular radius of Venus during encounter[a]

Time from closest approach, hr	Distance from probe to Venus, km	Angular radius of Venus, deg	Sun–probe–Venus angle (UV telescope to Sun), deg	Sun–Venus–probe angle, deg
−6	120,000	2.3	58	121
−5	118,000	2.8	60	119
(Turn-on) −4	98,000	3.5	63	116
−3	74,000	4.7	68	111
−2	54,000	6.7	78	101
−1	34,000	10.6	100	80
0	26,000	14.0	142	38

[a] Launch azimuth, 94 to 114 deg; Trajectory 1, nominal.

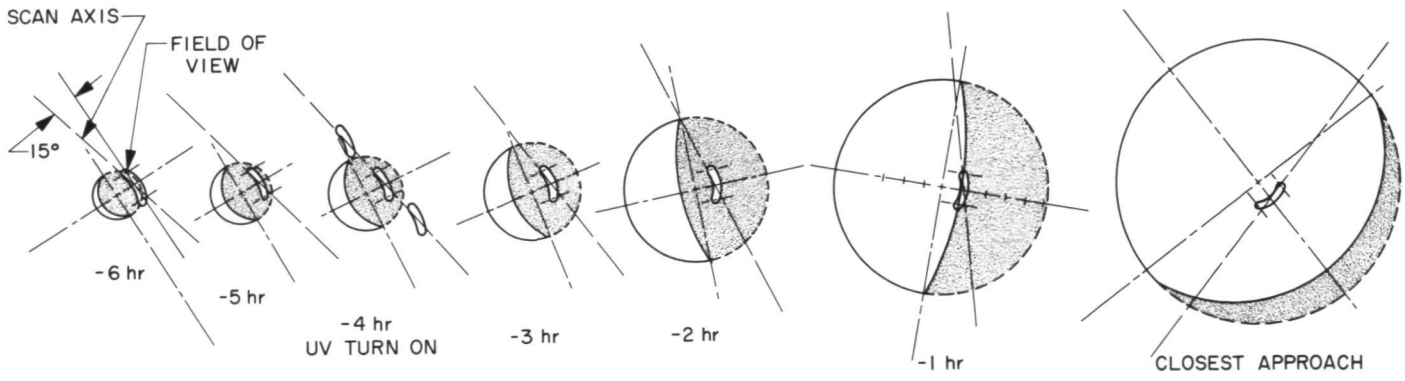

Figure 1. Venus aspects and UV spectrometer field of view

Table 3. Venus surface brightness vs wavelength

Approximate wavelength λ, Å	Brightness In Rayleighs (Estimated)		
	Day-side scatter and day-glow	Aurora	Night glow
5500	9×10^8	1×10^6	9×10^3
5000	1×10^9	—	—
4500	1×10^9	—	—
4000	6×10^8	1×10^6	—
3500	5×10^8	—	—
3000	7×10^7	—	7×10^3
2500	1×10^7 (3 × 1 if no ozone)	—	—
2000	1×10^6 (5 × 10^7 if no ozone)	—	—
1500	$< 1 \times 10^6$	1×10^6	—
1200	$< 1 \times 10^6$	1×10^6	—

Major problem areas of the ultraviolet spectrometer were immediately imposed by the scientific mission:

(1) Requirement for a telescope which could have large light gathering ability, and at the same time, attenuate off-axis light by a factor of at least 10^5 at 4 deg.

(2) Sensitivity that would detect 5 or 6 orders of magnitude below daylight cloud brightness; 2 orders below the threshold of human vision.

(3) Wide spectral response, from 1200 Å (vacuum ultraviolet) to 4200 Å in the visible, with freedom from scattered visible light mixing with the ultraviolet.

(4) Wide dynamic range in the detection circuitry; at least 10^6 dynamic range.

Other problems were associated with rotating the grating, and identifying both wavelength and intensity: (1) the requirement for low power, precise motor control to drive the grating, including stop–start repeatability; (2) a fiducial coding system to code data or grating position without consuming unnecessary computer storage; and (3) flight calibration, both intensity and wavelength.

a. Ultraviolet spectrometer description. Figure 2 illustrates the ultraviolet spectrometer engineering prototype. Following is a description of the subsystems incorporated.

Optics. Figure 3 shows the optical arrangement of the spectrometer. The Cassegrain telescope primary mirror diameter is 125 mm; telescope focal-length is 500 mm; exit beam is *f*/4. Telescope walls use sharpened thin blades to absorb off-axis light. The entrance and exit slits of the monochrometer are multiple slit assemblies to attenuate stray light.

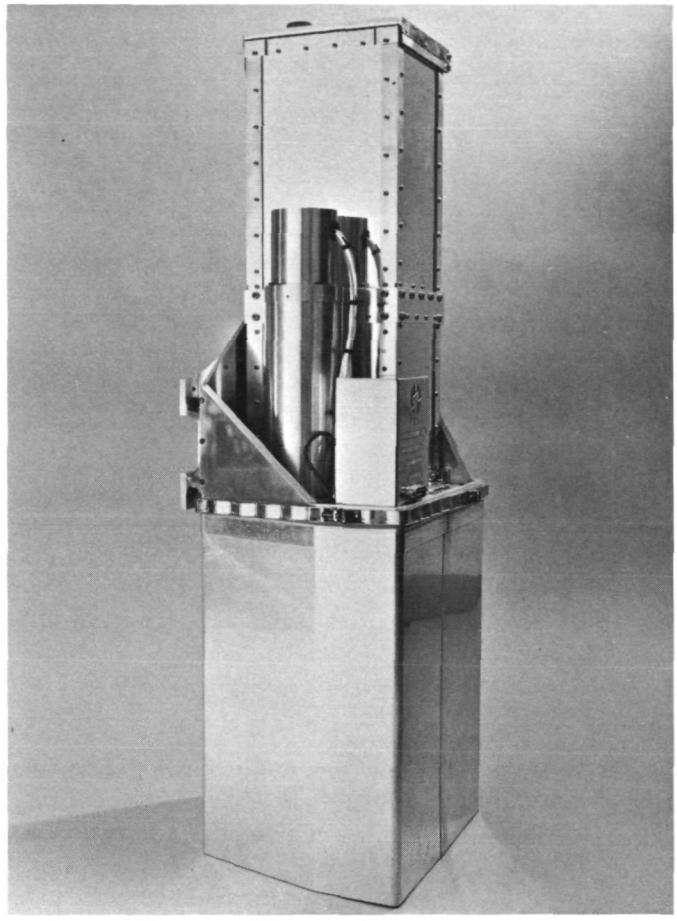

Figure 2. Engineering prototype ultraviolet spectrometer

The Ebert monochrometer has cylindrical symmetry for low dispersion and high resolution for its focal ratio. The 2160 lines/mm diffraction grating gives spectra from 1200 to 4200 Å; resolution is 10 Å. All optics have vacuum deposited magnesium fluoride coated over freshly deposited aluminum for 60 to 70% reflectivity at 1200 Å.

Detector circuitry. The detector (Fig 4) is an English EMI 15-stage phototube with S11 (blue sensitive) cathode, and response from 2000 to 6000 Å. For ultraviolet sensitivity, the window is coated with sodium salicylate. High voltage is supplied to the photocathode by a variable supply which is servo-controlled to keep anode current constant. AC chopping is performed by modulating the relative voltage of 2 multiplying dynodes. The 300-cps modulation signal cuts tube gain to zero 600 times/sec. To close the loop, 600-cps band-pass amplifica-

CONFIDENTIAL

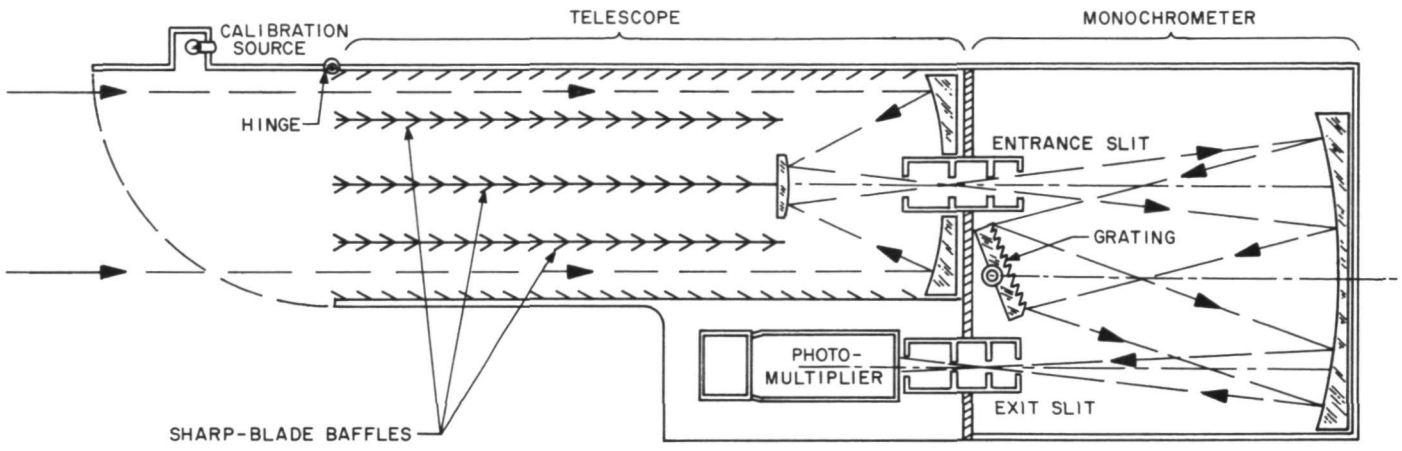

Figure 3. Ultraviolet spectrometer optical arrangement

tion and synchronous detection are used. Light intensity data is taken from the cathode voltage level. Near-logarithmic compression results because the phototube voltage varies as the log of light intensity when current is held constant. The intensity signal is sampled every 5 Å and digitized to 6 bits.

Grating drive control. The grating, gear train, and cam follower (Fig 5) are driven by a stepping motor. DC is controlled in the motor windings by countdown and logic circuitry. A stepping motor has the advantages of operating on dc power, allowing precise speed control, starting and stopping instantly without coasting. The motor is started by external pulse command. It is stopped by a signal from the magnetic code wheel when it reaches home position. After 1 start–stop cycle, the grating stops in the proper position to begin its next scan. During spacecraft boost and cruise, the cam follower is lifted off the cam and held rigidly in a lubricated track so it will survive shake.

Fiducial coding system. A 2-track magnetic code wheel (Fig 5) is geared to the cam. Magnetic Head 1 picks up the *home position* signal which stops the motor drive. Magnetic Head 2 reads the fiducial code which identifies grating position; this is especially important during intermittent telemetry reception. One scan from 1200 to 4200 Å provides 640 samples. Each 7-bit sample has

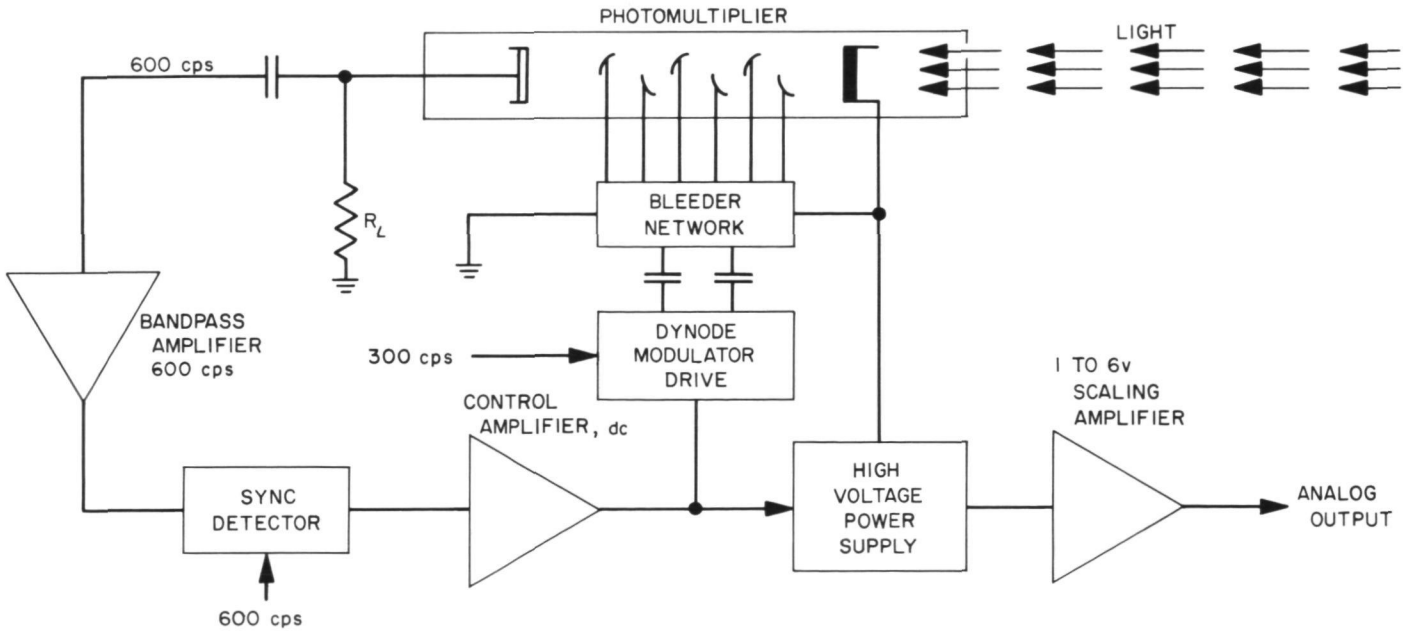

Figure 4. Ultraviolet detector

CONFIDENTIAL

CONFIDENTIAL

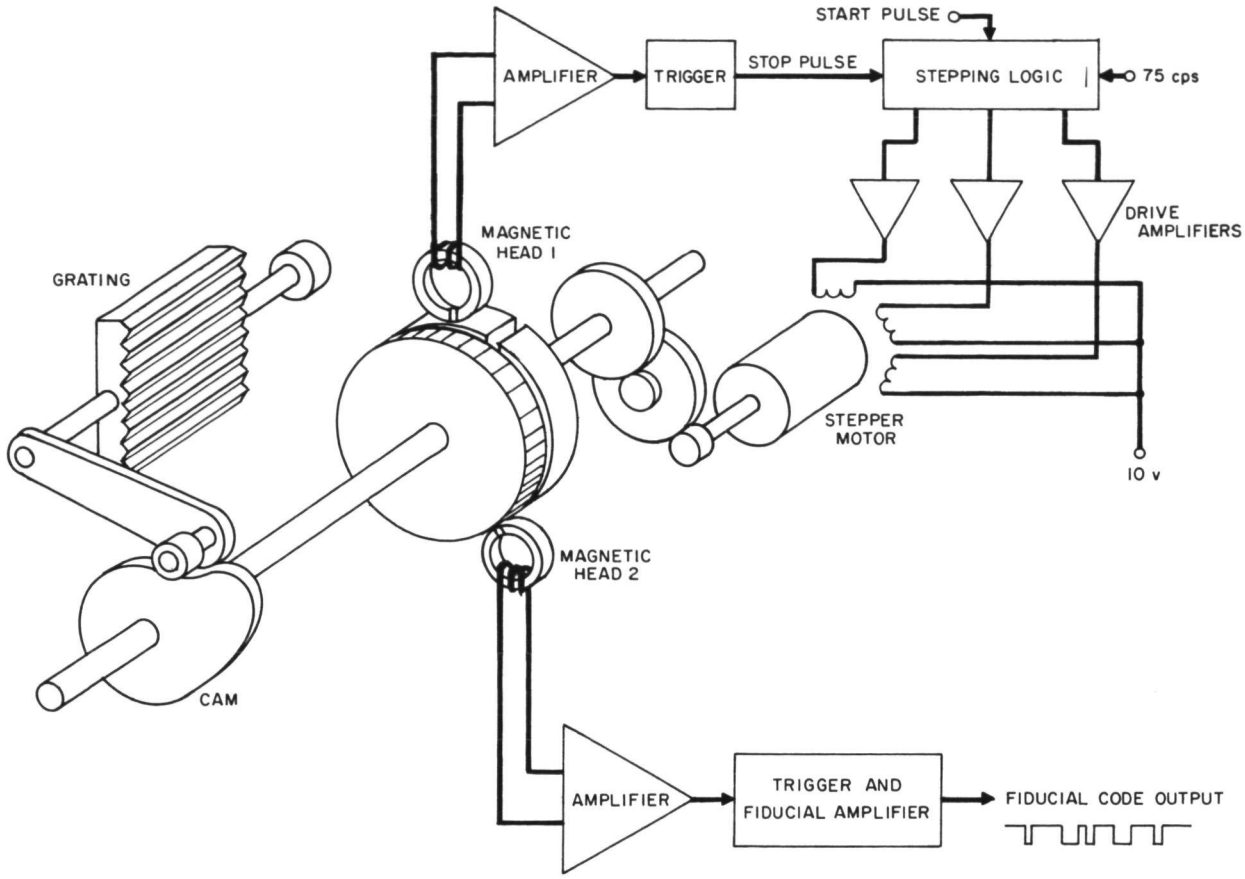

Figure 5. Ultraviolet grating drive and coding system

6 bits for intensity and 1 bit for fiducial code. The code positively identifies position if 15 or more consecutive data samples are received.

Calibration. Inflight calibration is desirable after the vibration of boost and the effect of space vacuum for 4 months. Just before the telescope opens, the instrument scans a built-in tungsten lamp for intensity calibration and a gas discharge lamp for spectral line identification. The lamps, built into the cover, move out of the field of view when the cover opens.

b. Future studies.

Solar-blind ultraviolet detector. The incorporation of a photomultiplier which would respond to ultraviolet, but not to visible light, would help solve 2 critical problems: (1) mixing of high intensity visible light into the low intensity ultraviolet because of grating and optical scatter, and (2) need for 10^5 attenuation at 4 deg off the telescope axis. Recent improvements have been made in the manufacture of solar–blind ultraviolet photomultipliers. The new detectors are not interchangeable, however, and must be designed into the instruments and tested.

Gratings. More study is being given to increase grating efficiency and reduce unwanted scatter. High sterilization temperatures will likely rule out replica gratings entirely. New sources of original gratings with good ultraviolet reflectivity will be needed.

Space lubrication and evaporation. Vacuum chambers are needed that are capable of holding the entire instrument near space vacuum.

Optical blacking. A good black surface is needed which will not evaporate or change properties in 4 months.

Telescope construction. The original method of making baffles was to cut or sharpen the edges of individual blades and to weld or rivet the individual blades into a herringbone pattern. Figure 6 shows the blades at the telescope entrance. Experiments are underway to produce a series of sharp-edged grid plates by chemical etching which will be lighter and easier to fabricate.

CONFIDENTIAL

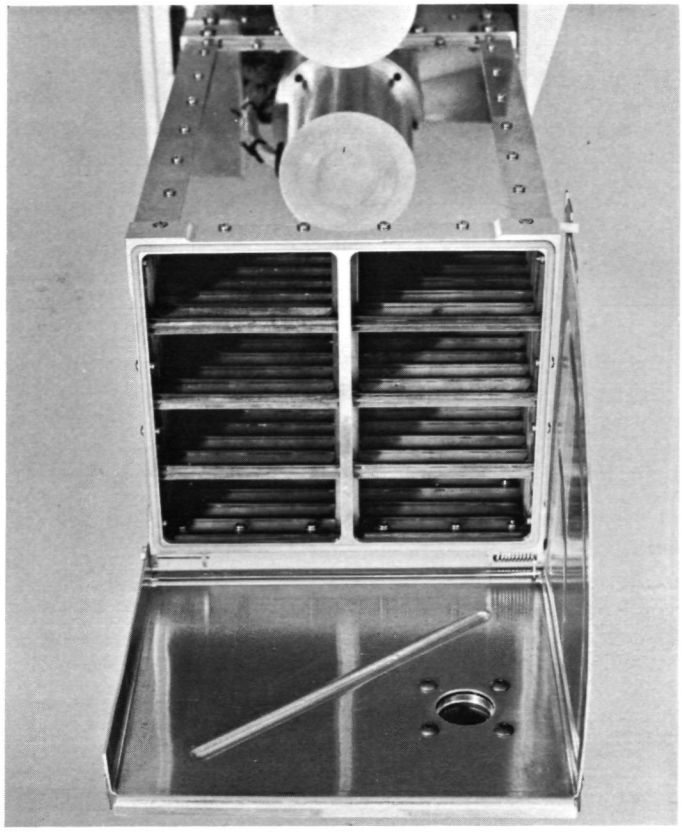

Figure 6. Entrance of ultraviolet spectrometer telescope with baffle blades

C. Spacecraft Secondary Power

1. Solar Concentrator

As was reported in *SPS 37-8*, JPL is acting as technical monitor of a NASA contract with Electro-Optical Systems (EOS), Incorporated, on a research and development program to investigate techniques for fabricating lightweight, efficient solar concentrators for space applications. Investigations have led to the fabrication of a number of mirrors which were evaluated both by JPL and EOS. The construction of a water flow calorimeter which is used in the evaluation program at JPL was described in *SPS 37-9*. The results of efficiency measurements performed on the first 5-ft diameter, nickle electroformed, solar concentrator delivered to JPL were reported in *SPS 37-10*. This concentrator was environmentally tested at JPL and the results reported in *SPS 37-11*.

Two 60-in. concentrators have been delivered to JPL and are undergoing performance tests prior to environmental testing. One is a nickel electroformed concentrator, the other a copper electroformed concentrator. Hardness of the skin in the copper concentrator is as expected, but lack of agitation in the electrolyte bath has produced unevenness and blisters on the back of the mirror. These blemishes show through on the prime surface giving it an orange peel appearance. Reflectivity of the prime surface also suffered, because during parting from the master, parts of the sensitizing silver film adhered to the master. Further investigation will be performed on copper electroforms concerning electrolyte bath agitation, since this determines the quality of the copper deposit and its distribution (thickness) along the full concentrator surface.

2. Thermionic Conversion System

The solar energy thermionic (SET) conversion system under development at EOS and Thermo Electron Engineering Corporation (TEC), has been described in *SPS 37-10* and *-11*. Work on the initial 6-month phase of this project was completed in November 1961 as scheduled; however, all of the initial objectives were not achieved. EOS fabricated a total of six 5-ft diameter parabolic concentrators during this period and has delivered 2 of these to JPL for performance evaluation. A mock SET type generator is shown (Figs 7 and 8) attached to Concentrator JM-1-1. Figure 7 shows the thermionic generator in the launch configuration. The generator would be actuated to the position shown in Figure 8 once in space.

TEC has fabricated and tested a total of 10 SET type converters during Phase I of the development program. The initial converter to be electrically tested failed after approximately 20 hr of operation. One later converter operated 650 hr at relatively constant output. A sudden decrease in output occurred at 650 hr and the converter output went to 0 after 960 hr. Another converter of this type operated for 850 hr without failure; however, the power output of this unit was from 10 to 15% less after 850 hr. A program for continued SET development is being formulated.

a. Thermionic energy converter. The basic configuration and materials of the SET thermionic converter are shown in Figure 9. The emitter (1) and thin walled tantalum spacer (4) are machined from rod material resulting in a 1-piece construction. The emitter area is 2.00 cm^2 and the spacer wall thickness 2.3 mil. The radiant and conduction heat transfer along the spacer accounts for most of the extraneous heat loss in the SET converter. Rupture of the thin walled spacer has been the major

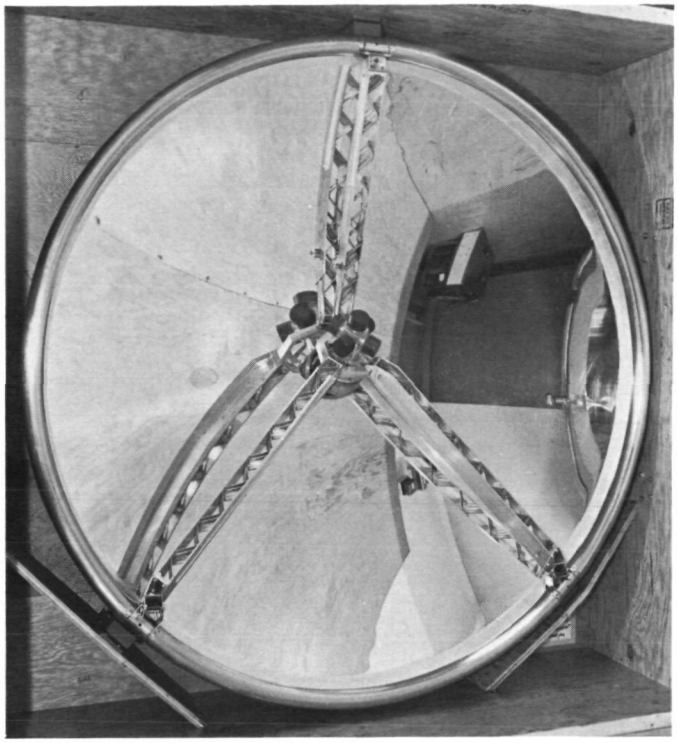

Figure 7. SET system with thermionic generator in launch position

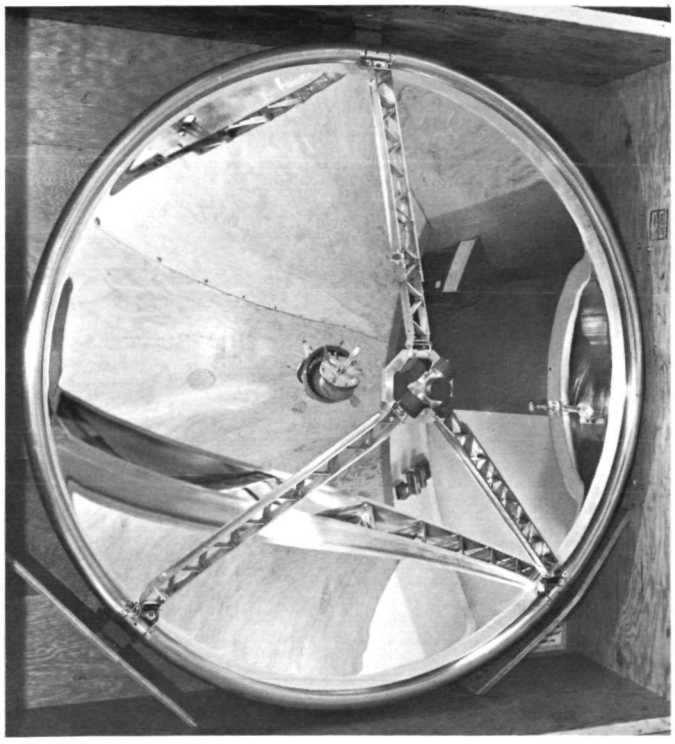

Figure 8. SET system with thermionic generator in operating position

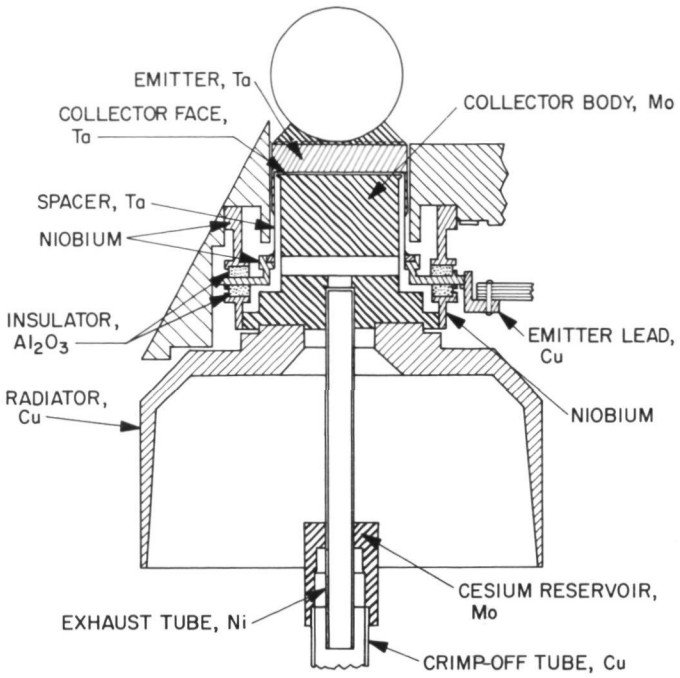

Figure 9. SET thermionic energy converter

cause of converter failure. The collector face is tantalum brazed to a molybdenum collector body. Nominal operating temperatures are:

Emitter face, °K: 1980.

Collector face, °K: 950.

Alumina seal, °K: 850 to 900.

Cesium reservoir, °K: 600 to 650.

Typical performance characteristics of 9 experimental set converters fabricated during Phase I are shown in Table 4. The results of life tests on these converters are shown in Figure 10. The converter design objective for the 10-month, 2-phase, development program was 14.4 w/cm² electrical power density at an output of 1.00 v and 1980°K emitter temperature. The performance of Converter IIb was 12.0 w/cm² at 1.00-v output and 2000°K emitter temperature and was greater than 80% of the design objective. However, Converter IIb failed after 20 hr operation. The tungsten–molybdenum combination used in Converter IIb was not continued in the later converters. Tantalum–molybdenum, and finally tantalum–tantalum, was substituted in an attempt to improve the operational lifetime. Converter Va operated 850 hr without failure; however, only 6.0 w/cm² electrical power density at 1.00 v and 1980°K emitter temperature was obtained. The current vs voltage characteristics of 4 Type-V converters are shown in Figure 11.

Table 4. SET converter electrical performance

Converter	Electrical Output at 1.00v, w/cm² at °K	Emitter material	Collector material	Optimum cesium temperature, °K	Calculated interelectrode spacing, mil
IIb	12 at 2000	W	MO	Not measured	1.61
IIIa	9.5 at 2000	W	TA	659	2.09
IVb	9.1 at 2000	TA	MO	647	2.09
IVc	5.0 ≈ 2000	TA	MO	658	2.09
Va	6.0 at 1980	TA	TA	617	2.3
Vb	5.5 at 1980	TA	TA	601	2.3
Vc	6.0 at 1980	TA	TA	617	2.3
Vd	5.5 at 1980	TA	TA	640	2.3
TE-1	5.5 at 1980	TA	TA	640	2.3

b. Solar concentrators. The performance of SET concentrators fabricated in Phase I is shown in Figure 12. The measured efficiency of concentrator JM-1-1 was 82% with a 0.5-in. cavity aperture diameter. The 10-month, 2-phase development program design objective was approximately 83% with the 0.5-in. cavity aperture diameter. Concentrator JM-1-2 was measured with the silver sensitizing surface uncoated. The silver surface is normally overcoated with vacuum deposited aluminum. The reflectance of the silver surface as measured with a water flow calorimeter was greater than 91%. The efficiency with a 0.5-in. aperture diameter was 89%. However, it is not anticipated that silver surfaces can be utilized on practical concentrators since the reflectance of silver degrades due to atmospheric exposure.

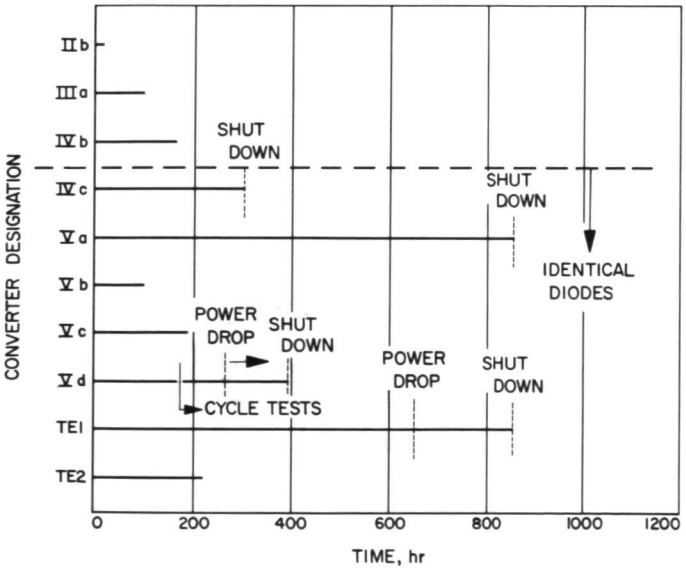

Figure 10. Results of life tests on SET thermionic converters

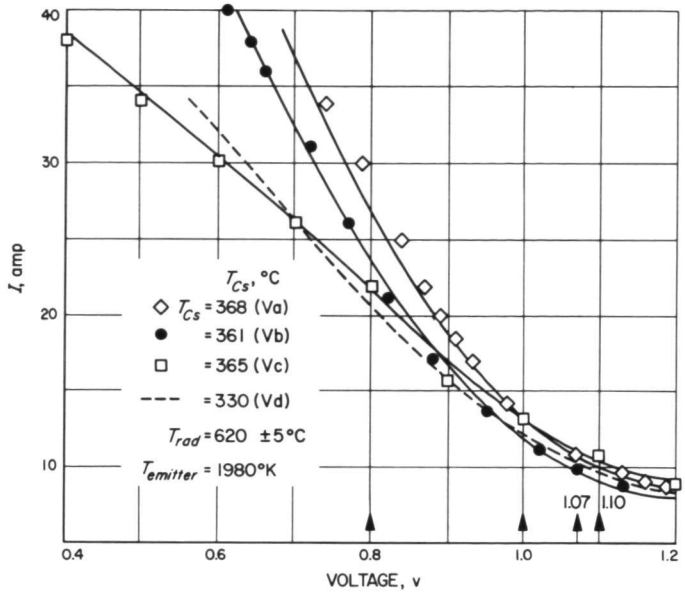

Figure 11. Current vs voltage characteristics of Va, Vc, and Vd

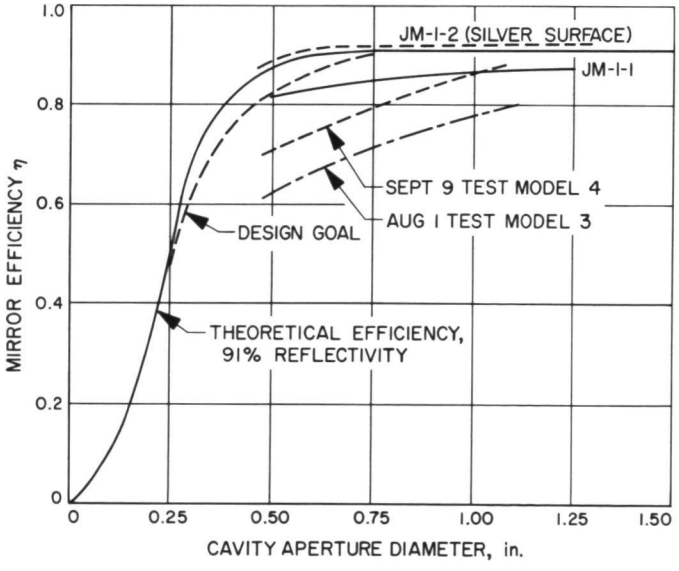

Figure 12. Efficiency measurements on SET concentrators

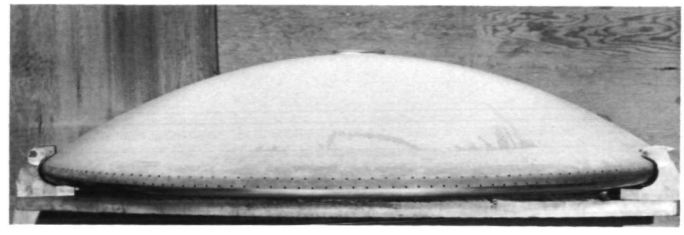

Figure 13. SET Concentrator JM-1-1

Concentrator JM-1-1 (Fig 13) successfully withstood low and high frequency vibration at the *Ranger*-type approval level for subsystems. Specific weight of the 5-ft diameter nickel concentrator is approximately 1.0 lb/ft^2.

D. Engineering Mechanics

1. Energy Absorbing Structures

As stated in *RS 36-5*, there was a need for a program (analytical and experimental) to determine the crushing stress of metallic honeycomb structures and the parameters controlling this stress.

The analytical program has been completed. The analysis was approximate, assuming a rigid-plastic material and applying limit analysis techniques to obtain upper and lower boundaries on the crushing stress. The resulting expression yielded the parameters that control the crushing stress and their relative significance.

The parameters of primary interest are: (1) yield strength to density ratio of the material, (2) structural density of the cellular array (i.e., wall thickness to cell diameter ratio), and (3) geometrical configuration of the cellular array.

The yield strength to material density ratio is subject to the limitation that the material should not be brittle, but have sufficient ductility to deform without fracturing. Experience has shown that materials with uniaxial elongations of approximately 8 to 10% or greater are satisfactory. In addition, for optimum response, a material with a near rigid-plastic stress–strain curve response is desirable. Assuming these 2 limitations, the greater the yield strength to material density, the greater the structural crushing stress.

The structural density, or ratio of cell wall thickness to cell diameter, is a parameter whose optimization depends on fabrication techniques to a limited extent. The greater this ratio, the greater the crushing stress; however, it has been found that there is a maximum density at which the structure will no longer collapse in a uniform manner, but fail in a lower energy mode (Fig 14).

The geometrical configurations of the cellular array may be of many types other than the typical hexagonal cell. Test specimens have been fabricated and tested utilizing tubular arrays, in both closed pack and open pack geometrical arrays (Fig 15).

Results indicated that an increase in crushing stress resulted in the use of tubular arrays as opposed to hexagonal cell arrays.

At present, several cell structures are being fabricated in which the parameters have been optimized in order to obtain a hexagonal cell structure with an energy absorbing property which is maximum for this system. The results of tests performed on these specimens will allow for an evaluation of the analytical work, as well as establish a truly representative energy absorbing value for the hexagonal cell system.

2. Extendable Booms

An extendable, retractable boom is being obtained from De Havilland Aircraft of Canada, Ltd, it can be made of either magnetic or nonmagnetic material and may have application in positioning experiments (such as a magnetometer) away from the spacecraft.

The boom consists of a metal strip heat treated to form a long tube when unrestrained. Prior to extension, the boom is stored on a reel as a flat tape (Fig 16). To extend the tubing, a Mylar tape (interwound with the tape on the storage drum) is reeled onto its own spool by a motor-drive gear train.

The erection unit is a self-contained package complete with power supply for extending the antenna length to the automatic power cutoff point. Early units put out an antenna of fixed length, using either a de-clutching device or a tripped cam for shutting off the drive motor. More recent designs can meter out several precise lengths and

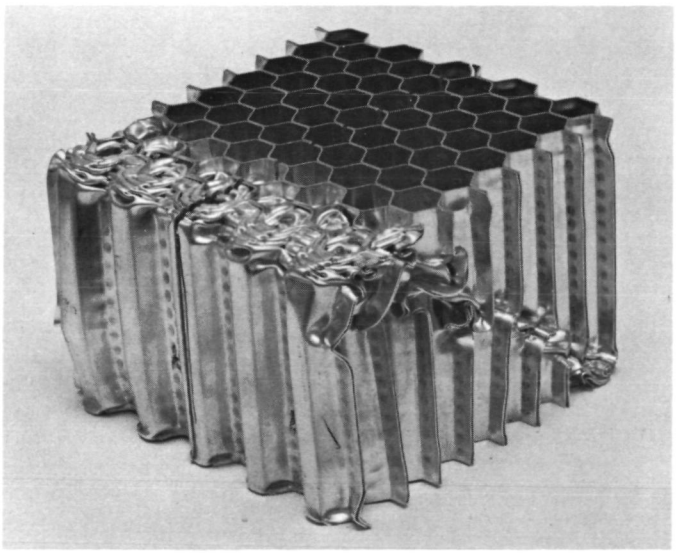

Figure 14. Nonuniform, low-energy-mode failure

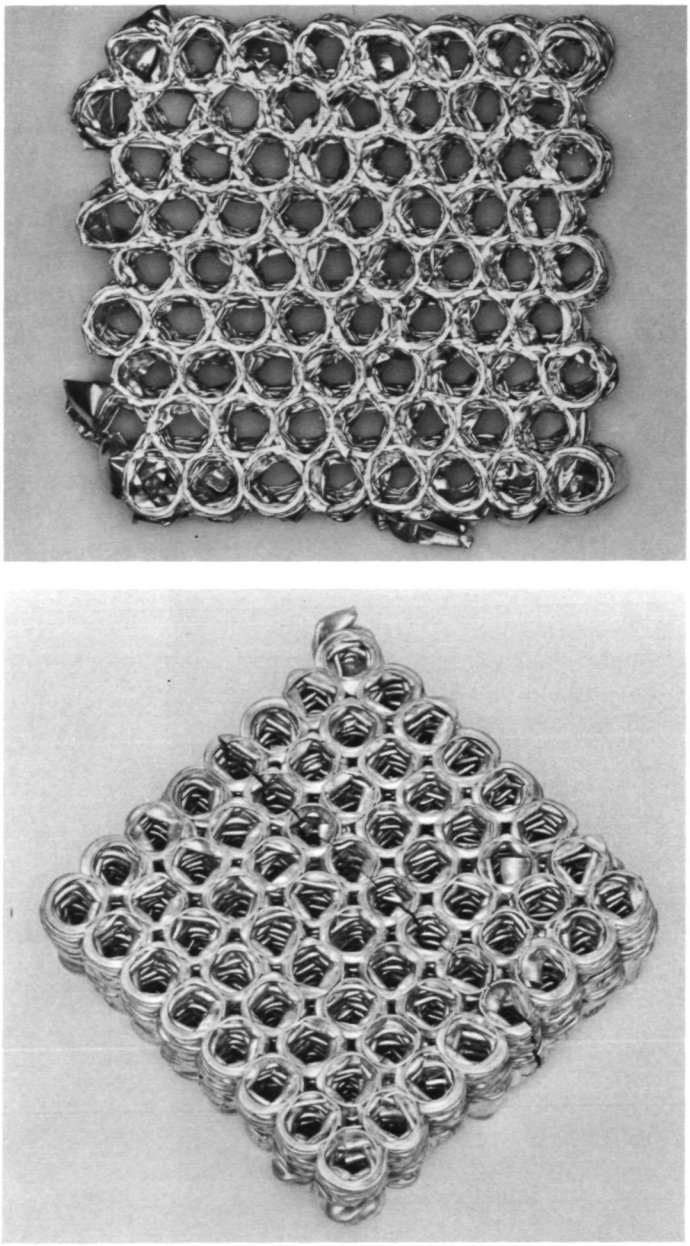

Figure 15. Crushed metallic honeycomb structures (a) closed and (b) open tubular arrays

also fully retract the antenna. To minimize the capacitance between antenna and satellite shell, the erection unit is made of nonmetallic materials and the element is centrally housed. Capacitance is rated at 40 $\mu\mu$f.

Extended, the boom will be approximately 20-ft long. It will incorporate 2 new developments that are not available in the present booms. One will be a method to increase the torsional positioning accuracy; the other will allow cables inside the tube to be extended with the boom. The boom and the cables will be retractable and re-extendable.

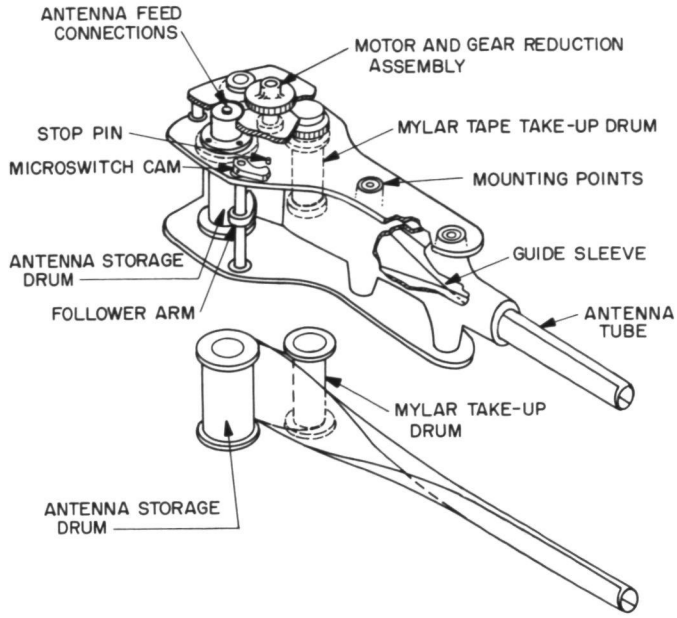

Figure 16. Tubular boom

E. Propulsion

1. Amine Nitrate Monopropellants

Current requirements for spacecraft in-transit maneuvering has led to the utilization of liquid monopropellants as the energy source. Monopropellant hydrazine is currently being utilized in a 50-lb-thrust rocket motor for mid-course trajectory correction of *Ranger* lunar-impact missions. Similar propulsion devices are planned for future planetary probes. For future missions, however, system studies indicate the desirability of more energetic liquid propellants, since propulsion system weights become appreciable as spacecraft weights increase (Ref 11). One such high energy liquid monopropellant, designated Cavea-B, has been undergoing experimental investigation at the Laboratory and the program progress has been reported in *RS 36-2* through *36-7*, and *SPS 37-9* through *37-12*. In addition, JPL rocket motor test results, reported in those publications up to *SPS 37-12*, are summarized in Reference 12.

Cavea-B is the designation of a liquid monopropellant consisting of a nitric acid solution of a quaternary amine

nitrate salt. At acid-to-salt ratios of 1.50 to 1.80, this propellant exhibits suitable physical properties along with a theoretical equilibrium flow specific impulse of 255 to 259 sec (depending on acid-to-salt ratio) at 1000-psia chamber pressure expanded to atmospheric pressure.

Additional theoretical performance data has been compiled during this reporting period. Calculations were made for solutions containing 2% water, since the monopropellant is normally prepared from as received Cavea-B salt and commercial grade white fuming nitric acid; each component contains a small amount of water, so the mixture normally contains from 1 to 2% water. The information was obtained on an IBM 7090 computer utilizing a modified Aerojet program. Table 5 is a compilation of theoretical characteristic exhaust velocities c^*; Figures 17, 18, and 19 are plots of the theoretical vacuum specific impulse I_s, as a function of expansion area ratio ε, for both 1.50 and 1.72 acid-to-salt ratio propellants for chamber pressures of 50, 150, and 300 psia. Curves are shown for anhydrous solutions as well as for those containing 2% water. Figure 20 presents combustion products

Table 5. Effect of water upon the theoretical performance of Cavea-B, equilibrium flow

p_c, psia	$r = 1.50$				$r = 1.72$			
	Anhydrous		2 % H_2O		Anhydrous		2 % H_2O	
	c^*	I_s	c^*	I_s	c^*	I_s	c^*	I_s
50	5063	150.9	5027	149.8	5027	149.5	4998	149.0
150	5099	202.0	5056	200.1	5074	203.0	5043	200.6
300	5116	224.9	5071	222.7	5102	226.3	5069	224.6
1000	5138	254.9	—	—	5146	258.5	—	—

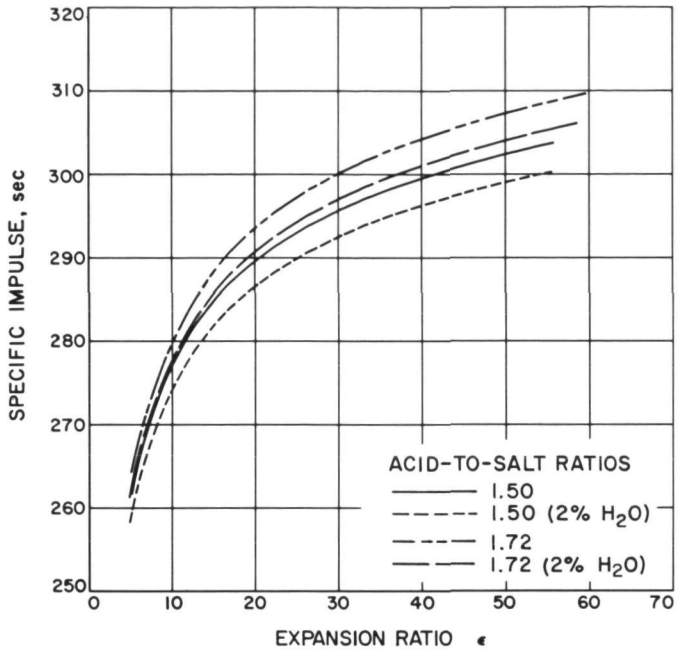

Figure 18. Theoretical vacuum performance of Cavea-B, equilibrium flow, $p_c = 150$ psia

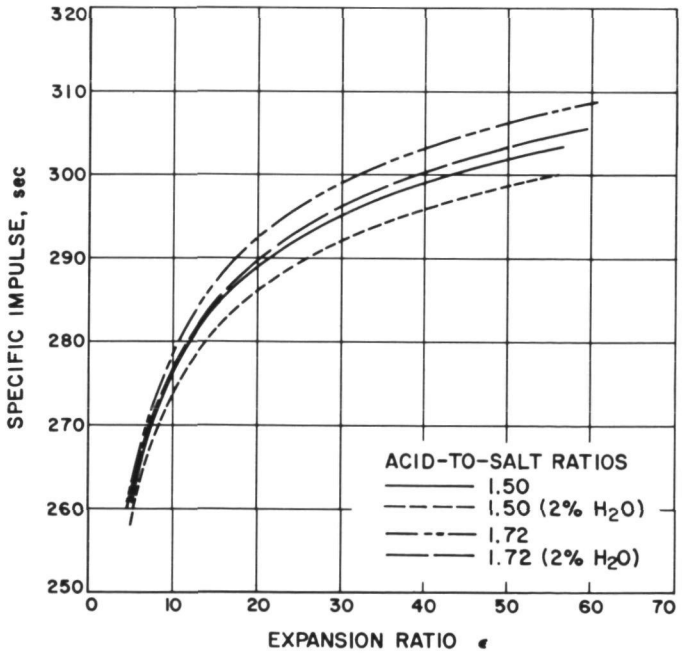

Figure 17. Theoretical vacuum performance of Cavea-B, equilibrium flow, $p_c = 50$ psia

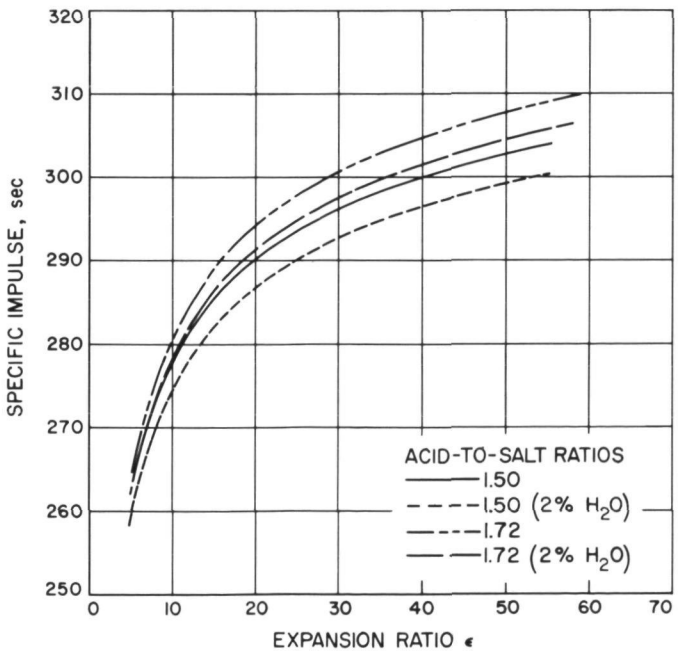

Figure 19. Theoretical vacuum performance of Cavea-B, equilibrium flow, $p_c = 300$ psia

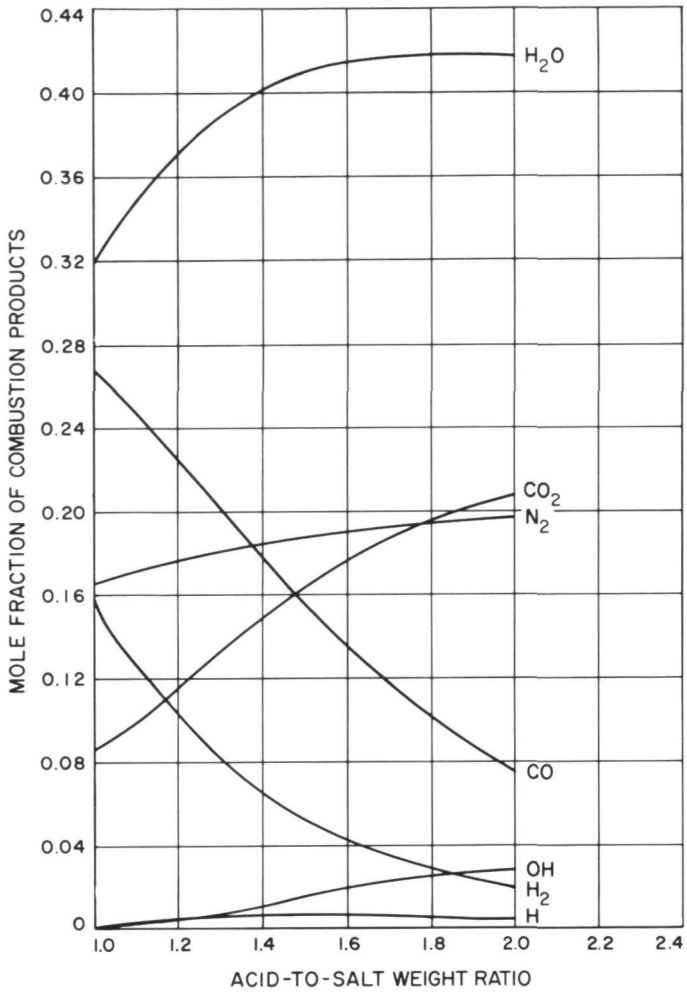

Figure 20. Chamber mole fraction of various combustion products as a function of Cavea-B acid-to-salt ratio, p_c = 300 psia

as a function of acid-to-salt weight ratio for the 300-psia chamber pressure case, assuming anhydrous monopropellant.

Experimental investigations to date reveal that efficient monopropellant combustion of this propellant depends strongly upon several factors, including combustion chamber pressure, degree of atomization, combustion chamber gas-side wall temperature, and residence time. At the 100-lb-thrust level, and at 300-psia chamber pressure, it has been necessary to utilize fairly high injector pressure drops (greater than 100 psid), ceramic insulated chambers, and chamber characteristic lengths L^*, in excess of 100 in. in order to obtain high percentages of theoretical specific impulse as well as stable combustion. Two types of injectors have been utilized: the impinging stream type, composed of multiple like-on-like doublet elements, and the multiple-spray type, composed of either 4 or 8 atomizing spray nozzles. *SPS 37-10* contained performance results of the impinging stream injector and *SPS 37-12* contained complete results obtained with the 4-spray configuration.

An evaluation of the 8-spray injector was completed during this reporting period. It was expected that the more uniform mass distribution per unit of chamber cross-sectional area and the better atomization provided by 8 individual spray nozzles would provide more stable combustion at lower L^* values than provided by the 4-spray configuration. Little improvement was noted, however. It was again necessary to utilize a characteristic length of approximately 165 in. in order to obtain high performance (c^* = 5000 ft/sec) and avoid severe low frequency instability. At an L^* value of 165 in. and a chamber pressure of 300 psia, pressure fluctuations were $\pm$18 psi ($\pm$6%) when an injector pressure drop of 140 psid was utilized. A change of spray nozzle sizes, to produce a pressure drop of 110 psid at the same flow rate resulted in rough combustion, with pressure fluctuations of $\pm$150 psi ($\pm$50%). Similar, although not as severe, results were obtained at an L^* value of 234 in.

It would appear that the atomizing spray-nozzle injector is satisfactory at a reasonable L^* only if it is possible to provide a high injector pressure drop (150 to 350 psid). On the other hand, the impinging stream injector produced combustion noise pressure fluctuations of only $\pm$6 psi ($\pm$2%) at an L^* of 34 in. and with a pressure drop of 140 psid. Thus, under the conditions of this test program, the impinging stream injector type is clearly the better of the 2 types tested.

2. Advanced Liquid Propulsion System

The Advanced Liquid Propulsion System (ALPS) Program has been established for the purpose of formulating and demonstrating solutions to problems in spacecraft propulsion. The program has been organized to cover these problems in a coordinated manner so that solutions are mutually compatible and suitable for practical application in a complete system. *SPS 37-8* through *37-12* contain details of the program.

a. Engine development. The thrust chamber for the ALPS must be capable of restart in space, of long-duration firings, and of throttled operation. It is proposed to employ a radiatively cooled thrust chamber. Several advantages which accrue from the use of nonregenerative cooled chambers are: (1) elimination of the coolant flow inadequacy at low thrust levels in a throttlable engine, (2) elimination of problems associated with space storage of the liquid holdup in cooling passages, (3) elimination of problems relating to compatibility of

materials with hot coolant, (4) reduction in engine weight due to elimination of liquid holdup. Presently, the most promising material appears to be pyrolytic graphite. This material can be fabricated with present technology, has an extremely high sublimation temperature, and has the highest strength-to-weight ratio at elevated temperatures of any substance known.

High Temperature Materials, Incorporated, was given a best-efforts contract to produce model-size thrust chambers of free-standing pyrolytic graphite. Six 100-lb-thrust and six 2000-lb-thrust chambers were ordered. Thus far, three 100-lb-thrust chambers and one 2000-lb-thrust chamber have been accepted.

The first of the three 100-lb-thrust chambers failed under hydrostatic proof test at 100 psig. It is believed that stresses caused by a test-fixture O-ring sealing the chamber throat contributed to the failure. In order to eliminate these stresses, flowing nitrogen gas was used for subsequent proof tests. The 2nd chamber (S/N M564) was successfully proof tested to 144 psig. The 3rd chamber failed in proof test at 130 psig. It is felt a minimum proof pressure of 140 psig is required since the chambers are designed to be fired at 135 psig. A rejected chamber whose injector flange was severely cracked was modified so as to be usable. This chamber (S/N M563) was successfully proof tested to 144 psig. Figure 21 shows a 100-lb-thrust pyrolytic graphite chamber.

The ALPS 100-lb-thrust pyrolytic graphite thrust chambers are currently being tested with the propellant combination N_2O_4–N_2H_4. The first chamber (S/N M564) was fired on December 12, 1961, and operated successfully for the full scheduled duration of 30 sec. The chamber wall thickness at the throat was about 0.045 in. and about 0.060 in. in the cylindrical portion. The injector used for the tests characteristically gives rather high erosion in certain areas and practically no erosion in other areas. In region of maximum erosion there was a 0.014 in. reduction of wall thickness at the throat and 0.012 in. near the injector. There was no measurable erosion over a large portion of the throat. Outside wall temperatures were measured with thermocouples which were spring loaded against the chamber. These thermocouples indicated temperatures of about 2000°F and appeared to reach steady-state in about 30 sec. Preliminary heat transfer calculations indicate that the inner wall temperatures were on the order of 3500°F. Nitrogen gas was flowed around the outside of the chamber in order to minimize oxidation of the outside wall. Postrun measurements indicate there was about 0.002-in. reduction in the outside diameter of the chamber. The chamber

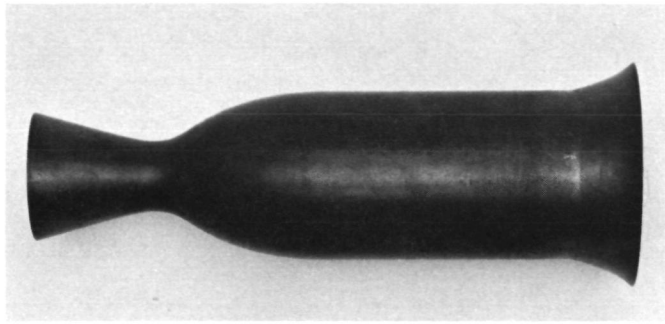

Figure 21. ALPS 100-lb-thrust free-standing pyrolitic graphite thrust chamber

was attached to the injector with a graphite flange. A Viton O-ring was used as a pressure seal between the inside surface of the pyrolytic graphite chamber and the injector. The O-ring charred during the firing but continued to seal. The test setup for the firing is shown in Figure 22.

This chamber was then rotated 180 deg with respect to the injector in order to get minimum erosion in those regions of the chamber which were most severely eroded in the first run. The chamber was then successfully fired again for 30 sec.

The chamber whose flange had been modified (S/N M563) was fired on December 18, 1961, and failed after 44 sec during a firing scheduled for 60-sec duration. Preliminary data shows that the failure occurred near

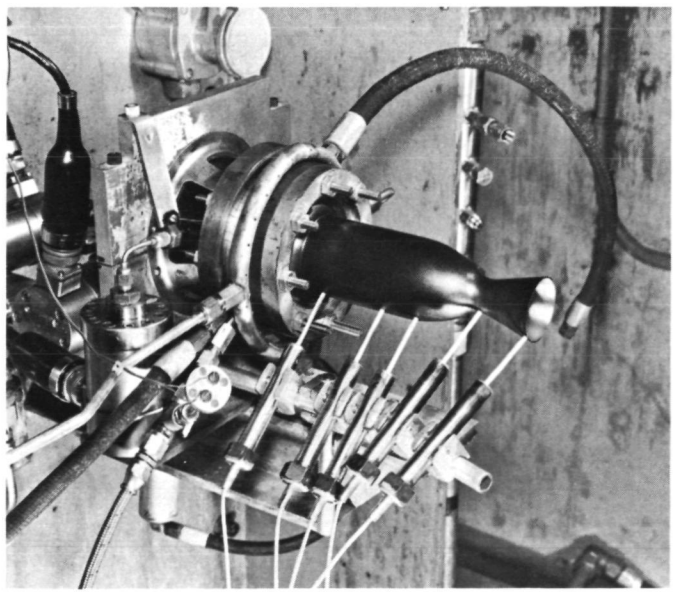

Figure 22. Test setup of ALPS 100-lb-thrust pyrolitic graphite thrust chamber

the injector, indicating the failure may be related to the cracked flange. No nitrogen gas was flowed around the chamber during the run, but it is not felt that appreciable oxidation occurred on the outer surface.

Data from these firings are given in Table 6. Additional firings will be made with pyrolytic graphite thrust chambers as the chambers become available.

b. Propellant performance comparison. A determination was made of the performance of several hydrazine-based fuels with nitrogen tetroxide operating at a chamber pressure of 150 psia. The data was calculated on the IBM 7090 digital computing system using the Aerojet-General Corporation program. Computation was based on shifting equilibrium flow in the nozzle and assumed no losses in either the characteristic exhaust velocity c^*, or the thrust coefficient C_F. The fuels considered are:

Hydrazine

Unsymmetrical dimethylhydrazine (UDMH)

Monomethylhydrazine (MMH)

50% hydrazine–50% UDMH (wt %)

Hydrazine Blend 1 (HB-1)
66.7% hydrazine, 4 moles
23.9% MMH, 1 mole
9.4% water, 1 mole

Hydrazine Blend 2 (HB-2)
73.6% hydrazine, 4 moles
26.4% MMH, 1 mole

Hydrazine Blend 3 (HB-3)
50% hydrazine–50% MMH (wt %)

Because impulse and density are of primary concern in the design of a propulsion system, some of the computed performance was plotted in a manner so that the relationship between impulse and density is displayed directly with mixture ratio as a parameter (Fig 23). In this figure the vacuum specific impulse I_s, at an expansion area ratio of 40:1, is plotted against density ρ, on a log-log scale, so that contours of constant $\rho^n I_s$ appear as straight lines, with a parallel family of contours for each value of n. The method of presenting this comparison was based on work described in Reference 13. Equations for the selection of an appropriate value of n for these types of vehicles are described below.

Table 6. Data from test firings of ALPS[a]

Date	Test	Chamber S/N	Chamber pressure p_c, psia	Mixture ratio r oxidizer/fuel	Characteristic velocity c*, ft/sec	Firing duration, sec
12-12-61	106	M-564	141	0.96	5470	30
12-15-61	108	M-564	140	0.99	—	30
12-18-61	109	M-563	140	1.01	5460	44

[a]100-lb-thrust free-standing pyrolytic graphite thrust chambers.

In all 3 types, the vehicle is accelerated to a high velocity, then coasts ballistically or aerodynamically. In the 1st type, part of the rocket burnout mass is fixed and the propellant volume is fixed. In the 2nd vehicle type, part of the rocket burnout mass is fixed and the gross mass is fixed. In the last type, the gross mass, the length and part of the burnout mass are fixed, but the diameter may vary. In the first 2 cases, the purpose is to maximize burnout velocity, and in the 3rd case, which is based on a boost-glide vehicle concept, the purpose is to maximize range. The equations for n for these 3 cases are shown below; the derivation of the equations can be found in Reference 13.

Case I. Propellant volume and part of burnout mass fixed:

$$n = \frac{m_p/m_0}{\ln (m_0/m_b)} = \frac{\nu}{\ln \dfrac{1}{1-\nu}}$$

Case II. Gross mass and part of burnout mass fixed:

$$n = \frac{m_{b2}/m_b}{\ln (m_0/m_b)}$$

Case III. Gross mass, length, and part of burnout mass fixed; variable diameter:

$$n = \frac{1}{p}\left\{1 - \frac{(m_0/m_b)\,(m_{b2}/m_b)}{(m_0/m_b) - 1}\right\} + \frac{m_{b2}/m_b}{\ln (m_0/m_b)}$$

where

m_0 = gross mass of the vehicle

m_b = burnout mass of the vehicle

m_{b1} = part of burnout mass which is proportional to propellant volume

m_{b2} = fixed portion of burnout mass

m_p = propellant mass

p = speed exponent: 0.6 for sharp-nosed missiles, 0.1 for blunt-nosed missiles

In Figure 23, it can be seen that, for any value of n shown on the plot, the hydrazine–nitrogen tetroxide combination is superior to any of the 6 combinations; i.e., the product of ρ^n and I_s is greater than that for the other combinations.

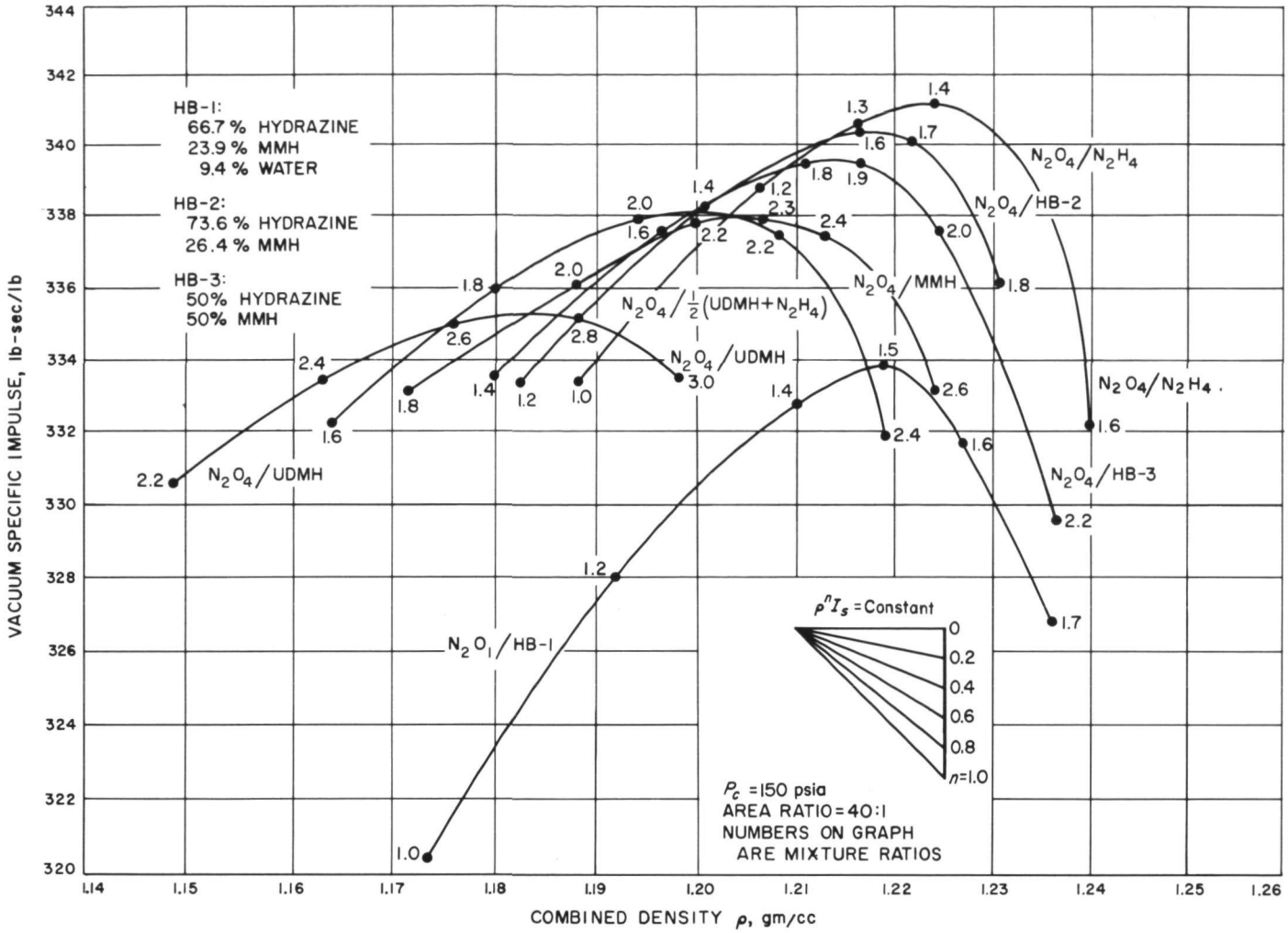

Figure 23. Density–impulse comparison

3. Cryogenic Propulsion System

a. Introduction. Efficient performance of current and possible future space exploration missions, depends on the use of propulsion equipment of increasingly higher performance (exhaust velocity).

The High-Energy Liquid Propellant Research Program has been concerned with storable liquid propellants, such as N_2O_4–N_2H_4 and ClF_3–N_2H_4 having theoretical exhaust velocities of approximately 8300 ft/sec. Liquid propellant systems using oxygen or fluorine as the oxidizer and hydrogen as the fuel have theoretical exhaust velocities in excess of 11,000 ft/sec (expanding to 14.7 psia from 300-psia chamber pressure). Various preliminary design studies indicate that insulation requirements associated with the use of these cryogenic propellants can, for most missions, be satisfied without appreciably depleting the performance advantage these propellants have over the storable liquid propellants. Further, the large tank volume required for low-density liquid hydrogen is not a limiting factor in upper-stage vehicles, although it might be a limiting factor if hydrogen were used as the fuel in a 1st stage booster.

Beyond the performance limits of chemical reaction rocket motors, exhaust velocities of 20,000 up to 64,000 ft/sec are expected to be obtained using, in order: hydrogen heated in a nuclear reactor, electrically-heated working fluids, plasma jets, and finally, ion expulsion devices. Cryogenic working fluids will be used in many of these propulsion systems.

Because of these considerations, the research program has been reoriented and renamed the Cryogenic Propulsion System Program and the stand at the Edwards Test Station which had been used for the recently com-

pleted ClF_3–N_2H_4 program is being modified to utilize cryogenic propellants.

The multiple objectives of the program are:

(1) To achieve an understanding of the properties of the cryogenic fluids, especially oxygen and hydrogen, and of the requirements imposed by these properties on the materials and equipment used with these fluids.

(2) To develop a competence in the handling, storage, and transfer of the cryogenic fluids, and in the design, fabrication, and operation of components used with the cryogenic fluids.

(3) To obtain experience in the design and operation of LH_2–LO_2 rocket motor systems in order to provide test and evaluation ability and engineering capability necessary for considering cryogenic propulsion systems in future JPL spacecraft programs.

The program will start with the installation of cryogenic storage tanks and test station equipment which will enable experience to be obtained in handling the cryogenic propellants and in the operation of the components in cryogenic systems. Engine problems will be investigated next. These include the areas of combustion chamber fabrication, injector design and fabrication, performance, combustion stability, heat transfer, and cooling. As soon as possible, the program will be broadened to simulate and solve problems which would arise in the design and operation of complete propulsion systems and vehicle stages using high energy cryogenic propellants. These problems include fluid metering devices and propellant utilization systems, instrumentation, ground handling and loading, insulation requirements, and flight-weight component development.

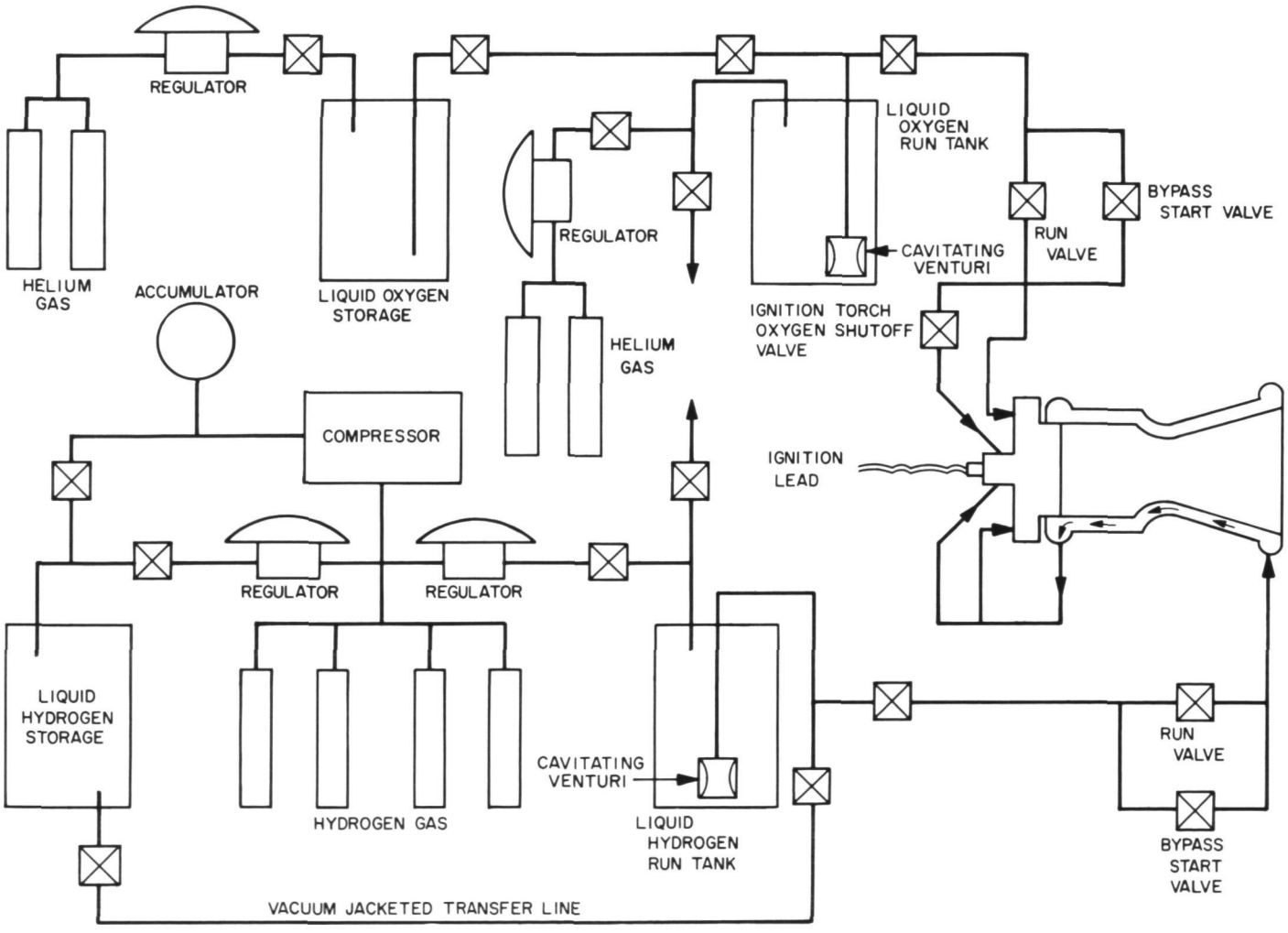

Figure 24. Liquid hydrogen–liquid oxygen test stand facilities

b. Test stand and facility. The C-stand area at the Edwards Test Station has been modified for testing liquid hydrogen–liquid oxygen rocket motors. The major modifications and new installations are indicated in Figure 24.

Test stand. A new motor mount, incorporating a flexure-hinge parallelogram linkage, has been installed to accommodate the modified JPL 6K motors which will be used for test purposes (Fig 25).

Propellant tanks. The chlorine trifluoride and hydrazine propellant tanks have been removed and replaced by new propellant tankage. Liquid oxygen is supplied from a 60-gallon, 1000-psi working-pressure tank located in an existing concrete-lined pit at the north side of the test stand. The oxygen tank is completely immersed in a liquid nitrogen jacket to prevent losses; the liquid nitrogen container is insulated with 2 in. of sprayed-on low-density polyurethane foam (Fig 26).

Liquid hydrogen is supplied from a 320-gallon, 1000-psi working-pressure tank which is located in a new concrete-lined pit a few feet south of the test stand. The liquid hydrogen tank is provided with a liquid nitrogen precooling jacket, and the whole assembly insulated with 9½ in. of sprayed-on low-density polyurethane foam (Fig 27).

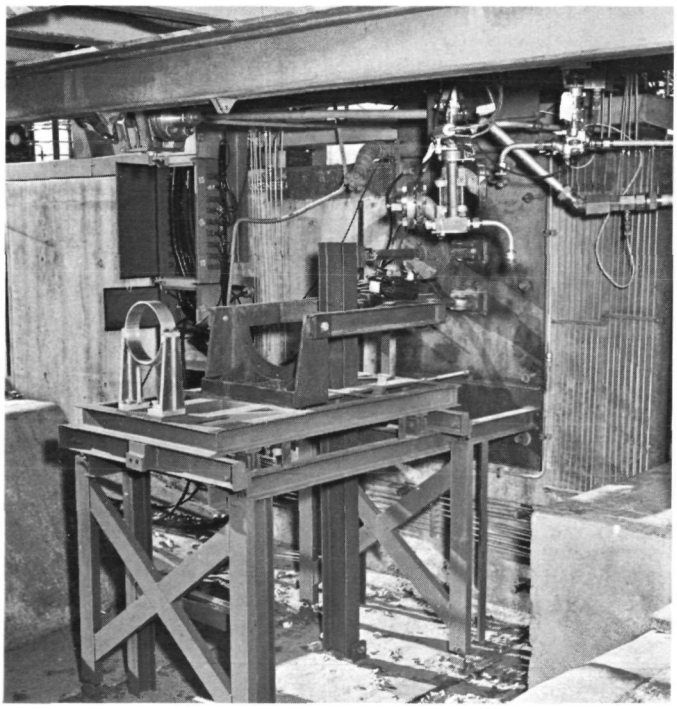

Figure 25. Flexure hinge parallelogram linkage test stand motor mount

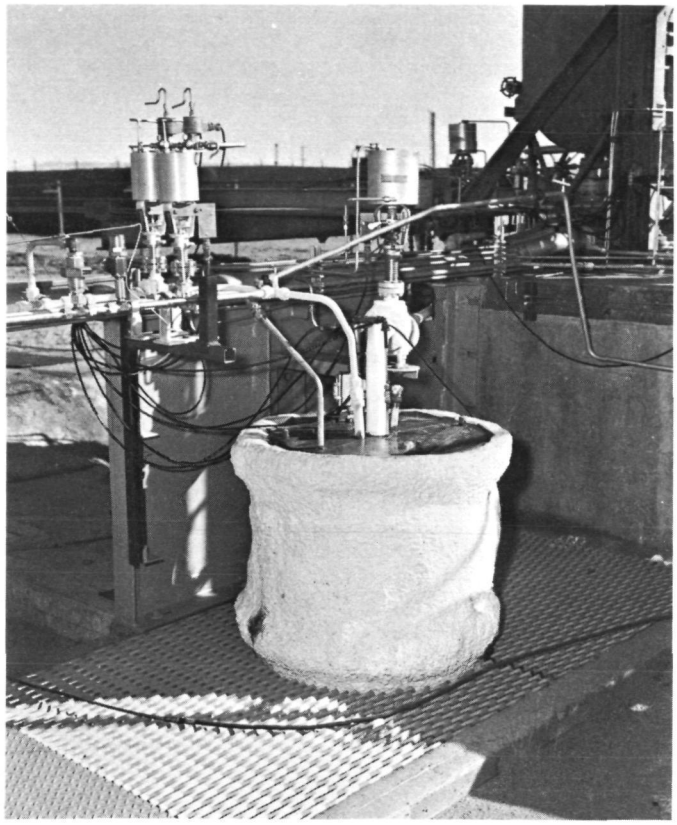

Figure 26. Liquid oxygen run tank in liquid nitrogen jacket

Liquid hydrogen storage. A 1285-gallon liquid hydrogen storage tank is located behind a barricade about 200 ft to the east and south of the test stand. This tank is vacuum jacketed and has a loss rate of not more than 2.6% of tank capacity per day. A vacuum jacketed transfer line connects this storage tank to the hydrogen run tank at the stand (Fig 28).

Liquid oxygen storage. A roadworthy trailer, originally made for liquid fluorine service, has been modified and mounted to the east, and north, of the test stand for storage of liquid oxygen (Fig 29). The oxygen tank is concentrically mounted inside a liquid nitrogen tank, which in turn is insulated by a vacuum jacket. Two Norelco liquefier units reclaim and return to the system the nitrogen boiloff. A transfer line connects the oxygen storage area to the oxygen run tank at the test stand.

Liquid nitrogen supply. A large liquid nitrogen storage tank (Fig 30, 250,000-standard-ft^3 gas capacity) has been installed at the Edwards Test Station to supply liquid nitrogen for cooling down and jacketing equipment at Stand C and to supply, through a high pressure

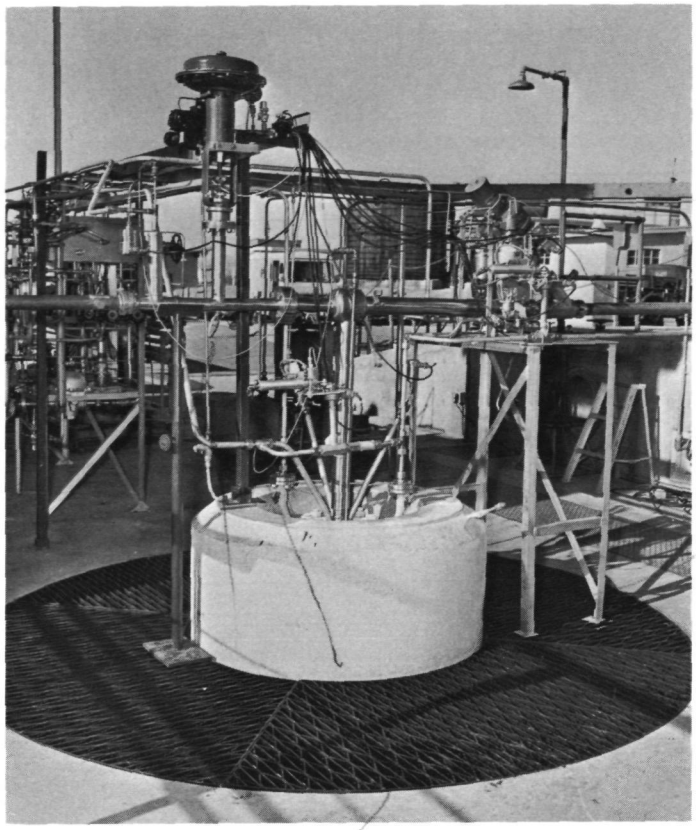

Figure 27. Liquid hydrogen run tank in pit near test stand

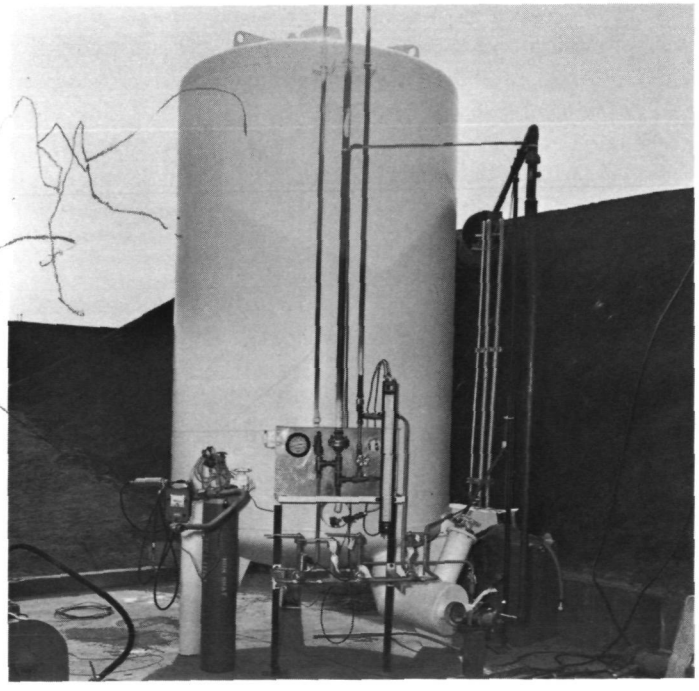

Figure 28. Liquid hydrogen storage tank behind barricade

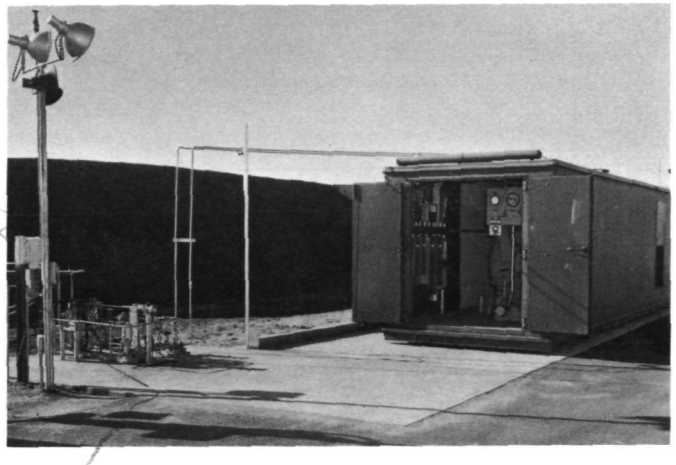

Figure 29. Liquid oxygen trailer and storage tank

Figure 30. Liquid nitrogen storage tank

pump and a heat exchanger, high pressure nitrogen gas which is used throughout the station.

Hydrogen gas compressor. The boiloff from the liquid hydrogen storage tank is collected in 2 accumulator tanks and then compressed and stored in high pressure gas bottles. The high pressure hydrogen gas is used for supply pressure in the liquid hydrogen run tank. The 2-stage Corblen diaphragm-type compressor (Fig 31) was selected because it does not introduce contamination into the gas being pumped.

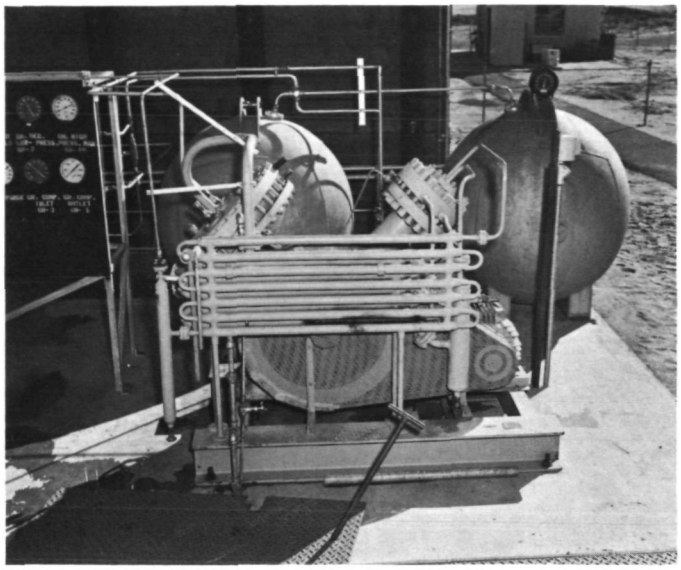

Figure 31. High pressure hydrogen gas compressor with low pressure inlet accumulator tanks

Introduction of liquid hydrogen as a propellant at the test station has required the development of competence in 2 new fields. Because of the wide inflammability limits of hydrogen with air (4.1 to 74% by volume), special attention has had to be given to the detection of hydrogen and of hydrogen–oxygen combustible mixtures; means used to purge, evacuate, and pump the system; and disposal of gaseous wastes through elevated stacks. Liquid hydrogen must be maintained at a very low temperature (37°R), requiring extremely efficient insulation of tanks and lines. Besides the introduction to low density polyurethane foam insulation technology, this requirement has led to the extensive use of vacuum jacketing for insulation, and to procurement and training in the use of high vacuum pumping systems and helium-leak detection equipment.

c. Preliminary studies. The major modifications of the C-stand area have been completed and most of the new equipment has been procured, is in use, or is being checked out. There remains a number of preliminary study and experimental projects to be performed before actual motor tests are initiated. These projects are designed to provide calibration information and checkout on instrumentation and flow-measuring systems or to provide information and design data about equipment and components which will be needed before the motor firing tests begin. At the same time the preliminary tests will develop familiarity with, and serve as proof tests of, the major subsystems which have been newly installed in the test stand area.

Injector element study. The recently completed work with ClF_3–N_2H_4 involved development of a *cup and plug* injector element for use in multielement injectors. This injector element is believed to be applicable to all types of propellants, and will be incorporated in some of the injectors being made for the LH_2–LO_2 program. Basically, the injector element involves the deflection of streams of propellant to form alternate interleaved thin sheets of propellant, with some mixing of side sprays within the protected confines of the cup. Most of the mixing occurs by mass transfer between the sheets of propellant as the sheets proceed down the combustion chamber. The original injector element involved 2 rows of holes drilled at angles of ± 30 deg to the axis of the element; it was desired to simplify the fabrication of this element by drilling the orifice holes parallel to the axis of the element and making simple changes in the deflection surfaces. A water test model was designed and fabricated and several modified deflection surfaces were investigated without achieving the desired results. A water test model similar to the original ClF_3–N_2H_4 injector element, but adjusted in size to fit the LH_2–LO_2 injector, was made to give a satisfactory spray pattern. Fabrication of an injector using this element is proceeding.

Igniter. The hydrogen–oxygen propellant combination is not hypergolic, but the electric spark ignition has been found satisfactory. A decision was made to use a low tension (2000 v) ignition system using a semiconductor-type ignition plug. It is essential that a properly mixed gas be present where the igniter is operated, and also that there be no flashback into the manifolds, or overheating of the spark plug. A test ignition torch has been built to examine the performance of the system before it is built into an injector. Tests will be made using gaseous hydrogen and oxygen.

Flowmeter calibration. Flow rates of the propellants are to be metered and controlled by cavitating venturis at the bottoms of the propellant tank standpipes. These venturis have been calibrated in a water system, but calibration to a higher Reynolds number is required. Liquid nitrogen calibration can be accomplished at high flow rate and high pressure by utilizing the 2 propellant run tanks and displacing the liquid nitrogen from 1 to the other through a line containing a water calibrated turbine type flowmeter of the appropriate range. The over-all error of such a calibration may approach ± 3 or 4%, but this will have to be accepted in order to place the system into initial operation and until properly calibrated mass flowmeters can be obtained.

Seal and component tests. Low temperature affects the operation of components, and it is important that problem areas be identified to avoid serious trouble. A particular problem is that of making mechanical joint seals which remain tight at low temperature. A small test chamber, 8 in. in diameter and 12 in. long, has been fabricated. Components placed within the chamber can be cooled by contact with a coolant coil after the surrounding space has been evacuated; then the component can be pressurized or actuated with helium gas, and leakage of helium into the vacuum space can be monitored with a leak detector. A lightweight, 2-in. pipe flange (of JPL design), and several commercial seals are ready for testing.

Temperature transducer calibration. Low temperatures will be measured with tungsten wire resistance elements and with copper-constantan thermocouples. In order to permit comparison of these transducers and to check calibration at a few points, an insulated vessel having 3 identical transducer wells has been fabricated. This vessel can be filled with any of the cryogenic fluids, and the boiloff vapor pressure can be adjusted to obtain a range of the corresponding saturation temperatures of the fluid.

d. Motor test program. The engineering study and preparation for the LH_2–LO_2 motor test program includes the following efforts:

Physical property data. Literature is being surveyed for what appears to be the most reliable values of the following properties: density, viscosity, thermal conductivity, specific heat, enthalpy, and entropy, as functions of pressure and temperature. The foot, second, pound-force, slug-mass, degree Rankin unit system has been selected as standard for all calculations, and where the property data cannot be conveniently put into these units, the appropriate conversion factors are being appended to the data. The collected data will serve as a common standard for measurements, calculations, and transmission of information by all personnel working on the LH_2–LO_2 program.

Heat transfer calculations. The heat transfer characteristics, wall temperature, and coolant conditions of an existing 6000-lb-thrust (vacuum) welded-rib thrust chamber (originally designed for use with the N_2O_4–N_2H_4 propellant) have been computed for the LH_2–LO_2 propellant, using hydrogen as the coolant. Gas-side heat transfer was computed using the enthalpy potential method described in Reference 14. The performance of liquid hydrogen as a coolant at supercritical pressure was computed by the method described in Reference 15. These calculations show that for operation at 150-psi chamber pressure and a mixture ratio of 5.0 (approximately 4200-lb-thrust at sea level for the version of the motor with an exit area ratio of 3.5), the motor wall temperatures are high enough to make satisfactory operation questionable. Further calculations are to be made to establish the requirements for water cooling of the existing thrust chambers and to establish the coolant passage modifications required if similar thrust chambers are to be built to cool with hydrogen when operated at chamber pressures from 50 to 300 psia. An estimate will also be made of the transient temperature rise to be expected in the wall of an uncooled thrust chamber duplicating the interior configuration of the cooled motor.

As indicated, the test stand modifications have been completed (with the exception of 1 length of high pressure, vacuum-jacketed propellant line which has been returned to the vendor for repairs); flowmeter calibration and component testing are underway. Initial component tests and system checks will be made using liquid nitrogen as a working fluid and as a refrigerant. The system will be ready for liquid hydrogen during January 1962, and rocket motor tests should start soon thereafter.

Several welded-rib cooled thrust chambers are available for the test program which can be used: (1) for low mixture ratio tests (r less than 5) at 150-psi chamber pressure, (2) at a later time for tests at 300-psi chamber pressure, or (3) with water cooling over the entire range of useful mixture ratios and at chamber pressures up to 300 psia. Several uncooled combustion chambers and nozzles are on hand for short duration tests to prove the system before the more costly cooled thrust chambers are used. Injectors of the multielement cup and plug-type previously described are being fabricated for use with both the cooled and the uncooled thrust chambers. Injectors of the concentric stream showerhead and the impinging stream types are also being considered for use.

4. Power Reactors

Research is being conducted into fuels to be used in advanced power reactors. The reactors are anticipated for long-range, nuclear-electric spacecraft missions requiring thermal outputs of 10 mw for time periods of 2 to 3 years.

Investigations show that a molten fuel reactor employing 70% UF_4, and 30% sodium fluoride will have approximately the same weight as a solid fuel reactor limited to an average burnup of 30,000 mwd/t. Both reactors will weigh in the neighborhood of 350 kilograms for core volume fractions of 0.6 fuel, 0.3 coolant (lithium) and 0.1 structure (zirconium). The assumed solid fuel burnup performance appears to be within the capability of solid

fuel elements; however, an average burnup of more than 30,000 mwd/t in an operating high temperature, high-power-density space power reactor cannot be predicted with confidence at this time. If the solid fuel is assumed to be uranium carbide, the high fuel density of this compound yields a significantly smaller core than the molten fluoride fueled reactor (approximately 49 vs 35 liters). Since payload shield weight must be minimized, the low fuel density of the fluoride fuel is definitely undesirable (although not completely prohibitive). For this reason, additional nonstructural fuels are under investigation which possess high fuel density and the ability to provide high burnup.

5. Corrosion of Liquid Metals

A Liquid Metals Corrosion Program has been initiated by the energy sources group to determine the compatibility of various container materials with liquid potassium, lithium, cesium rubidium, indium, uranium, uranium carbide, lithium fluoride and uranium fluoride.

Columbium-1Zr, tantalum 10W, B33 alloy and B77 alloy (Westinghouse Electric Company) will be evaluated for simple solution corrosion, alloying between liquid metal and solid metal, inter-granular penetration, and temperature-gradient mass transfer at 2200°F.

Static and dynamic corrosion and mass transfer mechanisms are to be investigated in 6 tilting furnaces capable of tilting 45 deg from the horizontal, from 0 to 4 cycles/min.

Test capsules will be in an argon atmosphere and instrumented at the hot and cold ends. An inert atmosphere chamber (capable of attaining 10^{-6} mm Hg) will be used for test capsule construction, liquid metal fill, and loop construction.

A 30 kw (thermal), lithium-boiling potassium loop will be constructed from Cb-1Zr and enclosed in an inert atmosphere chamber. This loop will operate at these conditions:

Material	Flow rate, gal/min	Temperature, °F	Pressure, psig
Lithium	1 to 10	2200	Up to 20
Potassium	0 to 1	1500 to 2000	200

In addition to obtaining liquid metal corrosion and heat transfer data, the following components are to be developed and operated at loop temperature for periods up to 10,000 hr.

(1) A liquid metal centrifugal 0 leakage pump capable of pumping lithium at 2200°F up to 10 gpm at 100 ft total dynamic head, constructed of Cb-1Zr.

(2) Two liquid metal swing gate valves for 2200°F lithium and potassium service, constructed of Cb-1Zr.

(3) An electromagnetic flow meter for 2200°F lithium flow measurements.

(4) A Cb-1Zr bellows to be statically tested in lithium at 2200°F for 500 cycles.

(5) A Cb-1Zr diaphragm for pressure measurements at 2200°F for lithium and potassium service.

(6) Three boiler designs for loop operation at loop design conditions.

(7) Potassium vapor separator.

(8) Instrumentation techniques for the measurement of boiling potassium temperatures in a single tube potassium boiler.

(9) A fission gas vent capable of venting fission products while containing core fuel will be investigated and tested.

In addition to the above, long time (10,000 hr) creep-to-rupture strength will be determined for various container materials for reactor service.

References

1. Heyden, F. J., Kiess, C. C., and Kiess, H. K. "Spectrum of Venus in the Violet and Near-Violet," *Science*; Vol 130, p 1195. 1959.

2. Kiess, C. C., Corliss, C. H., and Kiess, H. K. "High-Dispersion Spectra of Jupiter," *Astrophysical Journal;* Vol 132, p 221. 1960.

3. Kiess, C. C., Karrer, S., and Kiess, H. K. *Astrophysical Journal;* Vol 72, p 256. 1960.

4. Sinton, W. M. *Astrophysical Journal;* Vol 73, p 125. 1961.

5. Kaplan, L. D. "Studies of the Physical Properties of the Moon and Planets," *Rand Report, RM-2769-JPL;* Sec 5, p 29; Sec 8, p 62. Rand Corp., Santa Monica, Calif. 1961.

6. Kozyrev, N. A. *Crimean Astrophysical Observation;* Vol 12, p 177. 1954.

7. Harris, D. L. "Planets and Satellites," *The Solar System;* ed by G. P. Kuiper and B. M. Middlehurst, Vol 3, pp 272 ff. University of Chicago Press, Chicago. 1960.

8. Richardson, E. H. *Astronomical Journal;* Vol 65, p 56. 1960.

9. Heard, J. F. "Reports of Observatories," *Astronomical Journal;* Vol 64, p 274. 1959.

10. McFarland, R. K. "A Limit Analysis of the Collapse of Hexagonal Cell Structures Under Axial Loads," *Technical Report 32-186;* Jet Propulsion Laboratory, California Institute of Technology, Pasadena, Calif. December 1, 1961.

11. Lee, D. H., Breshears, R. R., Allen, D., Wrobel, J. R. "Applications for Monopropellants in Space Vehicles," *Technical Report 32-174;* Jet Propulsion Laboratory, California Institute of Technology, Pasadena, Calif. October 5, 1961. (Confidential).

12. Evans, D. D. "Rocket Motor Studies with Cavea-B Monopropellant," *Technical Memorandum 33-64;* Jet Propulsion Laboratory, California Institute of Technology, Pasadena, Calif. October 6, 1961.

13. Henry, I. G. "Relative Effects of Propellant Density and of Specific Impulse on Rocket Performance," *Journal of the British Interplanetary Society;* Vol 17, p 366. 1959-1960.

14. Welsh, W. E. Jr., and Witte, A. B. "A Comparison of Analytical and Experimental Local Heat Fluxes in Liquid-Propellant Rocket Thrust Chambers," *Technical Report 32-43;* Jet Propulsion Laboratory, California Institute of Technology, Pasadena, Calif. February 1, 1961.

15. Hendricks, R. C., Graham, R. W., Hau, Y. Y., and Medeiros, A. A. "Correlation of Hydrogen Heat Transfer in Boiling and Supercritical Pressure States," Paper presented at American Rocket Society Propellants, Combustion, and Liquid Rockets Conference, Palm Beach, Florida. April 26-28, 1961.

III. Syncom

1. Mission

The Goddard Space Flight Center (GSFC) formally undertook Project *Syncom* in August 1961. The objective is to provide narrow band communications with a lightweight Earth satellite in a 24-hr orbit. A 3-stage *Thor–Delta* vehicle will boost the spacecraft into an elliptical transfer orbit with the apogee at synchronous altitude. A solid-propellant rocket motor in the satellite will be fired at apogee to give the satellite near-synchronous velocity. A combination of hydrogen peroxide and nitrogen gas jet systems controlled from the ground will be used to position the satellite at the proper longitude and orient it to the proper attitude.

The most nearly adaptable *on-the-shelf* motor is a 13.5-in.-diameter spherical rocket motor, containing 67 lb of propellant in its present configuration. The motor is designated TE345 and was developed by the Thiokol Elkton Division. This motor will have to be modified and off-loaded to the mission, and is generally limited in its capability for this application. GSFC has implemented a dual program by adapting the TE345 and requesting JPL to develop a high performance motor optimized for the mission. This motor will provide a significant payload weight margin, and will be capable of off-loading within reasonable limits to accommodate more optimized trajectories and orbits.

2. Apogee Rocket Motor Design

The Laboratory has completed the detailed design of the rocket motor which is cylindrical in shape, with oblate-hemispherical ends, using a conical nozzle with a submerged entrance and throat (Fig 1). The grain perforation is conical except at the head-end web which has star points. The case material is AIS1410 stainless steel, fabricated of sheet-metal construction. The major motor characteristics are shown in Table 1.

A sketch of the motor incorporated into the *Syncom* satellite is shown in Figure 2. When cast in its off-loaded

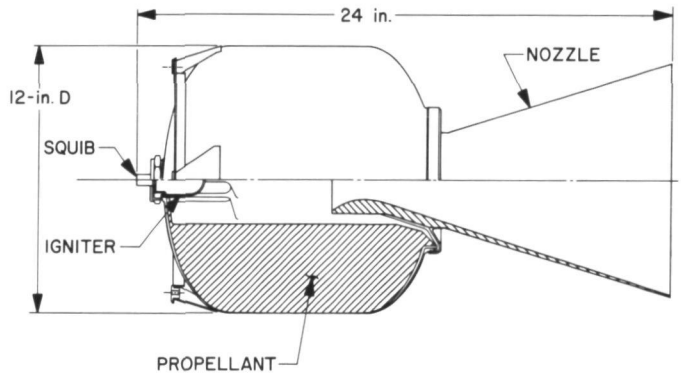

Figure 1. JPL *Syncom* apogee motor

Table 1. Estimated vacuum performance of 80°F propellant[a] temperature

Parameter	Value
Average thrust, lb	1030
Average pressure, psia	200
Action time, sec	20
Propellant specific impulse, lb-sec/lb	283
Nozzle expansion ratio	35
Propellant weight (maximum loading), lb	62
Initial motor mass ratio	0.90

[a]Propellant: SYN-3 : AP/64%, PU/20%, Al/16%.

condition, the motor will impart 4850-ft/sec velocity increment to a satellite weighing 125 lb initially, resulting in a minimum burn-out payload (less motor hardware) of 64 lb. Loaded with the maximum amount of propellant possible, the motor will impart 6090 ft/sec velocity to the same initial weight of satellite, resulting in a minimum burn-out payload (less motor hardware) of 54.7 lb. The latter mission would provide a less-inclined orbit than the former, dependent on the boost vehicle capability and trajectory. Alternatively, the fully loaded motor will deliver 4850 ft/sec to an initial satellite weighing 147.6 lb with a burn-out weight of 77.3 lb (less motor hardware).

3. Development Program

The program is scheduled for a flight date in the last quarter of 1962, resulting in a tight development schedule. Design work was initiated in October 1961, and all testing is expected to be completed 1 year later. Six heavy-walled motor tests, 16 development-type firings with the flight-weight cases, and 21 qualification tests of the flight configuration will be accomplished. Included in the 21

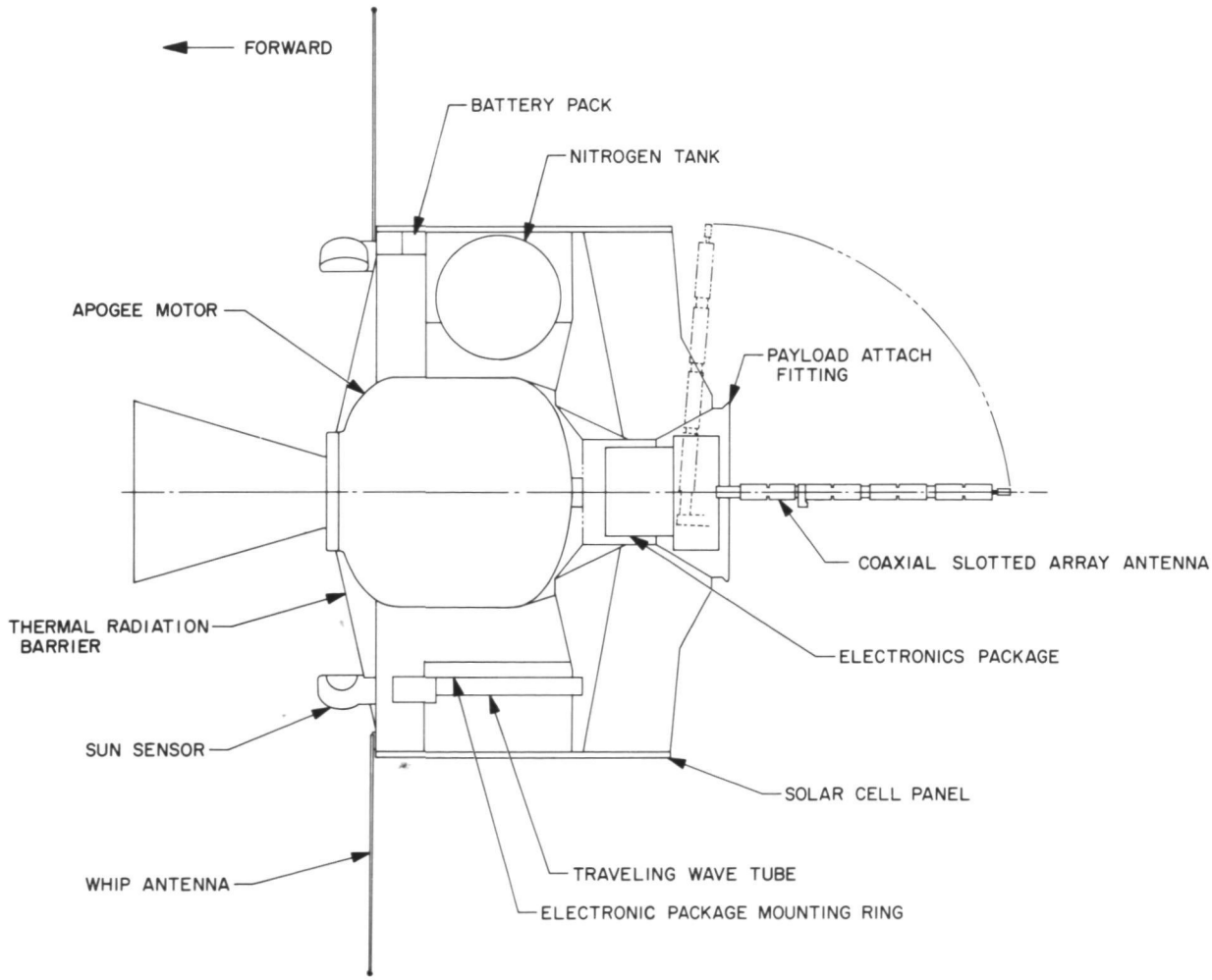

Figure 2. Preliminary assembly of JPL apogee motor in *Syncom* satellite

qualification rounds will be 2 spin-fired motors and 8 motors tested at the Arnold Engineering Development Center.

The propellant formulation has been selected and is now being characterized for its ballistic and physical properties. It is a 20% polyurethane, 64% ammonium perchlorate, 16% aluminum powder additive propellant. One of the significant advanced features of the motor design is the relatively low chamber operating pressure which allows a lightweight case design. However, investigation has revealed that unstable burning or chuffing may occur for any given propellant at well defined starting pressures and port-to-throat ratios, with the doubtful areas of operation occurring at low chamber pressures and low initial port-to-throat ratios. Accordingly, a task has been undertaken to determine the behavior of this propellant with tests being conducted with partially submerged nozzles to fully simulate the final *Syncom* motor design.

An igniter squib is being developed which will meet the more severe RF radiation safe requirements recently suggested by the Air Force Missile Test Center. The goal is to provide a squib which will not fire as a result of applying 1 w of direct current power for 5 min and the application of 1 amp direct current for 5 min. The squib detailed design and fabrication will be done by an outside contractor, and qualification and acceptance will be accomplished at JPL.

CONFIDENTIAL

This document contains information affecting the national defense of the United States, within the meaning of the Espionage Laws, Title 18, U.S.C., Sections 793 and 794, the transmission or revelation of which in any manner to an unauthorized person is prohibited by law.

CONFIDENTIAL